Micromechanical study of transgranular and intergranular ductile fractures of metals

Cédric Senac

▶ **To cite this version:**

Cédric Senac. Micromechanical study of transgranular and intergranular ductile fractures of metals. Mechanics of materials [physics.class-ph]. Université Paris-Saclay, 2023. English. NNT : 2023UP-AST142 . tel-04402724

HAL Id: tel-04402724
https://theses.hal.science/tel-04402724

Submitted on 18 Jan 2024

HAL is a multi-disciplinary open access archive for the deposit and dissemination of scientific research documents, whether they are published or not. The documents may come from teaching and research institutions in France or abroad, or from public or private research centers.

L'archive ouverte pluridisciplinaire **HAL**, est destinée au dépôt et à la diffusion de documents scientifiques de niveau recherche, publiés ou non, émanant des établissements d'enseignement et de recherche français ou étrangers, des laboratoires publics ou privés.

université
PARIS-SACLAY

Micromechanical study of transgranular and intergranular ductile fractures of metals

Étude micromécanique des ruptures ductiles transgranulaire et intergranulaire des métaux

Thèse de doctorat de l'université Paris-Saclay

École doctorale n° 579, Sciences mécaniques et énergétiques, matériaux et géosciences (SMEMaG)
Spécialité de doctorat : Mécanique des matériaux
Graduate School : Sciences de l'ingénierie et des systèmes
Référent : ENS Paris-Saclay

Thèse préparée au **Service d'Études des Matériaux Irradiés** (Université Paris-Saclay, CEA), sous la direction de **Benoît TANGUY**, directeur de recherche CEA, et le co-encadrement de **Jérémy HURE**, directeur de recherche CEA

Thèse soutenue à Paris-Saclay, le 17 novembre 2023, par

Cédric SÉNAC

Composition du jury

Membres du jury avec voix délibérative

Samuel Forest Directeur de recherche CNRS, Mines ParisTech	Président
Léo Morin Maître de conférences, Université de Bordeaux	Rapporteur & Examinateur
Thomas Pardoen Professeur, Université catholique de Louvain	Rapporteur & Examinateur
Renald Brenner Directeur de recherche CNRS, Sorbonne Université	Examinateur
Éric Lorentz Ingénieur de recherche, EDF R&D	Examinateur
Gilles Perrin Directeur scientifique, Framatome	Examinateur

Thèse de doctorat
NNT : 2023UPAST142

université PARIS-SACLAY

ÉCOLE DOCTORALE
Sciences mécaniques et énergétiques, matériaux et géosciences (SMEMAG)

Titre: Étude micromécanique des ruptures ductiles transgranulaire et intergranulaire des métaux

Mots clés: Rupture ductile, Rupture intergranulaire, Croissance et coalescence de cavités, Homogénéisation, Matériaux poreux, Plasticité cristalline

Résumé: La rupture ductile par germination, croissance et coalescence de cavités compte parmi les modes de rupture dominants pour les alliages métalliques et peut être transgranulaire aussi bien qu'intergranulaire. Dans le premier cas, l'endommagement se développe au sein des grains, tandis que dans le second cas, le phénomène de croissance et de coalescence de cavités se produit aux joints de grains du fait d'une intense localisation de la plasticité dans les zones intergranulaires. Selon la microstructure et les conditions de chargement, un grand éventail d'alliages métalliques peut présenter l'un de ces modes de rupture; certaines fractographies révèlent même des processus d'endommagement mixtes. Par exemple, le mode de ruine des alliages à durcissement structural est particulièrement sensible aux traitements thermiques qui peuvent favoriser ruptures ductiles intergranulaire et transgranulaire. Les métaux irradiés dans lesquels la transmutation génère des bulles d'hélium est aussi une classe de matériaux où la compétition entre les phénomènes d'endommagement ductiles a lieu. La prédiction du mode de rupture qui prévaut est d'une grande importance pour estimer la ductilité du matériau. Depuis des travaux précurseurs portant sur les matériaux isotropes, des efforts considérables ont été effectués afin de proposer une modélisation de la rupture ductile par homogénéisation du comportement mécanique des matériaux poreux. Ces dernières années, ces résultats n'ont été que partiellement étendus aux monocristaux avec des cavités internes, c'est-à-dire à la modélisation de la rupture ductile transgranulaire ; par ailleurs, la modélisation micromécanique de l'endommagement ductile des joints de grains poreux est toujours manquante.

Afin de faire progresser la prédiction de la compétition entre rupture ductile transgranulaire et rupture ductile intergranulaire, des contributions à la modélisation et la simulation de ces deux modes de ruine sont effectuées. En ce qui concerne la rupture ductile transgranulaire, un modèle homogénéisé pour monocristal poreux est proposé à partir d'études existantes dans la littérature et évalué à l'aune de simulations de cellules-unité poreuses. Ce modèle est ensuite utilisé pour simuler la rupture ductile transgranulaire d'éprouvettes mono- et polycristallines, mettant en évidence le changement d'échelle permis par le modèle homogénéisé ainsi que l'effet de la microstructure sur la fissuration. Enfin, un critère de plasticité pour la coalescence de cavités en colonnes est développé afin de permettre la prédiction de ce mode de localisation dans les monocristaux. En ce qui concerne la rupture ductile intergranulaire, des critères de plasticité pour la croissance et la coalescence de cavités situées aux joints de grains sont tout d'abord obtenus analytiquement et validés par des simulations numériques. Grâce à une comparaison vis-à-vis de leurs pendants transgranulaires, ces critères intergranulaires fournissent des éléments qualitatifs d'évaluation de la compétition entre les modes de rupture ductile. Ensuite, un modèle homogénéisé de croissance des cavités intergranulaires est proposé et comparé aux résultats de simulations correspondants. Finalement, une expérience modèle de rupture de joints de grains poreux dans un acier austénitique inoxydable est mise en place grâce à une implantation d'ions hélium. Ainsi, l'ensemble des contributions de cette thèse fournit les éléments nécessaires à la prédiction de la compétition entre rupture ductile intergranulaire et rupture ductile transgranulaire.

université PARIS-SACLAY

ÉCOLE DOCTORALE
Sciences mécaniques et énergétiques, matériaux et géosciences (SMEMAG)

Title: Micromechanical study of transgranular and intergranular ductile fractures of metals

Keywords: Ductile fracture, Intergranular fracture, Void growth and coalescence, Homogenization, Porous materials, Crystal plasticity

Abstract: The process of void nucleation, growth, and coalescence is among the dominant ductile failure modes in metallic alloys and can be transgranular as well as intergranular. In the former case, damage develops at grain interiors, whereas in the latter case, void growth and coalescence happen at grain boundaries due to intense intergranular plastic flow. Depending on microstructure and loading conditions, a broad class of metallic alloys can experience one of these fracture modes; some fractographies even reveal mixed damaging processes. For instance, the failure mode of precipitation-hardened alloys is especially sensitive to the aging treatment that can foster transgranular or intergranular ductile fracture. Irradiated metals in which transmutation produces helium bubbles are also a type of material where competition between ductile damage phenomena happens. Predicting the dominant damage process is paramount as it controls the material's ductility. Since seminal works on isotropic media, considerable efforts have been made to model ductile failure through homogenization of the mechanical behavior of porous materials. Until now, these results have only been partially extended to single crystals with internal cavities; furthermore, the micromechanical modeling of ductile damage at porous grain boundaries is still lacking.

In order to enhance the prediction of the competition between transgranular and intergranular ductile fractures, this thesis contributes to the modeling and simulation of these two failure modes. In the first part, which focuses on transgranular ductile fracture, a homogenized model for porous single crystals is proposed, building on results available in the literature and assessed against porous unit-cell simulations. This model is then used to simulate the transgranular ductile fracture of mono- and polycrystalline samples, demonstrating the scaling up it allows as well as the effect of microstructure on failure. Moreover, a yield criterion for necklace coalescence of cavities is developed to predict this localization mode in single crystals. In the second part, which dwells on intergranular ductile fracture, yield criteria for the growth and coalescence of voids located at grain boundaries are derived analytically and validated through numerical simulations. Comparing these criteria to their transgranular counterparts provides a qualitative assessment of the competition between ductile fracture modes. Furthermore, a homogenized model of intergranular void growth is proposed and compared to corresponding simulation results. Finally, a model experiment of porous grain boundary fracture in an austenitic stainless steel relying on helium implantation is developed. As a result, this thesis gathers the tools necessary to predict the competition between intergranular and transgranular ductile fractures.

Remerciements

À l'orée d'une nouvelle période de ma vie, je suis naturellement porté à revivre l'enchaînement de hasards qui m'a conduit à effectuer un doctorat en mécanique des matériaux au Commissariat à l'énergie atomique. Parmi ces derniers, la passion manifestée par mes professeurs à l'École polytechnique occupe une place importante : Jean-Jacques Marigo — son cours de *Plasticité et rupture* a constitué une véritable épiphanie profane — François Willaime, Sylvain David, Habibou Maitournam et Emmanuel de Langre. Je le dois également à Benoît Tanguy, mon directeur, et Jérémy Hure, mon encadrant (et deuxième directeur *de facto*) qui ont su m'interpeller avec ce sujet original — le concept de « rupture ductile intergranulaire » étonne souvent, même dans les cénacles avertis — qui mêlait modélisation, simulation et expériences. Au cours de ces années de doctorat, j'ai bénéficié de leurs conseils avisés et leur exigence m'a fait grandir. Qu'ils soient remerciés d'avoir toujours su se rendre disponibles.

Les membres du jury — Samuel Forest, Renald Brenner (tous deux ayant composé mon comité de suivi), Thomas Pardoen, Léo Morin, Eric Lorentz, Gilles Perrin et Pierre-Guy Vincent — me font un grand honneur en acceptant d'examiner ma thèse et d'abriter les premiers pas de ma carrière de docteur à l'ombre de leur stature scientifique ; beaucoup des résultats de ce manuscrit sont appuyés sur leurs travaux précurseurs.

L'équipe du SEMI mérite d'être citée pour son aide ponctuelle mais néanmoins cruciale pour la réussite de ce doctorat : Arnaud Courcelle, Damien Schildknecht, Hawa Bouyssou, Stéphane Urvoy, Marie Azera ainsi que le LCMI au complet et spécialement Sandrine Delogu, Catherine Lombard, Philippe Grange, Guillaume Zumpicchiat, Tom Petit, Sarah Saanouni, Thomas Le Jolu, Mohamed-Ali Bouaziz, David Le Boulch, Antoine Petit, Matthew Bono et Tuan-Hiep Pham. En dehors du service, les contributions de Thomas Helfer, Lionel Gélébart, Benoît Arnal, Nicolas Lochet et Patrick Olier ont aussi été précieuses. Il faut également reconnaître à sa juste valeur le concours essentiel du personnel du CNRS d'Orléans ; ainsi, j'ai une pensée particulière pour Thierry Sauvage, Pierre Desgardin, David Chaulin, Sébastien Bouillon, Virginie Bazin, Hélène Lecoq et les opérateurs du (regretté) cyclotron. Enfin, les bonnes volontés de PSI — Jia-Chao Chen et Peng Bi — et du GPM de Rouen — Solène Rouland — ne seront pas omises de ce panégyrique.

Que les doctorants (et doctorants émérites), qui ont occupé une place de premier choix lors de ces trois années et demie au CEA, reçoivent ma reconnaissance explicite pour avoir apporté de la jeunesse et de la légèreté dans cette institution octogénaire : Paul Lartaud, Pierrick François, Jean-Michel Scherer, Thomas-Xavier Masset (ou serait-ce François-Xavier Massenet ?), Jean-Baptiste Delattre, Clément Lafond, Nicolas Cerardi, Anne-Constance Stchepinsky, Rachma Azihari, Élodie Barrot et Pierre-Olivier Barrioz. Je n'oublie pas Solenn Fabre, à l'échelon inférieur dans la chaîne alimentaire du CEA mais que son engagement syndical mènera loin ! Qu'ils aient été croisés dans le décor gothique d'Oxford, le Connemara chanté par Sardou, à l'ombre du monolithe d'Aussois, ou pour le concours doctoral le plus mal organisé de la décennie, je me remémore avec plaisir les moments passés avec Caroline Vibert, Rachel Azulay, Bruno Masseron, Lucas Lapostolle, Xavier Morel, Clément Cadet, Sidonie Pinaroli, Shamanth Shiva Kumar, Riccardo Cocci, Pauline Fouquet-Métivier, Emmanuelle Catel, Camille Le Goff, Mathieu Reymond et Simon Lottier. Encore quelques années de pratique et je deviendrai bon au ChronoMéca...

Finalement, il va sans dire que le soutien de ma famille et mes amis a été inestimable, mais la séparation entre vie personnelle et vie professionnelle a déjà été suffisamment malmenée au cours de cette thèse pour ne pas y faire une infraction supplémentaire en les y citant nommément !

Table of contents

Remerciements i

Table of contents iii

1 Literature review 1
1 Overview of ductile fracture . . . 2
1.1 Physical mechanisms . . . 2
1.1.1 Ductile fracture classification . . . 2
1.1.2 Intergranular ductile fracture . . . 4
1.2 Intergranular void nucleation . . . 5
1.2.1 Grain boundary particles . . . 5
1.2.2 Pre-existing intergranular cavities . . . 8
1.3 Intergranular void growth and coalescence . . . 8
1.3.1 Diffusion-driven void growth . . . 9
1.3.2 Void growth by plastic flow . . . 10
1.3.3 Identifying the mechanism responsible for void growth . . . 12
2 Occurrence of intergranular ductile fracture in engineering alloys . . . 15
2.1 Unirradiated alloys . . . 15
2.1.1 Low homologous temperature . . . 15
2.1.2 High homologous temperature . . . 22
2.2 Irradiated alloys . . . 23
2.2.1 Fission reactor fuel cladding . . . 24
2.2.2 Light water reactor core internal components . . . 29
3 Simulation and modeling of ductile fracture . . . 35
3.1 Introduction . . . 35
3.2 Porous unit-cells . . . 35
3.3 Matrix with phenomenological plasticity . . . 36
3.3.1 Models of transgranular ductile fracture . . . 37
3.3.2 Simulation of intergranular ductile fracture . . . 39
3.4 Matrix with crystal plasticity . . . 41
3.4.1 Models of transgranular ductile fracture . . . 42
3.4.2 Simulation of intergranular ductile fracture . . . 43
3.5 Perspectives . . . 47

2 Transgranular ductile fracture 49
1 Homogenized models for void growth and coalescence in single crystals . . . 51
1.1 Introduction . . . 53
1.2 Database for porous single crystal unit-cell simulations . . . 55
1.2.1 Crystal plasticity constitutive equations . . . 55
1.2.2 Porous unit-cell simulations . . . 56
1.2.3 Analysis of the database . . . 58
1.3 Homogenized model for porous single crystals . . . 62
1.3.1 Constitutive equations . . . 62
1.3.2 Numerical implementation . . . 66
1.3.3 Calibration of numerical parameters . . . 67
1.3.4 Comparison to unit-cells results . . . 68
1.4 Discussion and perspectives . . . 74
1.5 Conclusion . . . 75
1.A Finite strain framework . . . 76

1.B Yield criteria flow direction . . . 77
1.B.1 Growth yield criterion . . . 77
1.B.2 Coalescence yield criterion . . . 78
1.C Summary of the two homogenized models . . . 78
2 Trangranular ductile fracture simulations . . . 80
2.1 Description of simulations . . . 81
2.1.1 Specimen geometries and loading conditions . . . 81
2.1.2 Material behavior . . . 82
2.1.3 Numerical implementation . . . 83
2.2 Simulation results . . . 84
2.2.1 Single crystal samples . . . 85
2.2.2 Polycrystalline samples . . . 92
2.3 Conclusion . . . 92
3 Necklace coalescence in porous crystals . . . 94
3.1 Introduction . . . 95
3.2 Problem statement . . . 97
3.2.1 Porous material description . . . 97
3.2.2 Kinematic limit analysis . . . 98
3.3 Yield surface for porous Hill materials . . . 99
3.3.1 From homogeneous yielding to inhomogeneous yielding in columns . . . 100
3.3.2 Trial velocity field and associated dissipation . . . 100
3.3.3 Yield criterion . . . 101
3.3.4 From homogeneous yielding to inhomogeneous yielding in layers . . . 104
3.3.5 Trial velocity field and associated plastic dissipation . . . 105
3.3.6 Yield criterion . . . 105
3.3.7 Numerical assessment . . . 109
3.4 Yield surface for rate-independent crystals . . . 112
3.4.1 Single crystal matrix behavior . . . 112
3.4.2 Approximate macroscopic dissipation . . . 112
3.4.3 Yield surface . . . 113
3.4.4 Numerical assessment . . . 115
3.5 Homogenized model for porous Hill materials . . . 117
3.5.1 Sequential limit analysis . . . 117
3.5.2 Discussion . . . 118
3.6 Conclusion and perspectives . . . 120
3.6.1 Conclusion . . . 120
3.6.2 Perspectives . . . 121
3.A Taylor surfaces of a porous single crystal . . . 122
4 Conclusion and perspectives . . . 123
A Contributions to the study of internal necking . . . 124
A.1 Internal necking criterion obtained from Thomason triangular trial field . . . 124
A.2 Internal necking criterion obtained from Keralavarma and Chockalingam trial field . . . 126

3 Intergranular ductile fracture **129**
1 Intergranular void growth criteria . . . 131
1.1 Introduction . . . 133
1.2 Numerical homogenization . . . 135
1.2.1 Crystal plasticity constitutive laws . . . 136
1.2.2 Unit-cell computations . . . 136
1.2.3 Simulation database . . . 138
1.3 Plastic yield criterion for spherical voids . . . 140
1.3.1 Limit-analysis on porous Hill bi-materials . . . 141
1.3.2 Porous bi-crystal correction . . . 142
1.3.3 Assessment of yield surfaces . . . 143
1.4 Viscoplastic potentials for porous bi-crystals with ellipsoidal voids . . . 145
1.4.1 Case $n = 1$: Hashin-Strikman estimates for periodical porous bi-crystals . . . 146
1.4.2 Case $n = 1$: Assessment of gauge surfaces . . . 148
1.4.3 Case $n > 1$: Heuristical variational extension . . . 149
1.4.4 Case $n > 1$: Assessment of gauge surfaces . . . 151
1.5 Application to the competition between intergranular and transgranular void growth . . . 154
1.6 Conclusion and perspectives . . . 156
1.A Definition and properties of Hill strain anisotropy tensor $\mathbb{H}^*$ . . . 157

1.B Coalescence micromechanical indicator . . . 157
1.C Crystalline laminate mechanical analysis . . . 159
1.D Analytic expressions of g-functions . . . 160
1.D.1 Ellipsoidal voids . . . 160
1.D.2 Elliptic-cylindrical voids . . . 160
1.E Porous crystal with infinite equivalent equiangular slip systems . . . 162
1.E.1 Pristine crystal . . . 162
1.E.2 Hollow sphere under hydrostatic loading . . . 163
2 Intergranular void coalescence criterion . . . 165
2.1 Introduction . . . 166
2.2 Problem statement . . . 168
2.2.1 Porous material description . . . 168
2.2.2 Kinematic limit analysis . . . 168
2.3 Void coalescence in a von Mises bi-material . . . 170
2.3.1 Material description and trial velocity fields . . . 170
2.3.2 Macroscopic dissipation . . . 171
2.3.3 Yield surface . . . 172
2.3.4 Numerical assessment . . . 173
2.4 Void coalescence at a crystal interface . . . 177
2.4.1 Single crystal matrix behavior . . . 177
2.4.2 Approximate macroscopic dissipation . . . 178
2.4.3 Yield surface . . . 179
2.4.4 Numerical assessment . . . 180
2.4.5 Coalescence by internal necking . . . 180
2.4.6 Coalescence under combined tension and shear . . . 182
2.5 Discussion . . . 185
2.5.1 Effect of the localization pattern on ductility . . . 185
2.5.2 Competition between transgranular and intergranular void coalescence . . . 185
2.5.3 Intergranular void growth and coalescence by internal necking . . . 187
2.6 Conclusion and perspectives . . . 189
2.A Location and number of localization bands . . . 189
2.B Explicit resolution for the Mises bi-material . . . 191
2.B.1 Macroscopic dissipation . . . 191
2.B.2 Yield surface . . . 193
2.C Explicit resolution for the grain boundary . . . 194
2.C.1 Macroscopic dissipation . . . 194
2.C.2 Yield surface . . . 196
3 Homogenized model for intergranular void growth . . . 198
3.1 Description of the homogenized model . . . 198
3.1.1 Finite strain framework . . . 198
3.1.2 Constitutive equations . . . 199
3.1.3 Numerical implementation . . . 200
3.2 Numerical assessment . . . 202
3.2.1 Porous unit cell simulations . . . 202
3.2.2 Comparison to the homogenized model . . . 203
3.2.3 Discussion . . . 206
3.3 Conclusion . . . 207
3.A Expression of useful derivatives . . . 207
3.A.1 Finite strain quantities . . . 207
3.A.2 Growth yield criterion . . . 208
4 Ductile fracture of a helium-implanted austenitic steel . . . 209
4.1 Sample description . . . 209
4.1.1 Model material . . . 209
4.1.2 Sample preparation . . . 212
4.1.3 Helium implantation . . . 213
4.1.4 Quantification of the implantation homogeneity . . . 221
4.1.5 Quantification of oxidation after implantation . . . 221
4.1.6 Post-implantation annealing . . . 223
4.1.7 Characterization of irradiation defects . . . 223
4.2 Fracture behavior . . . 226
4.2.1 Mechanical testing . . . 226
4.2.2 Fracture surface investigation . . . 228

4.3 Temporary conclusion 233
5 Conclusion and perspectives 234

Conclusion and perspectives **237**

Résumé du manuscrit **243**

Bibliography **251**

1

Literature review

Summary

The process of void nucleation, growth and coalescence is among the dominant ductile failure modes in metallic alloys and can be transgranular as well as intergranular. In the latter, the phenomenon of void growth and coalescence happens at grain boundaries due to intense intergranular plastic flow and is associated with fracture surfaces displaying intergranular facets covered in fine dimples. This failure mode usually exhibits a lower ductility than transgranular ductile fracture. Reliable physical observations of intergranular ductile fracture date back more than fifty years and span a large class of metallic alloys and loading conditions, including unirradiated materials — mainly precipitation-hardened alloys — and irradiated materials — where it usually arises from the presence of helium bubbles at grain boundaries. Physically-based modeling of transgranular ductile fracture relying on the homogenization of porous materials has proven fruitful in the last decades. This micro-mechanical framework enables to conduct large simulations of ductile fracture without accounting explicitly for all the cavities, which would be too computer-intensive. However, the modeling of transgranular ductile fracture at the crystal scale is still incomplete and a similar micro-mechanical approach is yet to be conducted for intergranular ductile fracture.

Contents

1 Overview of ductile fracture . . . **2**
1.1 Physical mechanisms . . . 2
1.1.1 Ductile fracture classification . . . 2
1.1.2 Intergranular ductile fracture . . . 4
1.2 Intergranular void nucleation . . . 5
1.2.1 Grain boundary particles . . . 5
1.2.2 Pre-existing intergranular cavities . . . 8
1.3 Intergranular void growth and coalescence . . . 8
1.3.1 Diffusion-driven void growth . . . 9
1.3.2 Void growth by plastic flow . . . 10
1.3.3 Identifying the mechanism responsible for void growth . . . 12
2 Occurrence of intergranular ductile fracture in engineering alloys . . . **15**
2.1 Unirradiated alloys . . . 15
2.1.1 Low homologous temperature . . . 15
2.1.2 High homologous temperature . . . 22
2.2 Irradiated alloys . . . 23
2.2.1 Fission reactor fuel cladding . . . 24
2.2.2 Light water reactor core internal components . . . 29
3 Simulation and modeling of ductile fracture . . . **35**
3.1 Introduction . . . 35
3.2 Porous unit-cells . . . 35
3.3 Matrix with phenomenological plasticity . . . 36
3.3.1 Models of transgranular ductile fracture . . . 37
3.3.2 Simulation of intergranular ductile fracture . . . 39
3.4 Matrix with crystal plasticity . . . 41
3.4.1 Models of transgranular ductile fracture . . . 42
3.4.2 Simulation of intergranular ductile fracture . . . 43
3.5 Perspectives . . . 47

1 Overview of ductile fracture

1.1 Physical mechanisms

1.1.1 Ductile fracture classification

Fracture of metallic materials is the process during which damage — in a broad sense, *i.e.* encompassing cracks — develops in a material subjected to mechanical loading. Macroscopically, it manifests by the progressive — gradual or sudden — loss of load-bearing capacity of the material. *Ductile fracture* refers to a material failure mode associated with significant irreversible deformation at the global or local scale. It opposes *brittle fracture* which exhibits almost no irreversible deformation. In the context of material science, irreversible deformation is referred to as *plastic* while reversible deformation is said to be *elastic*. The typical load-displacement curve of an austenitic stainless steel subjected to uniaxial straining is shown in Fig. I.1: this type of material usually exhibits ductile fracture, as evidenced by the large contribution of plastic deformation to the total displacement at fracture. Indeed, the propensity of ductile fracture varies significantly according to the material class considered; ductile fracture is also known to be favored by high temperature and low strain rates (Pineau et al., 2016).

Various ductile fracture physical processes have been observed and described experimentally depending on materials and loading conditions. In metallic materials, two main types of mechanisms can be distinguished (Noell et al., 2018):

- *void-driven* mechanisms in which ductile fracture occurs due to the nucleation, growth and coalescence of internal voids originating from second-phase particles or grain boundaries (Fig. I.2a,b,c,d).
- *void-free* mechanisms in which ductile fracture occurs due to the reduction of the effective section of the specimen — *i.e.* necking — until complete failure (Fig. I.2e) or the localization of plastic strain in specific planes (Fig. I.2f,g);

Mechanisms compete or facilitate each other, making some fracture occurrences difficult to interpret (Noell et al., 2018). However, in metallic alloys used in engineering applications, voids appear relatively early during mechanical loading due to many precipitates or inclusions, so void-free mechanisms can usually be neglected. Therefore, ductile fracture by void nucleation, growth, and coalescence is dominant, as shown in Fig. I.1. Under loading, void nucleation from second-phase particles either occurs due to their decohesion from the alloy matrix — if the bonding interface is weak — or by their fracture — if the particles are brittle. Then, void growth manifests as the slow and independent enlargement of voids. In that stage, plasticity is rather diffuse around the cavities. Finally, once cavities are large

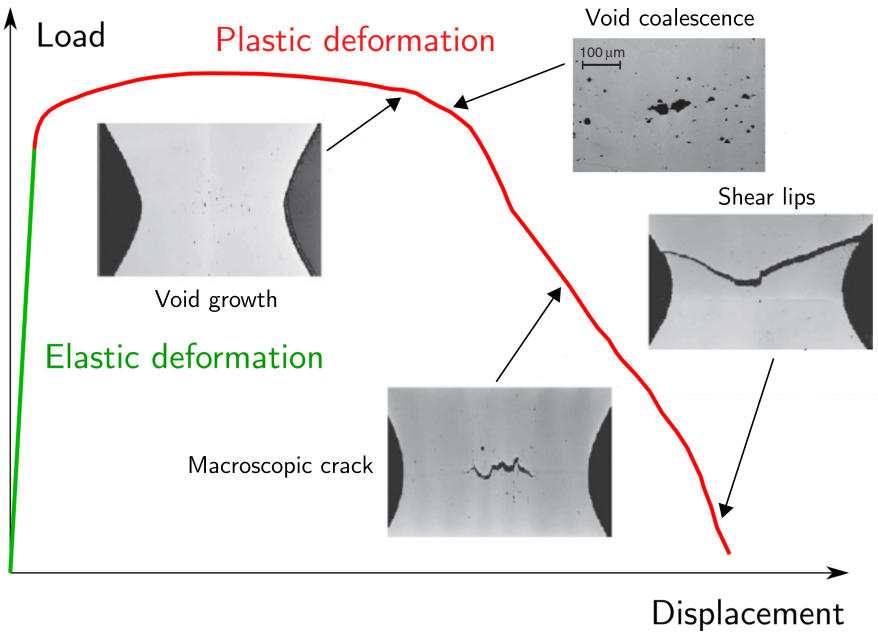

FIGURE I.1: Typical load-displacement curve of transgranular ductile fracture of an high-strength steel, adapted from Benzerga (2000) (the elastic zone was enlarged for clarity).

enough, strain localizes in zones linking the voids — referred to as *ligaments* — which soon leads to fracture by void linkage (Pineau et al., 2016). Different modes of coalescence are distinguished according to the geometry of ligaments (Benzerga and Leblond, 2010):

- *Coalescence in layers* is the mode in which plastic localization occurs mainly in planes perpendicular to the main loading direction. In the absence of shear, it is referred to as *internal necking* (Fig. I.2a). Otherwise, it is called shear-assisted coalescence and can be classified as *intervoid shearing* (Fig. I.2b) if void growth is significant or *void sheeting* (Fig. I.2c) if coalescence happens immediately after void nucleation (Noell et al., 2018). For instance, in Fig. I.1, void coalescence begins as internal necking before switching to shear-assisted coalescence when shear lips appear.
- *Coalescence in columns* is the mode in which plastic localization happens along the main loading direction within cylindrical ligaments (see Fig. II.37). Evidenced theoretically a few years after internal necking (Gologanu et

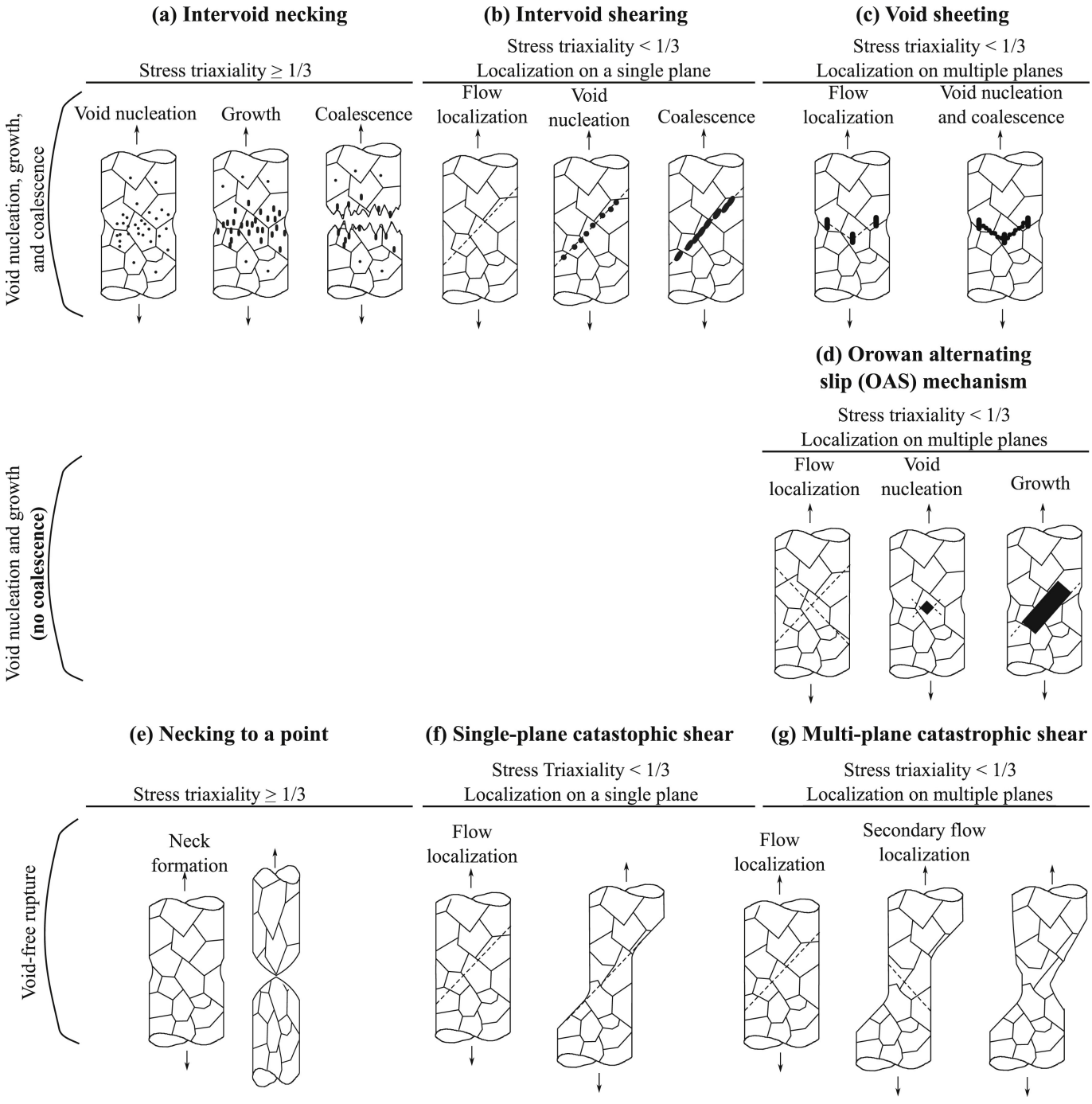

FIGURE I.2: Schematic representation of the various macroscopic ductile fracture mechanisms inventoried by Noell et al. (2018).

al., 2001a), it has since been neglected in most models due to rare experimental observations (Pardoen, 1998; Benzerga et al., 2004a). Indeed, it is believed to be less critical than coalescence in layers because fractured columns are less damaging than fractured layers. Yet, as shall be seen in Section II.3, its accounting may be determining to understand some situations of ductile fracture.

In engineering materials, void-driven ductile fracture is often *transgranular*, as shown in Fig. I.2a,b,c, meaning that crack propagation goes through the grains without notable influence from grain boundaries. Extensive reviews were compiled on the current understanding of this failure mode (Benzerga and Leblond, 2010; Benzerga et al., 2016; Pineau et al., 2016), so it shall not be dwelt upon further. However, an alternative ductile fracture mode exists in which void nucleation, growth, and coalescence happen at grain boundaries. This failure mechanism, known as *intergranular* ductile fracture, will be the object of the remainder of this part.

1.1.2 Intergranular ductile fracture

Intergranular fracture of polycrystalline alloys through void growth and coalescence is a widely documented phenomenon (Hull and Rimmer, 1959; Hancock, 1976; Riedel, 1987; Kassner and Hayes, 2003; Hojná, 2017; Qin et al., 2018). In this fracture process, material failure arises from the presence of grain boundary cavities and their evolution under mechanical loading. Reliable physical observations of void-driven intergranular fracture date back more than fifty years (Plateau et al., 1957) and span a large class of metallic alloys and loading conditions. At the microscopic scale, it is characterized by intergranular fracture surfaces whose facets are covered in fine dimples (Fig. I.3). The resulting fracture exhibits reduced ductility compared to the classical transgranular ductile fracture of alloys (Vasudévan and Doherty, 1987; Hojná, 2017).

Void-driven intergranular fracture should not be confused with classical brittle intergranular failure, which arises from atomic decohesion at grain boundaries and whose fracture surfaces are perfectly flat and exhibit no dimples (Briant, 1988). Furthermore, insufficient fractography magnification significantly hampers the precise determination of fracture modes (Hojná, 2017): in many available experiments, observations of intergranular failure may relate to void-driven intergranular fracture as well as intergranular brittle fracture. Even worse, a brittle fracture surface might exhibit fine dimples if grain boundaries are decorated with cavities whose ligaments fractured in a brittle manner (Hojná, 2017). This emphasizes the need for careful microscopic analyses. Fortunately, recent progress in SEM techniques has enabled better examinations of fracture surfaces, bringing additional evidence to confirm intergranular ductile failure occurrences. A handful of observations in typical engineering alloys will be commented on in Section I.2.

There is a broad consensus that void-induced intergranular fracture follows the same stages identified for ductile transgranular fracture: void nucleation, void growth, and void coalescence (Vasudévan and Doherty, 1987). Each stage can be driven by various mechanisms that depend on material properties and loading characteristics. In the following, the three phases of void-driven intergranular fracture in engineering materials will be described — the

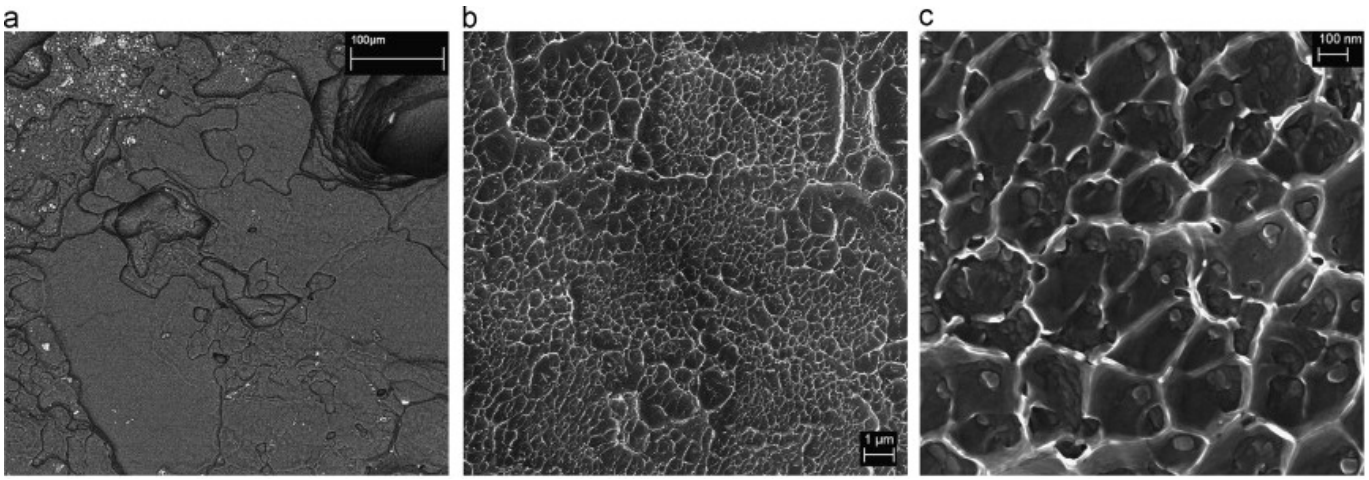

Figure I.3: Intergranular ductile fracture surface of a AA2198 (Al-Cu-Li alloy) sample aged 100 h at 155°C and subjected to tensile loading: increasing resolution from flat intergranular facets (**a**) to fine dimples containing small particles (**c**) (Decreus et al., 2013).

case of pure metals shall only be evoked incidentally. Void nucleation arises from various causes deeply linked with microstructure; it will be the object of Section I.1.2. Section I.1.3 will then detail void growth and coalescence as they determine the fracture mode. Indeed, void-induced intergranular fracture can be divided into two main fracture types according to the driving mechanism of stress-induced void growth: vacancy diffusion or plastic flow. Cavity enlargement by plastic flow will naturally be given precedence, as it is the subject of this work.

1.2 Intergranular void nucleation

In this section, void nucleation mechanisms will be briefly reviewed to evaluate qualitatively the circumstances of dimpled intergranular fracture. First, the role of grain boundary particles shall be discussed and the stress concentration mechanisms that enable nucleation at these particles will be listed (Section I.1.2.1). Then, the possible existence of pre-existing intergranular cavities will be tackled (Section I.1.2.2).

1.2.1 Grain boundary particles

In pure metals, nucleation can occur at microstructural elements such as grain boundaries, triple points — *i.e.* locations where three grains meet — or crystal defects (Kassner and Hayes, 2003). However, in engineering alloys, void nucleation was shown to predominate at second-phase particle (Ratcliffe and Greenwood, 1965; McClintock, 1968; Goods and Nieh, 1983; Wu and Sandström, 1995; Pineau et al., 2016). This finding is also verified in the context of intergranular ductile fracture (Riedel, 1987; Vasudévan and Doherty, 1987; Kassner and Hayes, 2003).

Mesoscopic processes of void nucleation

The mechanisms of void nucleation at second-phase particles during intergranular ductile fracture are very close to those occurring in transgranular void nucleation (Pineau et al., 2016).

Particle decohesion If the stress concentrations at a hard particle are sufficient, atomic decohesion can occur at the particle-grain interfaces (Riedel, 1987). It is also possible that vacancy condensation on second-phase particles plays a role in matrix-particle decohesion when the bonding energy is too high: the void may propagate at the interface from a vacancy nuclei arising from vacancy accumulation (Riedel, 1987; Pineau et al., 2016). However, a cavity nucleated on a particle that would not touch the grain boundary is unlikely to grow further by vacancy diffusion (Kassner and Hayes, 2003).

Particle cracking Brittle intergranular particles can break under the stresses induced by mechanical loading and concentrated by the mechanisms evoked below, especially when the matrix is harder than the second-phase particles. The traces of brittle particles can often be observed in SEM micrographs of fracture surfaces, such in as Fig. I.5 (Fu and Zhang, 2020).

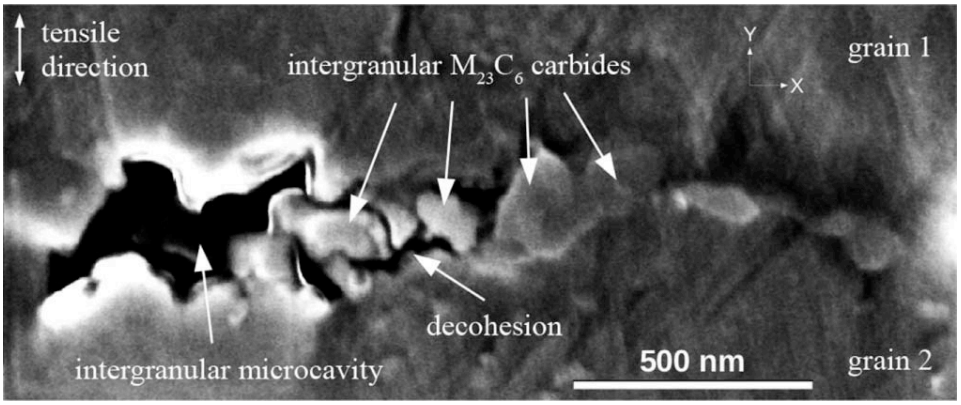

FIGURE I.4: SEM observation of intergranular $M_{23}C_6$ carbides partial decohesion, on the surface of a 316 steel tensile specimen deformed *in situ* to 11% true plastic strain during a creep testing at 550°C for 4313 hours (Pommier et al., 2016).

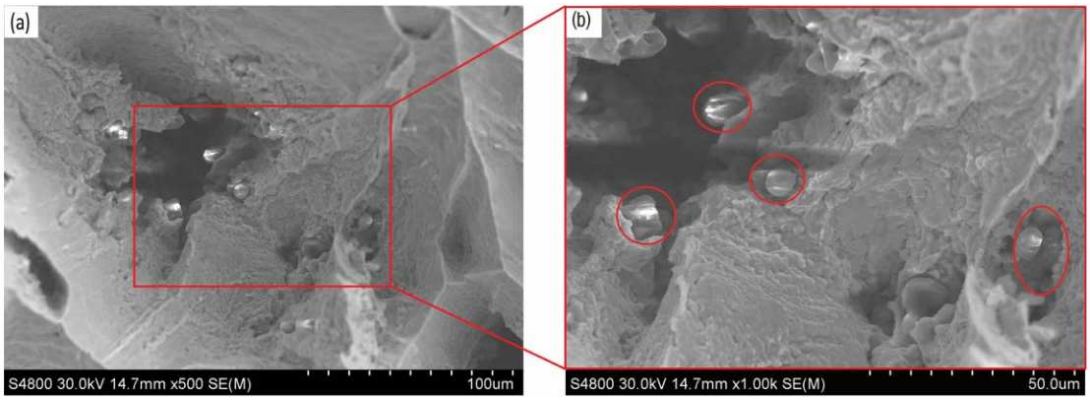

FIGURE I.5: SEM observation of: **(a)** intergranular fracture surface of a 316 austenitic steel loaded at 1150°C; **(b)** cracked brittle non-metallic particles (Al_2O_3?) that are responsible for void nucleation (Fu and Zhang, 2020).

Atomic processes of void nucleation

Mesoscopic events of particle debonding and particle cracking are enabled by elementary atomic processes. Two main phenomena can be distinguished: atoms' brittle decohesion and vacancies' condensation into void nuclei.

Brittle decohesion Voids can be created due to material decohesion. The separation of neighboring atomic planes in a crystal is known to require elevated local stresses (*e.g.* 10^4 MPa) (Riedel, 1987). Since the decohesion of grain boundaries benefits from releasing grain boundary energy, the rupture of atomic bonds is believed to be eased compared to the decohesion of the crystal lattice in grain interiors. Impurity segregation at grain boundaries by thermal diffusion (Herzig and Mishin, 2005) or radiation-induced segregation (RIS) (English et al., 1990) can lower the brittle decohesion stress, as well as intergranular corrosion (Tedmon et al., 1971). Nevertheless, to reach the required threshold, stress concentrations are needed (Riedel, 1987). Note that this process can also nucleate cracks instead of cavities.

Vacancy condensation The idea that a certain number of vacancies can agglomerate at grain boundaries to form voids was spotlighted early and explained by a phenomenon of vacancy supersaturation (Greenwood, 1952; Greenwood et al., 1954). This idea was later dismissed as unrealistic in standard engineering materials (McLean, 1966). On the contrary, vacancy supersaturation is likely to explain void swelling in irradiated materials (Lucki et al., 1975). The interest in vacancy condensation in unirradiated materials was revitalized a few decades later when stress was identified as a possible driving force for condensation in creep-like situations (Raj and Ashby, 1975). Suppose the free energy required to form two free surfaces at the grain boundary is inferior to the stress-induced free energy rise. In that case, vacancies will accumulate until equilibrium is reached, which leads to a fixed nucleated void radius (Kassner and Hayes, 2003). The stress threshold needed to trigger nucleation is usually very high (about 10^4 MPa), which can be considerably larger than macroscopic stresses leading to intergranular fracture. This implies that large stress concentrations are needed to trigger vacancy accumulation in unirradiated materials (Evans, 1984).

Stress concentration mechanisms

Atomic mechanisms for void nucleation evoked in the previous paragraphs must overcome energy barriers. Thus, the location of nucleated voids is by no means random: they form on particular grain boundary areas in which stress concentration arises. The main mechanisms responsible for these concentrations are listed below.

Grain boundary sliding In pure metals, grain boundaries slide easily, concentrating stresses at triple points. Such phenomena are also observed in superplastic metals (see Fig. I.7) (Tan and Tan, 2003). These stresses may be sufficient to nucleate cavities, since many observations of cavities at triple points have been made (Riedel, 1987). Grain boundary ledges (Fig. I.6a) are also privileged areas for stress concentrations from grain boundary sliding. These ledges can pre-exist mechanical loading or be induced by slip band transmission at a grain boundary (Riedel, 1987). The stresses concentrated at these ledges were alternatively deemed sufficient (Chen and Machlin, 1956; Watanabe and Davies, 1978) or insufficient (Fleck et al., 1975) for nucleation; the issue is still open. Independently of the ledge

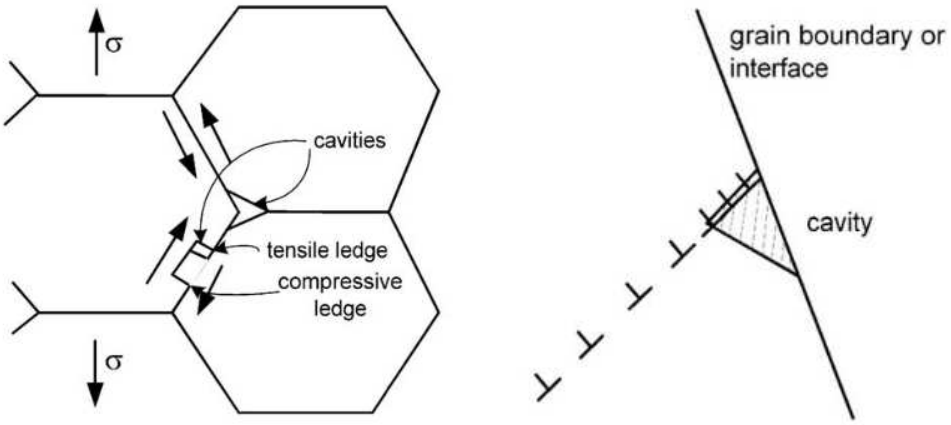

(**a**) Grain boundary sliding (**b**) Dislocation pile-up

FIGURE I.6: Stress concentration situations able to trigger void nucleation at grain boundaries (Kassner and Hayes, 2003).

type, nucleation at ledges only seems to be significant in pure metals since void nucleation at second-phase particles (see Section I.1.2.1) predominates in engineering alloys (Riedel, 1987).

Dislocation pile-up During plastic straining, dislocations move in slip bands located within the grains. A slip band can be transmitted or blocked when it reaches a grain boundary. In the first case, a grain boundary ledge is created, which can be the location of subsequent stress concentration by grain boundary sliding, as mentioned before. In the second case, dislocations pile up at the grain boundary (Fig. I.6b), which generates an increasing stress concentration (Riedel, 1987). As grain boundaries normal to applied stress will only experience mild grain boundary sliding, dislocation pile-up could explain the nucleation of voids there (Kassner and Hayes, 2003). Dislocation pile-up has also been thought to happen in the context of dislocation channeling — a deformation mode in which intense dislocation motion happens in a few shear bands due to the removal of hardening defects — as is shown in Fig. I.8. However, the reality of this phenomenon is questioned by some authors (Griffiths, 2023).

Neighboring cavities It has been suggested that stress concentration near existing cavities can trigger nucleation of other voids (Anderson and Shewmon, 2000). Such a phenomenon will likely lead to continuous void nucleation during fracture, significantly reducing ductility compared to when nucleation occurs before void growth and coalescence.

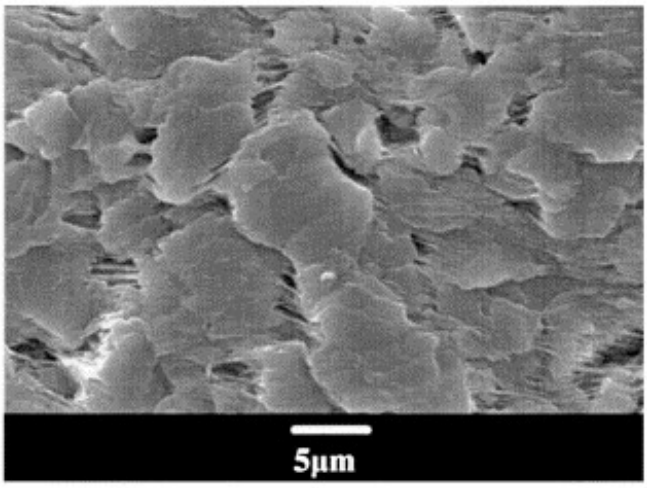

FIGURE I.7: Intergranular void nucleation by grain boundary sliding at 250°C in a superplastic Mg-3Al-1Zn alloy with finely recrystallized grains (6–8 μm) (Tan and Tan, 2003).

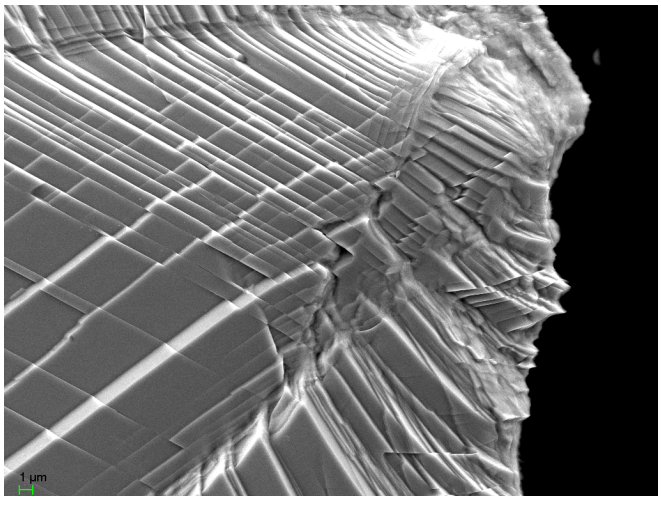

FIGURE I.8: Intergranular void nucleation by dislocation pile-up in proton-irradiated 304 steel (courtesy of P.-O. Barrioz, experimental details in Barrioz et al. (2019)).

Stress concentration at intergranular particles Intergranular second-phase particles themselves have significant interactions with the stress concentration mechanisms and the atomic processes. First, they impede grain boundary sliding so significant stress concentrations may arise (Riedel, 1987). Then, they can effectively stop the transmission of a slip band through a grain boundary. Finally, they can lower the threshold of vacancy condensation by increasing grain boundary free energy (Kassner and Hayes, 2003). However, they are not strictly necessary since void nucleation can happen at grain boundaries in pure metals (Noell et al., 2017).

1.2.2 Pre-existing intergranular cavities

Irradiation cavities Irradiation damage of metallic materials induces the formation of defects — vacancies and interstitial atoms — in the crystal lattice (Was, 2007). The vacancies created during the atom displacement cascades generated by ballistic damage can then migrate and form irradiation cavities. First observations of these nanometric voids were made at least half a century ago (Cawthorne and Fulton, 1967). It was evidenced in later experimental studies that neutron irradiation (*e.g.* Edwards et al. (2009), Griffiths (2021), and Hure et al. (2022)) or ion irradiation (*e.g.* Paccou et al. (2019) and Loyer-Prost et al. (2023)) do produce intergranular cavities that often have different properties (size, density, etc.) than intragranular cavities. However, some cavities appear in the presence of helium, which may indicate that they are helium bubbles instead (Paccou, 2019).

Spallation cavities Shock loading is known to produce mainly intergranular cavities (Curran et al., 1987), as was shown in pure copper (Luo et al., 2010; Perez-Bergquist et al., 2011; Perez-Bergquist et al., 2012) (Fig. I.9), steel (Li et al., 2016), aluminium (Chen et al., 2006) and tantalum (Cheng et al., 2018). A shocked (partially damaged) material will more likely experience intergranular ductile fracture when subjected to subsequent quasi-static loads.

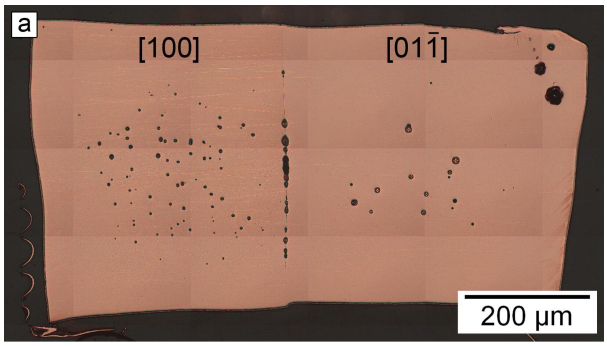

FIGURE I.9: Intergranular void nucleation due to room temperature shock loading on a pure copper bicrystal (Perez-Bergquist et al., 2011).

Helium bubbles As will be seen in Section I.2.2, grain boundary helium bubbles can act as nucleated cavities in the process of intergranular ductile fracture (Shiraishi, 1996; Demkowicz, 2020; Griffiths, 2023). Due to its low solubility in metals, helium concentration generally builds up by intrusion mechanisms (Trinkaus and Singh, 2003): (n, α) reactions — for instance on ^{10}B (Rowcliffe, 1966) and ^{59}Ni (Judge et al., 2012) — are known to produce helium, as well as the decay of tritium and — of course — direct α-bombardment. Gas bubbles then form in the material through various diffusion processes; high temperature and the presence of vacancies caused by irradiation are known to accelerate these fluxes (Trinkaus and Singh, 2003). The size of bubbles increases with the temperature of the material, either during irradiation or subsequent annealing (Griffiths, 2023). The nucleation of bubbles can be either homogeneous or heterogeneous; in the latter case, grain boundaries are generally among the privileged defect sinks (Trinkaus and Singh, 2003). Grain boundaries seem to display different sensitivities to bubble nucleation depending on their structure. The prevalence of grain boundary helium bubbles increases with grain boundary misorientation (Qin et al., 2018), very few bubbles being observed under 15° (low-energy grain boundary). Moreover, larger bubbles are observed at high-angle grain boundaries (HAGBs); this can explained by a greater diffusivity in HAGBs due to available space (Thorsen et al., 2004).

1.3 Intergranular void growth and coalescence

Void-driven intergranular fracture can be divided into two main fracture modes according to the driving mechanism of stress-induced void growth (Hancock, 1976; Riedel, 1987; Kassner and Hayes, 2003). The first one is the diffusion of vacancies from the grain boundary to intergranular voids, briefly described in Section I.1.3.1. Next, Section I.1.3.2 tackles void growth due to plastic flow, but only from a qualitative point of view since existing simulations and models are detailed in Section I.3. Note that void growth through grain boundary sliding also exists, but it is seldom encountered in engineering materials (Riedel, 1987; Kassner and Hayes, 2003), so it will not be dealt with. Finally,

discriminating criteria to determine the prevalent void growth mechanism in a given application are discussed in Section I.1.3.3.

1.3.1 Diffusion-driven void growth

Void growth controlled by the diffusion of vacancies is the most observed growth mechanism in creep tests, which are conducted at relatively high temperatures and low strain rates. Indeed, the occurrence of diffusion is favored by thermal agitation and long testing duration. Therefore, vacancy diffusion can take place at the boundaries (Coble creep) or in crystal lattices (Herring-Nabarro creep) (Riedel, 1987). Grain boundaries are known to be an important vacancy source; hence, in most engineering applications, loading conditions ensure that Coble creep dominates Herring-Nabarro creep (as will be seen later in Fig. I.12a). Thus, the intensity of diffusion-controlled void growth can be measured by diffusion length Λ (Needleman and Rice, 1980):

$$\Lambda = \left(\frac{\omega D_\mathrm{b}\sigma}{k_\mathrm{B}T\dot{\varepsilon}}\right)^{\frac{1}{3}} \text{ with } D_\mathrm{b} = D_\mathrm{b}^0 \exp\left(-\frac{Q_\mathrm{b}}{RT}\right) \tag{I.1}$$

where $k_B = 1.381 \cdot 10^{-23}\ \mathrm{J \cdot K^{-1}}$ is Boltzmann constant, $R = 8.314\ \mathrm{J \cdot mol^{-1} \cdot K^{-1}}$ the ideal gas constant, σ the grain boundary normal stress, $\dot{\varepsilon}$ the strain rate, T the absolute temperature (in kelvins), ω the atomic volume and D_b is the grain boundary diffusion coefficient (in $\mathrm{m^3 \cdot s^{-1}}$) which is assumed to follow an Arrhenius-type law with an activation energy of Q_b. This diffusion length arises directly from the derivation of Coble creep (Coble, 1963).

Alloy	ω ($\mathrm{m^3}$)	D_b^0 ($\mathrm{m^3 \cdot s^{-1}}$)	Q_b ($\mathrm{kJ \cdot mol^{-1}}$)
Fe (α-phase) (Frost and Ashby, 1982)	$1.18 \cdot 10^{-29}$	$1.1 \cdot 10^{-12}$	174
Fe (γ-phase) (Frost and Ashby, 1982)	$1.21 \cdot 10^{-29}$	$7.5 \cdot 10^{-14}$	159
316L(N) (Rieth et al., 2004)[a]	$1.21 \cdot 10^{-29}$	$3 \cdot 10^{-15}$	200
Nickel (Frost and Ashby, 1982)	$1.09 \cdot 10^{-29}$	$3.5 \cdot 10^{-15}$	115
Inconel 718 (Han and Chaturvedi, 1987)	-	-	280

TABLE I.1: Coble diffusion creep parameters given in the literature for various metals.

[a] Assuming that the grain boundary thickness is 0.5 nm.

The diffusive growth of an intergranular void through the migration of grain boundary vacancies was theorized early (Hull and Rimmer, 1959); over the years, many improvements to this model have been proposed and equations have been validated in a certain number of experiments. This phenomenon is called *unconstrained diffusive growth* since the limiting process is the grain boundary diffusion (Evans, 1984; Riedel, 1987; Kassner and Hayes, 2003). However, other diffusive growth modes exist. Indeed, the diffusive growth can be controlled by the diffusion of vacancies at the

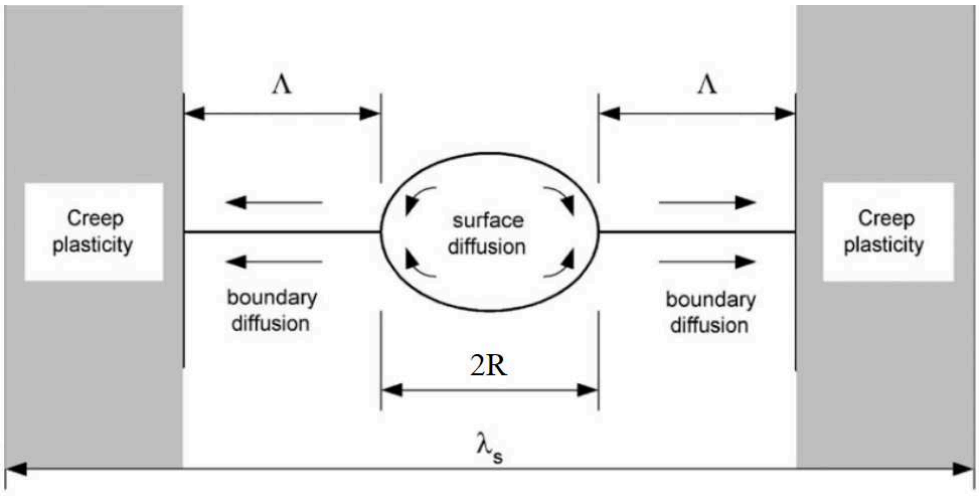

FIGURE I.10: Outline of coupled void growth, where the diffusion length Λ is enhanced by zones of plastic flow sufficient to accommodate deformation over the void spacing length λ_s (adapted from (Kassner and Hayes, 2003) and (Nix, 1988)). The diffusion arrows represent the flow of alloy atoms; vacancies move oppositely.

surface of the void if this phenomenon is slower than grain boundary diffusion; this can lead to nonequilibrium crack-shaped cavities (Riedel, 1987; Kassner and Hayes, 2003). Alternatively, when the supply of grain boundary vacancies is limited, the dominant process is the generation of new intergranular vacancies — by dislocation climb at grain boundaries for instance. This mode is called *inhibited diffusive growth* (Riedel, 1987). Finally, *constrained diffusive growth* refers to the situation in which porous grain boundaries are surrounded by a material composed of hard crystals with pristine grain boundaries, which results in impaired diffusive growth. The constraint imposed by the surroundings is often taken into account through a back-stress acting on intergranular cavities (Riedel, 1987; Kassner and Hayes, 2003).

All the theories outlined above deny any direct role of plasticity in the growth of cavities, but diffusive growth can be enhanced by plastic flow in some situations. Indeed, if the vacancy diffusion is slow enough, the diffusion length Λ will be inferior to half the void spacing length λ_s, meaning that a non-uniform thickening of the grain boundary will occur (Fig. I.10). The rigidity of grains opposes such a heterogeneous thickening, but plastic deformation can accommodate resulting deformation incompatibilities, thus assisting diffusive void growth (Riedel, 1987; Nix, 1988; Kassner and Hayes, 2003).

In any case, void coalescence eventually occurs due to grain boundary diffusion (Kassner and Hayes, 2003), but this process is expected a mere continuation of void growth and not a brutal damaging process as in the case of ductile fracture (Wilkinson, 1987).

1.3.2 Void growth by plastic flow

On the one hand, it has been shown in Section I.1.3.1 that plastic flow can enhance diffusion-controlled intergranular void growth. On the other hand, it has been known for decades that void growth leading to transgranular ductile fracture is controlled by the plastic flow of the surrounding matrix (McClintock, 1968; Pineau et al., 2016; Benzerga et al., 2016). Thus, as Hancock suggested in a seminal work, it seems that plastic flow is also responsible for intergranular void growth in a wide range of situations, including some creep tests (Hancock, 1976).

The case of creep testing has triggered a heated controversy. For instance, it was argued that common creep fracture was insufficiently ductile to be effectively explained by such a phenomenon, and that only room-temperature creep tests and creep of superplastic materials could display void growth by plastic flow (Riedel, 1987). Intergranular ductile void growth has indeed been evidenced in such conditions: for instance, in the low-temperature creep of pure silver (Kassner et al., 1998; Kassner and Pérez-Prado, 2000) and in the superplastic creep of an aluminum alloy between 500 and 550°C (Khaleel et al., 2001; Taylor et al., 2002). Nevertheless, the dismissal of plastic void growth at high temperatures can be questioned since this rebuttal relies on an analysis of void growth without coalescence while void coalescence is known to reduce material ductility strongly. It is thus impossible to rule out the influence of plastic flow at high temperatures, especially when the imposed strain rate is above the typical values for creep testing $\dot{\varepsilon} \in [10^{-10}\ \mathrm{s}^{-1}, 10^{-6}\ \mathrm{s}^{-1}]$ (Riedel, 1987). Indeed, it was found that the growth of cavities was controlled by power law

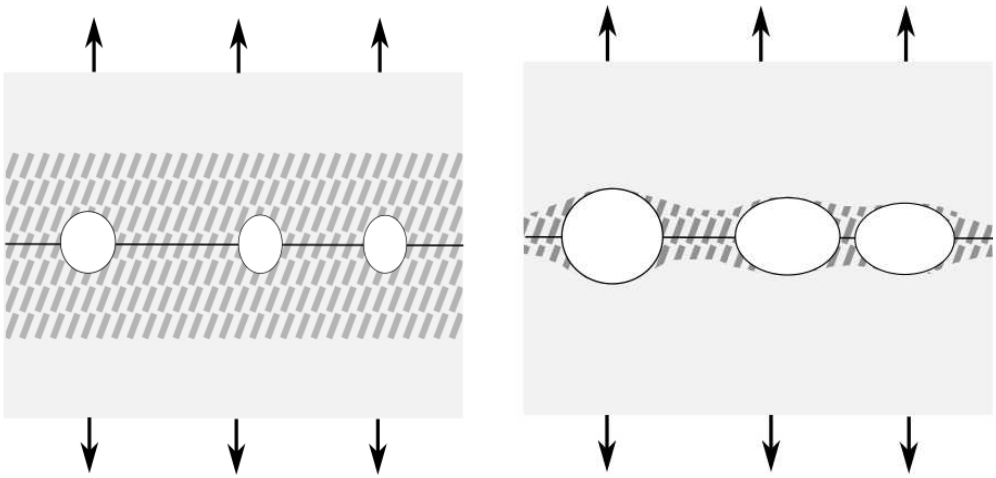

(**a**) Void growth (**b**) Void coalescence

FIGURE I.11: Intergranular void growth and void coalescence induced by plastic flow. During void growth, cavities do not interact with each other; on the contrary, plastic flow localizes in ligaments during the coalescence stage.

creep in polycrystalline copper containing silica dispersoids for strain rates ranging from $\dot{\varepsilon} \in [10^{-7}\ \mathrm{s}^{-1}, 10^{-4}\ \mathrm{s}^{-1}]$ and temperatures between 400 °C and 700°C (Pavinich and Raj, 1977). Other examples of creep fracture in engineering materials will be examined in Section I.2.1.2.

In creep situations, the shape of voids deforming plastically will result from the competition between surface diffusion, which favors equilibrium lenticular shapes, and plastic flow that deforms the void. If the cavity growth rate is relatively slow, equilibrium will have time to establish. The regime where contributions of both shape change mechanisms are equivalent is of complex handling for small expected benefits since void aspect ratio w only seems to have a second-order effect on the void growth rate (Riedel, 1987).

As a general rule, once intergranular voids are nucleated, the two last stages of intergranular ductile fracture are:

(a) *Void growth:* Cavities grow due to a plastic zone located in the grain boundary area. No void interactions are expected at this stage. Some authors consider that this stage is more limited than transgranular void growth due to the small distance between intergranular cavities and thus refer to intergranular ductile fracture as intergranular void coalescence (*e.g.* Schulz and McMahon (1973) and Hojná (2017)). However, significant intergranular void growth observations exist (Becker et al., 1989; Vincent et al., 2022).

(b) *Void coalescence:* During this stage, cavities interact with neighboring voids located on the same grain boundary. Plastic flow localizes in the ligaments interlinking the cavities, triggering void linkage. The stress-bearing capacity of the grain boundary thus drops, quickly leading to its fracture. As will be seen in experimental observations of Section I.2 (see also Fig. III.22), shear-assisted coalescence and internal necking, which are the main modes of transgranular void coalescence, can also be witnessed during intergranular fracture. Once a crack is initiated, two behaviors are conceivable:

- The ensuing crack propagates to other grain boundaries. Stress concentrations enhance void growth at the crack tips, enabling crack propagation. Alternatively, the crack may go transgranular, in which case the fracture mode is mixed intergranular-transgranular.
- The intergranular crack coalesces with other intergranular cracks that have formed on neighboring grain boundaries.

The nature of the plasticity involved in the growth and coalescence of intergranular cavities needs additional discussion. Indeed, plastic deformation varies greatly depending on temperature, applied load and strain rate. The three main deformation mechanisms in metallic alloys are (see Fig. I.12):

- *Dislocation glide:* Dislocation glide is metallic alloys' most common deformation mode. It consists of a motion of the dislocation axis in the direction given by the dislocation Burgers vector. A Burgers vector coupled to a slip plane defines a slip system. The slip planes are usually close-packed crystal planes. The more symmetric the crystal is, the more equivalent crystallographic planes — and therefore equivalent slip systems — there are (Kuhlmann-Wilsdorf and Wilsdorf, 1964). In face-centered cubic (FCC) metals, the usual slip systems are the twelve $\{111\} < 110 >$ systems. Body-centered cubic (BCC) metals have more slip systems, up to 48 in the case of α-iron. On the contrary, hexagonal close-packed (HCP) crystals usually exhibit limited slip due to few available slip systems. Dislocation glide is believed to be the active deformation mode in a wide range of loading conditions, especially at moderate strain rates such as those involved in typical tensile tests (see Fig. I.12).

- *Dislocation creep:* Dislocation creep is a combination of dislocation glide and dislocation climb, climbing being a dislocation motion perpendicular to slip planes due to vacancy diffusion. Dislocation climb can enhance the movement of dislocations by overcoming obstacles; in that case, the dislocation creep rate is controlled by the kinetics of dislocation climb. Note that low loading velocity favors creep deformation modes, including diffusion creep (Fig. I.12c compared with Fig. I.12b). At loading rates higher than 10^{-8} (Fig. I.12a), zones of dislocation creep and diffusion creep (Coble and Navarro-Herring) are further reduced. The shrinking of the diffusion zone is coherent with the decrease of diffusion length Λ with increasing $\dot{\varepsilon}$ (Eq. I.1). Dislocation creep is expected to be the dominant plastic void growth mode in creep conditions (Riedel, 1987; Kassner and Hayes, 2003); for instance, in the already-mentioned case of intergranular cavity growth in polycrystalline copper containing silica particles (Pavinich and Raj, 1977).

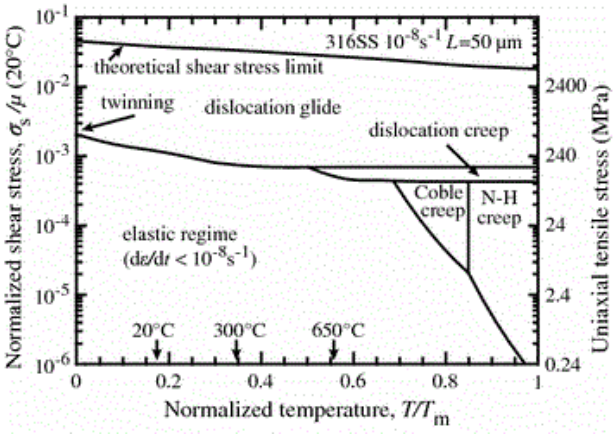

(**a**) Unirradiated, $\dot{\varepsilon} = 10^{-8}$

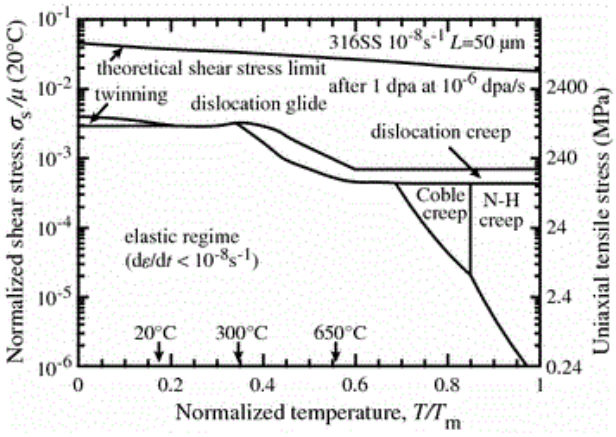

(**b**) Irradiated at 1 dpa, $\dot{\varepsilon} = 10^{-8}$ s^{-1}

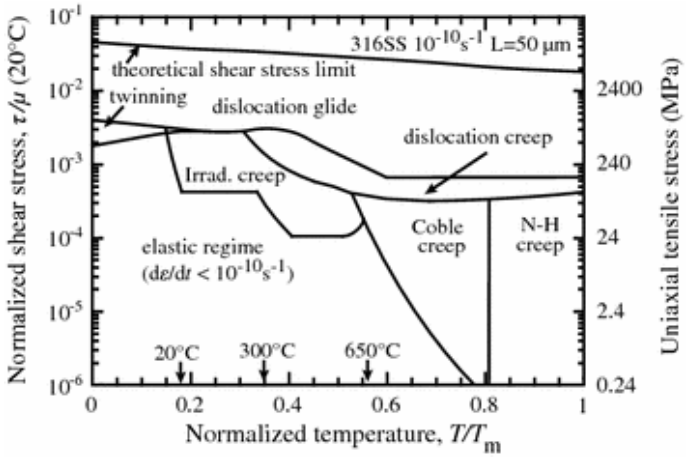

(**c**) Irradiated at 1 dpa, $\dot{\varepsilon} = 10^{-10}$ s^{-1}

FIGURE I.12: Deformation mechanism maps for 316 stainless steel with a grain size of 50 μm (Zinkle and Lucas, 2003).

- *Twinning:* Twinning is a plastic deformation mode generating deformation twins. It is triggered by a resolved shear stress acting on the normal to the plane of the twin. This deformation mode mainly occurs in HCP metals, which cannot accommodate deformation by dislocation glide. In cubic (FCC and BCC) metals, mechanical twinning only occurs at low temperatures or high strain rates (Clayton, 2011). In particular, in austenitic stainless steels used in the the nuclear industry, usual in-service temperatures forbid twinning (Fig. I.12a); however, irradiation can extend the deformation twinning conditions (Fig. I.12b). Intergranular fracture has been linked to twinning around grain boundaries in irradiated austenitic stainless steels at very low temperatures (Hojná, 2017). Moreover, molecular dynamics simulations predict that localized twinning happens at crack tips during intergranular fracture in pure nickel at $T = -240$°C and -170°C while dislocation glide prevails at 230°C; the deformation mode at room temperature is mixed (Wu and Zikry, 2016). No evidence of twinning-mediated grain boundary cavity growth currently exists, so the modeling and simulation of intergranular ductile fracture currently focus on dislocation glide and creep.

1.3.3 Identifying the mechanism responsible for void growth

In order to assess which mechanism prevails in a given situation, it is possible to compare quantitatively the viscous/plastic void growth rate and the diffusion void growth. For instance, Hancock did compare the classical Hull and Dimmer diffusion law (Hull and Rimmer, 1959) to McClintock's plastic void growth solution (McClintock and Argon, 1966; McClintock, 1968) adapted to creep, but more refined laws can be used. Since the diffusion growth rate fades to zero when the cavity grows while the plastic growth rate continues to increase, an equilibrium cavity size R_{eq} can always be computed. At this void radius, contributions arising from vacancy diffusion and plastic flow are equal

(Hancock, 1976).

A simplified assessment consists of introducing a normalized void radius ξ to weight the contribution of vacancy diffusion in the growth of cavities (Needleman and Rice, 1980):

$$\xi = \frac{R}{\Lambda} \tag{I.2}$$

where R is the void radius and Λ is given by Eq. I.1. When $\xi \gg 1$, plastic flow dominates the growth of cavities, whereas vacancy diffusion is the primary mechanism when $\xi \ll 1$. Both mechanisms are active when ξ is close to 1. ξ soars during damage since the void radius R increases. This is coherent with Hancock's approach in which a void size threshold marks the dominance of plastic flow (Hancock, 1976). In the case of creep, this is enhanced by the fact that the strain rate $\dot{\varepsilon}$ increases in the ternary phase of creep tests, which results in a decrease of the ratio $\sigma/\dot{\varepsilon}$ and therefore an increase of ξ. A model combining equations for plastic void growth, coupled growth and diffusive growth (Nix, 1988) confirmed that plastic flow plays an important role for $\xi \in [1, 10]$ and that diffusive growth is negligible for $\xi \geq 10$ (Fig. I.13). Even when diffusion is the predominant mechanism at the start of void growth, plastic flow will often become dominant at coalescence, as some authors pointed out (Venkiteswaran and Taplin, 1974; Hancock, 1976; Mannan and Sivaprasad, 2016). The successive occurrence of diffusive void growth, plastic void growth, and plastic void coalescence is likely to reduce ductility compared to simple plastic void growth and could lead to creep models compatible with experimental data.

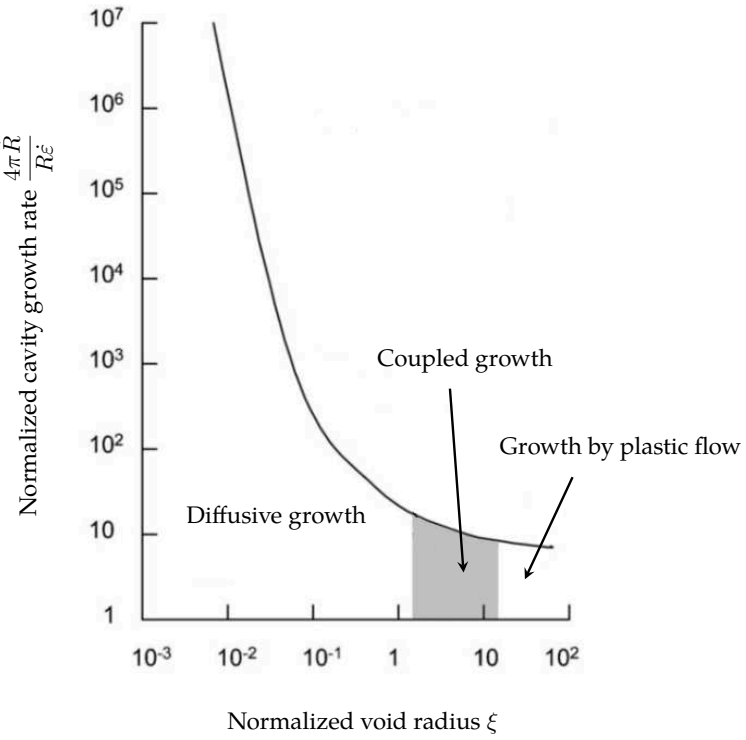

FIGURE I.13: Normalized void growth rate, as predicted by Chen and Argon model for equilibrium cavities, with the different growth regimes shown (adapted from Chen and Argon (1981) and Kassner and Hayes (2003)).

It is worth mentioning that void aspect ratios may give another way of distinguishing the underlying mechanism: plastic void growth usually favors prolate voids (Hancock, 1976) while diffusion shape oblate voids since additional vacancies come from the median plane containing the grain boundary (Riedel, 1987). In both cases, this shape effect can be opposed by surface diffusion: at equilibrium, vacancies migrate to minimize surface energy by forming lenticular voids, even if it is likely that surface diffusion can be neglected in situations where plastic flow dominates grain boundary diffusion (Kassner and Hayes, 2003). This criterion only holds for low triaxiality loadings; indeed, voids retain their sphericity under high triaxiality stress states (Riedel, 1987) — and could even become oblate if the trends of transgranular void growth are generalizable (Benzerga et al., 2016). Observations of void aspect ratios can be made in strained material before the onset of coalescence, but such characterization is uncommon. Nevertheless, the aspect ratio of fracture dimples might give access to the void aspect ratio at fracture.

Finally, molecular dynamics (MD) simulations can theoretically assess void growth mechanisms. For instance, studies on stress-induced grain boundary helium bubble growth were performed in copper (Zhu et al., 2023a; Zhu et al., 2023b), nickel (Demkowicz, 2020), and steel (Zhu et al., 2023c). MD studies on classical intergranular void growth are usually limited by the void size, the temperature (well above zero kelvin) and the duration associated with fracture processes (Bringa et al., 2010).

Due to its inherent simplicity, the approach relying on ξ to identify the mechanism responsible for void growth will be favored in the following. However, it should be noted that creep diffusion parameters are not available for all the alloys that will be reviewed (see Table I.1), and that existing data remain tainted with uncertainty; indeed, grain boundary diffusion is very sensitive to microstructure, including intergranular segregation and precipitation.

In the following, the focus is made on intergranular fracture through plastic growth and coalescence of cavities, leaving aside the identified cases of diffusion-controlled growth — as well as the few occurrences of grain boundary sliding.

Summary

Intergranular ductile fracture is a failure mode which presents the three following successive — or possibly simultaneous — stages:

1. *Void nucleation*, that manifests as the creation of intergranular cavities by atomic decohesion or vacancy condensation, both of which are made possible by stress concentration mechanisms — grain boundary sliding, dislocation pile-up, neighboring cavities — that usually occur at the grain boundary second-phase particles of engineering materials. Sometimes, cavities are not nucleated by quasi-static mechanical loading but preexist in the material, *e.g.* irradiation cavities, spallation voids and helium bubbles.

2. *Void growth*, which is characterized by the slow and relatively independent enlargement of intergranular cavities due to the plastic flow at grain boundaries. Plastic flow can originate from various deformation modes — dislocation glide, dislocation creep, twinning — and can sometimes be supplemented or substituted by the diffusion of grain boundary vacancies — a specificity of intergranular fracture. A dimensionless parameter ξ is introduced to distinguish diffusion from plasticity.

3. *Void coalescence*, which is defined by the fast enlargement of cavities interacting with each other. Voids coalesce into a unique intergranular crack, or multiple cracks that also undergo coalescence. For some authors, the process of intergranular ductile fracture is controlled almost entirely by void coalescence, contrary to transgranular ductile fracture in which void growth plays a significant role.

The ensuing fracture surfaces display intergranular facets covered in fine dimples, which distinguish them from two other fracture modes with which ductile intergranular fracture may be confused:

- *intergranular brittle fracture*, which lacks the ductile dimples due to the absence of plasticity;
- and *transgranular ductile fracture*, which do not show intergranular facets because void coalescence does not occur at grain boundaries.

This confusion is often caused by the insufficient magnification of fracture surfaces used to identify the fracture mode. The fracture strain associated with intergranular ductile fracture is generally superior to that of intergranular brittle fracture — because plasticity is significant — and inferior to transgranular ductile fracture. This last observation can be explained by the fact that intergranular ductile fracture usually results in less void growth than transgranular ductile fracture, as witnessed by the smaller dimples on fracture surfaces.

In the next section, occurrences of intergranular ductile fracture in engineering materials will be reviewed, which will enable uncovering the main parameters that influence this failure mode in the various alloy classes. In particular, it will be seen that intergranular and transgranular ductile fractures are often competing failure modes.

2 Occurrence of intergranular ductile fracture in engineering alloys

In this section, typical situations of intergranular ductile fracture in engineering materials are reviewed. In order to assess whether vacancy diffusion can be neglected compared to plastic flow, parameter ξ will be given when possible. When ξ is close to 1, both diffusion and plastic mechanisms are deemed active, which means that plasticity may be insufficient to describe the fracture process.

As the previous review on occurrences of intergranular ductile fracture dates back 25 years and was focused on aluminum alloys (Vasudévan and Doherty, 1987), this novel literature review aims at complementing it with most of the new observations of this fracture mode. Thus, it holds a significant wealth of technological and material science details which will not be directly used in the remainder of the study.

2.1 Unirradiated alloys

Dimpled intergranular fracture is reported in many engineering metals under various loading conditions. Representative examples in the two domains of low and high homologous temperature — the homologous temperature T_h is the ratio of the current temperature of the material to its melting-point temperature — are presented. In particular, alloys relevant to aerospace and nuclear applications will be dwelt upon.

2.1.1 Low homologous temperature

Precipitation-hardened alloys are extensively used in aerospace — planes, helicopters, space shuttles —, automobile, petrochemical, and nuclear industries where they provide excellent mechanical properties. At low homologous temperatures, these alloys can display intergranular fracture by plastic growth and coalescence of cavities.

Aluminum alloys

Aluminum alloys[1] form the class of materials for which intergranular ductile fracture mode was first undoubtedly highlighted (Varley et al., 1957; Thomas and Nutting, 1957; Thomas and Nutting, 1959; Unwin and Smith, 1969). Among the alloys subjected to this failure mode, the most cited are Al-Li (Vasudévan and Doherty, 1987; Kuramoto et al., 1996), Al-Cu (Kuramoto et al., 1996), Al-Cu-Li (Decreus et al., 2013), Al-Zn-Mg (Kawabata and Izumi, 1976; Gräf and Hornbogen, 1977; Kuramoto et al., 1996), Al-Zn-Mg-Cu (Alarcon et al., 1991; Deshpande et al., 1998; Morere et al., 1998) and Al-Mg-Si (Poole et al., 2019). Two factors seem to play an essential role in the occurrence of this fracture mode: grain boundary precipitates and precipitate-free zones (PFZ).

First, we shall examine the influence of precipitates. Aluminum alloys often display fracture surfaces whose facets are covered in small dimples where precipitates can sometimes be found. The dimple size and spacing are always correlated to grain boundary precipitate size and spacing even if, in some cases, too fine precipitates do not nucleate cavities (Vasudévan and Doherty, 1987). Intergranular ductile fracture usually corresponds to minimum resistance to

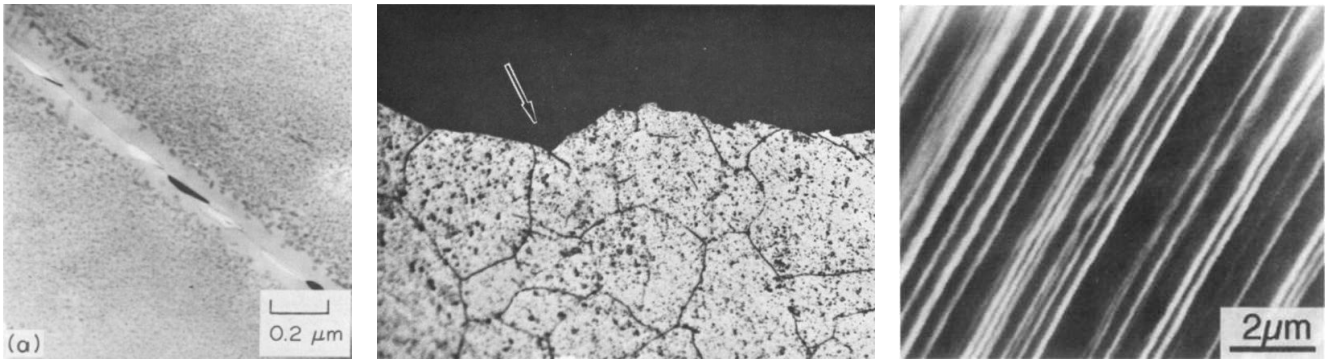

(**a**) (**b**) (**c**)

FIGURE I.14: Precipitation-hardened Al-Zn-Mg alloy: (**a**) TEM observation of a PFZ along a grain boundary (Kawabata and Izumi, 1976); (**b**) cross-section of the fracture surface of a peak-aged alloy (Gräf and Hornbogen, 1977); (**c**) intergranular fracture facet in the presence of intense planar slip (Kuramoto et al., 1996).

[1] No grain boundary diffusion data was found for aluminum alloys, thus ξ cannot be computed.

crack propagation — called *fracture toughness* —, justifying its careful study (Gräf and Hornbogen, 1977; Deshpande et al., 1998). In some aluminum alloys, the fracture toughness is well correlated with the fraction of grain boundary area covered with precipitates (Vasudévan and Doherty, 1987). The critical role of precipitates is corroborated by the fact that 7000 series alloys, which are more prone to intergranular ductile fracture than 6000 series alloys, also display more intense grain boundary precipitation (Chen et al., 2009).

Second, the role of precipitate-free zones is assessed. Indeed, in precipitation-strengthened aluminum alloys, precipitate-free zones (PFZ) are found along grain boundaries (see Fig. I.14a), arising from the lower stability of matrix precipitates compared to grain boundary precipitates. PFZs are thought to favor intergranular fracture through strain localization because the grain boundary area is softer than the precipitate-hardened grain interior (Kawabata and Izumi, 1976; Kuramoto et al., 1996). Peak aging is the most favorable state to localize deformation in the grain boundary area: in this aging state, the yield strength difference between the grain interior and the PFZ is maximal (Gräf and Hornbogen, 1977; Vasudévan and Doherty, 1987). However, a PFZ is not required to observe intergranular failure, as will be shown in the case of nickel superalloys.

Intergranular ductile fracture (Fig. I.15b) should not be confused with another failure mechanism arising in precipitation-hardened aluminum alloys and characterized by the prevalence of planar slip. This alternative fracture mode is specially observed in under-aged alloys, and can be spotted by the presence of multiple parallel lines on fracture surfaces (Fig. I.14c). Indeed, dislocation pileups due to planar slip can induce intergranular fracture by decohesion of the grain boundaries (Vasudévan and Doherty, 1987) (Fig. I.15a). Intergranular fracture by planar slip usually dominates over intergranular ductile fracture when precipitate-free zones are narrow and grain boundary precipitates are fine (Kuramoto et al., 1996). As will be seen later, lithium segregation in Al-Li alloys could enhance this phenomenon.

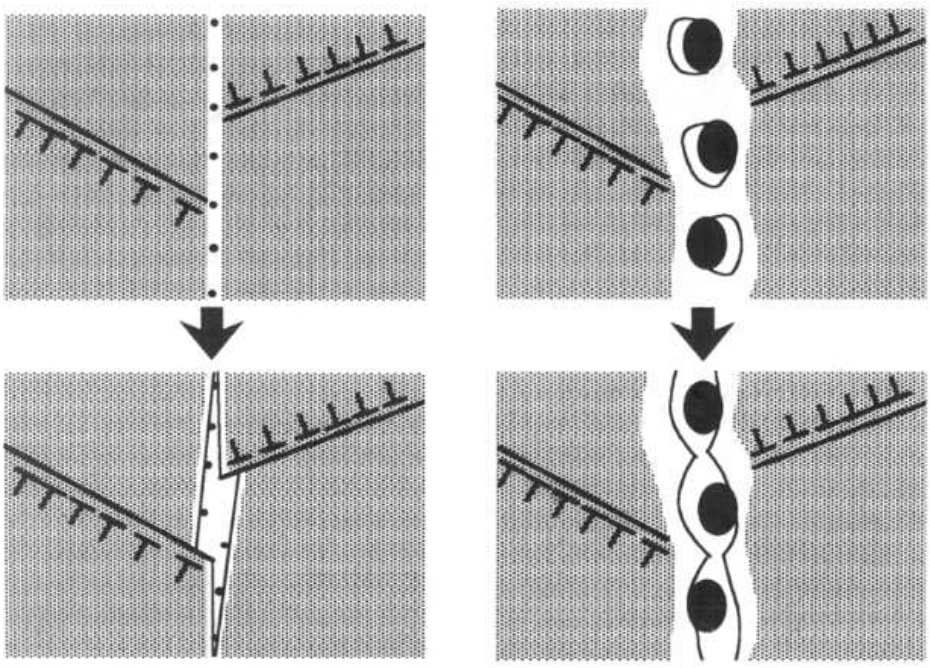

(a) Intergranular decohesion due to planar slip

(b) Growth and coalescence of cavities

FIGURE I.15: Alternative mechanisms of intergranular fracture in precipitation-hardened aluminum alloys (Kuramoto et al., 1996).

Al-Zn-Mg alloys (7000 series) 7000 series alloys are particularly prone to intergranular void growth due to their coarse grain boundary precipitates (see Table III.1) and wide precipitate-free zones (Vasudévan and Doherty, 1987). In 7075 alloy, E-phase (chromium dispersoids) grain boundary precipitates are believed to be the primary void nucleation source in usual aging conditions (Ludtka and Laughlin, 1982). In Al-Zn-Mg, grain boundaries tilted at 45° from the tensile direction seem more vulnerable to intergranular fracture than others. At peak aging, the fracture is not observed to be entirely intergranular and can present transgranular cracking such as in Fig. I.14b: the arrow shows the location of a partial transgranular crack that lost its competition with a more favorable 45° grain boundary. Thus,

cracking can become transgranular if a grain boundary tilt angle is too far from 45° — minus or plus 20° at peak-aging. Grain boundaries perpendicular to the loading direction are sometimes subjected to intergranular cracking; the internal necking coalescence mode they display is different from the shear-assisted void coalescence observed in tilted grain boundaries and that is believed to come — at least partially — from grain boundary sliding. When the precipitation is too important (over-aging) or too mild (solid solution), grain interiors can deform, increasing the transgranular fracture area ratio in the fracture surfaces. When intergranular fracture is prevalent, the cracking depends on the microstructure, with ductility decreasing with increasing grain size (Gräf and Hornbogen, 1977). In 7050 alloy (an Al-Zn-Mg-Cu-based alloy), intergranular ductile fracture seems to exhibit different characteristics since grain boundaries normal to the loading direction are favorable sites for cracking. Shear-assisted coalescence is therefore believed to be less important than internal void necking, possibly due to difficult grain boundary sliding. The fracture mode is always mixed, transgranular ductile fracture being prevalent under plane strain conditions while intergranular ductile fracture dominates under plane stress conditions (Deshpande et al., 1998).

Beyond precipitation-aging, heat treatments can induce unwanted partial recrystallization that harms fracture toughness, as often observed in commercial wrought alloys. In 7050 alloy, the degradation of mechanical properties is believed to come from enhanced intergranular ductile fracture. Indeed, partial recrystallization form numerous high-angle grain boundaries and a strong correlation between the proportion of high-angle grain boundaries normal to the loading direction and intergranular fracture is found. Transgranular fracture occurs after decohesion/cracking of intermetallic particles and extensive intergranular fracture, linking existing intergranular cracks by avoiding less favorable grain boundaries. The nucleation of these intergranular cracks seems attributable to dislocation pileup at high-angle grain boundaries (Deshpande et al., 1998). However, the effect of partial recrystallization is contested in another study in which authors find prevalent transgranular fracture in fast-quenched partially recrystallized specimens of 7010 alloy. Indeed, large intermetallic particles are located at grain boundaries in un-recrystallized specimens but are often within recrystallized grains since they provide ideal nucleation sites. Therefore, particle decohesion/cracking occurs in the interior of grains, favoring transgranular ductile fracture (see Fig. I.16, PRFQ). Slow quenching triggers the formation of a second population of precipitates on grain boundaries, which is responsible for the mixed fracture mode of the partially recrystallized slow-quenched material (see Fig. I.16, PRSQ) (Morere et al., 1998). Independent observations of a final fracture mechanism by the necking of transgranular ligaments between intergranular voids (Ludtka and Laughlin, 1982) are coherent with Fig. I.16 for UFQ condition.

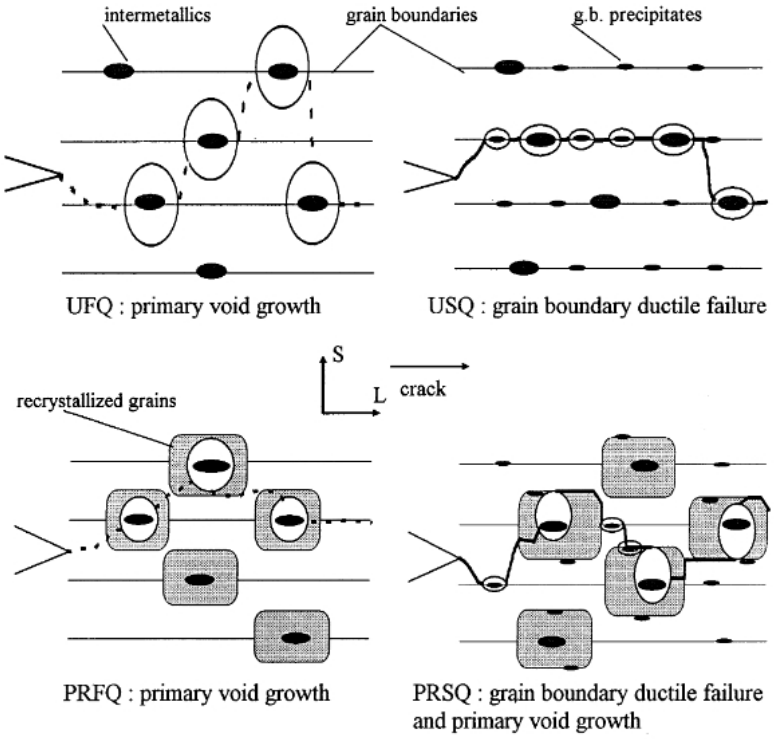

FIGURE I.16: Sketches of dominant fracture modes under tensile stress along direction S in various aluminum alloy microstructures: un-recrystallized with fast (UFQ) or slow (USQ) quenching and partially-recrystallized with fast (PRFQ) or slow (PRSQ) quenching (Morere et al., 1998).

Al-Li alloys Precipitation-hardened alloys containing both aluminum and lithium offer a good combination of low density, high stiffness and elevated strength. Commercially-available alloys include 8090 alloy and part of the 2000 series (2090, 2091, 2195, etc.). Despite their excellent facial mechanical properties, they have not experienced the promised market success. Indeed, it has been noticed that these alloys frequently present low ductility intergranular

fracture both in under-aged and aged conditions (Lewandowski and Holroyd, 1990; Pasang et al., 2012). For instance, the use of 8090 alloy in the structure of a military transport helicopter to reduce the weight of the aircraft (Fig. I.17a) has led to catastrophic damage upon heavy landing or crash (Fig. I.17b). Using 2195 alloy in the external tank of a space shuttle was luckier (Pasang et al., 2012).

FIGURE I.17: Agusta–Westland EH101 helicopter early model: (**a**) components made of Al-Li alloys (Pasang et al., 2012); (**b**) hard landing due to a tail-rotor failure attributed the low toughness of alloy 8090 (Wanhill et al., 2013).

In the first generation of Al-Li alloys, which contained up to 11% lithium, intergranular void growth at grain boundary precipitates was undoubtedly observed (Suresh et al., 1987; Vasudévan and Doherty, 1987). Indeed, a model alloy was subjected to carefully chosen heat treatments to vary the area fraction A_f of grain boundary precipitates whilst retaining the same matrix precipitation; while yield strength remained identical, fracture strain and fracture toughness were reported to vary as $1/\sqrt{A_f}$. Moreover, at constant matrix precipitation, slip lines became finer with grain boundary precipitation increase. This indicates that slip bands originate from grain boundaries instead of grain interiors. No proof of embrittlement by strain localization in the precipitate-free zone was found; instead, the reduced ductility of Al-Li compared to Al-Zn-Mg-Cu alloys was explained by the bigger grain boundary precipitates. A study also emphasized the fact that void nucleation and growth seem to arise from the same particle stress concentrations as observed in transgranular ductile fracture (Vasudévan and Doherty, 1987).

In the second generation, which includes 8090 alloy, the determination of the intergranular fracture mode triggered a heated controversy. Despite extensive experimental data collected on the presence of large dimples on the facets of fracture surfaces (*i.e.* the well-defined craters of zone A and the clear features of zones B in Fig. I.18) that indicate intergranular ductile fracture, some authors postulated the existence of an intergranular brittle fracture mode caused by two-dimensional lithium phases at grain boundaries (Lynch, 1991a; Lynch et al., 1993; Lynch et al., 2001; Lynch et al., 2002; Pasang et al., 2012). This inference is based on the observation that some under-aged Al-Li alloys display intergranular fracture surfaces devoid of dimples (zones C in Fig. I.18). However, this finding contradicts older studies discarding lithium segregation as the main factor of intergranular fracture of Al-Li alloys (Lewandowski and Holroyd, 1990). Therefore, two intergranular fracture modes seem at play in Al-Li alloys, as shown in Fig. I.19: an intergranular ductile fracture involving void growth and coalescence around grain boundary precipitates and a less ductile microvoid coalescence mode enhanced by lithium segregation and in which grain boundary precipitates play

no role (Lynch et al., 2002). This fracture can be seen as a form of intergranular fracture by planar slip (Fig. I.15a) (Kuramoto et al., 1996). The reduction of lithium atomic content under 2% appears to be required to avoid lithium-induced intergranular fracture, thus impacting the low-density asset of these alloys (Pasang et al., 2012).

In the recent context of competition between composite materials and aluminum alloys for aircraft structures and durably high fuel prices, new research campaigns on Al-Li alloys have led to the development of a third generation of Al-Li alloys: ternary Al-Cu-Li alloys with around 1% lithium, such as 2198 and 2050 alloys. Their efficient precipitation-hardening and eviction of brittle-like intergranular fracture due to lithium segregation fostered their commercial success in airplane programs, for instance under the brand Airware. However, intergranular ductile fracture still occurs in these alloys (Decreus et al., 2013), as shown in Fig. I.3.

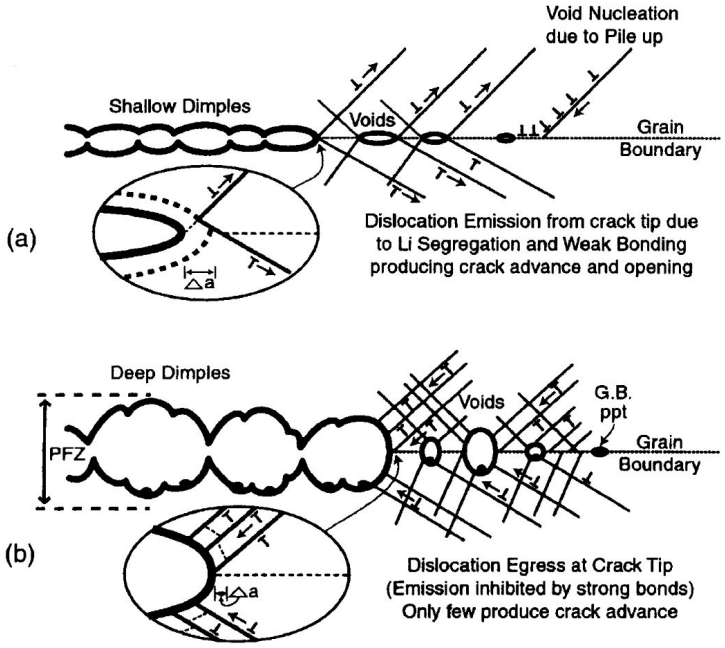

FIGURE I.19: Sketches of competing microvoid-coalescence processes in second-generation Al-Li alloys: (**a**) intergranular decohesion due to planar slip enhanced by lithium segregation; (**b**) void growth and coalescence due to large grain boundary precipitates and wide precipitate-free zone (Lynch et al., 2002).

Al-Mg-Si alloys The oil-quenching of an Al-Mg-Si was noticed to promote intergranular ductile fracture: when manganese content was low, the fracture was fully intergranular, whereas a higher manganese content triggered a mixed fracture mode. In both cases, the fracture strain was significantly lower than that displayed by the same materials subjected to water quench and which failed by transgranular ductile fracture. This is another proof of the reduced ductility associated with intergranular ductile fracture. Interestingly, dimples on the intergranular fracture surfaces were seen to be alternatively equiaxed (Fig. III.22a) and elongated (Fig. III.22b). This observation hints at the fact that the distinction between coalescence by internal necking — thought to create equiaxed dimples — and shear-assisted coalescence — believed to generate elongated dimples — that exists in transgranular ductile fracture can also be applied to intergranular ductile fracture (Poole et al., 2019). It was also shown that these alloys' grade composition can affect the grain boundary

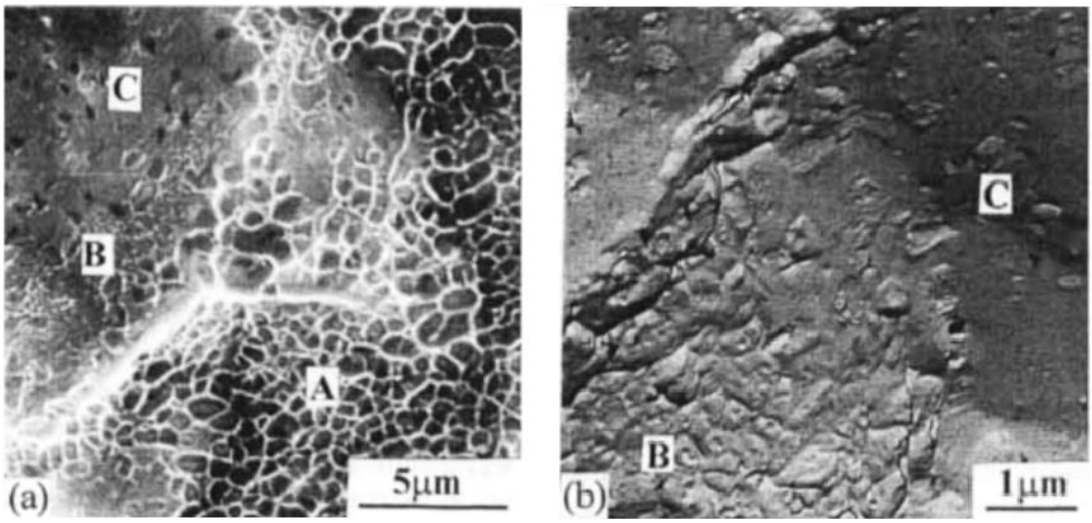

FIGURE I.18: Fracture surface of an alloy 8090 plate aged at 170°C for 32h and tested at room temperature: (**a**) Scanning Electron Microscopy (SEM) image; (**b**) TEM observation (Lynch et al., 2002).

type that fractures (Matsuda et al., 2008).

Metastable β-Ti alloys

Metastable β-titanium alloys share with Al-Li alloys an excellent density-normalized strength thanks to precipitation hardening of α-titanium, which make them attractive for aircraft — *e.g.* landing gear — and juggernaut materials. However, they are also vulnerable to room temperature intergranular ductile fracture, which is an obstacle to their wide use (Osovski et al., 2015). In lamellar β-titanium alloys such as β 21-S, Ti-10V-2Fe-3Al and Ti-5Al-5V-5Mo-3Cr, a thin α layer covers β grains boundaries, providing a favorable zone for void nucleation, growth and coalescence (Foltz et al., 2011; Li et al., 2017), as seen in Table III.1.

Nickel superalloys

Precipitation-hardened nickel superalloys are known for their excellent creep resistance at high temperatures due to yield strength anomaly, *i.e.* increasing yield strength with temperature. These alloys are less prone to intergranular void growth than aluminum alloys, probably because they do not exhibit precipitate-free zones at grain boundaries. Indeed, the absence of intergranular soft zones is associated with a lower strain localization at grain boundaries (Vasudévan and Doherty, 1987).

Grain boundary void nucleation at room temperature has been studied quite early in Astroloy and was explained by slip bands impinging at intergranular carbides, mainly $M_{23}C_6$. Nucleation was favored at grain boundaries parallel to the loading axis (Kikuchi and Weertman, 1980; Kikuchi et al., 1981). Observations of room temperature intergranular ductile fracture in nickel-based superalloys have followed. For instance, Inconel X-750, which also presents grain boundary $M_{23}C_6$, experiences intergranular fracture (see Fig. I.20) due to significant plastic flow around carbides and stress concentrations that cause matrix-particle decohesion. Total elongation at room temperature is quite unusual for this fracture mode (14-18%); a mixed transgranular-intergranular fracture mode is also observed at 316 °C and 427 °C (Mills, 1980). At room temperature, this fracture mode is associated[2] with $\xi \approx 4 \cdot 10^6$, which speaks plainly in favor of intergranular ductile fracture. Another example is Inconel 718, an alloy used in various applications in petrochemical, aerospace, and nuclear industries, and which has been obtained in the last decade by hot isostatic pressing powder metallurgy, a processing technique that can reduce component fabrication costs. However, when applying classical Inconel 718 heat treatments on this newly obtained Inconel 718, it was found that extensive precipitation of MC-carbides and δ-phase provided favorable sites for grain boundary void growth and coalescence, triggering intergranular fracture (here, $\xi \approx 2{\cdot}10^{10}$). This unwanted behavior was averted by developing a new heat treatment (Chang et al., 2014). A related issue is experienced in GH4169 superalloy where heat treatments supposed to harden the ma-

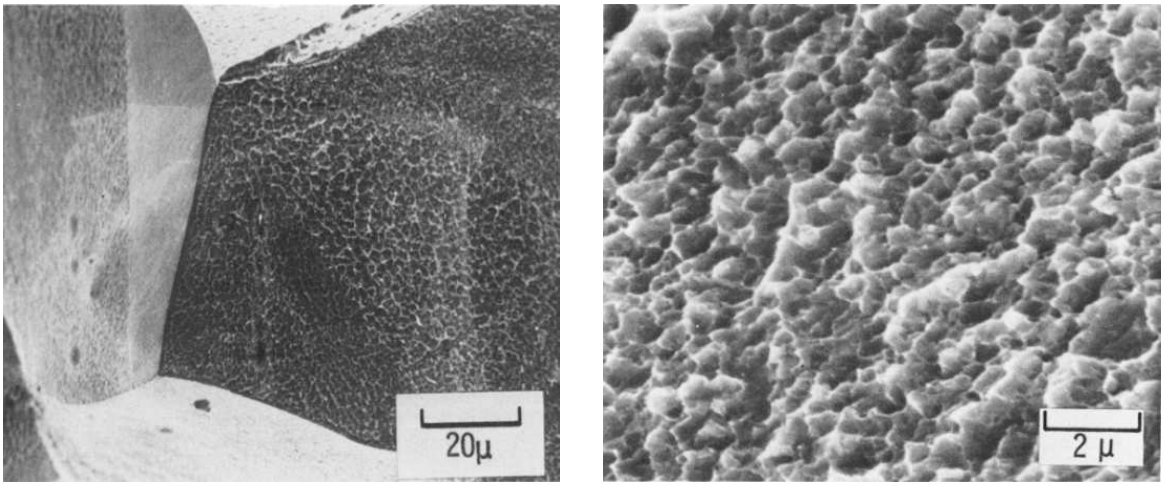

(**a**) (**b**)

FIGURE I.20: SEM fractographs of a sample of Inconel X-750 loaded at room temperature in a classical tensile test: (**a**) intergranular fracture surface; (**b**) dimples on an intergranular facet (Mills, 1980).

[2]No grain boundary vacancy diffusion activation energy was found for Inconel X-750; therefore, activation energy was set to the barycenter between pure Nickel and Inconel 718 weighted by their respective Nickel content, leading to $Q_b = 225$ kJ $\cdot$ mol^{-1}.

trix with γ' and γ'' precipitates simultaneously favor intergranular fracture, first by creating a discrepancy between grain interior and grain boundary strengths and then by triggering the precipitation of δ-phase at grain boundaries. Thus, intergranular crack-shaped cavities nucleate at δ particles and grow plastically (Lin et al., 2017). Carbon and boron-doping of MAR-M200 alloy are also reported to cause intergranular ductile fracture due to the grain boundary precipitation of titanium-carbide particles (Vasudévan and Doherty, 1987).

Magnesium alloys

Magnesium alloyed with rare earth elements can also experience intergranular ductile failure at room temperature. For instance, Mg-11Gd-2Nd-0.4Zr displays a fracture mode transition that has been thoroughly characterized: transgranular ductile fracture in the as-quenched condition, brittle transgranular cleavage in the peak-aged condition, brittle intergranular fracture in slightly-overaged condition and, finally, intergranular ductile fracture (see Table III.1) in fully-overaged condition (Zheng et al., 2008). The brittle intergranular fracture mode is akin to the failure by planar slip evidenced by Kuramoto et al. (1996) (Fig. I.15a). As already seen in aluminum alloys, the difference between the two last fracture modes arises from the fact that the slightly overaged condition is associated with fine grain boundary precipitates and narrow precipitate-free zones while subsequent aging triggers the formation of coarser precipitates and wider precipitate-free zones (see Table III.1) (Zheng et al., 2008). Intergranular ductile fracture is also seen at higher temperature (500°C) in a Mg-Gd-Y-Ag alloy (Xiao et al., 2022).

Austenitic steels

Intergranular fracture due to incoherent precipitation at grain boundaries induced by a heat treatment is observed in alloys that are not precipitation-hardened. Steel overheating during forging is a typical example of this phenomenon: when austenitic steels are heated or heat-treated above the overheating temperature (around 1200 °C), precipitation of intergranular manganese sulfide happens. Subsequent room temperature tests present intergranular fracture surfaces with large dimples containing MnS inclusions (Fig. I.21b) (Tsun, 1953; Schulz and McMahon, 1973) which display a stark contrast with brittle intergranular fracture surfaces (Fig. I.21a). Overheating was observed in forged aero-engine components such as connecting rods (Tsun, 1953).

Less known, unwanted heat-treatments of binary gold-platinum alloys can trigger sufficient grain boundary precipitation to shift fracture mode from transgranular ductile fracture to intergranular ductile fracture (Carpenter, 1967).

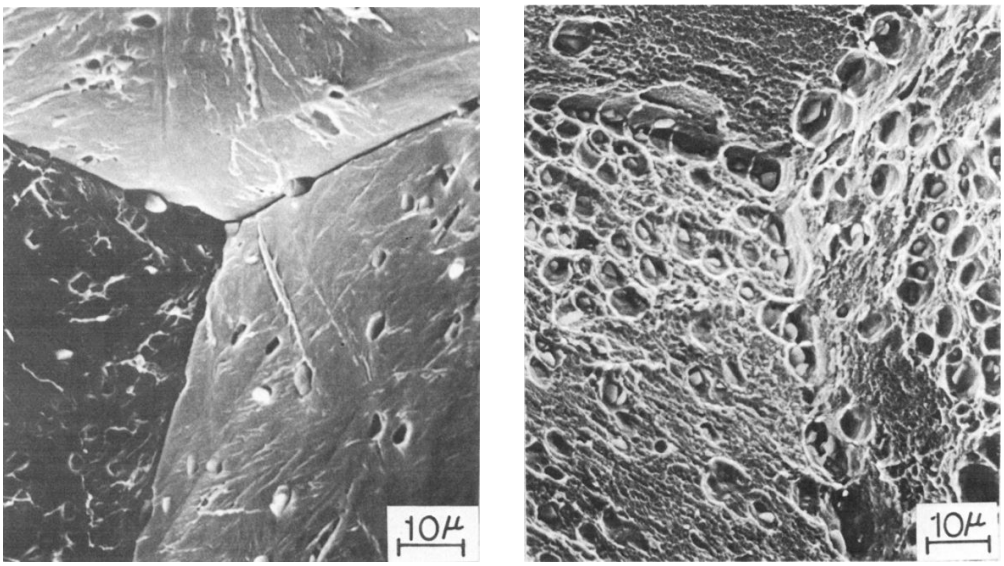

(**a**) 4h at 1250°C, 90h at 900°C, oil-quenched

(**b**) Heat treatment (**a**) followed by 2h at 650°C

FIGURE I.21: Intergranular fracture surfaces of a Fe - 3.5% Ni - 1.7% Cr steel tested at room temperature after overheating treatment (Schulz and McMahon, 1973).

2.1.2 High homologous temperature

In Section I.1.3.1, it has been highlighted that creep can occur in conditions where plastic flow dominates diffusion flow (Pavinich and Raj, 1977). Inconel X-750 is among the engineering materials in which such a fracture mechanism is thought to prevail (Venkiteswaran and Taplin, 1974). However, diffusion is evoked in most creep applications. Without a clear distinction between the diffusion and plasticity domains, it is not useful to list all the observations of intergranular growth and coalescence of cavities in creep-like conditions. Thus, in the following, only two types of occurrences of intergranular ductile fracture at high homologous temperature are summarized: first, stress relief cracking, as it is still a concern in the nuclear field and other industries; second, testing at high strain rates.

Stress relief cracking This phenomenon, also called stress relaxation cracking or reheat relief cracking, is observed in many alloys in which cracking occurs immediately after welding or within a slight delay — less than two years (Dhooge et al., 1978; Dhooge and Vinckier, 1987). Cracking is mainly found in heat-affected zones instead of the weld itself (Shoemaker et al., 2007). Stress relief cracking is often characterized by extensive cavity growth at grain boundaries leading to dimpled intergranular fracture surfaces (Shoemaker et al., 2007; Kant and Dupont, 2019; Dayalan et al., 2020). The driving mechanism is the relaxation of internal stresses induced by welding thermal incompatibilities; that relaxation occurs at temperatures between 500 and 700°C depending on the material. Localization of plastic deformation is often observed at grain boundaries due to the presence of a precipitate-free zone or to the hardening intragranular precipitates induced by aging (Kant and Dupont, 2019; Dayalan et al., 2020). Typical materials experiencing stress relief cracking are high-carbon stainless steels 304H, 316H, 321H, 347H and Ni-based alloys such as Incoloy 800HT, Inconel 601 and 617 (Shoemaker et al., 2007; Pommier et al., 2016; Dayalan et al., 2020). The high carbon content favors precipitation-hardening of grain interiors, which fosters stress relaxation cracking. In the following, occurrences of reheat relief cracking in low-carbon nuclear austenitic steels (304L, 316L, 321, 347) will be discussed to uncover the void growth mechanism.

In 321 and 347 steels, stress reaheat cracking is usually associated with grain interior hardening by Ti(C,N) (321 steel) or Nb(C,N) (347 steel) carbides (Pommier et al., 2016). For instance, the Russian version of 321 alloy is used for cooling water inlet and outlet tubes (Kasana and Pandey, 2021) and other core internals of WWER reactors. Two different kinds of fracture surfaces are highlighted in this austenitic steel: the cold-rolled and unaged steel (*i.e.* without intragranular precipitates) presents featureless facets (Fig. I.22a) while the cold-rolled and aged material exhibits well-defined intergranular dimples (Fig. I.22b). This hints at the existence of two intergranular deformation mechanisms, with only the second one being linked to the growth and coalescence of cavities at intergranular particles precipitated during aging (possibly chromium carbides or σ phase) (Chabaud-Reytier et al., 2003). ξ associated with the experiments of Fig. I.22b ranges between 10 and 25 at void nucleation and $\xi \approx 500$ at void coalescence.

304 and 316 series steels do not exhibit the intragranular precipitates of austenitic steels stabilized by titanium (321 steel) or niobium (347 steel); stress reheat cracking is thus less intense in these alloys. Yet, reheat cracking of heat-affected zones of thick welded parts of the 316L series was seen in industrial applications, such as at the junction

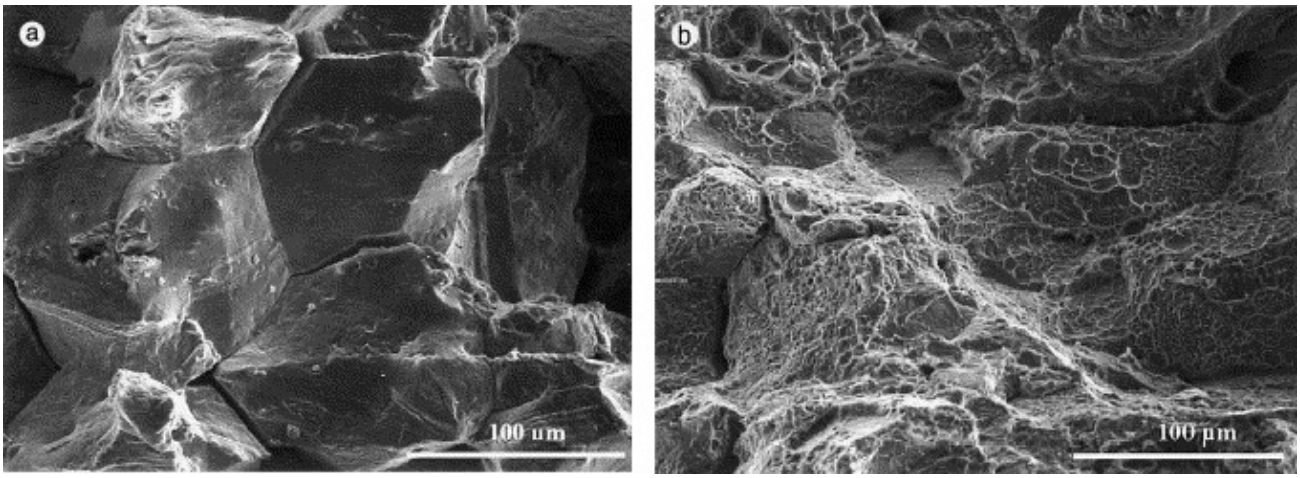

FIGURE I.22: Stress relief cracking fracture surfaces of 15% pre-strained 321 steel CT specimens tested at 600°C: (**a**) unaged state; (**b**) aged state (Chabaud-Reytier et al., 2003).

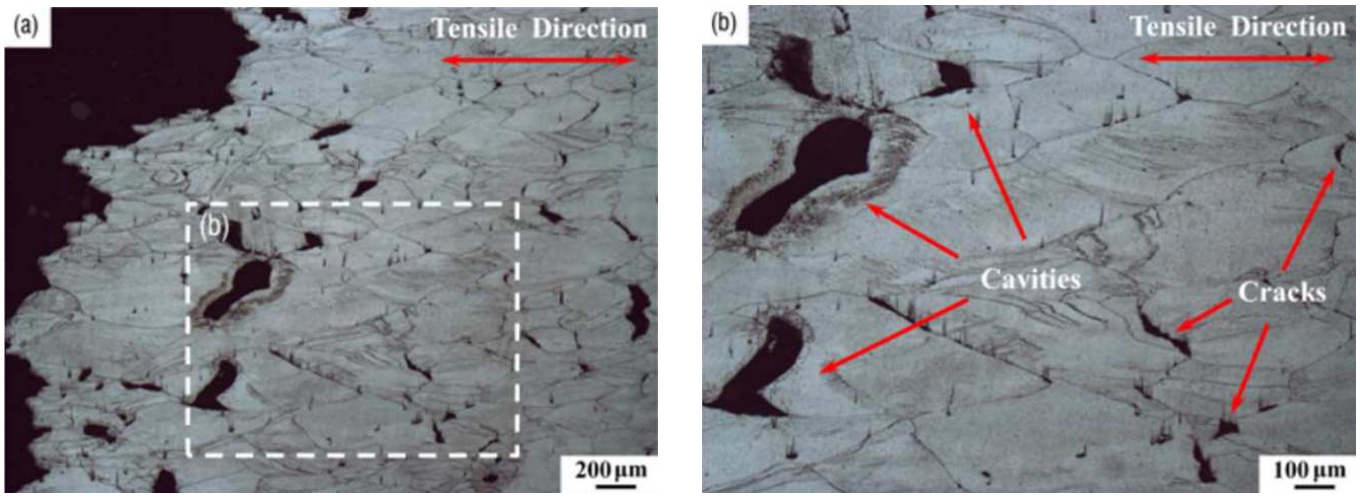

FIGURE I.23: Microstructure near the fracture zone and two-fold magnification for a 316 steel strained at $\dot{\varepsilon} = 0.5\ \mathrm{s}^{-1}$ at 900°C (Fu and Zhang, 2020).

between the steam header and the nozzle of advanced gas-cooled reactors (AGR) (Auzoux, 2004; Auzoux et al., 2010; Pommier et al., 2016; Pommier et al., 2017). It is always associated with the precipitation of intergranular $M_{23}C_6$ during aging at high service temperatures (around 550 °C); these carbides are usually located on grain boundaries normal to the principal residual stress caused by thermal incompatibilities. The stress relief cracking then takes place either during a subsequent heat treatment or during operation. Void nucleation at grain boundaries occurs mainly due to the decohesion of $M_{23}C_6$ carbides (see Fig. I.4), creating nanocavities whose mean diameter is 50 nm, while intergranular MnS inclusions are unaffected. Grain boundaries that exhibit 25° to 55° misorientation are preferentially affected because carbides precipitate easily on them (Pommier et al., 2016). Following void nucleation at carbides, voids grow and coalesce, leading to intergranular fracture (Pommier et al., 2017). In the compact tension specimens of Auzoux (2004) and Pommier et al. (2016), the dimensionless parameter ξ is such that $\xi \in [0.25, 1]$ at the start of void growth and $\xi \in [1.25, 5]$ at fracture. It is therefore believed that plastic flow plays an important role along vacancy diffusion from a certain void size threshold, even if the previously cited authors present reheat cracking as entirely diffusion-controlled.

Testing at high strain rates In cases where deformation is fast enough, the void growth mechanism is easy to decide. For instance, dimpled intergranular fracture occurs in 316LN austenitic steel at elevated temperature (900–1200°C) under high strain rate, with no preexisting cavities in the alloy. At such temperature, analysis is hampered since fracture is accompanied by recrystallization above 1050°C, and is sometimes opposed by grain boundary sliding. Nevertheless, it is found that triple points are weak spots and that voids nucleate at brittle inclusions such as aluminum oxide Al_2O_3 (see Fig. I.5). Void growth and coalescence can be either parallel (temperature under 1050°C, such as in Fig. I.23), perpendicular (1200°C), or with no directivity (1050–1150°C) relative to the tensile direction. This experimental data corresponds to $\xi \in [250, 2500]$ at the beginning of void growth and tenfold values at fracture, which means that in all likelihood plastic flow is responsible for void growth; curiously, the phenomenon is attributed by the authors to vacancy diffusion (Fu and Zhang, 2020).

2.2 Irradiated alloys

A large variety of alloys is used in nuclear applications: zirconium alloys, austenitic and ferritic steels, nickel alloys, etc. Under neutron irradiation, their mechanical properties undergo a progressive degradation that can endanger their ability to meet service requirements. Radiation damage can be divided into two fields: atomic displacement and transmutation. The first one arises from neutron collisions with atoms of a crystalline metal matrix that trigger displacement cascades, creating irradiation defects and enhancing diffusion. Ballistic damage is characterized by the number of displacements per atom (dpa), *i.e.* the average number of times that one atom of the initial lattice was hit out of its equilibrium position. This damage type is responsible for segregation, additional precipitation, void swelling, material growth and irradiation creep. The second one emerges from the nuclear reactions induced by incident neutrons and manifests by generating new radioisotopes such as helium — whose bubbles can act as

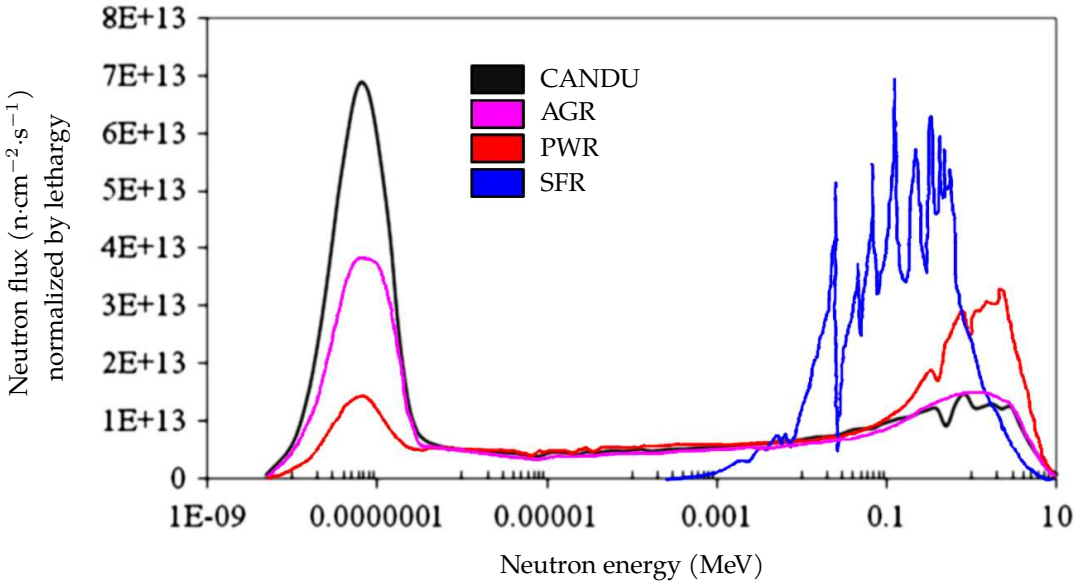

FIGURE I.24: Approximate neutron spectra of various reactor designs (adapted from Judge et al. (2015) with additional data from Lewis (2008) and Idaho National Laboratory (2011)). For material science applications, it is often sufficient to distinguish thermal (low energy) neutrons and fast (high energy) neutrons, the threshold being conventionally set to $E = 0.1$ MeV.

nucleated intergranular cavities, see Section I.1.2.2. Radiation damage in nuclear materials has been described for each type of alloy in comprehensive reviews which are referred to for additional information (Was, 2007; Garner, 2020; Onimus et al., 2020; Leonard and Taylor, 2020; Hashimoto et al., 2020; Griffiths and Boothby, 2020).

Reactor designs operate under various damaging environments which range from pressurized 300°C water to molten salt and 500°C liquid sodium, all of which can enhance damage through corrosion or diffusion of embrittling elements. Neutron energy spectrums also exhibit widely different thermal-to-fast fractions (Fig. I.24), which means that helium production rates for a given material vary according to the reactor design. Indeed, cross-sections of helium-producing nuclear reactions are large for thermal and fusion neutrons. In EBR-II fast reactor, austenitic and ferritic alloys suffer a helium production rate of 0.5 appm per dpa, while the mixed spectrum reactor HFIR induces a rate of 55 appm per dpa in 316 steel and a tokamak first wall made of steel is expected to produce 8-13 appm per dpa (Klueh, 1990). Such variations can even be observed at a local scale in a pressurized water reactor (PWR) given the axial dependence of thermal-to-fast neutron ratio: for 316 steel, it can range from 10 appm per dpa (ratio of 0.16) to 35 appm per dpa (ratio of 2.5) (Fukuya et al., 2006). Thus, the different neutron spectra combined with the various nickel and boron contents — boron can exist at trace levels — in materials can lead to different helium embrittlements (Mansur and Grossbeck, 1988). Therefore, this criterion must be considered in the choice of structural alloys.

In the following, two domains in which intergranular ductile fracture can be encountered in fission reactors are successively reviewed: fuel cladding (Section I.2.2.1) and light water reactor internals (Section I.2.2.2).

2.2.1 Fission reactor fuel cladding

In most reactor types, fuel cladding is designed to be the first containment barrier — *i.e.* its integrity is essential to retain radioisotopes in case of accident. This task is difficult due to the various damaging mechanisms exerted upon fuel cladding: fission gas internal pressure, fuel pellet-cladding mechanical and chemical interactions as well as more classical mechanisms such as irradiation creep, growth and swelling. Such high stakes justify the close study of fuel cladding fracture modes. Observations are divided according to reactor design to account for different loading conditions and helium per dpa ratios. Note that helium production is not observed in the cladding of light water reactors made from zirconium alloys (Onimus et al., 2020).

CANDU reactor – Nickel superalloy CANDU (standing for CANada Deuterium Uranium) reactor is a type of pressurized heavy water reactor (PHWR). In CANDU fuel channels, garter springs (Fig. I.25), also known as spacers, separate the calandria tube from the central hot pressure tube. Spacers used to be in Inconel 600, which was then changed to Inconel X-750 (Stopher, 2017). Tube creep induced by gravity effects applies a pinching loading on the

spacers during the service duration. The temperature of the spacers ranges from 120°C to 330°C (Judge et al., 2015).

Helium embrittlement of Nickel alloys is very significant in CANDU reactors because its neutron spectrum exhibits a high thermal-to-fast ratio (Fig I.24) (Judge et al., 2015). Indeed, thermalized neutrons promote intense helium production from Nickel-59, itself produced from Nickel-58 (Woo et al., 2011). At the end of a fuel channel's life, the spacers' helium content can reach 2 at. %. After 10 years of service, garter springs exhibit an entirely intergranular fracture mode (see Fig. I.26a) and which is responsible for a substantial ductility loss (Judge et al., 2012; Judge et al., 2015). In-service fracture of Inconel 600 spacers was observed a few times in CANDU reactors at approximately ten effective power years (Griffiths et al., 2012; Stopher, 2017). A high density of nanoscale helium bubbles located at grain boundaries is reported (see Fig. I.26b) (Judge et al., 2012). Room temperature micro-tensile tests on irradiated samples have shown that the grain boundary fracture is a ductile process (Howard et al., 2019) and molecular dynamics simulations have confirmed that void growth and coalescence are involved in this fracture mode (Demkowicz, 2020). Another study has shown that intergranular cracks run along brittle precipitates (Judge et al., 2015), cracking being only driven by the presence of voids at the grain boundaries (Griffiths, 2023). This is supplemented by the fact that helium-implanted X-750 was shown to develop the same mode of intergranular fracture as neutron-irradiated X-750 (Changizian et al., 2023). Fracture modeling based on helium bubbles coverage of grain boundaries has successfully predicted the ductility loss of irradiated X-750 spacers (Xu et al., 2022). In the standard mechanical tests conducted at in-service temperature (Judge et al., 2015), ξ is estimated to be between 50000 (T = 120°C) and 25 (T = 330°C) at the start of void growth and higher at fracture. Therefore, the dominant fracture mode is likely intergranular ductile fracture.

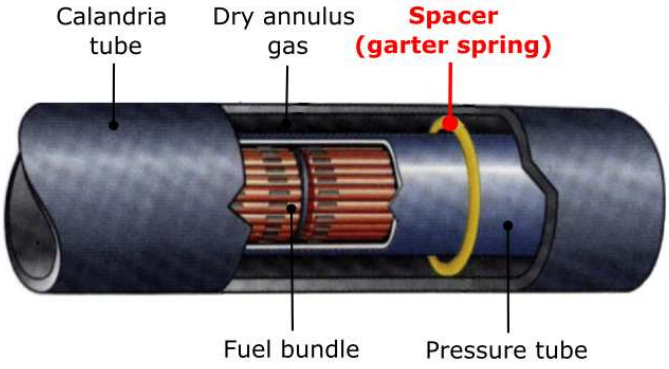

FIGURE I.25: Sketched view of a CANDU fuel channel (Judge et al., 2015).

Advanced gas reactor (AGR) – Austenitic steel In AGRs, a British reactor design, fuel cladding is made of 20Cr-25Ni-Nb stainless steel. The cladding can experience temperatures ranging from 400°C to 900°C depending on the power conditions (Lobb and Evans, 1987). Irradiation of this steel at fluences of $1.65 \cdot 10^{20}$ n·cm^{-2} (fast neutrons)

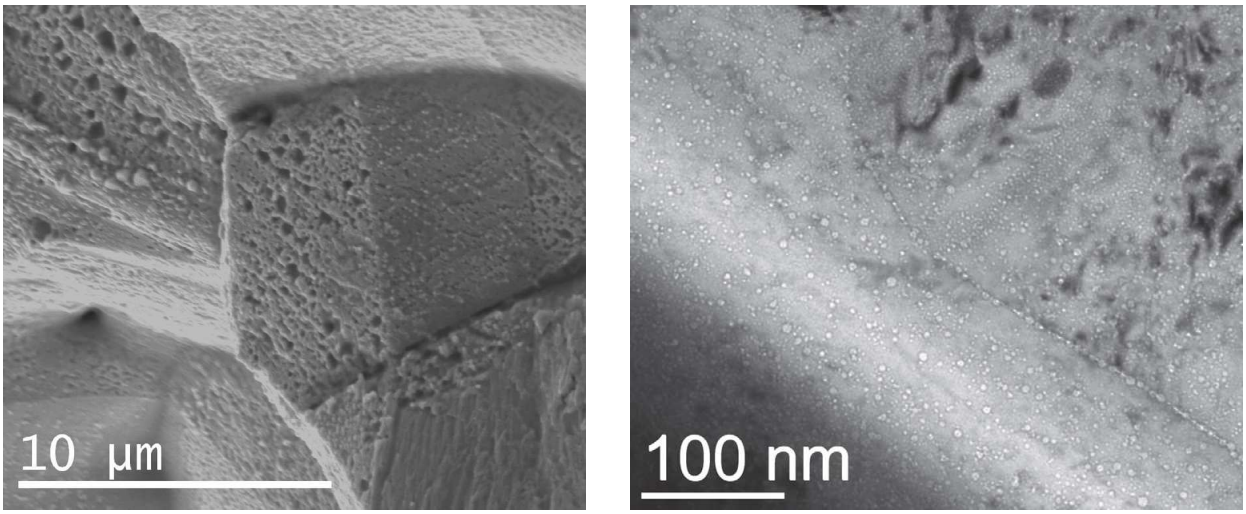

FIGURE I.26: Inconel X-750 CANDU spacer irradiated at 300 °C to 55 dpa (∼ 18000 appm of helium): **(a)** fracture surface after room-temperature loading; **(b)** TEM observation of intragranular and intergranular (the grain boundary is the descending diagonal) helium bubbles (Judge et al., 2015).

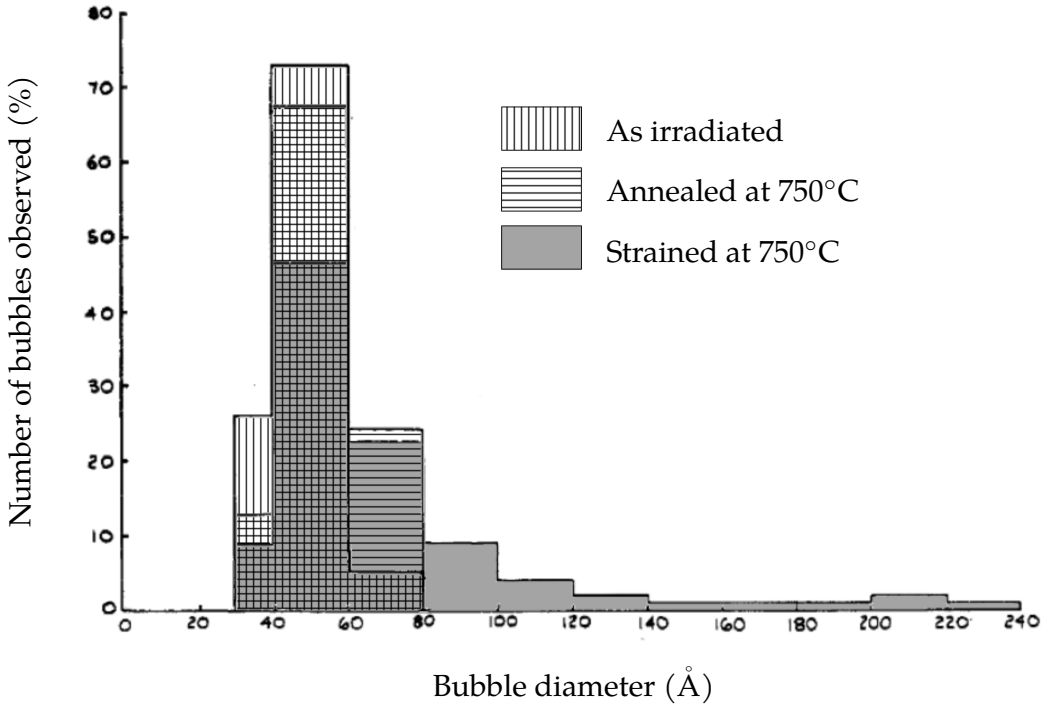

FIGURE I.27: Helium bubble size distribution in an irradiated 20Cr-25Ni-Ti steel (superposed diagrams from Rowcliffe (1966)).

and $5.7 \cdot 10^{20}$ n·cm^{-2} (thermal neutrons) at temperatures between 450°C and 750°C followed by tensile testing in the 650 - 800°C range triggered intergranular fracture (Hughes and Caley, 1963; Arkell and Pfeil, 1964). These conditions are coherent with both AGR in-service temperature and neutron spectrum (Fig. I.24). A 20Cr-25Ni-Ti steel irradiated at 623°C with a thermal-to-fast neutron ratio of 2.33 exhibited grain boundary He bubbles. Subsequent straining at 750°C and $\dot{\varepsilon} = 3 \cdot 10^{-4}$ triggered a significant cavity growth while the void enlargement generated by annealing of 30 minutes conducted at the same temperature was much weaker (Fig. I.27) (Rowcliffe, 1966), which underlines that stress plays a key role in void growth. At such a loading rate and temperature, the growth is believed to be partially induced by plasticity at the start of void growth ($\xi \approx 1$) and fully controlled by plasticity at fracture ($\xi \approx 20$)[3]. Therefore, AGR type-austenitic steels are likely prone to intergranular ductile fracture induced by grain boundary helium bubbles in AGR in-service conditions.

Sodium fast reactor (SFR) – Austenitic steel Austenitic steel cladding irradiated in SFR conditions — fast neutron spectrum, high temperature — exhibits intergranular fracture for a wide range of loading conditions, including low and high test temperatures. The case of low test temperature is illustrated by the case of a Russian analog of 321 steel (18Cr-10Ni-Ti), which is used in core internals of BOR-60 and BN-600 fast reactors and WWER light water reactors, making its study relevant for nuclear materials (Margolin et al., 2016). Occurrence of intergranular fracture is seen during tensile tests at 20°C and 290°C on this steel irradiated at 400–450°C in the fast reactor BOR-60 (Margolin et al., 2009). The insufficient magnification of fracture surfaces (Fig. I.28) makes it difficult to assess the fracture mechanisms, but such an intergranular failure is likely to be ductile (Hojná, 2017).

Intergranular fracture can also happen at high test temperatures, as seen on the putative fracture mode map of a 316 steel irradiated at 20 dpa with a fast neutron spectrum (Fig. I.29). In this map over the space of imposed stress and test temperature, the fracture mode that prevails is drawn (Matthews and Preusser, 1987). Even if irradiation is thought to lower the temperature transition from transgranular fracture to intergranular fracture, the temperature threshold between transgranular and intergranular fracture at 20 dpa (580°C) is coherent with the data at 55 dpa (600 ± 50 °C) (Huang, 1984). Failure modes 3 to 6 are intergranular: in modes 3 and 4, it seems that grain boundary cracks are nucleated at precipitates due to stress concentrations and then either grow and coalesce (mode 3) or propagate quickly (mode 4). In mode 3, it is claimed that the resolved shear stress controls fracture, contrary to

[3] In the absence of grain boundary vacancy diffusion data for 20Cr-25Ni-Ti steels, data from 316L series have been used.

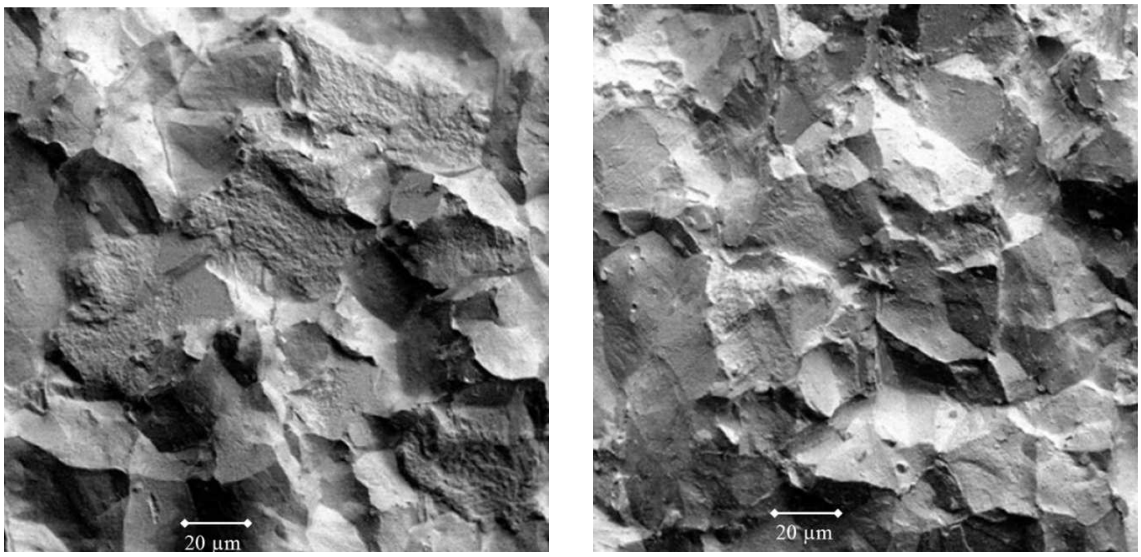

(**a**) 20°C (**b**) 290 °C

FIGURE I.28: Intergranular fracture surfaces of 321 steel tensile specimens irradiated at 400–450°C to 49 dpa in a BOR-60 reactor (3–13% void swelling) and loaded at two different temperatures. Rough zones display a transgranular fracture supposedly related to dislocation channeling (Margolin et al., 2009).

mode 4, which depends on the stress normal to the grain boundary. Mode 6 is intergranular fracture triggered by the stress-induced growth and coalescence of grain boundary helium bubbles. Mode 5 displays creep kinetics, and may be related to the underlying mechanisms of modes 3, 4, or 6 (Matthews and Preusser, 1987). The distinction between mode 3/4 (grain boundary cracks) and mode 6 (helium-filled spherical cavities) is also made by another study (Ford, 1992). Based on this interpretation, intergranular ductile fracture is believed to cover at least mode 3 and perhaps mode 4 (highlighted in red in Fig. I.29); nothing can be said of modes 5 and 6 except that, if intergranular ductile fracture were to be involved, it would concern the high-stress/medium-temperature zone. However, the mechanisms identified in Fig. I.29 should be treated carefully as the review by Bennetch and Jesser (1981) attributes the intergran-

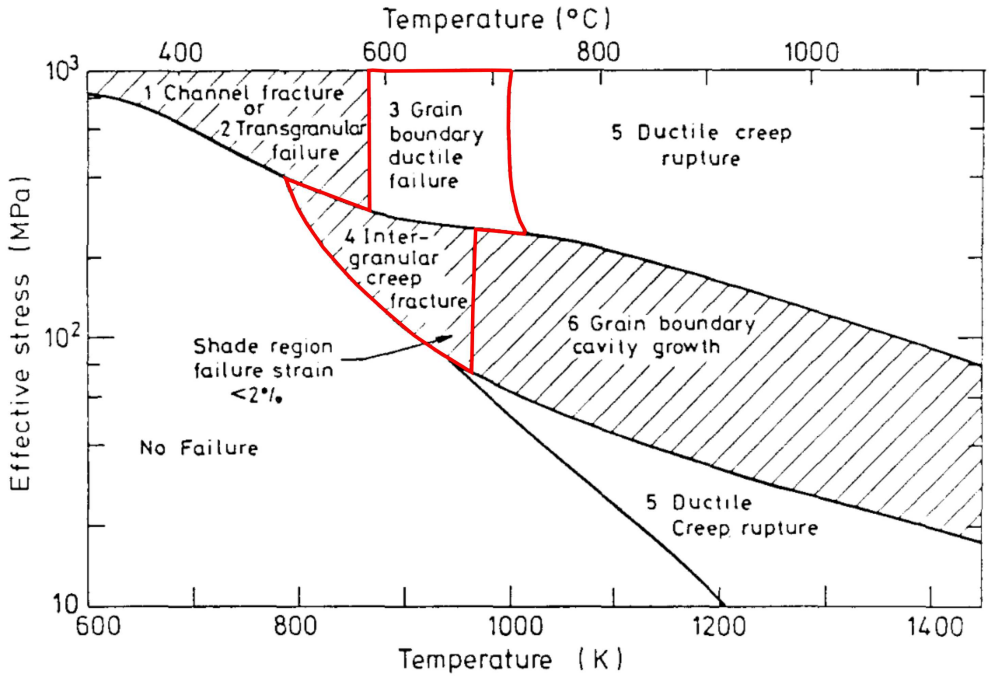

FIGURE I.29: Putative failure mode map for 316 stainless steel irradiated to 20 dpa at 400-600°C with a fast neutron spectrum (Matthews and Preusser, 1987). Zones in which intergranular ductile fracture is thought to occur are highlighted in red.

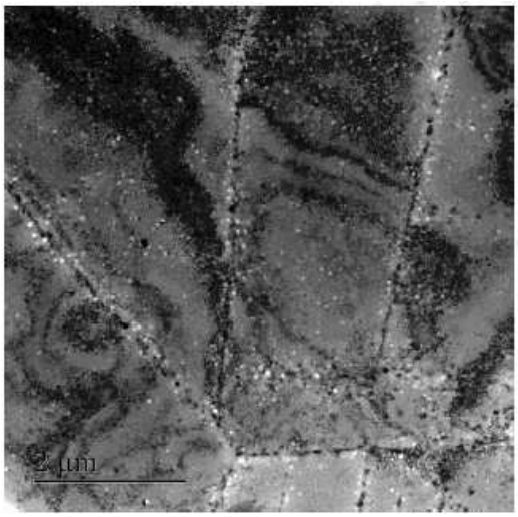

FIGURE I.30: TEM observation of a 15Cr-15Ni-Ti austenitic steel irradiated in the sodium fast reactor Phénix at 470°C and 91 dpa, displaying a swelling of 4,3% (Hure et al., 2022)

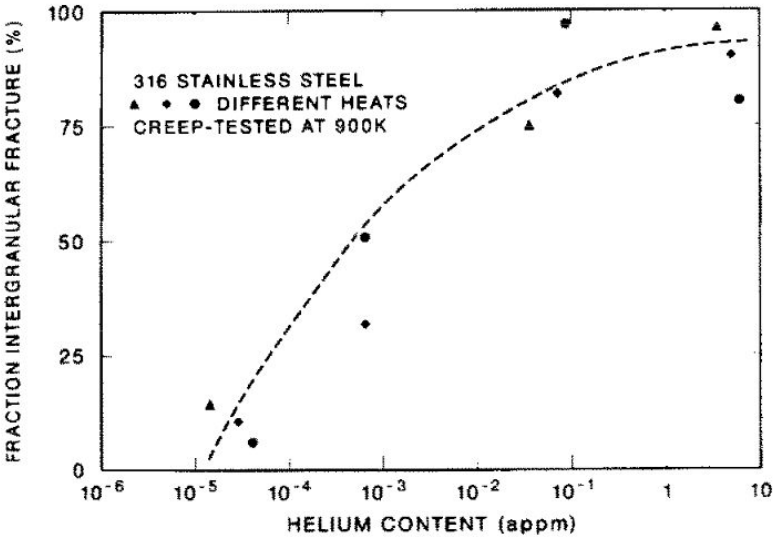

FIGURE I.31: Fraction of intergranular fracture versus helium content in 316 steel creep tests conducted at 630°C (Mansur and Grossbeck, 1988).

ular fracture of neutron-irradiated 316 steel to helium-filled cavities based on the finding that both neutron-irradiated and helium-implanted 316 steel display fractures that are at least partly intergranular above a test temperature threshold of 550°C. The critical role of helium bubbles in intergranular fracture of helium-implanted 316 steel is shown in Fig. I.31 for a test temperature around 600°C (Mansur and Grossbeck, 1988).

Finally, some studies point to a peculiar fracture mode in which fracture occurs along grain boundaries without coinciding with them; in the following, it will be referred to as *quasi-intergranular fracture*. For instance, deformation at 635°C of an irradiation-swollen 18Cr-10Ni-Ti austenitic steel (swelling of 20%, ion irradiation dose of 100 dpa) displayed a ductile fracture mode that is neither transgranular nor intergranular but whose path follows the edges of defect-denuded zones along grain boundaries (at a distance of $\sim 0.5\mu$m) due to an increased void concentration at that location (Borodin et al., 2004). Observations of two planes of greater porosity on either side of grain boundaries in an irradiated austenitic steel 15Cr-15Ni-Ti (Fig. I.30) associated with facet-like fracture surfaces also hint at quasi-intergranular fracture (Hure et al., 2022). These observations of void-free zones surrounded by void walls supplement previous data obtained from Fe–15Cr–15Ni, PNC316 (Sekio et al., 2015) as well as other irradiated materials (Liu et al., 2016b).

Sodium Fast Reactor (SFR) – Nickel superalloys In sodium fast reactor nickel-based fuel cladding, strong helium embrittlement is observed in the temperature range 450-725°C. This effect is particularly marked in Alloy 706 and PE16 (see Fig. I.32 where a saturation effect at 20 dpa is noticed) and is believed to come exclusively from stress-induced helium bubble growth and coalescence (Rowcliffe et al., 2009; Barnes, 1965). In fuel cladding, the hoop stresses induced by the fuel-pellet interaction at high temperatures are believed to favor the formation of helium bubbles at radial grain boundaries with high energies, which would be a major cause of embrittlement (Qin et al., 2018). ξ is estimated between 6 and 150 at the onset of void growth, which is consistent with inter-

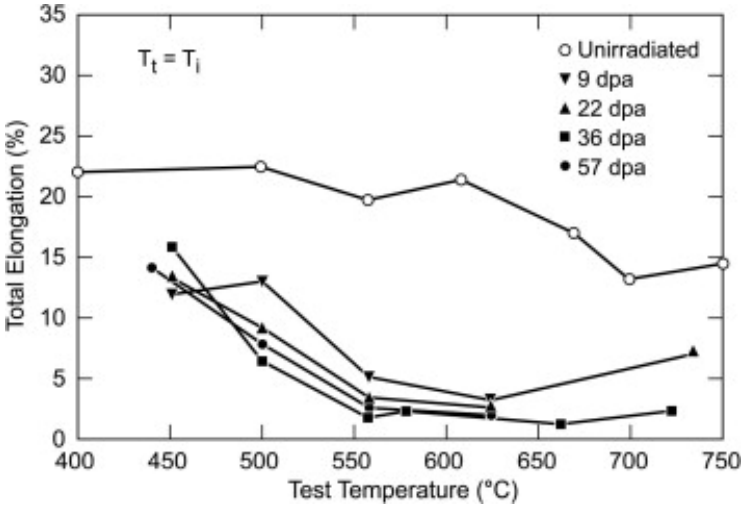

FIGURE I.32: Ductility of irradiated PE16 alloy at various doses and temperatures (Rowcliffe et al., 2009).

granular ductile fracture.

The research campaign on Alloy 706 and PE16, conducted in the United States during the 1970s, has led to the abandonment of nickel-based superalloys for SFR cladding in the subsequent decades. Research projects on Generation IV Nickel-based superalloys have then resumed, focusing on developing alloys resistant to helium embrittlement such as ternary alloys Fe-Cr-Ni (Rowcliffe et al., 2009).

2.2.2 Light water reactor core internal components

Light water reactor (LWR) internals used in pressurized and boiling water reactors (PWR/BWR) worldwide are mainly made of austenitic stainless steels, which combine excellent ductility and good resistance to corrosion. In French PWRs, the dominant grades are 304L and 316L steels. The core structures made of austenitic stainless steels in a Westinghouse PWR design are presented in Fig. I.33. Since the degradation of mechanical properties of LWR internals has been summarized elsewhere (*e.g.* (Fukuya, 2013)), this review shall only dwell on irradiation-induced damage relevant to the subject. Indeed, irradiated LWR internals sometimes experience intergranular fracture. Alternative mechanisms have been proposed for these observations. Two of them are characterized by plastic deformation at grain boundaries that do not correspond *stricto sensu* to intergranular ductile fracture. They shall be summarized in the first part. Then, the role of helium bubbles in promoting intergranular ductile fracture by growth and coalescence

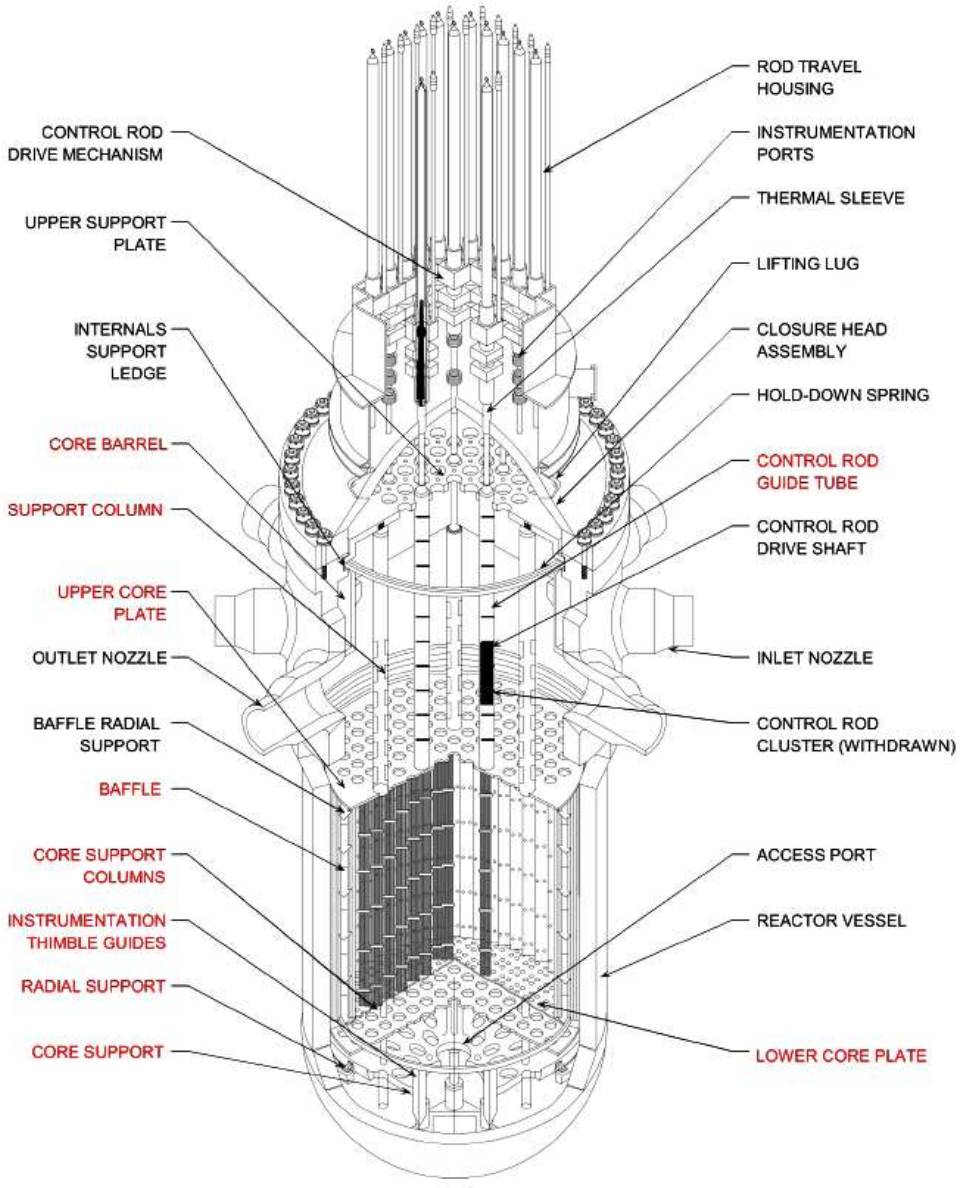

FIGURE I.33: Cutaway view of a Pressurized Water Reactor vessel (Westinghouse, 2020). Internal structures made of austenitic stainless steel are shown in red.

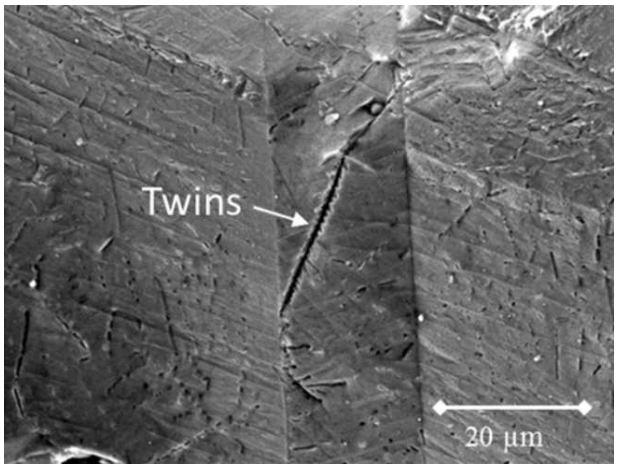

FIGURE I.34: Localized twinning on the grain boundary of an 18Cr-10Ni-Ti compact tension specimen irradiated at 2.4 dpa and tested at -100°C (Hojná, 2017).

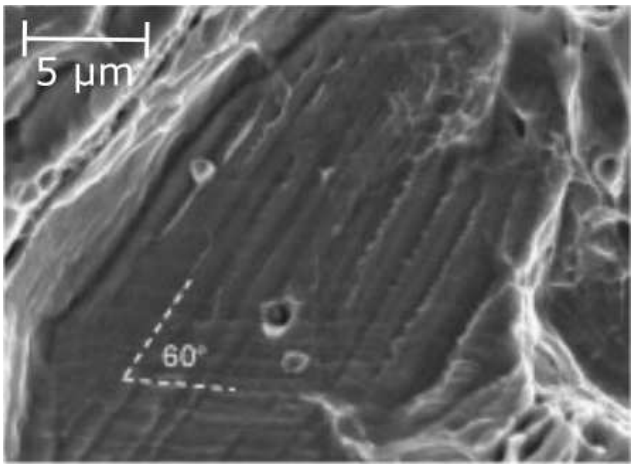

FIGURE I.35: Intergranular facet on the fracture surface of a 316 impact test sample irradiated to 38 dpa and loaded at 30 °C in air (Fukuya et al., 2008).

of cavities will be discussed.

Dimple-free intergranular fracture

Intergranular decohesion by twinning It has been known for long that irradiation can foster twinning in austenitic steels under loading; it was recently shown that micro-twinning can occur in zones localized at the grain boundary (see Fig. I.34) (Hojná, 2017). To reconcile intergranular fracture occurrences at low temperatures (room temperature or below) and high strain rate (conventional tensile testing and impact testing) of irradiated LWR internals, a mechanism of intergranular decohesion due to twin formation was proposed. First, various locations of a grain boundary decohere due to deformation twinning — although the microscopic mechanism involved is unknown (Griffiths, 2023). Then, cracks grow and coalesce, either along grain boundaries — which leads to a fully intergranular failure — or by fracturing grain interiors — which leads to a mixed failure mode. Fracture surfaces display facets covered with parallel ridges coherently with twinning directions (see Fig. I.35). These ridges are equally spaced with a distance of around 1 µm that does not depend on dose and temperature. Intergranular facets can be conterminous or embedded in transgranular ductile fracture zones. Since high stress trixialities favor twinning, it accounts correctly for the location of intergranular fracture at the center of tensile specimens. This explanation also agrees with the observation that intergranular fracture is fostered when the strain rate increases or the temperature is lowered (Fukuya et al., 2008). Occurrences of intergranular fracture during tensile testing in air at room temperature of a BWR 304 wide range neutron monitor (irradiated at 80 dpa, *i.e.* 29 years of service) and a PWR 316 flux thimble tubes (irradiated at 65 dpa, *i.e.* 20 years of service, and 73 dpa) are believed to fall into this category (Hojná, 2017; Fukuya et al., 2008). Multiple impact tests of PWR 316 flux thimble tubes (irradiated between 22 dpa and 73 dpa) at room temperature and below also displayed this fracture mode (Fig. I.35) (Fukuya et al., 2008).

This theory is far from being fully validated. The evidence of grain boundary helium bubbles of 1-3 nm size and bubble-free zones in a 316 PWR thimble tube irradiated at 35 dpa and 70 dpa may also indicate helium embrittlement (Edwards et al., 2009). Moreover, strain-induced formation of brittle martensite at grain boundaries is also possible, which would rule out ductile fracture (Hojná, 2017; Griffiths, 2023). Unfortunately, fracture area magnification is often insufficient to decide on the existence of nano-features such as twins, martensite, or dimples (Hojná, 2017).

Intergranular fracture by channeled slip To account for the observations of intergranular fracture at moderate temperature (room temperature and above) and low strain rates ($\dot{\varepsilon} = 10^{-2}$ s^{-1} and below), a mechanism relying on dislocation channeling was put forward. This fracture mode is thus explained by the localization of plastic strain in clear bands that could concentrate stresses upon grain boundaries that they cross. Decohesion along these lines then happens simultaneously and merges along the grain boundary. It explains that this intergranular fracture mode shares the affinities of the dislocation channeling process: predominant appearance at the edges of tensile specimens (Fig. I.36a) and at high temperatures. As in the previous fracture mode, intergranular fracture can be mixed with

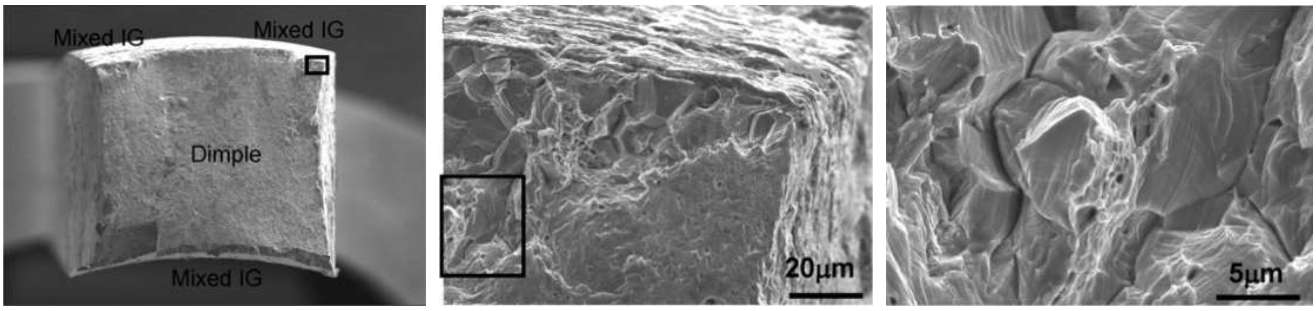

(a) (b) (c)

FIGURE I.36: Fracture surface of 316 thimble tubes irradiated to 73 dpa and fractured by slow tensile testing ($\dot{\varepsilon} = 7 \cdot 10^{-8}$ s^{-1}) at 320 °C (Fukuya et al., 2008).

transgranular fracture (Fig. I.36b) and intergranular facets present parallel steps (Fig. I.36c) (Fukuya et al., 2008). Given this observation, it seems that this fracture mechanism corresponds closely to the intergranular fracture by planar slip noticed in aluminum alloys (see Figs. I.14c and I.15a) (Kuramoto et al., 1996). For instance, this fracture mode was mainly observed in PWR flux thimble tubes (15% cold-worked 316 steel) irradiated to 73 dpa and tested at 320 °C and in a PWR rod control cluster assembly (304 steel) irradiated to 7 dpa and tested in argon at 310 °C (Fukuya et al., 2008; Hojná, 2017). Intergranular fracture in 21Cr-6Ni-9Mn austenitic steel at room temperature due to the presence of solute helium atoms can also be understood in the context of this failure mechanism (Rawl et al., 1980). However, the process described in this section is challenged by some authors who contest that dislocation pile-up can occur due to dislocation channeling (Griffiths, 2023), and the role of helium bubbles is still to be clarified. Indeed, the latter may promote an intergranular ductile fracture at the nano-scale.

Helium-induced intergranular ductile fracture

Room temperature helium embrittlement In PWR conditions, helium bubbles are observed in 316 austenitic steels irradiated to doses above 1 dpa (Fukuya et al., 2001; Fujii et al., 2001; Fukuya and Fujii, 2001; Fukuya et al., 2006). Whatever the irradiation dose, bubbles are homogeneously present in the material without notable segregation at grain boundaries; the bubble size ranges from 0.5 to 1.5 nm with an average size of 1 nm (Fukuya et al., 2006). This cavity structure differs significantly from the one seen in 316 steel irradiated in a fast neutron reactor (Fukuya and Fujii, 2001). However, recent evidence of favorable nucleation of helium bubbles of 2 nm size at grain boundaries as well as bubble-free zones was provided by the examination of a 316 steel PWR thimble tube irradiated at 35 dpa and 70 dpa (Edwards et al., 2009); in the long run, such bubbles might promote intergranular ductile fracture. Two possible thresholds have been evidenced by studies on helium-implanted 316 steel tested at low temperatures:

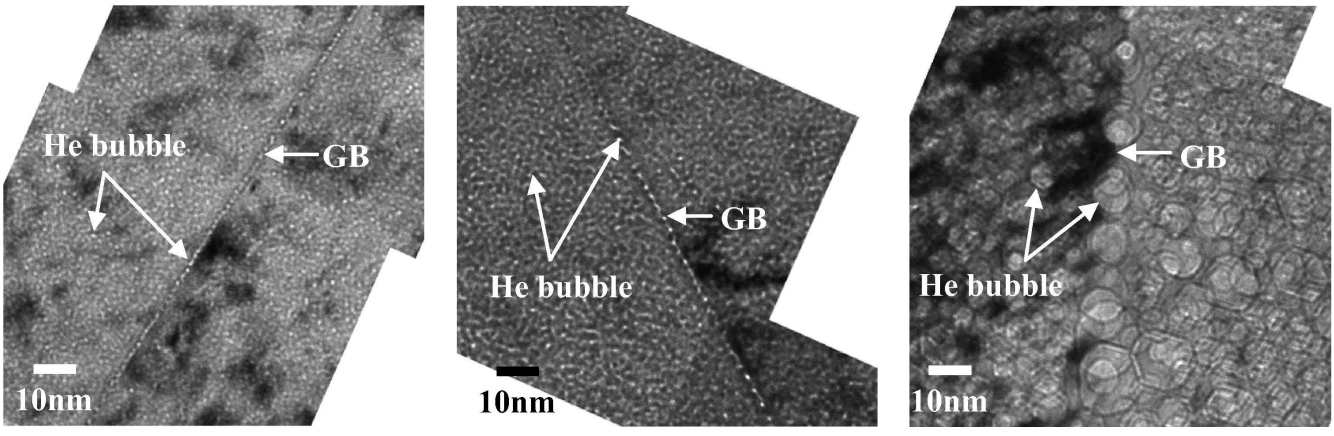

(a) No annealing, 1.2 at.% He (b) No annealing, 6 at.% He (c) 650°C annealing, 6 at.% He

FIGURE I.37: Cross-sectional TEM micrographs of grain boundaries of 316 steel irradiated at room temperature with various helium concentrations (Miura et al., 2015).

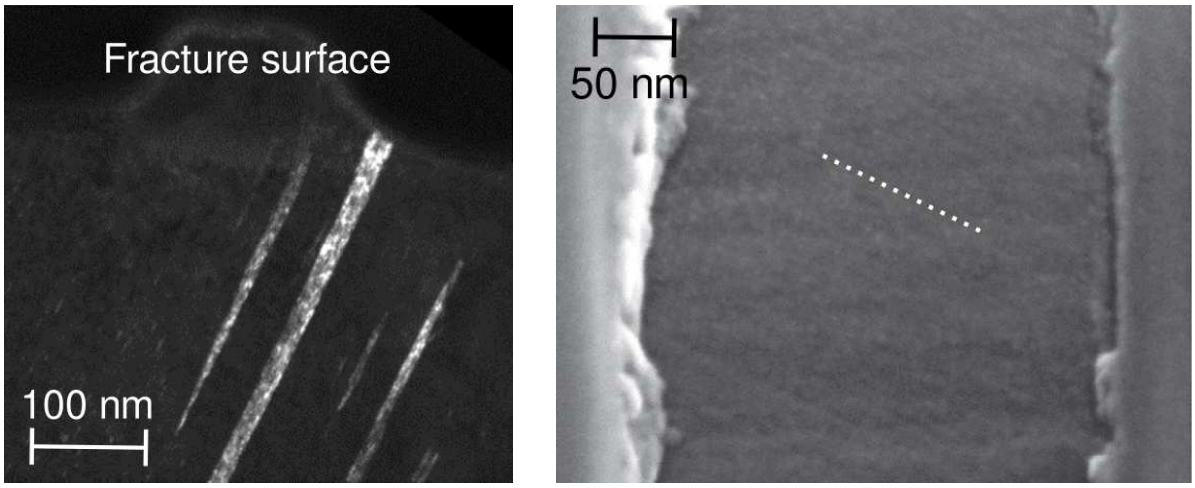

(a) (b)

FIGURE I.38: Examination of the fracture surface of micro-sample with 10% helium atomic content: (a) TEM observation of deformation twinning; (b) SEM observation of small shear steps on top of the fracture surface (Miura et al., 2015).

1. Presence of helium bubbles at grain boundaries above 2 at. % has been reported to cause intergranular fracture of 316 steel (Miura et al., 2015). In LWR components, helium generation is not expected to exceed 2500 appm at doses lower than 60 dpa (Fukuya et al., 2006), which is one order of magnitude inferior to this threshold concentration. However, the threshold may be reduced in neutron-irradiated austenitic steel by the contribution of other factors — irradiation hardening, oxidation and hydrogen content as in irradiation-assisted stress corrosion cracking (IASCC), annealing etc.

2. Bennetch and Jesser (1981) has shown that grain boundary bubbles with a diameter inferior to 4 nm and a spacing inferior to 30 nm were required to trigger fractures that were partly intergranular. The study of Miura et al. (2015) is consistent with this result: small helium bubble size (less than 2 nm diameter) and close spacing (4 nm) were seen to promote a fracture mode without dimples (Fig. I.37a,b).

It seems that condition #1 is harsher than condition #2 since condition #1 usually implies condition #2 but not the other way around (Miura et al., 2015). Thus, it can be envisioned that neutron-irradiated stainless steels may fulfill condition #2 under operating LWR conditions, which could explain the intergranular fracture occurrences seen in the two previous sections. Indeed, helium embrittlement is not incompatible with localized twinning, as also evidenced by the study of Miura et al. (2015) which reported nano-twins along one of the fractured grain boundaries (Fig. I.38a) and shear traces on the intergranular facets (Fig. I.38b).

Finally, it is worth noting that intergranular ductile fracture was undeniably noticed in the study of Miura et al. (2015) for farther (9 nm) and larger bubbles (5-6 nm diameter) — thus not strictly abiding by condition #2 — obtained after subsequent annealing (Fig. I.37c). They were associated with a fracture surface that displayed apparent ductile features believed to be coalesced cavities ($\xi \approx 10^7$). This observation may be useful to rationalize the fracture with smaller bubbles (for which these features may be too small to be observed) or on the contrary may stem from a distinct fracture process.

Welding of helium-embrittled components The lifetime extension of second-generation nuclear reactors has raised issues about repairing and replacing irradiated structural components. Thus, research has been conducted on welding irradiated light-water reactor materials. However, conventional gas tungsten arc (GTA) welding generates high temperatures and important thermal stresses in heat-affected zones that trigger intergranular helium bubble nucleation, growth, and coalescence. In 316 steels, intergranular fracture in the HAZ occurs at helium concentrations as low as 1 appm (Li et al., 2011). Vanadium alloy V-15Cr-5Ti (Lin and Braski, 1994) and ferritic 12Cr-1Mo-VW (Sandvik HT-9) (Lin and Chin, 1991) were also reported to display intergranular fracture during welding. Fracture usually happens at a distance of one to three grains from the melted zone and follows a path parallel to the weld (Fig. I.39a). Cracking occurs one second after the weld pool passage. The facets of intergranular fracture surfaces

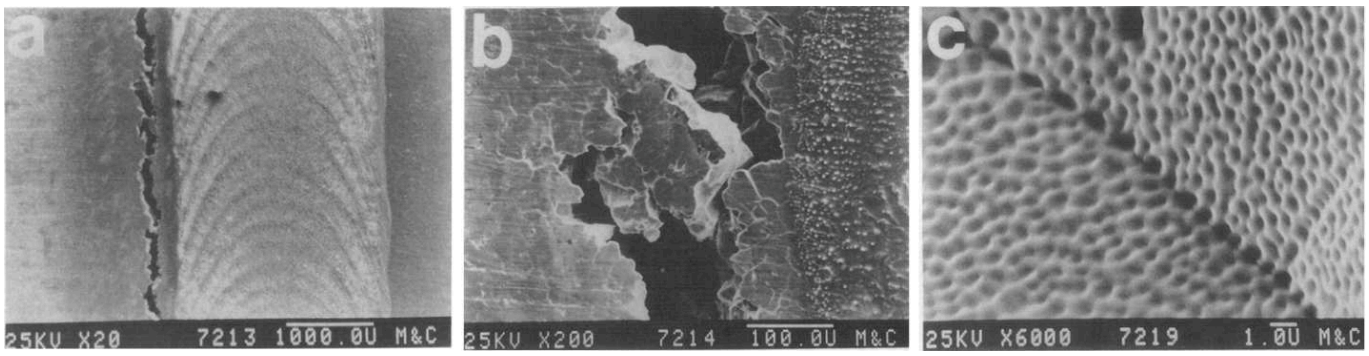

FIGURE I.39: SEM micrographs of HAZ intergranular cracking in a type 316 steel containing 2.5 appm of helium (Lin et al., 1990).

display fine dimples of 1 μm diameter (Fig. I.39c), testifying to the occurrence of void growth and coalescence. Based on observations on 316 stainless steels provided by the previous studies, ξ is estimated to be around 0.01 at the onset of void growth and reaches 20 at fracture. Void growth is therefore initially controlled by vacancy diffusion, but void coalescence is believed to fall within the plastic domain. It means that HAZ cracking is likely to be intergranular ductile fracture from cavities originating from grain boundary bubbles which grew due to vacancy diffusion (Li et al., 2011). It seems that the vacancy diffusion process can be separated into three distinct regimes (Fig. I.40): in regime I, compressive stress opposes vacancy diffusion; in regime II, thermal diffusion is the only mechanism of vacancy condensation; in regime III, tensile stress enhance the growth of helium bubbles (Lin et al., 1990).

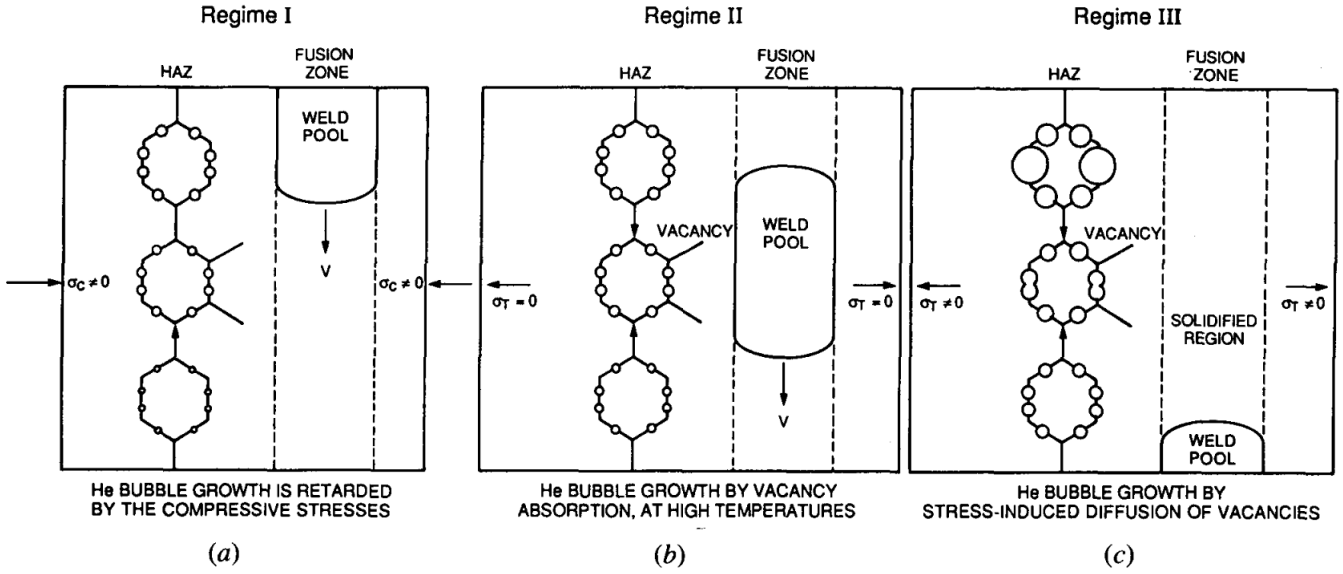

FIGURE I.40: Void growth by vacancy diffusion during GTA welding of an irradiated material containing intergranular helium bubbles (Lin et al., 1990).

To alleviate the difficulties arising from GTA welding, alternative techniques such as low-heat gas metal arc (GMA) welding, stress-modified welding and Yttrium Aluminum garnet (YAG) laser welding are under testing, with promising results (Kuroda, 2000; Wang et al., 1996; Li et al., 2011).

Summary

Intergranular ductile fracture can be witnessed in many engineering alloys, irradiated or not, under various loading conditions. For testing at low homologous temperature, the occurrence of this fracture mode was seen to be associated with the following microstructure types:

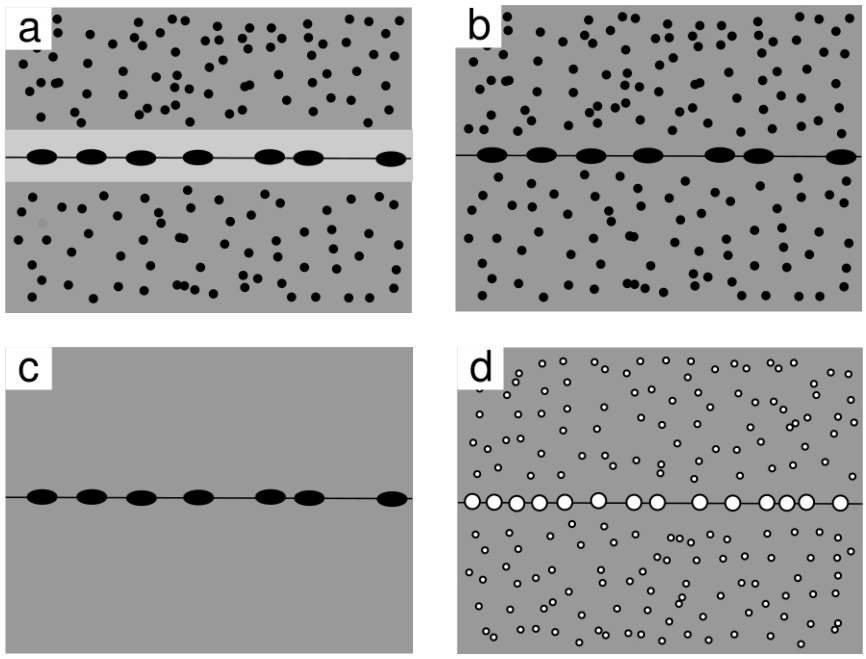

In each of these simplified micro-structures, the material parameters that control the prevalence of ductile fracture and the related engineering alloys are listed below:

(a) **Precipitation-hardened alloy with precipitate-free zone:** important parameters are precipitate-free zone width, intergranular particle size and spacing, easiness of nucleation at grain boundary particles, yield strength mismatch between precipitate-free zone and grain interiors, shearability of intragranular precipitates (?). The corresponding materials are aluminum alloys, metastable β-titanium alloys, nickel superalloys and magnesium alloys.

(b) **Precipitation-hardened alloy without precipitate-free zone:** important parameters are intergranular particle size and spacing, easiness of nucleation at grain boundary particles, strength of grain interiors (?), shearability of intragranular precipitates (?). The corresponding materials are metastable β-titanium alloys, nickel superalloys and aged austenitic stainless steels.

(c) **Solid solution alloy with intergranular particles :** important parameters are intergranular particle size and spacing, easiness of nucleation at grain boundary particles. The corresponding materials are austenitic stainless steels and gold-platinum alloys.

(d) **Helium-embrittled alloy:** important parameters are size and spacing of grain boundary helium bubbles, propensity to experience localized twinning (?) or dislocation channeling (?). The corresponding materials are neutron-irradiated austenitic stainless steels and nickel superalloys with high thermal-to-fast spectrum as well as helium-implanted austenitic stainless steels and nickel superalloys.

As all the mechanisms of intergranular ductile fracture have not yet been uncovered experimentally, the effect of some parameters of the previous list is still hypothetical. As could be expected, parameters of interest are related to void nucleation (nucleation potential of particles), growth (particle and bubble size), coalescence (particle and bubble spacing) or plasticity characteristics (precipitate-free zone existence, yield strength, deformation mechanisms). Depending on those parameters, the aforementioned alloys can experience intergranular ductile fracture, transgranular ductile fracture or a mix of these two failure modes. Intergranular ductile fracture can also happen for high homologous temperatures, but plastic void growth is usually difficult to separate from diffusive void growth, so each particular case should be analyzed with care to determine the failure mode.

Having identified the materials and the mechanisms involved in intergranular ductile fracture, it is now necessary to model this phenomenon as well as the competing process of transgranular ductile fracture; this is the object of the next section.

3 Simulation and modeling of ductile fracture

3.1 Introduction

In this section, the current state of simulation and modeling of ductile fracture relying on micro-mechanics is briefly reviewed. As underlined previously, ductile fracture occurs by successive (or simultaneous) void nucleation, growth, and coalescence.

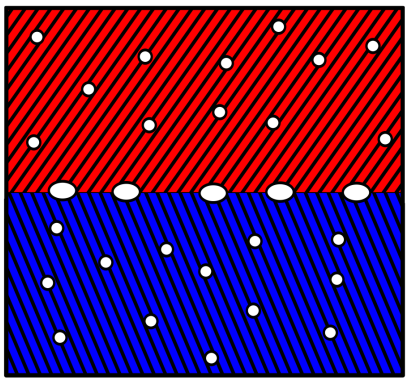

FIGURE I.41: Porous bi-crystal.

Physically-based modeling or simulation of void nucleation being still elusive, two main approaches exist towards that process: the first one is the use of phenomenological criteria that can be stress-based or strain-based (see Benzerga and Leblond (2010)); the second one is to consider that voids nucleate immediately. The latter is valid when dealing with materials with pre-existing cavities (*e.g.* porous materials, irradiated materials) or with loadings involving sufficient stresses/strain rates to induce quick nucleation (Pineau et al., 2016). The void nucleation stage is thus described by a set of initial porosity parameters which will be an input of the detailed void growth and coalescence mechanical model. This framework is adopted here; thus, only the void growth and coalescence stages are considered in the following. As a result, the situation of interest in this work is that of a porous polycrystal with preexisting cavities in grain interiors and at grain boundaries, as shown in Fig. I.41.

Due to the required physical grounding, damage mechanics, which do not resort to a microscopic description of fracture and often rely on a single damage variable to account for this gradual process, are excluded from this review. Instead, it will be devoted to the micro-mechanical modeling of ductile fracture, usually based on considering unit cells.

3.2 Porous unit-cells

When simulating or modeling the mechanical behavior of a material with a given microstructure, it is useful to consider a representative (or statistical) volume element whose behavior will be assimilated to that of the studied material. The simpler the unit cell is, the more straightforward simulation or modeling will be, but it will come at the expense of material representativeness. In the context of ductile fracture studies, these unit-cells contain one or more voids (or cracks) and are called *porous unit-cells* (see Benzerga and Leblond (2010)). In this work, only porous unit cells with a single void are considered, which is associated with an idealized microstructure containing a regular array of voids (see Fig. I.42). However, it should be noted that random or clustered distribution of voids — which are more realistic — can induce deviations from the regular distribution (*e.g.* Hure (2021), Cadet et al. (2021), and Vishnu et al. (2023))

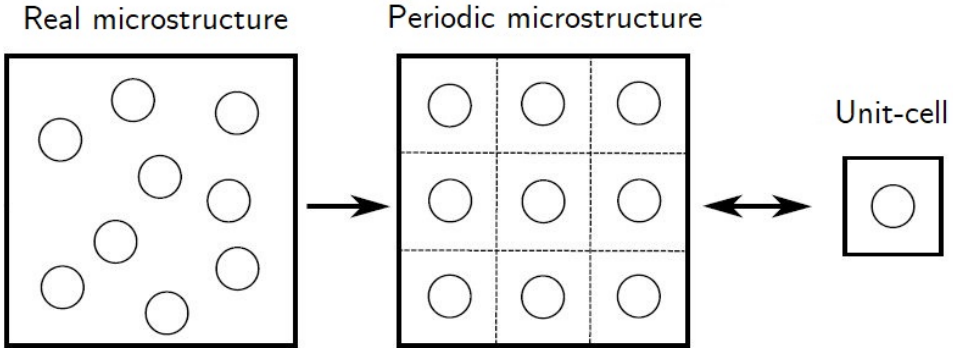

FIGURE I.42: Cubic unit-cell obtained through the approximation of a real porous microstructure by a periodic microstructure with a cubic array of cavities (Ling, 2017).

Unit cells considered in the micro-mechanical approach of ductile fracture are usually loaded with a Cauchy stress tensor $\boldsymbol{\Sigma}$ whose component ratios are imposed; this loading is usually referred to as *proportional stress loading* (Benzerga and Leblond, 2010). On the one hand, when the imposed stress tensor is diagonal — *i.e.* its principal

components are along the reference axes of the unit-cell —, it is defined by two dimensionless factors: the stress triaxiality ratio T and the Lode parameter L (or alternatively the Lode angle θ). Their definitions are the following:

$$T = \frac{\Sigma_{\mathrm{m}}}{\Sigma_{\mathrm{eq}}^{\mathrm{vM}}} \ , \quad L = \frac{2\Sigma_{\mathrm{II}} - \Sigma_{\mathrm{I}} - \Sigma_{\mathrm{III}}}{\Sigma_{\mathrm{I}} - \Sigma_{\mathrm{III}}} \ , \quad \cos 3\theta = \frac{27}{2} \frac{\det\left(\boldsymbol{\Sigma} - \Sigma_{\mathrm{m}} \boldsymbol{I}\right)}{\left(\Sigma_{\mathrm{eq}}^{\mathrm{vM}}\right)^3} \tag{I.3}$$

where Σ_{m} is the hydrostatic stress, $\Sigma_{\mathrm{eq}}^{\mathrm{vM}}$ is the von Mises equivalent stress and $\Sigma_{\mathrm{I}} \geq \Sigma_{\mathrm{II}} \geq \Sigma_{\mathrm{III}}$ are the ordered eigenvalues of $\boldsymbol{\Sigma}$. The family of stress tensors associated with (T, L) is then:

$$\boldsymbol{\Sigma} \propto \begin{pmatrix} \cos\theta + \frac{3}{2}T & 0 & 0 \\ 0 & -\cos\left(\theta + \frac{\pi}{3}\right) + \frac{3}{2}T & 0 \\ 0 & 0 & -\cos\left(\theta - \frac{\pi}{3}\right) + \frac{3}{2}T \end{pmatrix} \tag{I.4}$$

On the other hand, when the stress tensor is arbitrary, it is defined by T, L, and the rotation matrix involved in its diagonalization[4]

Explicit simulation of the mechanical behavior of a unit cell can be performed using a finite-element modeling or fast Fourier transform (Moulinec and Suquet, 1998) solver. They can be either conducted within finite strain (*i.e.* with geometry update) or small strain (*i.e.* without geometry update) theories according to the phenomenon investigated. The former is used to compute the complete mechanical behavior of the material represented by the unit-cell (*e.g.* Koplik and Needleman (1988)) whereas the latter is used to compute the yield stress of that same material (*e.g.* Madou and Leblond (2012b)). Unit cells are useful for modeling ductile fracture, as mechanical analysis can be performed on these simple geometries to derive analytical models, which will be seen later.

Micro-mechanical studies on ductile fracture can be divided according to the type of plasticity used for the matrix material: either phenomenological plasticity (*e.g.* Mises (1913) or Hill (1948) plasticity) or crystal plasticity. Approaches related to the first case are treated in a first part, and the ones belonging to crystal plasticity are gathered in a second part.

3.3 Matrix with phenomenological plasticity

The most commonly used phenomenological plasticity models are those proposed by Mises (1913) and Hill (1948). The first one accounts for isotropic materials whereas the second concerns anisotropic materials. On the one hand, von Mises' yield criterion writes:

$$\phi_{\mathrm{vM}} = \sigma_{\mathrm{eq}}^{\mathrm{vM}} - \sigma_0 \quad \text{where} \quad \sigma_{\mathrm{eq}}^{\mathrm{vM}} = \sqrt{\frac{3}{2}\boldsymbol{\Sigma} : \mathbb{K} : \boldsymbol{\Sigma}} \tag{I.5}$$

where $\mathbb{K}$ is the fourth-order deviatoric projector and σ_0 is the yield stress. On the other hand, Hill's yield criterion writes:

$$\phi_{\mathrm{H}} = \sigma_{\mathrm{eq}}^{\mathrm{H}} - \sigma_0 \quad \text{where} \quad \sigma_{\mathrm{eq}}^{\mathrm{H}} = \sqrt{\frac{3}{2}\boldsymbol{\Sigma} : \mathbb{H} : \boldsymbol{\Sigma}} \tag{I.6}$$

where $\mathbb{H}$ is the fourth-order Hill tensor associated with the anisotropy of the material and σ_0 is the yield stress. Both of these criteria are used in an associated framework, which means that the plastic strain rate $\boldsymbol{d}$ derives from the expression of the criterion through the normality rule:

$$\boldsymbol{d} = \dot{p} \frac{\partial \phi}{\partial \boldsymbol{\Sigma}} \tag{I.7}$$

where $\dot{p}$ is the plastic multiplier.

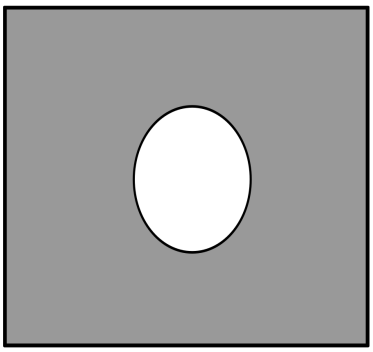

FIGURE I.43: Porous material whose matrix follows phenomenological plasticity.

The aforementioned plasticity yield criteria are relevant to model the macroscopic behavior of large polycrystals in a phenomenological approach. Yet, many models of ductile fracture consider Mises or Hill associated plasticity

[4]Remember that the symmetry of the stress tensor makes it diagonalizable.

for the matrix material (see Fig. I.43) (Benzerga and Leblond, 2010). These models are applicable for polycrystalline materials where voids are significantly larger than the grain size, so that the matrix material at the scale of the voids is composed of many grains and can be described by conventional plasticity models. Alternatively, these models are used to describe the average behavior of cavities at the crystal scale, but with less physical grounding.

3.3.1 Models of transgranular ductile fracture

The state of the art of physically-based transgranular ductile fracture modeling is described in a handful of reviews (Besson, 2010; Benzerga and Leblond, 2010; Pineau et al., 2016; Benzerga et al., 2016). The models described therein account for the micro-mechanics of fracture through homogenization over a unit cell of the porous material to obtain a plastic yield criterion. Following a generic formulation inspired by non-porous models and proposed by Besson (2010), a yield criterion i can be expressed as:

$$\phi_i = \sigma_i^* - \sigma_0 \tag{I.8}$$

where σ_0 is the yield stress and σ_i^* is an effective scalar matrix stress implicitly defined by an equation $S_i(\sigma_i^*, \boldsymbol{\Sigma}, \alpha_j) = 0$ where (α_j) are internal variables which describe void geometry, void distribution, and matrix characteristics. The normality rule (Eq. I.7) is usually kept. Homogenized model closure is obtained by giving evolution laws for internal variables (α_j). By establishing plastic criteria for void growth and coalescence, the successive stages of ductile fracture can be modeled by gradually activating these yield functions.

Void growth Gurson established the most popular void growth model through the theoretical and numerical limit analysis of a spherical hollow sphere contained in a perfect-plastic von Mises matrix (Gurson, 1977). Many improvements have been proposed to generalize this yield criterion and its associated flow rule: *e.g.*, calibration parameters (Tvergaard, 1982; Tvergaard and Needleman, 1984), spheroidal (Gologanu et al., 1997) and ellipsoidal void shape (Madou and Leblond, 2012a), isotropic and kinematic hardening (Mear and Huntchinson, 1985; Leblond et al., 1995; Morin et al., 2017), interfacial stresses (Dormieux and Kondo, 2010), inhomogeneous boundary strain rate (Gologanu et al., 1997), void shear (Nahshon and Hutchinson, 2008), Hill matrix (Benzerga and Besson, 2001; Monchiet et al., 2008; Keralavarma and Benzerga, 2010; Morin et al., 2015c), Tresca matrix (Cazacu et al., 2014), Mohr-Coulomb matrix (Anoukou et al., 2016) and matrix strain gradients (Wen et al., 2005). The unit cell that was used to derive those models is shown in Fig. I.44. A generalized form of Gurson yield criterion is obtained with σ_{g}^* defined through the following expression:

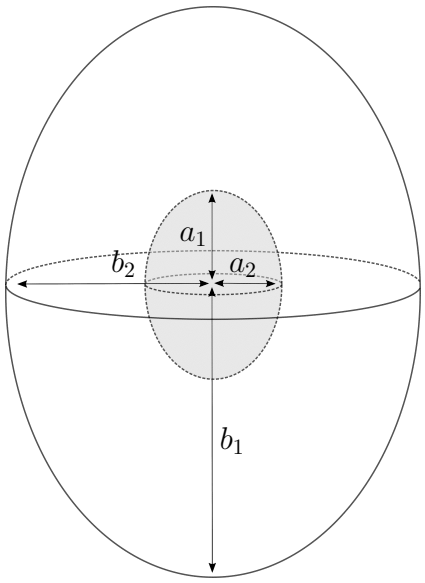

FIGURE I.44: Spheroidal unit cell with a spheroidal cavity used in the limit analysis of void growth.

$$S_{\mathrm{g}}(\sigma_{\mathrm{g}}^*, \boldsymbol{\Sigma}, \alpha_j) \equiv A(\alpha_j) \left(\frac{\mathcal{F}(\boldsymbol{\Sigma})}{\sigma_{\mathrm{g}}^*} \right)^2 + 2B(\alpha_j) \cosh\left(\frac{3}{2} C(\alpha_j) \frac{\mathcal{G}(\boldsymbol{\Sigma})}{\sigma_{\mathrm{G}}^*} \right) - D(\alpha_j) \tag{I.9}$$

where $\boldsymbol{\Sigma} = \frac{1}{V} \int_V \boldsymbol{\sigma} \mathrm{d}V$ is the macroscopic Cauchy stress tensor, (α_j) a set of microstructural parameters describing void geometry (*e.g.*, void volume fraction $f = (a_1 a_2^2)/(b_1 b_2^2)$, void aspect ratio $w = a_1/a_2$, void orientation) and matrix anisotropy (*e.g.* Hill tensor $\mathbb{H}$), $\mathcal{F}$ and $\mathcal{G}$ scalar equivalent stresses and A, B, C and D scalar functions that only depend on microstructural parameters.

Table I.2 details a few interesting versions of this criterion. In the GTN model, calibration parameters q_1 and q_2 increase the agreement to numerical simulations (Tvergaard and Needleman, 1984). In the GLD model, functions A, B, η and the second porosity g depend on the void aspect ratio w, and Σ_{h} is a linear combination of the components of $\boldsymbol{\Sigma}$ whose coefficients vary with w (Gologanu et al., 1994). The original criterion of (Gurson, 1977) is plotted in Fig. I.46.

Version	$\mathcal{F}$	$\mathcal{G}$	A	B	C	D
Gurson (1977)	$\Sigma_{\text{eq}}^{\text{vM}}$	Σ_{m}	1	f	1	$1+f^2$
Tvergaard and Needleman (1984)	$\Sigma_{\text{eq}}^{\text{vM}}$	Σ_{m}	1	$q_1 f$	q_2	$1+(q_1 f)^2$
Gologanu et al. (1994)	$\Sigma_{\text{eq}}^{\text{vM}}+\eta(w)\Sigma_{\text{h}}$	Σ_{h}	$A(w)$	$(g(w)+1)(g(w)+f)$	$C(w)$	$(g(w)+1)^2+(g(w)+f)^2$
Benzerga and Besson (2001)	$\Sigma_{\text{eq}}^{\text{H}}$	Σ_{m}	1	f	$C(\mathbb{H})$	$1+f^2$

TABLE I.2: Scalar equivalent stresses and multipliers for various versions of Gurson model.

Void coalescence Similarly to Gurson, Thomason set the path for internal necking modeling through limit-load analysis of a porous unit-cell containing a square-prismatic void (Thomason, 1985). In this study, he found a critical stress upon which localization of plastic deformation occurs in the intervoid ligament, triggering necking. Interpreting this maximum stress in the context of porous material homogenization yields a plastic criterion for void coalescence. Many improvements have been proposed to generalize this yield criterion: *e.g.* rigorous upper bounds (Benzerga and Leblond, 2014; Morin et al., 2015b), matrix anisotropy (Keralavarma and Chockalingam, 2016; Morin, 2012), flat voids (Hure and Barrioz, 2016), elliptic-cylindrical voids (Barrioz et al., 2018a), interfacial stresses (Gallican and Hure, 2017), hardening (Pardoen and Hutchinson, 2000; Scheyvaerts et al., 2011), secondary voids (Fabregue and Pardoen, 2008) and shear-assisted coalescence (Scheyvaerts et al., 2011; Tekoğlu et al., 2012; Torki et al., 2015; Torki et al., 2017). Most models were derived using kinematic limit analysis on the unit-cell shown in Fig. I.45. A generalized form of coalescence yield criterion under combined tension and shear is obtained with σ_{c}^* defined through the following expression, $\underline{e}_3$ being normal to the coalescence plane:

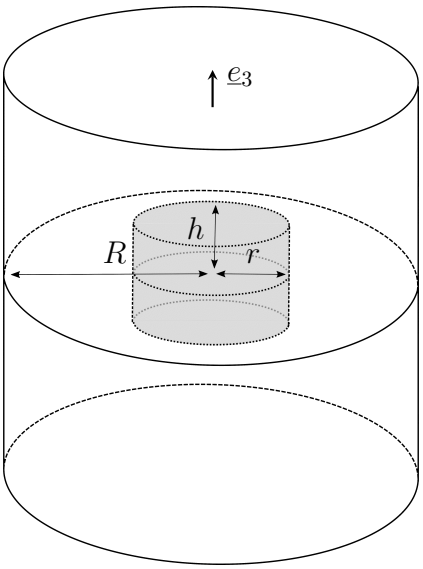

FIGURE I.45: Cylindrical unit cell with coaxial cylindrical cavity used in the limit analysis of void coalescence.

$$S_{\text{c}}(\sigma_{\text{c}}^*,\boldsymbol{\Sigma},\alpha_j)\equiv\left[\frac{1}{A(\alpha_j)}\left(\frac{|\Sigma_{33}|}{\sigma_{\text{c}}^*}-B(\alpha_j)\right)_+\right]^2+\left[C(\alpha_j)\frac{\mathcal{H}\left(\widetilde{\boldsymbol{\Sigma}}\right)}{\sigma_{\text{c}}^*}\right]^2-1 \tag{I.10}$$

Version	$\mathcal{H}$	A	B	C
Thomason (1985)	—	$(1-\chi^2)\left[0.1\left(\frac{1-\chi}{\chi w}\right)^2+1.2\frac{1}{\sqrt{\chi}}\right]$	0	0
Benzerga and Leblond (2014)	—	$\frac{1}{\sqrt{3}}\left[2-\sqrt{1+3\chi^4}+\ln\frac{1+\sqrt{1+3\chi^4}}{3\chi^2}\right]$	$\frac{\chi^3-3\chi+2}{3\sqrt{3}\chi w}$	0
Torki et al. (2015)	$\widetilde{\Sigma}_{\text{eq}}^{\text{vM}}$	$\frac{1}{\sqrt{3}}\left[2-\sqrt{1+3\chi^4}+\ln\frac{1+\sqrt{1+3\chi^4}}{3\chi^2}\right]$	$\frac{\chi^3-3\chi+2}{3\sqrt{3}\chi w}$	$\frac{1}{1-\chi^2}$
Keralavarma and Chockalingam (2016)[a]	$\widetilde{\Sigma}_{\text{eq}}^{\text{H}}$	$a\left[\sqrt{b^2+1}-\sqrt{b^2+\chi^4}+b\ln\left(\frac{1}{\chi^2}\frac{b+\sqrt{b^2+\chi^4}}{b+\sqrt{b^2+1}}\right)\right]$	0	$\frac{1}{1-\chi^2}$

TABLE I.3: Scalar equivalent stresses and multipliers for various versions of the yield function for void coalescence in layers.

[a] The model is given here in a simplified quadratic form, see the original publication for the detailed hyperbolic version.

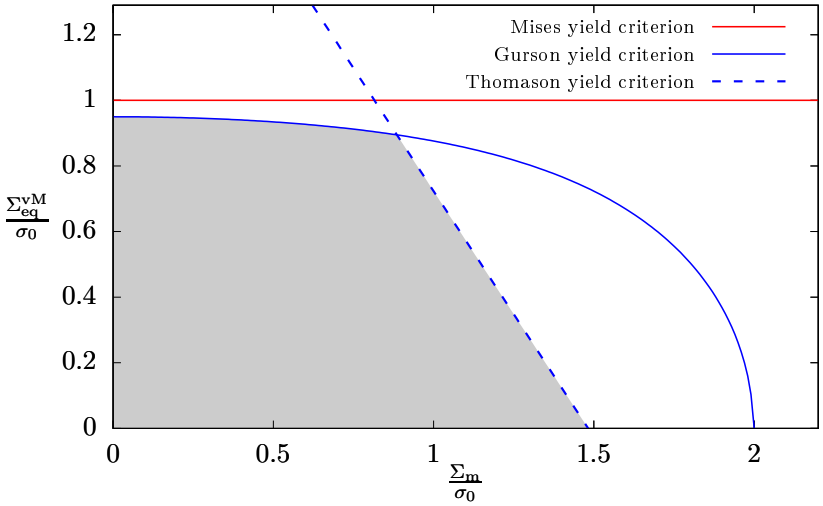

FIGURE I.46: Comparison of the yield surface for a pristine isotropic material modeled by the Mises (1913) criterion and the yield surface (shown in gray) of a porous isotropic material with $f = 0.05$ ans $w = 1$ whose void growth criterion is that of Gurson (1977) and whose coalescence follows Thomason (1985) criterion. The surfaces are plotted in the meridian plane (Σ_{eq}, Σ_m).

In the previous equation, $(\cdot)_+ = \max(0, \cdot)$, (α_j) is a set of microstructural parameters describing void geometry (*e.g.*, ligament size ratio $\chi = r/R$, void aspect ratio $w = h/r$) and matrix anisotropy (*e.g.* Hill tensor $\mathbb{H}$), $\mathcal{H}$ is a scalar equivalent stress depending on the shear stress tensor $\widetilde{\boldsymbol{\Sigma}}$ and A, B and C are scalar functions that only depend on microstructural parameters. Table I.3 details a few interesting versions of this criterion, that may $(C \neq 0)$ or may not $(C = 0)$ take into account shear-assisted coalescence. In the model of Keralavarma and Chockalingam (2016) designed to account for matrix anisotropy, a is a function of $\mathbb{H}$ and b depends simultaneously on w and $\mathbb{H}$. Finally, note that to apply the results of Eq. I.10 and Table I.3 to a periodic array of cavities with other unit-cell geometries than Fig. I.45, the ligament size ratio χ should be defined by $\chi = \sqrt{f_b}$, f_b being defined as the void volume fraction in the coalescence band (Torki et al., 2015). The original criterion of Thomason (1985) is plotted in Fig. I.46.

Combined void growth and coalescence Using limit analysis on Fig. I.45 with appropriate velocity fields, yield criteria accounting for both void growth and void coalescence can be derived for an isotropic von Mises matrix. They cover void growth and internal necking (Morin et al., 2016a), void growth and coalescence under combined tension and shear (Torki, 2019), and void growth together with coalescence in columns (Torki et al., 2023).

Homogenized model Prediction of yield surfaces for porous materials is only the first step in modeling ductile fracture. As a matter of fact, microstructure parameters evolve under plastic flow, gradually modifying the yield surface. Accounting for this coupling is paramount to predict the behavior of materials until failure, and therefore to estimate ductility. Thus, the yield criterion must be supplemented with evolution laws for the microstructure. Various homogenized models of ductile fracture combining void growth and coalescence in layers have been proposed in the literature for isotropic materials (Benzerga and Leblond, 2010; Keralavarma, 2017; Torki and Benzerga, 2018b; Vishwakarma and Keralavarma, 2019; Reddi et al., 2019; Keralavarma et al., 2020; Torki et al., 2021; Torki and Benzerga, 2022).

3.3.2 Simulation of intergranular ductile fracture

Building on the successful development of micro-mechanical models dedicated to transgranular fracture, Gurson's model and its variants were used for intergranular ductile fracture. The first application that motivated such studies was the fracture of precipitation-hardened aluminum alloys. Becker et al. (1989) conducted the first of these works by simulating the intergranular ductile fracture of a polycrystal using finite element modeling. Grain interiors were simplified as an isotropic pristine material whereas grain boundaries were assimilated to an isotropic porous material following the GTN model. A significant issue is the fact that transgranular fracture models rely on volume homogenization whereas grain boundaries are two-dimensional domains; Becker et al. (1989) recommended setting the width of the homogenized grain boundary microstructure to the average grain boundary precipitate spacing. However, this length can also be linked to the precipitate-free zone width, if any (Pardoen et al., 2003).

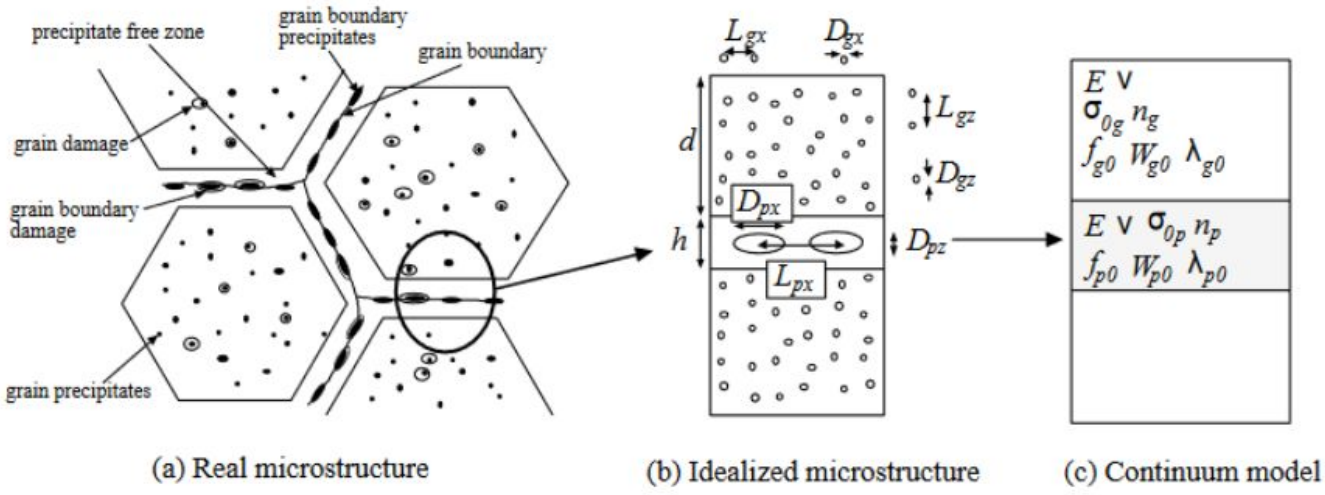

FIGURE I.47: Description of: (**a**) the real microstructure of precipitation-hardened alloys and their damage mechanisms; (**b**) the idealized two-band microstructure and (**c**) the continuum bilayer micromechanical model (Pardoen et al., 2003).

In a related approach, a two-band model was proposed for simulating the competition between intergranular and transgranular ductile fracture by considering the grain boundary zone and the grain interiors as porous isotropic elastoplastic materials with isotropic hardening (Pardoen et al., 2003). Material parameters — such as yield strength, initial porosity and hardening capacity — differed between the grain boundary and grain interiors to account for dissimilar mechanical properties (Fig. I.47). In the case of precipitation-hardened alloys, these differences were mainly due to the existence of precipitate-free zones around grain boundaries. In the original study of Pardoen et al. (2003), the growth yield function used was the GLD model (Gologanu et al., 1997), whereas the coalescence criterion was an extension of Thomason's yield function to strain hardening materials (Pardoen and Hutchinson, 2000). The bilayer homogenized model was validated against two-band porous unit-cell simulations and showed satisfactory agreement. Thus, its predictions on the competition between transgranular and intergranular fracture are worth noting: it was concluded that the most important microstructural parameters are on the one hand, the ratio of initial grain boundary width to the initial intergranular void spacing, and on the other hand, the grain boundary void coverage; both increase the likeliness of intergranular fracture. Moreover, grain boundary void growth is promoted by increasing the yield strength inside the grains as well as decreasing the grain boundary hardening capacity. However, no effect of grain boundary width and initial intergranular void aspect ratio w on this competition was found. Transgranular fracture was characterized by a higher ductility upon which the grain boundary void coverage was without effect. Overall, this work shed new light on the effect of heat treatment and quenching speed on promoting intergranular fracture in precipitation-hardened alloys (Pardoen et al., 2003). After this qualitative study, Pardoen's bilayer model was used to study quantitatively the competition between transgranular and intergranular fracture in polycrystalline aggregates of typical aluminum precipitation-hardened alloys (Pardoen et al., 2010).

A similar method was adopted for an aluminum AA7075-T651 alloy with a periodic network of hexagonal grains loaded with various stress triaxialities and Lode parameters (Fourmeau et al., 2015). Furthermore, intergranular crack growth in metastable β-titanium alloys with continuous grain boundary α-phase was investigated using finite element where α- and β-phases both followed GTN model. It enabled a careful study of the decoupled effects of microstructural parameters and hinted at increased ductility when the grain boundary α-phase continuity was below 80% (Osovski et al., 2015). In a subsequent study, the effect of void shearing was also incorporated in the micromechanical model of lamellar β-titanium (Fig. I.48) (Li et al., 2017). In an indirect approach, bilayer modeling was also used to conduct theoretical assessments such as evaluating intergranular crack propagation resistance prediction through a discrete graph of grain boundaries in the J-resistance space. It was found that the graph model reproduced qualitatively the predictions of the bilayer model and thus can be used to optimize grain size in the engineering of tough bimodal materials (Molkeri et al., 2020).

When grain boundary damage is closer to cracks than cavities, the aforementioned bilayer model is no longer suited to simulate intergranular ductile fracture. Therefore, cracked two-band unit-cell simulations were performed

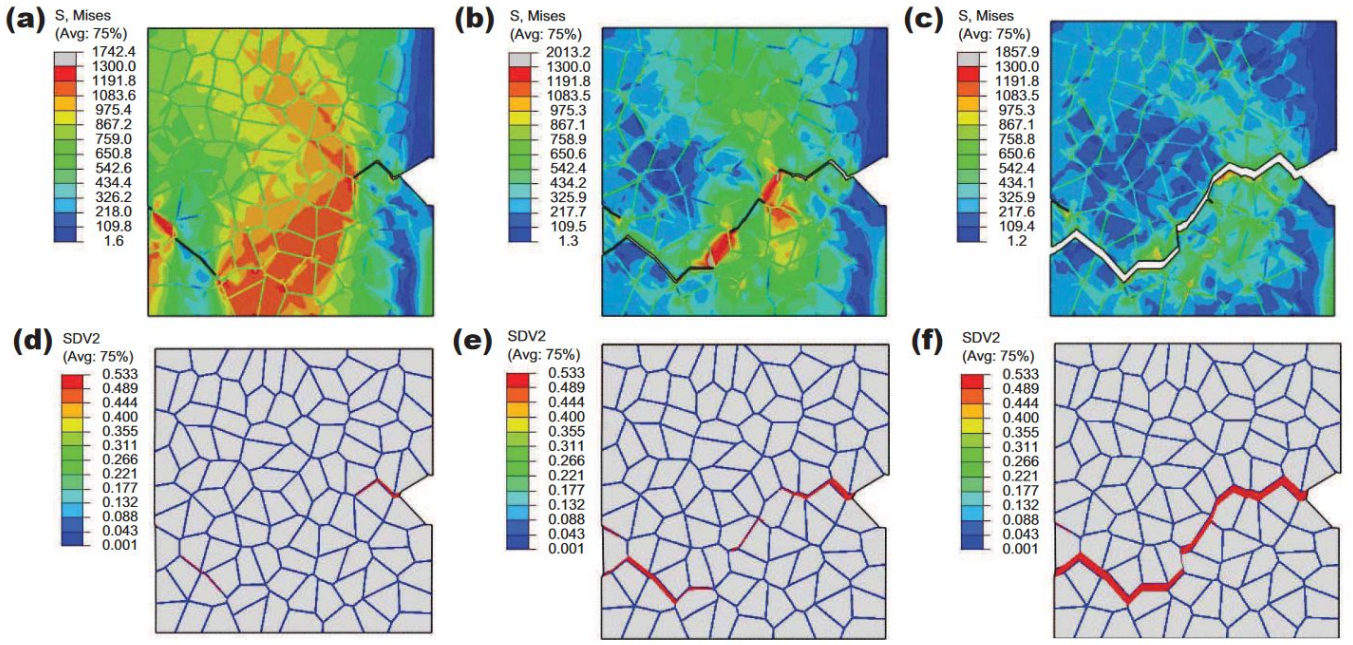

FIGURE I.48: Intergranular crack ductile propagation simulation in lamellar Ti-5553: von Mises stress (**a-c**) and damage evolution (**d-f**) for displacements of 0.04 mm (a,d), 0.08 mm (**b,e**) and 0.3 mm (**c,f**) (Lin et al., 2017).

using extended finite element modeling (XFEM), enabling arbitrary crack propagation in the FEM mesh (Moës et al., 1999). The authors studied a cubical unit cell containing a grain boundary presenting an initial crack of variable shape and size surrounded by a precipitate-free zone and a matrix. This unit cell was loaded with uniaxial tension to assess crack propagation, and predicts that intergranular fracture susceptibility increases and then decreases with precipitate-free zone width. Cracks tend to stay in the grain boundary plane and to become circular; fracture strain is higher for low aspect ratio cracks but also for elongated cracks with high aspect ratio. The study predicts that peak-aging corresponds to intergranular fracture, under-aging to transgranular fracture and over-aging to mixed fracture mode (Liu et al., 2014).

The outcomes of these first studies are valuable but show some limitations. First, numerical homogenization has shown that macroscopic yield surfaces of macroscopically isotropic polycrystalline aggregates with intergranular voids are quite distinct from the ones obtained by supposing that voids are in a von Mises isotropic matrix (Lebensohn et al., 2011; Nervi and Idiart, 2015). Then, at the mesoscale of the porous boundaries, all conventional plasticity models previously mentioned are intrinsically not adapted to model complex effects coupling crystallographic orientations, material non-linearity, and void size/shape. Therefore, the conventional ductile modeling approach is challenged for macroscopic and mesoscopic applications.

3.4 Matrix with crystal plasticity

Models and simulations detailed in Section I.3.3.1 assume that the matrix material at the voids' scale comprises many grains. However, observations of fracture surfaces' dimples resulting from void coalescence (Pineau et al., 2016), and X-ray tomography experiments (Maire and Withers, 2014) on various metal alloys show voids smaller than the grain size. Void size ranges typically from micrometric when nucleated from particles down to nanometric in specific conditions, such as neutron irradiation (Neustroev and Garner, 2009). Given that the grain size is rarely below a few microns, it means that voids are adjacent to a few crystals only, and most probably are either located in a single crystal or at the boundary of two crystals. At that scale, conventional plasticity yield criteria such as the ones of Mises (1913) and Hill (1948) are inadequate. Physically-based modeling of such alloys may require to model porous single crystals (Fig. I.49) and porous grain boundaries (Fig. I.50) with

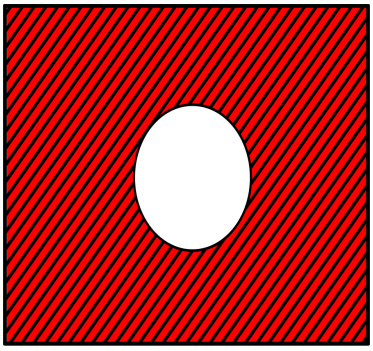

FIGURE I.49: Porous single crystal.

crystal plasticity laws.

In the following, crystal plasticity is assumed to be related to the glide of dislocations (see Section I.1.3.2), that can happen in a limited number of planes and directions, called crystallographic slip systems, defined by a slip plane (whose normal is along unit vector $\underline{m}_s$) and a slip direction (of unit vector $\underline{n}_s$), and represented by the following symmetric Schmid tensor: $\boldsymbol{\mu}_s = \frac{1}{2}(\underline{m}_s \otimes \underline{n}_s + \underline{n}_s \otimes \underline{m}_s)$. Plastic twinning is disregarded. Using viscoplastic regularization, the plastic strain rate generated by a microscopic stress tensor $\boldsymbol{\sigma}$ writes (Hutchinson, 1976):

$$\boldsymbol{d} = \sum_{s=1}^{K} \left[\dot{\gamma}_0 \left(\frac{|\boldsymbol{\sigma} : \boldsymbol{\mu}_s|}{\tau_\mathrm{c}^s} \right)^n \mathrm{sgn}(\boldsymbol{\sigma} : \boldsymbol{\mu}_s) \right] \boldsymbol{\mu}_s = \sum_{s=1}^{K} \dot{\gamma}_s \boldsymbol{\mu}_s \tag{I.11}$$

In that equation, τ_c^s is the critical resolved shear stress of slip system s; when it is identical for all slip systems, it is usually denoted τ_0. Then, $\dot{\gamma}_0$ is a reference slip-rate and $\dot{\gamma}_s$ is the slip rate of system s. n denotes the Norton exponent: the case $n \to +\infty$ corresponds to rate-independent plasticity. In rate-independent plasticity, $(\dot{\gamma}_k)$ may be determined from $\boldsymbol{d}$ as the set that verifies Eq. I.11 while minimizing $\sum |\dot{\gamma}_s|$, as suggested by Taylor (1938).

3.4.1 Models of transgranular ductile fracture

In the last decade, transgranular models based on phenomenological plasticity were extended to crystal plasticity. As in Section I.3.3.1, void growth and void coalescence criteria are given separately and their conjunction provides the entire yield surface (Benzerga and Leblond, 2010).

Void growth The first model for void growth in single crystals with rate-independent plasticity was obtained using an approximate variational method; despite that fact, it bears a striking resemblance to Gurson-like models (Eq. I.9) derived through limit analysis. For each slip system $s \in [\![1, M]\!]$, an equivalent yield stress $\sigma^*_{\mathrm{G},s}$ is defined through (Han et al., 2013):

$$S_{\mathrm{G},s}(\sigma^*_{\mathrm{G},s}, \boldsymbol{\Sigma}, f) \equiv \left(\frac{|\boldsymbol{\mu}_s : \boldsymbol{\Sigma}|}{\sigma^*_{\mathrm{G},s}} \right)^2 + \alpha \frac{2}{45} f \left(\frac{\Sigma_\mathrm{eq}}{\sigma^*_{\mathrm{G},s}} \right)^2 + 2qf \cosh\left(\kappa \frac{\Sigma_\mathrm{m}}{\sigma^*_{\mathrm{G},s}} \right) - 1 - (qf)^2 \tag{I.12}$$

Then, the yield criterion writes:

$$\phi_\mathrm{G} = \max_{s \in [\![1,M]\!]} \left(\sigma^*_{\mathrm{G},s} - \tau_\mathrm{c}^s \right) \tag{I.13}$$

This model was then written within finite strain theory by Ling et al. (2016). An alternative criterion, obtained through approximate limit analysis, is even closer to Eq. I.9, containing only one equivalent yield stress (Paux et al., 2015):

$$S_\mathrm{G}(\sigma^*_\mathrm{G}, \boldsymbol{\Sigma}, f) \equiv \left(\frac{\left(\sum_{s=1}^{M} |\boldsymbol{\mu}_s : \boldsymbol{\Sigma}|^m \right)^{\frac{1}{m}}}{\sigma^*_\mathrm{G}} \right)^2 + 2qf \cosh\left(\kappa \frac{\Sigma_\mathrm{m}}{\sigma^*_\mathrm{G}} \right) - 1 - (qf)^2 = 0 \tag{I.14}$$

with $m \to +\infty$ a regularization parameter. The model was extended to account for strain hardening (Paux et al., 2018) and void size effects by using a strain gradient plasticity model in the crystal matrix (Khavasad and Keralavarma, 2021; Khavasad and Keralavarma, 2023). In the aforementioned models, $\kappa \in [0.489, 0.513]$ (Han et al., 2013; Paux et al., 2018; Hure, 2019), while q is a calibration parameter varying between 1.4 (Han et al., 2013) and 2.2 (Paux et al., 2018).

Finally, another variational method relying on Hashin-Strikhman bounds for linear composites and heuristic simplifications was proposed by Mbiakop et al. (2015b). Contrary to the previous criteria (Eqs. I.12 and I.14), it accounts for material non-linearity n and void aspect ratio w as it allows ellipsoidal voids. In its rate-independent form, it can be written using Eq. I.13 with equivalent stresses defined as:

$$\sigma^*_{\mathrm{G},s} = \frac{1}{1-f} \sqrt{\boldsymbol{\Sigma} : (\boldsymbol{\mu}_s \otimes \boldsymbol{\mu}_s + \mathbb{A} + (q_\mathrm{J}(f)^2 - 1)\, \mathbb{J} : \mathbb{A} : \mathbb{J}) : \boldsymbol{\Sigma}} \quad \text{with} \quad \mathbb{A} = \frac{(\tau^\mathrm{c})^2}{K} \left[(1-f) \overline{\mathbb{S}}(f, w) - \mathbb{S} \right] \tag{I.15}$$

where $\overline{\mathbb{S}}$ and $\mathbb{S}$ are respectively the pseudo-compliance of the linear porous and pristine single crystal; q_J is a scalar depending on f. Heuristic approximations were later eliminated at the expense of simplicity (Song and Ponte-Castañeda, 2017a): the model is no longer analytical and requires solving large non-linear systems of equations.

Void coalescence A first heuristic criterion for void coalescence in porous single crystals was presented in Yerra et al. (2010). It was later formalized and extended to combined tension and shear in Hure (2019) which adapted the model of Torki et al. (2015) to single crystals using average Taylor factors. The local Taylor factor associated with a single crystal subjected to a strain rate $\boldsymbol{d}$ is defined as:

$$M(\boldsymbol{d}) = \frac{\sum_{s=1}^{K} \dot{\gamma}_k \left[\boldsymbol{d}\right]}{d_{\text{eq}}^{\text{iso}}} \quad \text{with} \quad d_{\text{eq}}^{\text{iso}} = \sqrt{\frac{2}{3}\boldsymbol{d} : \boldsymbol{d}} \tag{I.16}$$

Then, the model expresses as Eq. I.10 with:

$$A(\mu_s, \chi) = M_2(\mu_s, \chi) A_0(\chi) \ , \quad B(\mu_s, \chi, w) = M_1(\mu_s) B_0(\chi, w) \ , \quad C(\mu_s, \chi) = M_3(\mu_s) C_0(\chi) \tag{I.17}$$

where M_1, M_2 and M_3 are well-chosen average Taylor factors whose definition can be found in Hure (2019) and A_0, B_0 and C_0 are those from Torki et al. (2015) (see Table I.3).

Homogenized model Very few homogenized models exist for porous single crystals. Most of them only consider the void growth stage, such as Khadyko et al. (2021) using Eq. I.12. The only model to gather void growth and void coalescence is the one from Scherer et al. (2021) where the void growth criterion is Eqs. I.12-I.13 but the coalescence criterion is the conventional plasticity yield function of Thomason (1985).

3.4.2 Simulation of intergranular ductile fracture

To this date, no intergranular ductile fracture model can account for the interplay between crystal plasticity and void evolution, which would amount to predicting the mechanical behavior of the material element shown in Fig. I.50. Nevertheless, a handful of numerical simulations were conducted to assess this coupling. When performing these simulations, the first question that arises is the way grain boundary should be modeled, which is tackled in the first subsection. Porous unit cell simulations of intergranular ductile fracture will be the object of the second subsection.

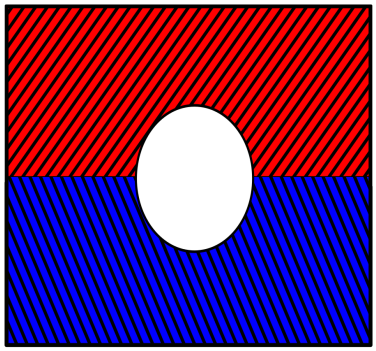

FIGURE I.50: Porous grain boundary.

Grain boundary modeling Wide use of crystal plasticity-based finite element modeling (CPFEM) of polycrystals has raised interest in grain boundary modeling. Grain boundaries are often considered as simple geometric interfaces without intrinsic mechanical properties (Peralta et al., 1993; Chen et al., 1998; Chen et al., 2000; Wan and Yue, 2004; Liu et al., 2019). Comparisons between aluminum bicrystal mechanical experiments and FEM simulations have shown that even if the agreement on strain data was not perfect, the most relevant features were well predicted (Fig. I.51) (Zaefferer et al., 2003). In a 6061 alloy polycrystal, CPFEM identified well regions of highest strain localization but significant differences were observed elsewhere (Güler et al., 2018). A closer comparison led on a 316L bicrystal bending sample showed that total strains can be predicted by classical crystal plasticity laws within 20% error margin, but that elastic strains are overestimated. Moreover, predicted slip systems in zones adjacent to a grain boundary can be occasionally flawed (Plancher et al., 2019). Finally, in a bicrystal tensile specimen, classical modeling predicts simple necking at the grain boundary whereas double necking is usually observed at room temperature, which is attributed to the hardening capacity of the grain boundary (Lu et al., 2003; Guo et al., 2013).

The fact that strain hardening laws can influence local stresses or strains should not be overlooked and better hardening modeling could bridge part of the gap between experiments and simulations (Kysar, 2001). However, many alternative crystal plasticity modelings of grain boundaries were proposed; a comprehensive summation of those is beyond the scope of this review but some ideas are worth noting. For instance, some authors advocate for physical grain boundary simulation by implementing a finite thickness boundary with a higher rate sensitive ratio m, which enables recovering qualitative agreement with double necking observations, and predicts higher stress/strain concentration at grain boundaries (Lu et al., 2003). Besides, Gurtin's model was proposed to account for slip interactions at grain boundaries (Gurtin, 2008; Yalçinkaya et al., 2018). Interactions between dislocation densities and grain boundary based on slip transmission criteria (Bayerschen et al., 2016) can also influence hardening close to the grain

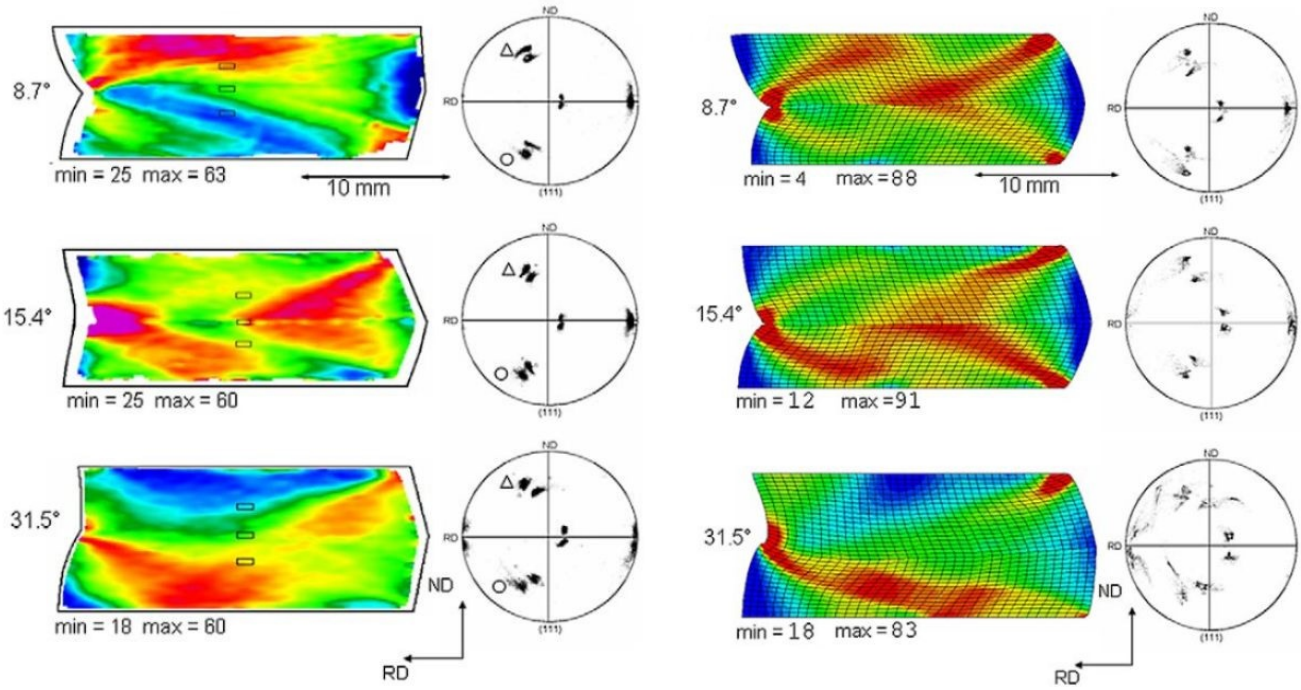

(**a**) Experiment (**b**) Conventional crystal plasticity simulation

FIGURE I.51: Von Mises strain measured (a) and computed (b) for 30%-strained aluminum bicrystals with various initial grain boundary misorientations; red indicates maximum strain while blue marks minimum strain (Zaefferer et al., 2003).

boundary (Ashmawi and Zikry, 2001; Wu et al., 2016; Zhou et al., 2021). Finally, gradient models can enhance crystal plasticity predictions: for instance, directional dependence of crack growth along a grain boundary was successfully predicted using lattice incompatibility hardening gradient (Tang et al., 2005); more generally, strain gradient models are known to uncover physical effects overlooked by local plasticity laws (Cordero et al., 2012).

Porous grain boundary unit-cell simulations As already stated in this section, crystallographic orientations strongly affect both void growth and void coalescence stages when cavities are at the crystal scale (Crépin et al., 1996; Ding et al., 2016; Barrioz et al., 2019). In transgranular ductile fracture, this influence has been studied through porous single crystal unit-cell simulations for almost two decades (among other works, see Potirniche et al. (2006), Ha and Kim (2010), Yerra et al. (2010), Han et al. (2013), Paux et al. (2015), Ling et al. (2016), Paux et al. (2018), and Selvarajou et al. (2019)). In those FEM simulations, the void is explicitly meshed in a matrix that follows crystal plasticity laws; it is a reliable way to study the effect of microstructural parameters and provide assessment for homogenized porous crystal yield criteria (Han et al., 2013; Paux et al., 2015; Ling et al., 2016; Paux et al., 2018). Concomitantly to the study of transgranular fracture, some efforts have been carried out to simulate the behavior of intergranular cavities through voided bicrystal unit-cell simulations (see Fig. I.52a) conducted within finite strain framework. As stated at the beginning of Section I.3.4.2, those computations consider grain boundaries as simple geometric interfaces. In crystal plasticity simulations, it is generally assumed that hardening can result in different critical shear resolved stresses τ_c^s for each slip system s. The following latent hardening law was chosen in all unit cell studies (except that of Li et al. (2015)):

$$\dot{\tau}_c^s = h_0 \sum_{k=1}^{N} h_{sk} h_k \left|\dot{\gamma}_k\right| \quad \text{with} \quad h_{sk} = \begin{cases} 1 & (s = k) \\ \delta & (s \neq k) \end{cases} \tag{I.18}$$

where δ is the latent hardening coefficient, generally chosen to be 1.4 (Zhang et al., 2008; Liu et al., 2009; Liu et al., 2010; Jeong et al., 2018; Dakshinamurthy et al., 2021) or 1 (Wen and Yue, 2007; Asim et al., 2019b; Chen et al., 2019). In the latter case, all τ_c^s keep the same value and only depend on the cumulated slip $\gamma = \sum_s \int_{[0,t]} |\dot{\gamma}_s|$. h_s is function of τ_c^s that tends towards a value h when τ_c^s reaches a given saturation value τ_{sat}: h is set to 0 (Wen and Yue, 2007; Zhang et al., 2008; Yang and Dong, 2009; Liu et al., 2009; Liu et al., 2010; Jeong et al., 2018; Asim et al., 2019b; Dakshinamurthy

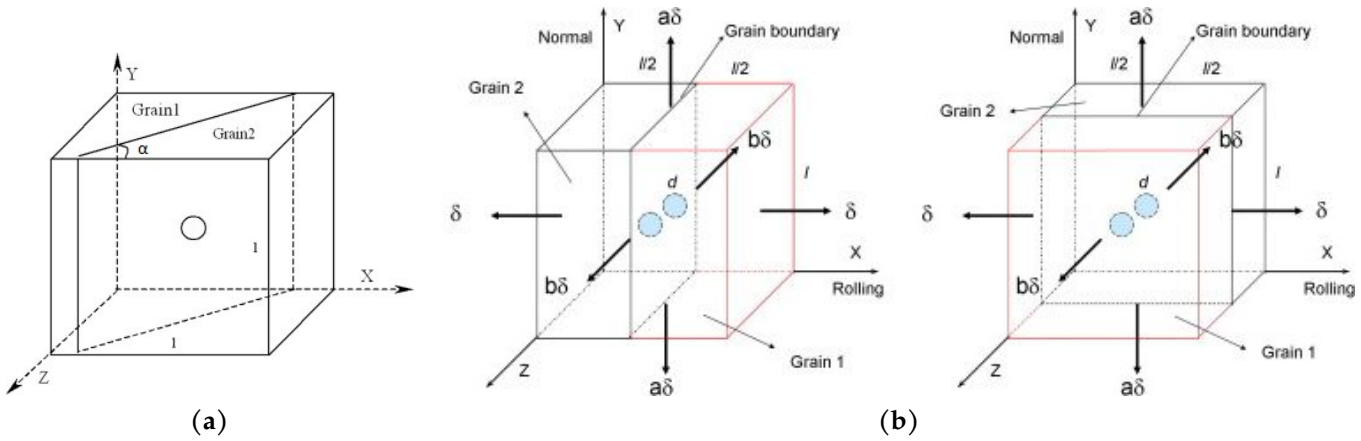

FIGURE I.52: Porous bicrystal unit-cells: (a) unique spherical void, α is the angle between the grain boundary plane and the X-axis, which is the main loading direction (Liu et al., 2009); (b) double void to study coalescence along and through the grain boundary (Liu et al., 2010).

et al., 2021) except in one study (Chen et al., 2019). Mechanical loadings prescribed in the different studies are shown in Table I.4: T is the stress triaxiality ratio and θ is the Lode angle (see Eq. I.4), whereas α is the angle between the grain boundary plane and the main loading direction X (see Fig. I.52a). The number of different crystallographic orientation couples investigated is denoted N. The crystal lattices are also indicated in the table: FCC stands for face-centered cubic, BCC refers to body-centered cubic and HCP is hexagonal close-packed.

Some findings emerge from this literature survey. First, all the studies have confirmed that the main patterns associated with transgranular void growth remain true for intergranular cavities:

- Crystal orientation couples influence yield stress (Yang and Dong, 2009; Jeong et al., 2018; Asim et al., 2019b), void growth rate (Wen and Yue, 2007; Yang and Dong, 2009; Jeong et al., 2018; Chen et al., 2019; Asim et al., 2019b; Dakshinamurthy et al., 2021), void shape (Wen and Yue, 2007; Jeong et al., 2018; Chen et al., 2019; Asim et al., 2019b; Dakshinamurthy et al., 2021) and plastic strain fields (Liu et al., 2009; Jeong et al., 2018; Dakshinamurthy et al., 2021).
- The void growth rate increases exponentially with stress triaxiality; when the stress triaxiality is high, void volume fraction increases with equivalent plastic strain and an opposite behavior is seen at low stress triaxiality (Chen et al., 2019; Asim et al., 2019b; Dakshinamurthy et al., 2021).

Study	Lattice	T	θ	α	N	Notes
Wen and Yue (2007)	FCC	$\frac{1}{3}$	0	$\{0, \frac{\pi}{4}, \frac{\pi}{2}\}$	2	
Zhang et al. (2008)	FCC	$\frac{1}{3}$	0	$\{0, \frac{\pi}{4}, \frac{\pi}{3}\}$	3	
Yang and Dong (2009)	FCC	Axisymmetric strain		$\{0, \frac{\pi}{2}\}$	3	Strain ratio set to -0.235
Liu et al. (2009)	FCC	Axisymmetric strain		$\frac{\pi}{2}$	4	Strain ratio set to -0.235
Liu et al. (2010)	FCC	Axisymmetric strain		$\{0, \frac{\pi}{2}\}$	4	*Idem*, cluster of two voids
Li et al. (2015)	FCC	$\frac{1}{3}$	0	$\{0, \frac{\pi}{4}, \frac{\pi}{2}\}$	1	Creep study
Jeong et al. (2018)	BCC	$\{1, 3\}$	0	$\frac{\pi}{2}$	2	Tricrystals and 75%-25% bicrystals also studied
Chen et al. (2019)	FCC	$\{\frac{1}{3}, \frac{1}{2}, 1, 2\}$	0	$\frac{\pi}{2}$	4	
Asim et al. (2019b)	BCC-HCP	1	0	$\frac{\pi}{2}$	3	
		$\{0, \frac{1}{3}, \frac{2}{3}, 1\}$	0		4	Orientation and α are tied
Dakshinamurthy et al. (2021)	FCC	$\{\frac{1}{3}, 1, 2, 3\}$	$\{0, \frac{\pi}{6}, \frac{\pi}{3}\}$	$\frac{\pi}{2}$	3	
Zhu et al. (2022)	FCC	$\{0.7, 3\}$	0	$\frac{\pi}{2}$	6	
				Random	6	Embedded in polycrystals

TABLE I.4: Characteristics of porous grain boundary unit cell computations in the literature.

- Triaxial stress loadings tend to elongate cavities along the main loading axis (Wen and Yue, 2007; Zhang et al., 2008; Li et al., 2015) and that effect decreases with increasing stress triaxiality (Chen et al., 2019); yet, cavities are not perfectly ellipsoidal but exhibit irregular shapes (Wen and Yue, 2007; Jeong et al., 2018; Chen et al., 2019; Asim et al., 2019b), sometimes with sharp corners (Zhang et al., 2008; Liu et al., 2009; Liu et al., 2010).
- Lode angle θ has an effect on void shape; furthermore, the void growth rate is negatively correlated with θ (Dakshinamurthy et al., 2021).
- Lattice rotation in the unit-cell increases with stress triaxiality (Chen et al., 2019).

Second, all unit cell computations underlined the significant differences between the mechanical behavior of porous grain boundaries and that of corresponding porous single crystals. Furthermore, some trends have been noticed — even if they may need confirmation due to the low number of simulations conducted:

- A large crystallographic orientation difference between grains generates strain and stress concentrations at the grain boundary, which can then favor intergranular fracture over transgranular fracture. These concentrations increase with α (Wen and Yue, 2007; Zhang et al., 2008). For instance, the small orientation differences — only one axial rotation — shown in Chen et al. (2019) generate no such concentrations.
- Void growth rate seems to be faster when the grain boundary is perpendicular to the main loading direction than when it is tilted at 45°, itself being faster than when the grain boundary is parallel to the main loading direction (Wen and Yue, 2007; Zhang et al., 2008; Yang and Dong, 2009; Li et al., 2015).
- The void growth rate and the stress-strain curve of the porous bicrystal seem somewhat to be an average of those of the corresponding porous single crystals (Jeong et al., 2018; Zhu et al., 2022).
- Void growth is usually faster in the softer[5] half-crystal (Wen and Yue, 2007; Zhang et al., 2008; Li et al., 2015; Dakshinamurthy et al., 2021; Zhu et al., 2022), contrary to what is seen in porous single crystals (Jeong et al., 2018). This is due to stress redistribution in the bicrystal resulting in a mean T and θ in each half-crystal different from the macroscopic T and θ (Dakshinamurthy et al., 2021). At low macroscopic triaxialities, it can result in a highly irregular void shape (crack-like in the hard crystal, ellipsoidal in the soft crystal) while voids tend to stay ellipsoidal at high stress triaxiality ratios (Dakshinamurthy et al., 2021). Both crystals thus exert an important influence on each other.
- The active slip systems seem to be the same as those activated in corresponding porous single crystals, but their relative intensity differs from these reference cases (Jeong et al., 2018; Chen et al., 2019).

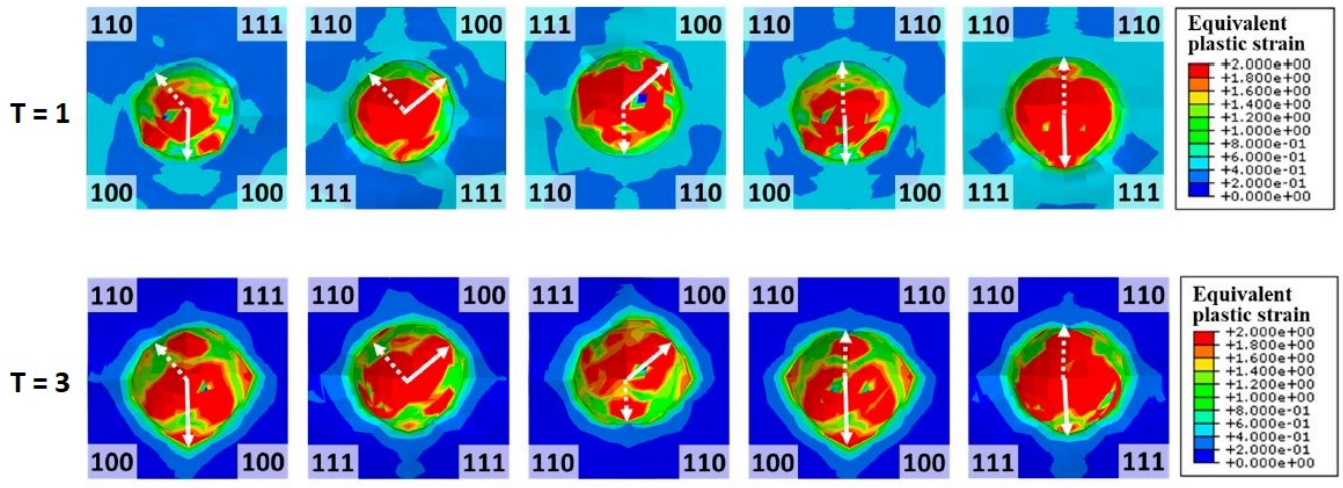

FIGURE I.53: Plastic strain map of various porous bicrystals and tricrystals loaded with two different stress triaxialities T, the main loading direction being normal to the plane shown in the figure; the full arrow shows the direction of maximal void growth while the dotted arrow marks the minimum void growth direction (Jeong et al., 2018).

[5] In the following, a grain shall be referred to as "soft" or "hard" according to its yield limit under the prescribed mechanical loading.

- The direction of maximal and minimal void growth seems to be left unchanged by stress triaxiality, as seen in Fig. I.53 (Jeong et al., 2018).
- The amount of lattice rotation occurring around the void is strongly dependent on the crystallographic orientation couple (Chen et al., 2019), and seems more important in the hard crystal — where the formation of new grain boundaries may be possible (Dakshinamurthy et al., 2021).
- When the void size is of the same order of magnitude as the grain size, porous grain boundaries embedded in a polycrystal display a reduced influence of the crystallographic orientation couple on void growth rate due to the effect of neighboring grains on the local mechanical loading (Zhu et al., 2022).

Alternatively to porous unit-cell results, XFEM can also be coupled to crystal plasticity laws to study intergranular ductile cracking (Liu et al., 2016a). Such simulations also underline the important influence of the crystallographic orientation couple on this fracture mode.

As a whole, this review highlights that the specificity of porous grain boundaries is too important to be accurately modeled by existing transgranular fracture models. Yet, the similarities are sufficient to consider that a model for intergranular ductile fracture could be expressed within a framework similar to that of transgranular ductile fracture.

3.5 Perspectives

After underlining the current state of ductile fracture micromechanics, it is useful to point out the developments required to enhance our understanding of that failure mode at the crystal scale. Three main axes can be privileged:

1. As was detailed in Section I.3.4.1, porous single crystal yield criteria for void growth and coalescence in layers are available. Yet, coalescence in columns still lacks a dedicated study that will adapt the results of Torki et al. (2023) to a crystalline matrix. Then, together with appropriate evolution laws for microstructure parameters, a full homogenized model incorporating void growth, internal necking, coalescence in shear and coalescence in columns could be obtained to predict the mechanical behavior of the material element shown in Fig. I.54a.
2. To model intergranular ductile fracture, a path parallel to that of transgranular ductile can probably be followed, this time applied to the material element of Fig. I.54b. However, the amount of work is considerable since only the starting point, *i.e.* unit-cell simulations (see Section I.3.4.2), is available. It would therefore require deriving yield criteria for void growth and coalescence in layers along with related evolution laws to obtain a full homogenized model. Models could then be specialized to study the particular case of intergranular cracks (Fig. I.54c), which seems especially relevant for some applications (see Section I.2).
3. The simulation of the competition between transgranular and intergranular fracture at the crystal scale (Fig. I.41) appears as a milestone. Explicit numerical simulations of voided polycrystals — akin to that Pardoen et al. (2003) with conventional plasticity laws — were never conducted while they could shed an interesting light on competition phenomena. Besides, once homogenized models of points #1 and #2 are developed, they could be used to predict the crack propagation in finite element modeling computations and simulate mixed fracture modes — *e.g.* Pardoen et al. (2010).

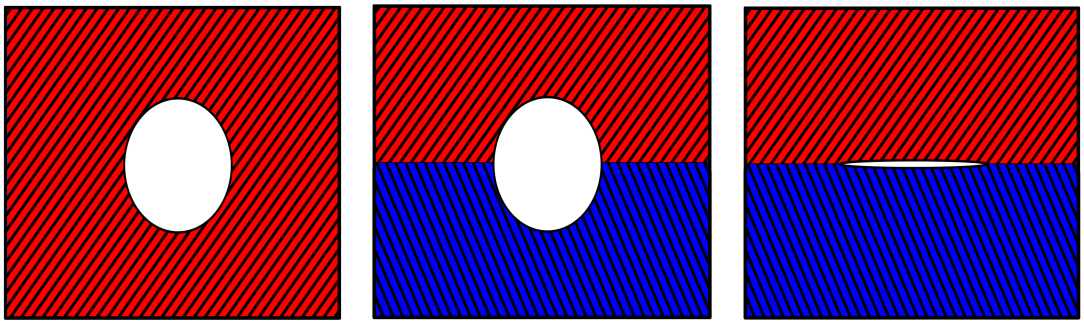

(**a**) Transgranular void (**b**) Intergranular void (**c**) Intergranular crack

FIGURE I.54: Material elements whose mechanical behavior should be modeled to predict transgranular and intergranular ductile fracture.

Summary

Following seminal contributions dating back to half a century ago, physically-based prediction of ductile fracture was attempted using micro-mechanical approaches based on the homogenization of porous materials. In that framework, the three successive stages of ductile fracture are accounted for by dedicated models. On the one hand, the understanding of void nucleation is still limited. In this work, the assumption that voids preexist in the material, or at least are nucleated quite early during mechanical loading, is adopted. On the other hand, void growth and coalescence are modeled according to the scale at which cavities are:

- if cavities are *larger than grains*, the material around voids can be accurately represented by phenomenological plasticity laws such as those of Mises (1913) and Hill (1948);
- if cavities are *at the crystal scale*, the approach based on phenomenological plasticity may still be used to represent an average mechanical behavior of voids; however, this framework accounts imperfectly for microstructure effects because crystal plasticity can no longer be neglected, prompting the need of models for porous single crystals and porous grain boundaries.

In the first case, abundant literature has developed plasticity criteria fit for various applications (non-spherical cavities, anisotropic matrix etc.). Furthermore, homogenized models gathering yield criteria for void growth and void coalescence along with evolution laws for the microstructure were used to simulate transgranular ductile fracture. In the second case, only a handful of studies on porous single crystals are available. In particular, a full homogenized based on porous single crystal plasticity criteria is missing, as well as a criterion for coalescence in columns. Finally, the modeling of porous grain boundaries is still a fallow field. As a result, simulations of intergranular ductile fracture still rely on the explicit meshing of grain boundary cracks (as in XFEM computations) or cavities (as in porous unit cell computations).

Based on this diagnosis, the objective set to this thesis is to bridge the modeling gaps evidenced for porous single crystals and porous grain boundaries to simulate the competition between transgranular and intergranular ductile fracture in a microstructure as the one shown in Fig. I.41. Contributions to the study of transgranular ductile fracture are gathered in Chapter 2 whereas advances in the accounting of intergranular ductile fracture can be found in Chapter 3.

2

Transgranular ductile fracture

Summary

Transgranular ductile fracture of metallic alloys is often governed by the nucleation, growth and coalescence of micro-voids smaller than the grain size. Thus, at short distances, the matrix material surrounding these voids is a single crystal. As a result, classical models developed to model ductile fracture, as the Gurson-Tvergaard-Needleman model and its extensions — which assume either an isotropic or a Hill-type anisotropic matrix material —, might fail to capture the influence of crystal plasticity on the evolution of voids. In order to account for these effects, the mechanical behavior of porous single crystals has to be studied.

In a first part, a homogenized model for void growth and coalescence by internal necking in single crystals is obtained building on yield criteria available in the literature. Its results are compared to a database of finite strain porous single crystal unit cell computations, showing qualitative agreement but underlying the need for a precise account of crystal lattice rotations and hardening. Then, in a second part, this homogenized model is employed to perform simulations of ductile tearing on monocrystalline and polycrystalline test samples, highlighting the effects of microstructure on fracture. Finally, in a third part, a yield criterion for coalescence in columns in porous single crystals is obtained and is shown to account correctly for this deformation mode.

All the contributions presented in this chapter pave the way towards a comprehensive homogenized model for transgranular ductile fracture including void growth, coalescence in layers and coalescence in columns at the crystal scale.

Contents

1 Homogenized models for void growth and coalescence in single crystals **51**
1.1 Introduction 53
1.2 Database for porous single crystal unit-cell simulations 55
1.2.1 Crystal plasticity constitutive equations 55
1.2.2 Porous unit-cell simulations 56
1.2.3 Analysis of the database 58
1.3 Homogenized model for porous single crystals 62
1.3.1 Constitutive equations 62
1.3.2 Numerical implementation 66
1.3.3 Calibration of numerical parameters 67
1.3.4 Comparison to unit-cells results 68
1.4 Discussion and perspectives 74
1.5 Conclusion 75
1.A Finite strain framework 76
1.B Yield criteria flow direction 77
1.B.1 Growth yield criterion 77
1.B.2 Coalescence yield criterion 78
1.C Summary of the two homogenized models 78
2 Trangranular ductile fracture simulations **80**
2.1 Description of simulations 81
2.1.1 Specimen geometries and loading conditions 81
2.1.2 Material behavior 82
2.1.3 Numerical implementation 83
2.2 Simulation results 84

2.2.1 Single crystal samples . . . 85
2.2.2 Polycrystalline samples . . . 92
2.3 Conclusion . . . 92
3 Necklace coalescence in porous crystals . . . **94**
3.1 Introduction . . . 95
3.2 Problem statement . . . 97
3.2.1 Porous material description . . . 97
3.2.2 Kinematic limit analysis . . . 98
3.3 Yield surface for porous Hill materials . . . 99
3.3.1 From homogeneous yielding to inhomogeneous yielding in columns . . . 100
3.3.2 Trial velocity field and associated dissipation . . . 100
3.3.3 Yield criterion . . . 101
3.3.4 From homogeneous yielding to inhomogeneous yielding in layers . . . 104
3.3.5 Trial velocity field and associated plastic dissipation . . . 105
3.3.6 Yield criterion . . . 105
3.3.7 Numerical assessment . . . 109
3.4 Yield surface for rate-independent crystals . . . 112
3.4.1 Single crystal matrix behavior . . . 112
3.4.2 Approximate macroscopic dissipation . . . 112
3.4.3 Yield surface . . . 113
3.4.4 Numerical assessment . . . 115
3.5 Homogenized model for porous Hill materials . . . 117
3.5.1 Sequential limit analysis . . . 117
3.5.2 Discussion . . . 118
3.6 Conclusion and perspectives . . . 120
3.6.1 Conclusion . . . 120
3.6.2 Perspectives . . . 121
3.A Taylor surfaces of a porous single crystal . . . 122
4 Conclusion and perspectives . . . **123**
A Contributions to the study of internal necking . . . **124**
A.1 Internal necking criterion obtained from Thomason triangular trial field . . . 124
A.2 Internal necking criterion obtained from Keralavarma and Chockalingam trial field 126

1 Homogenized models for void growth and coalescence in single crystals

As underlined in Section I.3, significant challenges remain for predicting ductile fracture in a physically-based framework. In particular, the modeling of the mechanical behavior of voids at the crystal scale is still in an early stage, motivating the studies carried out during this thesis. The current chapter is devoted to contributions to transgranular ductile fracture prediction. This section develops a homogenized model for porous single crystals based on results available in the literature.

Ideally, simulating the ductile fracture of full components would require to account for every void in the structure — keeping aside the nucleation stage. In finite element modeling, that means that the various populations of cavities — which can be located at different scales — would have to be meshed. This would require a degree of prior knowledge of the microstructure which is in most cases unrealistic. Even with that data at hand, such simulations would still be impossible — at least at the time being — due to the necessary mesh resolution which would result in a huge computational burden. Thus, there is a necessity to bridge a gap between the void scale, in which material heterogeneity plays a key role, and the computation scale, which should only consider homogeneous continuum mechanics. In this work, the micromechanical framework chosen to scale up ductile fracture relies on the homogenization of porous materials (Fig. II.1). In that stance, the porous material is simplified as a homogeneous material with the following characteristics:

- A set of internal variables that accounts for the homogenized microstructure; since the underlying microstructure can change under mechanical loading, evolution laws for internal variables should be provided.
- A material behavior law that relates the macroscopic stress and the macroscopic strain rate; for elastoplastic metals, it is constituted of a Hooke-type law for the elastic stage and a yield surface which delineates the elasticity domain of the material. The yield surface depends on the internal variables and the plastic flow rule is usually obtained from the yield surface through the normality rule (*i.e.* associated plasticity).

On the one hand, in *coupled* models (*e.g.* Gurson (1977)), internal variables influence the material behavior law, which itself impacts the mechanical loading, which itself triggers the evolution of internal variables. On the other hand, *uncoupled* models (*e.g.* Rice and Tracey (1969)) do not display such feedback mechanisms because damage variables do not appear in the material behavior law. In the following, the focus will be on coupled models.

In order to carry out the homogenization of the porous material, a geometry (*e.g.* the cubic porous unit cell shown in Fig. II.1) and a loading type must be selected. Then, under the prescribed loading, the homogenized material should have a behavior as close as possible to that of the chosen porous unit cell. In particular, high triaxialities ($T \approx 3$) are

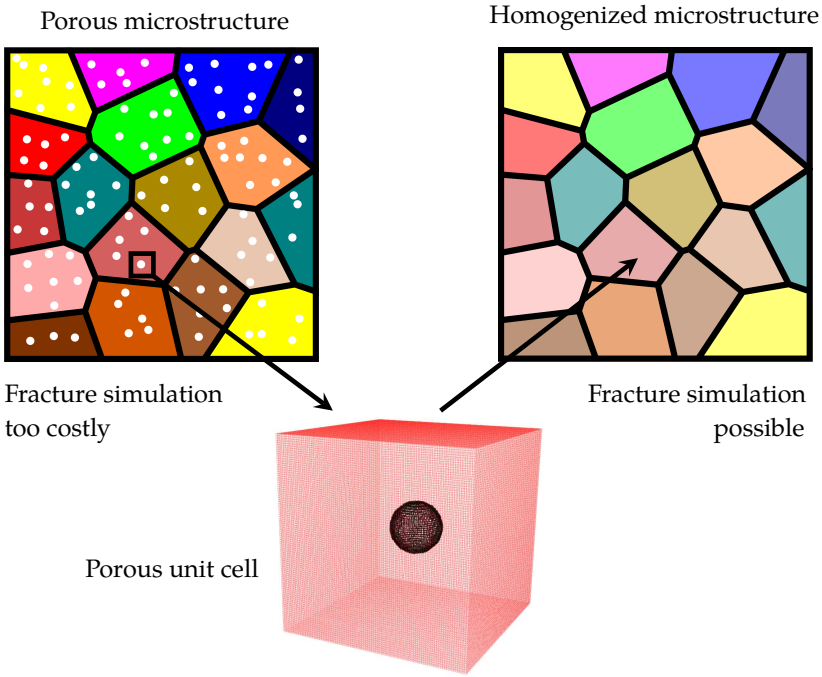

FIGURE II.1: Homogenization of porous materials applied to ductile fracture.

Model	Growth stage	Coalescence stage	Finite strain framework
Ling et al. (2016)	• Han et al. (2013)		$\boldsymbol{F}_\mathrm{e}\boldsymbol{F}_\mathrm{p}$
Frodal et al. (2021)	• Rice and Tracey (1969)		Hypoelastic (Jaumann)
Khadyko et al. (2021)	• Han et al. (2013)		Hypoelastic (Jaumann)
Scherer et al. (2021)	• Han et al. (2013)	• Thomason (1985)	$\boldsymbol{F}_\mathrm{e}\boldsymbol{F}_\mathrm{p}$

TABLE II.1: Homogenized models for transgranular ductile fracture at the crystal scale available in the literature. They are classified according to the modeling of growth and coalescence, which can be based on conventional (•) or crystal (•) plasticity.

of special interest for the ductile fracture of cracked structures (Pineau et al., 2016).

Coupled homogenized models for porous single crystals available in the literature are presented in Table II.1 along with their modeling of ductile fracture stages. First, the model of Frodal et al. (2021) is based on crystal plasticity laws (Eq. I.11) in which the effective Lemaitre stress tensor (Lemaitre, 1985) $\tilde{\boldsymbol{\Sigma}} = \boldsymbol{\Sigma}/(1-D)$ is used instead of the Cauchy stress tensor $\boldsymbol{\Sigma}$. $D \in [0,1]$ is a damage variable linked to void growth that follows a law inspired by Rice and Tracey (1969):

$$\dot{D} = \frac{3}{4} q_1 q_2 D(1-D) \sinh\left(\frac{3}{2} q_2 T\right) \dot{\gamma} \quad \text{with} \quad \dot{\gamma} = \sum_s |\dot{\gamma}_s| \tag{II.1}$$

In this model, the effect of the crystallographic orientation on the damage rate is only accounted for through the cumulated slip rate $\dot{\gamma}$, which is an oversimplification. Second, the model used by Khadyko et al. (2021) builds on the void growth criterion of Han et al. (2013) (see Eqs. I.12-I.13) and, as such, incorporates the effect of crystal orientation on the growth of internal cavities. Both models rely on hypoelasticity with the Jaumann objective derivative (Zhang et al., 2014) to account for finite strains with a plastic spin derived from crystal plasticity. Third, the model of Ling et al. (2016) (the earliest of all) extends the void growth criterion of Han et al. (2013) to finite strains using the multiplicative decomposition framework $\boldsymbol{F} = \boldsymbol{F}_\mathrm{e}\boldsymbol{F}_\mathrm{p}$, which is recognized as the most physically-grounded approach (Helfer and Ling, 2014). The first three models overlook void coalescence as well as void nucleation, which is likely to impact their predictions of ductility. Finally, the model found in Scherer et al. (2021) incorporates both growth and coalescence by using yield criteria from Han et al. (2013) and Thomason (1985) (Eq. I.10). Thus, the effect of crystal orientation on ductile fracture is accounted for in the void growth stage but not for the void coalescence stage. This model also uses the $\boldsymbol{F} = \boldsymbol{F}_\mathrm{e}\boldsymbol{F}_\mathrm{p}$ framework for finite strains. Based on this review, it appears that the next logical step is to combine crystal plasticity-based void growth and void coalescence criteria into a homogenized model. This is carried out in the remainder of this section — which is the manuscript of a published scientific paper (Sénac et al., 2022).

Homogenized constitutive equations for porous single crystals plasticity

Cédric Sénac, Jean-Michel Scherer, Jérémy Hure, Thomas Helfer, Benoît Tanguy

European Journal of Mechanics / A Solids — 2022

Abstract

Ductile fracture through void growth to coalescence occurs at the grain scale in numerous metallic alloys encountered in engineering applications. Classical models used to perform numerical simulations of ductile fracture, like the Gurson-Tvergaard-Needleman model and its extensions, are relevant for the case of large voids compared to the grain size, in which a homogenization of the material behavior over a large number of grains is used. Such modeling prevents assessing the effects of microstructure on both crack path and propagation resistance. Therefore, homogenized constitutive equations for porous single-crystal plasticity are proposed, featuring void growth and void coalescence stages, hardening, and void shape evolutions. An original numerical implementation based on the coupling of Newton-Raphson and fixed point algorithms is described. In order to assess the accuracy of the proposed model as well as another one described recently in the literature, an extended database of porous unit-cell simulation results is gathered, investigating the effect of crystallographic orientations and hardening behavior for an FCC material. Strengths and weaknesses of both models are detailed with respect to the reference simulations, leading to the definition of the validity domain of the current model and to pinpoint necessary refinements.

1.1 Introduction

Ductile fracture refers to a failure mode associated with a significant amount of plasticity either at the global or local scale. Various ductile fracture physical mechanisms have been observed and described experimentally depending on materials and loading conditions (Noell et al., 2018). One of these ductile fracture mechanisms is related to the nucleation, growth and coalescence of internal voids originating from inclusions or second-phase particles, widely observed in metallic alloys used in engineering applications. Ductile fracture through void growth to coalescence has been extensively studied from experimental, theoretical and numerical perspectives, and the reader is referred to the exhaustive reviews on the topic (Benzerga and Leblond, 2010; Besson, 2010; Benzerga et al., 2016; Pineau et al., 2016). Modeling is based on the homogenization of porous materials (Fig. II.2) through different techniques (Gurson, 1977; Rousselier, 1981; Ponte Castañeda, 1991), and a key ingredient is the mechanical behavior of the material surrounding voids. Classical homogenized models, such as the widely used Gurson-Tvergaard-Needleman (GTN) model (Tvergaard, 1982; Tvergaard and Needleman, 1984) and its anisotropic extensions (Danas and Castañeda, 2009; Morin et al., 2015c), consider von Mises or Hill associated plasticity for the matrix material. These models are relevant for

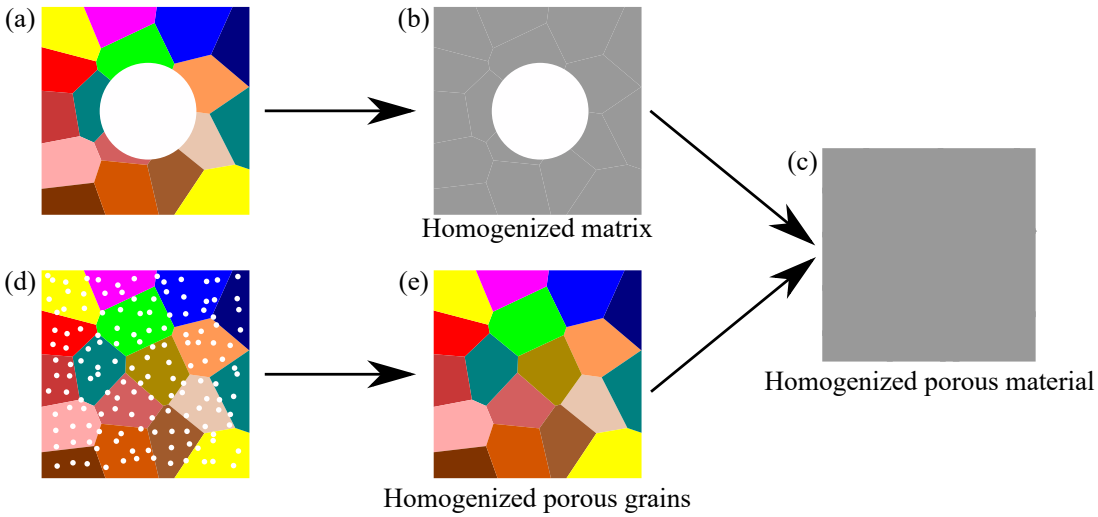

Figure II.2: Homogenization strategies for porous polycrystals, for voids size larger (**a**) or smaller (**d**) than the grain size.

polycrystalline materials where voids are significantly larger than the grain size, so that the matrix material at the scale of the voids is composed of a large number of grains (Fig. II.2a) and can be described by conventional plasticity models (Fig. II.2b). Interestingly, observations of fracture surfaces' dimples (Pineau et al., 2016), resulting from void coalescence, and X-ray tomography experiments (Maire and Withers, 2014) on various metal alloys indicate that voids may be smaller than the grain size. Austenitic stainless steels (such as AISI 304 and 316) (Mills, 1997), aluminum alloys (AA 6xxx) (Thomesen et al., 2020) and Inconel alloys (IN718) (Stout and Gerberich, 1978) figure prominently among these materials. Void size ranges typically from micrometric when nucleated from inclusions down to nanometric in specific conditions — *e.g.* nanocavities induced by irradiation (Neustroev and Garner, 2009). In these cases, each grain is a porous single crystal (Fig. II.2d).

Any physically-based modeling of such materials thus requires to model porous single crystals. The final material behavior is then obtained either by performing a secondary homogenization over the microstructure (Fig. II.2c), or by performing simulations of polycrystals (Fig. II.2e). Experimental studies and theoretical modeling of porous single crystals have been tackled only recently. While detailed experimental observations of voids in single crystals under mechanical loading remain scarce, the influence of crystallographic orientation is clearly documented on both void growth mechanisms (Crépin et al., 1996; Ding et al., 2016; Barrioz et al., 2019) and plasticity (Gan et al., 2006; Biswas et al., 2013). Plasticity of porous single crystals has been assessed more extensively through porous unit-cell simulations (Potirniche et al., 2006; Ha and Kim, 2010; Yerra et al., 2010; Selvarajou et al., 2019; Paux et al., 2018) where the main results are the strong dependence of void volume fraction evolution to the crystallographic orientation, as well as a complex interplay between matrix material hardening and void growth softening as a function of stress triaxiality. Homogenized yield criteria for porous single crystals have been recently developed. Regarding void growth, several yield criteria have been proposed in the last decade based on various techniques, extending GTN-like models to single crystals. Most of them fall within the scope of multi-surface plasticity criterion (Han et al., 2013; Mbiakop et al., 2015b; Song and Ponte-Castañeda, 2017a; Joëssel et al., 2018; Vincent et al., 2020) where each crystal slip system is kept in the homogenization procedure, while another one (Paux et al., 2015) considers a single plasticity surface. Regarding void coalescence, the well-known Thomason yield criterion model (Thomason, 1985) has also been extended in the context of porous single crystals (Yerra et al., 2010; Hure, 2019; Scherer et al., 2021). Void nucleation, mostly described classically through phenomenological laws (Besson, 2010), has not yet triggered dedicated models for single crystals to the authors' knowledge. All these models lead mostly to consistent and accurate predictions (with respect to reference porous unit-cell simulations) for the effect of porosity and crystallographic orientation on the yield stress of porous single crystals.

A task that is still challenging is to propose a complete set of constitutive equations for porous single crystals able to reproduce evolution problems, *i.e.* stress-strain curves. This entails accounting for hardening, microstructural parameters evolution (porosity, crystallographic orientations, void shape) and finite strains. A first set of equations has been proposed in Ling et al. (2016) based on the calibration and extension to finite strains of the yield criterion proposed in Han et al. (2013). Comparisons of the predictions of the model to a handful of finite strain porous unit-cell simulations (Ling et al., 2016) indicate that the main features are correctly predicted, although accurate modeling of hardening is delicate. A rather complex physically-based porous single crystal hardening model has been proposed in Paux et al. (2018), showing promising results. Models based on the variational approach (Song and Ponte-Castañeda, 2017b) have also shown predictions in good agreement with some reference simulations. For completeness, it should also be noted that other constitutive equations have been proposed for porous single crystals belonging to the damage mechanics framework (Siddiq, 2019; Frodal et al., 2021). In both cases, a damage variable is introduced affecting the critical resolved shear stress, and its evolution is dictated either by a phenomenological law (Siddiq, 2019) or motivated by Rice & Tracey model (Frodal et al., 2021). To date, the only micromechanical-based model accounting for both void growth and void coalescence is the one proposed by Scherer et al. (2021).

The main focus of this article is bridging scales for simulating polycrystals (Fig. II.2d → Fig. II.2e). Indeed, numerical simulations of ductile fracture in single and polycrystalline structures can now be achieved, as pioneered in Ling et al. (2016) for a U-notch specimen and pursued in Scherer et al. (2021) on pre-cracked specimens. Efficient numerical implementation recently allows to perform ductile fracture simulations of a polycrystalline sample having a few thousand grains (Khadyko et al., 2021), showing that the objective of assessing in detail the effect of microstructure on fracture resistance is now within reach. Moreover, simulating ductile fracture at the polycrystalline scale opens the way to design microstructures of metal alloys — *e.g.* thanks to advanced material processing methods such as additive manufacturing — resistant to crack propagation. However, quantitative and efficient predictions

require at least two ingredients. First, homogenized constitutive equations for porous single crystals should be validated and/or calibrated against an extended database of reference finite strain porous unit-cell simulations. Previous works give only a few results, especially regarding the effect of crystallographic orientations that are often restricted to symmetric ones. Such a database will be required to develop refined homogenized models, and is the first objective of this study. Second, constitutive equations accounting for both void growth and coalescence, as proposed in Scherer et al. (2021), may be numerically heavy due to the large number of internal variables involved. Finding a compromise between the complexity of the model and the predictive capability is definitely required, which is the second objective of this study.

The paper is organized as follows: in a first part, a database of porous unit-cell simulation results is gathered and described for a face-centered cubic material, including a large set of parameters (crystallographic orientations, hardening laws, initial void volume fractions). In a second part, a homogenized model for porous single crystals is presented, featuring both void growth and void coalescence stages, as well as simple modeling of hardening and void shape evolution. The model differs from the one proposed in Scherer et al. (2021), and is designed as simple as possible in an effort towards industrial structure calculation scale. An original numerical implementation is proposed to increase numerical efficiency. The model proposed, as well as the alternative model (Scherer et al., 2021), are assessed quantitatively to the database reference simulations. These results are then used to derive the strengths and weaknesses of these complementary modeling approaches and plan future improvements of constitutive equations for porous single-crystal plasticity.

1.2 Database for porous single crystal unit-cell simulations

In this section, crystal plasticity constitutive equations are first recalled. Then, finite strain porous single crystal unit-cell simulations are presented. All simulation results are finally gathered into a database and analyzed.

1.2.1 Crystal plasticity constitutive equations

Crystal plasticity constitutive equations used in the following are briefly recalled here in the context of finite strains (Roters et al., 2010). A face-centered cubic (FCC) material is considered, but equations can be easily adapted to other crystal lattices. The deformation gradient $\boldsymbol{F}$ is split multiplicatively into an elastic part $\boldsymbol{F}_\mathrm{e}$ and a plastic part $\boldsymbol{F}_\mathrm{p}$:

$$\boldsymbol{F} = \boldsymbol{F}_\mathrm{e}\,\boldsymbol{F}_\mathrm{p} \tag{II.2}$$

Within the framework of crystal plasticity governed by dislocation glide, the plastic strain rate is decomposed as a sum of slip rates $\dot{\gamma}_s$ on slip systems $(\underline{n}_s, \underline{m}_s)$, where $\underline{n}_s$ denotes a slip plane normal and $\underline{m}_s$ a slip direction:

$$\dot{\boldsymbol{F}}_\mathrm{p}\boldsymbol{F}_\mathrm{p}^{-1} = \sum_{s=1}^{N} \dot{\gamma}_s\, \underline{m}_s \otimes \underline{n}_s = \sum_{s=1}^{N} \dot{\gamma}_s\, \boldsymbol{\mu}_s \tag{II.3}$$

where $\boldsymbol{\mu}_s$ is the Schmid tensor. Plastic slip rates are determined from a set of yield criteria S_s and rate-(in)dependent flow rules (Busso and Cailletaud, 2005; Forest and Rubin, 2016). Yield criteria are based on Schmid's law:

$$S_s(\tau_\mathrm{c}^s, \boldsymbol{\sigma}) = |\boldsymbol{\sigma} : \boldsymbol{\mu}_s| - \tau_\mathrm{c}^s = |\tau_s| - \tau_\mathrm{c}^s \tag{II.4}$$

where $\boldsymbol{\sigma}$ is the Cauchy stress tensor, complemented with a Norton-type viscous flow rule, mainly for numerical purposes:

$$\dot{\gamma}_s = \left(\frac{S_s}{K}\right)_+^m \tag{II.5}$$

where $(\cdot)_+ = \max(0, \cdot)$, K and m are viscoplastic parameters that are chosen such that the results given hereafter are approximately rate-independent ($K = 10$ MPa, $m = 15$). Cubic elasticity is described by Hooke's law using Green-Lagrange strain tensor $\boldsymbol{E}_\mathrm{GL} = \frac{1}{2}\left(\boldsymbol{F}_\mathrm{e}^T\boldsymbol{F}_\mathrm{e} - 1\right)$. Cubic symmetry elasticity moduli are given in Table II.2. The critical resolved shear stress (CRSS) τ_c^s represents the shear stress to be applied in order to activate dislocation glide and therefore accounts for strain hardening effects. The first hardening law is the dislocation density-based model introduced in Franciosi et al. (1980) (see also Kubin et al. (2008)) which will be referred to as FBZ hardening in this

article. In this law, the critical resolved shear stress τ_c^s of a given system s is composed of a thermal component due to lattice friction τ_0 and an athermal component due to dislocation interactions:

$$\tau_c^s = \tau_0 + \mu \sqrt{\sum_{k=1}^{N} a_{sk} r_D^k} \tag{II.6}$$

where μ is the shear modulus and (a_{sk}) a matrix describing interactions between dislocations. For FCC crystals with the $\{111\}\langle 110\rangle$ slip system family, the latter is only composed of six independent coefficients a_i, with $i \in [\![1, 6]\!]$, describing the intensity of different dislocation interactions, namely: self-hardening interactions, coplanar interactions, Hirth locks, colinear interactions, glissile junctions, and Lomer locks. The shape of this matrix can for instance be found in Franciosi and Zaoui (1982). r_D^k denotes the adimensional dislocation density ($r_D^k = b^2 \rho_D^k$ where ρ_D^k is the usual dislocation density, *i.e.* the length of dislocation lines per unit volume, b being the norm of the dislocation Burgers vector $\underline{b}$). The following rate equations give the evolution of dislocation densities:

$$\dot{r}_D^s = \left(\frac{1}{K_0} \sqrt{\sum_{k=1}^{N} (1 - \delta_s^k) r_D^k} - G_0 r_D^s \right) |\dot{\gamma}_s| \tag{II.7}$$

where δ_k^s is the Kronecker symbol which is equal to 1 if $s = k$ and 0 otherwise. Parameter K_0 is related to the pinning of dislocations while G_0 accounts for the annihilation of dislocation dipoles during dynamical recovery. Numerical values used for porous single crystal unit-cell simulations are given in Table II.2 and correspond to a 304L stainless steel (Han et al., 2013; Hure et al., 2016), in which case $b = 0.254$ nm.

The second hardening law is the phenomenological model proposed by Peirce et al. (1983), referred to as the Peirce-Asaro-Needleman (PAN) hardening law, which links the evolution of the critical resolved shear stress τ_c^s of system s to the plastic slip rates $\dot{\gamma}_k$ as follows:

$$\dot{\tau}_c^s = \sum_{k=1}^{N} h_{sk} h(\gamma) |\dot{\gamma}_k| \quad \text{with} \quad h(\gamma) = h_0 \cosh\left(\frac{h_0 \gamma}{\tau_{sat} - \tau_0} \right)^{-2} \quad \text{and} \quad h_{sk} = \delta + (1 - \delta)\delta_k^s \tag{II.8}$$

where $\gamma = \sum_k \int_0^t |\dot{\gamma}_k| \mathrm{d}t$ is the accumulated plastic slip. Matrix h represents the interaction between slip systems, while function h defines the evolution of hardening as a function of γ. τ_0 is the initial critical resolved shear stress, while h_0 is the strain hardening slope at the initiation of plastic slip. $h(\gamma)$ tends to 0 when γ goes to infinity and leads to the saturation of τ_c^s towards τ_{sat}. If the parameter δ is equal to 0, the plastic slip rate on a given system s does not induce strain hardening on any other slip system ($k \neq s$) than itself, *i.e.* only self-hardening is considered, whereas for $\delta = 1$ all critical resolved shear stresses τ_c^s have the same evolution. Several combinations of the parameters τ_0, h_0, τ_{sat} and δ are considered in the following to model low to medium hardening. Numerical values of these parameters are presented in Table II.2. Finally, as a reference, simulations are also performed without hardening, *i.e.* $\tau_c^s = \tau_0$.

Numerical integration of the crystal plasticity constitutive equations detailed above has been performed according to a fully implicit scheme solved with a Newton-Raphson algorithm. Details about the implementation and finite strain framework can be found elsewhere (Hure et al., 2016).

1.2.2 Porous unit-cell simulations

Finite strain porous unit-cell simulations have been used extensively to assess porous materials' behavior in the context of ductile fracture and to validate homogenized models. This technique was used for porous single crystals in a relatively limited number of studies (Potirniche et al., 2006; Ha and Kim, 2010; Yerra et al., 2010; Ling et al., 2016; Selvarajou et al., 2019). Non-linear simulations being numerically expensive, these studies usually consider few crystallographic orientations and only one set of hardening parameters. In order to construct a database on which homogenized models can be validated, 13 different FCC crystallographic orientations are considered (Fig. II.3). In the Inverse pole figure (IPF) representation, the axes of the axisymmetric loading ($\underline{e}_1$, $\underline{e}_2$) are given in the crystal frame. Eight symmetric orientations were chosen in order to activate simultaneously multiple slip systems, which is favorable for void growth. Five other orientations were picked randomly from a uniformly distributed orientation density function. These less symmetric orientations are less favorable to multiple slip system activation, but still lead to void

Viscosity parameters			**Elasticity stiffness moduli (Mandel notation)**		
K (MPa)	m		C_{11} (GPa)	C_{12} (GPa)	C_{44} (GPa)
10	15		199	136	105

Strain hardening law

Franciosi-Berveiller-Zaoui (Franciosi et al., 1980) — numerical values from Han (2012)

	τ_0 (MPa)	μ (GPa)	$r_{\mathrm{D}}^k(0)$	a_1	a_2	a_3	a_4	a_5	a_6	G_0	K_0
1a	88	65.6	$5.38 \cdot 10^{-11}$	0.124	0.124	0.07	0.625	0.137	0.122	10.4	42.8

Peirce-Asaro-Needleman (Peirce et al., 1983)

	τ_0 (MPa)	τ_{sat} (MPa)	h_0 (MPa)	δ
2a	100	150	250	1
2b	100	150	500	1
2c	100	200	250	1
2d	100	200	500	1
2e	100	150	250	0.75
2f	100	150	500	0.75
2g	100	200	250	0.75
2h	100	200	500	0.75

TABLE II.2: Material parameters used for porous unit-cell crystal plasticity simulations.

growth due to the heterogeneous stress field around the void and because lattice rotation can turn the crystal to a more symmetric orientation favoring multiple slip.

Cubic unit cells containing a centered single spherical void are considered with two different initial porosities $f \in \{0.01, 0.001\}$. Periodic boundary conditions are used along with axisymmetric loading conditions (Ling et al., 2016), principal axis $\underline{e}_1$ being aligned with the initial axis of the cell:

$$\boldsymbol{\Sigma} = \Sigma_{11} \begin{pmatrix} 1 & 0 & 0 \\ 0 & \beta & 0 \\ 0 & 0 & \beta \end{pmatrix} \quad , \qquad T = \frac{\Sigma_{\mathrm{m}}}{\Sigma_{\mathrm{eq}}^{\mathrm{vM}}} = \frac{1+2\beta}{3(1-\beta)} \tag{II.9}$$

where $\Sigma_{\mathrm{m}} = \frac{1}{3}\,\mathrm{Tr}(\boldsymbol{\Sigma})$ is the hydrostatic stress and $\Sigma_{\mathrm{eq}}^{\mathrm{vM}}$ is the equivalent von Mises stress.

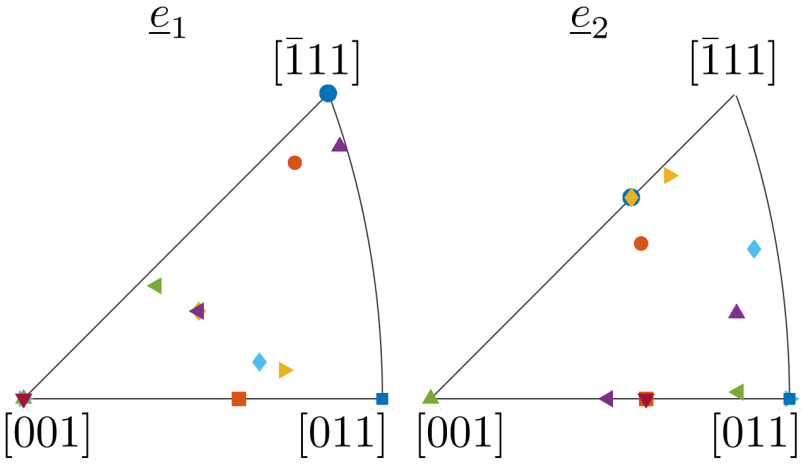

(a)

	#	ϕ_1 (°)	Φ (°)	ϕ_2 (°)
●	0	125.3	45	180
■	1	333.4	0	0
◆	2	114.1	90	63.4
◀	3	112.1	80.2	86.1
▲	4	0	0	0
▶	5	0	45	0
▼	6	0	26.6	0
■	7	315	0	0
●	r1	124.4	34.2	267.6
▶	r2	117.8	107.4	66.8
▲	r3	141.7	101	29.1
◀	r4	16.8	55	63.5
◆	r5	142.7	53.4	29.4

(b)

FIGURE II.3: (**a**) Inverse pole figure representation and (**b**) Euler angles (Bunge convention) of the crystallographic orientations.

Four different values of stress triaxiality are used: $T \in \{1, 1.5, 2, 3\}$. Simulations have been performed under finite strain either in the FEM-based solver `Z-set` (Besson and Foerch, 1998) or in the FFT-based solver `AMITEX FFTP` (CEA, 2020). Mechanical loading is applied by imposing one component of the macroscopic deformation gradient rate $\dot{F}_{11} = 10^{-4}$ (FEM), $2.5 \cdot 10^{-4}$ (FFT with $T = 3$) or $7.5 \cdot 10^{-4}$ (FFT for $T = 1$), reminding that the constitutive equations used are almost rate-independent. Only cases in which $\dot{F}_{11} > 0$ are considered. The FEM mesh holds 16464 elements and is shown in Fig. II.4. The FFT mesh is constituted of 41^3 voxels. Selected simulations have been performed in both solvers to check the consistency of the results and discretization convergence. In particular, FFT simulations were compared to computations with 61^3 voxels. In the FEM-based solver, the stress triaxiality is imposed by controlling the macroscopic deformation gradient. Multiple point constraints are applied in order to impose periodic boundary conditions on homologous nodes. Details about the implementation of the boundary and loading conditions can be found elsewhere (Ling et al., 2016). The method available in `AMITEX FFTP` is in the spirit of the work of Kabel et al. (2016) and extended to impose proportionality on the Cauchy stress tensor.

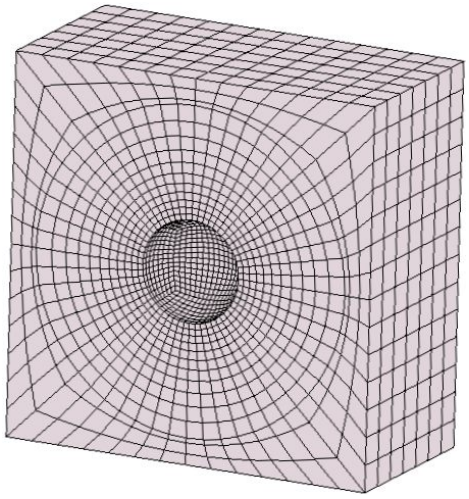

FIGURE II.4: Half of the mesh used for FEM computations in case in which $f_0 = 0.01$.

Combining the different crystallographic orientations (Fig. II.3), hardening behaviors (Table II.2), initial porosities and stress triaxialities, 240 finite strain porous single crystal unit-cell simulations inputs and results have been gathered into a database freely accessible (Sénac et al., 2021b).

1.2.3 Analysis of the database

Under mechanical loading, the cell and the void deform from their initial shapes. Except for highly symmetric crystallographic orientations, complex shapes are obtained as strain increases, requiring the definition of simplified geometrical parameters for analyzing and comparing different simulations. Due to the boundary and loading conditions considered, cell shape remains close to orthorhombic, with the same principal axes as the initial cube and lengths L_1, L_2 and L_3 (Fig. II.5). Void shape evolution is more complex, and is described as an ellipsoid of radii R_1, R_2 and R_3 (Fig. II.5). This allows defining geometrical ratios of interest such as the cell aspect ratio λ (Eq. II.10), void aspect ratio w (Eq. II.11), intervoid normalized distance χ (Eq. II.16), in addition to the porosity f (Eq. II.14). The parameters λ, w and χ should be viewed as average values (according to the transverse directions) and other definitions are possible. However, in the limit of spheroidal void shape ($R_2 = R_3$) and tetragonal cell ($L_2 = L_3$) used to derive most homogenized models, classical definitions are recovered. Apart from these geometrical parameters, standard outputs of the simulations include average (over the cell volume) stress $\boldsymbol{\Sigma}$ and deformation gradient $\boldsymbol{F}$ tensor components.

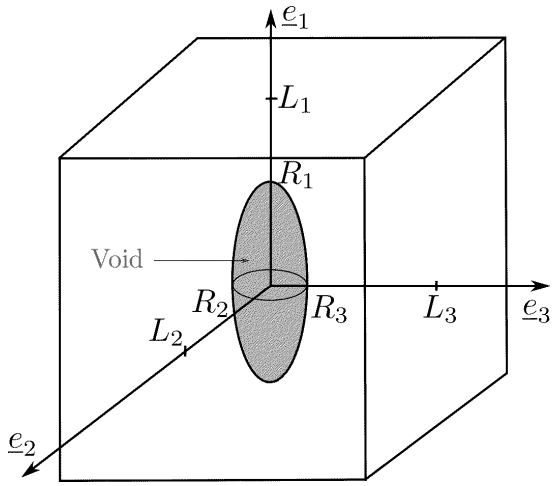

$$\lambda = \frac{L_1}{\sqrt{L_2 L_3}} \quad \text{with} \quad L_1 > L_2, L_3 \tag{II.10}$$

$$w = \frac{R_1}{\sqrt{R_2 R_3}} \tag{II.11}$$

$$V_{\text{void}} = \frac{4}{3}\pi R_1 R_2 R_3 \tag{II.12}$$

$$V_{\text{tot}} = L_1 L_2 L_3 \tag{II.13}$$

$$f = \frac{V_{\text{void}}}{V_{\text{tot}}} \tag{II.14}$$

$$f_{\text{b}} = \frac{V_{\text{void}}}{2 R_1 L_2 L_3} \tag{II.15}$$

$$\chi = \sqrt{f_{\text{b}}} \tag{II.16}$$

FIGURE II.5: Simplified porous unit-cell geometry (left) and definition of geometrical quantities (right).

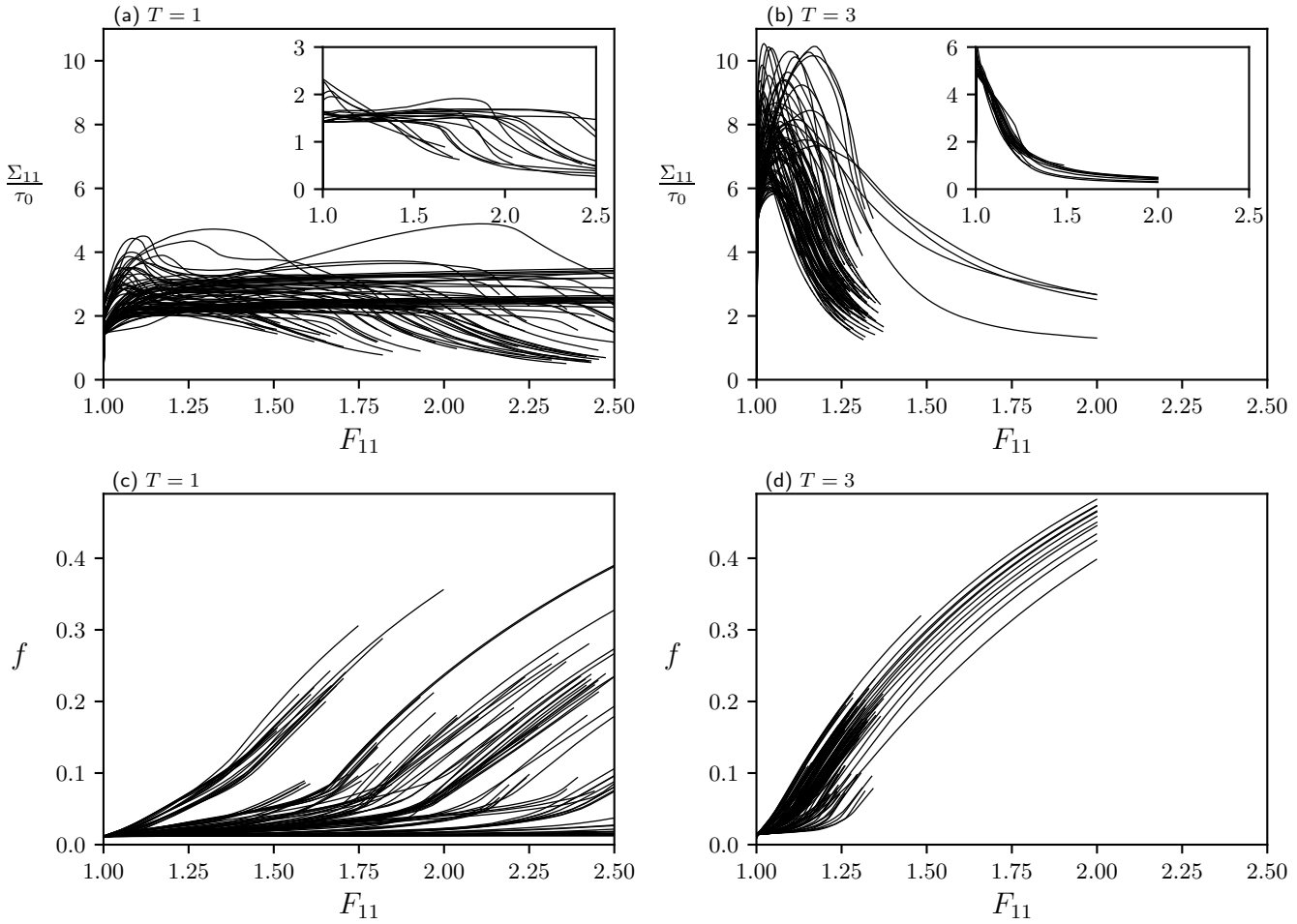

FIGURE II.6: Evolution of the stress Σ_{11} **(a,b)** and porosity f **(c,d)** as a function of the deformation gradient F_{11}, for stress triaxiality $T = 1$ **(a,c)** and $T = 3$ **(b,d)**. In **(a,b)**, simulations with strain hardening are shown in the main plot, while simulations without hardening are shown in insets.

The evolution of output variables of the porous unit-cell simulations is shown in Fig. II.6. Considering the entire database, a large variability is observed for the evolution of the stress Σ_{11} as a function of the deformation gradient F_{11} (Fig. II.6a,b where perfect plasticity simulations are shown in insets). Accounting for such variability, coming from the interplay between the crystallographic orientation and the hardening behavior of the matrix material, is the main challenge of developing homogenized constitutive equations for porous single crystals. Previous attempts, *e.g.* Ling et al. (2016) and Paux et al. (2018), have shown that this task is rather difficult. The large number of simulations in the current database allows however to gain some insights by restricting to selected subsets of entry parameters, which was not possible in previous studies that considered only a few cases. Without hardening, for given stress triaxiality and initial porosity, the differences are solely due to the crystallographic orientations. For low stress triaxiality $T = 1$, as shown in Fig. II.6a, a slight effect of crystallography on the apparent yield stress is observed. The effect of crystal orientation is much stronger on the value of the deformation gradient above which stress decreases abruptly (which corresponds to the onset of coalescence as discussed below). As evidenced in Fig. II.6c, the increase of porosity prior to coalescence depends strongly on the crystallographic orientation. For higher stress triaxiality $T = 3$, the effect of crystallographic orientation is much weaker (Fig. II.6b,d), dispersion on Fig. II.6d being imputable to different hardening law parameters. Basically, a higher applied stress triaxiality involves a higher number of activated slip systems in the porous unit cell. As the plastic anisotropy of FCC material is relatively weak due to the presence of 12 slip systems, a high number of activated systems results in an almost homogeneous deformation behavior whatever the crystallographic orientation. The qualitative observations made from Fig. II.6 are expected to hold also for BCC materials having even more slip systems available. HCP materials are however expected to have more complicated behavior, as described in Selvarajou et al. (2019), due to a lower number of slip systems (with potentially different

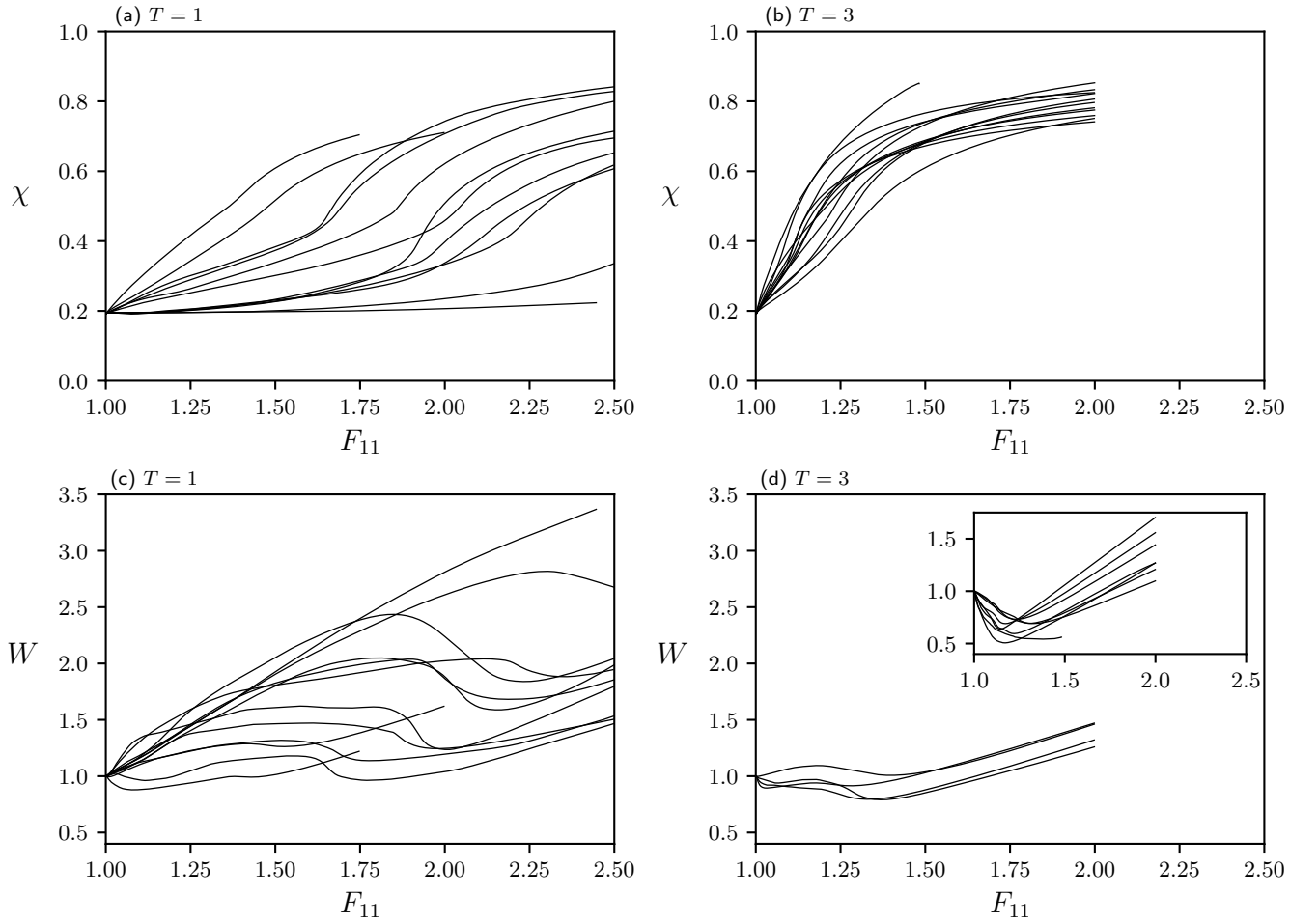

FIGURE II.7: Evolution of intervoid normalized distance χ **(a,b)** and void aspect ratio w **(c,d)** as a function of the deformation gradient F_{11}, for stress triaxiality $T = 1$ **(a,c)** and $T = 3$ **(b,d)**. Inset of **(d)** corresponds to cases without hardening, while the main plot displays simulation with hardening. Only FEM simulations are plotted here, contrary to Fig. II.6 in which both FEM and FFT computations are shown.

initial critical resolved shear stresses) and the occurrence of mechanical twinning.

Typical evolutions of χ and w are shown in Fig. II.7. In agreement with the description made in Fig. II.6, more scattering is observed at low stress triaxiality ($T = 1$) compared to high stress triaxiality ($T = 3$) for both void aspect ratio and intervoid normalized distance. On average, void tends to become prolate ($w > 1$) for $T = 1$ and oblate ($w < 1$) for $T = 3$ — at least for low values of applied strain, and before void coalescence sets in. This corresponds to the typical behavior observed for isotropic porous materials (Benzerga and Leblond, 2010). However, compared to perfect plasticity cases (inset of Fig. II.7d), FBZ hardening (main plot of Fig. II.7d) mitigate the initial decrease of w, cavities staying almost spheroidal.

In order to gain some insights into the effects of crystallographic orientation with or without hardening, characteristic points are extracted from the curves of Fig. II.6. The effective yield stress Σ_{11}^0 is defined as the value of Σ_{11} for 0.2% plastic strain (similarly to conventional yield stress measured on a tensile test). The maximal stress Σ_{11}^{m} is also extracted, the difference with the effective yield stress allowing to quantify hardening. Finally, the onset of coalescence is defined as the occurrence of a uniaxial straining mode such as $\max\left(\dot{F}_{22}, \dot{F}_{33}\right) \leq \alpha \dot{F}_{11}$. In practice, α is set to 3%. This definition disregards the other components of the deformation gradient and thus does not account for shear-assisted coalescence mode (Torki et al., 2015). This is justified by the initial void distribution considered — a cubic array — for which coalescence occurs mainly in the $(\underline{e}_2, \underline{e}_3)$ plane as voids are closer in that plane compared to arbitrary planes. Onset of coalescence is then defined by the corresponding values of stress Σ_{11}^{c} and deformation gradient F_{11}^c. Note that for some simulations — mostly at low stress triaxiality — coalescence is not attained and the corresponding values of $\Sigma_{11}^{\mathrm{c}}, F_{11}^{\mathrm{c}}$ are not available.

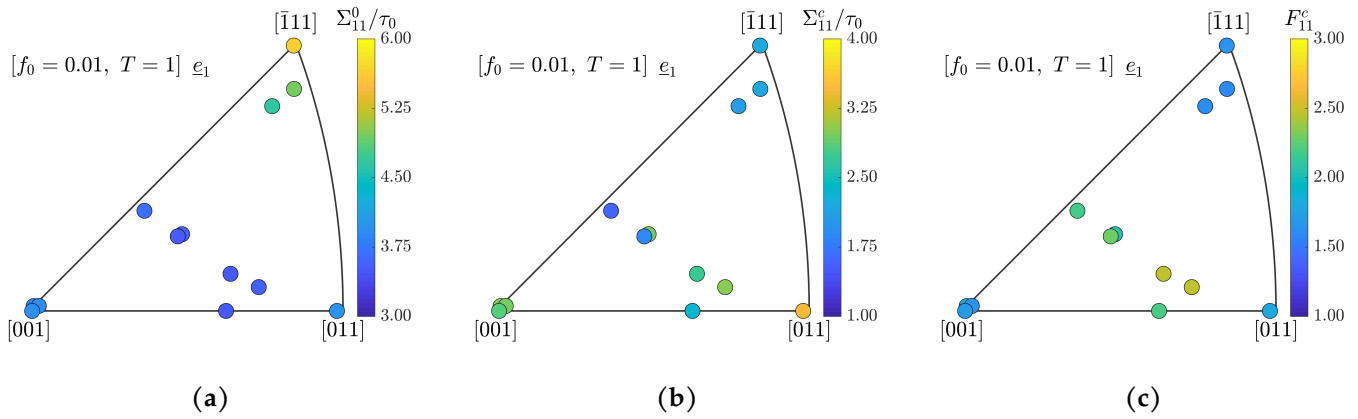

(a) **(b)** **(c)**

FIGURE II.8: Inverse pole figure representation of **(a)** effective yield stress Σ^0_{11}, **(b)** coalescence stress Σ^c_{11} and **(c)** coalescence deformation gradient F^c_{11} for porous single crystals with initially cubic distribution of spherical voids of porosity 1%, without hardening, for axisymmetric loading conditions with stress triaxiality $T = 1$.

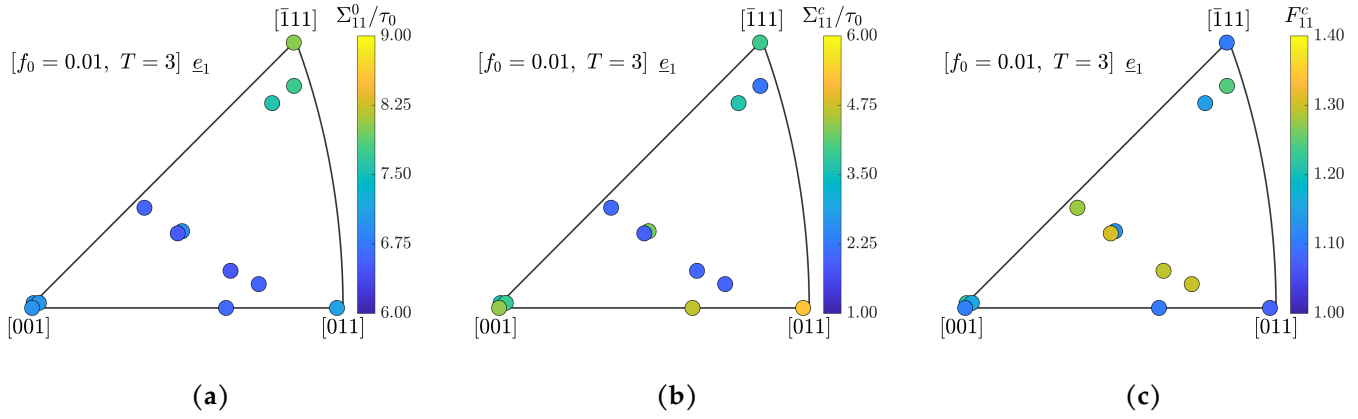

(a) **(b)** **(c)**

FIGURE II.9: Inverse pole figure representation of **(a)** effective yield stress Σ^0_{11}, **(b)** coalescence stress Σ^c_{11} and **(c)** coalescence deformation gradient F^c_{11} for porous single crystals with initially cubic distribution of spherical voids of porosity 1%, without hardening, for axisymmetric loading conditions with stress triaxiality $T = 3$.

The dependence of these characteristic points to the crystallographic orientations is shown in Figs. II.8, II.9 without hardening, and Figs. II.10, II.11 with hardening, using Inverse pole figure representation for the loading axis $\underline{e}_1$. For $T \in \{1, 3\}$, effective yield stress is higher for loading direction along <111>[1] (Figs. II.8a, II.9a), consistently with the results obtained in Paux et al. (2018). More interestingly, without hardening, coalescence stress (respectively deformation gradient) appears to be lower (respectively higher) in low symmetry crystallographic orientations (corresponding to the interior of the IPF) compared to high symmetry orientations (edges and corners of the IPF) especially for high stress triaxiality (Fig. II.9b,c). Thus, without hardening, the void growth deformation regime is active up to larger strains for low symmetry orientations. This may be explained by the fact that the increase of porosity in the void growth regime for low symmetry orientations is low, and that void coalescence depends more on the distance between voids than on the crystallographic orientations (Hure, 2019). Hence, higher strains are needed to obtain the critical porosity for coalescence to happen.

The effect of hardening is assessed in Figs. II.10, II.11. For the hardening law denoted $2a$, the dependence of the maximal stress to the crystallographic orientation (Fig. II.10a) is similar to the one observed for the effective yield stress (Fig. II.8a). This may be understood by the fact that the hardening law defined by Eq. II.8 does not depend explicitly on the orientation ($\delta = 1$ in Eq. II.8): in that case, the CRSS of all slip systems remains the same during hardening. For the physically-based hardening law (denoted FBZ, see Eq. II.6), differences are observed between the orientation dependence of yield stress (Fig. II.8a) and maximal stress (Fig. II.11a): maximal stress is for example higher for the loading direction along <011> compared to <111>, whereas the opposite is observed for the effective

[1] <111> refers to the family of equivalent FCC crystallographic directions [111], $[\bar{1}11]$, $[1\bar{1}1]$ etc.

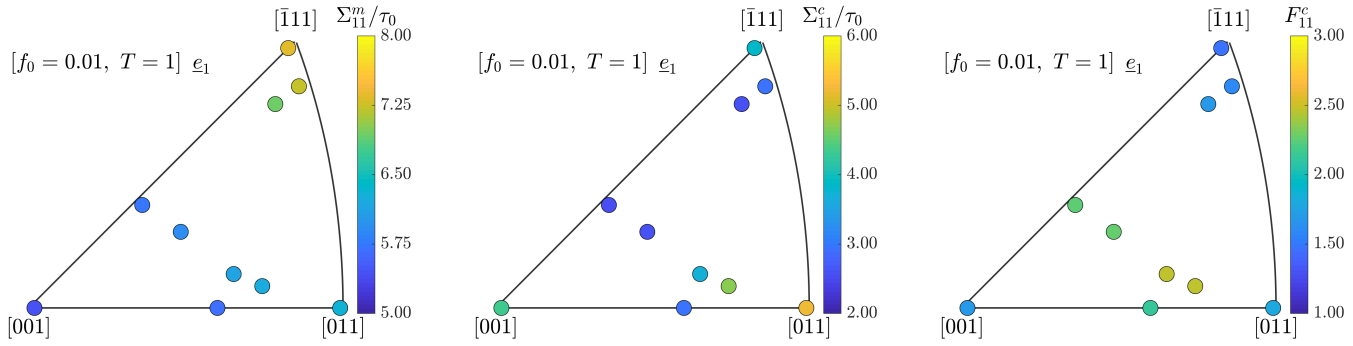

(a) **(b)** **(c)**

FIGURE II.10: Inverse pole figure representation of **(a)** maximal stress Σ^{m}_{11}, **(b)** coalescence stress Σ^{c}_{11} and **(c)** coalescence deformation gradient F^{c}_{11} for porous single crystals with initially cubic distribution of spherical voids of porosity 1%, with hardening $2a$, for axisymmetric loading conditions with stress triaxiality $T = 1$.

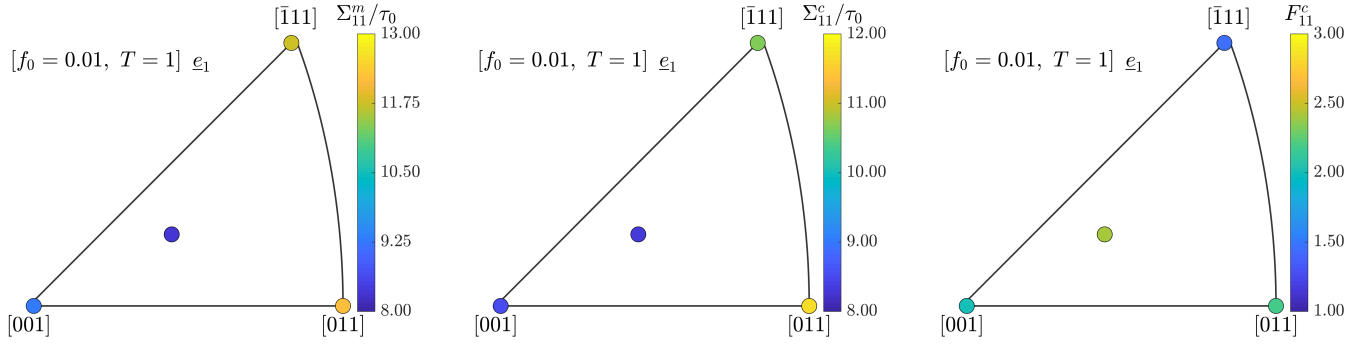

(a) **(b)** **(c)**

FIGURE II.11: Inverse pole figure representation of **(a)** maximal stress Σ^{m}_{11}, **(b)** coalescence stress Σ^{c}_{11} and **(c)** coalescence deformation gradient F^{c}_{11} for porous single crystals with initially cubic distribution of spherical voids of porosity 1%, with FBZ hardening, for axisymmetric loading conditions with stress triaxiality $T = 1$.

yield stress. The hardening rate is thus stronger along <011> than <111>. The interpretation of the coalescence stress values (Figs. II.10b, II.11b) is more complex, notably because fewer crystallographic orientations were tested than in Fig. II.10. However, the same conclusions than without hardening can be drawn for the coalescence deformation gradient (Figs. II.10c, II.11c): higher values are observed for low symmetry orientations, explained through the lower increase rate of porosity compared to high symmetry orientations.

The analysis of the database of the mechanical behavior of porous FCC single crystals under axisymmetric loading conditions clearly shows the complexity associated with the interplay between porosity, crystallographic orientations, and hardening. Without hardening, the crystallographic orientation effect is dominant for low stress triaxiality. The effect of hardening is more difficult to interpret for physically-based hardening laws where the CRSS of the different slip systems evolve differently. The challenge is thus to propose a homogenized model for porous single crystals rich enough to capture quantitatively the evolutions described in this section, but simple enough to be used in large-scale finite element simulations.

1.3 Homogenized model for porous single crystals

1.3.1 Constitutive equations

In this part, a homogenized model for porous single crystal plasticity is first presented under small strains assumption, and then extended to finite strains. $\boldsymbol{\Sigma}$ is the Cauchy stress tensor of the material point and is analogous to the macroscopic stress of the unit cell. Elasticity obeys Hooke's law with cubic symmetry, $\mathbb{C}$ being the fourth-order stiff-

ness tensor.

Yield criteria Following a generic formulation proposed in Besson (2010), a yield criterion $i \in \{\mathrm{g}, \mathrm{c}\}$ ('g' stands for growth and 'c' for coalescence) will be expressed as:

$$\phi_i = \sigma_i^* - \tau^* \tag{II.17}$$

where τ^* is the critical resolved shear stress and σ_i^* is an equivalent scalar matrix stress implicitly defined by an equation such as $S_i(\sigma_i^*, \boldsymbol{\Sigma}) = 0$. The void growth regime is described by Paux-Brenner-Kondo yield criterion (Paux et al., 2015), associated with an equivalent stress σ_g^* defined through the following expression:

$$S_\mathrm{g}(\sigma_\mathrm{g}^*, \boldsymbol{\Sigma}) \equiv \left(\frac{\left(\sum_{k=1}^{N} \left| \boldsymbol{\mu}_k^{(\mathrm{s})} : \boldsymbol{\Sigma} \right|^n \right)^{\frac{1}{n}}}{\sigma_\mathrm{g}^*} \right)^2 + 2qf \cosh\left(\kappa \frac{\Sigma_\mathrm{m}}{\sigma_\mathrm{g}^*} \right) - 1 - (qf)^2 \tag{II.18}$$

In Eq. II.18, κ and q are parameters that require calibration (Paux et al., 2018), $\boldsymbol{\mu}_k^{(\mathrm{s})}$ is the symmetric Schmid tensor of slip system k and n is a parameter used to regularize Schmid's law (Arminjon, 1991; Gambin, 1991) set to $n = 100$. Plastic flow is assumed to follow the normality rule, that is:

$$\dot{\boldsymbol{\varepsilon}}^\mathrm{p} \equiv \dot{p}_\mathrm{g} \boldsymbol{n}_\mathrm{g} = \dot{p}_\mathrm{g} \frac{\partial \phi_\mathrm{g}}{\partial \boldsymbol{\Sigma}} = \dot{p}_\mathrm{g} \frac{\partial \sigma_\mathrm{g}^*}{\partial \boldsymbol{\Sigma}} \tag{II.19}$$

where $\dot{p}$ is the plastic multiplier and $\boldsymbol{n}$ is the flow direction, indexed by g in the case of the growth criterion. For the sake of conciseness, the analytical expression of $\boldsymbol{n}_\mathrm{g}$ can be found in Appendix II.1.B.

A second yield criterion is considered to describe void coalescence by internal necking. During this phase, the yield criterion used is a variation on the Thomason model proposed in Hure (2019), whose equivalent stress σ_c^* is defined as follows:

$$S_\mathrm{c}(\sigma_\mathrm{c}^*, \boldsymbol{\Sigma}) \equiv \frac{\Sigma_\mathrm{I}}{\sigma_\mathrm{c}^*} - \underbrace{\left[\frac{b}{\sqrt{3}} \left(2 - \sqrt{1+3\chi^4} + \ln \frac{1+\sqrt{1+3\chi^4}}{3\chi^2} \right) M_1 + t(w,\chi) \left(\frac{\chi^3 - 3\chi + 2}{3\sqrt{3} w \chi} \right) M_2 \right]}_{C_\mathrm{f}(\boldsymbol{\Sigma})} \tag{II.20}$$

where M_1 and M_2 are average Taylor factors[2], Σ_I is the largest absolute value among principal stresses and $b = 0.9$ and $t(w, \chi)$ are fitting parameters that were calibrated in Torki et al. (2015). The expression of t is given below:

$$t(w,\chi) = \frac{(12.9\chi - 0.84)w}{1 + (12.9\chi - 0.84)w} \tag{II.21}$$

Definition of M_1 and M_2 integrals can be found in Hure (2019). Since the coalescence criterion was derived under uniaxial extension, the expression of M_1 and M_2 depend only on the normal to the coalescence plane. To avoid computing the integrals M_1 and M_2, a Fourier interpolation is used:

$$M_i \approx \sum_{m=-L}^{L} \sum_{n=-L}^{L} \hat{M}_i(m,n) \left[\cos(2m\theta) \cos(n\phi) - \sin(2m\theta) \sin(n\phi) \right] \tag{II.22}$$

where $\{\theta, \phi\}$ are the spherical coordinates of the normal to the coalescence plane in the crystal frame. As shown in Fig. II.12a, a good agreement is obtained between the analytical values given by Eq. II.22 and the numerical values, calibrating the Fourier coefficients $\hat{M}_i(m,n)$ for $L = 5$. The orientation dependence of the parameter M_1 given by Eq. II.22 is shown in Fig. II.12b. Numerical values of $\hat{M}_i(m,n)$ are given in the numerical implementation of the constitutive equations (Sénac et al., 2021a). The flow rule associated with the coalescence yield criterion is:

$$\dot{\boldsymbol{\varepsilon}}^\mathrm{p} = \dot{p}_\mathrm{c} \frac{\partial \phi_\mathrm{c}}{\partial \boldsymbol{\Sigma}} = \dot{p}_\mathrm{c} \frac{1}{C_\mathrm{f}} \frac{\partial \Sigma_\mathrm{I}}{\partial \boldsymbol{\Sigma}} \tag{II.23}$$

[2]Taylor factor is defined as $M = \frac{1}{d_\mathrm{eq}} \sum_s \dot{\gamma}_s$ $\left(\text{with } d_\mathrm{eq} = \sqrt{\frac{2}{3}\dot{\epsilon} : \dot{\epsilon}}\right)$ to quantify the amount of plastic slip in a single crystal (Hure, 2019).

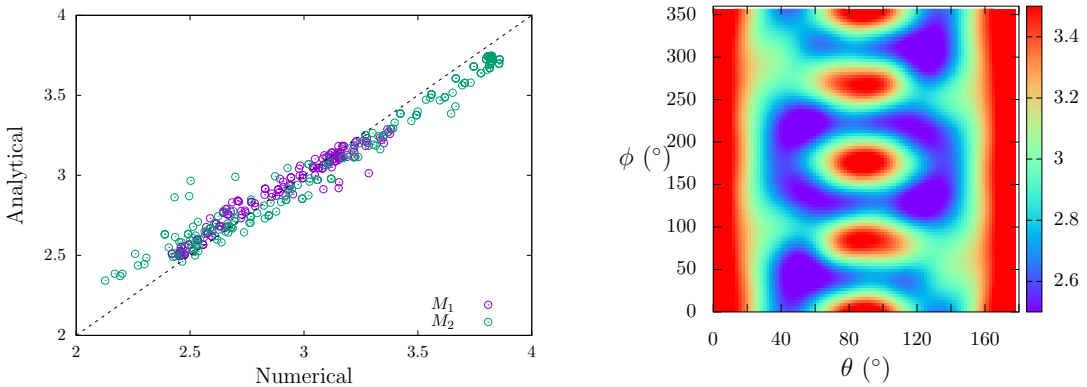

FIGURE II.12: **(a)** Analytical values of the coalescence parameters M_1 and M_2 given by Eq. II.22 as a function of the numerical values computed according to Hure (2019); **(b)** Orientation dependence of the parameter M_1 given by Eq. II.22. θ and ϕ are the spherical coordinates of the coalescence plane normal in the crystal frame.

where the dependence of M_1 and M_2 to $\boldsymbol{\Sigma}$ is disregarded as the parameters are fixed once coalescence sets in. Eq. II.23 is detailed in Appendix II.1.B and corresponds to uniaxial straining, consistently with coalescence by internal necking.

The model belongs to the multi-surface plasticity framework. In order to combine the void growth and void coalescence criteria, a viscoplastic regularization approach similar to crystal plasticity (see Section II.1.2.1) is adopted. Plastic multipliers related to void growth and void coalescence are chosen such as:

$$\forall i \in \{\mathrm{g}, \mathrm{c}\}, \dot{p}_i = \left(\frac{\phi_i}{K}\right)^m_+ \tag{II.24}$$

where K and m are viscoplastic parameters and τ^* is the critical stress for both yield criteria (see Eq. II.17); its evolution will be detailed in next section. These quantities are used to define the plastic strain increment:

$$\dot{\boldsymbol{\varepsilon}^{\mathrm{p}}} = \dot{p}_{\mathrm{g}} \boldsymbol{n}_{\mathrm{g}} + \dot{p}_{\mathrm{c}} \boldsymbol{n}_{\mathrm{c}} \tag{II.25}$$

with $\boldsymbol{n}_{\mathrm{g}}$ and $\boldsymbol{n}_{\mathrm{c}}$ being the flow directions of the two yield criteria defined above. At the transition from growth to coalescence, the two deformations modes are allowed to coexist in order to smooth the mechanical behavior and avoid angular points. This overlap is for numerical purposes and is not meant to describe a physical mechanism; most of the time, only one deformation mode is active — or neither of them in the elastic regime. The smoothing depends on parameters $\{K, m\}$ used.

Hardening The homogenized model should be able to handle different kinds of crystal-scale hardening behaviors such as the ones described in Section II.1.2.2. Following Gurson's approach (Gurson, 1977), the starting point is the Hill-Mandel lemma, which states that:

$$\boldsymbol{\Sigma} : \dot{\boldsymbol{\varepsilon}} = \frac{1}{V_{\mathrm{tot}}} \int_{V_{\mathrm{tot}}} \boldsymbol{\sigma} : \dot{\boldsymbol{\epsilon}} \, dV \tag{II.26}$$

expressing that macroscopic work (on the left-hand side) is equal to microscopic work (on the right-hand side). The assumption that elastic strain increments are negligible in the plastic phase is made, allowing to rewrite the lemma with plastic strains instead of total strains. It is first assumed that the critical resolved shear stress τ^* is locally the same for all slip systems and depends only on the accumulated plastic slip γ. This assumption holds exactly for the PAN hardening law with $\delta = 1$, but is an approximation in other cases considered in Section II.1.2.2. Considering secondly an average value of the accumulated plastic slip over the matrix material in the unit-cell, denoted Γ, Eq. II.26 can be written as:

$$\boldsymbol{\Sigma} : \dot{\boldsymbol{\varepsilon}}^{\mathrm{p}} = (1 - f)\tau^* \dot{\Gamma} \tag{II.27}$$

in the growth regime. Eq. II.27 stands as the definition of the average accumulated plastic slip Γ as τ^* is assumed to depend only on Γ. In the coalescence phase, the hypothesis that plasticity occurs only in the ligament — *i.e.* the

intervoid area — leads to a slightly different expression (Vishwakarma and Keralavarma, 2019):

$$\boldsymbol{\Sigma} : \dot{\boldsymbol{\varepsilon}}^{\mathrm{p}} = \left(\frac{1}{f_{\mathrm{b}}} - 1\right) f\tau^* \dot{\Gamma} \tag{II.28}$$

where f_{b} is defined in Fig. II.5. However, these two equations tend to overestimate strain hardening for low triaxialities as well as for high plastic strains. A parameter named C is thus introduced to tone it down in these cases, defined as:

$$C(\Gamma, \boldsymbol{\Sigma}) = \exp\left(\beta \frac{\Gamma}{T}\right) \tag{II.29}$$

with β a calibration parameter. It should be remembered that Eq. II.29 only deals with the range of trixialities covered by the database, but can be truncated with constant functions outside of this interval. Finally, Eq. II.27 and Eq. II.28 become the following evolution law for Γ:

$$\dot{\Gamma} = \begin{cases} \dfrac{1}{C} \dfrac{\boldsymbol{\Sigma} : \dot{\boldsymbol{\varepsilon}}^{\mathrm{p}}}{(1-f)\tau^*} & \text{(growth)} \\ \dfrac{1}{C} \dfrac{\boldsymbol{\Sigma} : \dot{\boldsymbol{\varepsilon}}^{\mathrm{p}}}{\left(\frac{1}{f_{\mathrm{b}}} - 1\right) f\tau^*} & \text{(coalescence)} \end{cases} \tag{II.30}$$

The homogenized evolution of the critical resolved shear stress τ^* is then established using hardening microscopic laws, by averaging the values on all slip systems to get a unique value. In the case of PAN hardening, Eq. II.8 gives:

$$\dot{\tau}^* = h_0 \frac{1 + 11\delta}{12} \cosh\left(\frac{h_0 \Gamma}{\tau_{\mathrm{sat}} - \tau_0}\right)^{-2} \dot{\Gamma} \tag{II.31}$$

The same reasoning applied to FBZ hardening, along with the fact that $\sum_k a_{sk}$ does not depend on s [3], brings the following homogenized hardening laws:

$$\dot{r_{\mathrm{D}}} = \left(\frac{1}{K_0}\sqrt{N-1}\sqrt{r_{\mathrm{D}}} - G_0 r_{\mathrm{D}}\right) \frac{\dot{\Gamma}}{12} \tag{II.32}$$

$$\tau^* = \tau_0 + \mu \sqrt{\sum_k a_{1k}} \sqrt{r_{\mathrm{D}}} \tag{II.33}$$

which can be simplified into this single formula:

$$\dot{\tau}^* = \frac{\mu}{24} \sqrt{\sum_{k=1}^{N} a_{1k}} \left(\frac{1}{K_0}\sqrt{N-1} - G_0 \frac{\tau^* - \tau_0}{\mu \sqrt{\sum_k a_{1k}}}\right) \dot{\Gamma} \tag{II.34}$$

Evolution of microstructural variables Homogenization theory makes use of microstructural parameters to describe the ductile material microstructure without accounting for the explicit evolution of voids. The microstructural parameters of interest have been defined in Section II.1.2.3. These parameters are treated as internal variables of the model and follow evolution laws detailed hereafter. Porosity f follows a classical evolution law derived from mass conservation (see Benzerga and Leblond (2010)):

$$\dot{f} = (1-f)\mathrm{Tr}\left(\dot{\boldsymbol{\varepsilon}}^{\mathrm{p}}\right) \tag{II.35}$$

The case of void aspect ratio w is more complex, its evolution being dependent on the ductile fracture stage. During coalescence, its evolution law is obtained from geometrical considerations, as explained in Benzerga and Leblond (2010). In the case where voids are spheroidal (with a shape factor of $\gamma = \frac{1}{2}$) and the unit-cell is orthorhombic, it leads to:

$$\dot{w} = \frac{9\lambda}{4\chi}\left[1 - \frac{2}{\pi}\frac{1}{\chi^2}\right] \dot{\varepsilon}^{\mathrm{p}}_{\mathrm{eq}} \tag{II.36}$$

[3] For all $s \in [\![1, N]\!]$, $\sum_k a_{sk} = a_1 + 2a_2 + 2a_3 + a_4 + 4a_5 + 2a_6$ (see Kubin et al. (2008)).

where $\dot{\varepsilon}^{\mathrm{p}}_{\mathrm{eq}} = \sqrt{\frac{2}{3}\left(\mathbb{K} : \dot{\boldsymbol{\varepsilon}}^{\mathrm{p}}\right) : \left(\mathbb{K} : \dot{\boldsymbol{\varepsilon}}^{\mathrm{p}}\right)}$ and $\mathbb{K} = \mathbb{I} - \frac{1}{3}\boldsymbol{I} \otimes \boldsymbol{I}$. However, exact evolution laws for w in the growth phase are of tedious handling (see Song and Ponte-Castañeda (2017a) for instance). Therefore, a heuristic formula depending on triaxiality is proposed:

$$\dot{w} = \begin{cases} \dfrac{1}{w}\left|T-2\right|\dot{\varepsilon}_{\mathrm{I}} & (T < 2) \\ -w\left|T-2\right|\dot{\varepsilon}_{\mathrm{I}} & (T \geq 2) \end{cases} \tag{II.37}$$

where ε_{I} is the largest principal strain. With this evolution law, voids become oblate for triaxialities under 2 and prolate for triaxialities above 2, which is qualitatively in agreement with unit-cell simulations presented in Section II.1.2.3, as well as in Yerra et al. (2010) and Ling et al. (2016). The simple prefactor allows to recover, on average, quantitative predictions when compared to the results shown in Fig. II.7c,d, as well as a saturating behavior. The normalized intervoid distance χ appearing in Eq. II.20 is computed according to:

$$\chi = q_\chi \left(\frac{6}{\pi}\frac{f\lambda}{w}\right)^{\frac{1}{3}} = q_\chi \sqrt{\frac{6}{\pi} f_{\mathrm{b}}} \tag{II.38}$$

This formula accounts for the difference between the unit-cell geometry from which the coalescence criterion was derived (*i.e.* a cylindrical unit-cell with a cylindrical void, see Hure (2019)) and the unit-cell geometry used to homogenize the material behavior (*i.e.* a cubical unit-cell with a spheroidal void) through the factor $\frac{6}{\pi}$. q_χ is a calibration parameter close to 1 that will be discussed later.

The small strain constitutive equations presented hereabove are extended to finite strain by using the logarithmic formalism proposed in Miehe et al. (2002) where the Hencky strain tensor $\boldsymbol{\varepsilon} = \frac{1}{2}\log\left(\boldsymbol{F}^{\mathrm{T}}\boldsymbol{F}\right)$ is used. As detailed in Appendix II.1.A, the final model is thus restricted in principle to highly symmetric crystallographic orientations or large porosity as rotations are disregarded[4]. This limitation will be evaluated in Section II.1.3.4 when comparing the model's predictions to the unit-cell simulations. Finally, the unit-cell aspect ratio λ (Fig. II.5) is defined as:

$$\lambda \equiv \left(\frac{\left(C_{\mathrm{I}}\right)^2}{C_{\mathrm{II}}C_{\mathrm{III}}}\right)^{\frac{1}{4}} = \frac{e^{\varepsilon_{\mathrm{I}}}}{e^{\frac{1}{2}\left(\varepsilon_{\mathrm{II}}+\varepsilon_{\mathrm{III}}\right)}} \tag{II.39}$$

where $C_{\mathrm{I}} > C_{\mathrm{II}}, C_{\mathrm{III}}$ are the eigenvalues of Cauchy-Green tensor $\boldsymbol{C} = \boldsymbol{F}^T\boldsymbol{F}$ and where the equality is obtained by using logarithmic strain.

Equations of both this homogenized model (referred to as the "PBKH model") and the one presented in Scherer et al. (2021) (referred to as the "HLS model") are summarized in Appendix II.1.C for comparison and convenience. For a detailed description of the HLS model, the reader is referred to Scherer et al. (2021). These two models account for both void growth and coalescence and are at the state of the art of homogenized porous crystal plasticity. However, their constituents are not identical, either on the finite strain framework (multiplicative decomposition of the deformation gradient $\boldsymbol{F} = \boldsymbol{F}_{\mathrm{e}}\boldsymbol{F}_{\mathrm{p}}$ versus logarithmic strain formalism) or on the level of description developed for growth and coalescence. On the one hand, the HLS model uses a more complex growth criterion with one yield criterion per slip system (proposed in Han et al. (2013) and extended in Ling et al. (2016)) that theoretically allows a better description of cross-hardening between slip systems but is in return more computation-intensive. On the other hand, coalescence modeling is more elaborated in the PBKH model since it takes into account void shape evolution while voids retain their aspect ratio in the HLS model. In their current state of development, the PBKH model is implemented with both PAN and FBZ hardening whereas only FBZ hardening has been considered for the HLS model.

1.3.2 Numerical implementation

The constitutive equations detailed in Section II.1.3.1 form a set of nonlinear differential equations which is integrated numerically for each total strain increment $\boldsymbol{\Delta\varepsilon}$. The state variables are the elastic strain tensor $\boldsymbol{\varepsilon}^{\mathrm{el}}$, the porosity f, the void aspect ratio w, the average cumulated plastic slip Γ and the homogenized critical stress τ^* — the last two being gathered in a unique hardening state variable H since their evolution is intertwined. Other parameters involved in the constitutive equations can be deduced from these state variables, such as the stress tensor $\boldsymbol{\Sigma}$ from Hooke's law,

[4] This is a result of both the definition of Hencky strain and the use of symmetric Schmid tensor $\boldsymbol{\mu}_k^{(\mathrm{s})}$ in the void growth criterion (Eq. II.18).

as well as the cell aspect ratio λ and the intervoid distance χ from geometrical relations. Equivalent matrix stresses $\sigma^*_{i\in\{\mathrm{g,c}\}}$ are obtained by solving Eqs. II.18 and II.20. The discretized version of the set of equations to be solved are:

$$\begin{aligned}
\mathcal{R}_{\Delta\boldsymbol{\varepsilon}^{\mathrm{el}}} &= \Delta\boldsymbol{\varepsilon}^{\mathrm{el}} + \Delta p_{\mathrm{g}}\boldsymbol{n}_{\mathrm{g}} + \Delta p_{\mathrm{c}}\boldsymbol{n}_{\mathrm{c}} - \Delta\boldsymbol{\varepsilon} &&= 0\\
\mathcal{R}_{\Delta f} &= \Delta f - \mathcal{F}\left(f, \boldsymbol{n}_i, \Delta p_i\right) &&= 0\\
\mathcal{R}_{\Delta w} &= \Delta w - \mathcal{W}\left(\boldsymbol{\varepsilon}^{\mathrm{el}}, f, w, \Delta p_i, \boldsymbol{n}_i\right) &&= 0\\
\mathcal{R}_{\Delta H} &= \begin{pmatrix}\Delta\Gamma\\ \Delta\tau^*\end{pmatrix} - \mathcal{H}\left(\boldsymbol{\varepsilon}^{\mathrm{el}}, f, w, \Gamma, \tau^*, \Delta p_i, \boldsymbol{n}_i\right) &&= 0
\end{aligned} \tag{II.40}$$

A fully implicit integration scheme for the set of Eqs. II.40 would solve the equations considering that the value of each variable corresponds to the one at the end of the time step. However, such a system is notoriously difficult to solve numerically using a Newton-Raphson algorithm due to the highly nonlinear nature of Eqs. II.40. This may also be related to the absence of uniqueness of the incremental problem solution. Different approaches have been proposed in the literature, from a fully implicit integration scheme (Benzerga et al., 2001) to the explicit integration of the geometrical variables (Enakoutsa and Leblond, 2009). In the latter case, it can be shown that the incremental problem falls within the scope of generalized standard materials (Morin et al., 2015a), where the uniqueness of the solution is guaranteed.

In order to alleviate these numerical difficulties, a mixed Newton-Raphson / fixed-point algorithm is proposed in this study. Eq. II.40$_a$ is solved by a Newton Raphson algorithm with respect to the increment of elastic stain tensor $\Delta\boldsymbol{\varepsilon}^{\mathrm{el}}$, the other state variables being constant. The Newton-Raphson algorithm requires the computation of the derivative of Eq. II.40$_a$:

$$\frac{\partial\mathcal{R}_{\Delta\varepsilon^{\mathrm{el}}}}{\partial\Delta\boldsymbol{\varepsilon}^{\mathrm{el}}} = \mathbb{I} + \sum_{i\in\{\mathrm{g,c}\}}\left[\Delta p_i\left(\frac{\partial\boldsymbol{n}_i}{\partial\boldsymbol{\Sigma}}\cdot\mathbb{C}\right) - \frac{m}{K}\left(\frac{(\sigma_i^* - \tau^*)_+}{K}\right)^{m-1}\Delta t\left(\boldsymbol{n}_i\otimes(\boldsymbol{n}_i:\mathbb{C})\right)\right] \tag{II.41}$$

where flow directions $\boldsymbol{n}_{i\in\{\mathrm{g,c}\}}$ and their derivatives are detailed in Appendix II.1.B. Upon convergence of the Newton-Raphson algorithm, Eqs. II.40$_{b,c,d}$ are used to compute the increments of the state variables. These two steps are repeated until the stationarity of these increments. This algorithm ensures a fully implicit integration scheme of the system defined by Eqs. II.40. The consistent tangent operator, required for some finite element solvers, can be computed based on Eq. II.41 (Helfer, 2020). The numerical integration has been implemented in the `MFront` code generator (Helfer et al., 2015), and the different steps are summarized in Algorithm 1. As the intervoid distance χ increases close to 1, the coalescence yield surface shrinks to a point, representing material failure. In order to avoid numerical issues in the vicinity of this point, a boolean state variable `broken` is added and set to `true` when χ reaches a critical value χ_c. In that case, the numerical integration simply returns zero stresses. As mentioned above, in order to extend these constitutive equations and their numerical integration to finite strains, the logarithmic strain framework is used. The full numerical implementation is freely available (Sénac et al., 2021a) and can be used in a large number of finite element solvers (*e.g.* with a UMAT-compatible interface) (Helfer et al., 2015).

1.3.3 Calibration of numerical parameters

The first use of the database described in Section II.1.2 is the calibration of numerical parameters that were not fixed in the homogenized model definition. Thereby, computation of κ and q from the growth yield criterion can be performed as follows: for each unit-cell simulation without hardening, a fixed number of points in the growth phase is sampled. κ and q are then computed with a least-square method to ensure that $|S_{\mathrm{g}}(\tau_0, \boldsymbol{\Sigma}, \kappa, q)|^2$ is as close to zero as possible over the sample of points, with $\boldsymbol{\Sigma}$ the macroscopic stress of the unit-cell and τ_0 the critical resolved shear stress. Note that the regularization parameter $n = 100$ is chosen for the yield criterion (Eq. II.18). The minimization brings $\kappa \approx 0.49$ and $q \approx 1.66$, which is close to the values provided in Paux et al. (2018) ($\kappa = 0.49$ and $q = 2$).

A similar calibration is performed on q_χ by minimizing the sum of $|S_{\mathrm{c}}(\tau_0, \boldsymbol{\Sigma}, q_\chi)|^2$ at the onset of coalescence phase of all unit-cell simulations without hardening. This optimization brings $q_\chi \approx 0.822$. However, direct comparisons between homogenized model computations and unit-cell simulations underline a discrepancy depending on stress triaxiality: coalescence occurs too early for high triaxialities ($T > 2$) and too late for low triaxialities ($T < 2$). In order to achieve a better agreement, the coalescence equivalence stress σ_{c}^* must be reduced for high triaxialities and *vice versa*. This can be achieved by a dependence of q_χ on T, as proposed in Scherer and Hure (2019). Using the database,

Algorithm 1 Numerical integration of constitutive equations.

Require: State variables at the beginning of the time step $\left\{\boldsymbol{\varepsilon}_n^{\text{el}}, f_n, w_n, \Gamma_n, \tau_n^*, \texttt{broken}\right\}$
Require: Total strain increment $\Delta\boldsymbol{\varepsilon}$
if `broken` **then**
  $\left\{\boldsymbol{\varepsilon}_{n+1}^{\text{el}}, f_{n+1}, w_{n+1}, \Gamma_{n+1}, \tau_{n+1}^*\right\} \leftarrow \left\{0, f_n, w_n, \Gamma_n, \tau_n^*\right\}$
else
  Compute elastic trial stress $\boldsymbol{\Sigma}_{\text{trial}} = \mathbb{C} : \left(\boldsymbol{\varepsilon}_n^{\text{el}} + \Delta\boldsymbol{\varepsilon}\right)$
  if $\mathcal{Y}\left(\boldsymbol{\Sigma}_{\text{trial}}, f_n, w_n, \Gamma_n, \tau_n^*\right) \leq 0$ **then** ▷ Elastic evolution
    $\left\{\boldsymbol{\varepsilon}_{n+1}^{\text{el}}, f_{n+1}, w_{n+1}, \Gamma_{n+1}, \tau_{n+1}^*\right\} \leftarrow \left\{\boldsymbol{\varepsilon}_n^{\text{el}} + \Delta\boldsymbol{\varepsilon}, f_n, w_n, \Gamma_n, \tau_n^*\right\}$
  else ▷ Elasto-plastic evolution
    $\left\{\Delta f, \Delta w, \Delta\Gamma, \Delta\tau^*\right\} \leftarrow \left\{0, 0, 0, 0\right\}$
    repeat ▷ Fixed-point algorithm for $\left\{\Delta f, \Delta w, \Delta\Gamma, \Delta\tau^*\right\}$
      $\left\{f, w, \Gamma, \tau^*\right\} \leftarrow \left\{f_n + \Delta f, w_n + \Delta w, \Gamma_n + \Delta\Gamma, \tau_n^* + \Delta\tau^*\right\}$
      while $\left|\mathcal{R}_{\Delta\boldsymbol{\varepsilon}^{\text{el}}}\right| \geq \varepsilon$ **do** ▷ Newton-Raphson algorithm on $\Delta\boldsymbol{\varepsilon}^{\text{el}}$
        $\Delta\boldsymbol{\varepsilon}^{\text{el}} \leftarrow \Delta\boldsymbol{\varepsilon}^{\text{el}} - \boldsymbol{J}^{-1}_{\Delta\boldsymbol{\varepsilon}^{\text{el}}}\mathcal{R}_{\Delta\boldsymbol{\varepsilon}^{\text{el}}}$
      end while
      $\left\{\Delta f, \Delta w, \Delta\Gamma, \Delta\tau^*\right\} \leftarrow \left\{\mathcal{F}, \mathcal{W}, \mathcal{H}\right\}\left(\varepsilon^{\text{el}} + \Delta\boldsymbol{\varepsilon}^{\text{el}}, f, w, \Gamma, \tau^*\right)$
    until $\max\left|\Delta f^{k+1} - \Delta f^k, \Delta w^{k+1} - \Delta w^k, \Delta\Gamma^{k+1} - \Delta\Gamma^k, (\Delta\tau^*)^{k+1} - (\Delta\tau^*)^k\right| \leq \delta$
    $\left\{\boldsymbol{\varepsilon}_{n+1}^{\text{el}}, f_{n+1}, w_{n+1}, \Gamma_{n+1}, \tau_{n+1}^*\right\} \leftarrow \left\{\boldsymbol{\varepsilon}_n^{\text{el}} + \Delta\boldsymbol{\varepsilon}^{\text{el}}, f_n + \Delta f, w_n + \Delta w, \Gamma_n + \Delta\Gamma, \tau_n^* + \Delta\tau^*\right\}$
    if $\chi > \chi_c$ **then**
      `broken` $\leftarrow$ `true` ▷ Material failure
    end if
  end if
end if

we perform a linear fit of q_χ according to T, which brings[5]:

$$q_\chi(\boldsymbol{\Sigma}) = 0.912 - 0.039T \tag{II.42}$$

As with Eq. II.29, the validity of this formula only holds over the range of trixialities covered by the database, *i.e.* for values of T that are not too low or too high. Values of κ, q, and q_χ were calibrated on unit-cell simulations without strain hardening, but will be used in the homogenized model for plasticity with hardening as well. The only parameter that is calibrated with the database of unit-cell simulations with hardening is β. Since PAN hardening saturates naturally, the value of β has almost no effect in this case. β is thus calibrated on FBZ hardening simulations only: minimization of the sum of $|S_{\text{g}}(\beta, \boldsymbol{\Sigma})|^2$ over the growth phase of these unit-cell calculations gives $\beta \approx 2.88$.

Numerical parameters of the HLS model were either fitted in previous work using a handful of small strain simulations (Han et al., 2013) (κ, q) or calibrated using the finite strain unit-cell simulation database of Section II.1.2 (κ^{c}, q^{c}, q_χ). Numerical parameters for both models are summarized in Appendix II.1.C.

1.3.4 Comparison to unit-cells results

Once the numerical parameters are calibrated, the agreement of the homogenized model to the unit-cell database can be assessed to ensure that it can reproduce the great diversity of results contained therein. Note that the objective is not to confront PBKH and HLS models directly but to evaluate the agreement of the PBKH model with the simulation database; in case of discrepancy and when it is relevant, the HLS model will be used to check the effects of alternative working hypotheses. Two assessments were conducted: the first to qualify the yield criteria ability to predict the stress state given the internal variables and the second to compare homogenized model predictions with the unit-cell axisymmetrical simulations. In all cases, only part of the unit-cell stress-strain curves is used for the comparison, from effective yield stress (to avoid elasticity) until stress equals 40% of the maximal stress. Beyond that point, meshes are strongly distorted in numerical simulations, making the stress values questionable.

In the first assessment, points are sampled over the growth phase for each set of parameters present in the database: crystallographic orientation, triaxiality T, initial porosity f_0 and hardening law, as shown in Fig. II.13. The axisymmetric stress tensor $\boldsymbol{\Sigma}$ is computed through equation $S_{\text{g}}(\boldsymbol{\Sigma}, f, \tau^*) = 0$ with f and τ^* given by the unit-cell

[5]Note that in the framework of associated plastic flow, this induces in principle an additional term in Eq. II.23. However, this term can be disregarded since it is at least one order of magnitude below the main term, ensuring that coalescence plastic flow is still compatible with uniaxial straining.

computation. $(\Sigma_{11})_{\text{YC}}$ can then be compared to the unit-cell simulation stress $(\Sigma_{11})_{\text{UC}}$. The same procedure is repeated by sampling points in the coalescence phase and computing $(\Sigma_{11})_{\text{YC}}$ using $S_c(\mathbf{\Sigma}, w, \chi, \tau^*) = 0$ with w, χ, τ^* given by the unit-cell simulation (see Fig. II.13). Both aforementioned sets of points are then displayed in Figure II.14; each subgraph corresponds to a homogenized model and a hardening law[6]. For simulations without hardening τ^* is equal to the initial critical resolved shear stress τ_0, but for simulations with hardening τ^* is not directly given by the unit-cell computation, being a homogenized variable. Homogenization equations II.27-II.34 are therefore used to compute τ^* from the unit-cell simulation stress and strain history[7]. The interest of this comparison is the assessment of the yield criteria and strain-hardening homogenization equations; this assessment is conducted independently of evolution laws, including flow rules, since geometrical internal variables are provided by unit-cell simulations. The results of this first assessment are shown in Fig. II.14. Without hardening, Fig. II.14a indicates that the yield criteria used in the PBKH model are very accurate *for fixed values of microstructural parameters*. This is in agreement with Paux et al. (2018) and Hure (2019) where each yield criterion has been validated. The same conclusion holds for the HLS model as shown in Fig. II.14b. With hardening (Fig. II.14c,d,e), more discrepancies are observed in the coalescence stage between the predictions of the homogenized models and the unit-cell results, especially in the case of FBZ hardening for which stress values are generally underestimated (Fig. II.14c,d). It should be noted that the values of the parameters for FBZ hardening lead to a very strong hardening with almost no saturation unless unrealistic strain values are reached. It fosters steep hardening gradients between the bulk material that remains soft and the layer around the cavity whose hardness displays no upper bound; such heterogeneities are particularly tricky to account for with homogenized models. Restricting to low and medium hardening (PAN model), a very good agreement is obtained (Fig. II.14e) between model predictions and unit-cell results whatever the parameters used (see Table II.2). This shows that the extension of Gurson's modeling of hardening for crystal plasticity through Eq. II.27, although simple, is effective for such situations. It should also be noted that some of the PAN hardening set of parameters correspond to cases where $\delta \neq 1$, *i.e.*, critical resolved shear stress may be locally different in each slip system. The assumption made in the homogenized model to consider a single accumulated plastic slip Γ variable does not seem to degrade the results compared to cases where $\delta = 1$.

The second assessment is more straightforward: for each set of parameters present in the database, a comparison of stress values is conducted between the unit-cell computation and the predictions of both homogenized models *for fixed strain values*. Strain values are sampled for each set of parameters, *e.g.* crystallographic orientation #0 under triaxiality $T = 1.5$ without hardening. Each of those strain values corresponds to a point in Figure II.15, the x-coordinate being the unit-cell normalized stress Σ_{11}/τ_0 at that strain value and the y-coordinate being the homogenized model

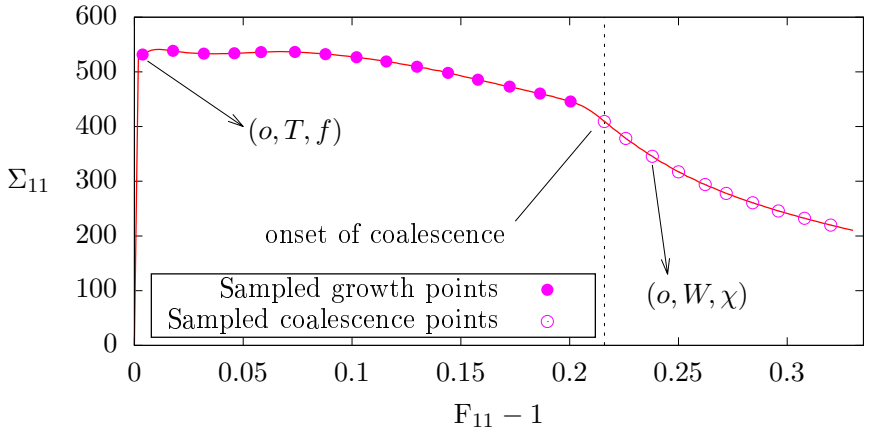

FIGURE II.13: Outline of the sampling of points from a unit-cell simulation conducted in the first assessment: for each point, internal variables are recovered, as well as entry parameters: orientation o — for both phases — and triaxiality T — in the growth phase. The simulation represented here corresponds to $f_0 = 0.01$, $T = 2$, orientation #7 and no hardening. In the presence of strain hardening, τ^* is also computed at each sampled point.

[6] In the case of the HLS model, $(\Sigma_{11})_{\text{YC}}$ predicted by the growth yield criterion is the minimal value such as plasticity occurs in a given slip system $s \in [\![1, N]\!]$. The procedure applied for the coalescence criterion is the same as the PBKH model with $S_c = \frac{\Sigma_{11}}{\sigma_c^*} - C_f$. Relevant equations are detailed in Appendix II.1.C.

[7] Since there is no obvious way of translating this procedure for the HLS model, the same hardening homogenization equations II.27-II.34 were applied regardless of the fact that HLS model has one homogenized critical resolved shear stress for each slip system instead of a global homogenized critical stress τ^*.

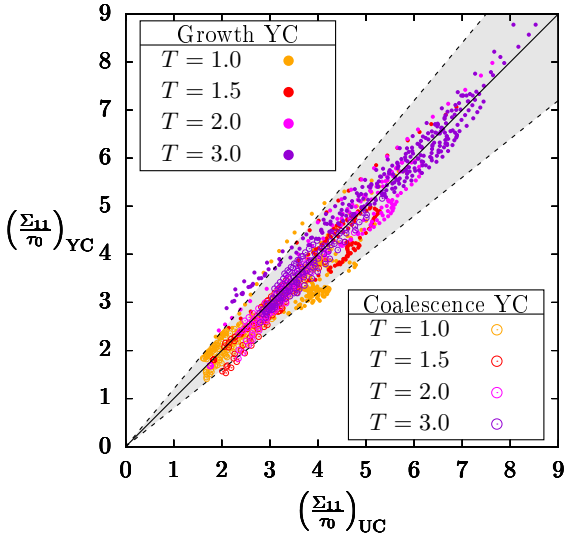

(a) PBKH yield criteria without hardening
($R_g^2 = 0.943$, $R_c^2 = 0.971$)

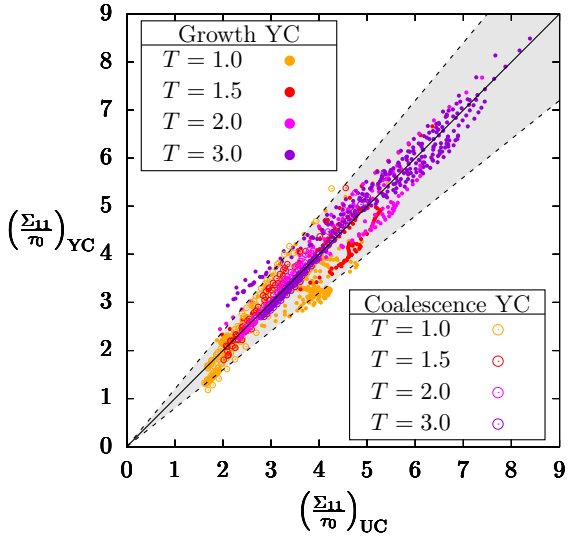

(b) HLS yield criteria without hardening
($R_g^2 = 0.937$, $R_c^2 = 0.974$)

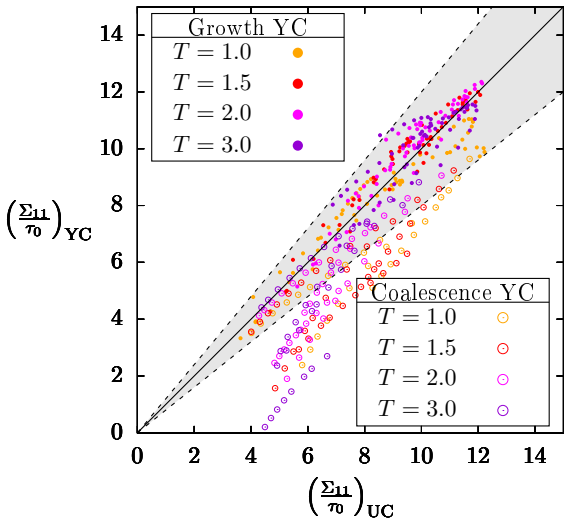

(c) PBKH yield criteria with FBZ hardening
($R_g^2 = 0.938$, $R_c^2 = 0.836$)

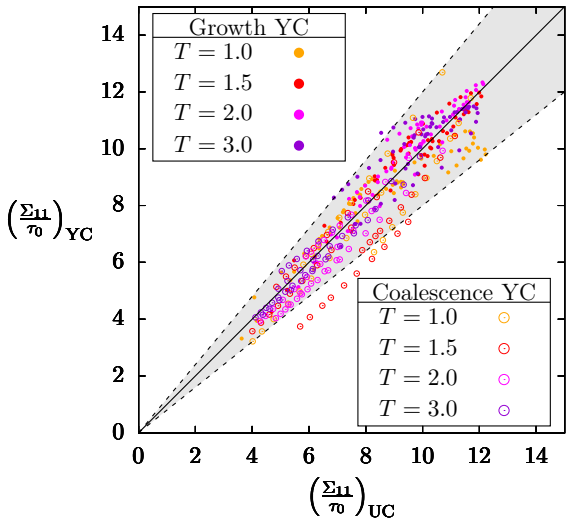

(d) HLS yield criteria with FBZ hardening
($R_g^2 = 0.923$, $R_c^2 = 0.917$)

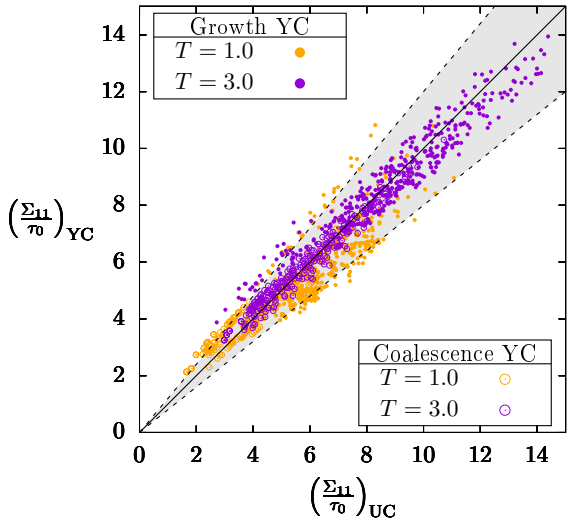

(e) PBKH yield criteria with PAN hardening
($R_g^2 = 0.948$, $R_c^2 = 0.983$)

FIGURE II.14: Assessment of yield criteria of the homogenized models: the normalized stress $\frac{\Sigma_{11}}{\tau_0}$ of the unit-cell computation and the one predicted by the yield criterion considered are plotted against each other, each point corresponding to a sampled set of internal variables from a given database simulation. Pearson correlation coefficients are given for both the growth phase and the coalescence phase of each graph. Dashed lines correspond to vertical deviations of $\pm 20\%$ from the $y = x$ line.

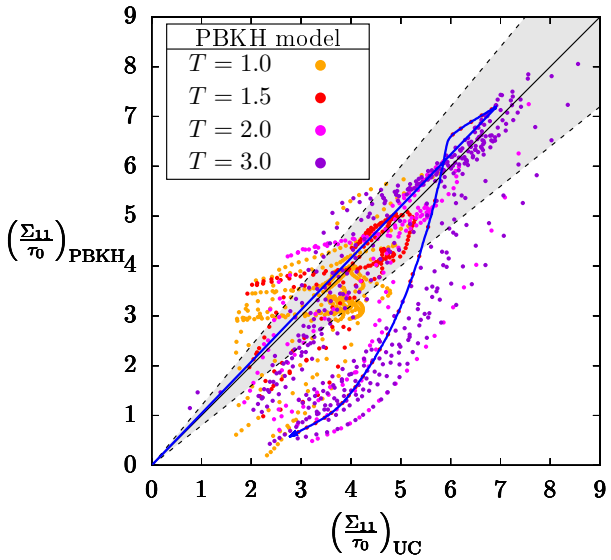

(a) PBKH model without hardening ($R^2 = 0.750$)

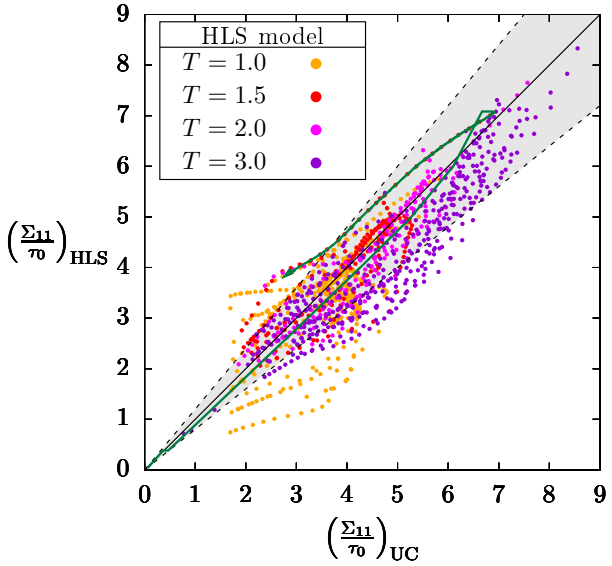

(b) HLS model without hardening ($R^2 = 0.859$)

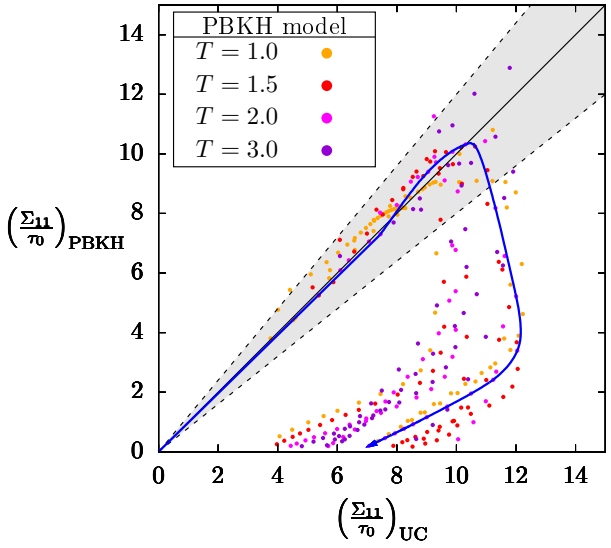

(c) PBKH model with FBZ hardening ($R^2 = 0.318$)

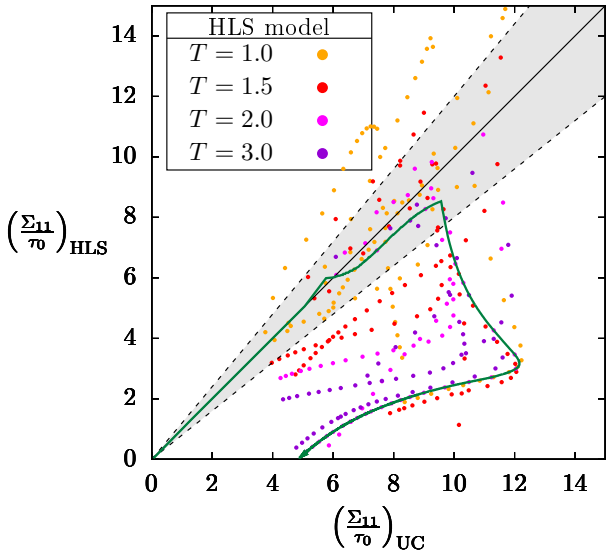

(d) HLS model with FBZ hardening ($R^2 = 0.255$)

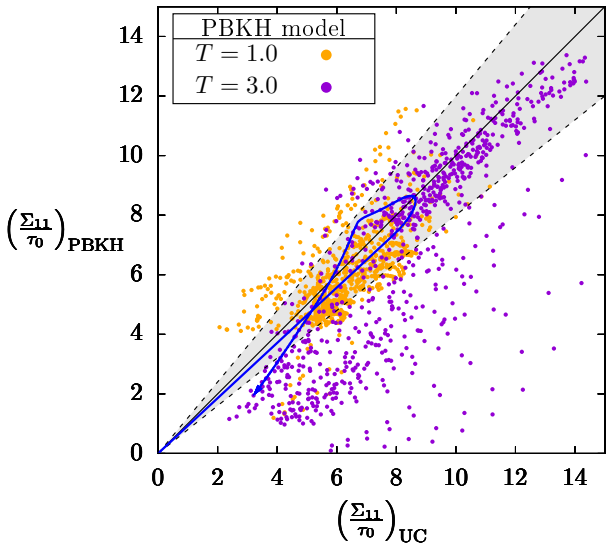

(e) PBKH model with PAN hardening ($R^2 = 0.752$)

FIGURE II.15: Assessment of the homogenized models: normalized stress $\frac{\Sigma_{11}}{\tau_0}$ of both the unit-cell computation and the homogenized model considered are plotted against each other, each point corresponding to a sampled strain level in a given database simulation. Colored arrows represent simulation trajectories whose stress-strain curves are plotted in Fig. II.16. Pearson correlation coefficients are given for each graph. Dashed lines correspond to vertical deviations of $\pm 20\%$ from the $y = x$ line.

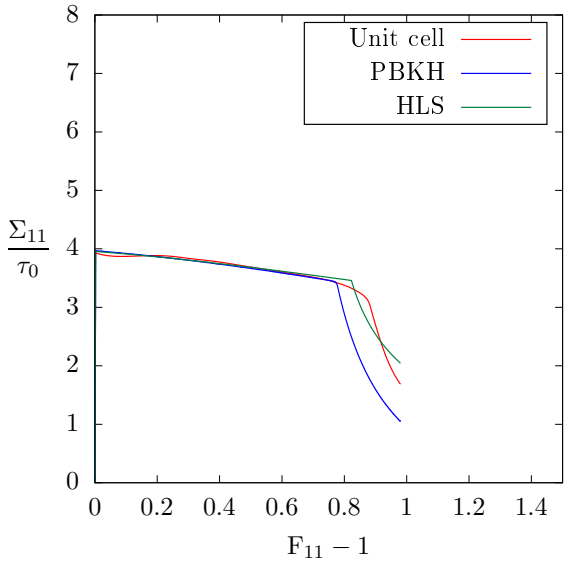

(a) Orientation #5: $[1\,0\,0] - [0\,1\,\bar{1}] - [0\,1\,1]$, $T = 1$, without hardening

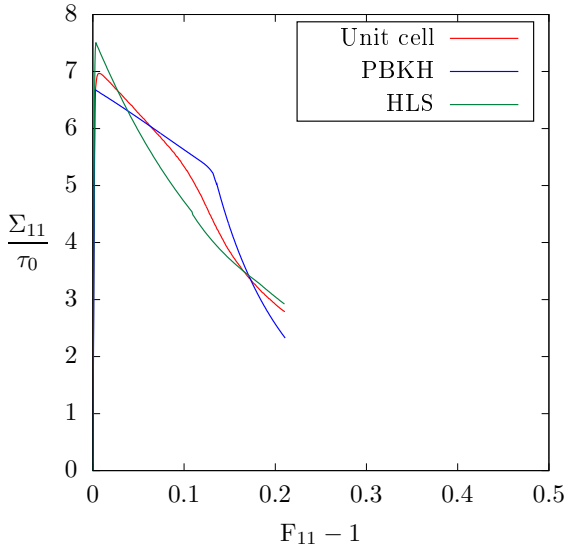

(b) Orientation #3: $[\bar{1}\,2\,5] - [0\,\bar{5}\,2] - [29\,2\,5]$, $T = 3$, without hardening

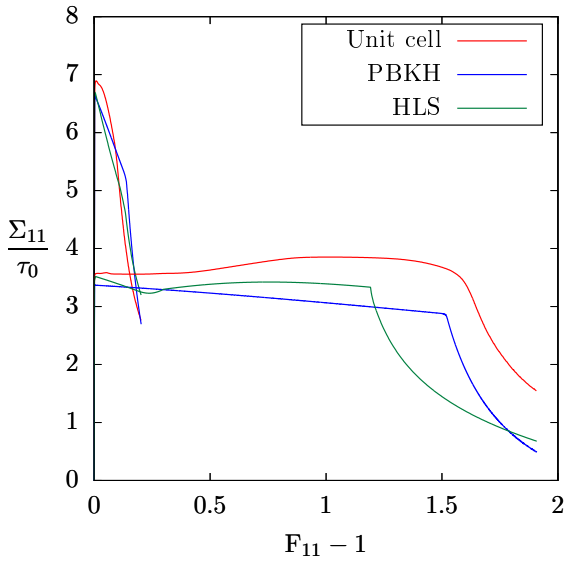

(c) Orientation #1: $[2\,1\,0] - [\bar{1}\,2\,0] - [0\,1\,1]$, $T \in \{1, 3\}$, without hardening

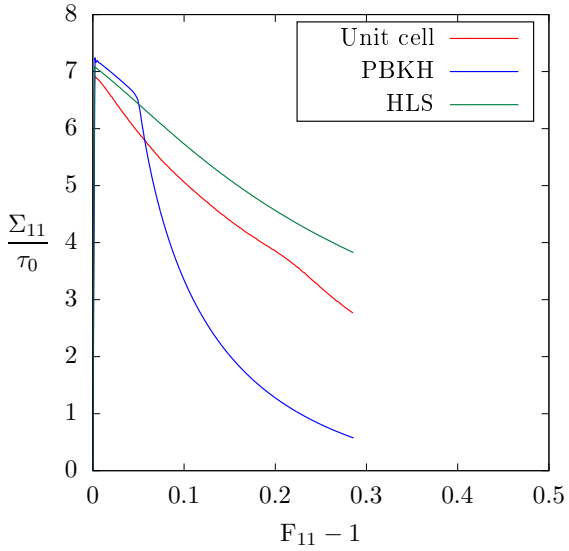

(d) Orientation #0: $[1\,1\,1] - [\bar{2}\,1\,1] - [0\,\bar{1}\,1]$, $T = 1.5$, without hardening

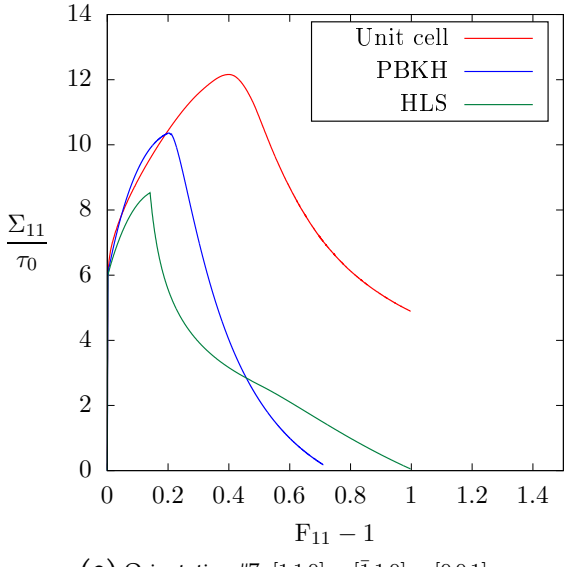

(e) Orientation #7: $[1\,1\,0] - [\bar{1}\,1\,0] - [0\,0\,1]$, $T = 2$, FBZ hardening

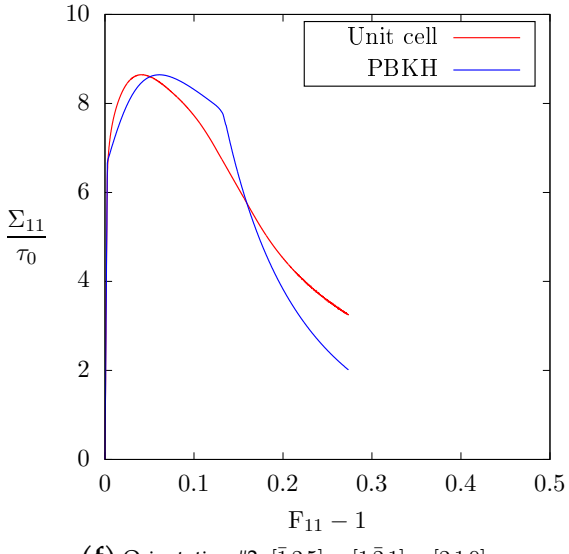

(f) Orientation #2: $[\bar{1}\,2\,5] - [1\,\bar{2}\,1] - [2\,1\,0]$, $T = 3$, PAN hardening (2b)

FIGURE II.16: Stress-strain curves of a representative set of simulations: various orientations, triaxialities and hardening laws are considered. Comparisons are made between the results of the unit-cell computation and predictions of the two homogenized models (PBKH and HLS).

normalized stress Σ_{11}/τ_0 at the same strain value. Contrary to Figure II.14, no distinction is made between growth and coalescence as the homogenized models should be able to predict the active deformation mode and, more importantly, the stress level. This comparison allows to assess the predictive capability of the homogenized models as a whole, including yield criteria, modeling of hardening, as well as evolution laws describing plastic flow and microstructural parameters. As yield criteria, and to a lesser extent hardening, have been shown to be rather accurate in Fig. II.14, Fig. II.15 stands as a test for evolution laws used in the homogenized models. For each subgraph of Figure II.15, a single set of parameters is chosen and corresponding points are linked by a colored arrow in ascending strain order. The stress-strain curves of these distinctive simulations are plotted in Figure II.16d,e,f.

Without hardening, Fig. II.15a indicates that most of the predictions of the PBKH homogenized model fall within $\pm$20% of the unit-cell results. However, strong discrepancies are observed in certain cases where the model underestimates the stress levels. They can easily be understood by looking at the stress-strain curves (Figure II.16a,b,c,d): while the model correctly predicts the first part of these curves — corresponding to void growth regime — the onset of coalescence is not predicted accurately enough, triggering a sudden stress drop that is either too late or too early. As coalescence deformation mode induces a very strong decrease of stress, the differences between the unit-cell results and the homogenized model increase drastically, explaining the strong deviations observed in Fig. II.15a. In general, the representation used in Fig. II.15 tends to amplify the differences, which should be kept in mind in the analysis. The HLS homogenized model appears to be in good agreement with the unit-cell results (Fig. II.15a). The different behavior exhibited by the PBKH model is believed to come from at least two features. First, since the logarithmic strain framework used in the PBKH model cannot reproduce crystal lattice rotation (see Appendix II.1.A), the structural hardening coming from the progressive activation of slip systems with increasing yield limits cannot be predicted, as can be seen in Fig. II.16c. In such situations, a qualitative agreement is obtained for the HLS model — which uses the multiplicative decomposition of the deformation gradient. This structural hardening effect, which can be strong at low triaxialities, is almost negligible at high triaxialities. Second, orientations displaying only one activated slip system under mechanical loading are not accurately predicted by the PBKH model, as shown in Fig. II.16d. As discussed in the model definition, this was expected due to the use of Hencky strain tensor and symmetric Schmid tensor. In fact, orientation #0 explains the main discrepancies seen in Fig. II.15a — the colored arrows on Fig. II.15a,b correspond to the simulation shown in Fig. II.16d — while random orientations are well predicted.

The agreement between homogenized model predictions and unit-cell results deteriorates with hardening (Fig. II.15c,d,e). The initial hardening regime is captured for the PBKH model with FBZ hardening (Fig. II.15c), but the model systematically predicts an early coalescence. For its part, the HLS model (Fig. II.15d) predicts coalescence either too late or too early depending on situations, the latter being less frequent. This should not be surprising; indeed, the latter neglects the void aspect ratio evolution and thus has simplified modeling of coalescence. The simulations marked by colored arrows in Figs. II.15c,d are displayed in Fig. II.16e, showing that the case of strong hardening is still tricky to handle, even though the phenomenological modification used (Eq. II.29) helps to recover a prediction in closer agreement with unit-cell results. Overall, predictions made by the PBKH model with FBZ hardening display a qualitative agreement in the absence of quantitative agreement during the coalescence phase. Restricting to low to medium hardening (Fig. II.15e), the agreement improves: most of the predictions fall within $\pm$20% of the reference results, even in the coalescence regime. The simulation marked by a colored arrow is shown in Fig. II.16f where a very good agreement is observed in this particular case.

The detailed assessments conducted in this section allow for drawing some conclusions regarding the current state of modeling of porous single crystals. Firstly, the model proposed in this study (PBKH), designed with a limited number of internal variables and a simplified finite strain framework, leads to predictions that are mostly in agreement with unit-cell simulations and compare reasonably well with the level of compliance reached by the HLS model. This implies that ductile fracture simulations can be performed using this model instead of isotropic models, *e.g.* that of Benzerga and Leblond (2010), with limited additional numerical costs while accounting for the material's microstructure. Secondly, yield criteria, and to a lesser extent hardening, are shown to be quite accurate *for fixed values of internal variables* under axisymmetric conditions, as shown in Fig. II.14. This indicates that more efforts should be put into other factors such as the interplay between void shape changes and hardening, for example, using models derived from different approaches (Song and Ponte-Castañeda, 2017a), but also on more complex — non-axisymmetric — loading conditions. Finally, the proposed model displays a validity domain in which accurate predictions can be made; this will be discussed in the following section.

1.4 Discussion and perspectives

The comparisons made in the previous section call for the assessment of the domain of validity of the model proposed in this study. First, as shown in Appendix II.1.A, the finite strain framework cannot capture single slip and/or crystal lattice rotation, which is at the origin of the discrepancies observed in Figs. II.16c,d. Thus, the model should be used for rather large porosity or triaxiality values, such as those considered in this study. This is the case in highly irradiated materials where a high void volume fraction — up to tens of percent — is formed at the grain scale (Neustroev and Garner, 2009). Another potential application is the case of materials from additive manufacturing (DebRoy et al., 2018). Note that this limitation could be removed by considering the multiplicative decomposition of the deformation gradient. Secondly, strong local hardening, like the one resulting from FBZ equations (Eq. II.6), cannot be captured quantitatively for all situations, even by introducing additional phenomenological modifications (Eq. II.29). Considering the similar behavior displayed by the HLS model, deviations observed for the proposed model are not related to the simplifications made to account for hardening with a single hardening variable (Eq. II.27). Instead, a hard shell appears around the void for strong hardening, and the local strain field is highly heterogeneous. Models have been proposed to handle this phenomenon for isotropic materials (Morin et al., 2017) that would benefit from being extended to single crystals. Considering only low and medium hardening — such as the PAN law with the set of parameters named *2a* and *2b* in Table II.2 — as well as perfect plasticity cases, comparisons between unit-cell results and model predictions are shown in Fig. II.17. An overall very good agreement is observed, confirming the model's validity for low to medium hardening material.

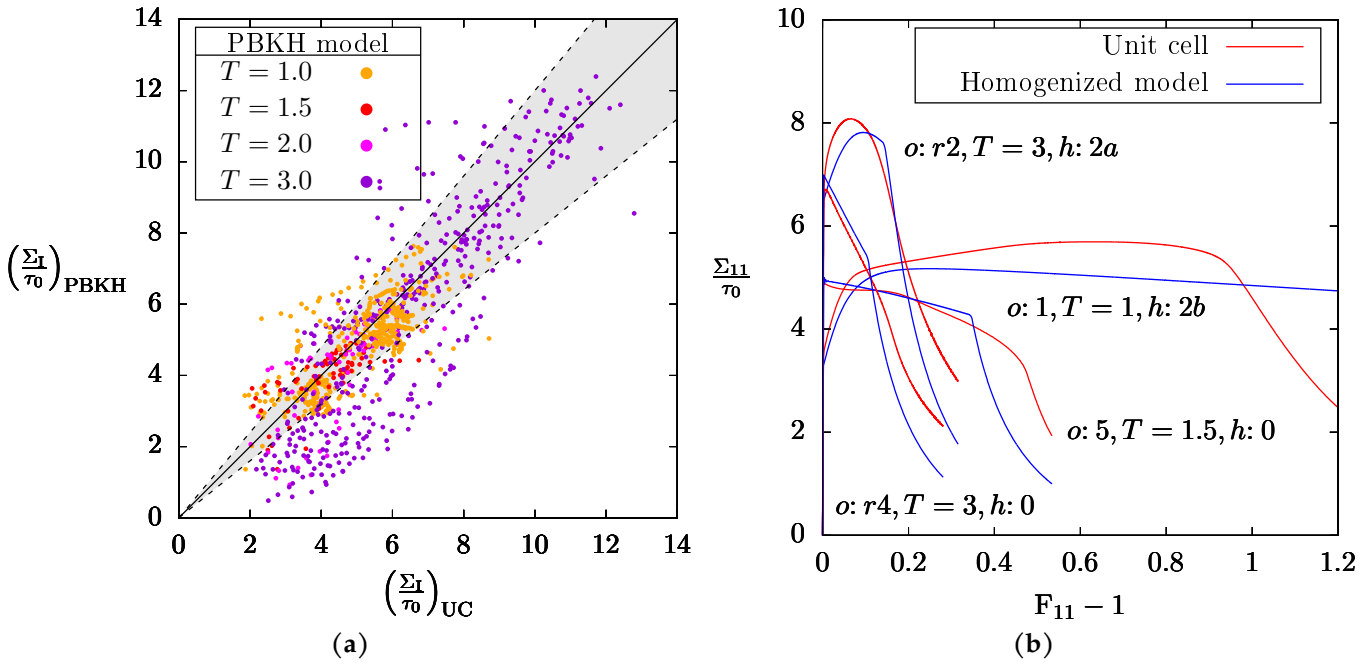

FIGURE II.17: Assessment of the homogenized model against unit-cell data corresponding to absence of hardening or *2a* / *2b* PAN hardening: **(a)** normalized stress $\frac{\Sigma_{11}}{\tau_0}$ of both the unit-cell computation and the homogenized model plotted against each other, each point corresponding to a sampled strain level in a given database simulation; **(b)** stress-strain curves of a representative set of simulations with various orientations (o), triaxialities (T) and hardening laws (h) considered.

While a general perspective lies in improving the models to reproduce reference unit-cell results better, an interesting improvement perspective is related to the distribution of voids. An initially cubic array of voids has been considered for both unit-cell simulations and the two homogenized models. As shown for isotropic porous materials (Fritzen et al., 2012), void distribution affects both void growth and void coalescence modeling. In the former case, calibration of the parameters of the yield criteria is required. In the latter case, other deformation modes, such as shear-assisted coalescence, can be observed. As an example, the results of a simulation considering a random distribution of voids in a non-hardening single crystal are shown in Fig. II.18 and compared to the case of a single void, for the same initial porosity, crystallographic orientation and mechanical loading condition. Slight differences are observed on the stress-strain curves (Fig. II.18a), but the main difference lies in the coalescence deformation mode. Indeed, shear bands are seen to link adjacent voids in the random porous crystal (Fig. II.18b). A shear-assisted coalescence

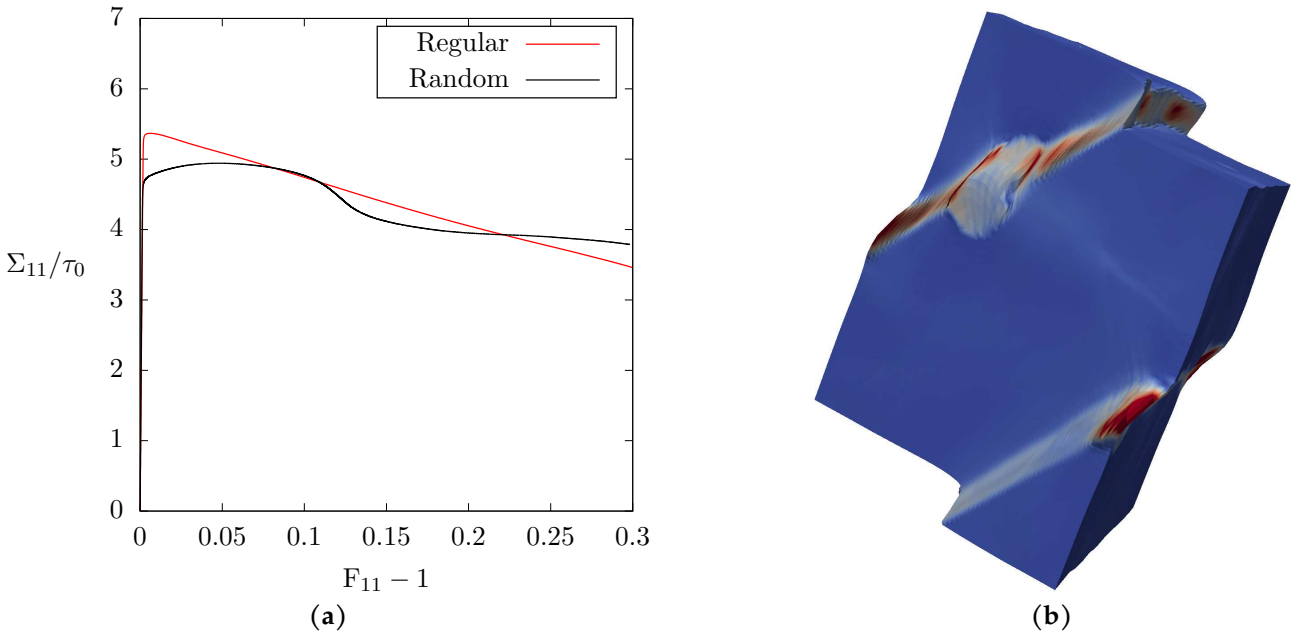

FIGURE II.18: Finite strain porous ($f_0 = 1\%$) single crystal ($\phi_1 = 124.4°$, $\Phi = 34.2°$, $\phi_2 = 267.6°$) unit-cell simulations under axisymmetric loading conditions ($T = 1$) without hardening, for regular (cubic void distribution) and random (with 8 voids): **(a)** stress-strain curves and **(b)** typical local deformation gradient field in the coalescence regime in the random case for $F_{11} = 1.2$.

yield criterion has been proposed for such situations (Hure, 2019) and its implementation is the next evolution step foreseen for the porous crystal models studied here. More importantly, finite strain porous single crystals unit-cell simulations considering random distributions of voids are definitely required to assess the occurrence of different coalescence modes (internal necking *vs.* shear-assisted). These simulations are numerically challenging, even for isotropic porous materials (Hure, 2021; Cadet et al., 2021), but appear as a milestone for validating homogenized models for porous single-crystal plasticity.

Besides the perspectives of model improvement drawn previously, the main prospect is to use such models to perform ductile fracture simulations in single and poly-crystals, as done in Khadyko et al. (2021) and Scherer et al. (2021). Different homogenized models should be studied to assess alternative modeling hypotheses' effect on fracture strain/toughness and crack paths. Eventually, direct comparisons to experimental results — very limited in the literature — will be mandatory to validate the models.

1.5 Conclusion

Homogenized constitutive equations for porous single-crystal plasticity have been proposed in this study, accounting for both void growth and void coalescence deformation regimes. This set of equations is based on yield criteria available in the literature, and evolution laws are proposed to account for hardening and void shape. The homogenized model is designed to be as simple as possible from a numerical point of view by limiting the number of internal variables. This is reached by considering a single yield criterion for void growth regime, a single scalar value to describe hardening, a simplified finite strain framework and a numerical implementation coupling Newton-Raphson and fixed point algorithms. A database of finite strain porous unit-cell simulations has been gathered for FCC materials, including various hardening laws, crystallographic orientations, porosities, and stress triaxiality ratios for axisymmetric loading conditions. The homogenized model predictions are found to be in good agreement with unit-cell simulations for low and medium hardening, whereas discrepancies are observed for strong hardening. The fact that deviations from unit-cell computations are of the same magnitude as the ones of a homogenized model with more physical modeling of the growth phase (Scherer et al., 2021) indicates that most of the features of porous single crystals plasticity are kept in the model proposed in this study. However, the model of Scherer et al. (2021) underlines the importance of particular features such as structural hardening induced by lattice rotation. In conclusion, the model proposed in this study can be used effectively to describe porous single crystals accurately in situations where rotation can be neglected, from low to medium hardening, with a limited number of internal variables and thus potentially as

numerically efficient as homogenized models used for porous isotropic materials.

1.A Finite strain framework

The constitutive equations described in Section II.1.3.1 for small strain theory are extended to finite strain theory using the logarithmic framework described in Miehe et al. (2002). This framework's advantage is relying on pre- and post-processors for the small strain numerical implementation of the constitutive equations. The pre-processor is based on the definition of Hencky total strain as:

$$\boldsymbol{\varepsilon} = \frac{1}{2}\log\left(\boldsymbol{F}^T\boldsymbol{F}\right) \tag{II.43}$$

where $\boldsymbol{F}$ is the deformation gradient. Hencky strain tensor $\boldsymbol{\varepsilon}$ is used as the input for integrating constitutive equations. The corresponding stress tensor $\boldsymbol{T}$ is not the Cauchy stress tensor $\boldsymbol{\sigma}$ required by the finite element solver, but the latter is found assuming duality: $\boldsymbol{T} : \dot{\boldsymbol{\varepsilon}} = \boldsymbol{\sigma} : \boldsymbol{D}$, where $\boldsymbol{D}$ is the Eulerian strain increment $\boldsymbol{D} = \dot{\boldsymbol{F}}\boldsymbol{F}^{-1}$ (Abbas, 2016). This framework thus allows to extend the applicability of small strain constitutive equations to finite strain, ensuring objectivity, and is available in the code generator `MFront` used in this study (Helfer and Ling, 2014). This framework has been shown to lead to good agreement for anisotropic plasticity to reference simulations using the multiplicative decomposition of the deformation gradient $\boldsymbol{F} = \boldsymbol{F}_\mathrm{e}\boldsymbol{F}_\mathrm{p}$ (Miehe et al., 2002). However, using the logarithmic framework for crystal plasticity, as done in this study in the limit $f \to 0$ for the growth yield criterion, has obvious limitations that are assessed here. Single slip, *e.g.*, $\boldsymbol{F} = \mathbf{1} + \gamma\, \underline{m} \otimes \underline{n}$ with associated eulerian strain increment $\boldsymbol{D} = \dot{\gamma}\, \underline{m} \otimes \underline{n}$ cannot be captured by Eq. II.43, being symmetric, leading to $\dot{\boldsymbol{\varepsilon}} = \frac{\gamma}{2}(\underline{m} \otimes \underline{n} + \underline{n} \otimes \underline{m})$. This is confirmed in Fig. II.19a

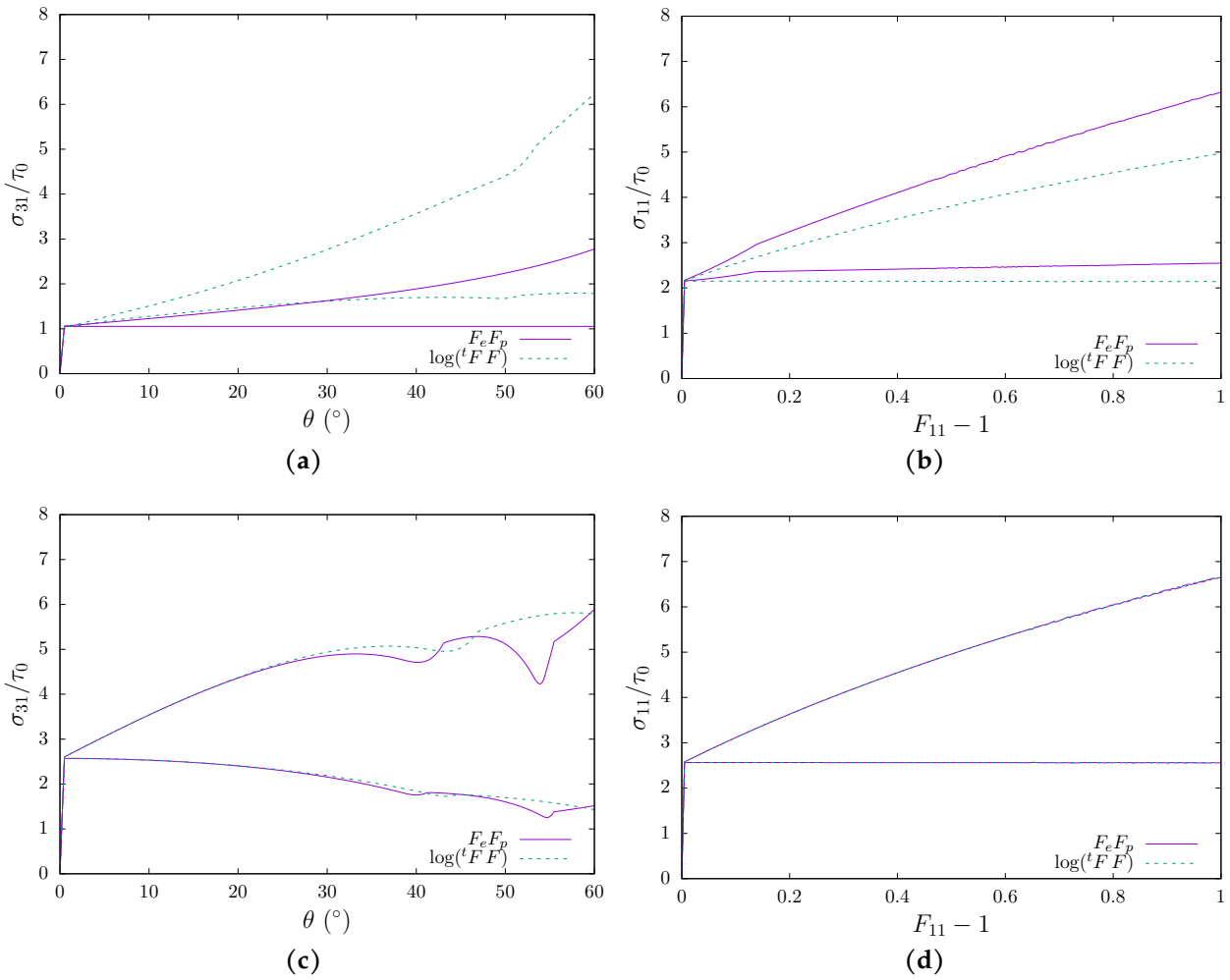

FIGURE II.19: Comparisons between finite strain crystal plasticity implementations based on the multiplicative decomposition of the deformation gradient ($\boldsymbol{F}_\mathrm{e}\boldsymbol{F}_\mathrm{p}$) and on the logarithmic framework: **(a,c)** simple shear: $\boldsymbol{F} = F_{31}\underline{e}_3 \otimes \underline{e}_1$ (with $\theta = \mathrm{atan}\, F_{31}$); **(b,d)** uniaxial tensile: $\boldsymbol{\sigma} = \sigma \underline{e}_1 \otimes \underline{e}_1$. 12 FCC slip systems are considered, and two sets of curves are plotted in each figure corresponding to different values of the Taylor hardening slope $H \in \{0, 100\}$ ($\tau_\mathrm{c} = \tau_0 + H\sum|\gamma_i|$). The crystal orientations along the 1-axis are **(a)** [111] **(b)** [$\bar{1}$25] **(c,d)** [100].

where numerical simulations of simple shear with single slip are performed using multiplicative and logarithmic frameworks, without and with hardening. Similarly, the logarithmic framework fails to recover the correct behavior for tensile loading on a crystal direction activating only single slip (Fig. II.19b).

However, for symmetric orientations (Fig. II.19c,d), the logarithmic framework closely follows the results obtained with the multiplicative framework up to high strain levels. For simple shear (Fig. II.19c), deviations appear for shear angle higher than 60°. A perfect agreement is observed between the two frameworks for tensile loading (Fig. II.19d). Therefore, the constitutive equations proposed in this study using the logarithmic framework should be restricted in principle to symmetric orientations or high porosity / high mean stress levels where isotropic volumetric strain dominates. This corresponds in practice to high stress triaxiality or high porosity, which is the main focus of this study.

1.B Yield criteria flow direction

Numerical implementation of the constitutive equations in the `MFront` code generator requires analytical expressions of yield criteria flow directions and their partial derivatives with respect to $\boldsymbol{\Sigma}$. They are provided below.

1.B.1 Growth yield criterion

When dealing with yield criteria defined by $S(\sigma^*, \boldsymbol{\Sigma}) = 0$, the two following equations are used:

$$\delta S = \frac{\partial S}{\partial \boldsymbol{\Sigma}} : \delta\boldsymbol{\Sigma} + \frac{\partial S}{\partial \sigma^*}\delta\sigma^* = 0 \tag{II.44}$$

$$\frac{\partial^2 \sigma^*}{\partial \boldsymbol{\Sigma}^2} = -\left(\frac{1}{\frac{\partial S}{\partial \sigma^*}}\right)\frac{\partial}{\partial \boldsymbol{\Sigma}}\left[\frac{\partial S}{\partial \boldsymbol{\Sigma}}(\cdot, \sigma^*(\cdot), ...)\right] - \frac{\partial S}{\partial \boldsymbol{\Sigma}} \otimes \frac{\partial}{\partial \boldsymbol{\Sigma}}\left[\frac{1}{\frac{\partial S}{\partial \sigma^*}(\cdot, \sigma^*(\cdot), ...)}\right] \tag{II.45}$$

Useful notations

$$S_{\mathrm{g}}^{(0)} \equiv \sum_{k=1}^{N} \left|\boldsymbol{\mu}_k^{(\mathrm{s})} : \boldsymbol{\Sigma}\right|^n \tag{II.46}$$

$$\boldsymbol{S}_{\mathrm{g}}^{(\mathbf{1})} \equiv \sum_{k=1}^{N} \mathrm{sgn}\left(\boldsymbol{\mu}_k^{(\mathrm{s})} : \boldsymbol{\Sigma}\right)\left|\boldsymbol{\mu}_k^{(\mathrm{s})} : \boldsymbol{\Sigma}\right|^{n-1} \boldsymbol{\mu}_k^{(\mathrm{s})} \tag{II.47}$$

$$\mathbb{S}_{\mathrm{g}}^{(2)} \equiv \sum_{k=1}^{N} \left|\boldsymbol{\mu}_k^{(\mathrm{s})} : \boldsymbol{\Sigma}\right|^{n-2} \boldsymbol{\mu}_k^{(\mathrm{s})} \otimes \boldsymbol{\mu}_k^{(\mathrm{s})} \tag{II.48}$$

Flow direction

$$\frac{\partial S_{\mathrm{g}}}{\partial \boldsymbol{\Sigma}} = \frac{2}{\sigma_{\mathrm{g}}^*}\left[\frac{1}{\sigma_{\mathrm{g}}^*}\left(S_{\mathrm{g}}^{(0)}\right)^{\frac{2}{n}-1} \boldsymbol{S}_{\mathrm{g}}^{(\mathbf{1})} + \frac{1}{3} q f \kappa \sinh\left(\kappa \frac{\Sigma_{\mathrm{m}}}{\sigma_{\mathrm{g}}^*}\right)\boldsymbol{I}\right] \tag{II.49}$$

$$\frac{\partial S_{\mathrm{g}}}{\partial \sigma_{\mathrm{g}}^*} = -\frac{2}{(\sigma_{\mathrm{g}}^*)^2}\left[\frac{1}{\sigma_{\mathrm{g}}^*}\left(S_{\mathrm{g}}^{(0)}\right)^{\frac{2}{n}} + q f \kappa \sinh\left(\kappa \frac{\Sigma_{\mathrm{m}}}{\sigma_{\mathrm{g}}^*}\right)\Sigma_{\mathrm{m}}\right] \tag{II.50}$$

$$\boldsymbol{n}_{\mathrm{g}} = \frac{\partial \sigma_{\mathrm{g}}^*}{\partial \boldsymbol{\Sigma}} = -\left(\frac{1}{\frac{\partial S_{\mathrm{g}}}{\partial \sigma_{\mathrm{g}}^*}}\right)\frac{\partial S_{\mathrm{g}}}{\partial \boldsymbol{\Sigma}} \tag{II.51}$$

Flow direction first-order derivative

$$\frac{\partial^2 S_{\mathrm{g}}}{\partial \boldsymbol{\Sigma}^2} = \frac{2}{\left(\sigma_{\mathrm{g}}^*\right)^2}\left[\left(S_{\mathrm{g}}^{(0)}\right)^{\frac{2}{n}-2}\left((n-1)S_{\mathrm{g}}^{(0)}\mathbb{S}_{\mathrm{g}}^{(2)} - (n-2)\boldsymbol{S}_{\mathrm{g}}^{(\mathbf{1})} \otimes \boldsymbol{S}_{\mathrm{g}}^{(\mathbf{1})}\right) + \frac{1}{9} q f \kappa^2 \cosh\left(\kappa \frac{\Sigma_{\mathrm{m}}}{\sigma_{\mathrm{g}}^*}\right)\boldsymbol{I} \otimes \boldsymbol{I}\right] \tag{II.52}$$

$$\frac{\partial^2 S_{\mathrm{g}}}{\partial \boldsymbol{\Sigma} \partial \sigma_{\mathrm{g}}^*} = -\frac{2}{(\sigma_{\mathrm{g}}^*)^2}\left[\frac{2}{\sigma_{\mathrm{g}}^*}\left(S_{\mathrm{g}}^{(0)}\right)^{\frac{2}{n}-1} \boldsymbol{S}_{\mathrm{g}}^{(\mathbf{1})} + \frac{1}{3} q f \kappa \sinh\left(\kappa \frac{\Sigma_{\mathrm{m}}}{\sigma_{\mathrm{g}}^*}\right)\boldsymbol{I} + \frac{1}{3}\frac{q f \kappa^2}{\sigma_{\mathrm{g}}^*} \cosh\left(\kappa \frac{\Sigma_{\mathrm{m}}}{\sigma_{\mathrm{g}}^*}\right)\Sigma_{\mathrm{m}}\boldsymbol{I}\right] \tag{II.53}$$

$$\frac{\partial^2 S_{\mathrm{g}}}{(\partial \sigma_{\mathrm{g}}^*)^2} = \frac{2}{(\sigma_{\mathrm{g}}^*)^3}\left[\frac{3}{\sigma_{\mathrm{g}}^*}\left(S_{\mathrm{g}}^{(0)}\right)^{\frac{2}{n}} + 2 q f \kappa \sinh\left(\kappa \frac{\Sigma_{\mathrm{m}}}{\sigma_{\mathrm{g}}^*}\right)\Sigma_{\mathrm{m}} + \frac{q f \kappa^2}{\sigma_{\mathrm{g}}^*} \cosh\left(\kappa \frac{\Sigma_{\mathrm{m}}}{\sigma_{\mathrm{g}}^*}\right)\Sigma_{\mathrm{m}}^2\right] \tag{II.54}$$

$$\frac{\partial \boldsymbol{n}_{\mathrm{g}}}{\partial \boldsymbol{\Sigma}} = \frac{\partial^2 \sigma_{\mathrm{g}}^*}{\partial \boldsymbol{\Sigma}^2} = -\left(\frac{1}{\frac{\partial S_{\mathrm{g}}}{\partial \sigma_{\mathrm{g}}^*}}\right)\left[\frac{\partial^2 S_{\mathrm{g}}}{\partial \boldsymbol{\Sigma}^2} + \frac{\partial^2 S_{\mathrm{g}}}{\partial \boldsymbol{\Sigma} \partial \sigma_{\mathrm{g}}^*} \otimes \frac{\partial \sigma_{\mathrm{g}}^*}{\partial \boldsymbol{\Sigma}}\right] + \left(\frac{1}{\frac{\partial S_{\mathrm{g}}}{\partial \sigma_{\mathrm{g}}^*}}\right)^2 \left[\frac{\partial S_{\mathrm{g}}}{\partial \boldsymbol{\Sigma}} \otimes \left(\frac{\partial^2 S_{\mathrm{g}}}{\partial \boldsymbol{\Sigma} \partial \sigma_{\mathrm{g}}^*} + \frac{\partial^2 S_{\mathrm{g}}}{(\partial \sigma_{\mathrm{g}}^*)^2} \frac{\partial \sigma_{\mathrm{g}}^*}{\partial \boldsymbol{\Sigma}}\right)\right] \tag{II.55}$$

1.B.2 Coalescence yield criterion

As detailed in Section II.1.3.1, M_1 and M_2 vary according to the coalescence plane normal $\underline{n}_{\mathrm{I}}$, but are kept fixed once coalescence sets in. $\underline{n}_{\mathrm{I}}$, $\underline{n}_{\mathrm{II}}$ and $\underline{n}_{\mathrm{III}}$ are the eigenvectors associated with principal stresses $\Sigma_{\mathrm{I}} \geq \Sigma_{\mathrm{II}} \geq \Sigma_{\mathrm{III}}$.

Flow direction

$$\boldsymbol{n}_{\mathrm{c}} = \frac{1}{C_{\mathrm{f}}} \frac{\partial \Sigma_{\mathrm{I}}}{\partial \boldsymbol{\Sigma}} = \frac{1}{C_{\mathrm{f}}} \underline{n}_{\mathrm{I}} \otimes \underline{n}_{\mathrm{I}} \tag{II.56}$$

Flow direction first-order derivative

$$\frac{\partial \boldsymbol{n}_{\mathrm{c}}}{\partial \boldsymbol{\Sigma}} = \frac{1}{C_{\mathrm{f}}} \frac{\partial^2 \Sigma_{\mathrm{I}}}{\partial \boldsymbol{\Sigma}^2} = \frac{1}{C_{\mathrm{f}}} \sum_{J \in \{\mathrm{II},\mathrm{III}\}} \frac{1}{\Sigma_{\mathrm{I}} - \Sigma_J} \left[\underline{n}_{\mathrm{I}} \otimes \underline{n}_J \otimes \underline{n}_{\mathrm{I}} \otimes \underline{n}_J + \underline{n}_J \otimes \underline{n}_{\mathrm{I}} \otimes \underline{n}_J \otimes \underline{n}_{\mathrm{I}}\right] \tag{II.57}$$

1.C Summary of the two homogenized models

The values of numerical parameters of the two homogenized porous models mentioned in this article are given in Table II.3. Moreover, the main equations for both models are summarized in Table II.4.

Parameter	PBKH model	HLS model
n	100	\
α	\	6.456
κ	0.49	0.513
q	1.66	1.471
κ^{c}	\	1.047
q^{c}	\	1.384
q_χ	$0.912 - 0.039T$	0.624
β	2.88	\

TABLE II.3: Numerical values of parameters used in the homogenized models.

Model equation	**PBKH model**	**HLS model**
Growth		
Yield criterion	$\left(\frac{\left(\sum_{k=1}^{N}\left\lvert\boldsymbol{\mu}_k^{(\mathrm{s})}:\boldsymbol{\Sigma}\right\rvert^n\right)^{\frac{1}{n}}}{\sigma_{\mathrm{g}}^*}\right)^2+2qf\cosh\left(\kappa\frac{\Sigma_{\mathrm{m}}}{\sigma_{\mathrm{g}}^*}\right)-1-(qf)^2=0$	$\forall s\in[\![1,N]\!],\ \left(\frac{\lvert\boldsymbol{\mu}_s:\boldsymbol{\Sigma}\rvert}{\tau_s^*}\right)^2+\alpha\frac{2}{45}f\left(\frac{\Sigma_{\mathrm{eq}}^{\mathrm{vM}}}{\tau_s^*}\right)^2+2qf\cosh\left(\kappa\frac{\Sigma_{\mathrm{m}}}{\tau_s^*}\right)-1-(qf)^2=0$
Flow direction	$\boldsymbol{n}_{\mathrm{g}}=\frac{\partial\sigma_{\mathrm{g}}^*}{\partial\boldsymbol{\Sigma}}$	$\forall s\in[\![1,N]\!],\ \boldsymbol{n}_{\mathrm{g},s}=\frac{\partial\tau_s^*}{\partial\boldsymbol{\Sigma}}$
Coalescence		
Yield criterion	$\frac{\Sigma_{\mathrm{I}}}{\sigma_{\mathrm{c}}^*}-C_{\mathrm{f}}=0$	
C_{f}	$\frac{b}{\sqrt{3}}\left(2-\sqrt{1+3\chi^4}+\ln\frac{1+\sqrt{1+3\chi^4}}{3\chi^2}\right)M_1+t(w,\chi)\left(\frac{\chi^3-3\chi+2}{3\sqrt{3}w\chi}\right)M_2$	$(1-\chi^2)\left(0.1\left(\frac{1-\chi}{\chi w}\right)^2+1.2\sqrt{\frac{1}{\chi}}\right)$
Flow direction	$\boldsymbol{n}_{\mathrm{c}}=\frac{1}{C_{\mathrm{f}}}\frac{\partial\Sigma_{\mathrm{I}}}{\partial\boldsymbol{\Sigma}}$	
Evolution laws		
Flow rule	$\dot{\boldsymbol{\varepsilon}}^{\mathrm{p}}=\dot{p}_{\mathrm{g}}\boldsymbol{n}_{\mathrm{g}}+\dot{p}_{\mathrm{c}}\boldsymbol{n}_{\mathrm{c}}$ $\dot{p}_i=\left(\frac{(\sigma_i^*-\tau^*)_+}{K}\right)^m$	$\dot{\boldsymbol{\varepsilon}}^{\mathrm{p}}=\sum_{k=1}^{N}\dot{\gamma}_k\boldsymbol{n}_{\mathrm{g},k}+\dot{p}_{\mathrm{c}}\boldsymbol{n}_{\mathrm{c}}$ $\dot{\gamma}_s=\left(\frac{(\tau_s^*-\tau_{\mathrm{c}}^s)_+}{K}\right)^m,\dot{p}_{\mathrm{c}}=\left(\frac{(\sigma_{\mathrm{c}}^*-\tau^*)_+}{K}\right)^m$ $\left(\frac{\Sigma_{\mathrm{eq}}^{\mathrm{vM}}}{\tau^*}\right)^2+2q^{\mathrm{c}}f\cosh\left(\kappa^{\mathrm{c}}\frac{\Sigma_{\mathrm{m}}}{\tau^*}\right)-1-(q^{\mathrm{c}}f)^2\equiv0$
f	$\dot{f}=(1-f)\mathrm{tr}\,(\dot{\boldsymbol{\varepsilon}}^{\mathrm{p}})$	
w	$\dot{w}=\begin{cases}\frac{1}{w}\lvert T-2\rvert\dot{\varepsilon}_{\mathrm{I}} & (\text{growth},T<2)\\ -w\lvert T-2\rvert\dot{\varepsilon}_{\mathrm{I}} & (\text{growth},T\geq2)\\ \frac{9\lambda}{4\chi}\left[1-\frac{2}{\pi}\frac{1}{\chi^2}\right]\dot{\varepsilon}_{\mathrm{eq}}^{\mathrm{p}} & (\text{coalescence})\end{cases}$	$\dot{w}=0$
λ	$\left(\frac{(C_{\mathrm{I}})^2}{C_{\mathrm{II}}C_{\mathrm{III}}}\right)^{\frac{1}{4}}$	$\lambda_{\mathrm{c}}^0\left(\frac{L_{\mathrm{I}}}{L_{\mathrm{I}}^0}\right)^{\frac{3}{2}}\sqrt{\frac{1-f}{1-f_0}}$
χ	$q_\chi\left(\sqrt{\frac{6}{\pi}}\frac{f\lambda}{w}\right)^{\frac{1}{3}}$	
FBZ hardening		
	$\dot{\Gamma}=\begin{cases}\frac{1}{C}\frac{\boldsymbol{\Sigma}:\dot{\boldsymbol{\varepsilon}}^{\mathrm{p}}}{(1-f)\tau^*} & (\text{growth})\\ \frac{1}{C}\frac{\boldsymbol{\Sigma}:\dot{\boldsymbol{\varepsilon}}^{\mathrm{p}}}{\left(\frac{1}{f_{\mathrm{b}}}-1\right)f\tau^*} & (\text{coalescence})\end{cases}$ $\dot{r_{\mathrm{D}}}=\left(\frac{1}{K_0}\sqrt{N-1}\sqrt{r_{\mathrm{D}}}-G_0r_{\mathrm{D}}\right)\frac{\dot{\Gamma}}{12}$ $\tau^*=\tau_0+\mu\sqrt{\sum_{k=1}^{N}a_{1k}\sqrt{r_{\mathrm{D}}}}$	$\forall s\in[\![1,N]\!],$ $\dot{r}_{\mathrm{D}}^s=\left(\frac{1}{K_0}\sqrt{\sum_{k=1}^{N}(1-\delta_s^k)r_{\mathrm{D}}^k}-G_0r_{\mathrm{D}}^s\right)\lvert\dot{\gamma}_s\rvert$ $\tau_{\mathrm{c}}^s=\tau_0+\mu\sqrt{\sum_{k=1}^{N}a_{sk}r_{\mathrm{D}}^k}$

TABLE II.4: Summary of the main equations used in the homogenized models.

2 Trangranular ductile fracture simulations

Until now, physically-based ductile tearing simulations carried out using porous homogenized models relying on isotropic and Hill-type anisotropic phenomenological plasticity (Benzerga and Leblond, 2010; Besson, 2010) have been shown to agree well with some experimental results (*e.g.* Skallerud and Zhang (1997), Rivalin et al. (2001), Bron and Besson (2006), Østby et al. (2007), and Steglich et al. (2008)). Although these models have proven useful in studying the fracture behavior of structures, their validity in investigating ductile fracture in oligo-crystals can be questioned. The quantitative assessment of microstructural effects on fracture toughness (Pardoen and Hutchinson, 2003) may also require to account for crystal plasticity.

The model presented in the previous section enables the simulation of ductile fracture while incorporating the effects of the grain microstructure. This type of computation was only carried out in a handful of studies anterior and contemporary to the present work, which we briefly review here. All related homogenized models were already presented at the beginning of Section II.1. In the work of Ling et al. (2015), tensile and single-edge-notch tension

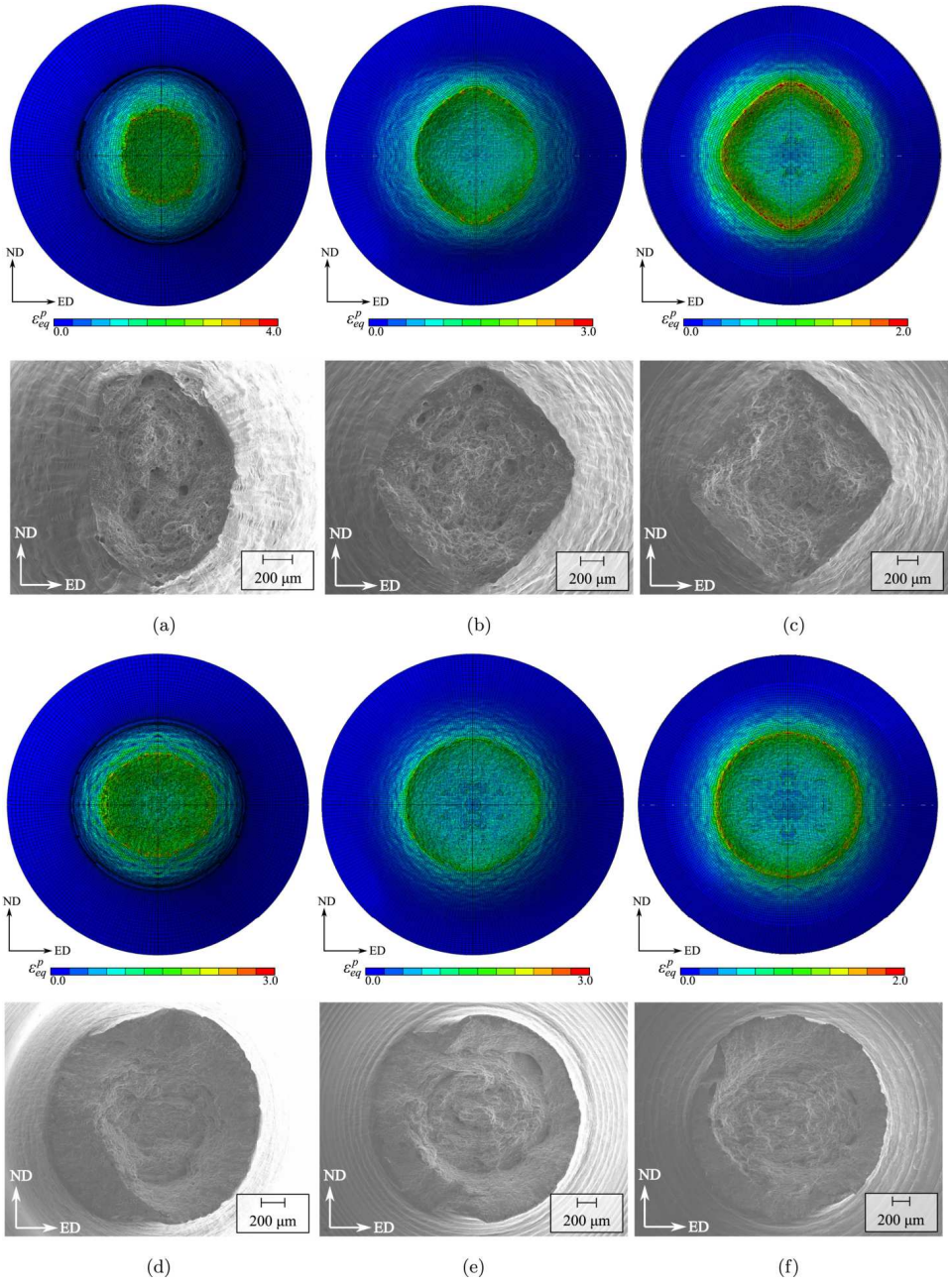

FIGURE II.20: Simulated and experimental fracture surfaces of cylindrical axisymmetric samples: smooth (**a,d**), large radius notch (**b,e**) and small radius notch (**f,g**). Two extruded aluminum alloys are considered: AA6063 (**a-c**) and AA6110 (**d-f**) (Frodal et al., 2021).

(SENT) specimina were simulated using the non-regularized homogenized model. Both mono- and polycrystalline samples of irradiated and non-irradiated 304L austenitic stainless steel were considered. The prediction of plastic slip activity at the notch area was seen to agree with an experiment conducted on a 316L sample (Ling, 2017). A polycrystalline aggregate of 343 cubic grains — each meshed with 27 elements — was also simulated under axisymmetric loading with various stress triaxialities (Ling, 2017). In the study of Frodal et al. (2021), the homogenized model was used to simulate the fracture of 3D smooth and notched round bars of two different aluminum alloys. In this work, each mesh element was a different single crystal, the two alloys exhibiting different crystallographic textures. All the grade-dependent model parameters were calibrated to reproduce macroscopic loading curves for the smooth tensile specimen. The first outcome of the simulations was the macroscopic load-displacement curves for notched specimens, which were correctly predicted. Furthermore, the morphology of the fracture surface foreseen by the polycrystalline simulations bore a striking resemblance to that of the experimental samples, as seen in Fig. II.20. The study by Khadyko et al. (2021) of a 3D polycrystalline aluminum plate (3000 equiaxed grains with crystal texture and 750000 elements) subjected to uniaxial tension also managed to reproduce the appearance of the experimental fracture surface. Moreover, the authors conducted a 2D-plane strain computation (384400 elements) with a more realistic grain morphology. Finally, Scherer et al. (2021) used their homogenized model with strain gradient regularization to simulate single crystal compact tension specimina and compute their fracture toughness. The results show a strong effect of the crystal orientation on the resistance to crack propagation but no experimental comparisons were conducted.

In this section, the homogenized model of Section II.1 is used in the plane strain simulations of three test sample geometries (tensile, bending, and CT) to demonstrate the possibility of simulating ductile fracture at the polycrystalline scale with this refined model. Both monocrystalline and polycrystalline specimina are considered and the effect of grain orientations on ductile fracture is investigated by analyzing the macroscopic load-curve, the local fields of internal variables and the crack path. A classical isotropic GTN model is also used as a reference to uncover the significant influence of crystal plasticity anisotropy on the fracture behavior.

2.1 Description of simulations

2.1.1 Specimen geometries and loading conditions

In the following, three different specimen geometries are considered in order to study different loading conditions that may be encountered in usual test samples:

(a) A tensile specimen (Fig. II.21a) of dimensions $L_1/L_2 = 0.6$ with two symmetric circular notches of radius R such that $R/L_2 = 0.1$.

(b) A bending specimen (Fig. II.21b) of dimensions $L_2/L_1 = 0.6$ with one circular notch of radius R such that $R/L_1 = 0.1$.

(c) A normalized compact tension specimen (Fig. II.21c); as a reminder, its dimensions are such that $L_2/L_1 = 0.96$, pin centers are initially separated by a length of L_{L}^0 where $L_{\mathrm{L}}^0/L_1 = 0.44$ and the distance between the center of the pins and the vertical end of the specimen is W with $W/L_1 = 0.8$. The initial crack length is a_0 with $a_0/W = 0.61$. Details can be found in the ASTM standard (ASTM E1820, 2017). The quantity $\Delta L_{\mathrm{L}} = L_{\mathrm{L}} - L_{\mathrm{L}}^0$ will be referred as *load line displacement*.

The microstructure of polycrystalline specimina is detailed in Fig. II.21; the location of grain centers was chosen randomly and microstructure was generated through Voronoi tessellation. The tensile specimen has 27 grains, whereas the bending specimen has 195 grains; no polycrystalline CT specimina is considered. Grain boundaries are located at the interface between mesh elements, so each element belongs to a unique grain.

The corresponding loading conditions are:

(a) The top line of the tensile specimen is subjected to a displacement rate $\dot{U}_0$ along $\underline{e}_2$ such that $\dot{U}_0/L_2(0) = 2 \cdot 10^{-4}\ \mathrm{s}^{-1}$, while the bottom surface cannot move along $\underline{e}_2$. The bottom and the upper lines are constrained so that no displacement is permitted along $\underline{e}_1$.

(b) The strain rate along $\underline{e}_1$ of lateral lines is set to $\pm\frac{1}{20} y_0 \dot{U}_0$, y_0 being the initial coordinate along $\underline{e}_2$. Thus, one point of each surface, located at a quarter of L_2, is fixed in the plane $(\underline{e}_1, \underline{e}_2)$. $\dot{U}_0$ is such that $\dot{U}_0/L_1(0) = 2 \cdot 10^{-4}\ \mathrm{s}^{-1}$.

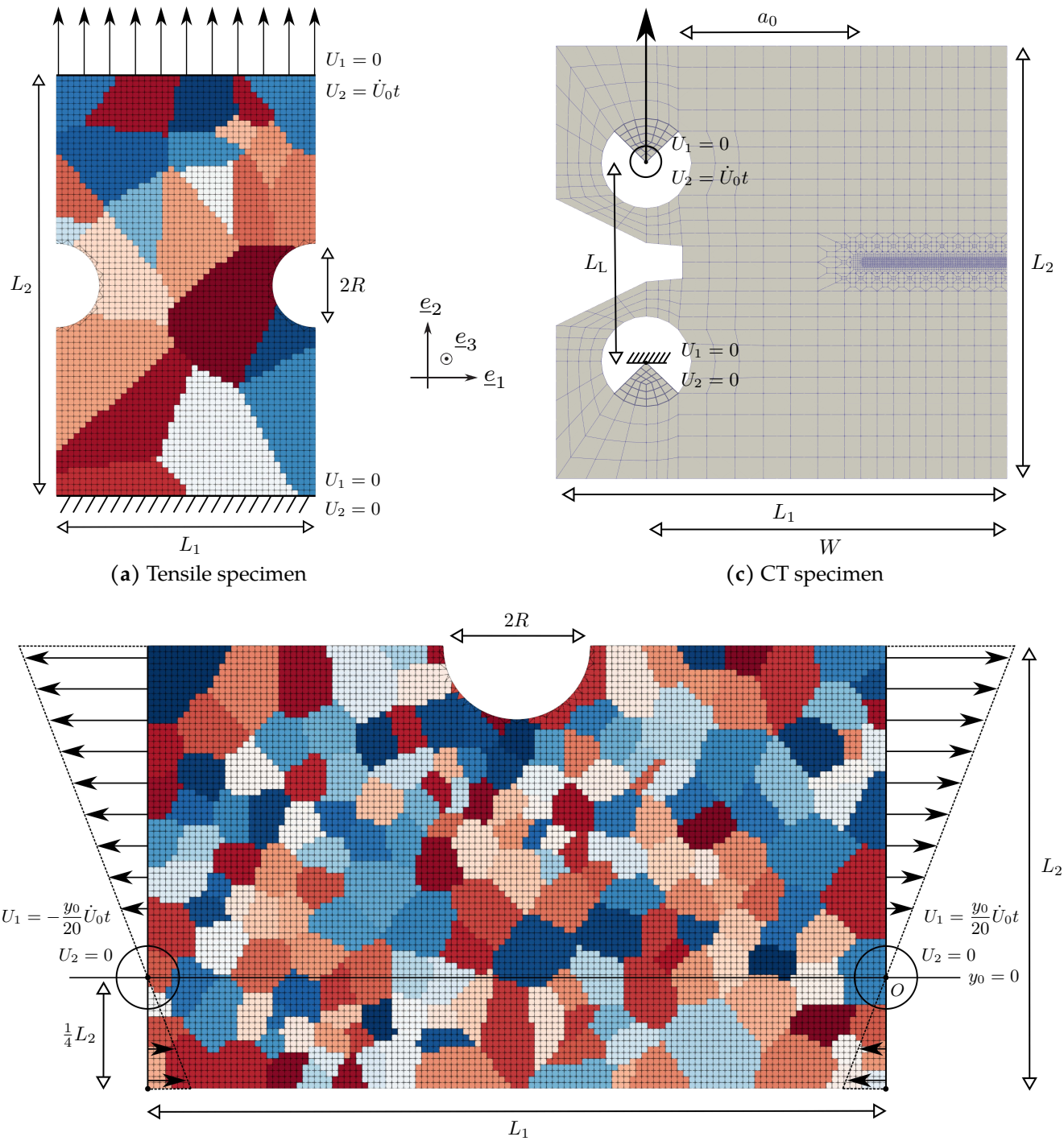

(**a**) Tensile specimen

(**c**) CT specimen

(**b**) Bending specimen

FIGURE II.21: Meshes, boundary conditions and grain positions (only applicable for polycrystalline specimens) for the test samples used in the finite element simulations.

(c) The center of the lower pin is fixed in the plane $(\underline{e}_1, \underline{e}_2)$ while the displacement of the top pin is only allowed along $\underline{e}_2$ with a displacement rate of $\dot{U}_0$ such that $\dot{U}_0/L_1(0) = 2 \cdot 10^{-2}$ s^{-1}.

The aforementioned loading conditions are shown in Fig. II.21. Plane strain conditions are enforced upon all specimens by constraining displacement along $\underline{e}_3$: $U_3 = 0$. This condition is known to increase stress triaxiality and therefore will favor void-driven ductile fracture.

2.1.2 Material behavior

Simulations on these three geometries are performed for both single and polycrystalline samples. Two single crystals are considered, whose crystallographic orientations are defined by the expression of two of their orthotropy axes $\underline{X}_i$

in the frame of reference of the simulations: $(\underline{X}_1, \underline{X}_2) = (\underline{e}_1, \underline{e}_2)$ (regular orientation) and $(\underline{X}_1, \underline{X}_2) = (0.37678\underline{e}_1 + 0.73643\underline{e}_2 - 0.56188\underline{e}_3, -0.46879\underline{e}_1 + 0.67476\underline{e}_2 + 0.57002\underline{e}_3)$ (random orientation). Using (approximate) Miller indexes, they correspond to $[100] - [010] - [001]$ and $[19\ \bar{2}4\ 40] - [37\ 34\ 3] - [\bar{2}8\ 29\ 30]$. For polycrystalline specimina, two different sets of random orientations are employed. Each grain follows the behavior of a porous single crystal, using the homogenized model presented in Section II.1.3. The initial porosity is set to $f_0 = 10^{-2}$, the initial void aspect ratio to $w_0 = 1$ and the critical resolved stress to $\tau_0 = 88$ MPa. The hardening law is the homogenized FBZ model (see Table II.4). The material parameters are those of Table II.2 and numerical parameters are from Table II.3. For each grain microstructure and each sample, two simulations are conducted, one without strain hardening and one with strain hardening; in total, it amounts to 24 computations whose results will be presented below.

To ease the convergence of the Newton-Raphson algorithm when a crystal material point is heavily damaged, the stress tensor is set to $\boldsymbol{\Sigma} = 0$ when $f > (1-\epsilon)f_{\mathrm{R}}$ (if the material is in the void growth stage[8]) or $\chi > 1 - \epsilon$ (if the material is in the void coalescence stage), with $\epsilon = 10^{-2}$. Such a modification is believed to have only mild effects on simulations.

Note that, in the CT specimen, the two pins behave as a linear elastic material with a Young modulus $E_0 = 10E$ where E is the Young modulus of a single crystal for uniaxial tension on an axis of orthotropy:

$$E = \frac{C_{11}^3 + 2C_{12}^3 - 3C_{11}C_{12}^2}{C_{11}^2 - C_{12}^2} \tag{II.58}$$

with the value of C_{ij} given in Table II.2. This choice of E_0 is rigid enough so that pins do not influence the simulation and soft enough to avoid numerical issues.

Finally, three additional simulations were conducted using the samples presented in Section II.2.1.1 with an elastoplastic material following the Gurson-Tvergaard-Needleman (GTN) model (Tvergaard and Needleman, 1984) with perfect-plasticity to assess the effect of crystal plasticity on ductile fracture. Isotropic Hooke elasticity is chosen with parameters $E = 200$ GPa and $\nu = 0.3$ and the initial porosity is set to $f_0 = 10^{-2}$. As the behavior of random polycrystals is close to the Mises model (see Bui (1969)), Mises plasticity is adopted with a yield stress under uniaxial tension $\sigma_0 = M_{\mathrm{US}}\tau_0$ (Taylor, 1938), where $M_{\mathrm{US}} \approx 3.066$ is the mean Taylor factor of an FCC polycrystal subjected to uniaxial tension. GTN parameters are:

$$q_1 = 1.5\ ,\quad q_2 = 1\ ,\quad f_{\mathrm{C}} = 0.045\ ,\quad f_{\mathrm{R}} = 0.25 \tag{II.59}$$

The values of q_1 and q_2 are the classical values of Tvergaard (1982); the value of f_{R} is recommended by Tvergaard and Needleman (1984) and f_{C} lie in the range fitted by Koplik and Needleman (1988) for unit-cell simulations with an initial porosity around 1%.

2.1.3 Numerical implementation

Ductile tearing computations are conducted using the finite-element solver `Cast3M` (CEA, 2018), developed at CEA, coupled with a user-defined library built with the code generator `MFront` (Helfer et al., 2015) (see Section II.1.3.2). Since the material behavior law is three-dimensional, the meshes are required to have a finite thickness (one element). The tensile specimen is meshed with 3420 quadratic elements (mostly hexahedrons, but some triangular prismatic elements are used on the edge of notches). The bending single-notched specimen holds 10469 quadratic elements; as in the tensile specimen, triangular prismatic elements were required to smooth the notch. Finally, the compact tensile specimen is composed of 5440 quadratic hexahedrons, the smaller of which being cubes of dimension l (with $l/L_1 = 1/750$) located in the crack propagation zone, which is very refined. The three meshes are shown in Fig. II.21. Reduced integration is performed using only eight Gauss points per quadratic hexahedron and six Gauss points per quadratic prism, which is recommended for ductile fracture simulations. Grain boundaries are modeled by perfect bonding between mesh elements whose behavior is that of porous single crystals.

In order to alleviate computational issues, elements that have experienced a lot of damage are removed from the mesh at each time step with a dedicated user procedure that suppresses elements in which at least half (for hexahedrons) or at least a third (for prismatic elements) of Gauss points are broken. A Gauss point is considered to be broken if its stress has been set to 0 due to the material behavior law (see Section II.2.1.2) or if it verifies the

[8] In the growth criterion (Eq. II.18), the stress state reaches zero when $f = f_{\mathrm{R}} = \frac{1}{q}$.

following condition:

$$p \equiv \int_{\tau=0}^{t} \sqrt{\frac{2}{3}\dot{\varepsilon}^{\mathrm{p}} : \dot{\varepsilon}^{\mathrm{p}}}\mathrm{d}\tau > p_{\max} \tag{II.60}$$

This condition is designed to eliminate very distorted elements. In the simulations described below, it was seldom used and had a limited effect on the load-displacement curves due to the values chosen for $p_{\max}$: 10 (bending and CT specimina, monocrystalline tensile samples) or 3 (polycrystalline tensile samples).

The initial time increment is $\Delta t_0 = 5 \cdot 10^{-3}$ s (tensile and CT specimina) or $2 \cdot 10^{-3}$ s (bending specimen). However, a condition is set so that the maximum porosity difference Δf between two consecutive time steps does not exceed $\delta = 10^{-3}$. If such a situation arises, the duration of the next time step is divided by $\max(\frac{\Delta f}{\delta}, 2)$, and time step reduction goes on until the porosity increment has dropped below the threshold. Then, the time step may be increased again by a factor $\max(2, \frac{\delta}{\Delta f})$ if $\Delta f < \frac{1}{2}\delta$. This procedure allows for the computation to be efficient as well as numerically stable when damage starts to soar in some elements.

The effect of the time discretization was studied on the GTN bending specimen by comparing the computation with parameters given above (full black line on Fig. II.29a) with a more refined scheme with $\Delta t_0 = 1 \cdot 10^{-3}$ s and $\delta = 5 \cdot 10^{-4}$ (dotted black line on Fig. II.29a). As seen on the loading curve, the first part of the computation is unchanged while a small effect is seen when the load-bearing capacity is below 50%. Therefore, it is concluded that the initial value of those parameters is chosen correctly to ensure convergence and enable an efficient computation.

Note that no spatial regularization is performed here so that numerical results exhibit a dependence on the element size. Indeed, if the mesh is refined, damage localization will increase, leading to a drop in the dissipated plastic energy. Such issues can be solved by dedicated methods such as strain gradient plasticity (Scherer et al., 2021). In the following, conventional plasticity is retained and the element size is considered a material parameter.

2.2 Simulation results

The results of ductile tearing computations are presented in this section. Monocrystalline samples are discussed first, and polycrystalline samples are dwelt upon in a second time.

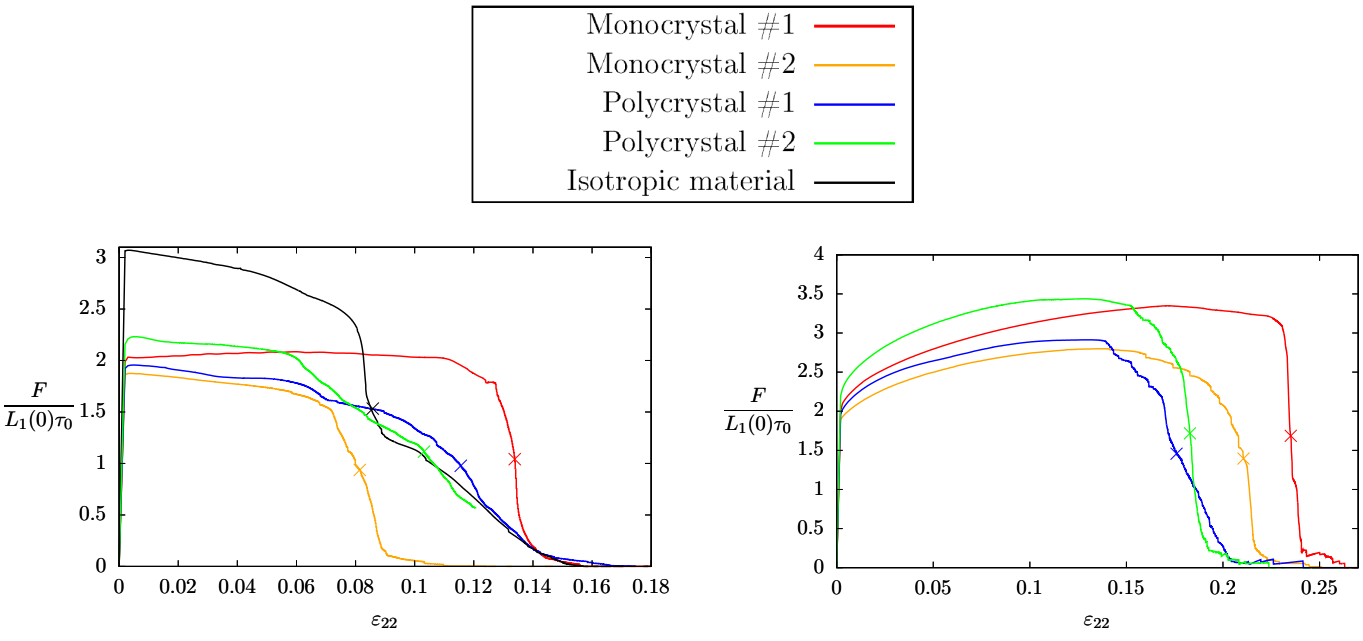

(**a**) Tension specimen, no hardening

(**b**) Tension specimen, with hardening

FIGURE II.22: Load-displacement curves of the tensile tests: the force per unit thickness F acting on the upper line (averaged on the initial upper line length $L_1(0)$) is plotted against the macroscopic true strain $\varepsilon_{22} = \log\left(L_2(t)/L_2(0)\right)$. Crosses mark the point at which the stress drops to half the maximum stress value.

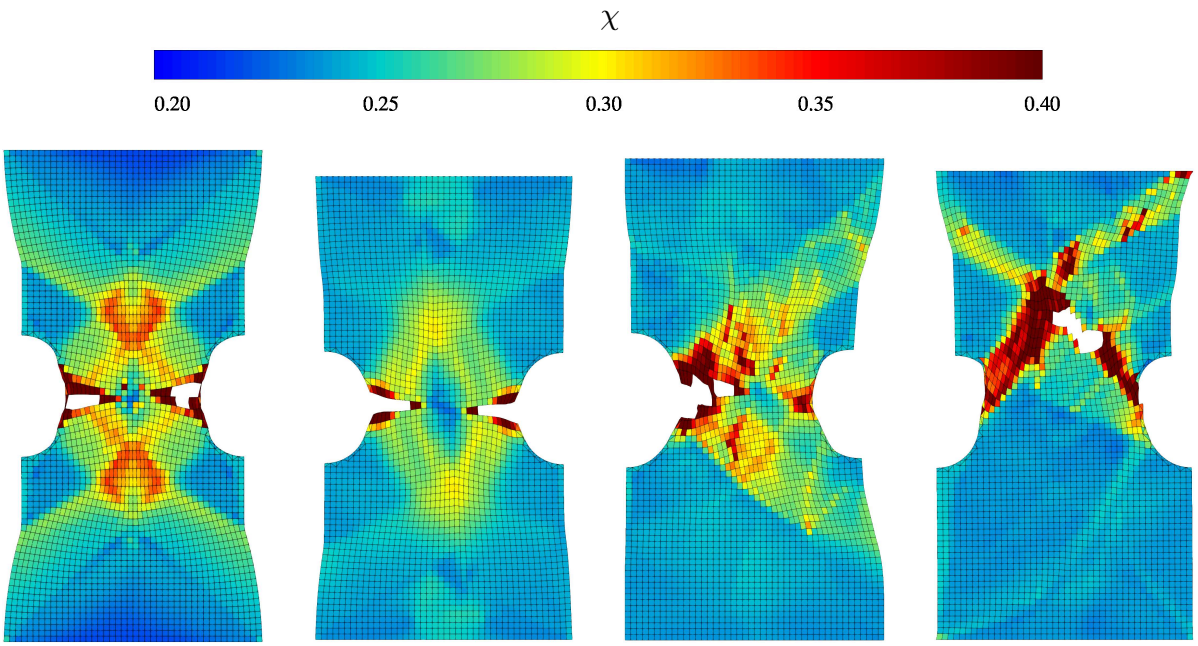

(a) Monocrystal #1 (b) Monocrystal #2 (c) Polycrystal #1 (d) Polycrystal #2

FIGURE II.23: Fields of χ at half the maximum load for perfectly-plastic specimens loaded in tension.

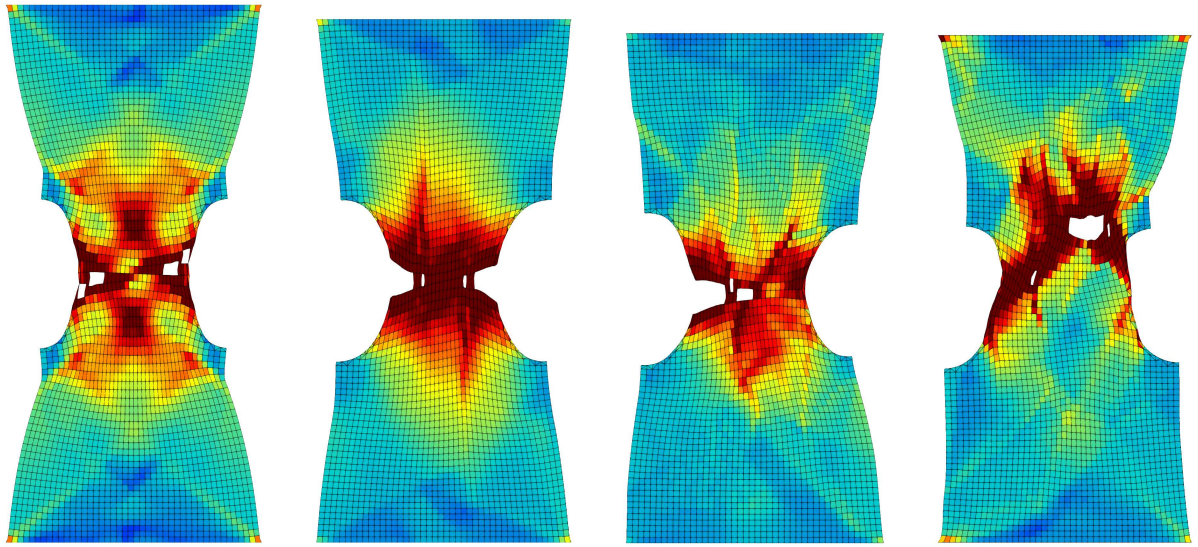

(a) Monocrystal #1 (b) Monocrystal #2 (c) Polycrystal #1 (d) Polycrystal #2

FIGURE II.24: Fields of χ at half the maximum load for specimens loaded in tension and in the presence of strain hardening.

2.2.1 Single crystal samples

The load-displacement curves of the monocrystalline tensile specimina are shown in Fig. II.22a,b. As expected, the two single crystal samples have different macroscopic yield stresses, both in simulations with and without hardening. After yielding, this difference increases. For instance, for perfectly plastic materials (Fig. II.22a), the regular crystallographic orientation displays a structural hardening due to the rotation of the crystallographic orientation relative to the loading (see the rotated elements near the notches on Fig. II.23a) whereas softening occurs very early for the random crystallographic orientation. As a result, the ductility of monocrystal #2 is significantly lower than that of monocrystal #1. This difference is also seen on hardening monocrystals (Fig. II.22b) but with a lower intensity. Note that the evaluation of structural hardening is complicated by the fact that the crystal orientation rotation induced by the plastic spin is neglected in the logarithmic finite strain framework, as highlighted in Section II.1.A.

The macroscopic response of monocrystalline bending specimina also differs (Fig. II.29a,b): the yield stress and the maximum stress of monocrystal #1 are much higher, while the ductility of monocrystal #2 is more important. Different trends are noticed compared to the tensile specimen because the loading axis is along $\underline{e}_1$, instead of $\underline{e}_2$ as

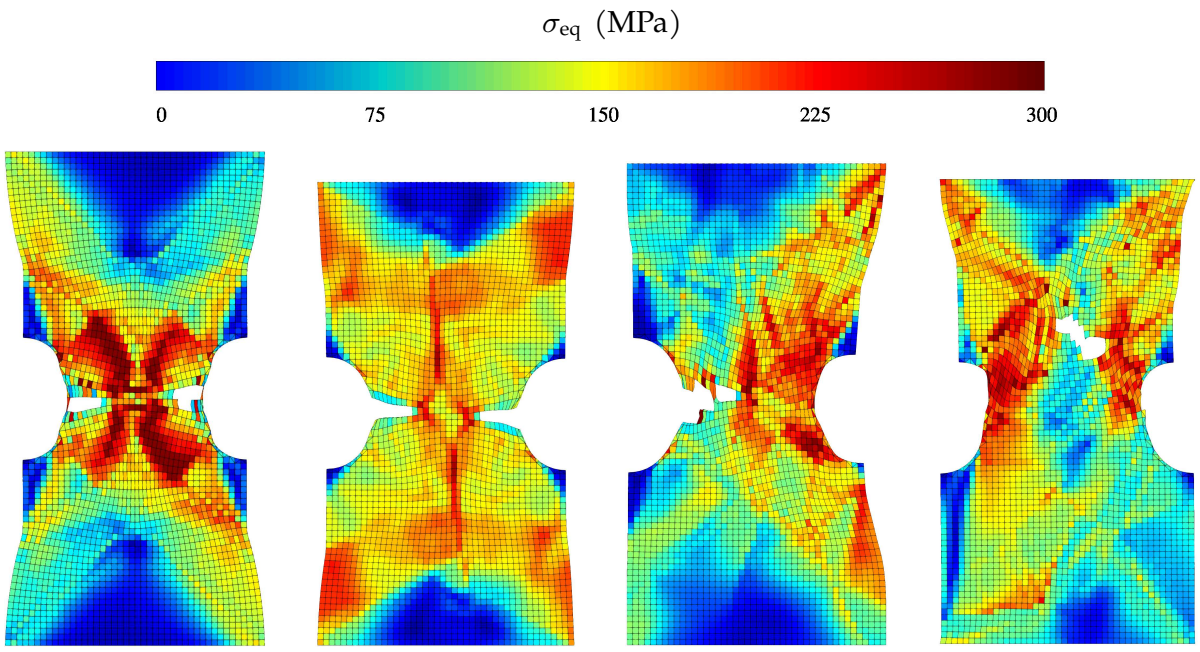

(**a**) Monocrystal #1 (**b**) Monocrystal #2 (**c**) Polycrystal #1 (**d**) Polycrystal #2

FIGURE II.25: Fields of von Mises stress σ_{eq} at half the maximum load for perfectly-plastic specimens loaded in tension.

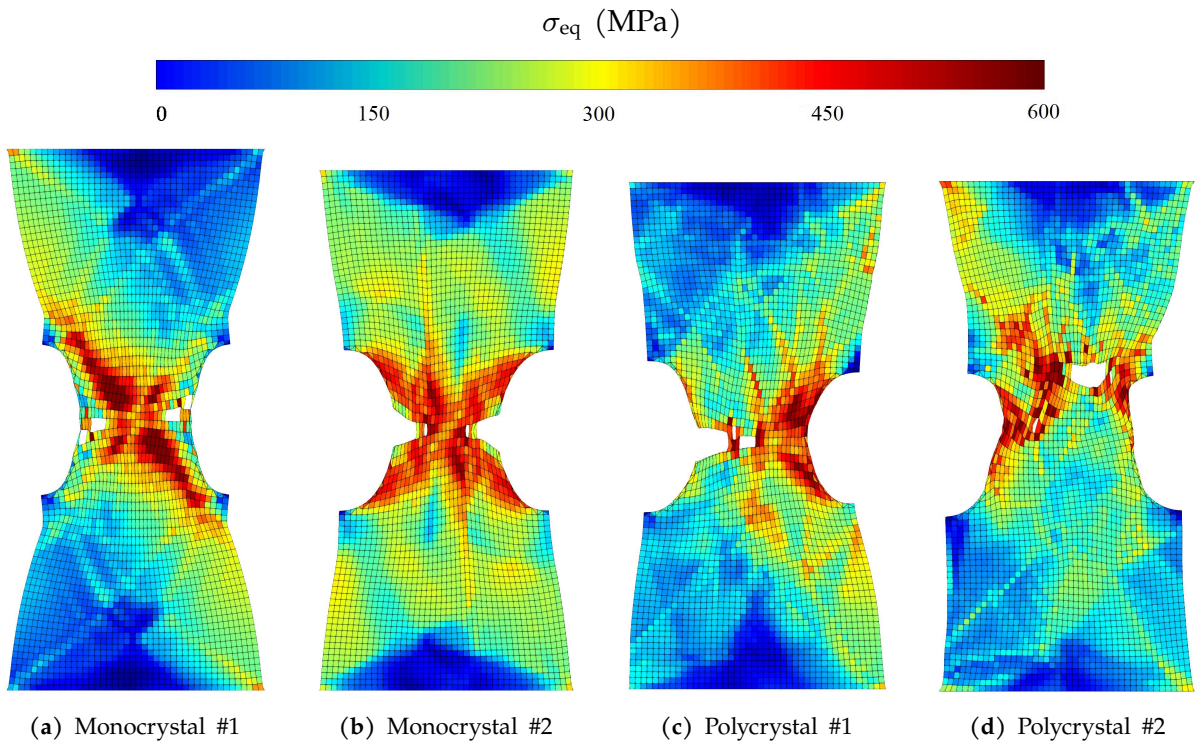

(**a**) Monocrystal #1 (**b**) Monocrystal #2 (**c**) Polycrystal #1 (**d**) Polycrystal #2

FIGURE II.26: Fields of von Mises stress σ_{eq} at half the maximum load for specimens loaded in tension and in the presence of strain hardening.

previously. The higher macroscopic ductility of monocrystal #2 is partly due to very diffuse damage before crack initiation (see around the notch of Fig. II.30b), compared to monocrystal #1 (Fig. II.30a).

Among the three geometries, the CT specimen is associated with the most dissimilar load-displacement curves (Fig. II.33a,b). The ductility exhibited by monocrystal #2 is at least four times higher than that of monocrystal # 1 in both perfectly-plastic and hardening computations (taking respectively a threshold at 50% and 80% of maximum stress to define the point at which failure is reached), which constitutes a very significant dispersion. It is also surprising to note that the crystal orientation exhibiting the larger maximum stress is not the same when hardening is implemented, meaning that the two crystal orientations have very different susceptibility to strain hardening under the considered

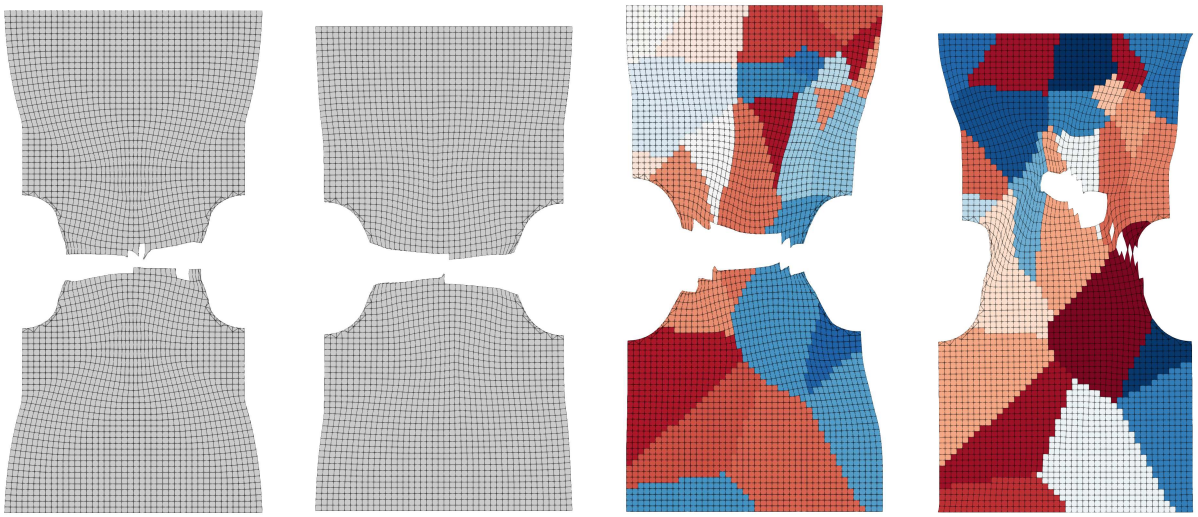

(**a**) Monocrystal #1 (**b**) Monocrystal #2 (**c**) Polycrystal #1 (**d**) Polycrystal #2

FIGURE II.27: Crack paths for perfectly-plastic specimens loaded in tension.

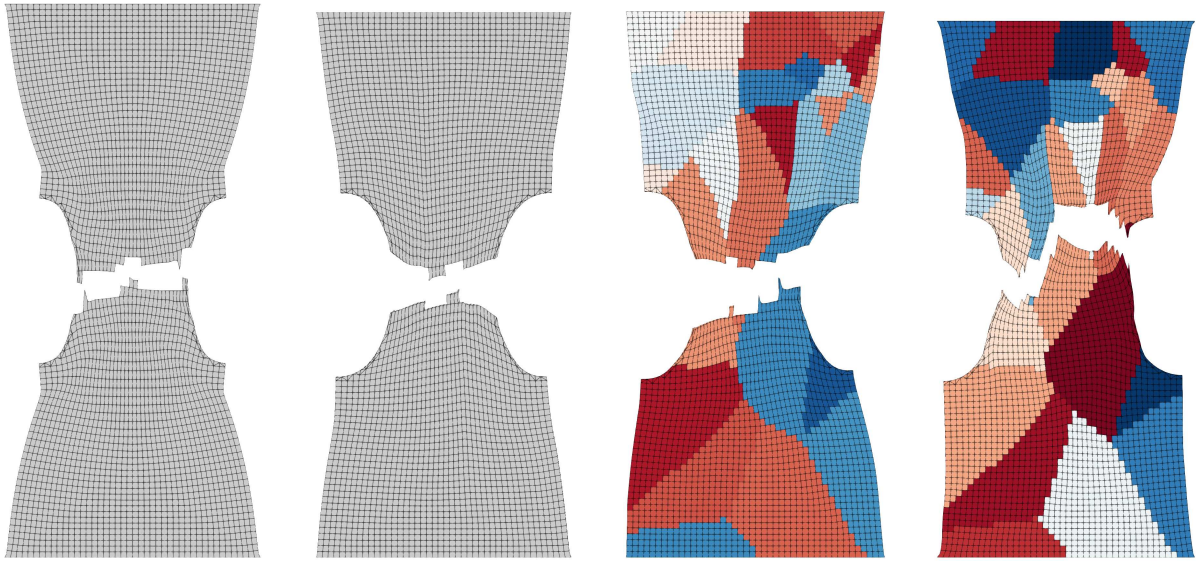

(**a**) Monocrystal #1 (**b**) Monocrystal #2 **c**) Polycrystal #1 (**d**) Polycrystal #2

FIGURE II.28: Crack paths for specimens loaded in tension and in the presence of strain hardening.

loading.

The local fields of χ (defined in Section II.1.3.1) and σ_{eq} (corresponding to the microscopic Cauchy stress $\boldsymbol{\sigma}$) taken at half the maximum stress also display striking differences between the two crystal orientations. On the one hand, due to the symmetric character of the regular orientation, the fields of χ for tensile and bending specimina (Fig. II.23a, II.24a and II.30a), as well as that of σ_{eq} for the bending and the CT specimina (Figs. II.30a, II.35a,c) display a mirror symmetry along a median axis parallel to $\underline{e}_2$ (or parallel to $\underline{e}_1$ for the CT specimen). The asymmetry seen on the crack paths (Figs. II.27a, II.27a and II.32a) and on the field of σ_{eq} of the tensile specimen (Fig. II.25a and II.26a) only originates from bifurcation events. On the other hand, the fields of specimens with the random orientation (Figs. II.23-II.32b, II.35b,d) all exhibit an asymmetry grounded in the effective behavior of the porous crystal.

Contrary to local fields and macroscopic behavior, the crack path of tensile specimens is quite similar between the regular orientation (Figs. II.27a, II.28a) and the random orientation (Figs. II.27b, II.28b). However, differences are noticed for bending and CT specimina, which seems to indicate that these test geometries are more discriminating than the tensile geometry. Without surprise, crack paths for the regular orientation are almost flat and perpendicular to the loading axis (Figs. II.32a and II.35a,c) while the crack paths corresponding to the random orientation have a strong tendency to leave the original plane: on Fig. II.35b it goes upward while it goes downward on Fig. II.35d.

For CT specimina, the fracture toughness is post-processed according to the ASTM standard E1820 (ASTM E1820, 2017). Due to the absence of elastic unloadings during the test, which may have caused convergence issues, no crack

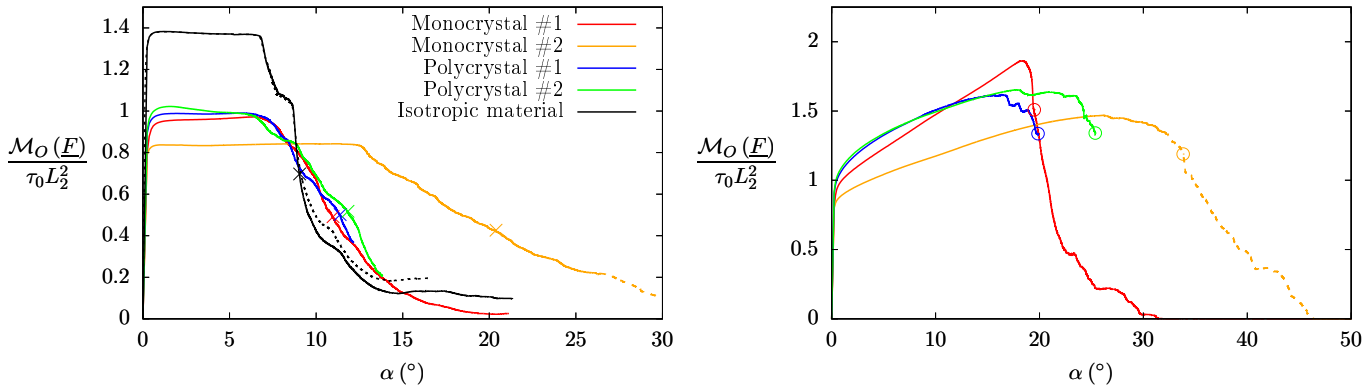

(**a**) With hardening (**b**) Without hardening

FIGURE II.29: Load-displacement curves of the bending tests: the moment $\mathcal{M}_O(\underline{F})$ of reaction forces per unit thickness $\underline{F}$ acting on the right-hand side lateral surface computed at point O (see Fig. II.21b) is plotted against the angle α of lateral surfaces relatively to $\underline{e}_2$. Crosses mark the point at which the stress drops to half the maximum stress value, while circles mark the point at which the stress drops to 80% of the maximum value. Dashed lines show the part where results become nonphysical: it happens due to the fracture of an element on which the boundary condition is applied (see Fig. II.32b). The dotted line on (**a**) is associated with a more precise time discretization scheme.

growth correction is applied. Thus, on the one hand, the elastic part J_{el} of the line integral J can be obtained as:

$$J_{\text{el}} = \frac{(1-\nu^2)}{E} K^2 \quad \text{where} \quad K = \frac{F}{\sqrt{W}} f\left(\frac{a_0}{W}\right) \tag{II.61}$$

with F the force per unit thickness applied on the upper pin and $f(\frac{a_0}{W})$ a geometric correction factor that evaluates as 14.21. This formula is designed for an isotropic material, but it is used on monocrystals by taking E and ν related to

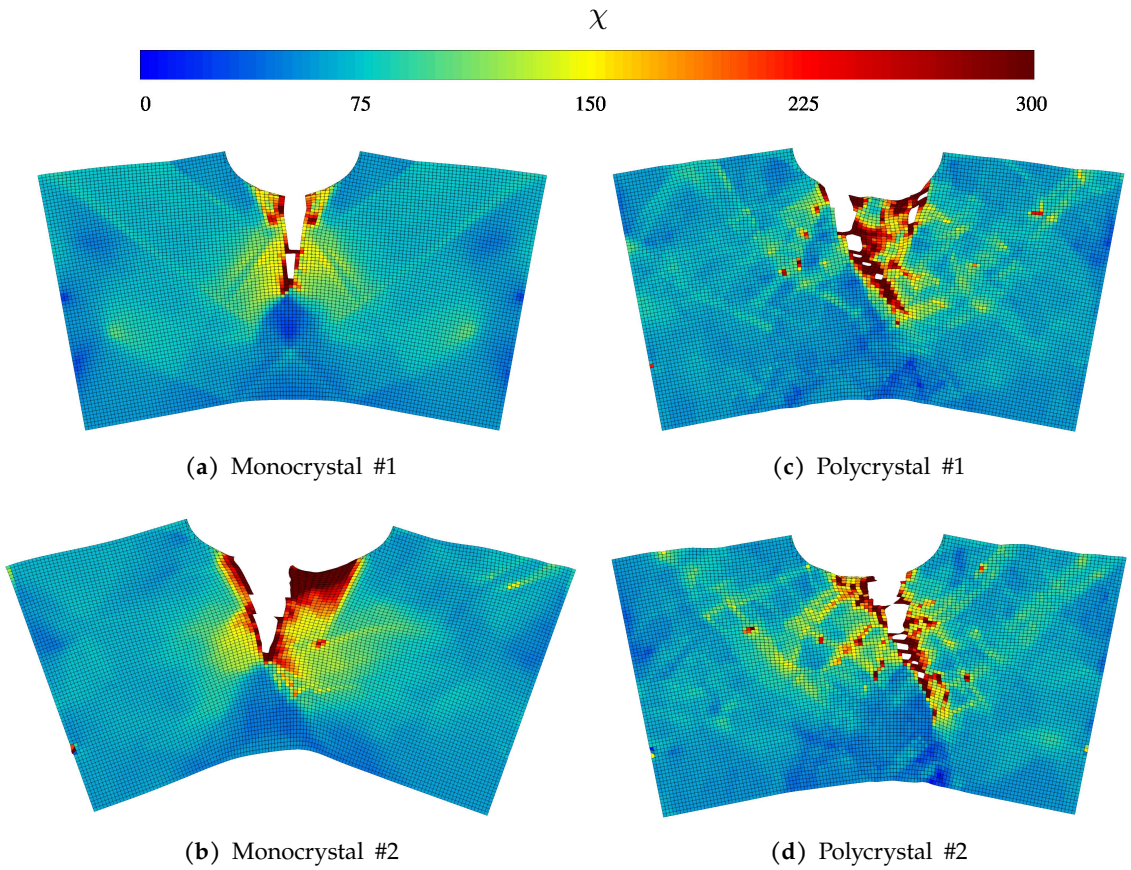

(**a**) Monocrystal #1 (**c**) Polycrystal #1

(**b**) Monocrystal #2 (**d**) Polycrystal #2

FIGURE II.30: Fields of χ at half the maximum load for plastically-perfect specimens loaded in bending.

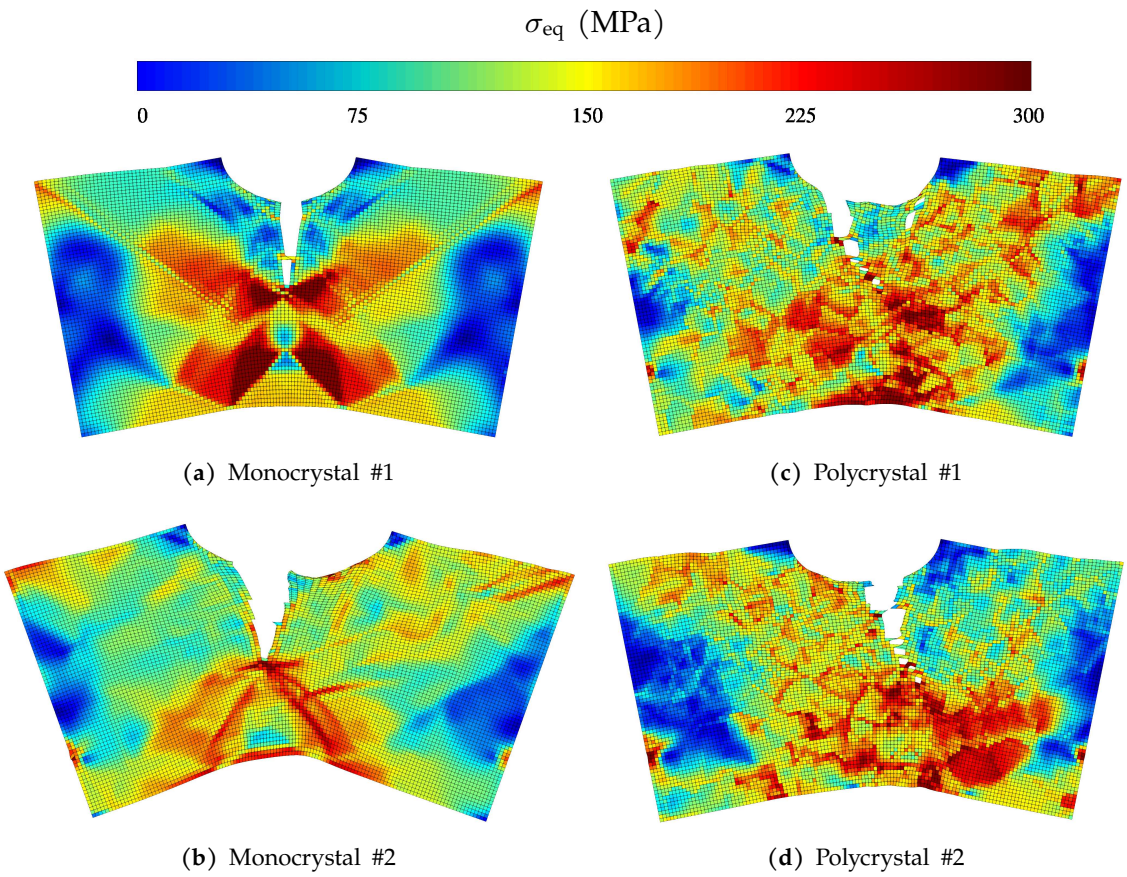

(**a**) Monocrystal #1 (**c**) Polycrystal #1

(**b**) Monocrystal #2 (**d**) Polycrystal #2

FIGURE II.31: Fields of von Mises stress σ_{eq} at half the maximum load for plastically-perfect specimens loaded in bending.

the tensile direction $\underline{e}_2$. For monocrystal #1, $E = 89$ GPa and $\nu = 0.406$, while $E = 174$ GPa and $\nu = 0.370$ (arithmetic mean of $\nu_{21} = 0.476$ along $\underline{e}_1$ and $\nu_{23} = 0.264$ along direction $\underline{e}_3$) for monocrystal #2. On the other hand, the plastic

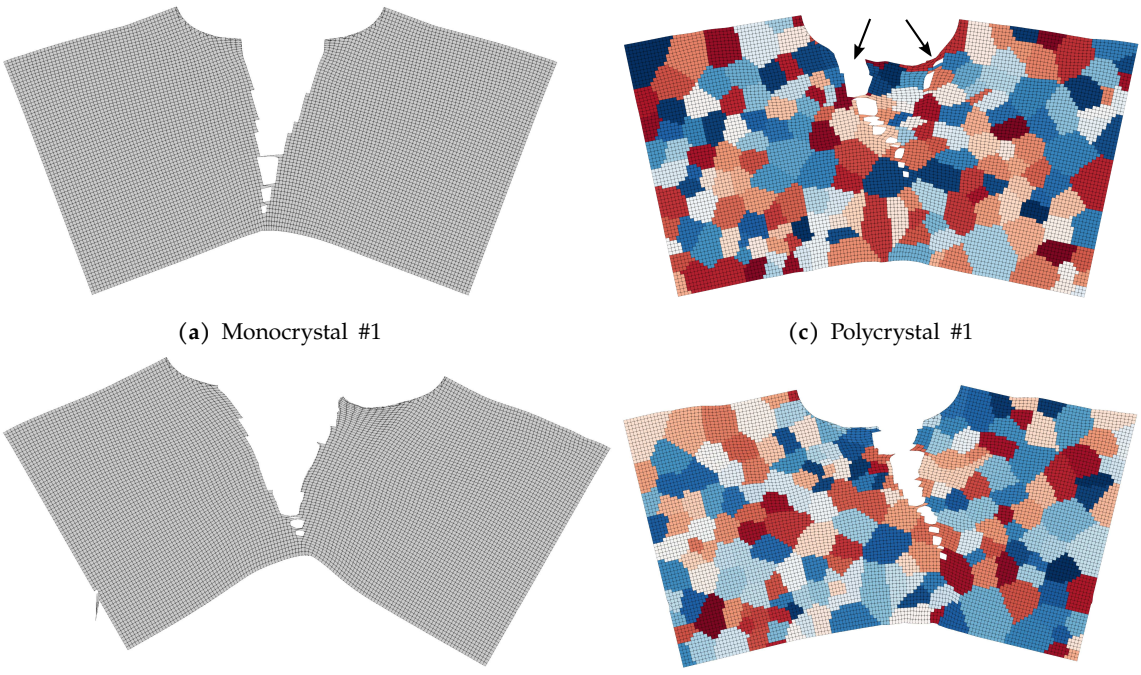

(**a**) Monocrystal #1 (**c**) Polycrystal #1

(**b**) Monocrystal #2 (**d**) Polycrystal #2

FIGURE II.32: Crack paths for plastically-perfect specimens loaded in bending. Arrows in (**c**) show the two crack initiation sites.

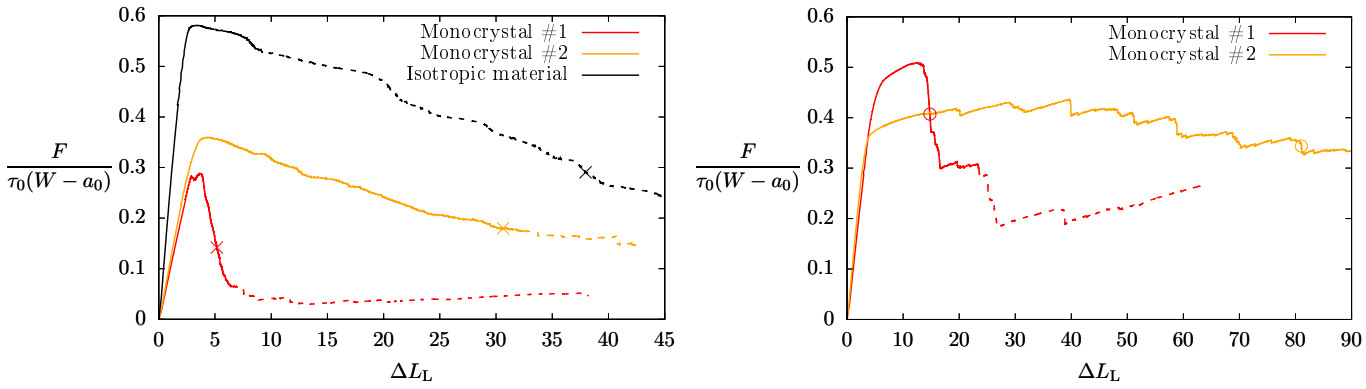

(**a**) Without hardening (**b**) With hardening

FIGURE II.33: Load-displacement curves of the CT tests: the reaction force per unit thickness F along $\underline{e}_2$ exerted by the upper pin is plotted against load line displacement ΔL_L. Crosses mark the point at which the stress drops to half the maximum stress value, while circles mark the point at which the stress drops to 80% of the maximum value. Dashed lines show the part where results become nonphysical: it happens when the crack starts to propagate outside of the refined mesh zone.

part J_p of the line integral J is given by:

$$J_\mathrm{p} = \frac{\eta A_\mathrm{p}}{W - a_0} \quad \text{where} \quad \eta = 2.522 - 0.522\frac{a_0}{W} \tag{II.62}$$

with A_p the plastic area under the graph displaying the force per unit thickness F against the load-line displacement ΔL_L (Fig. II.33a,b). J is plotted in Fig. II.34 against the crack extension Δa, where a is the projection along direction $\underline{e}_1$ of the total crack length. Δa was reported manually from the support mesh extracted at each time step. This figure again underlines that the regular and the random orientation are associated with different fracture toughness, in line with the findings of Scherer et al. (2021). In particular, crack initiation is easier for monocrystal #1 in both hardening conditions, and the subsequent crack propagation is much easier in that same orientation. As expected, the slope of the curves in Fig. II.34b is higher than in Fig. II.34a due to increased plastic dissipation related to material hardening. In fact, this effect explains the steps on Fig. II.34b for monocrystal #2: the crack propagates and then stops for a period during which the material at the crack tip hardens, which means that the plastic area A_p increases at constant Δa (high $\frac{\partial J}{\partial \Delta a}$), before crack propagation resumes (low $\frac{\partial J}{\partial \Delta a}$).

In conclusion, the results for single crystal specimina highlight the strong effect of crystal orientation on both macroscopic load-displacement curves, local fields and crack paths for all test geometries considered.

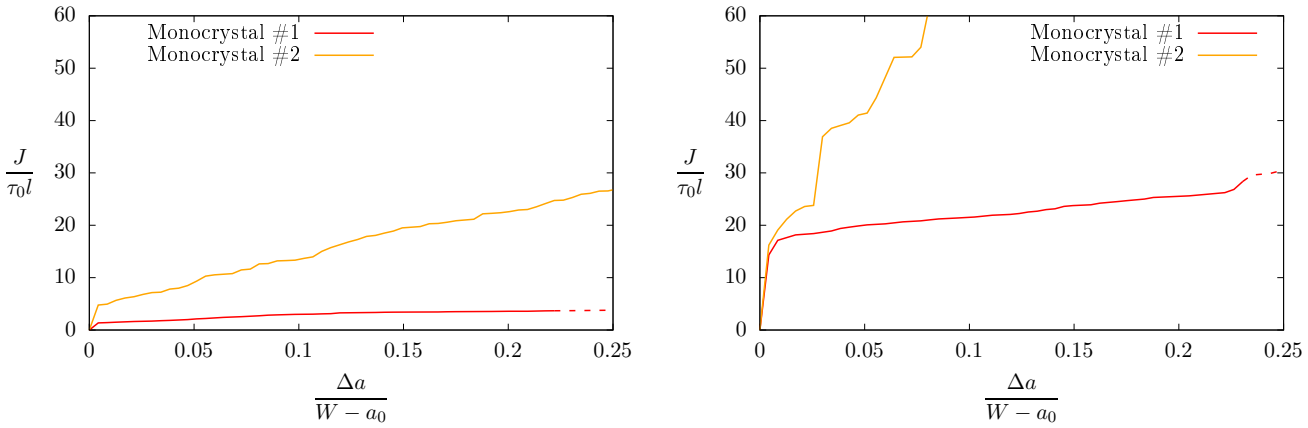

(**a**) In the absence of hardening (**b**) In the presence of hardening

FIGURE II.34: Integral J as a function of the crack advance Δa normalized by the ligament size $W - a_0$. The minimum mesh element size l is used for normalization purposes of integral J.

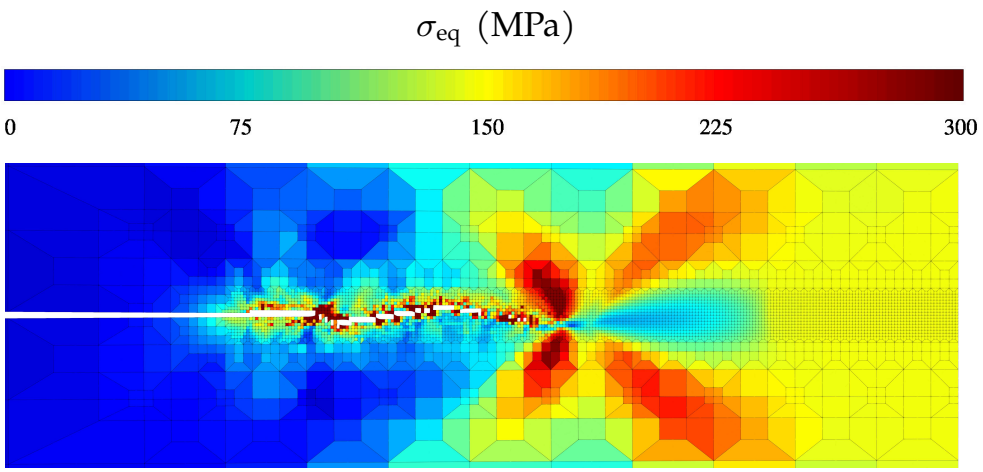

(**a**) Monocrystal #1, no hardening

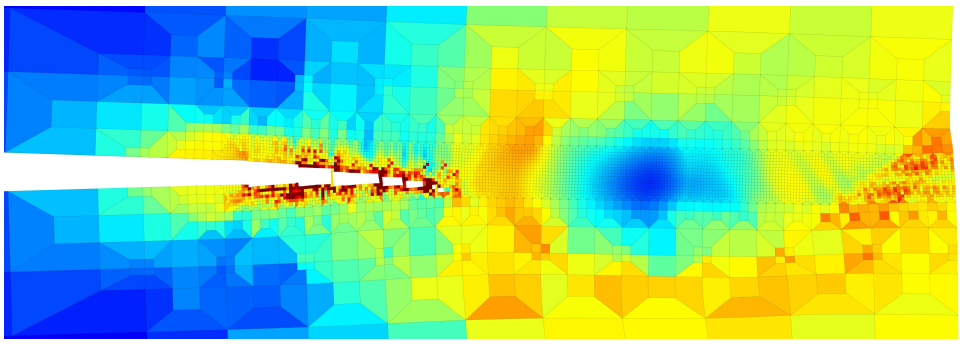

(**b**) Monocrystal #2, no hardening

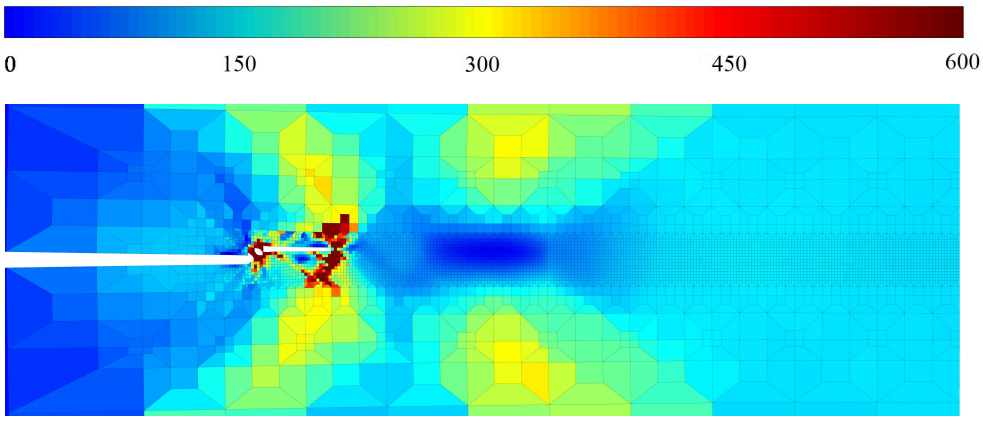

(**c**) Monocrystal #1, hardening

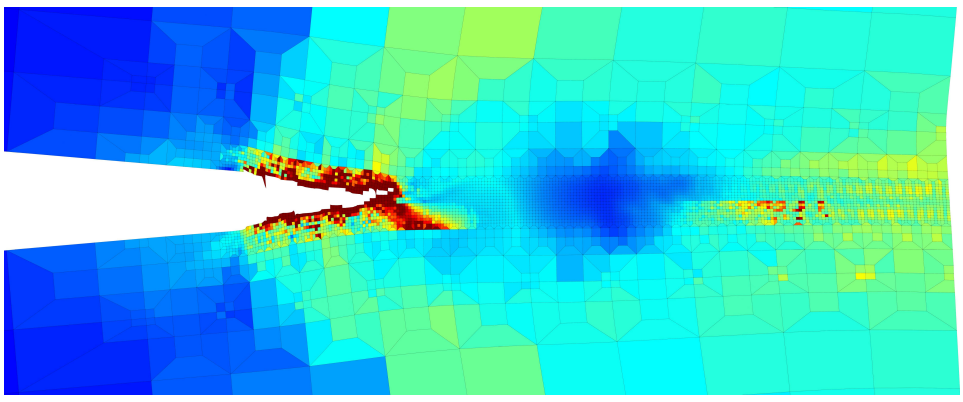

(**d**) Monocrystal #2, hardening

FIGURE II.35: Fields of von Mises stress σ_{eq} at half of the maximum load for CT specimens without strain hardening and 80 percent of the maximum load for monocrystal CT specimens with strain hardening.

2.2.2 Polycrystalline samples

Considering the load-displacement curves of the four polycrystalline tensile specimina (Fig. II.22a,b) and the four polycrystalline bending specimina (Fig. II.29a,b), it can be noticed that the difference of macroscopic effective behavior is much less critical than in the case of monocrystalline specimina. This can be traced to the fact that multiple grains enable to average the yield and fracture properties at the macroscopic scale. As expected, this averaging effect increases with the number of grains considered: indeed, the tensile geometry, which holds 27 grains, is associated with load curves with significant differences, whereas the bending geometry, which holds 195 grains, displays load curves that are very close — yet distinct, see for instance the maximum stress in the absence of hardening (Fig. II.29a) and the predicted ductility in the presence of hardening (Fig. II.29b).

On the one hand, local stress fields of polycrystals (Fig. II.25c,d, II.26c,d and II.31c,d) are more heterogeneous than local stress field for single crystals. Indeed, some grains are harder regarding the imposed loading (*e.g.* Fig. II.31d) and plastic incompatibilities can localize stress at grain boundaries (*e.g.* Fig. II.26d). Damage fields (Fig. II.23c,d, II.24c,d and II.30c,d), on the other hand, display a similar level of localization as in the case of single crystals.

Finally, the effect of polycrystal grain orientations on the crack path is unmistakable. For the tensile test, polycrystal #1 is associated with a flat fracture in the absence of hardening (Fig. II.27c) and a slightly slanted fracture in the presence of hardening (Fig. II.28c) whereas the path displayed by polycrystal #2 is entirely different (see Fig. II.27d and II.28d), due to a soft grain located in the upper part of the specimen. The location of crack initiation also differs: it occurs in the left-hand side notch in polycrystal #1 (see Fig. II.25c and II.26c) while it happens at a triple point in polycrystal #2 (see Fig. II.25d and II.26d). Coalescence by internal necking happens quickly in the damaged elements of polycrystal #1 while this coalescence mode is less intense in the fracture of polycrystal #2 (a significant number of elements was removed due to Eq. II.60, *i.e.* with $\chi < 0.99$). Thus, grain orientations seem to influence the fracture mode.

Despite the higher number of grains in the bending geometry, the effect of grain orientations on the crack path is also significant. As can seen in Fig. II.32c, two cracks initiated at the notch for polycrystal #1 before the left one took precedence, whereas a unique crack propagated in polycrystal #2 (see Fig. II.32d). All three crack-nucleating elements are located in different grains, underlying the influence of microstructure on the crack path.

2.3 Conclusion

The ductile tearing simulations presented in the previous section show the importance of accounting for crystal orientations to predict the ductile tearing of single crystals and oligo-crystals, as was already underlined by Scherer et al. (2021) for single crystals. In all test geometries considered, grain orientations influence the load curve, the local fields of stress and damage, and the crack path. In the three samples geometries considered, the ductility predicted by the simulation using the isotropic GTN model (Fig. II.22a, Fig. II.29a, Fig. II.33a) differ significantly from that observed for single crystals and polycrystals, emphasizing the interest of the homogenized model to account for microstructure effects. Naturally, when the number of grains increases, this dependence decreases. However, based on the results gathered, it is foreseen that the macroscopic behavior will converge faster than the local fields and the crack path. For instance, the latter still displays a significant dispersion in the bending samples. The fracture behavior being local, it seems that a relevant parameter to study microstructure effects in notched specimina could be the ratio between the grain size and the notch size.

As underlined at the beginning of this chapter, porous homogenized models are needed in order to perform large-scale simulations of ductile fracture. Using the model developed in Section II.1, it was shown that it was possible to simulate ductile tearing in mono- and polycrystalline samples of various geometries under plane strain. As a perspective, 3D simulations can also be conducted, as highlighted in Fig. II.36 which depicts the uniaxial straining of a cylinder with 100 grains (see Fig. II.36a). The homogenized model is used in the absence of hardening. As shown on the load curve of Fig. II.36b, the fracture process can be simulated almost entirely before numerical convergence becomes impossible (Fig. II.36c). As expected in such a round bar, the crack nucleates at the center of the specimen (see Fig. II.36d). These 2D and 3D simulations pave the way towards the microstructure-informed prediction of the ductile fracture of real polycrystalline samples, as pioneered by Frodal et al. (2021) and Khadyko et al. (2021) with simpler homogenized models. This goal is believed to be reachable by optimizing the material behavior law (in `MFront`) — not attempted in this work — and by taking advantage of massively parallel computation. Indeed, the FEM code used here (`Cast3M`) is not suited for multi-threading, so dedicated FEM codes — or FFT solvers, which are

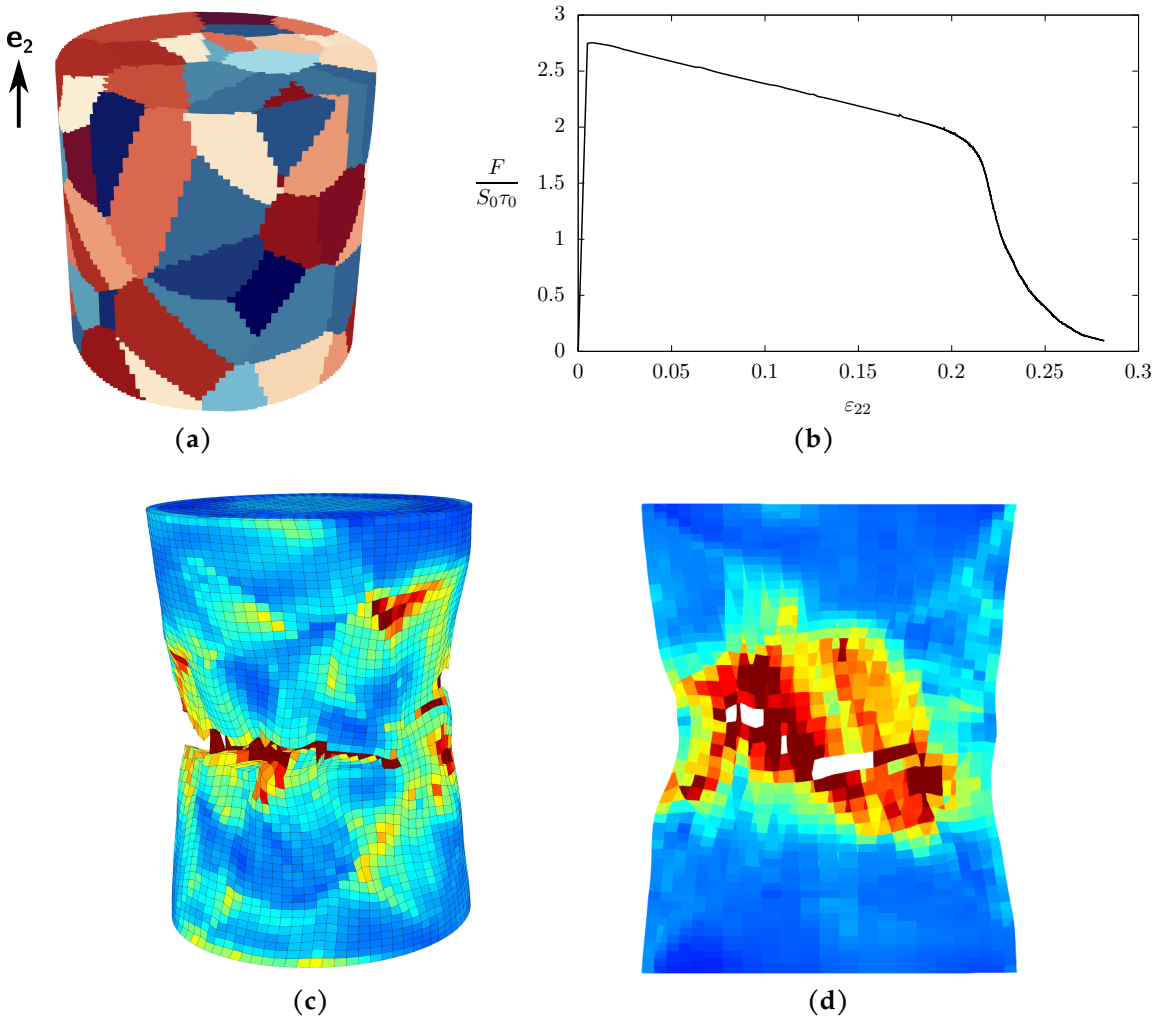

FIGURE II.36: Uniaxial tension simulation on a cylindrical specimen with 100 non-hardenable grains and 27050 quadratic sub-integrated elements: (**a**) initial microstructure; (**b**) load-displacement curve where F is the load on the upper surface, S_0 is the initial section of the cylinder and $\varepsilon_{22} = \log\left(\frac{L_2(t)}{L_2(0)}\right)$ with L_2 the time-dependent cylinder length along $\underline{e}_2$; (**c**) χ at the surface of the specimen at $\varepsilon_{22} = 0.282$; (**b**) χ in a longitudinal section at $\varepsilon_{22} = 0.223$.

more efficient — should be employed. One application could be the prediction of the effect of microstructure (*e.g.* presence and shape of inclusions, grain morphology, and texture) on fracture toughness — even if such computations would require regularization with a local length-scale to solve the issue of mesh size dependence. Eventually, if the microstructure of materials can be numerically reproduced, numerical optimization of the fracture toughness will become possible, which would constitute a significant advancement in material design.

Finally, it is highlighted that model experiments are needed to validate the quantitative predictions obtained using the homogenized model. These experiments are scarce because they require small specimens with few grains, as well as an extensive characterization to estimate correctly material and model parameters. The benchmark of simulations on identical samples and materials using different porous single-crystal homogenized models could also be conducted to assess competing modeling approaches. Such experimental and numerical comparisons were not carried out due to insufficient time.

3 Necklace coalescence in porous crystals

Since the beginning of this chapter, the deformation regimes considered are void growth and coalescence by internal necking (or *coalescence in layers*). However, it has been known for long that another coalescence mode, *coalescence in columns* (or *necklace coalescence*), can happen during ductile fracture (see Section I.1). In that regime, voids interact in a direction parallel to the main loading axis, as shown in Fig. II.37 at two different scales. Coalescence in columns is believed to have effects less drastic than coalescence in layers since damaged columns are less dangerous than damaged layers (Benzerga and Leblond, 2010). Still, this deformation regime can influence transgranular ductile fracture (Gologanu et al., 2001a). In Fig. II.37b, the cavities are larger than the average grain size (8–10 µm), so phenomenological models are suitable to study this phenomenon. However, in Fig. II.37a, the cavities are below the average grain size. Thus, following the governing theme of this thesis, studying necklace coalescence at the grain scale — as void growth and coalescence in layers — would enable to better account for microstructure effects in that type of application.

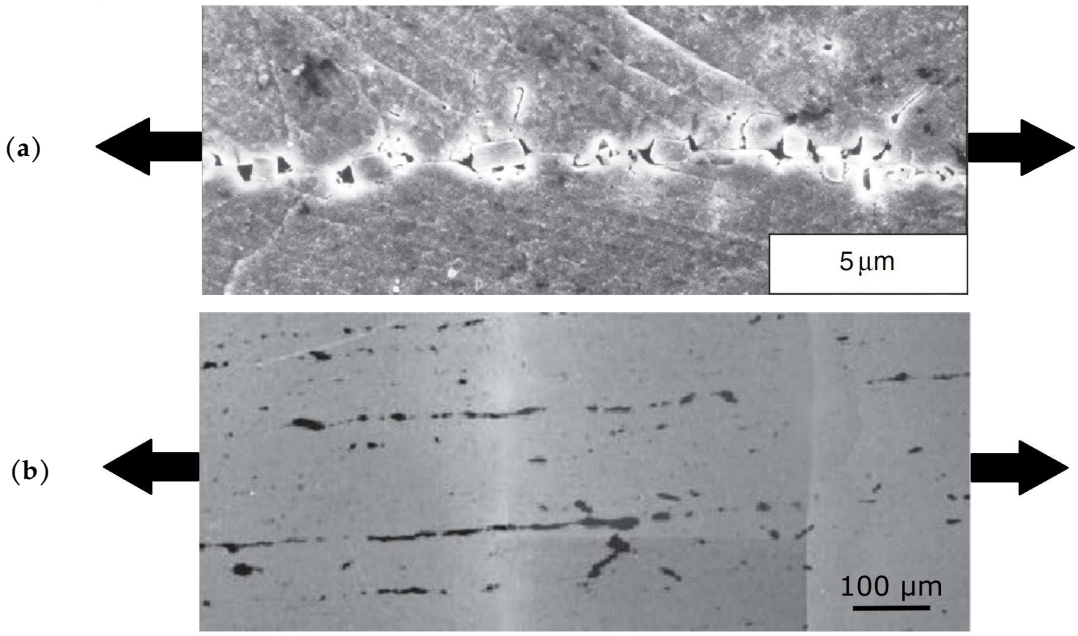

Figure II.37: Historical observations of coalescence in columns: **(a)** cold-drawn pure copper with around 0.2% copper oxides (Pardoen, 1998); **(b)** low alloyed ferrito-pearlitic steel with elongated MnS particles along the rolling direction (Benzerga, 2000). In both cases, the loading is horizontal.

Walking in the footsteps of Gurson (1977) and Thomason (1985), most of porous yield criteria of the literature were built using a multi-surface framework which considered on the one hand, a void growth surface derived in the geometry of Fig. I.44, and on the other hand, a coalescence in layers surface derived in the geometry of Fig. I.45. Given the difference in trial velocity field used, supplemented by the unit cell geometry discrepancy, non-differentiable points on the final yield surface were inevitable. To alleviate such a difficulty, Morin et al. (2015c) and later Torki (2019) proposed unified yield criteria for combined growth and coalescence, based on the cylindrical unit cell of Fig. I.45, by using a family of velocity field displaying gradual localization in layers. An account of gradual columnar localization in the cylindrical unit cell was inspired by this approach (Torki et al., 2023). As a result, to predict the yield surface of a porous unit cell, two different strategies coexist:

1. combining a void growth and a coalescence in layers criteria, neglecting coalescence in columns;
2. combining a criterion for gradual localization in layers and a criterion for gradual localization in columns, accounting simultaneously for void growth, coalescence in layers, and coalescence in columns;

The first strategy was used in Sections II.1 and II.2 (and will be used again in Sections III.1, III.2 and III.3); the second strategy will be adopted here. Thus, the remainder of the section is dedicated to developing a full yield surface for porous single crystal, including the necklace coalescence regime; it is reproduced from a scientific publication (Sénac et al., 2023b).

Yield surface for void growth and coalescence of porous anisotropic materials under axisymmetric loading

Cédric Sénac, Jérémy Hure, Benoît Tanguy

Journal of the Mechanics and Physics of Solids — 2023

Abstract

Ductile fracture in metallic alloys occurs by growth and coalescence of cavities. Growth, also referred to as homogeneous yielding, refers to rather diffuse plasticity around cavities, while coalescence, also termed inhomogenous yielding, corresponds to the localization of plasticity along some planes or directions. Coalescence can develop in various patterns; three coalescence modes have been observed experimentally: internal necking, coalescence in columns and void sheeting. Plastic anisotropy of the material is known to affect both homogeneous and inhomogeneous yielding significantly. Therefore, in the present study, yield criteria accounting for the transition from homogeneous yielding to inhomogeneous yielding modes in anisotropic porous materials are obtained using kinematic limit analysis on a cylindrical unit cell with a coaxial cylindrical cavity. Two types of plastic anisotropy are considered: Hill (1948) plasticity and crystal plasticity. The proposed analytical yield criteria are compared to numerical limit analysis computations and are found to agree with simulations qualitatively. In particular, plastic anisotropy, void shape effects and their coupling are captured well, especially regarding yield stresses and deformation modes. Finally, a homogenized model for Hill porous materials is obtained by supplementing evolution laws for microstructural parameters (void aspect ratio and ligament size ratios) derived from sequential limit analysis. Proposed evolution laws are then discussed in the light of numerical results and experimental evidence.

3.1 Introduction

It has been known for decades that the process of ductile fracture in most metallic alloys happens through the growth and coalescence of cavities originating from inclusions (*e.g.* Benzerga and Leblond (2010) and Pineau et al. (2016)). On the one hand, void growth manifests as a rather homogeneous yielding of the material, with diffuse plasticity at the scale of cavities. On the other hand, void coalescence arises from the inhomogeneous distribution of the plastic flow: due to strong interactions between cavities, strain localizes in specific zones linking voids. Following the seminal contributions of Rice and Tracey (1969) and Gurson (1977), homogeneous yielding in porous materials (Fig. II.38a) has been thoroughly studied: for isotropic materials, yield criteria for spherical voids (Gurson, 1977), spheroidal voids (Gologanu et al., 1997) and ellipsoidal voids (Madou and Leblond, 2012a) have been proposed. These criteria were extended to anisotropic materials through Hill (1948) plasticity, respectively in Benzerga and Besson (2001), Monchiet et al. (2008), Keralavarma and Benzerga (2010) and Morin et al. (2015c), and to porous single crystals by Han et al. (2013), Paux et al. (2015) and Mbiakop et al. (2015b). Thus, further improvements in the prediction of yield criteria for porous materials lie in the accurate modeling of inhomogeneous yielding and the transition from homogeneous yielding to inhomogeneous yielding.

Inhomogeneous yielding in porous materials has been modeled more recently than homogeneous yielding. Experimental observations of coalescence reveal various possible types of interactions between cavities (Benzerga et al., 2004a). Internal necking and necklace coalescence are the most commonly observed coalescence modes. The former, where localization occurs mainly perpendicular to the main loading direction, is alternatively referred to as coalescence in layers (Fig. II.38b), while in the latter, also denoted as coalescence in columns, localization happens along the main loading direction (Fig. II.38c). In a major contribution, Thomason (1985) used limit-analysis to derive a coalescence stress for internal necking later employed as a yield criterion. Thomason's yield criterion was used and improved by a certain number of studies (Pardoen and Hutchinson, 2000; Benzerga, 2002; Benzerga et al., 2004b) or specialized to anisotropic materials (Yerra et al., 2010) until analytical expressions were finally obtained by Benzerga and Leblond (2014), Morin et al. (2015b) (cylindrical voids), Hure and Barrioz (2016) (flat cylindrical voids) and Barrioz et al. (2018a) (elliptic-cylindrical voids). Shear-assisted coalescence has been incorporated in the model by Tekoğlu et al. (2012), Torki et al. (2015) and Torki et al. (2017). These inhomogeneous yield criteria have been combined with homogeneous yield criteria using multi-surface plasticity framework (Benzerga and Leblond,

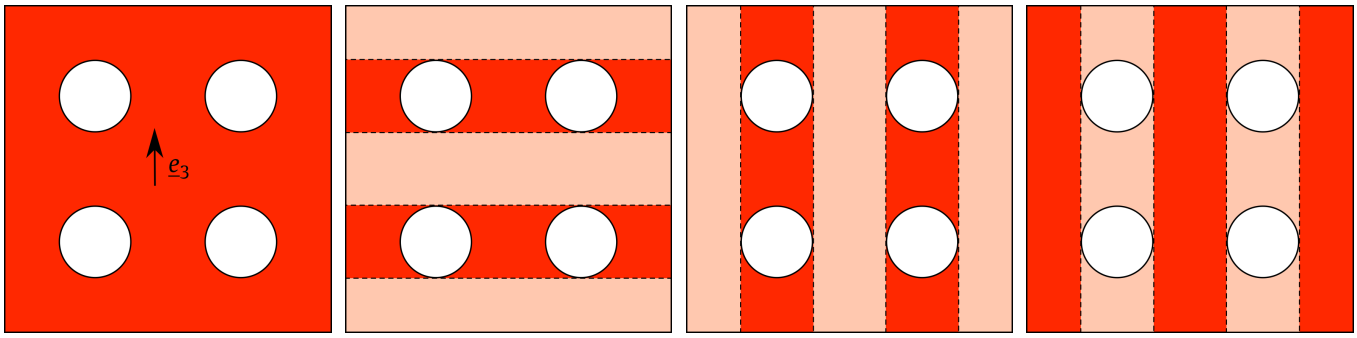

(**a**) Homogeneous growth (**b**) Internal necking (**c**) Coalescence in columns (**d**) Columnar shielding

FIGURE II.38: Possible modes of yielding of a periodic array of voids subjected to an axisymmetric loading of principal axis $\underline{e}_3$.

2010; Keralavarma, 2017; Torki et al., 2021). Another approach has been proposed recently consisting of deriving a single yield criterion able to represent both homogeneous and inhomogeneous yielding using limit-analysis with suitable velocity fields (Morin et al., 2016a; Torki, 2019). All these advances have focused on coalescence in layers; nonetheless, necklace coalescence is important in predicting ductile fracture of many materials, as shown below.

From an experimental perspective, the historical observations of coalescence in columns (Pardoen, 1998; Benzerga, 2000) were scarce, which has led to a false sentiment that this deformation mode was anecdotal and could be neglected. The paucity of experimental evidence was explained by the fact that coalescence in columns usually cannot be identified on fracture surfaces — contrary to shear-assisted coalescence and internal necking — and must therefore be glimpsed through metallographic examinations of areas away from fracture surfaces or on samples subjected to interrupted mechanical tests. The recent development of X-ray tomography has revealed that this phenomenon is in fact more common (Fig. II.39a) (Requena et al., 2014; Seo et al., 2015; Guo et al., 2022b). Observations of necklace coalescence, initially limited to steels (Benzerga, 2000) and almost-pure copper (Pardoen, 1998) with strings of second-phase particles caused by metal forming and oriented along the loading direction, were also diversified to other materials. In pure tantalum with equiaxed grains, coalescence in columns was shown to be dominant (Boyce et al., 2013), underlying that a specific distribution of inclusions is not a prerequisite to observe this phenomenon (Fig. II.39b). Furthermore, it was seen that necklace coalescence can give birth to micro-cracks (Fig. II.39c) in annealed bainitic steels (Saeidi et al., 2015). Outside of metallic materials, intense coalescence in columns was unambiguously identified during the fracture of aged polyethylene films (Fig. II.39d) in which void nucleation at the amorphous phase was enabled by chemical micro-cracks (Rodriguez et al., 2020). When coalescence in columns is significant, it influences the fracture process and the material's ductility, although its effect is eminently ubiquitous. On the one hand, fracture strain can be reduced if the final crack originates from a necklace coalescence micro-crack (Saeidi et al., 2015), if internal necking occurs between voids formed through necklace coalescence (Requena et al., 2014) or if a shear instability is fostered by elongated coalesced cavities (Rodriguez et al., 2020). On the other hand, coalescence in columns can be responsible for delaminations (Benzerga and Leblond, 2010) that lower the stress triaxiality, making crack propagation perpendicularly to the loading direction more difficult (Bramfitt and Marder, 1977; Pala and Dzioba, 2018; Wang et al., 2022), which can result in an increase of the fracture strain. For instance, coalescence in columns seems partially responsible for the observed ductility of pure tantalum (Boyce et al., 2013).

From a numerical perspective, porous plasticity models that do not incorporate coalescence in columns display discrepancies when compared to numerical results with general boundary conditions, as seen in Chouksey et al. (2019). Another localization mode, in which the central column of the unit-cell is shielded from plasticity — referred to as *columnar shielding* in the following — was also reported multiple times in unit-cell simulations (Chouksey et al., 2019; Chouksey et al., 2020; Chouksey and Basu, 2021). An earlier model of coalescence in columns was provided by Gologanu et al. (2001b) on a cylindrical unit-cell: the central column was modeled as a homogeneous porous material experiencing void growth, while the outer hollow cylinder followed plastic incompressibility laws. However, the approximate nature of implicit velocity fields considered in this model had detrimental effects on the micromechanics of coalescence (Torki et al., 2023). Recently, explicit limit-analysis of coalescence in columns and columnar shielding was performed by Torki et al. (2023) for an isotropic von Mises matrix; their results confirmed that accounting for

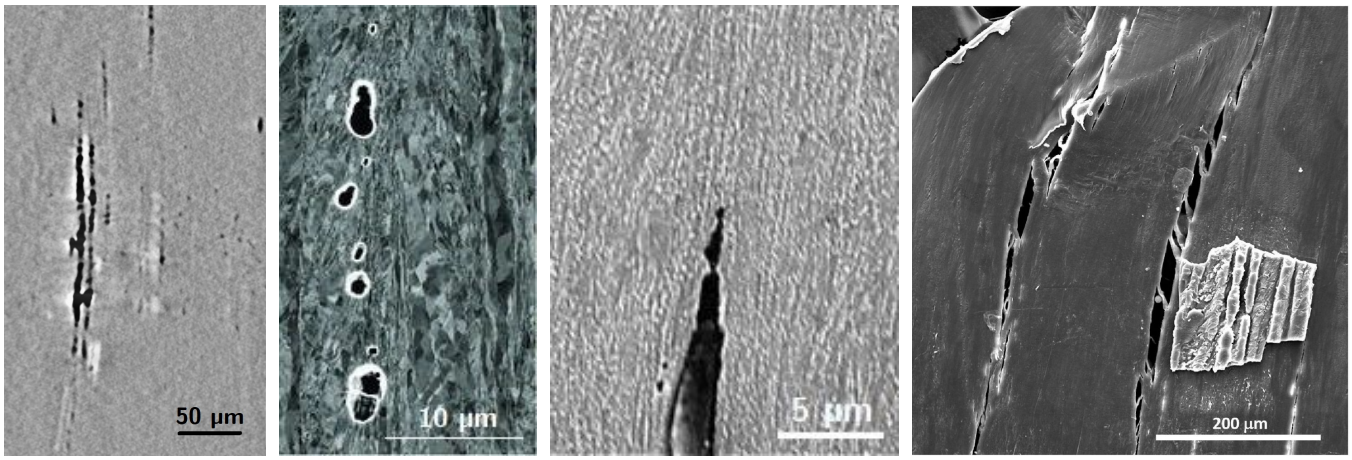

FIGURE II.39: Experimental evidence of necklace coalescence in various materials: **(a)** dual-phase steel (Requena et al., 2014); **(b)** pure tantalum (Boyce et al., 2013); **(c)** upper bainitic steel (Saeidi et al., 2015); **(d)** UV-aged low-density polyethylene (Rodriguez et al., 2020). The applied loading was vertical in all cases; however, note that specimen **(d)** has rotated a little following fracture.

these additional localization modes allowed for a better prediction of yield surfaces provided by unit-cell simulations.

It is known from experiments (Benzerga et al., 2004a; Benzerga and Leblond, 2010), theory (Keralavarma and Chockalingam, 2016; Hure, 2019) and simulations (Keralavarma et al., 2011; Yerra et al., 2010; Ling et al., 2016; Sénac et al., 2022) that plastic anisotropy has a strong influence on material ductility, through significant effects on both homogeneous and inhomogeneous yielding. Since metal forging and forming are known to induce strong anisotropy in metallic components, it means that specific yield surfaces for porous materials exhibiting plastic anisotropy are needed. As stated before, numerous studies have been carried out on the homogeneous yielding of anisotropic materials. Criteria for internal necking have also been established in Hill materials (Keralavarma and Chockalingam, 2016) and single crystals (Hure, 2019). Therefore, the goal set for the present study is to develop a yield criterion for both Hill materials and single crystals that would account for homogeneous yielding (Fig. II.38a), inhomogeneous yielding (Fig. II.38b,c,d), and the transition from one mode to another, for axisymmetric loading conditions.

The paper is divided into three main parts. In the first part, a multi-surface yield criterion for anisotropic porous materials following Hill's criterion is developed; this model is relevant for polycrystalline materials where voids are significantly larger than the grain size. It is derived through limit-analysis of two velocity fields: a field accounting for the transition from homogeneous yielding (Fig. II.38a) to coalescence in columns (Fig. II.38c,d), as in Torki et al. (2023), and a field accounting for the transition from homogeneous yielding to internal necking (Fig. II.38b), as in Morin et al. (2016a). Subsequently, the final criterion is checked against unit-cell simulations. Since this first model cannot be applied to alloys in which voids are smaller than the grain size, a yield surface for porous single crystals is developed in a second part. It is obtained using an approximate method relying on average Taylor factors and compared to numerical yield surfaces. In a third part, a complete homogenized model is obtained for Hill materials by supplementing the multi-surface yield criterion with microstructure evolution laws derived from sequential limit analysis. Finally, the model is discussed in the light of numerical velocity fields and ductile fracture experimental evidence.

3.2 Problem statement

In the following, vectors are shown as $\underline{a}$ of norm a, second-order tensors as $\boldsymbol{a}$ and fourth-order tensors as $\mathbb{A}$. Einstein's summation convention is used on Latin indices but not Greek ones. Finally, $\odot$ stands for the symmetrized tensor product.

3.2.1 Porous material description

This study considers a porous material with a homogeneous matrix where cavities of identical size and shape are embedded. As a first approximation, cavities are supposed to be spheroidal of aspect ratio w and the actual distribution

of voids is modeled as a periodic array of hexagonal lattice, with the void main axis and the lattice main axis being along $\underline{e}_3$ (Fig. II.40a).

The above-defined material is subjected to axisymmetric boundary conditions. This material is approximated by a cylindrical unit-cell Ω of main axis along $\underline{e}_3$, as shown in Fig. II.40b. The unit cell half-height is called H and its radius R; it contains a coaxial cylindrical void ω and is characterized by three dimensionless ratios:

$$\chi = \frac{r}{R} \ , \quad c = \frac{h}{H} \ , \quad w = \frac{h}{r} \tag{II.63}$$

χ is the transverse ligament size ratio, c is the axial ligament size ratio and w is the void aspect ratio. If $w > 1$, the void is prolate, and $w < 1$ means the void is oblate. This approximated unit cell is loaded axisymmetrically with the following velocity boundary conditions:

$$v_\rho(R, z) = RD_{\rho\rho} \ , \quad v_z(\rho, \pm H) = \pm H D_{33} \tag{II.64}$$

with $\boldsymbol{D}$ the (volume-averaged) macroscopic strain rate tensor. As discussed in Benzerga and Leblond (2014) and later shown in Morin et al. (2016a), these boundary conditions allow for both homogeneous and inhomogeneous yielding. The microscopic Cauchy stress tensor is referred to as $\boldsymbol{\sigma}$ and the macroscopic one as $\boldsymbol{\Sigma}$, these tensors being related by $\boldsymbol{\Sigma} = \int_\Omega \boldsymbol{\sigma} / |\Omega|$.

3.2.2 Kinematic limit analysis

In this work, the plastic yielding of the approximated unit-cell is studied using kinematic limit analysis (Suquet, 1982). Limit analysis relies on finding a (trial) velocity field that is both incompressible and compatible with boundary conditions. This trial velocity field is then used to estimate the yield surface (Benzerga and Leblond, 2010). The set of trial velocity fields $\underline{v}$ that satisfy boundary conditions (Eq. II.64) as well as matrix incompressibility $\mathrm{Tr}\,(\boldsymbol{d}) = 0$ is denoted $\mathcal{K}(\boldsymbol{D})$. The microscopic plastic dissipation of such a velocity field is:

$$\varpi\left(\underline{v}\left(\underline{x}\right)\right) \equiv \sup_{\boldsymbol{\sigma}^* \in \mathscr{C}} \left(\boldsymbol{\sigma}^* : \boldsymbol{d}\left(\underline{x}\right)\right) \tag{II.65}$$

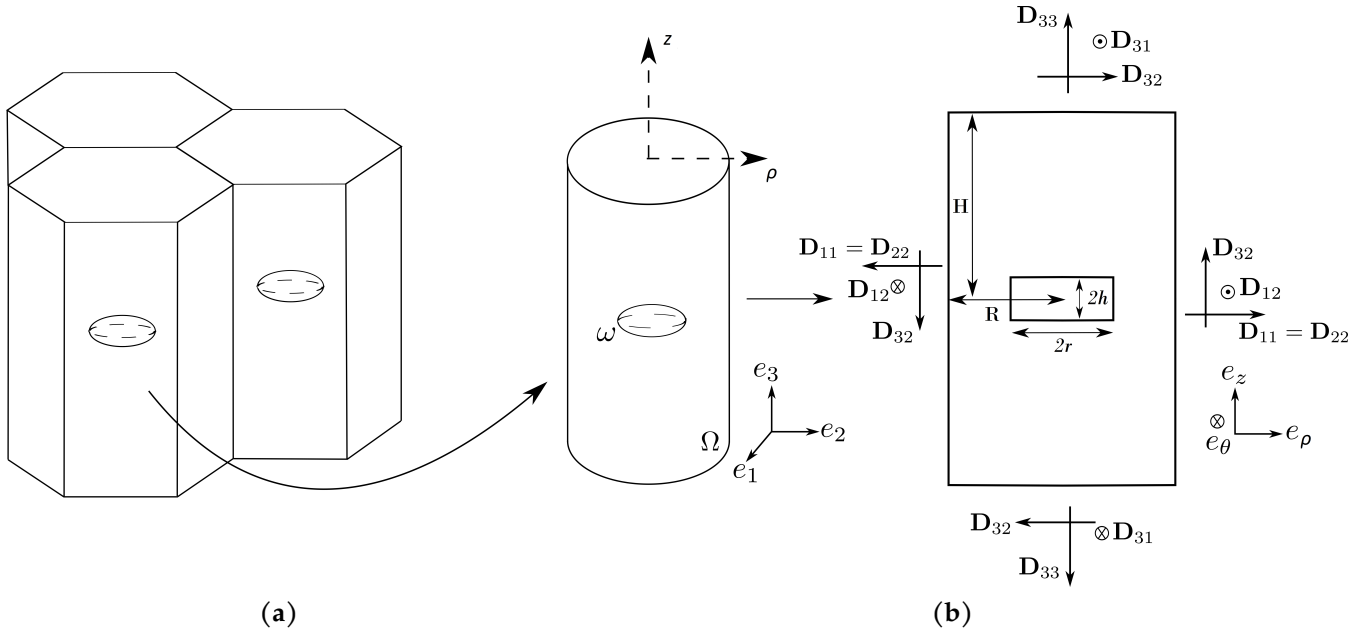

FIGURE II.40: Cylindrical unit-cell considered as an approximation of a unit-cell of a periodic array of voids of hexagonal lattice under periodic boundary conditions.

where $\boldsymbol{d}$ is the strain rate field deriving from $\underline{v}$ and $\mathscr{C}$ is the microscopic elasticity domain of the matrix. Each element $\underline{v} \in \mathcal{K}(\boldsymbol{D})$ provides an upper bound Π_+ for the macroscopic dissipation Π, defined as:

$$\Pi(\boldsymbol{D}) = \inf_{\underline{v} \in \mathcal{K}(\boldsymbol{D})} \frac{1}{|\Omega|} \int_\Omega \varpi\left(\underline{v}\left(\underline{x}\right)\right) \tag{II.66}$$

If the velocity field exhibits a discontinuity $\Delta\underline{v} = |\Delta\underline{v}|\,\underline{t}$ on a given surface $\mathcal{S}_d$ of normal $\underline{n}$ ($\underline{t}$ and $\underline{n}$ are unit vectors), an additional dissipation term has to be added to the dissipation upper-bound Π_+ (Salençon, 1983):

$$\Pi_+^{\text{surf}}(\boldsymbol{D}) = \frac{1}{|\Omega|} \int_{\mathcal{S}_d} |\Delta\underline{v}| \sup_{\boldsymbol{\sigma}^* \in \mathscr{C}} \left(\boldsymbol{\sigma}^* : \boldsymbol{d}^{(\mathrm{I})}\right) \quad \text{with} \quad \boldsymbol{d}^{(\mathrm{I})} = \underline{t} \odot \underline{n} \tag{II.67}$$

Hill-Mandel lemma (*e.g.* Nemat-Nasser and Hori (1993)) along with Eqs. II.65, II.66 allows to write that:

$$\forall \boldsymbol{D}\ , \quad \boldsymbol{\Sigma} : \boldsymbol{D} \leq \Pi\left(\boldsymbol{D}\right) \tag{II.68}$$

which is used to assess the yield surface. Indeed, the yield surface of the material is the boundary of the elasticity domain described by Eq. II.68. This means that for each $\boldsymbol{\Sigma}$ on the yield surface, there is a strain rate $\boldsymbol{D}$ for which $\boldsymbol{\Sigma} : \boldsymbol{D} = \Pi\left(\boldsymbol{D}\right)$. Thus, the hyperplane $\boldsymbol{\Sigma} : \boldsymbol{D}$ must be tangent to surface $\Pi(\boldsymbol{D})$. On the one hand, if Π is differentiable at the point $\boldsymbol{D}_0$ where multi-dimensional tangency occur, then tangency implies that:

$$\boldsymbol{\Sigma} : \boldsymbol{D}_0 = \Pi(\boldsymbol{D}_0)\ , \quad \boldsymbol{\Sigma} = \frac{\partial \Pi}{\partial \boldsymbol{D}}(\boldsymbol{D}_0) \tag{II.69}$$

On the other hand, if Π is not differentiable, then multi-dimensional tangency becomes:

$$\boldsymbol{\Sigma} : \boldsymbol{D}_0 = \Pi(\boldsymbol{D}_0)\ , \quad \boldsymbol{\Sigma} \in \partial\Pi(\boldsymbol{D}_0) \tag{II.70}$$

with $\partial\Pi(\boldsymbol{D}_0)$ denoting the subdifferential of Π at point $\boldsymbol{D}_0$, *i.e.* the set of subgradients $\boldsymbol{S}$ such that

$$\Pi(\boldsymbol{D}) - \Pi(\boldsymbol{D}_0) \geq \boldsymbol{S} : (\boldsymbol{D} - \boldsymbol{D}_0) \tag{II.71}$$

For each trial velocity field, Eq. II.69$_b$ (or Eq. II.70$_b$) provides an upper-bound Π_+ of the macroscopic dissipation Π and thus an upper-bound of the yield surface. In the following, for each trial field, the corresponding Π_+ and its subsequent upper bounds will still be denoted Π for convenience.

3.3 Yield surface for porous Hill materials

In the first part, plastic anisotropy will be modeled by the well-known Hill plasticity (Hill, 1948). The matrix material is supposed to be elastoplastic, obeying the associated Hill criterion:

$$\mathcal{F}\left(\boldsymbol{\sigma}\right) = \left(\frac{\sigma_{\text{eq}}^{\text{H}}}{\sigma_0}\right)^2 - 1 = \frac{3}{2}\frac{\boldsymbol{\sigma} : \mathbb{h} : \boldsymbol{\sigma}}{\sigma_0^2} - 1 \tag{II.72}$$

with $\mathbb{h}$ the Hill stress anisotropy tensor and σ_0 the uniaxial yield strength in a given direction. The matrix material is incompressible, thus $\mathbb{J} : \mathbb{h} = \mathbb{h} : \mathbb{J} = 0$ with $\mathbb{J} = \frac{1}{3}\boldsymbol{I} \otimes \boldsymbol{I}$. The associated equivalent strain rate is $d_{\text{eq}} = \sqrt{\frac{2}{3}\boldsymbol{d} : \hat{\mathbb{h}} : \boldsymbol{d}}$ with $\hat{\mathbb{h}}$ a tensor verifying $\hat{\mathbb{h}} : \mathbb{h} = \mathbb{h} : \hat{\mathbb{h}} = \mathbb{K}$, where $\mathbb{K} = \mathbb{I} - \mathbb{J}$. In a base of orthotropy, the components of $\hat{\mathbb{h}}$ can be obtained from the components of $\mathbb{h}$ following the formulas given in Morin (2012). More fundamentally, $\hat{\mathbb{h}}$ is linked to $\mathbb{h}$ through linear algebra, as shown in Sénac et al. (2023a). Microscopic plastic dissipation (Eq. II.65) writes:

$$\sup_{\boldsymbol{\sigma}^* \in \mathscr{C}} \left(\boldsymbol{\sigma}^* : \boldsymbol{d}\right) = \sigma_0 d_{\text{eq}} \tag{II.73}$$

The yield surface for porous Hill materials under axisymmetric loading will be obtained through the conjunction of a yield criterion describing the gradual localization of strain in vertical zones (Section II.3.3.1) and a yield criterion describing the gradual localization of strain in horizontal layers (Section II.3.3.4).

3.3.1 From homogeneous yielding to inhomogeneous yielding in columns

In this section, the transition from homogeneous yielding (Fig. II.38a) to columnar localization, which can manifest either as columnar shielding (Fig. II.38c) or as coalescence in columns (Fig. II.38d), is considered to obtain the related yield criterion. This yield criterion is therefore an extension of the criterion developed by Torki et al. (2023) to anisotropic materials following Hill's criterion (Eq. II.72).

3.3.2 Trial velocity field and associated dissipation

The trial velocity field proposed in Torki et al. (2023) is used to account for the situation depicted in Fig. II.38a,c,d and is defined in the geometry shown in Fig. II.41a:

$$\begin{aligned} &\text{Outer zone:} \quad v_\rho^{(\mathrm{O})}(\rho) = \frac{1}{2}\left(\frac{R^2}{\rho}D_{kk} - \rho D_{33}\right), \qquad v_z^{(\mathrm{O})}(z) = zD_{33} \\ &\text{Plugs:} \qquad\quad v_\rho^{(\mathrm{P})}(\rho) = \frac{1}{2}\left(\frac{\rho}{\chi^2}D_{kk} - \rho D_{33}\right), \quad v_z^{(\mathrm{P})}(z) = \frac{H-z}{\chi^2}D_{kk} + zD_{33} \end{aligned} \tag{II.74}$$

This trial velocity field is incompressible, kinematically admissible with Eq. II.64 and displays a purely tangential discontinuity along $\mathcal{S}_d$ ($\rho = r$). As this field has been shown in Torki et al. (2023) to lead to results in good agreement with numerical simulations for isotropic materials, it will be adopted to study general anisotropic materials. Then, the macroscopic plastic dissipation is the sum of volume terms corresponding to the plugs (P) and the outer zone (O), as well as a surface term originating from the velocity tangential discontinuity at the interface between zones P and O:

$$\Pi(\boldsymbol{D}) = \underbrace{\frac{1}{|\Omega|}\int_{\Omega_\mathrm{P}} \sigma_0 d_{\mathrm{eq}}^{(\mathrm{P})}}_{\Pi^{(\mathrm{P})}} + \underbrace{\frac{1}{|\Omega|}\int_{\Omega_\mathrm{O}} \sigma_0 d_{\mathrm{eq}}^{(\mathrm{O})}}_{\Pi^{(\mathrm{O})}} + \underbrace{\frac{1}{|\Omega|}\int_{\mathcal{S}_d} |\Delta \underline{v}|\, \sigma_0 d_{\mathrm{eq}}^{(\mathrm{I})}}_{\Pi^{\mathrm{surf}}} \tag{II.75}$$

Strain rates related to the trial velocity field are taken from Torki et al. (2023):

$$\begin{aligned} d_{\rho\rho}^{(\mathrm{O})} &= -\frac{1}{2}\left(\frac{R^2}{\rho^2}D_{kk} + D_{33}\right) & d_{\theta\theta}^{(\mathrm{O})} &= \frac{1}{2}\left(\frac{R^2}{\rho^2}D_{kk} - D_{33}\right) & d_{zz}^{(\mathrm{O})} &= D_{33} \\ d_{\rho\rho}^{(\mathrm{P})} &= \frac{1}{2}\left(\frac{1}{\chi^2}D_{kk} - D_{33}\right) & d_{\theta\theta}^{(\mathrm{P})} &= \frac{1}{2}\left(\frac{1}{\chi^2}D_{kk} - D_{33}\right) & d_{zz}^{(\mathrm{P})} &= D_{33} - \frac{1}{\chi^2}D_{kk} \end{aligned} \tag{II.76}$$

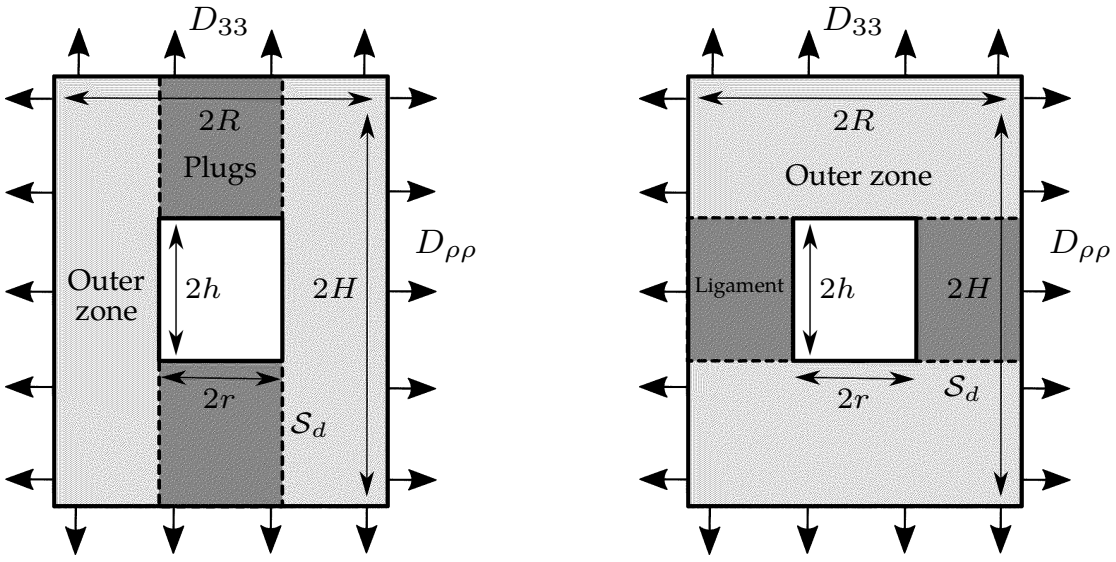

(**a**) Columnar localization (**b**) Layered localization

FIGURE II.41: Geometry of the zones used to define trial velocity fields kinematically admissible with the boundary conditions.

The tangential velocity jump on $\mathcal{S}_d$ is along $\underline{e}_3$:

$$|\Delta \underline{v}| = \frac{H-z}{\chi^2}\,|D_{kk}| \tag{II.77}$$

Eq. II.75 requires to perform the integration of the equivalent strain rate d_{eq}, which depends on cylindrical coordinate ρ (or z) due to $\boldsymbol{d}$ and on θ due to tensor $\hat{\mathbb{h}}$. At fixed ρ (or z), the θ-integral of d_{eq} does not admit an analytic expression in general; resorting to Cauchy-Schwarz inequality yields:

$$\frac{1}{2\pi}\int_0^{2\pi} d_{\text{eq}}(\rho,\theta)\,\mathrm{d}\theta \leq \sqrt{\frac{1}{2\pi}\int_0^{2\pi} d_{\text{eq}}^2(\rho,\theta)\,\mathrm{d}\theta} \equiv \sqrt{\left\langle d_{\text{eq}}^2\right\rangle_\theta(\rho)} \tag{II.78}$$

Note that if $\hat{\mathbb{h}}$ does not depend on θ (*i.e.* transverse isotropy), then inequality turns into equality. Writing $\hat{\mathbb{h}}$ in the cylindrical frame of reference, lengthy but elementary evaluation leads to:

$$\left\langle \left(d_{\text{eq}}^{(\text{O})}\right)^2\right\rangle_\theta = \hat{h}_q D_{33}^2 + \frac{\hat{h}_t}{3}\left(\frac{R}{\rho}\right)^4 D_{kk}^2\ ,\quad \left\langle \left(d_{\text{eq}}^{(\text{P})}\right)^2\right\rangle_\theta = \hat{h}_q\left(\frac{1}{\chi^2}D_{kk}-D_{33}\right)^2\ ,\quad \left\langle \left(d_{\text{eq}}^{(\text{I})}\right)^2\right\rangle_\theta = \frac{\hat{h}_a}{3} \tag{II.79}$$

where $\hat{h}_q$, $\hat{h}_t$ and $\hat{h}_a$ are scalar anisotropy factors also used in the anisotropic yield criteria of Benzerga and Besson (2001) and Keralavarma and Benzerga (2010) (void growth) as well as Keralavarma and Chockalingam (2016) (coalescence in layers). They are related to the coefficients of the Voigt-Mandel representation of $\hat{\mathbb{h}}$ and, as expected, are left unchanged by rotations of the frame of reference around void axis $\underline{e}_3$:

$$\hat{h}_q = \frac{\hat{h}_{11}+\hat{h}_{22}+4\hat{h}_{33}-4\hat{h}_{23}-4\hat{h}_{31}+2\hat{h}_{12}}{6}\ ,\quad \hat{h}_t = \frac{\hat{h}_{11}+\hat{h}_{22}+2\hat{h}_{66}-2\hat{h}_{12}}{4}\ ,\quad \hat{h}_a = \frac{\hat{h}_{44}+\hat{h}_{55}}{2} \tag{II.80}$$

After straightforward integration, volume terms of the macroscopic dissipation write:

$$\Pi^{(\text{P})} = \sigma_0(1-c)\sqrt{\hat{h}_q}\,|D_{kk}-\chi^2 D_{33}|\ ,\quad \Pi^{(\text{O})} = \sigma_0\left[\sqrt{\frac{\hat{h}_t}{3}}\mathcal{A}\left(\sqrt{\frac{\hat{h}_t}{3\hat{h}_q}}\xi\right)|D_{kk}| + \sqrt{\hat{h}_q}\mathcal{B}\left(\sqrt{\frac{\hat{h}_t}{3\hat{h}_q}}\xi\right)|D_{33}|\right]$$
$$\text{where}\quad \xi = \frac{D_{kk}}{D_{33}}\quad\text{and}\quad \begin{cases}\mathcal{A}(x) &= \log\left[\dfrac{x^2}{\chi^2}\left(-1+\sqrt{1+\dfrac{1}{x^2}}\right)\left(1+\sqrt{1+\dfrac{\chi^4}{x^2}}\right)\right]\\ \mathcal{B}(x) &= \sqrt{1+x^2}-\sqrt{\chi^4+x^2}\end{cases} \tag{II.81}$$

Finally, using Eqs. II.67 and II.77, the surface term reads:

$$\Pi^{\text{surf}} = \frac{\sigma_0}{\pi R^2 H}\frac{|D_{kk}|}{\chi^2}\int_h^H 2\pi r(H-z)\sqrt{\left\langle\left(d_{\text{eq}}^{(\text{I})}\right)^2\right\rangle_\theta}\,\mathrm{d}z = \frac{\sigma_0}{\sqrt{3}}\frac{w}{c}(1-c)^2\sqrt{\hat{h}_a}\,|D_{kk}| \tag{II.82}$$

For an isotropic Von Mises matrix $\hat{h}_q = \hat{h}_t = \hat{h}_a = 1$, so Eqs. II.81 and II.82 recover the expressions found in Torki et al. (2023).

3.3.3 Yield criterion

Eqs. II.68-II.70 are used to obtain the yield surface; under axisymmetric loading, Eq. II.68 can be written:

$$\boldsymbol{\Sigma} : \boldsymbol{D} = \Sigma_{\rho\rho} D_{kk} + (\Sigma_{33}-\Sigma_{\rho\rho})D_{33} \tag{II.83}$$

Two cases should be considered depending on the differentiability of Π. $\Pi^{(\text{O})}$ is a differentiable function of (D_{kk}, D_{33}) on $\mathbb{R}^2\setminus\{(0,0)\}$ whereas Π^{surf} is non-differentiable on strain rates verifying $D_{kk}=0$ and $\Pi^{(\text{P})}$ is non-differentiable on strain rates verifying $D_\chi \equiv D_{kk}-\chi^2 D_{33}=0$. Thus, the condition of differentiability on Π is $D_{kk}D_\chi \neq 0$. For cases

where Π is differentiable, Eq. II.69 specifies into[9]:

$$\begin{aligned}\Sigma_{\rho\rho} = \frac{\partial \Pi}{\partial D_{kk}} &= \operatorname{sgn}(D_{33})\,\sigma_0 \left[\operatorname{sgn}(\xi-\chi^2)(1-c)\sqrt{\hat{h}_q} + \operatorname{sgn}(\xi)\left(\sqrt{\frac{\hat{h}_t}{3}}\mathcal{A}\left(\sqrt{\frac{\hat{h}_t}{3\hat{h}_q}}\xi\right) + \frac{w}{\sqrt{3}}\frac{(1-c)^2}{c}\sqrt{\hat{h}_a}\right)\right] \\ \Sigma_{33}-\Sigma_{\rho\rho} = \frac{\partial \Pi}{\partial D_{33}} &= \operatorname{sgn}(D_{33})\,\sigma_0 \left[-\operatorname{sgn}(\xi-\chi^2)(1-c)\chi^2\sqrt{\hat{h}_q} + \sqrt{\hat{h}_q}\mathcal{B}\left(\sqrt{\frac{\hat{h}_t}{3\hat{h}_q}}\xi\right)\right]\end{aligned} \tag{II.84}$$

which gives a parametrization of the yield surface in terms of $\xi \in \mathbb{R}$ and $\operatorname{sgn}(D_{33})$. Next, simple algebra can eliminate parameter ξ in Eq. II.84 in order to obtain a closed-form of the yield criterion. Then, using $\cosh(\log x) = \left(x + x^{-1}\right)/2$ leads to:

$$\cosh\mathcal{A} = \frac{1}{\chi^2}\left[\sqrt{1+\xi^2}\sqrt{\chi^4+\xi^2} - \xi^2\right] \tag{II.85}$$

which, using $\mathcal{B}$, can be rewritten as a Gurson-like criterion, χ^2 being the relative volume occupied by the central zone:

$$\mathcal{B}^2 + 2\chi^2\cosh\mathcal{A} - (1+\chi^4) = 0 \tag{II.86}$$

Inversion of the linear system of Eq. II.84 in order to express $(\mathcal{A},\mathcal{B})$ according to $(\Sigma_{\rho\rho}, \Sigma_{33}-\Sigma_{\rho\rho})$ lead to the following family of criteria:

$$\begin{aligned}&\left[\sqrt{\frac{1}{\hat{h}_q}}\frac{\Sigma_{33}-\Sigma_{\rho\rho}}{\sigma_0} + \epsilon_1(1-c)\chi^2\right]^2 + 2\chi^2\cosh\left[\sqrt{\frac{3}{\hat{h}_t}}\left(\frac{\Sigma_{\rho\rho}}{\sigma_0} - \epsilon_1(1-c)\sqrt{\hat{h}_q} - \epsilon_2\frac{w}{\sqrt{3}}\frac{(1-c)^2}{c}\sqrt{\hat{h}_a}\right)\right] \\ &\qquad - (1+\chi^4) = 0\end{aligned} \tag{II.87}$$

where $\epsilon_1 = \operatorname{sgn}(D_\chi)$ and $\epsilon_2 = \operatorname{sgn}(D_{kk})$. Thus, Eq. II.87 corresponds to four curved parts on the yield surface.

Then, the zones where Π is not differentiable are considered. The case in which $D_{kk} = 0$ and $D_\chi \neq 0$ is considered, which corresponds to $\xi = 0$. Since $\Pi(D_{kk}, D_{33})$ is differentiable in the second variable and left- and right- differentiable in the first variable, the subdifferential writes:

$$\partial\Pi(0,D_{33}) = \left[\left.\frac{\partial\Pi}{\partial D_{kk}}\right|_{0^-}(0,D_{33}),\ \left.\frac{\partial\Pi}{\partial D_{kk}}\right|_{0^+}(0,D_{33})\right] \times \left\{\frac{\partial\Pi}{\partial D_{33}}(0,D_{33})\right\} \tag{II.88}$$

so that Eq. II.70 yields:

$$\left|\Sigma_{\rho\rho} + \operatorname{sgn}(D_{33})\sigma_0(1-c)\sqrt{\hat{h}_q}\right| \leq \sigma_0\frac{w}{\sqrt{3}}\frac{(1-c)^2}{c}\sqrt{\hat{h}_a}\ ,\quad \Sigma_{33}-\Sigma_{\rho\rho} = \operatorname{sgn}(D_{33})\sigma_0\sqrt{\hat{h}_q}\left(1-c\chi^2\right) \tag{II.89}$$

The case in which $D_\chi = 0$ ($\xi = \chi^2$) and $D_{kk} \neq 0$ (or alternatively $D_{33} \neq 0$) can be treated by recasting Π as a function of D_χ and D_{33}. Since $\boldsymbol{\Sigma} : \boldsymbol{D} = \Sigma_{\rho\rho}D_\chi + \left(\Sigma_{33} - (1-\chi^2)\Sigma_{\rho\rho}\right)D_{33}$, Eq. II.70 writes:

$$\left(\Sigma_{\rho\rho}, \Sigma_{33}-(1-\chi^2)\Sigma_{\rho\rho}\right) \in \partial\Pi(0,D_{33}) = \left[\left.\frac{\partial\Pi}{\partial D_\chi}\right|_{0^-}(0,D_{33}),\ \left.\frac{\partial\Pi}{\partial D_\chi}\right|_{0^+}(0,D_{33})\right] \times \left\{\frac{\partial\Pi}{\partial D_{33}}(0,D_{33})\right\} \tag{II.90}$$

which means that

$$\begin{aligned}&\left|\Sigma_{\rho\rho} - \operatorname{sgn}(D_{33})\sigma_0\left[\sqrt{\frac{\hat{h}_t}{3}}\mathcal{A}\left(\sqrt{\frac{\hat{h}_t}{3\hat{h}_q}}\chi^2\right) + \frac{w}{\sqrt{3}}\frac{(1-c)^2}{c}\sqrt{\hat{h}_a}\right]\right| \leq \sigma_0(1-c)\sqrt{\hat{h}_q} \\ &\Sigma_{33}-(1-\chi^2)\Sigma_{\rho\rho} = \operatorname{sgn}(D_{33})\sigma_0\left[\sqrt{\frac{\hat{h}_t}{3}}\chi^2\mathcal{A}\left(\sqrt{\frac{\hat{h}_t}{3\hat{h}_q}}\chi^2\right) + \sqrt{\hat{h}_q}\mathcal{B}\left(\sqrt{\frac{\hat{h}_t}{3\hat{h}_q}}\chi^2\right) + \frac{1}{\sqrt{3}}\frac{w}{c}(1-c)^2\chi^2\sqrt{\hat{h}_a}\right]\end{aligned} \tag{II.91}$$

Eqs. II.89 and II.91 together describe four plat parts that complete the yield surface by connecting the four curved parts described previously.

The yield surface is therefore described by the conjunction of Eqs. II.84, II.89 and II.91; this is one of the main

[9] Remark that terms related to $\mathcal{A}'$ and $\mathcal{B}'$ cancel out because $\mathcal{A}'(x) = -|x|\,\mathcal{B}'(x)$.

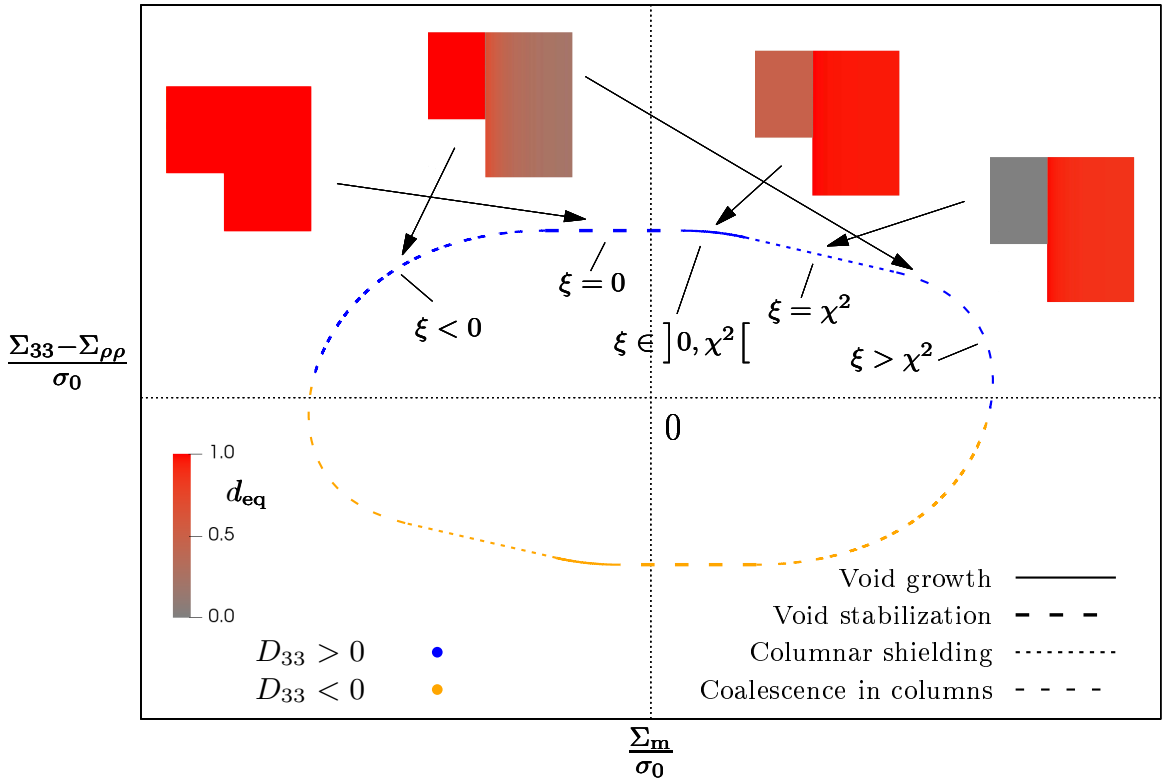

FIGURE II.42: Sketch of the yield surface associated with the trial field defined by Eq. II.74. Each section of the yield surface is linked to the deformation mode experienced by the unit cell; the corresponding equivalent deformation maps are shown (with d_{eq} normalized so its maximum is 1) for an isotropic material. The strain ratio ξ values and the sign of D_{33} are also displayed on the graph.

results of this study. It can be verified that the surface is continuous; indeed, Eq. II.84 is compatible with Eq. II.89 when D_{kk} goes to 0, and compatible with Eq. II.91 when D_χ goes to 0. In fact, it is fully differentiable, as shown in Morin et al., 2016a. A graphical representation of the obtained yield criterion in the meridian plane $(\Sigma_{\mathrm{m}}, \Sigma_{33} - \Sigma_{\rho\rho})$ where $\Sigma_{\mathrm{m}} \equiv \Sigma_{kk}/3$ is provided in Fig. II.42. The yield surface displays four different modes of deformation:

- a homogeneous yielding mode (Eq. II.89) where $\mathrm{Tr}(\boldsymbol{D}) = 0$, meaning that the volume of void will not change;
- a heterogeneous yielding mode (Eq. II.84 with $0 < \xi < \chi^2$), in which plasticity happens preferentially in the outer zone;
- a heterogeneous yielding mode (Eq. II.84 with $\xi < 0$ or $\xi > \chi^2$), in which plasticity happens preferentially in the plugs;
- a localized yielding mode (Eq. II.91) in which plasticity occurs exclusively in the outer zone, *i.e.* a hollow cylinder, while the plugs are elastically unloaded;

In the literature, the first two deformation modes are generally described as void growth (in this study, the first one will be distinguished and denoted *void stabilization* for convenience) and the third one is denoted as coalescence in columns (*e.g.* Torki et al. (2023)). The fourth deformation mode has been discussed less frequently but previous evidence has been collected through unit-cell simulations (Chouksey et al., 2019; Chouksey et al., 2020; Chouksey and Basu, 2021); since no clear denomination has emerged, it shall be denoted *columnar shielding* in the remainder of the study.

Some limit behaviors are worth considering in order to compare the criterion to known theoretical results. When χ goes to 0 — *i.e.* no porosity — Eq. II.87, II.89$_b$ and II.91$_b$ all lead to the same expression $|\Sigma_{33} - \Sigma_{\rho\rho}| = \sqrt{\hat{h}_q}\sigma_0$, which is Hill's criterion. When c goes to 0, Eq. II.89 yields the same result. When c goes to 1, Eq. II.87 recovers the anisotropic criterion of Benzerga and Besson (2001) for a hollow cylinder (whereas Eq. II.89 and II.91 reduce to subcases of Eq. II.87). Finally when χ goes to 1, the curved parts of Eq. II.85 reduce to points; thus, only the flat parts remain. On the one hand, Eq. II.89$_b$ becomes $|\Sigma_{33} - \Sigma_{\rho\rho}| = (1-c)\sqrt{\hat{h}_q}\sigma_0$ which is comfortingly Hill's criterion for

the remaining upper (or lower) cylinder. On the other hand, a positive yield limit on $|\Sigma_{33}|$ is predicted by Eq. II.91$_b$, which is unphysical because the voided horizontal band should imply $\Sigma_{33} = 0$. This is explained by the fact that the discontinuity surface $\mathcal{S}_d$ no longer exists when $\chi = 1$ so that Π^{surf} should vanish, allowing to recover $\Sigma_{33} = 0$.

It can then be useful to specialize the criterion for cracks through extreme values of w: needle-like (*i.e.* one-dimensional) when w goes to infinity, in which case the criterion becomes $|\Sigma_{33} - \Sigma_{\rho\rho}| = \sqrt{\hat{h}_q}\sigma_0(1 - c\chi^2)$, and penny-shaped (*i.e.* two-dimensional) when w goes to 0, in which case one of the two flat parts (Eq. II.89) of the criterion disappears.

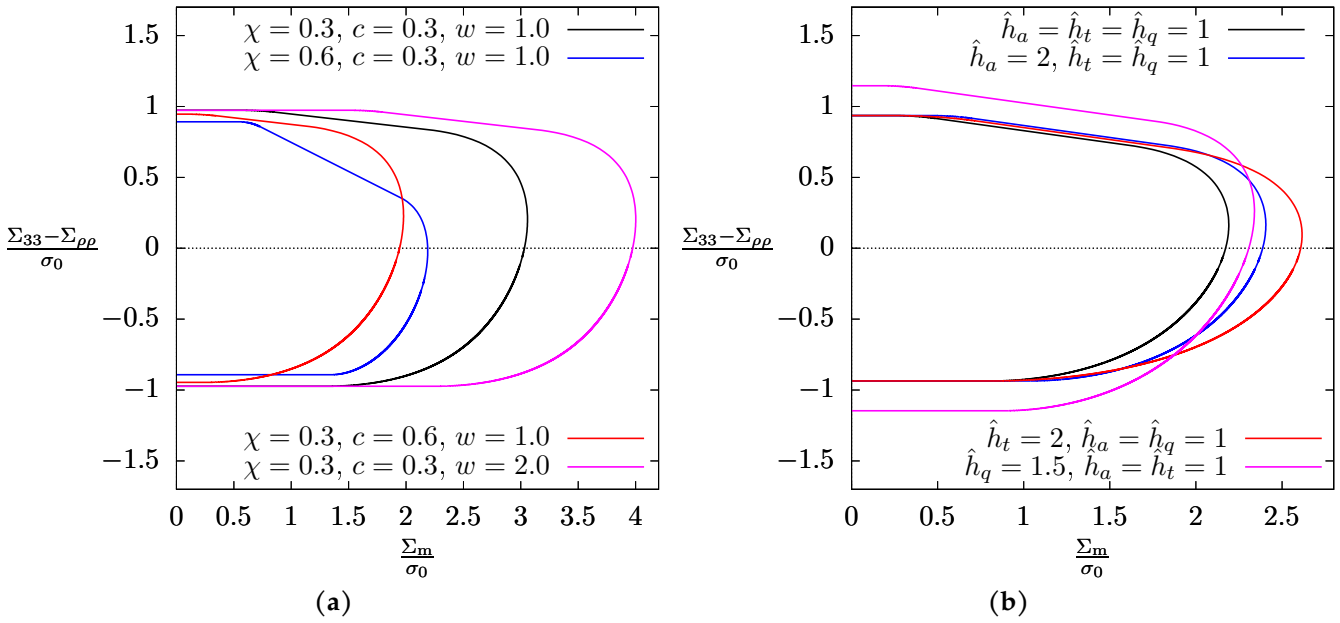

FIGURE II.43: Graphical investigation of the yield criterion: (a) effect of the geometry on the yield surface in the isotropic case ($\hat{h}_q = \hat{h}_t = \hat{h}_a = 1$); (b) effect of the anisotropy factors on the yield surface at $\chi = c = 0.4$ and $w = 1$.

It is shown in Fig. II.43a that χ, c and w all significantly influence the yield criterion. Although the figure is plotted for an isotropic material, the trends it displays also hold for anisotropic materials. Increasing χ induces a contraction of the yield surface as well as a noticeable shape change of the columnar shielding section since χ controls directly the slope of the slanted straight-lined part (Eq. II.91$_b$). As expected, increasing c also has a strong damaging effect and this change dominates the one induced by χ as far as coalescence in columns is concerned. Finally, increasing w expands the yield surface at high stress triaxiality ratios, meaning that coalescence in columns and columnar shielding are hindered for prolate voids compared to oblate voids, but that void growth and stabilization are left unaffected by the aspect ratio of the cavity. This is coherent with the fact that void growth is known to be affected only by void volume fraction $f = c\chi^2$ upon which w has no influence.

The influence of the three coefficients $\hat{h}_q$, $\hat{h}_t$, $\hat{h}_a$ that characterize the anisotropy of the matrix relatively to velocity fields is shown in Fig. II.43b. Increasing one of these values results in the extension of the yield surface, but modes of expansion are different. In the case of $\hat{h}_a$ and $\hat{h}_t$, this effect is restricted to rather high stress triaxiality ratios, *i.e.* the section where coalescence in columns is active. It is noticed that $\hat{h}_t$ has a stronger influence than $\hat{h}_a$, except on columnar shielding (Eq. II.91$_b$). In the case of $\hat{h}_q$, the effect on the yield surface is somehow uniform, which means that it affects both void stabilization, columnar shielding and coalescence in columns; note that the diagonal part accounting for columnar shielding (Eq. II.91$_a$) occupies a larger section of the yield surface.

3.3.4 From homogeneous yielding to inhomogeneous yielding in layers

In this section, the transition from homogeneous yielding (Fig. II.38a) to internal necking (Fig. II.38b) is accounted for using a dedicated yield surface describing the gradual localization of strain in layers perpendicular to the main loading axis. This yield surface is therefore an extension of the work of Morin et al. (2016a) to anisotropic materials following Hill's criterion (Eq. II.72).

3.3.5 Trial velocity field and associated plastic dissipation

The trial velocity field proposed in Morin et al. (2016a) accounts for the situations depicted in Fig. II.38a,b and is defined in the geometry shown in Fig. II.41b:

$$\begin{aligned}
&\text{Ligament:} \quad v_\rho^{(\mathrm{L})}(\rho) = \frac{1}{2}\left\{\frac{D_{kk}}{c}\frac{R^2}{\rho} - \left[\left(\frac{1}{c}-1\right)D_{kk} + D_{33}\right]\rho\right\}\ , \quad v_z^{(\mathrm{L})}(z) = \left[\left(\frac{1}{c}-1\right)D_{kk} + D_{33}\right]z \\
&\text{Outer zone:} \quad\quad v_\rho^{(\mathrm{E})}(\rho) = \frac{1}{2}\left(D_{kk} - D_{33}\right)\rho\ , \quad\quad\quad\quad v_z^{(\mathrm{E})}(z) = (D_{33} - D_{kk})z + HD_{kk}
\end{aligned} \tag{II.92}$$

This trial velocity field is incompressible, kinematically admissible with Eq. II.64, and displays a purely tangential discontinuity at the interface $\mathcal{S}_d$ ($z = h$). As this field has been shown in Morin et al. (2016a) to lead to results in good agreement with numerical simulations for isotropic materials, it will be adopted to study general anisotropic materials. In the transverse ligament (L) and the outer zone (E), the strain rates associated with this trial field write:

$$\begin{aligned}
d_{\rho\rho}^{(\mathrm{L})} &= -\frac{1}{2}\left[\frac{D_{kk}}{c}\left(\frac{R^2}{\rho^2}+1-c\right)+D_{33}\right] \quad d_{\theta\theta}^{(\mathrm{L})} = \frac{1}{2}\left[\frac{D_{kk}}{c}\left(\frac{R^2}{\rho^2}-1+c\right)-D_{33}\right] \quad d_{zz}^{(\mathrm{L})} = \frac{1-c}{c}D_{kk} + D_{33} \\
d_{\rho\rho}^{(\mathrm{E})} &= \frac{1}{2}\left(D_{kk} - D_{33}\right) \quad\quad\quad d_{\theta\theta}^{(\mathrm{E})} = \frac{1}{2}\left(D_{kk} - D_{33}\right) \quad\quad\quad d_{zz}^{(\mathrm{E})} = D_{33} - D_{kk}
\end{aligned} \tag{II.93}$$

The tangential velocity jump at $\mathcal{S}_d$ writes (see Appendix C of Morin et al. (2016a)):

$$|\Delta \underline{v}| = \frac{D_{kk}}{2c}\left(\frac{R^2}{\rho} - \rho\right) \tag{II.94}$$

Next, computations are similar to those that brought Eq. II.79:

$$\begin{aligned}
\left\langle \left(d_{\mathrm{eq}}^{(\mathrm{L})}\right)^2 \right\rangle_\theta &= \hat{h}_q \left(\frac{1-c}{c}D_{kk} + D_{33}\right)^2 + \frac{\hat{h}_t}{3}\left(\frac{R}{\rho}\right)^4\left(\frac{D_{kk}}{c}\right)^2 \\
\left\langle \left(d_{\mathrm{eq}}^{(\mathrm{E})}\right)^2 \right\rangle_\theta &= \hat{h}_q \left(D_{kk} - D_{33}\right)^2\ , \quad \left\langle \left(d_{\mathrm{eq}}^{(\mathrm{I})}\right)^2 \right\rangle_\theta = \frac{\hat{h}_a}{3}
\end{aligned} \tag{II.95}$$

which combine into the following upper bound for the macroscopic dissipation:

$$\Pi = \Pi^{(\mathrm{E})} + \Pi^{(\mathrm{L})} + \Pi^{\mathrm{surf}} \tag{II.96}$$

where dissipation terms write:

$$\begin{aligned}
&\Pi^{(\mathrm{E})} = \sigma_0(1-c)\sqrt{\hat{h}_q}\,|D_{kk} - D_{33}| \quad , \quad \Pi^{\mathrm{surf}} = \sigma_0 \frac{\chi^3 - 3\chi + 2}{3\sqrt{3}w\chi}\sqrt{\hat{h}_a}\,|D_{kk}| \\
&\Pi^{(\mathrm{L})} = \sigma_0\left[\sqrt{\frac{\hat{h}_t}{3}}\mathcal{A}\left(\sqrt{\frac{\hat{h}_t}{3\hat{h}_q}}\frac{\xi}{\bar{\xi}}\right)|D_{kk}| + \sqrt{\hat{h}_q}\mathcal{B}\left(\sqrt{\frac{\hat{h}_t}{3\hat{h}_q}}\frac{\xi}{\bar{\xi}}\right)|(1-c)D_{kk} + cD_{33}|\right] \quad \text{with} \quad \bar{\xi} = (1-c)\xi + c
\end{aligned} \tag{II.97}$$

3.3.6 Yield criterion

The yield surface is obtained from the fundamental equation of limit-analysis (Eq. II.68) following the path laid in Section II.3.3.3. $\Pi^{(\mathrm{E})}$ is non-differentiable when $D_{kk} - D_{33} = 0$, Π^{surf} when $D_{kk} = 0$ and $\Pi^{(\mathrm{L})}$ when $D_{kk} = D_{33} = 0$.

For cases where Π is differentiable, *i.e.* $D_{kk}(D_{kk}-D_{33})\neq 0$, the yield criterion is written in parametric form as[10]:

$$\begin{aligned}\Sigma_{33}-\Sigma_{\rho\rho}=\frac{\partial\Pi}{\partial D_{33}}&=\operatorname{sgn}(D_{33})\,\sigma_0\left[-\operatorname{sgn}(\xi-1)(1-c)\sqrt{\hat{h}_q}+\operatorname{sgn}(\bar{\xi})c\sqrt{\hat{h}_q}\mathcal{B}\left(\sqrt{\frac{\hat{h}_t}{3\hat{h}_q}}\frac{\xi}{\bar{\xi}}\right)\right]\\ \Sigma_{33}=\frac{\partial\Pi}{\partial D_{33}}+\frac{\partial\Pi}{\partial D_{kk}}&=\operatorname{sgn}(D_{33})\,\sigma_0\left\{\operatorname{sgn}(\xi)\left[\sqrt{\frac{\hat{h}_t}{3}}\mathcal{A}\left(\sqrt{\frac{\hat{h}_t}{3\hat{h}_q}}\frac{\xi}{\bar{\xi}}\right)+\frac{\chi^3-3\chi+2}{3\sqrt{3}w\chi}\sqrt{\hat{h}_a}\right]\right.\\ &\qquad\left.+\operatorname{sgn}(\bar{\xi})\sqrt{\hat{h}_q}\mathcal{B}\left(\sqrt{\frac{\hat{h}_t}{3\hat{h}_q}}\frac{\xi}{\bar{\xi}}\right)\right\}\end{aligned}\tag{II.98}$$

which can be rewritten using Eq. II.85 as:

$$\left[\sqrt{\frac{1}{\hat{h}_q}}\frac{\Sigma_{33}-\Sigma_{\rho\rho}}{c\sigma_0}+\epsilon_3\frac{1-c}{c}\right]^2+2\chi^2\cosh\left[\sqrt{\frac{3}{\hat{h}_t}}\left(\frac{\Sigma_{\rho\rho}-(1-c)\Sigma_{33}}{c\sigma_0}-\epsilon_3\frac{1-c}{c}\sqrt{\hat{h}_q}-\epsilon_2\frac{\chi^3-3\chi+2}{3\sqrt{3}cw\chi}\sqrt{\hat{h}_a}\right)\right]-(1+\chi^4)=0\tag{II.99}$$

where $\epsilon_3=\operatorname{sgn}(D_{\rho\rho})$.

For cases where Π is not differentiable, the same method used in Section II.3.3.3 is followed to get the corresponding parts of the yield criterion. When $D_{kk}=0$ ($\xi=0$) and $D_{kk}-D_{33}\neq 0$, it is obtained that:

$$\left|\Sigma_{\rho\rho}+\operatorname{sgn}(D_{33})\sigma_0(1-c)\chi^2\sqrt{\hat{h}_q}\right|\leq\sigma_0\frac{\chi^3-3\chi+2}{3\sqrt{3}w\chi}\sqrt{\hat{h}_a}\quad,\quad\Sigma_{33}-\Sigma_{\rho\rho}=\operatorname{sgn}(D_{33})\sigma_0\sqrt{\hat{h}_q}\left(1-c\chi^2\right)\tag{II.100}$$

whereas $D_{kk}-D_{33}=0$ ($\xi=1$) and $D_{kk}\neq 0$ leads to:

$$\begin{aligned}\left|\Sigma_{33}-\Sigma_{\rho\rho}-\operatorname{sgn}(D_{33})c\sigma_0\mathcal{B}\left(\sqrt{\frac{\hat{h}_t}{3\hat{h}_q}}\right)\sqrt{\hat{h}_q}\right|&\leq\sigma_0(1-c)\sqrt{\hat{h}_q}\\ \Sigma_{33}=\operatorname{sgn}(D_{33})\sigma_0\left[\sqrt{\frac{\hat{h}_t}{3}}\mathcal{A}\left(\sqrt{\frac{\hat{h}_t}{3\hat{h}_q}}\right)+\sqrt{\hat{h}_q}\mathcal{B}\left(\sqrt{\frac{\hat{h}_t}{3\hat{h}_q}}\right)+\frac{\chi^3-3\chi+2}{3\sqrt{3}w\chi}\sqrt{\hat{h}_a}\right]&\end{aligned}\tag{II.101}$$

A graphical representation of the obtained yield criterion in the meridian plane $(\Sigma_{\mathrm{m}},\Sigma_{33}-\Sigma_{\rho\rho})$ is provided in Fig. II.44. The yield surface displays three different modes of deformation:

- a homogeneous yielding mode (Eq. II.100) where $\operatorname{Tr}(\boldsymbol{D})=0$, meaning that the volume of void will not change;
- a heterogeneous yielding mode (Eq. II.98), in which plasticity happens preferentially in the transverse ligament, inducing a change of porosity (positive to the right-hand side of the homogeneous part and negative to the left-hand side);
- a localized yielding mode (Eq. II.101), in which plasticity occurs exclusively in the transverse ligament while the upper and the lower zones are elastically unloaded.

In the literature, the first two deformation modes are generally described as void growth (in this study, the first one will be distinguished and denoted *void stabilization* for convenience) whereas the last one corresponds to internal necking (*e.g.* Morin et al. (2016a)).

Again, some limit behaviors are worth considering in order to compare the criterion to known theoretical results. When χ goes to 0 — *i.e.* no porosity — the yield criterion reduces to Hill's criterion $|\Sigma_{33}-\Sigma_{\rho\rho}|=\sqrt{\hat{h}_q}\sigma_0$. When χ goes to 1, Eq. II.99 yield $\Sigma_{33}=0$ and $|\Sigma_{\rho\rho}|=\sigma_0\sqrt{\hat{h}_q}(1-c)$ which is exactly what may be expected from a Hill material laminated with void along $\underline{e}_3$. When c goes to 1, Eq. II.99 recovers the anisotropic criterion of Benzerga and Besson (2001) for a hollow cylinder whereas Eqs. II.100-II.101 reduce to points. When c goes to 0, Eq. II.99 reduces to points so the yield surface becomes a parallelogram whose sides are Hill's criterion (from Eq. II.100) since the material has no

[10] See footnote 9.

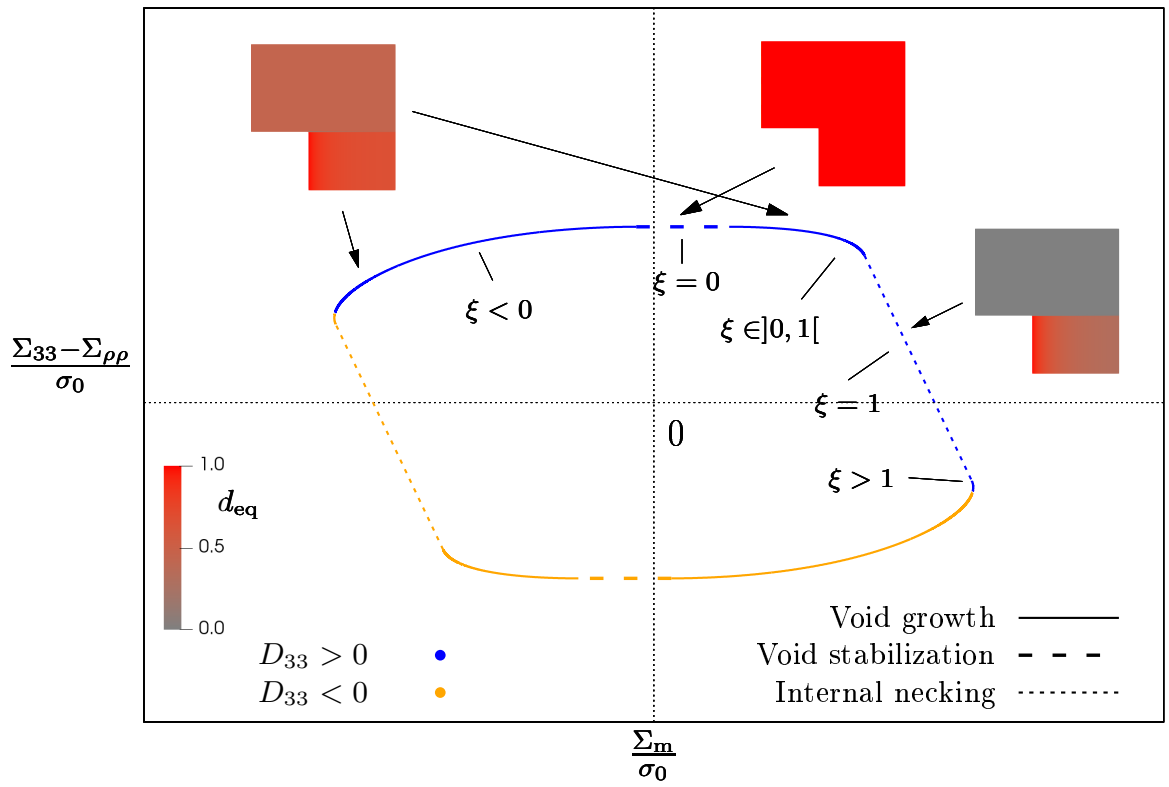

FIGURE II.44: Sketch of the yield surface associated with the trial field defined by Eq. II.92. Each section of the yield surface is linked to the deformation mode experienced by the unit cell; the corresponding equivalent deformation maps are shown (with d_{eq} normalized so its maximum is 1) for an isotropic material. The strain ratio ξ values and the sign of D_{33} are also displayed on the graph.

porosity and an anisotropic version of the internal necking criterion of Benzerga and Leblond (2014) (from Eq. II.101) because the material can still coalesce in a horizontal plane without prior void growth.

The criterion can be used to make novel predictions for cracks by considering extreme values of w. Needle-like (*i.e.* one-dimensional) cracks are obtained when w goes to infinity, in which case one of the two flat parts (Eq. II.100) of the criterion disappears. Penny-shaped (*i.e.* two-dimensional) cracks are obtained when w goes to 0, in which case

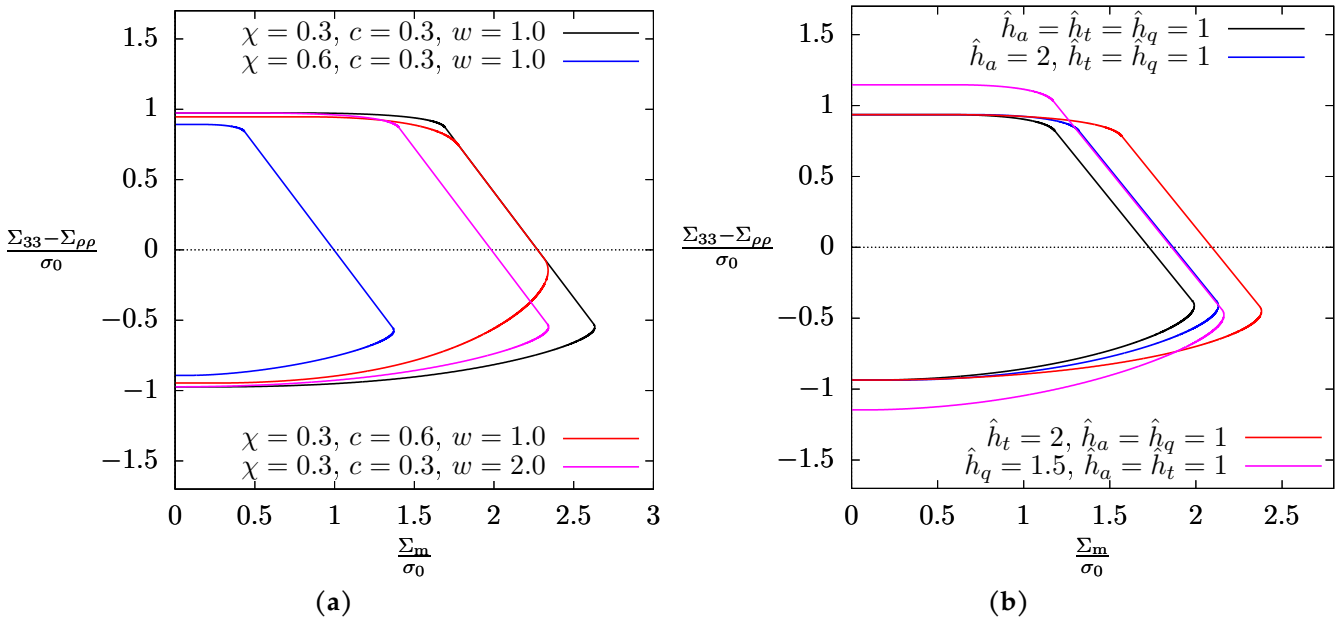

FIGURE II.45: Graphical investigation of the yield criterion: (a) effect of the geometry on the yield surface in the isotropic case ($\hat{h}_q = \hat{h}_t = \hat{h}_a = 1$); (b) effect of the anisotropy factors on the yield surface at $\chi = c = 0.4$ and $w = 1$.

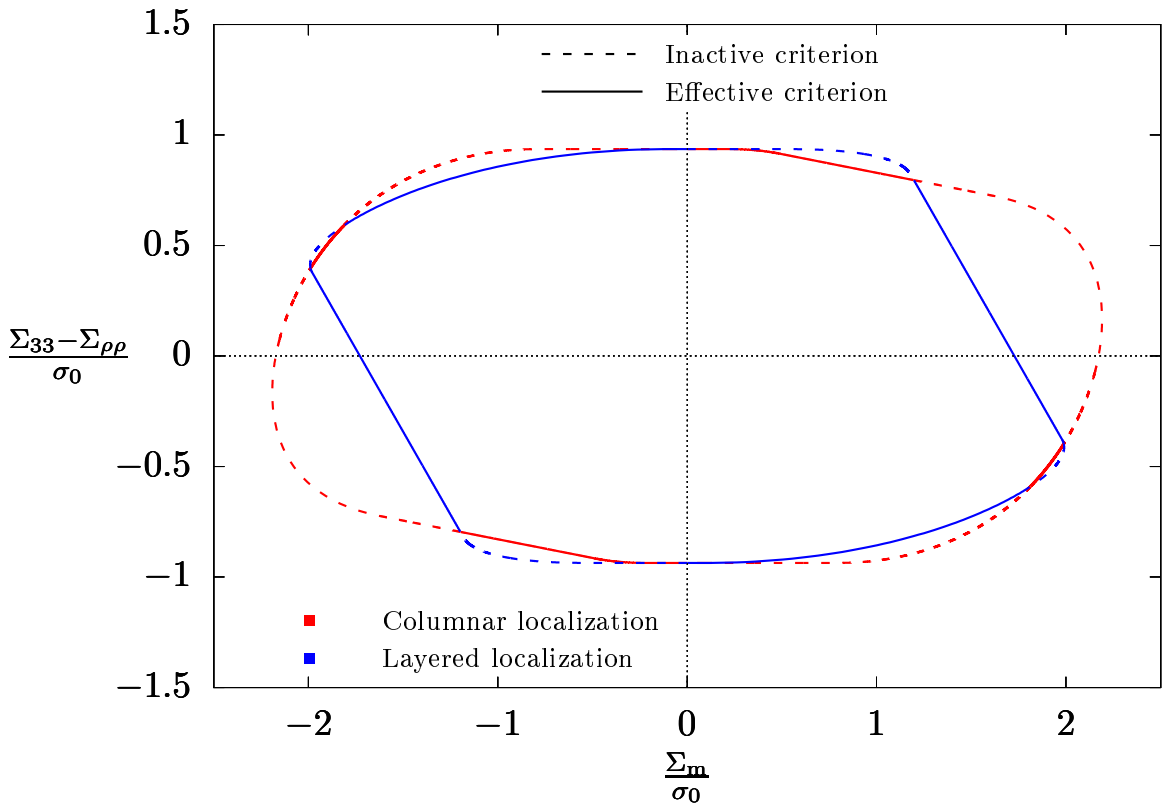

FIGURE II.46: Total yield criterion for porous anisotropic Hill materials obtained by the intersection of two individual elasticity domains associated with the criteria of Section II.3.3.1 and II.3.3.4. (The figure has been plotted for an isotropic material using $\chi = c = 0.4$ and $w = 1$).

the criterion becomes $|\Sigma_{33} - \Sigma_{\rho\rho}| = \sqrt{\hat{h}_q}\sigma_0(1 - c\chi^2)$. This is an oversimplification since internal necking still occurs for penny-shaped cracks, as shown in Hure and Barrioz (2016); this discrepancy emerges from the fact that when $w = 0$, the trial field cannot accommodate the axial strain rate D_{33} due to the absence of transverse ligament.

For isotropic materials, the internal necking criterion (Eq. II.101) becomes:

$$\Sigma_{33} = \mathrm{sgn}(D_{33})\sigma_0 \left[\frac{1}{\sqrt{3}} \mathcal{A}\left(\frac{1}{\sqrt{3}}\right) + \mathcal{B}\left(\frac{1}{\sqrt{3}}\right) + \frac{\chi^3 - 3\chi + 2}{3\sqrt{3}w\chi} \right] \tag{II.102}$$

which has been shown by Torki et al. (2015) to require a correction to improve the agreement to numerical results and recover an acceptable yield criterion in the limit $w \to 0$. The calibration led in the aforementioned study resulted in the multiplication of the third term of Eq. II.102 by a function t given by:

$$t(x, \chi) = \frac{(t_0 + t_1\chi)w}{1 + (t_0 + t_1\chi)w} \quad \text{where} \quad (t_0, t_1) = (-0.84, 12.9) \tag{II.103}$$

Note that the parameter b introduced in Torki et al. (2015) is discarded since it would induce uncontrolled shape changes in the yield surface. The correction for isotropic materials (Eq. II.103) is extended to anisotropic materials in by replacing $\sqrt{\hat{h}_a}$ by $t(w, \chi)\sqrt{\hat{h}_a}$ in Eqs. II.99, II.100 and II.101.

The yield surface strongly depends on microstructure parameters, as seen in Fig. II.45a. On the one hand, the internal necking section (Eq. II.101) is determined entirely by w and χ, as shown in the original study of Benzerga and Leblond (2014). Increasing any of those parameters results in the shrinking of the yield surface, mainly through the shift of the straight-lined part. Note that the effect of w on columnar localization is the opposite of the one it has on layered localization since prolate voids promote internal necking. On the other hand, the void stabilization part does not depend on w and is mainly determined by the value of c. The effect of anisotropy factors on the yield surface is shown in Fig. II.45b; these parameters appear to have the same qualitative influence on the yield surface as they did in Fig. II.43b: $\hat{h}_q$ has a relatively homogeneous effect no matter the triaxiality whereas $\hat{h}_a$ and $\hat{h}_t$ only modify the high-triaxiality section (*i.e.* coalescence).

As stated at the beginning of Section II.3.3, the complete yield criterion for porous Hill materials under axisymmetric loading is obtained by combining the two yield criteria obtained in Section II.3.3.3 and Section II.3.3.6 using the multi-surface framework described in Benzerga and Leblond (2010). In this framework, the final elasticity domain is the intersection of individual domains associated with the (two) sub-criteria, as shown in Fig II.46.

3.3.7 Numerical assessment

The analytical criterion is then assessed by resorting to numerical limit analysis. Small strain finite element simulations (Madou and Leblond, 2012b) are conducted on the unit-cell shown in Fig. II.40 using the FEM solver `Cast3M` (CEA, 2018). As in Keralavarma and Chockalingam (2016), the criterion shall be tested on materials whose orthotropy axes are aligned with the void axes. In that frame of reference, Hill equivalent stress writes:

$$\begin{aligned}\left(\sigma_{\text{eq}}^{\text{H}}\right)^2 &= \frac{3}{2}\left(h_{11}{\sigma'_{11}}^2 + h_{22}{\sigma'_{22}}^2 + h_{33}{\sigma'_{33}}^2 + 2h_{44}\sigma_{23}^2 + 2h_{55}\sigma_{31}^2 + 2h_{66}\sigma_{12}^2\right)\\ &= \frac{2(h_{11}+h_{22})-h_{33}}{6}(\sigma_{11}-\sigma_{22})^2 + \frac{2(h_{22}+h_{33})-h_{11}}{6}(\sigma_{22}-\sigma_{33})^2 + \frac{2(h_{11}+h_{33})-h_{22}}{6}(\sigma_{11}-\sigma_{33})^2\\ &\quad + 3h_{44}\sigma_{23}^2 + 3h_{55}\sigma_{31}^2 + 3h_{66}\sigma_{12}^2\end{aligned} \tag{II.104}$$

where (h_{ij}) are the coefficient of the Voigt-Mandel representation of $\mathbb{h}$.

In the case of transverse isotropy with respect to $\underline{e}_3$, equality of yield stress for stress states $\boldsymbol{\sigma} = (\cos\theta)^2\underline{e}_1\otimes\underline{e}_1 + (\sin\theta)^2\underline{e}_2\otimes\underline{e}_2 - 2\cos\theta\sin\theta\,\underline{e}_1\odot\underline{e}_2$ brings $h_{11} = h_{22} = h_{66}$. Same considerations about $\boldsymbol{\sigma} = \underline{e}_i\odot\underline{e}_3$ with $i\in\{1,2\}$ yield $h_{44} = h_{55}$. These relations also hold for $\hat{\mathbb{h}}$. Taking σ_0 as the transverse yield stress gives $h_{33} = 6-5h_{11}$. Thus, material anisotropy can be described by only two parameters that are chosen according to Keralavarma and Chockalingam (2016): the ratio R_{a} of the axial yield stress relative to the transverse yield stress and the ratio R_{s} of the out-of-plane shear yield stress to the transverse yield stress, multiplied by $\sqrt{3}$ to normalize it to 1 in the isotropic case. Using Eq. II.104, it can be shown that:

$$R_{\text{a}} = \frac{1}{\sqrt{4-3h_{11}}}\,,\quad R_{\text{s}} = \frac{1}{\sqrt{h_{44}}} \tag{II.105}$$

Then, relationships between coefficients of $\hat{\mathbb{h}}$ and $\mathbb{h}$ bring:

$$\hat{h}_q = R_{\text{a}}^2\,,\quad \hat{h}_t = \frac{3R_{\text{a}}^2}{4R_{\text{a}}^2-1}\,,\quad \hat{h}_a = R_{\text{s}}^2 \tag{II.106}$$

Exploiting the symmetries of the loading as well as those of the material, only a quarter of a section of the unit cell is effectively simulated under the assumption of axisymmetry. The corresponding mesh is shown in Fig II.47a (Fig. II.47b will be discussed later); it holds 19200 quadratic quadrangular elements. The material behavior is chosen to be elastoplastic: elasticity obeys an isotropic Hooke law of Young modulus $Y = 10^3$ MPa and Poisson ratio $\nu = 0.49$ whereas perfect plasticity follows Hill's criterion. As a classical result of limit analysis, the results presented in the following do not depend on elastic parameters. Mesh convergence is duly checked. The displacements of the nodes lying on the boundaries $\mathcal{S}_{\text{top}}$ and $\mathcal{S}_{\text{lat}}$ are constrained to have the same vertical (for $\mathcal{S}_{\text{top}}$) and horizontal (for $\mathcal{S}_{\text{lat}}$) values consistently with imposing D_{33} and $D_{\rho\rho}$. The macroscopic stress $\boldsymbol{\Sigma}$ is computed by averaging the microscopic stress field $\boldsymbol{\sigma}$ over Ω. Simulations are performed by imposing the displacement on one boundary ($\mathcal{S}_{\text{top}}$ or $\mathcal{S}_{\text{lat}}$) and enforcing the ratio of stresses $\Sigma_{\rho\rho}/\Sigma_{33}$ by adjusting the displacement of the other boundary during the iterations of the Newton-Raphson algorithm. The imposed displacement is increased linearly until small strain yielding of the unit cell occurs. This manifests by the saturation of $\boldsymbol{\Sigma}$ to values corresponding to the yield stress of the unit cell.

The comparison between numerical yield stresses and the analytical criterion is displayed in Fig. II.48. Two unit-cell geometries are studied: on the one hand, $\chi = 0.4$ and $c = 0.4$ (left row of Fig. II.48), and on the other hand, $\chi = 0.3$ and $c = 0.6$ (right row of Fig. II.48). Both configurations were chosen with a cavity of aspect ratio $w = 1$. In all cases, the numerical results are seen to be interior to the surfaces delimited by the two expressions constituting the yield criterion, confirming their character of upper bound[11].

In Fig. II.48a,b, the assessment is performed for a material with $R_{\text{a}} < 1$, meaning that the material is softer in

[11] Note that this property is not to be taken for granted in the case of the layered localization surface: indeed, a numerical correction (Eq. II.103) was adopted.

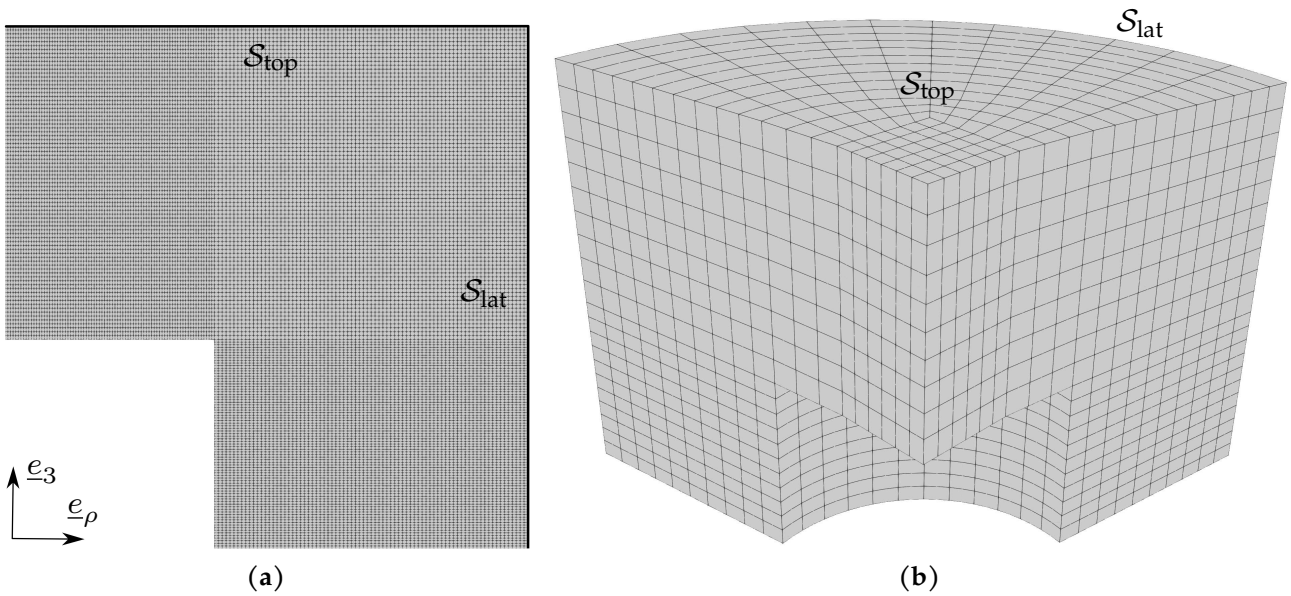

FIGURE II.47: Meshes used for numerical limit-analysis at $\chi = c = 0.4$ and $w = 1$: (a) axisymmetric mesh used for the transverse isotropy matrix; (b) one-eighth of the total mesh used for the crystal matrix.

the axial direction than in the transverse direction, and compared to corresponding data for an isotropic material ($R_{\text{a}} = 1$). The final criterion accounts satisfactorily for the decrease of yield strength at the deviatoric point compared to the isotropic case, which can be traced back to the decrease of $\hat{h}_q$ (see Eq. II.106$_a$ and purple curve of Figs. II.43b and II.45b). The yield function also predicts a larger yield stress at the hydrostatic point correctly, meaning that the opposing effects of $\hat{h}_q$ (increasing function of R_{a}) and $\hat{h}_t$ (decreasing function of R_{a}) are correctly balanced in the analytical expressions. In Fig. II.48a, the layered localization surface better approximates the yield surface at high stress triaxialities (notice the straight-line of slope $-3/2$ which characterizes internal necking), but as was pointed out in Torki et al. (2023), two sections of the final yield surface originate from columnar localization: a larger one at dominant axial stress (columnar shielding), and a smaller one at dominant radial stress (coalescence in columns), highlighting the interest of the expression developed in Section II.3.3.3. Such a conclusion is also supported by Fig. II.48b in which the columnar localization surface reproduces quantitatively the numerical results for both the isotropic and the anisotropic material. The difference between isotropic and anisotropic unit-cell simulations at moderate and high triaxialities also confirms that plastic anisotropy of the matrix significantly affects strain localization, both in layers and in columns.

Similar comments can be made on Fig. II.48c,d (beware that axes bounds are not the same as Fig. II.48a,b) which displays results for an anisotropic material with $R_{\text{a}} > 1$. This time, the yield stress of the anisotropic material is more significant than that of the isotropic material over the entire yield surface. A third characteristic behavior also exists, not shown here: at values $R_{\text{a}} \in]0.6, 1[$ close to 1, the yield surface of the anisotropic material is fully interior to that of the isotropic material: indeed, the effect of a slight decrease of R_{a} from 1 has a stronger effect on $\hat{h}_q$ than on $\hat{h}_t$ (see Eq. II.106), enabling to reduce the yield stress at the hydrostatic point effectively.

In Fig. II.48e,f, the assessment is performed for anisotropic materials with different R_{s}. $R_{\text{s}} = 3$ means that the matrix material is three times harder than the corresponding isotropic material when loaded in shear. It is seen that void growth yield stress is left unchanged but that coalescence is affected by the modification of R_{s}. Again, the criterion accounts satisfactorily for this effect, which can be linked to the increase of $\hat{h}_a$ (see Eq. II.106$_c$ and blue curve of Figs. II.43b and II.45b). In Fig. II.48e, the yield surface at high stress triaxialities is better approximated by the surface for internal necking whereas the necklace coalescence surface reproduces quantitatively the numerical results of Fig. II.48f.

From that numerical assessment, it can be concluded that plastic anisotropy has a strong effect on coalescence, whatever the pattern of strain localization, and that this effect is quantitatively captured by the yield criterion proposed in this study; depending on whether localization is columnar or in layers, the expression of Section II.3.3.3 or Section II.3.3.6 will be selected through the multi-criteria framework. This has been shown in the case of materials with transverse isotropy but the model is applicable to materials in which the orthotropy axes are not aligned with

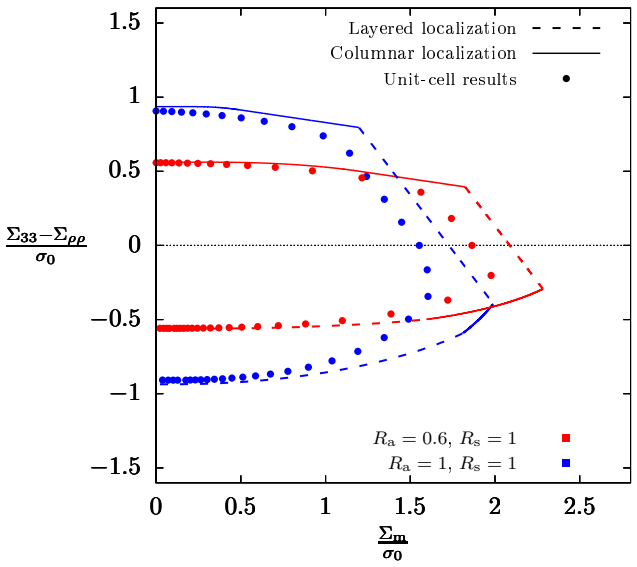

(a) $\chi = 0.4$, $c = 0.4$

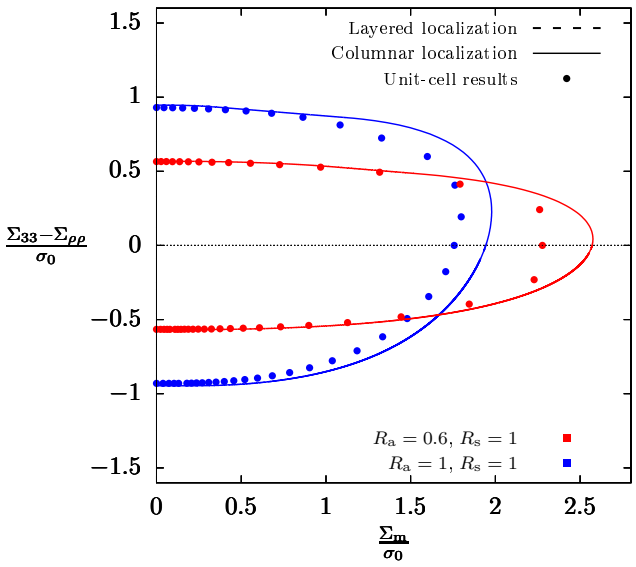

(b) $\chi = 0.3$, $c = 0.6$

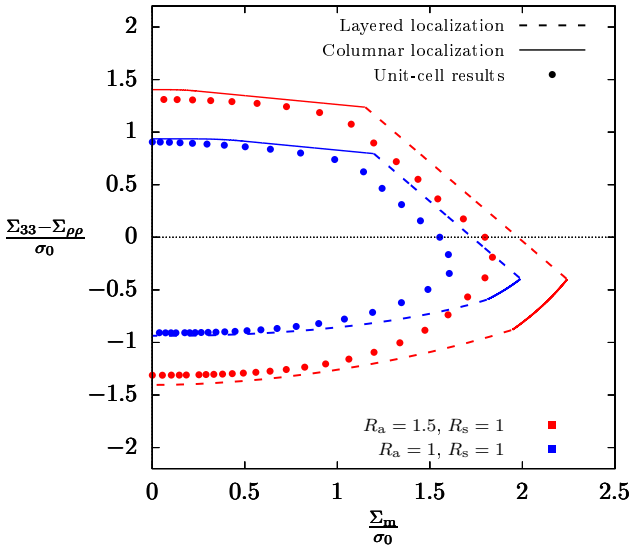

(c) $\chi = 0.4$, $c = 0.4$

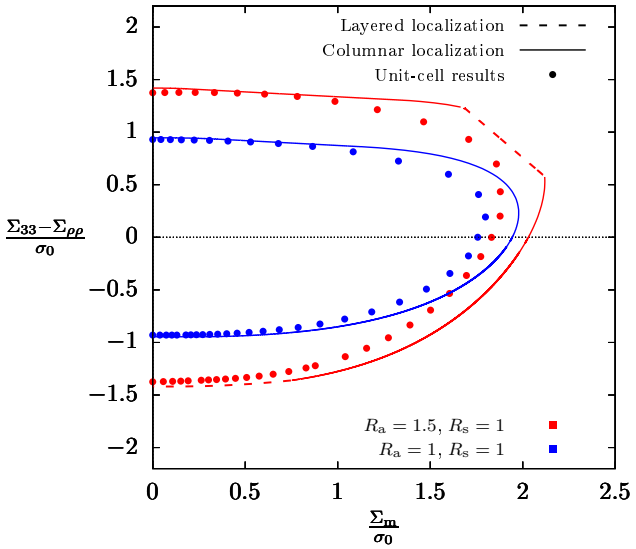

(d) $\chi = 0.3$, $c = 0.6$

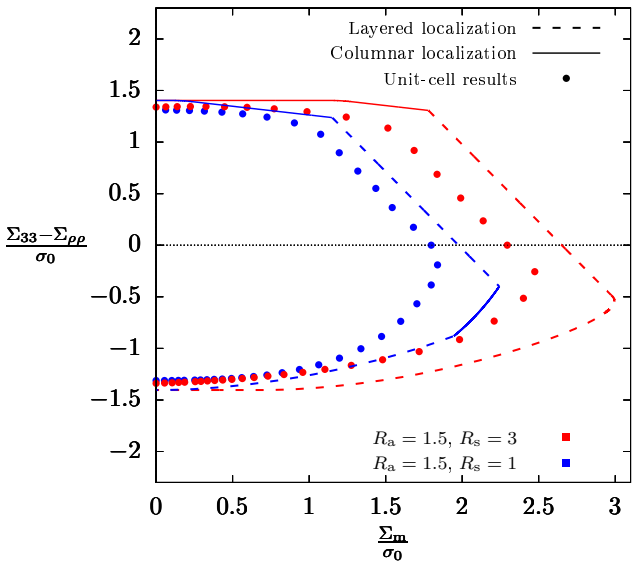

(e) $\chi = 0.4$, $c = 0.4$

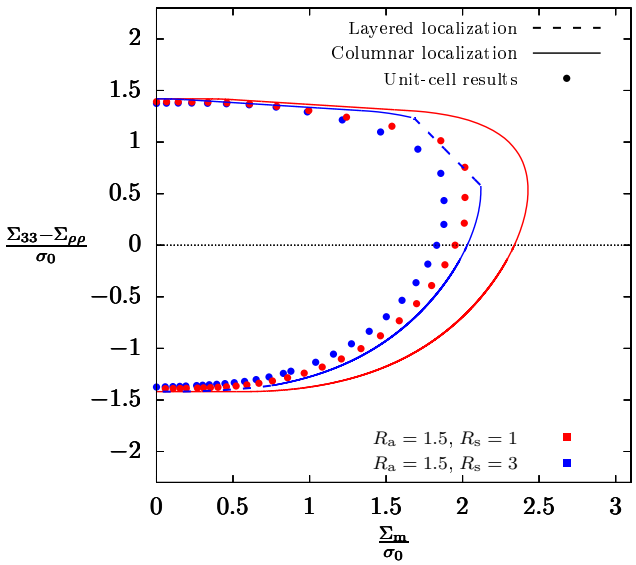

(f) $\chi = 0.3$, $c = 0.6$

FIGURE II.48: Comparison between the numerical limit-analysis (points) and the analytical criterion (columnar localization shown with full lines and layered localization drawn with dashed lines) for a set of transverse isotropic materials defined by yield stress ratios R_a and R_s. Two void geometries are considered: **(a,c,e)** $\chi = 0.4$, $c = 0.4$, $w = 1$; **(b,d,f)** $\chi = 0.3$, $c = 0.6$, $w = 1$.

void axes. Full three-dimensional numerical simulations being numerically heavy and time-consuming, further numerical assessment is left for future research. Such a model has interesting outcomes for material science because it quantifies plastic anisotropy's effects on ductile fracture so that materials suitable for a given application can be knowingly chosen or designed.

The criterion developed in this section is relevant for polycrystalline materials where voids are significantly larger than the grain size, so that the matrix material at the scale of the voids is composed of a large number of grains and can be described by Hill (1948) plasticity which accounts for large-scale anisotropy. However, it is well-known that voids are smaller than the grain size in many metals (Pineau et al., 2016). In these cases, each grain is a porous single crystal and this low-scale anisotropy has to be taken into account in the yield criterion, motivating the model presented in the next section.

3.4 Yield surface for rate-independent crystals

The second part deals with crystalline plastic anisotropy, meaning that the same unit-cell as in Section II.3.3 is considered, this time with a single crystal matrix. A yield surface for porous single crystals under axisymmetric loading is searched by extending the previous yield criterion using the method presented in Hure (2019).

3.4.1 Single crystal matrix behavior

Plasticity is assumed to be related to the glide of dislocations, that can happen in a limited number of planes and directions, called crystallographic slip systems, defined by a slip plane (whose normal is along unit vector $\underline{m}_s$) and a slip direction (of unit vector $\underline{n}_s$), and represented by the following symmetric Schmid tensor: $\boldsymbol{\mu}_s = \frac{1}{2}(\underline{m}_s \otimes \underline{n}_s + \underline{n}_s \otimes \underline{m}_s)$. A face-centered cubic (FCC) material is considered, with $K = 12$ independent slips systems — the $\{111\}\langle 110\rangle$ family. Using viscoplastic regularization, the plastic strain rate writes (Hutchinson, 1976):

$$\boldsymbol{d} = \sum_{s=1}^{K} \left[\dot{\gamma}_0 \left(\frac{|\boldsymbol{\sigma} : \boldsymbol{\mu}_s|}{\tau_0} \right)^n \operatorname{sgn}(\boldsymbol{\sigma} : \boldsymbol{\mu}_s) \right] \boldsymbol{\mu}_s = \sum_{s=1}^{K} \dot{\gamma}_s \boldsymbol{\mu}_s \tag{II.107}$$

where τ_0 is the critical resolved shear stress (identical for all slip systems), $\dot{\gamma}_0$ a reference slip-rate (set to $1\,\mathrm{s}^{-1}$) and $\dot{\gamma}_s$ the slip rate of system s. n denotes the Norton exponent: the case $n \to +\infty$ corresponds to rate-independent plasticity, which is of interest here.

The local Taylor factor associated with a single crystal subjected to a strain rate $\boldsymbol{d}$ is defined as:

$$M(\boldsymbol{d}) = \frac{\sum_{s=1}^{K} \dot{\gamma}_k \, [\boldsymbol{d}]}{d_{\mathrm{eq}}^{\mathrm{iso}}} \quad \text{with} \quad d_{\mathrm{eq}}^{\mathrm{iso}} = \sqrt{\frac{2}{3}\boldsymbol{d} : \boldsymbol{d}} \tag{II.108}$$

where $d_{\mathrm{eq}}^{\mathrm{iso}}$ is the von Mises equivalent deformation. In rate-independent plasticity, $(\dot{\gamma}_k)$ may be determined from $\boldsymbol{d}$ as the set that verifies $\sum \dot{\gamma}_s \boldsymbol{\mu}_s = \boldsymbol{d}$ while minimizing $\sum |\dot{\gamma}_s|$, as suggested by Taylor (1938). Since this problem is a minimization under linear hard constraints involving inequalities, it can be solved through classical linear programming algorithms (see Van Houtte (1988) for this specific case). M strongly depends on the crystallographic orientation through the set of Schmid tensors $(\boldsymbol{\mu}_s)$. This quantity is of great interest to our study since, in a single crystal, the microscopic plastic dissipation writes:

$$\sup_{\boldsymbol{\sigma}^* \in \mathscr{C}} \boldsymbol{\sigma}^* : \boldsymbol{d} = \sum_k \tau_0 \dot{\gamma}_k = M(\boldsymbol{d}) \tau_0 d_{\mathrm{eq}}^{\mathrm{iso}} \tag{II.109}$$

Eq. II.109 can then be used to re-apply the limit analysis framework of Section II.3.3 considering $\sigma_0 = M(\boldsymbol{d})\tau_0$.

3.4.2 Approximate macroscopic dissipation

At the macroscopic scale, the following approximation can be performed on a volume A:

$$\Pi^{(\mathrm{A})} = \frac{1}{|\Omega|} \int_{\Omega_\mathrm{A}} M(\boldsymbol{d}) \tau_0 d_{\mathrm{eq}}^{\mathrm{iso}} \approx \left(\frac{1}{|\Omega_\mathrm{A}|} \int_{\Omega_\mathrm{A}} M(\boldsymbol{d}) \right) \left(\frac{1}{|\Omega|} \int_{\Omega_\mathrm{A}} \tau_0 d_{\mathrm{eq}}^{\mathrm{iso}} \right) = \left(\frac{1}{|\Omega_\mathrm{A}|} \int_{\Omega_\mathrm{A}} M(\boldsymbol{d}) \right) \Pi_{\mathrm{iso}}^{(\mathrm{A})} \tag{II.110}$$

with $\Pi_{\text{iso}}^{(\text{A})}$ the corresponding dissipation in an equivalent isotropic material of uniaxial yield stress τ_0. Additional details can be found in Hure (2019). Supposing that the velocity field given in Torki et al. (2023) for columnar localization in isotropic material can be used to describe approximately the same localization mode in crystals, Eq. II.110 is successively applied to the three zones of the unit-cell (plugs, matrix, and interface), leading to:

$$\Pi \approx \underbrace{\left(\frac{1}{2\pi}\int_0^{2\pi} M\left(\boldsymbol{d}^{(\text{I})},\theta\right)\,\mathrm{d}\theta\right)}_{M_1}\Pi_{\text{iso}}^{\text{surf}} + \underbrace{\left(\frac{1}{\pi(1-\chi^2)}\int_\chi^1\int_0^{2\pi} M\left(\boldsymbol{d}^{(\text{O})},\rho,\theta\right)\rho\,\mathrm{d}\theta\,\mathrm{d}\rho\right)}_{M_2(\chi,\xi)}\Pi_{\text{iso}}^{(\text{O})} + \underbrace{\left(\frac{1}{2\pi}\int_0^{2\pi} M\left(\boldsymbol{d}^{(\text{P})},\theta\right)\,\mathrm{d}\theta\right)}_{M_4}\Pi_{\text{iso}}^{(\text{P})} \quad \text{(II.111)}$$

where $\boldsymbol{d}^{(\text{O})}$ and $\boldsymbol{d}^{(\text{P})}$ are given by Eq. II.76, and $\boldsymbol{d}^{(\text{I})}$ can be found in Eq. II.67. Expressions for $\Pi_{\text{iso}}^{(\text{O})}$, $\Pi_{\text{iso}}^{(\text{P})}$ and $\Pi_{\text{iso}}^{\text{surf}}$ are obtained by specializing Eqs. II.81 and II.82 with $\hat{h}_q = \hat{h}_t = \hat{h}_a = 1$ and $\sigma_0 = \tau_0$. The dependence of M_1, M_2 and M_4 on loading and geometry have been established by keeping in mind that $M(\boldsymbol{d})$ is homogeneous of degree 0, *i.e.* colinear strain rates tensors share the same Taylor factor. Note that the present M_1 is equal to the M_1 defined in Hure (2019), and that $M_2(\chi)$ of the aforementioned paper corresponds to $M_2(\chi,1)$ of the present study. It is also easily seen that $M_2(\chi,0) = M_4$.

Similarly, the macroscopic dissipation associated with the trial field of Morin et al. (2016a) can be approximated by:

$$\Pi \approx \underbrace{\left(\frac{1}{2\pi}\int_0^{2\pi} M\left(\boldsymbol{d}^{(\text{I})},\theta\right)\,\mathrm{d}\theta\right)}_{M_1}\Pi_{\text{iso}}^{\text{surf}} + \underbrace{\left(\frac{1}{\pi(1-\chi^2)}\int_\chi^1\int_0^{2\pi} M\left(\boldsymbol{d}^{(\text{L})},\rho,\theta\right)\rho\,\mathrm{d}\theta\,\mathrm{d}\rho\right)}_{M_2\left(\chi,\frac{\xi}{\bar{\xi}}\right)}\Pi_{\text{iso}}^{(\text{L})} + \underbrace{\left(\frac{1}{2\pi}\int_0^{2\pi} M\left(\boldsymbol{d}^{(\text{E})},\theta\right)\,\mathrm{d}\theta\right)}_{M_4}\Pi_{\text{iso}}^{(\text{E})} \quad \text{(II.112)}$$

On the one hand, the dependence of M_2 on χ is relatively weak, as seen in Fig. II.49a for a handful of crystal orientations defined in Table II.5. Therefore, as already suggested in Sénac et al. (2022), it is discarded and M_2 is evaluated for $\chi = 0.3$, since it is usually preferable to predict correctly the beginning of localization rather than the later stages. On the other hand, the dependence of M_2 on ξ is quite significant, as shown in Fig. II.49b. Thus, the ξ-derivative of M_2 cannot be neglected in determining yield surfaces and will be denoted M_2'. It is also worth noticing that M_2 is not a perfectly even function of ξ, the slight difference being attributable to the constant terms in $\boldsymbol{d}^{(\text{O})}$.

3.4.3 Yield surface

As shown in Appendix II.3.A, two surfaces can be derived (using Eqs. II.69-II.70) from the approximated expressions of the macroscopic potential given in the previous section. However, these *Taylor surfaces* present two major limitations: first, the use of Eqs. II.111 and II.112 offers no guarantee on the convexity of Π so the convexity of Taylor surfaces cannot be assured; then, they require the computation of M_2 and its derivative for each crystallographic orientation, which is quite cumbersome. Thus, a pragmatic approach consists of identifying an equivalent Hill porous

#	Euler angles			Miller indexes		
	ϕ_1 (°)	Φ (°)	ϕ_2 (°)	$\underline{e}_1$	$\underline{e}_2$	$\underline{e}_3$
● Regular orientation #1	0	0	0	[100]	[010]	[001]
● Regular orientation #2	90	24.09	333.43	[1$\bar{2}$1]	[210]	[$\bar{1}$25]
● Random orientation	93.48	53.17	315.41			

TABLE II.5: Definition of the crystallographic orientations. Euler angles are given using the Bunge convention; Miller indexes define loading axes in the crystal frame.

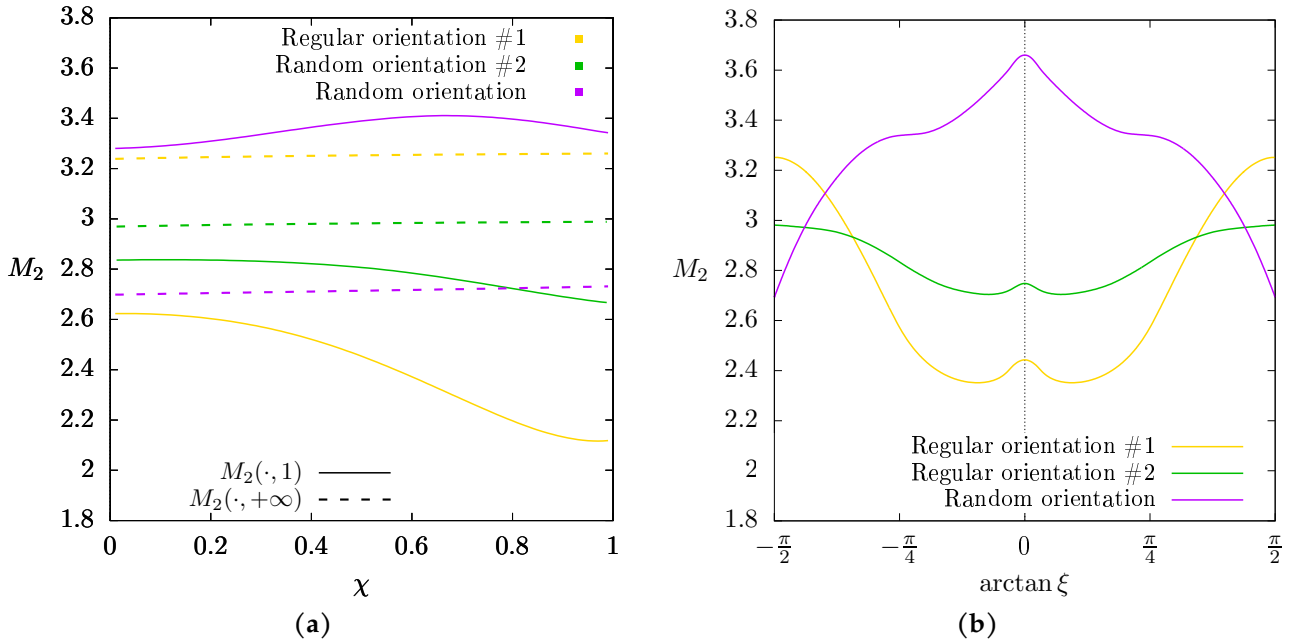

FIGURE II.49: Average Taylor factor M_2 for various crystal orientations: (a) effect of χ at fixed $\xi \in \{1, +\infty\}$; (b) effect of ξ for fixed $\chi = 0.3$.

material whose two individual yield surfaces are close to the Taylor surfaces of the porous single crystal. As seen in Section II.3.3, each individual yield surface (either columnar localization or layered localization) of a porous Hill material is characterized by three factors: $\hat{h}_a$, $\hat{h}_t$ and $\hat{h}_q$.

Since it has been noticed on Figs. II.43b and II.45b that the effects of $\hat{h}_a$ and $\hat{h}_t$ on the shape of yield surfaces are almost impossible to distinguish, $\hat{h}_a$ is arbitrarily fixed to 0 to reduce the number of freedom degrees. Then, $\hat{h}_t$ and $\hat{h}_q$ are chosen so that the flat parts of the Taylor surface and the flat parts of the porous Hill material yield surface coincide. For both columnar and layered localization, the equality of the deviatoric point of the yield surface (either Eq. II.89$_b$ or II.100$_b$) and that of the Taylor surface (either Eq. II.123$_b$ or Eq. II.126$_b$) yields:

$$\sqrt{\hat{h}_q} = M_4 \tag{II.113}$$

Then, in the case of the layered localization, identifying the internal necking stresses of both surfaces (Eq. II.101$_b$ and Eq. II.127$_b$) leads to:

$$\sqrt{\frac{\hat{h}_t^{\mathrm{l}}}{3}}\mathcal{A}\left(\frac{1}{M_4}\sqrt{\frac{\hat{h}_t^{\mathrm{l}}}{3}}\right) + M_4\mathcal{B}\left(\frac{1}{M_4}\sqrt{\frac{\hat{h}_t^{\mathrm{l}}}{3}}\right) = M_2\left(1\right)\left[\frac{1}{\sqrt{3}}\mathcal{A}\left(\frac{1}{\sqrt{3}}\right) + \mathcal{B}\left(\frac{1}{\sqrt{3}}\right)\right] + M_1\frac{\chi^3 - 3\chi + 2}{3\sqrt{3}w\chi} \tag{II.114}$$

Similarly, in the case of columnar localization, identifying the columnar shielding stresses of both surfaces (Eq. II.91$_b$ and Eq. II.124$_b$) leads to:

$$\sqrt{\frac{\hat{h}_t^{\mathrm{c}}}{3}}\chi^2\mathcal{A}\left(\frac{\chi^2}{M_4}\sqrt{\frac{\hat{h}_t^{\mathrm{c}}}{3}}\right) + M_4\mathcal{B}\left(\frac{\chi^2}{M_4}\sqrt{\frac{\hat{h}_t^{\mathrm{c}}}{3}}\right) = M_2(\chi^2)\left[\frac{\chi^2}{\sqrt{3}}\mathcal{A}\left(\frac{\chi^2}{\sqrt{3}}\right) + \mathcal{B}\left(\frac{\chi^2}{\sqrt{3}}\right)\right] + M_1\frac{w}{\sqrt{3}}\frac{(1-c)^2}{c}\chi^2 \tag{II.115}$$

Eqs. II.114 and II.115 respectively constitute implicit definitions of function $\hat{h}_t^{\mathrm{l}}(M_1, M_2(1), M_4, \chi, w)$ and function $\hat{h}_t^{\mathrm{c}}(M_1, M_2(\chi^2), M_4, \chi, c, w)$. Obviously, $\hat{h}_t^{\mathrm{c}}$ (corresponding to columnar localization) will be different from $\hat{h}_t^{\mathrm{l}}$ (related to layered localization). For FCC crystals, it can be assessed numerically that the dependence of $\hat{h}_t$ on the crystal orientation is weak compared to its dependence on void parameters. Thus, the crystallographic dependence of $\hat{h}_t$ can be ignored. As a consequence, $\hat{h}_t$ are evaluated for each set of (χ, c, w) through Eqs. II.114-II.115 by replacing Taylor

Crystal	• Regular orientation #1	• Regular orientation #2	• Random orientation
$\sqrt{\hat{h}_q}$	2.45	2.76	3.67
Void geometry		$\chi = c = 0.4$	$\chi = 0.3$, $c = 0.6$
$\sqrt{\hat{h}_t^{\mathrm{c}}}$		6.13	3.03
$\sqrt{\hat{h}_t^{\mathrm{l}}}$		3.97	4.19

TABLE II.6: Anisotropy factors of the equivalent yield surfaces for porous single crystals.

factors by their mean values:

$$\langle M_1 \rangle \approx 3.197 \ , \quad \langle M_2(1) \rangle \approx 2.806 \ , \quad \left\langle M_2(\chi, \chi^2) \right\rangle \approx \begin{cases} 2.884 & (\chi = 0.3) \\ 2.845 & (\chi = 0.4) \\ 2.775 & (\chi = 0.6) \end{cases} , \quad \langle M_4 \rangle \approx 2.929 \tag{II.116}$$

For instance, the values of $\hat{h}_q$, $\hat{h}_t^{\mathrm{c}}$ and $\hat{h}_t^{\mathrm{l}}$ are given in Table II.6 for the three crystallographic orientations of Table II.5 and two void geometries with $w = 1$: on the one hand, $\chi = c = 0.4$, and on the other hand $\chi = 0.3$ and $c = 0.6$.

As in the case of porous Hill materials, the final predicted yield criterion for porous single crystals is given by the intersection of the equivalent surfaces corresponding to columnar localization and layered localization.

3.4.4 Numerical assessment

In this section, the numerical assessment of the criterion defined in the previous section is conducted on a set of three crystallographic orientations given in Table II.5.

In order to assess the predicted yield criterion, numerical limit-analysis is conducted with `Cast3M` for the aforementioned crystallographic orientations. Crystal elasticity is chosen to obey an isotropic Hooke law of Young modulus $Y = 10^3$ MPa and Poisson ratio $\nu = 0.49$. As stated before, the results presented in the following do not depend on these values. In the following, the value $n = 100$ is chosen in Eq. II.107 to ensure crystal behavior is quasi-rate-independent. Since transverse isotropy is no longer verified, the full unit-cell has to be meshed; one-eighth of the mesh is shown in Fig. II.47b. Note that due to the computational burden associated with three-dimensional computations, the mesh is coarser (20400 quadratic elements with reduced integration) than in Fig. II.47a. Still, it was checked for convergence against a similar mesh of 160000 elements: the relative error was found to be below 1%.

The boundary conditions are consistent with the axisymmetric case, described in Section II.3.3.7: the radial displacement is homogeneous along the lateral exterior surface of the unit cell, the axial displacements are homogeneous on the top and the bottom surface (with opposite signs) and the angular displacement is set to 0 on the whole exterior surface. Note that no rigid-body motion can occur with these conditions. As in the previous part, the ratio of axial displacement on radial displacement is continuously adjusted in the Newton-Raphson iterations to reach the prescribed macroscopic stress ratio $\Sigma_{\rho\rho}/\Sigma_{33}$.

The criterion quality is checked against numerical limit analysis simulations in Fig. II.50. Given the fact that trial velocity fields used in Section II.3.4.2 were initially designed for isotropic materials, they diverge significantly from the real velocity fields and therefore cannot be expected to be tight upper bounds for the macroscopic dissipation. In an effort to acknowledge this gap, the predicted criterion plotted in Fig. II.50 is scaled down in order to recover the best possible agreement at the deviatoric point:

$$\left(\Sigma_{\mathrm{m}}, \Sigma_{\mathrm{eq}}\right)_{\mathrm{model}} = q \cdot \left(\Sigma_{\mathrm{m}}, \Sigma_{\mathrm{eq}}\right)_{\mathrm{analytical}} \tag{II.117}$$

where the analytical model is constituted from the expressions of Sections II.3.3.3 and II.3.3.6 used with anisotropy values from Table II.6 and where $q = 0.85$ is a single calibration parameter.

Comparisons between the ensuing yield surface and the numerical surface are shown in Fig. II.50 for two different void parameters: $\chi = c = 0.4$ (left-hand side), and $2\chi = c = 0.6$ (right-hand side); w is set to 1 in both cases. Despite the strong influence of crystal orientation on plastic yielding, the displayed agreement is quite satisfying. First, the characteristic sections of coalescence in columns, internal necking and columnar shielding are well visible in the nu-

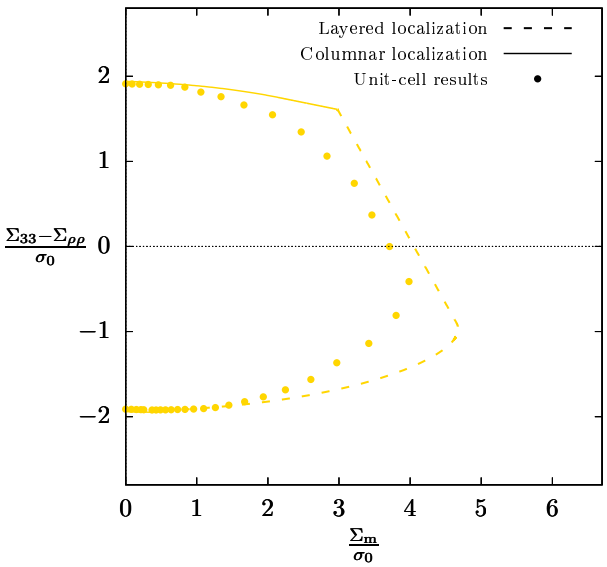

(**a**) $\chi = 0.4$, $c = 0.4$, regular orientation #1

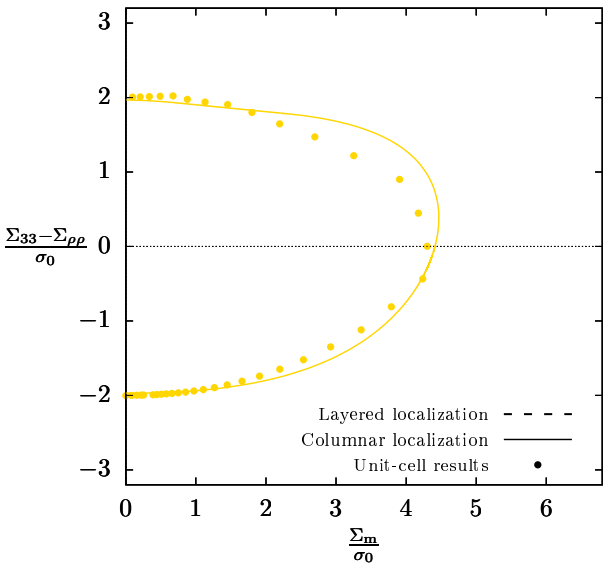

(**b**) $\chi = 0.3$, $c = 0.6$, regular orientation #1

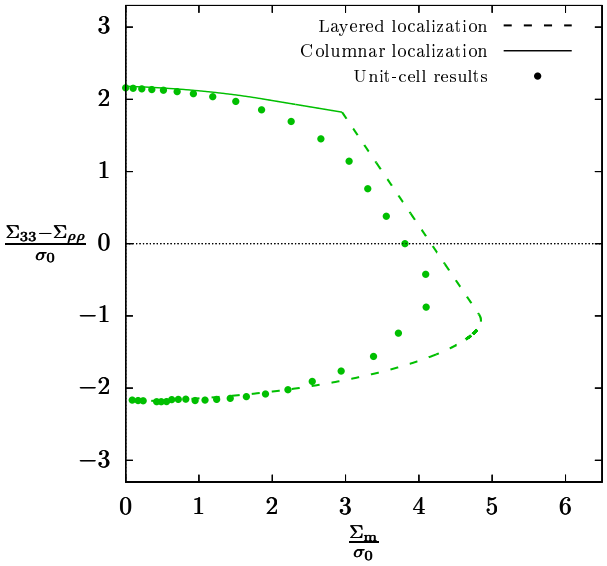

(**c**) $\chi = 0.4$, $c = 0.4$, regular orientation #2

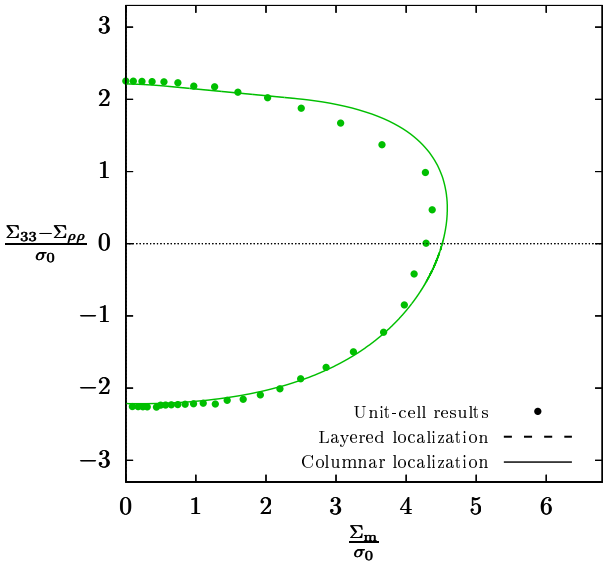

(**d**) $\chi = 0.3$, $c = 0.6$, regular orientation #2

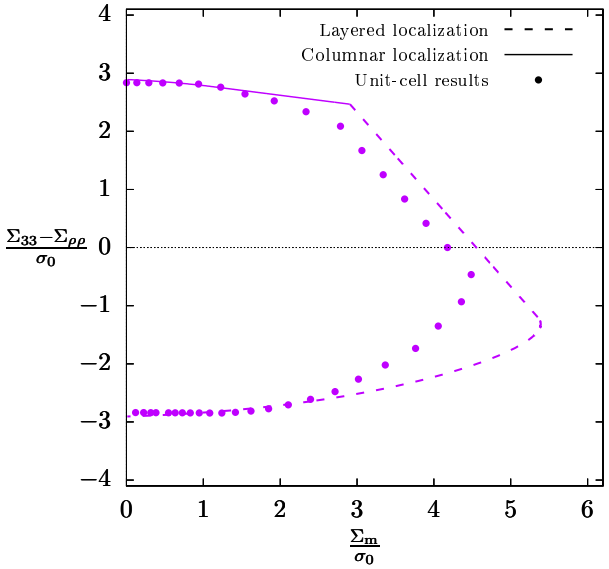

(**e**) $\chi = 0.4$, $c = 0.4$, random orientation

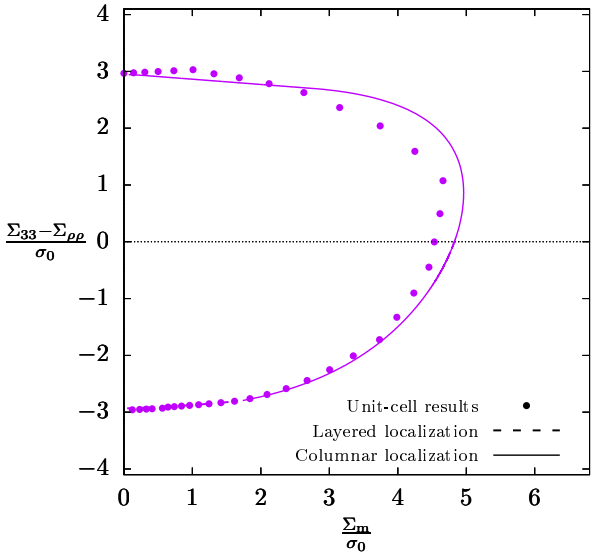

(**f**) $\chi = 0.3$, $c = 0.6$, random orientation

FIGURE II.50: Comparison between the numerical limit-analysis (points) and the calibrated analytical criterion, with its sections of columnar localization (full lines) and layered localization (dashed lines) for a set of porous single crystals. Two void geometries are considered: **(a,c,e)** $\chi = 0.4$, $c = 0.4$, $w = 1$; **(b,d,f)** $\chi = 0.3$, $c = 0.6$, $w = 1$.

merical surfaces, which justifies qualitatively the approach used in Section II.3.4.3. Then, the effect of crystallographic orientations is well accounted for: note that the rankings of deviatoric yield stress are identical for numerical and predicted surfaces (this can be seen on all subfigures of Fig. II.50), and the same can be said about internal necking yield stress (see Fig. II.50a,b,c). Overall, the quantitative predictions are of similar quality compared to those observed in Section II.3.3.7 for porous Hill materials.

3.5 Homogenized model for porous Hill materials

Prediction of yield surfaces for porous materials is only the first step in modeling ductile fracture. As a matter of fact, microstructure parameters evolve under plastic flow, gradually modifying the yield surface. Accounting for this coupling is paramount to predict the behavior of materials until failure, and therefore to estimate ductility. Thus, the yield criterion must be supplemented with evolution laws for the microstructure. Various homogenized models of ductile fracture combining void growth and coalescence in layers have been proposed in the literature for isotropic materials (Benzerga and Leblond, 2010; Keralavarma, 2017; Torki and Benzerga, 2018b; Vishwakarma and Keralavarma, 2019; Reddi et al., 2019; Keralavarma et al., 2020; Torki et al., 2021; Torki and Benzerga, 2022) as well as porous single crystals (Scherer et al., 2021; Sénac et al., 2022) but none of them include coalescence in columns.

3.5.1 Sequential limit analysis

In the following, the evolution under plastic flow of the unit-cell shown in Fig. II.40 with a Hill matrix is studied assuming that both the void and the unit-cell remain cylindrical. Thus, the four geometry parameters that define microstructure are R, H, r and h. Boundary conditions are such that $\dot{H} = D_{33}H$ and $\dot{R} = D_{\rho\rho}R$, leaving two unknown evolution laws for r and h or, alternatively, for χ and c. Therefore, the mere application of the incompressibility of the matrix material cannot close the equations and an additional hypothesis is needed. In Gurson's analysis, spherical invariance was such a hypothesis; in the approach of internal necking by Thomason (1985), the rigid character of the upper and lower zones provided an additional constraint, as well as in coalescence under combined tension and shear (Torki et al., 2017; Torki and Benzerga, 2018b; Torki and Benzerga, 2018a). In the present case, none of these hypotheses are acceptable. Therefore, it is resorted to sequential limit analysis (Leblond et al., 2018), *i.e.* the trial velocity fields given by Eqs. II.74 and II.92 will be used to derive evolution equations of the microstructure. In that framework, $\dot{r} = v_\rho(r,0)$ and $\dot{h} = v_z(0,h)$.

On the one hand, for the trial velocity field corresponding to columnar localization, it leads to:

$$\dot{c} = \frac{\dot{h}}{H} - \frac{\dot{H}h}{H^2} = \frac{1-c}{\chi^2} D_{kk} \quad , \quad \dot{\chi} = \frac{\dot{r}}{R} - \frac{\dot{R}r}{R^2} = \frac{1}{2}\left(\frac{1}{\chi} - \chi\right) D_{kk} \quad , \quad \dot{w} = \frac{\dot{h}}{r} - \frac{\dot{r}h}{r^2} = \frac{w}{\chi^2}\left(\frac{1}{c} - \frac{3}{2}\right) D_{kk} + \frac{3}{2} w D_{33} \tag{II.118}$$

On the other hand, for the trial velocity field corresponding to layered localization, sequential limit-analysis yields:

$$\dot{c} = (1-c) D_{kk} \quad , \quad \dot{\chi} = \frac{1}{2c}\left(\frac{1}{\chi} - \chi\right) D_{kk} \quad , \quad \dot{w} = \frac{w}{2}\left[3\left(\frac{1}{c} - 1\right) - \frac{1}{c\chi^2}\right] D_{kk} + \frac{3}{2} w D_{33} \tag{II.119}$$

Note that Eqs. II.119 are an extension of the evolution laws for λ, χ and w given by Benzerga and Leblond (2010) in the case $\gamma = \frac{1}{3}$. The incompressibility condition of the matrix writes

$$\frac{\partial}{\partial t}\left[2\pi H R^2 - 2\pi h r^2\right] = H R^2 \left[D_{kk}(1 - c\chi^2) - \chi^2 \dot{c} - 2c\chi\dot{\chi}\right] = 0 \tag{II.120}$$

and is compatible with Eqs. II.118 and II.119, which is no surprise since trial velocity fields were chosen to verify the incompressibility of the matrix material.

The homogenized model for Hill porous materials is the combination of the multi-surface yield criterion obtained previously (see Sections II.3.3.3 and II.3.3.6) along with the corresponding evolution laws (respectively Eqs. II.118 and II.119). The set of microstructure equations to be applied is chosen according to the stress criterion currently activated. The issue of surface intersections can be solved by combining criteria using a viscoplastic framework such as the one used in Sénac et al. (2022) or a perfect plastic framework following Koiter (1953). Note that since the matrix deforms during ductile fracture, evolution equations for the orthotropy axes of the matrix are also needed. However, given the absence of macroscopic shear in the axisymmetric loadings considered here, it will be supposed that these axes do not rotate significantly.

3.5.2 Discussion

Evolution laws do not benefit from the variational framework associated with classical limit analysis (Eq. II.66), and thus Eqs. II.118 and II.119 have no guarantee of holding unless the trial velocity fields are very close from the real field. Besides, spatial inhomogeneities of the velocity field on the void surface can also lead to the evolution of the void towards shapes that are no longer cylindrical (see for instance Keralavarma et al. (2011), Morin et al. (2016b) and Hosseini et al. (2022) for the same issue with ellipsoidal cavities), which would reduce the predictive capability of the model. Finally, since the chosen trial fields do not depend on material anisotropy, they result in evolution laws that are also independent of it, providing that the strain rate is fixed; this simplifying hypothesis needs to be assessed.

Numerical velocity fields for various plastic anisotropy are presented in Fig. II.51 in the case where $\chi = 0.3$ and $c = 0.6$ for two displacement boundary conditions. For an isotropic material, they correspond to two different deformation modes: columnar shielding ($D_{33} = -D_{\rho\rho} = 1$, see Fig. II.51a) and coalescence in columns ($D_{\rho\rho} = -2D_{33} = 1$, see Fig. II.51b). On the one hand, the velocity field for the first loading condition remains the same for anisotropic materials (Fig. II.51c,e), except for the material with lower axial strength (Fig. II.51b) where slight deviations arise: notice that the plugs are no longer shielded from plasticity. On the other hand, the velocity field associated with the second loading condition seems more sensible to anisotropy as the material with $R_\mathrm{s} = 3$ deviates strongly from the isotropic field while the material with $R_\mathrm{a} = 0.6$ displays reduced velocity magnitude in the plugs. The influence of anisotropy on internal necking is studied in Fig. II.52 at $\chi = 0.4$ and $c = 0.4$. The velocity field is found to be relatively stable when varying plastic anisotropy: compare the isotropic field (Fig. II.52a) to the anisotropic field that displays the strongest deviations from it (Fig. II.52b).

The conclusion to be drawn from these comparisons is the following: supposing that evolution laws are accurate enough to model damage evolution in the isotropic material, the velocity field mismatches highlighted in the case of coalescence in columns (right-hand side of Fig. II.51) would require a correction depending on material anisotropy to account satisfactorily for microstructure evolution. Such a correction seems to be less necessary in the case of columnar shielding (left-hand side of Fig. II.51) and useless in the case of internal necking (Fig. II.52).

A sense of the accuracy of evolution laws derived by sequential limit analysis can be obtained by comparing the velocity fields from numerical limit analysis in the isotropic material and the trial fields used in the theoretical analysis. When velocity fields are compared *at equal displacement boundary conditions* (*i.e.* fixed ξ), the result is rather disappointing. Indeed, as seen in Fig. II.53a, the trial velocity field predicts coalescence in columns instead of columnar shielding (Fig. II.51a), and the coalescence in columns of Fig. II.53b misses the fact that the void lateral surface moves faster than the unit-cell lateral surface (see Fig. II.51b). These discrepancies are likely to result in inaccurate evolution for internal parameters. However, when numerical velocity fields are compared *at equal stress triaxialities*, the picture is entirely different. This time, columnar shielding is correctly predicted (Fig. II.53c), and the void surface moves faster than the unit-cell exterior surface (Fig. II.53d). In Fig. II.53d, it is also visible that the ratio of the void upper surface axial velocity on the lateral surface radial velocity is more coherent with numerical fields (right-hand side of Fig. II.51) than that of Fig. II.53b. Finite strain unit-cell computations at fixed stress triaxiality ratios would be needed for definitive assessment of evolution laws obtained by sequential limit-analysis (Eqs. II.118 and II.119) but these simulations are left for future research. In finite-element computations, mechanical solving at material points couples stress and displacement conditions, so the resulting velocity fields might lie between those obtained using pure boundary conditions. This observation is yet another reminder that a satisfying analytical yield surface must approximate correctly yield stresses as well as their derivatives (*e.g.* Leblond and Morin (2014)).

Assuming for now that Eq. II.118 are a good approximation of microstructure evolution during necklace coalescence, they can be invoked to explain the observations of Benzerga (2002) and Benzerga et al. (2004a) which reported coalescence in columns occurring between close-packed prolate cavities. Torki et al. (2023) have put forward that at fixed unit-cell aspect ratio λ, increasing w contracts the yield surface and therefore favors coalescence in columns; however, at fixed c and χ, increasing w hinders necklace coalescence (see Fig. II.43a) and fosters internal necking (see Fig. II.45a). Thus, one cannot say that necklace coalescence *occurs* preferentially for prolate cavities; in fact, tensile necklace coalescence *produces* prolate cavities. This observation arises from Eq. II.118$_c$: for $c \leq \sqrt{2/3}$ and $D_{kk} > 0$, coalescence in columns leads to very significant increase of w. From Eq. II.118$_a$, it also inferred that tensile coalescence in columns is a self-sustaining phenomenon since $\dot{c} > \dot{\chi}$ for c verifying the following inequality:

$$c \leq 1 - \frac{1}{2}\,\chi\,(1 - \chi^2) \tag{II.121}$$

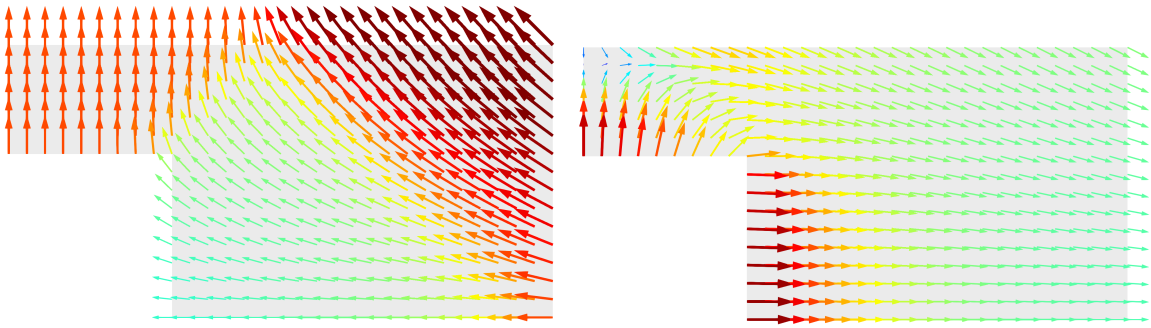

(**a**) $R_\mathrm{a} = R_\mathrm{s} = 1$, $D_{33} = -D_{\rho\rho} = 1$, $\Sigma_{\rho\rho}/\Sigma_{33} = -0.668$

(**b**) $R_\mathrm{a} = R_\mathrm{s} = 1$, $D_{\rho\rho} = -2D_{33} = 1$, $\Sigma_{\rho\rho}/\Sigma_{33} = 1.636$

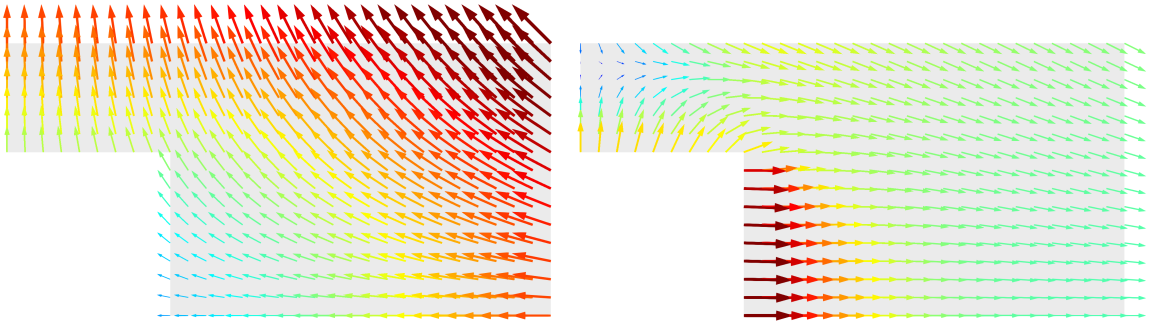

(**c**) $R_\mathrm{a} = 0.6$, $R_\mathrm{s} = 1$, $D_{33} = -D_{\rho\rho} = 1$, $\Sigma_{\rho\rho}/\Sigma_{33} = -0.678$

(**d**) $R_\mathrm{a} = 0.6$, $R_\mathrm{s} = 1$, $D_{\rho\rho} = -2D_{33} = 1$, $\Sigma_{\rho\rho}/\Sigma_{33} = 1.098$

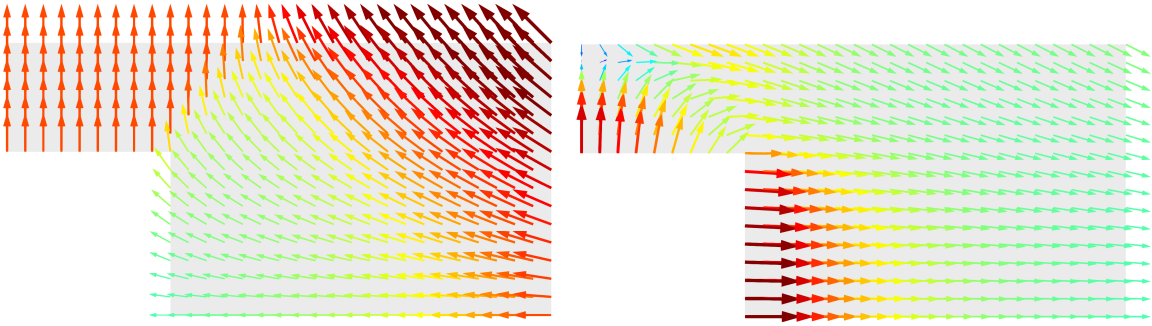

(**e**) $R_\mathrm{a} = 1.5$, $R_\mathrm{s} = 1$, $D_{33} = -D_{\rho\rho} = 1$, $\Sigma_{\rho\rho}/\Sigma_{33} = -0.235$

(**f**) $R_\mathrm{a} = 1.5$, $R_\mathrm{s} = 1$, $D_{\rho\rho} = -2D_{33} = 1$, $\Sigma_{\rho\rho}/\Sigma_{33} = 3.437$

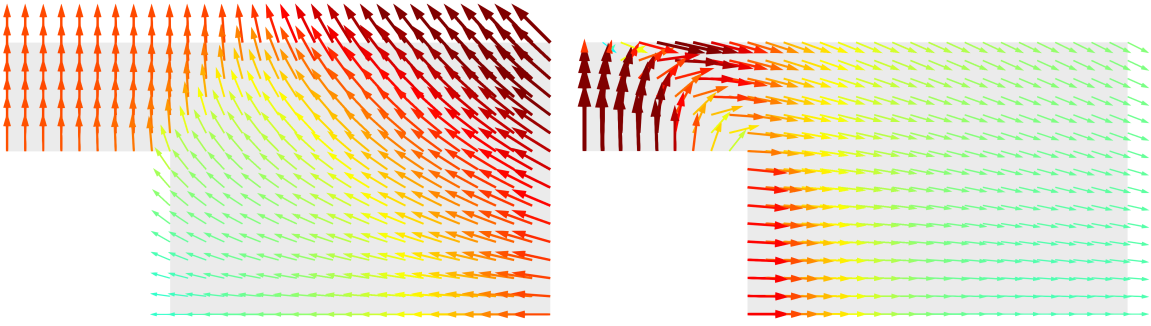

(**g**) $R_\mathrm{a} = 1.5$, $R_\mathrm{s} = 3$, $D_{33} = -D_{\rho\rho} = 1$, $\Sigma_{\rho\rho}/\Sigma_{33} = -0.403$

(**h**) $R_\mathrm{a} = 1.5$, $R_\mathrm{s} = 3$, $D_{\rho\rho} = -2D_{33} = 1$, $\Sigma_{\rho\rho}/\Sigma_{33} = 3.030$

FIGURE II.51: Comparison of the numerical kinematic limit analysis velocity fields for $\chi = 0.4$, $c = 0.6$, $w = 1$, corresponding to $D_{33} = -D_{\rho\rho} = 1$ (left row) or $D_{\rho\rho} = -2D_{33} = 1$ (right row). Different ratios R_a and R_s are presented.

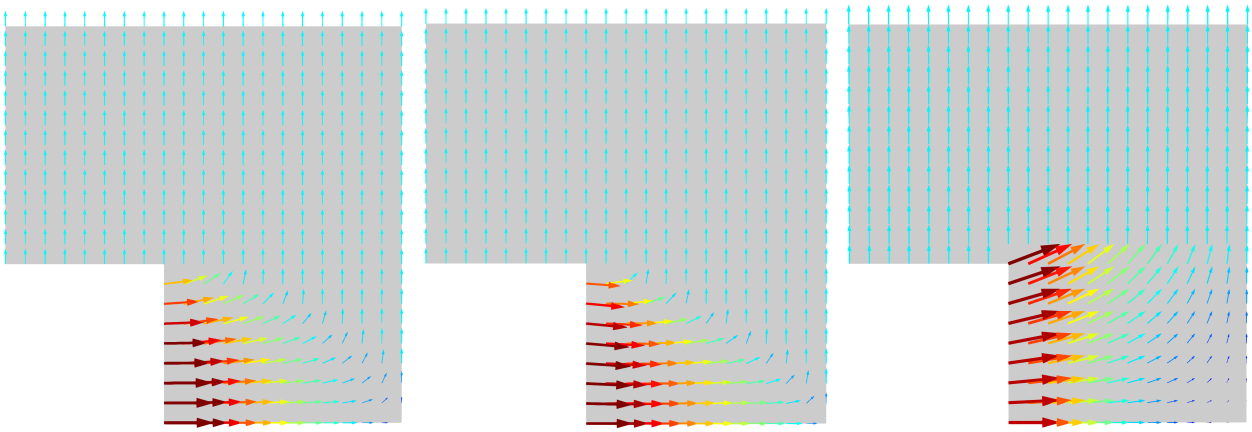

(**a**) $R_a = R_s = 1$, $D_{\rho\rho} = 0$ (**b**) $R_a = 1.5$, $R_s = 1$, $D_{\rho\rho} = 0$ (**c**) Trial velocity field, $D_{\rho\rho} = 0$

FIGURE II.52: Numerical limit-analysis velocity fields and trial velocity field (Eq. II.92) for $\chi = 0.4$, $c = 0.4$, $w = 1$.

That should ensure — apart from significant loading changes — that once necklace coalescence has begun, internal necking does not activate until high c are reached.

3.6 Conclusion and perspectives

3.6.1 Conclusion

In this study, a yield criterion for porous anisotropic materials — Hill-type and single crystal — under axisymmetric loading has been developed using limit analysis. In particular, it accounts for the transition from homogeneous yielding (void growth) to various inhomogeneous deformation modes: internal necking, columnar shielding and coalescence in columns. A strong effect of plastic anisotropy on strain localization modes, both in Hill materials and single crystals, is observed. When compared to the yield surface obtained through numerical limit analysis, a good agreement is reached after limited calibration. In particular, the following findings about coalescence in columns, already made by Torki et al. (2023) for isotropic materials, are extended to anisotropic materials:

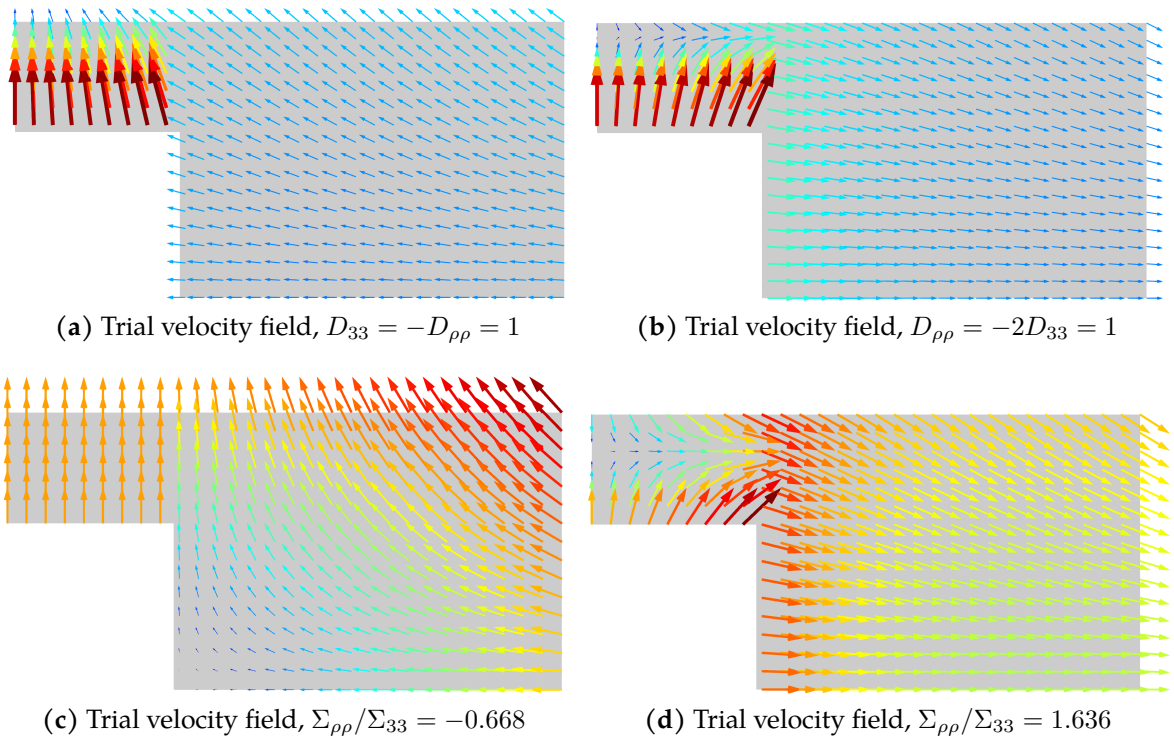

(**a**) Trial velocity field, $D_{33} = -D_{\rho\rho} = 1$ (**b**) Trial velocity field, $D_{\rho\rho} = -2D_{33} = 1$

(**c**) Trial velocity field, $\Sigma_{\rho\rho}/\Sigma_{33} = -0.668$ (**d**) Trial velocity field, $\Sigma_{\rho\rho}/\Sigma_{33} = 1.636$

FIGURE II.53: Trial velocity field of Eq. II.74 for $\chi = 0.4$, $c = 0.6$, $w = 1$.

- coalescence in columns depends both on the axial ligament size c and the radial ligament size χ, as opposed to internal necking which only exhibits a variation with χ;
- depending on the microstructure and the plastic anisotropy, coalescence in columns can be favored over coalescence in layers over a significant range of loading conditions, including stress states with Lode angle $\theta = 0$ (hydrostatic tension superposed with uniaxial compression);
- contrary to internal necking, this deformation mode does not lead to complete loss of bearing capacity, which is confirmed by available experimental evidence (Benzerga et al., 2004a).

The occurrence of columnar shielding over a significant range of stress triaxialities is also predicted, which confirms previous numerical evidence (Chouksey et al., 2019).

Due to this clear physical grounding, the multi-surface plasticity model presented here outperforms the previous attempts to predict ductile fracture in anisotropic materials for axisymmetric loading conditions. In order to provide a complete homogenized model for porous Hill materials, the final yield surface was supplemented by a set of evolution laws for the microstructure so that the gradual process of ductile fracture can be simulated.

3.6.2 Perspectives

The perspectives are the following:

- In cases where the void axis and the main loading direction differ, equivalent voids could be defined using the method found in Torki and Benzerga (2018b) in order to use the expressions derived in this article, but this deserves additional validation.
- Yield surfaces for anisotropic materials can be extended to account for macroscopic shear which can lead to shear-assisted coalescence in layers. This would amount to adapting the work of Torki (2019) to anisotropic materials. It would also be interesting to study the effect of shear boundary conditions on columnar shielding and coalescence in columns, something that was not carried out in isotropic materials to begin with.
- Alternative evolutions laws could be obtained using continuous trial fields (*e.g.* the continuous field of Torki et al. (2023) for columnar localization and the internal necking field of Keralavarma and Chockalingam (2016) instead of the one of Benzerga and Leblond (2014) for layered localization). In any case, finite strain unit-cell simulations need to be conducted to assess the quality of evolution laws definitively.
- Once sound evolution laws are calibrated, it would be possible to study the effect of plastic anisotropy on material ductility, for instance by exploring failure loci for proportional loadings, *i.e.* fixed Lode angle and stress triaxiality (see Vishwakarma and Keralavarma (2019) for the corresponding study on isotropic materials). Such results would be paramount for using plastic anisotropy to design tougher materials.
- In single crystals, the issue of evolution laws is more complicated since strain inhomogeneities can have deeper consequences on plastic yielding. Indeed, even at the homogeneous yielding stage, Guo et al. (2020) has shown that local microstructure evolution can have a significant effect on void growth at large strains; for instance, even if the macroscopic strain tensor has no shear terms, void shearing can occur due to local lattice rotation. The picture gets increasingly tangled when twinning occurs (Selvarajou et al., 2019; Indurkar et al., 2022). Therefore, an in-depth investigation of these phenomena is required.

3.A Taylor surfaces of a porous single crystal

Deriving the tangent surface associated with the macroscopic potential given by Eq. II.111 can be carried out following the lines of Section II.3.3.3. It brings, for $\xi \neq 0$ and $\xi \neq \chi^2$:

$$\begin{aligned}\Sigma_{\rho\rho} &= \mathrm{sgn}(D_{33})\,\tau_0 \left[\mathrm{sgn}(\xi)\left(\frac{M_2(\xi)+M_2'(\xi)\xi}{\sqrt{3}}\mathcal{A}\left(\frac{\xi}{\sqrt{3}}\right)+M_1\frac{w}{\sqrt{3}}\frac{(1-c)^2}{c}\right)\right.\\ &\qquad\left.+\,\mathrm{sgn}(\xi-\chi^2)M_4(1-c)+M_2'(\xi)\mathcal{B}\left(\frac{\xi}{\sqrt{3}}\right)\right]\\ \Sigma_{33}-\Sigma_{\rho\rho} &= \mathrm{sgn}(D_{33})\,\tau_0 \left[-\mathrm{sgn}(\xi-\chi^2)M_4(1-c)\chi^2-\mathrm{sgn}(\xi)\frac{\xi^2 M_2'(\xi)}{\sqrt{3}}\mathcal{A}\left(\frac{\xi}{\sqrt{3}}\right)\right.\\ &\qquad\left.+\,\left(M_2(\xi)-\xi M_2'(\xi)\right)\mathcal{B}\left(\frac{\xi}{\sqrt{3}}\right)\right]\end{aligned} \tag{II.122}$$

whereas $\xi = 0$ results in:

$$\begin{aligned}\left|\Sigma_{\rho\rho}+\mathrm{sgn}(D_{33})\tau_0\left[(1-c)M_4-(1-\chi^2)M_2'(0)\right]\right| &\leq \tau_0 M_1\frac{w}{\sqrt{3}}\frac{(1-c)^2}{c}\sqrt{\hat{h}_a}\\ \Sigma_{33}-\Sigma_{\rho\rho} &= \mathrm{sgn}(D_{33})\tau_0(1-c\chi^2)M_4\end{aligned} \tag{II.123}$$

and $\xi = \chi^2$ yields:

$$\begin{aligned}&\left|\Sigma_{\rho\rho}-\mathrm{sgn}(D_{33})\tau_0\left[\frac{M_2(\chi^2)+\chi^2M_2'(\chi^2)}{\sqrt{3}}\mathcal{A}\left(\frac{\chi^2}{\sqrt{3}}\right)+M_2'(\chi^2)\mathcal{B}\left(\frac{\chi^2}{\sqrt{3}}\right)+M_1\frac{w}{\sqrt{3}}\frac{(1-c)^2}{c}\right]\right| \leq \tau_0 M_4(1-c)\\ &\Sigma_{33}-(1-\chi^2)\Sigma_{\rho\rho} = \mathrm{sgn}(D_{33})\tau_0\left[\frac{M_2(\chi^2)}{\sqrt{3}}\chi^2\mathcal{A}\left(\frac{\chi^2}{\sqrt{3}}\right)+M_2(\chi^2)\mathcal{B}\left(\frac{\chi^2}{\sqrt{3}}\right)+M_1\frac{w}{\sqrt{3}}\frac{(1-c)^2}{c}\chi^2\right]\end{aligned} \tag{II.124}$$

Similarly, the tangent surface associated with the macroscopic potential given by Eq. II.112 can be obtained following the lines of Section II.3.3.6, for $\xi \neq 0$ and $\xi \neq 1$:

$$\begin{aligned}\Sigma_{33}-\Sigma_{\rho\rho} &= \mathrm{sgn}(D_{33})\,\tau_0\left\{-\mathrm{sgn}(\xi-1)M_4(1-c)-\mathrm{sgn}(\xi)\frac{c}{\sqrt{3}}\left(\frac{\xi}{\bar{\xi}}\right)^2 M_2'\left(\frac{\xi}{\bar{\xi}}\right)\mathcal{A}\left(\frac{\xi}{\sqrt{3\bar{\xi}}}\right)\right.\\ &\qquad\left.+\,\mathrm{sgn}(\bar{\xi})c\left[M_2\left(\frac{\xi}{\bar{\xi}}\right)-\frac{\xi}{\bar{\xi}}M_2'\left(\frac{\xi}{\bar{\xi}}\right)\right]\mathcal{B}\left(\frac{\xi}{\sqrt{3\bar{\xi}}}\right)\right\}\\ \Sigma_{33} &= \mathrm{sgn}(D_{33})\,\tau_0\left\{\left[M_2\left(\frac{\xi}{\bar{\xi}}\right)+\left(1-\frac{\xi}{\bar{\xi}}\right)M_2'\left(\frac{\xi}{\bar{\xi}}\right)\right]\left[\frac{\mathrm{sgn}(\xi)}{\sqrt{3}}\mathcal{A}\left(\frac{\xi}{\sqrt{3\bar{\xi}}}\right)+\mathrm{sgn}(\bar{\xi})\mathcal{B}\left(\frac{\xi}{\sqrt{3\bar{\xi}}}\right)\right]\right.\\ &\qquad\left.+\,\mathrm{sgn}(\xi)M_1\frac{\chi^3-3\chi+2}{3\sqrt{3}w\chi}\right\}\end{aligned} \tag{II.125}$$

The flat part corresponding to $\xi = 0$ is:

$$\begin{aligned}\left|\Sigma_{\rho\rho}+\mathrm{sgn}(D_{33})\tau_0\left[(1-c)\chi^2M_4-(1-\chi^2)M_2'(0)\right]\right| &\leq \tau_0 M_1\frac{\chi^3-3\chi+2}{3\sqrt{3}w\chi}\\ \Sigma_{33}-\Sigma_{\rho\rho} &= \mathrm{sgn}(D_{33})\tau_0(1-c\chi^2)M_4\end{aligned} \tag{II.126}$$

while $\xi = 1$ is associated to:

$$\begin{aligned}&\left|\Sigma_{33}-\Sigma_{\rho\rho}-\mathrm{sgn}(D_{33})c\tau_0\left[-\frac{M_2'(1)}{\sqrt{3}}\mathcal{A}\left(\frac{1}{\sqrt{3}}\right)+\left(M_2(1)-M_2'(1)\right)\mathcal{B}\left(\frac{1}{\sqrt{3}}\right)\right]\right| \leq \tau_0(1-c)M_4\\ &\Sigma_{33} = \mathrm{sgn}(D_{33})\tau_0\left\{M_2(1)\left[\frac{1}{\sqrt{3}}\mathcal{A}\left(\frac{1}{\sqrt{3}}\right)+\mathcal{B}\left(\frac{1}{\sqrt{3}}\right)\right]+M_1\frac{\chi^3-3\chi+2}{3\sqrt{3}w\chi}\right\}\end{aligned} \tag{II.127}$$

It is found that the coalescence stress established in Hure (2019) for internal necking is a particular case of the result given above (Eq. II.127$_b$).

4 Conclusion and perspectives

This chapter's contributions to transgranular ductile fracture prediction were developed using the micromechanical framework of porous material homogenization. Indeed, the physical-based simulation of ductile fracture cannot afford to account explicitly for all the cavities in a material and requires the derivation of homogenized models able to reproduce correctly the gradual growth and coalescence of cavities as an average behavior. While most of the literature has focused on a framework that considers voids larger than the grain size, this work was mainly devoted to the accounting of internal cavities inside single crystals, as it is a situation witnessed in many engineering materials (see Section I.3.4).

Homogenized models rely heavily on porous plasticity criteria, which must describe the yielding of the material as precisely as possible and thus incorporate various deformation modes. In this chapter, two competing approaches were adopted:

- As ductile fracture occurs by void growth and coalescence, the yield criterion can be obtained from individual criteria associated directly with these two deformation modes. The first two sections belonged to this framework:
  - First, a homogenized model for porous single crystals was proposed based on yield criteria for transgranular void growth and internal necking available in the literature, as well as *ad hoc* evolution laws for internal variables. This model was validated against an extensive database of unit cell simulations, showing satisfying agreement when the hardening is limited, and compared to the homogenized model of Scherer et al. (2021), underlying that a finite strain framework that accounts for lattice rotations is necessary.
  - Then, this homogenized model was used to perform 2D plane strain ductile tearing simulation of mono- and polycrystalline specimina, highlighting the effect of grain orientation on the fracture behavior (load curve, local field, and crack path) of full samples. A first 3D ductile tearing simulation was also carried out. These achievements pave the way toward microstructure-informed simulation of structures and numerical optimization of material properties such as fracture toughness.
- In another approach, the yield criterion can be obtained from combined criteria corresponding to gradual localization in layers and gradual localization in columns. Using this framework, a yield surface accounting for void growth, internal necking, and coalescence in columns in anisotropic materials (Hill plasticity and crystal plasticity) was developed in the last section. Indeed, accounting for coalescence in columns is required to correctly predict ductile fracture in various situations, as highlighted by both experimental and numerical findings. Evolution laws associated with this yield surface were derived to develop a dedicated homogenized model.

Through these two axes, this work has significantly enhanced the physical-based modeling of ductile fracture at the scale of crystals. On the one hand, natural extensions of this work include the following:

- application to crystal lattices that are more anisotropic than FCC crystals, *e.g.* HCP crystals. In the HCP case, twinning systems may also be accounted for using a similar framework as slip systems;
- development of a homogenized model including void growth, coalescence in layers, and coalescence in columns, based on the criterion proposed in Section II.3;
- improvement of the efficiency of ductile tearing simulations by optimization of the material law behavior and massive parallelization of mechanical solving.

On the other hand, longer-term perspectives foreseen in order to pursue the prediction of transgranular fracture are:

- to conduct model experiments of fracture using single crystals and oligo-crystals, enabling the establishment of benchmarks and increasing confidence in homogenized models. In this process, the small size of grains in most engineering alloys is a severe hurdle that needs to be overcome by designing micro-specimens or developing coarse-grained materials.
- to improve the modeling of microstructure evolution at finite strain, which is still a significant issue due to its highly coupled nature. Possible developments include the use of the multiplicative decomposition of the deformation gradient, which will improve the estimation of the plastic spin. Yet, the challenge of homogenizing hardening and crystal lattice rotation remains.

A Contributions to the study of internal necking

In this appendix, two minor contributions to the limit analysis of internal necking of materials with phenomenological plasticity are made. The starting point of the first contribution is that Thomason (1985) originally used limit analysis on two trial velocity fields in a tetragonal unit cell and took the minimum of the corresponding coalescence stresses. Indeed, depending on the microstructure parameters (w, χ), a trial field could bring a lower limit load than the other. However, only the rectangular trial field was adapted by Benzerga and Leblond (2014) to a cylindrical unit cell. Thus, the first section provides an analytical expression of the coalescence stress of the triangular velocity field of Thomason (1985). As foresaw based on the original study, it shows some improvement on existing coalescence criteria for low ligament size ratio χ. In the second section, an analytical expression of the coalescence stress of Keralavarma and Chockalingam (2016) is derived, avoiding the approximation that the authors performed.

A.1 Internal necking criterion obtained from Thomason triangular trial field

In this section, an upper-bound for the macroscopic plastic dissipation of internal necking is derived, providing an alternative to those of Benzerga and Leblond (2014), Keralavarma and Chockalingam (2016) and Hure and Barrioz (2016). The cylindrical unit-cell whose geometry is shown in Fig II.54a is considered, with the triangular trial field of Thomason (1985):

$$v_\rho(\rho) = \frac{D_{33}}{2}\frac{R-r}{c}\left(\frac{R}{\rho}+1\right) \quad , \quad v_z(\rho,z) = -\frac{D_{33}}{2}\frac{R-r}{c}\frac{z}{\rho} \tag{II.128}$$

while in the rigid zone $\underline{v} = \pm D_{33} H \underline{e}_3$. This field is kinematically admissible with the uniaxial straining boundary conditions commonly used when studying internal necking (Eq. II.64 with $D_{\rho\rho} = 0$). It is shown in Fig. II.54b for a given set of microstructure parameters.

At the upper interface between the ligament and the rigid zone, the velocity leap is such as:

$$\begin{aligned}\llbracket \underline{v} \rrbracket &= \left(v_\rho \underline{e}_\rho + v_z \underline{e}_3\right) - D_{33} H \underline{e}_3 \\ &= \frac{D_{33}}{2c}\left(\frac{R}{\rho}+1\right)\left[(R-r)\underline{e}_\rho - h\underline{e}_3\right]\end{aligned} \tag{II.129}$$

which is a purely tangential discontinuity; the same can be verified at the lower interface. It is recalled that for every microscopic statically admissible field $\boldsymbol{\sigma}$ and kinematically admissible field $\boldsymbol{d}$, the difference between the macroscopic

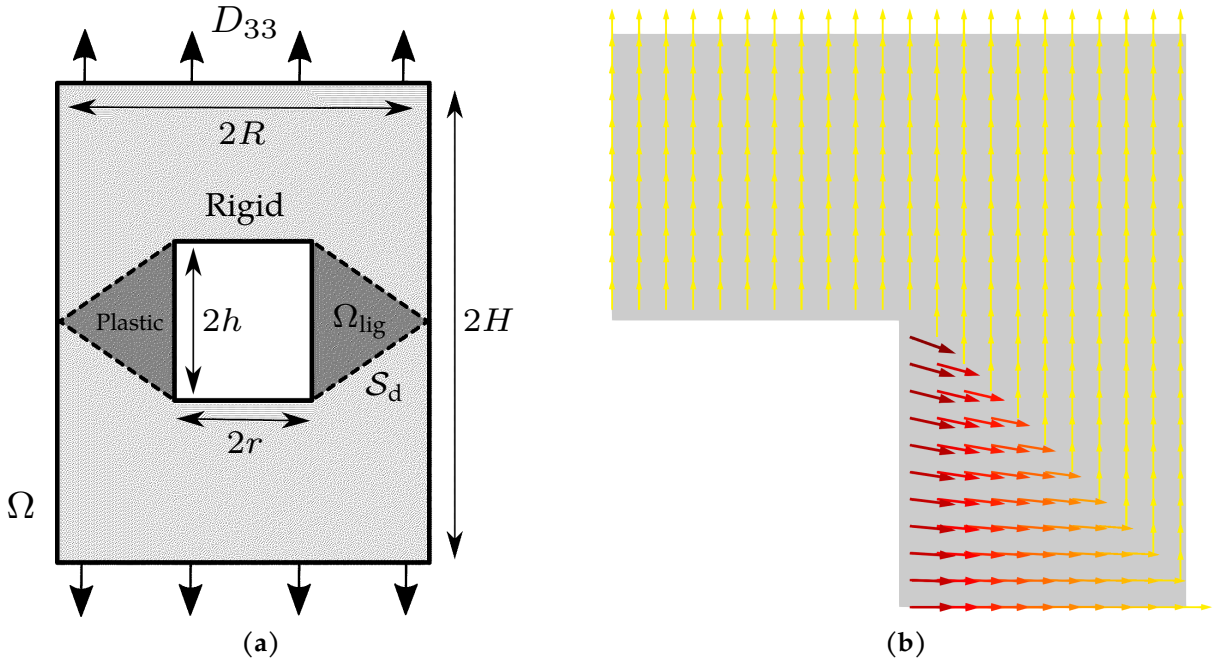

FIGURE II.54: Cylindrical unit-cell subjected to the triangular trial velocity field of Thomason (1985): (**a**) cell geometry; (b) triangular velocity field for $\chi = \frac{r}{R} = 0.5$ and $w = \frac{h}{r} = 1$.

and the microscopic plastic dissipation can be written according to boundary data (Nemat-Nasser and Hori, 1993):

$$\boldsymbol{\Sigma} : \boldsymbol{D} - \frac{1}{|\Omega|}\int_{\Omega} \boldsymbol{\sigma} : \boldsymbol{d} = \frac{1}{|\Omega|}\int_{\partial\Omega} [\underline{v} - \boldsymbol{D}\cdot\underline{x}] \cdot [(\boldsymbol{\Sigma} - \boldsymbol{\sigma})\cdot\underline{n}] \tag{II.130}$$

In the present case, $\underline{v} - \boldsymbol{D}\cdot\underline{x}$ is null on $\partial\Omega$ except on the circle $\{(R,\theta,0)\,,\ \theta \in [0,2\pi]\}$ which is a set of measure zero. Therefore, the right-hand side of Eq. II.130 evaluates as 0, which proves that the Hill-Mandel theorem is valid for this

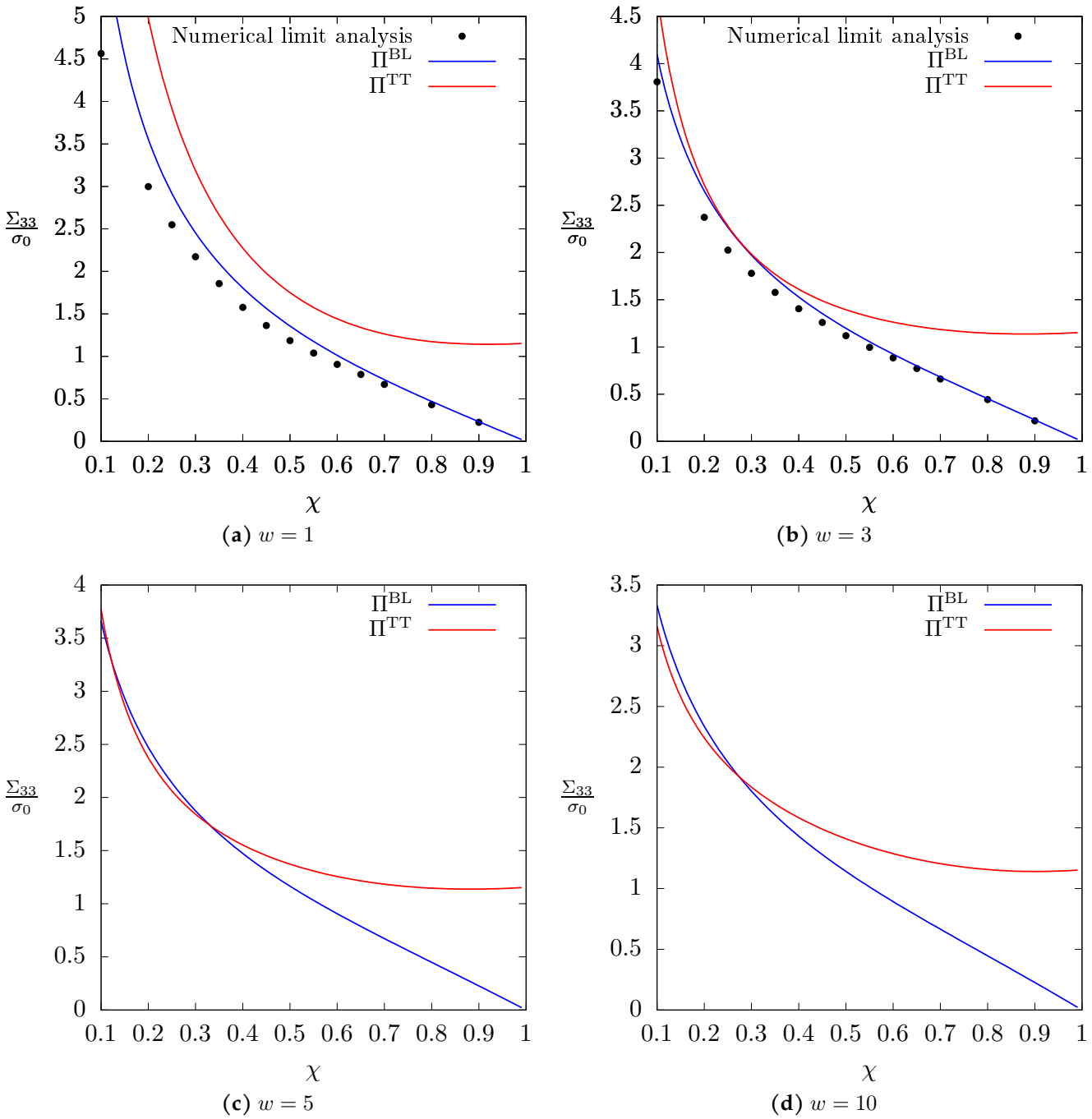

(a) $w = 1$ (b) $w = 3$ (c) $w = 5$ (d) $w = 10$

FIGURE II.55: Comparison between the predicted stresses to coalescence of various models (analytical Π^{BL} of Benzerga and Leblond (2014) and numerical Π^{TT} given by Eq. II.131) and FEM numerical limit analysis, according to the ligament size ratio χ and for a handful of void aspect ratios w. FEM results are reproduced from Morin et al. (2015b) ($0.2 < \chi \leq 0.7$) and Hure and Barrioz (2016) ($\chi \leq 0.2$ and $\chi > 0.7$).

trial field. The macroscopic plastic dissipation is:

$$\Pi^{\mathrm{TT}}(\boldsymbol{D}) = \underbrace{\frac{1}{|\Omega|}\int_{\Omega_{\mathrm{lig}}} \sup_{\boldsymbol{\sigma}^*\in\mathscr{C}} \boldsymbol{\sigma}^* : \boldsymbol{d}}_{\Pi^{\mathrm{TT}}_{\mathrm{vol}}} + \underbrace{\frac{1}{|\Omega|}\int_{\mathcal{S}_{\mathrm{d}}} \sup_{\boldsymbol{\sigma}^*\in\mathscr{C}} |(\boldsymbol{\sigma}^*\cdot\underline{n})\cdot[\![\underline{v}]\!]|}_{\Pi^{\mathrm{TT}}_{\mathrm{surf}}} \tag{II.131}$$

Note that the elementary surface element $\mathrm{d}S$ of $\mathcal{S}_{\mathrm{d}}$ is:

$$\mathrm{d}S = \frac{\sqrt{(1-\chi)^2+\chi^2w^2}}{1-\chi}\mathrm{d}\rho\times\rho\mathrm{d}\theta \tag{II.132}$$

With the chosen trial field, the surface term $\Pi^{\mathrm{TT}}_{\mathrm{surf}}$ becomes:

$$\begin{aligned}\Pi^{\mathrm{TT}}_{\mathrm{surf}}(\boldsymbol{D}) &= \frac{1}{\pi R^2 H}\frac{\sigma_0}{\sqrt{3}}\int_{\rho=r}^{R}\int_{\theta=0}^{2\pi}\frac{\sqrt{(1-\chi)^2+\chi^2w^2}}{1-\chi}\rho\,|[\![\underline{v}]\!]|\;\mathrm{d}\theta\,\mathrm{d}\rho\\ &= \frac{\sigma_0}{\sqrt{3}}\frac{|D_{33}|}{\chi w}\frac{(1-\chi)^2+\chi^2w^2}{1-\chi}\int_{\overline{\rho}=\chi}^{1}(1+\overline{\rho})\,\mathrm{d}\rho\\ &= \frac{\sigma_0}{2\sqrt{3}}|D_{33}|\frac{3+\chi}{\chi w}\left[(1-\chi)^2+\chi^2w^2\right]\end{aligned} \tag{II.133}$$

whereas the volume term $\Pi^{\mathrm{TT}}_{\mathrm{vol}}$ writes:

$$\begin{aligned}\Pi^{\mathrm{TT}}_{\mathrm{vol}}(\boldsymbol{D}) &= \frac{1}{\pi R^2 H}\sqrt{\frac{2}{3}}\sigma_0\int_{\rho=r}^{R}\int_{z=0}^{h\frac{R-\rho}{R-r}}\int_{\theta=0}^{2\pi}\rho\sqrt{\left(\frac{\partial v_\rho}{\partial\rho}\right)^2+\left(\frac{v_\rho}{\rho}\right)^2+\left(\frac{\partial v_z}{\partial z}\right)^2+\frac{1}{2}\left(\frac{\partial v_z}{\partial\rho}\right)^2}\,\mathrm{d}\theta\,\mathrm{d}z\,\mathrm{d}\rho\\ &= \sigma_0|D_{33}|\frac{1-\chi}{\sqrt{3}}\int_{\overline{\rho}=\chi}^{1}\int_{\overline{z}=0}^{\frac{1-\overline{\rho}}{1-\chi}}\frac{1}{\overline{\rho}}\sqrt{Q(\overline{\rho},\overline{z})}\,\mathrm{d}\overline{z}\,\mathrm{d}\overline{\rho}\quad\text{with}\quad Q(X_1,X_2)=4(X_1^2+X_1+1)+(\chi w)^2X_2^2\\ &= \sigma_0|D_{33}|\frac{1-\chi}{2\sqrt{3}}\int_{\overline{\rho}=\chi}^{1}\frac{1}{\overline{\rho}}\left[\frac{1-\overline{\rho}}{1-\chi}\sqrt{Q\left(\overline{\rho},\tfrac{1-\overline{\rho}}{1-\chi}\right)}+\frac{Q(\overline{\rho},0)}{w\chi}\log\left(\frac{\frac{1-\overline{\rho}}{1-\chi}w\chi+\sqrt{Q\left(\overline{\rho},\frac{1-\overline{\rho}}{1-\chi}\right)}}{\sqrt{Q(\overline{\rho},0)}}\right)\right]\mathrm{d}\overline{\rho}\end{aligned} \tag{II.134}$$

The stresses to coalescence predicted with Π^{TT} are plotted in Fig. II.54 and compared to the results of Benzerga and Leblond (2014) at various void aspect ratios w. On the one hand, the triangular velocity field does not improve the coalescence stress prediction compared to the parallel trial field when $w \leq 3$ (see Fig. II.55a,b). In particular, the triangular trial field fails when $\chi \to 1$ because the surface term $\Pi^{\mathrm{TT}}_{\mathrm{surf}}(\chi=1)$ is strictly positive. This is because the surface $\mathcal{S}_{\mathrm{d}}$ does not vanish when $\chi = 1$ as it should but becomes vertical instead. In comparison, the parallel field of Benzerga and Leblond (2014) brings $\Sigma_{33} = 0$ when $\chi = 1$. On the other hand, a small improvement is noticed for $w > 3$ around $\chi = 0.2$. This is coherent with the statement of Thomason (1985) that the trial triangular field is best suited for the regime where $w/\left(\frac{1}{\chi}-1\right)$ is high. Overall, the enhancement of the triangular velocity field seems very limited since the parallel velocity field used in Benzerga and Leblond (2014) provides a better upper bound for most practical applications.

A.2 Internal necking criterion obtained from Keralavarma and Chockalingam trial field

With the trial field chosen by Keralavarma and Chockalingam (2016) in the context of a cylindrical cell with coaxial void and Hill matrix material, the macroscopic plastic dissipation writes, after an approximation similar to Eq. II.78:

$$\Pi^{\mathrm{KS}}(\boldsymbol{D}) = \sigma_0|D_{33}|\sqrt{\frac{6}{5}}\int_{\chi^2}^{1}\frac{1}{x}\sqrt{\frac{1}{3}\hat{h}_t+\hat{h}_q x^2+\frac{5}{24}\hat{h}_a\frac{R^2}{h^2}x(1-x)^2}\,\mathrm{d}x \tag{II.135}$$

The elliptic integral of Eq. II.135 can be expressed from the three Legendre canonical forms, *i.e.* incomplete elliptic integrals of the first kind F, second kind E and third kind P. Defining S as:

$$S(X) = \frac{1}{3}\hat{h}_t+\hat{h}_qX^2+\frac{5}{24}\hat{h}_a(w\chi)^{-2}X(1-X)^2 = aX^3+bX^2+cX+d \tag{II.136}$$

it is possible to obtain:

$$\int_{\chi^2}^{1} \frac{\sqrt{S(x)}}{x}\,\mathrm{d}x = \frac{2}{3}\left\{\sqrt{S(x)}\frac{x+b-\rho_1}{x-\rho_1} + i\frac{\sqrt{a}}{\sqrt{\rho_1-\rho_2}}\left((\rho_1-\rho_2)bE\left[i\,\mathrm{arcsinh}\left(\frac{\sqrt{\rho_1-\rho_2}}{\sqrt{x-\rho_1}}\right), \frac{\rho_1-\rho_3}{\rho_1-\rho_2}\right]\right.\right.$$
$$+\ (\rho_1-\rho_2)(\rho_2+2\rho_3)F\left[i\,\mathrm{arcsinh}\left(\frac{\sqrt{\rho_1-\rho_2}}{\sqrt{x-\rho_1}}\right), \frac{\rho_1-\rho_3}{\rho_1-\rho_2}\right]$$
$$\left.\left.+\,3\rho_2\rho_3 P\left[\frac{\rho_1}{\rho_1-\rho_2}, i\,\mathrm{arcsinh}\left(\frac{\sqrt{\rho_1-\rho_2}}{\sqrt{x-\rho_1}}\right), \frac{\rho_1-\rho_3}{\rho_1-\rho_2}\right]\right)\right\}_{x=\chi^2}^{x=1} \quad \text{(II.137)}$$

with ρ_1, ρ_2 and ρ_3 the three roots of S for which explicit expressions exist (*e.g.* Cardan formulas). Considering that Legendre canonical forms are well-known special functions as they intervene in a wide class of physical problems, Eq. II.137 can be deemed an analytic form of Eq. II.135. Note that S is real-valued with $S(x) > 0$ for $x \geq 0$, so roots are either all strictly negative or $\rho_1 < 0$ and $\rho_3 = \overline{\rho_2}$. In the isotropic case, $S = \frac{1}{3} + X^2 + \frac{5}{24}(w\chi)^{-2}X(1-X)^2$, which has a strictly negative determinant. All arguments of E, F, and P can thus be negative or complex numbers, which might prove challenging for some numerical implementations.

3

Intergranular ductile fracture

Summary

Despite its numerous occurrences in metallic alloys, intergranular ductile fracture by growth and coalescence of grain boundary cavities has not been yet the subject of modeling efforts as intense as transgranular ductile fracture. In particular, the effect of crystal orientation couples was mostly disregarded to this day. In this chapter, the aforementioned theoretical gap is bridged by a handful of contributions. As in the case of trangranular ductile fracture, the ultimate goal set to this work is the development of a homogenized model ready to be implemented in a structural calculation.

In a first part, two yield criteria for intergranular void growth are derived using two different frameworks: kinematic limit analysis and variational methods. The first criterion is designed for spherical cavities, while the second one can account for ellipsoidal voids; both are validated against suitable unit cell computations. Then, in a second part, a yield criteria for intergranular void coalescence is developed for cylindrical cavities and tested successfully against numerical results. Next, a homogenized model for void growth is proposed in the third part and compared to finite strain unit cell computations. Finally, in a fourth part, experimental results on the intergranular fracture of an helium-implanted model austenitic stainless steel are described and discussed.

Contents

1 Intergranular void growth criteria **131**
- 1.1 Introduction 133
- 1.2 Numerical homogenization 135
  - 1.2.1 Crystal plasticity constitutive laws 136
  - 1.2.2 Unit-cell computations 136
  - 1.2.3 Simulation database 138
- 1.3 Plastic yield criterion for spherical voids 140
  - 1.3.1 Limit-analysis on porous Hill bi-materials 141
  - 1.3.2 Porous bi-crystal correction 142
  - 1.3.3 Assessment of yield surfaces 143
- 1.4 Viscoplastic potentials for porous bi-crystals with ellipsoidal voids 145
  - 1.4.1 Case $n = 1$: Hashin-Strikman estimates for periodical porous bi-crystals . 146
  - 1.4.2 Case $n = 1$: Assessment of gauge surfaces 148
  - 1.4.3 Case $n > 1$: Heuristical variational extension 149
  - 1.4.4 Case $n > 1$: Assessment of gauge surfaces 151
- 1.5 Application to the competition between intergranular and transgranular void growth 154
- 1.6 Conclusion and perspectives 156
- 1.A Definition and properties of Hill strain anisotropy tensor $\mathbb{H}^*$ 157
- 1.B Coalescence micromechanical indicator 157
- 1.C Crystalline laminate mechanical analysis 159
- 1.D Analytic expressions of g-functions 160
  - 1.D.1 Ellipsoidal voids 160
  - 1.D.2 Elliptic-cylindrical voids 160
- 1.E Porous crystal with infinite equivalent equiangular slip systems 162
  - 1.E.1 Pristine crystal 162
  - 1.E.2 Hollow sphere under hydrostatic loading 163

2 Intergranular void coalescence criterion **165**
- 2.1 Introduction 166
- 2.2 Problem statement 168
  - 2.2.1 Porous material description 168

2.2.2 Kinematic limit analysis . . . 168
2.3 Void coalescence in a von Mises bi-material . . . 170
2.3.1 Material description and trial velocity fields . . . 170
2.3.2 Macroscopic dissipation . . . 171
2.3.3 Yield surface . . . 172
2.3.4 Numerical assessment . . . 173
2.4 Void coalescence at a crystal interface . . . 177
2.4.1 Single crystal matrix behavior . . . 177
2.4.2 Approximate macroscopic dissipation . . . 178
2.4.3 Yield surface . . . 179
2.4.4 Numerical assessment . . . 180
2.4.5 Coalescence by internal necking . . . 180
2.4.6 Coalescence under combined tension and shear . . . 182
2.5 Discussion . . . 185
2.5.1 Effect of the localization pattern on ductility . . . 185
2.5.2 Competition between transgranular and intergranular void coalescence . 185
2.5.3 Intergranular void growth and coalescence by internal necking . . . 187
2.6 Conclusion and perspectives . . . 189
2.A Location and number of localization bands . . . 189
2.B Explicit resolution for the Mises bi-material . . . 191
2.B.1 Macroscopic dissipation . . . 191
2.B.2 Yield surface . . . 193
2.C Explicit resolution for the grain boundary . . . 194
2.C.1 Macroscopic dissipation . . . 194
2.C.2 Yield surface . . . 196
3 Homogenized model for intergranular void growth . . . **198**
3.1 Description of the homogenized model . . . 198
3.1.1 Finite strain framework . . . 198
3.1.2 Constitutive equations . . . 199
3.1.3 Numerical implementation . . . 200
3.2 Numerical assessment . . . 202
3.2.1 Porous unit cell simulations . . . 202
3.2.2 Comparison to the homogenized model . . . 203
3.2.3 Discussion . . . 206
3.3 Conclusion . . . 207
3.A Expression of useful derivatives . . . 207
3.A.1 Finite strain quantities . . . 207
3.A.2 Growth yield criterion . . . 208
4 Ductile fracture of a helium-implanted austenitic steel . . . **209**
4.1 Sample description . . . 209
4.1.1 Model material . . . 209
4.1.2 Sample preparation . . . 212
4.1.3 Helium implantation . . . 213
4.1.4 Quantification of the implantation homogeneity . . . 221
4.1.5 Quantification of oxidation after implantation . . . 221
4.1.6 Post-implantation annealing . . . 223
4.1.7 Characterization of irradiation defects . . . 223
4.2 Fracture behavior . . . 226
4.2.1 Mechanical testing . . . 226
4.2.2 Fracture surface investigation . . . 228
4.3 Temporary conclusion . . . 233
5 Conclusion and perspectives . . . **234**

1 Intergranular void growth criteria

As seen in the previous chapter dedicated to the micromechanical approach to transgranular ductile failure, such a framework enables a physical-based prediction of fracture at the crystal scale. Given the similarities between the mechanical evolution of cavities under mechanical loading in transgranular and intergranular ductile fracture evidenced in Section I.1, it seems natural to use the same approach to account for intergranular ductile fracture. This permits to benefit from all the methodological developments already available to homogenize porous materials.

Before detailing them, it may be appropriate to recall some theoretical results. Let us consider the representative volume element (RVE) Ω of a porous material with multiple phases i (voids being one of them) of domains Ω_i, each phase admitting a microscopic dissipation potential ϖ_i (*e.g.* generalized standard materials (Halphen and Nguyen, 1975)) such that:

$$\boldsymbol{\sigma} = \frac{\partial \varpi_i}{\partial \boldsymbol{d}} \ , \quad \boldsymbol{d} = \frac{\partial u_i}{\partial \boldsymbol{\sigma}} \quad \text{with} \quad u_i(\boldsymbol{\sigma}) = \sup_{\boldsymbol{d}} \left[\boldsymbol{\sigma} : \boldsymbol{d} - \varpi_i(\boldsymbol{d}) \right] \tag{III.1}$$

where $\boldsymbol{\sigma}$ and $\boldsymbol{d}$ are the microscopic Cauchy stress and strain-rate tensors. The effective stress potential u_i is defined from ϖ_i using the Legendre-Fenchel transform. It has been shown that the porous material also admits (macroscopic) potentials that verify (Hill, 1967; Hutchinson, 1976):

$$\boldsymbol{\Sigma} = \frac{\partial \Pi}{\partial \boldsymbol{D}} \ , \quad \boldsymbol{D} = \frac{\partial U}{\partial \boldsymbol{\Sigma}} \tag{III.2}$$

where $\boldsymbol{\Sigma}$ and $\boldsymbol{D}$ are (volume-averaged) macroscopic Cauchy and strain-rate tensors. Thus, determining the behavior law of the homogenized porous material amounts to computing Π or U. On the one hand, the macroscopic dissipation potential Π can be expressed as (Salençon, 1983; Benzerga and Leblond, 2010):

$$\Pi(\boldsymbol{D}) = \inf_{\underline{v} \in \mathcal{K}(\boldsymbol{D})} \frac{1}{|\Omega|} \sum_i \int_{\Omega_i} \varpi_i \left(\underline{v} \left(\underline{x} \right) \right) \tag{III.3}$$

where $\mathcal{K}(\boldsymbol{D})$ is the space of velocity fields $\underline{v}$ that are compatible with boundary conditions and consistent with $\boldsymbol{D}$, *i.e.* $\int_\Omega \boldsymbol{d}(\underline{v}) = \boldsymbol{D}$. On the other hand, the macroscopic stress potential writes (Idiart, 2006):

$$U(\boldsymbol{\Sigma}) = \inf_{\boldsymbol{\sigma} \in \mathcal{S}(\boldsymbol{\Sigma})} \frac{1}{|\Omega|} \sum_i \int_{\Omega_i} u_i \left(\boldsymbol{\sigma} \left(\underline{x} \right) \right) \tag{III.4}$$

where $\mathcal{S}(\boldsymbol{\Sigma})$ is the space of stress fields $\boldsymbol{\sigma}$ that are compatible with boundary conditions and consistent with $\boldsymbol{\Sigma}$, *i.e.* $\int_\Omega \boldsymbol{\sigma} = \boldsymbol{\Sigma}$. However, calculation of these potentials is usually a formidable task that can only be performed numerically; thus, additional simplifications are required for an analytical treatment. Among those approximations, two stand out by their versatility and efficiency:

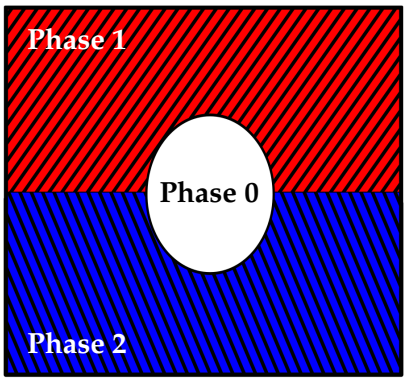

FIGURE III.1: Representative volume element of a material experiencing intergranular void fracture. Crystals are shown in colors and the void is depicted in white.

- **Approximate limit analysis:** In this framework, boundary conditions are generally considered to be kinematic ($\underline{v}(\underline{x}) = \boldsymbol{D} \cdot \underline{x}$ on $\partial\Omega$), static ($\boldsymbol{\sigma} \cdot \underline{n} = \boldsymbol{\Sigma} \cdot \underline{n}$ with $\underline{n}$ the normal to the boundary $\partial\Omega$) or periodic, as these three choices are consistent with the Hill-Mandel lemma (*e.g.* Nemat-Nasser and Hori (1993)). In its most common use, approximate limit analysis consists of substituting the space $\mathcal{K}(\boldsymbol{D})$ of trial velocity fields by a subspace of $\mathcal{K}(\boldsymbol{D})$ whose elements all admit an analytical potential (Salençon, 1983). For instance, this was used by Rice and Tracey (1969) to obtain their famous law of void growth, and in Section II.3. Note that, in this case, approximate limit analysis is an *exterior* method because it brings an upper bound of Π. Alternatively, this method can consist of reducing the space $\mathcal{S}(\boldsymbol{\Sigma})$ of trial stress fields to a subspace whose elements are such that an analytical potential can be computed for each of them (Benzerga and Leblond, 2010). This time, it is an *interior* method because it brings an upper bound of U and thus a lower bound of Π.

- **Variational method by linear composite comparison:** A linear material corresponding to the porous material

is obtained by supposing that all phases are linear materials, *i.e.* for each phase i, there is a fourth-order tensor $\mathbb{S}_i$ such that $u_i(\boldsymbol{\sigma}) = \frac{1}{2}\boldsymbol{\sigma} : \mathbb{S}_i : \boldsymbol{\sigma}$ (or equivalently $\varpi_i(\boldsymbol{d}) = \frac{1}{2}\boldsymbol{d} : \mathbb{S}_i^{-1} : \boldsymbol{d}$). The stress potential of the linear composite for a trial stress field $\boldsymbol{\sigma}$ shall be referred as $U_{\mathrm{L}}(\boldsymbol{\sigma})$. Then, a triangular inequality yields:

$$U(\boldsymbol{\Sigma}) \geq \inf_{\boldsymbol{\sigma} \in \mathcal{S}(\boldsymbol{\Sigma})} \langle U_{\mathrm{L}}(\boldsymbol{\sigma}) \rangle_{\Omega} - \inf_{\boldsymbol{\sigma} \in \mathcal{S}(\boldsymbol{\Sigma})} \langle U(\boldsymbol{\sigma}) - U_{\mathrm{L}}(\boldsymbol{\sigma}) \rangle \tag{III.5}$$

Sound variational estimates inspired by the work of Hashin and Shtrikman (1963) can be obtained for the first term by supposing that the stress is homogeneous in each phase of the linear composite (*e.g.* Willis (1977) and Nemat-Nasser et al. (1993)):

$$\inf_{\boldsymbol{\sigma} \in \mathcal{S}(\boldsymbol{\Sigma})} \langle U_{\mathrm{L}}(\boldsymbol{\sigma}) \rangle_{\Omega} \approx \frac{1}{2}\boldsymbol{\Sigma} : \mathbb{S}\left(\mathbb{S}_i\right) : \boldsymbol{\Sigma} \tag{III.6}$$

where $\mathcal{S}$ is a modulus tensor depending on all $\mathcal{S}_i$. The major challenge remains to find an estimate for the second term of Eq. III.5 and maximize the sum of the two terms relative to the set of linearization moduli $\mathbb{S}_i$, *i.e.* the linear comparison composite has to be chosen carefully. The inequality of Eq. III.5 indicates an exterior method but later approximations can endanger the lower-bound character: for most practical applications, a simple estimate of U is sufficient. For additional details on this method, see for instance Castañeda and Suquet (1997) and Idiart (2006).

In the following, both methods will be used to obtain yield criteria for void growth at porous grain boundaries: one for spherical voids and the other for ellipsoidal voids. Indeed, the RVE of a porous grain boundary is a three-phased material (see Fig. III.1): void (phase 0), crystal 1 (phase 1), and crystal 2 (phase 2). The dissipation potential of the void ϖ_0 is taken as 0 and the stress potential of single crystals can be obtained by direct integration of Eq. I.11 (see Eq. III.25). This is carried out in the remainder of this section, reproduced from a scientific publication (Sénac et al., 2023a).

Void growth yield criteria for intergranular ductile fracture

Cédric Sénac, Jérémy Hure, Benoît Tanguy

Journal of the Mechanics and Physics of Solids — 2023

Abstract

Ductile fracture through growth and coalescence of intergranular cavities is a failure mode observed experimentally in many metallic alloys used in industrial applications. Simulation of this fracture process in polycrystalline aggregates requires modeling the plastic yielding of porous boundaries. However, classical yield criteria for porous materials such as the Gurson–Tvergaard–Needleman model and its current extensions cannot account for the complex coupling between loading state, crystallographic orientations, void shape, and material behavior at grain boundaries. In order to bridge this modeling gap, two yield criteria for intergranular ductile void growth are proposed. The first one is a GTN-like model derived from limit analysis which, once calibrated, accounts for spherical voids at the interface of rate-independent crystals. The second one is developed from a variational approach and predicts yielding in viscoplastic crystals containing intergranular ellipsoidal cavities. Both models are validated against a wide database of numerical limit-analysis of porous bi-crystals using an FFT solver. Satisfying agreements are obtained, paving the way to microstructure-informed intergranular ductile fracture simulation. The interplay between plastic yielding inside grains and along grain boundaries is finally studied based on the proposed yield criterion.

1.1 Introduction

The process of void nucleation, growth and coalescence is among the dominant ductile failure modes in metallic alloys and can be transgranular as well as intergranular. In the latter, void growth and coalescence occur at grain boundaries due to intense intergranular plastic flow (Hornbogen and Kreye, 1982; Vasudévan and Doherty, 1987). In that case, fracture surfaces display intergranular facets covered in fine dimples. Reliable physical observations of ductile intergranular fracture date back more than fifty years (Plateau et al., 1957) and span a large class of metallic alloys and loading conditions. However, due to insufficient magnification, these facets may appear flat at first glance and can be mistakenly identified as proof of intergranular brittle fracture, impairing comprehensive identification of intergranular ductile fracture occurrences (Lynch, 1991b).

Precipitation-hardened alloys are especially prone to dimpled intergranular fracture at low homologous temperature, regardless of crystal lattice structures (Table III.1). First and foremost, aluminum alloys are the material class for which this fracture mode was first undoubtedly highlighted (Varley et al., 1957; Thomas and Nutting, 1957; Thomas and Nutting, 1959; Unwin and Smith, 1969). Among the most cited alloys: Al-Zn-Mg (Vasudévan and Doherty, 1987), Al-Cu (Kuramoto et al., 1996) and Al-Mg-Si (Poole et al., 2019; Ringdalen et al., 2021). Aluminum alloys containing lithium, divided in three successive generations, form a whole class of materials vulnerable to intergranular fracture by growth and coalescence of cavities (Suresh et al., 1987; Vasudévan and Doherty, 1987; Lynch et al., 2002; Pasang et al., 2012; Decreus et al., 2013). All precipitation-hardened aluminum alloys display precipitate-free zones (PFZ) around grain boundaries; softer than grain interiors, they play an important role in the localization of plasticity (Gräf and Hornbogen, 1977; Vasudévan and Doherty, 1987). The second most common occurrence of intergranular ductile fracture is in nickel superalloys: for instance, Inconel X-750 (Mills, 1980), MAR-M200 (Vasudévan and Doherty, 1987) and Inconel 718 (Chang et al., 2014; Lin et al., 2017). The absence of PFZ in some of these alloys uncovers another elementary phenomenon in which grain boundary precipitation is so detrimental that intergranular soft zones are not mandatory to foster grain boundary cavity growth (Vasudévan and Doherty, 1987). Similar behaviors are observed in other metallic materials: magnesium alloyed with rare earth elements (*e.g.* Mg-11Gd-2Nd-0.4Zr) experiences this failure mode at specific precipitation aging (Zheng et al., 2008); metastable β-titanium alloys exhibit dimpled intergranular fracture due to grain boundary precipitates of phase α, which is a hurdle to their wider use in aerospace field (Foltz et al., 2011).

Leaving precipitation aging aside, overheating of sulfur-rich steels during austenitization favors intergranular ductile fracture by enhancing grain boundary MnS precipitation (Tsun, 1953; Schulz and McMahon, 1973). Besides, intergranular ductile fracture may be promoted by neutron irradiation (Hojná, 2017), especially when helium bubbles

Crystal lattice	**FCC:** peak-aged A1-4.5Zn-1.5Mg (Kuramoto et al., 1996)	**BCC**: lamellar Ti-5Al-5Mo-5V-3Cr-0.5Fe (Foltz et al., 2011)	**HCP:** aged Mg-11Gd-2Nd-0.4Zr (Zheng et al., 2008)
Grain boundary	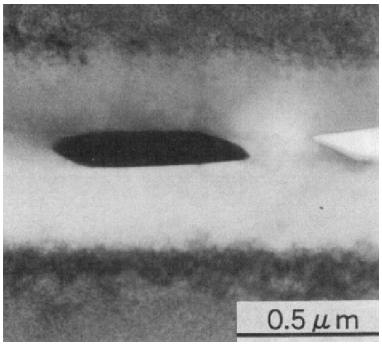	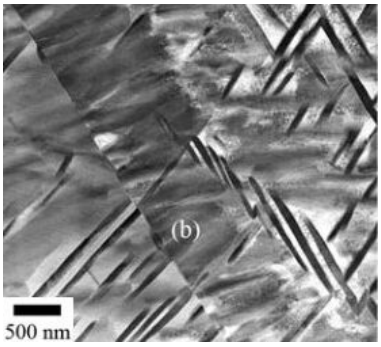	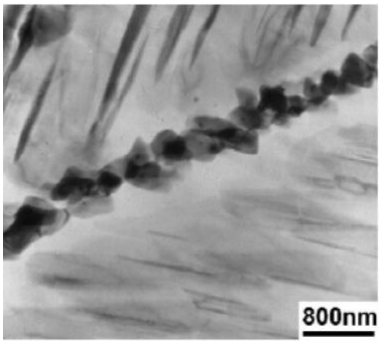
Fracture surface	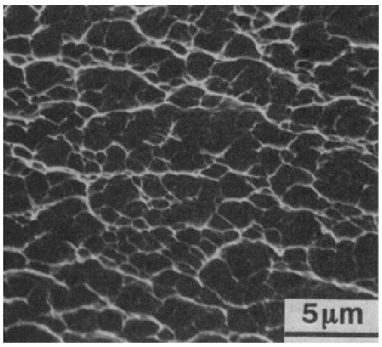	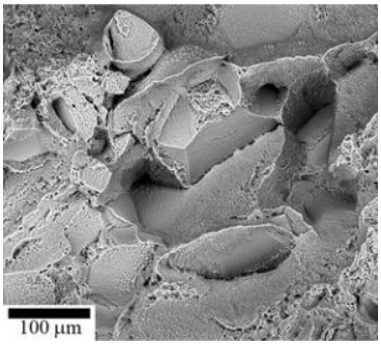	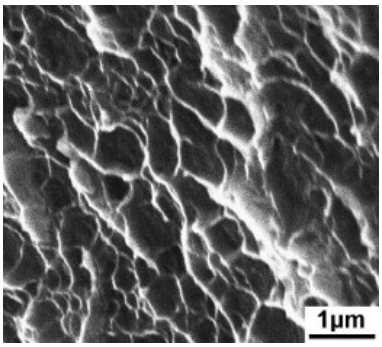
f_p	0.05	0.1	0.5

TABLE III.1: Typical literature observations of low homologous temperature dimpled intergranular fracture in precipitation-hardened alloys for different crystal structures: face-centered cubic (FCC), body-centered cubic (BCC) and hexagonal close-packed (HCP). f_p is the volume fraction of grain boundary precipitates in an inter-crystalline layer of width equal to the grain boundary precipitate spacing.

form at grain boundaries, as reported in austenitic steels (Miura et al., 2015) and Nickel-based alloys (Judge et al., 2012; Judge et al., 2015; Demkowicz, 2020). Finally, for the sake of completeness, it should be noted that intergranular fracture at high homologous temperature can also be classified as ductile fracture when purely plastic contributions exceed the intensity of diffusion phenomena associated with creep (Pavinich and Raj, 1977; Riedel, 1987; Kassner and Hayes, 2003). Examples of such situations may be the high strain rate deformation (Fu and Zhang, 2020) and stress-relief cracking (Hornbogen and Kreye, 1982; Chabaud-Reytier et al., 2003) of austenitic steels and the fracture of Inconel X-750 (Venkiteswaran and Taplin, 1974; Mills, 1980).

Since the seminal works of Rice and Tracey (1969), Gurson (1977) and Thomason (1985), considerable efforts have been made to model ductile failure through homogenization of the mechanical behavior of porous materials, and extensive reviews were published on the matter (Besson, 2010; Benzerga and Leblond, 2010; Pineau et al., 2016). Results contained therein, which mainly concern voids in isotropic or Hill materials, have been extended to single crystals with internal cavities in the last decade (Han et al., 2013; Paux et al., 2015; Mbiakop et al., 2015b; Ling et al., 2016; Song and Ponte-Castañeda, 2017a; Hure, 2019; Khavasad and Keralavarma, 2021). All these studies consider homogeneous matrix materials and are thus designed to model transgranular fracture. Nevertheless, the GTN model, relevant for isotropic porous materials, was used to conduct finite element computations of intergranular ductile fracture in precipitation-hardened alloys, either with void-nucleating boundaries and pristine grains (Becker et al., 1989; Molkeri et al., 2020), or with different material parameters in the PFZ and in the grain interior (Pardoen et al., 2003; Pardoen et al., 2010; Fourmeau et al., 2015) to study competition between fracture modes. This yield function was also used in the context of metastable β-titanium alloys (Osovski et al., 2015; Li et al., 2017). These models rely on volume homogenization, but grain boundaries are two-dimensional domains; Becker et al. (1989) recommend setting the width of the homogenized microstructure to grain boundary precipitate spacing: conventional precipitate volume fraction f_p is reported in Table III.1 for alloys taken as examples. The outcomes of these first studies are valuable but show some limitations. First, numerical homogenization has shown that macroscopic yield surfaces of

macroscopically isotropic polycrystalline aggregates with intergranular voids are quite distinct from the ones obtained by supposing that voids are in a von Mises isotropic matrix (Lebensohn et al., 2011; Nervi and Idiart, 2015). Then, at the mesoscale of the porous boundaries, all isotropic models previously mentioned are intrinsically not adapted to model complex effects coupling crystallographic orientations, material non-linearity and void size/shape. Therefore, the isotropic ductile modeling approach is challenged for macroscopic and mesoscopic applications.

From the earliest times of porous materials homogenization, unit-cell computations have accompanied analytic developments by providing numerical evaluations of yield surfaces (Koplik and Needleman, 1988), which is of paramount importance for the calibration and validation of models. Following their successful application to isotropic and monocrystalline matrices, finite strain unit-cell simulations were performed on voided bi-crystals in a handful of studies. The majority of these works focused on the void growth stage, *i.e.* deformation situations where plasticity is diffuse and cavities do not significantly interact with each other in the periodic void lattice; face-centered cubic (FCC) crystals were mostly considered (Wen and Yue, 2007; Zhang et al., 2008; Liu et al., 2009; Yang and Dong, 2009; Li et al., 2015; Chen et al., 2019; Dakshinamurthy et al., 2021) except for one study which conducted simulations on a body-centered cubic (BCC) material (Jeong et al., 2018) and another one which considered BCC-HCP bi-crystals (Asim et al., 2019a). Void coalescence — *i.e.* the stage in which plasticity localizes in ligaments between cavities — was considered in FCC bi-crystals in Liu et al. (2010). The main conclusion to be drawn is the fact that void growth at grain boundaries is not reducible to void growth in single crystals, all the more to void growth in an isotropic matrix.

Both unit-cell computations and homogenized modeling of ductile intergranular fracture have focused on (initially) spherical voids. However, the void shape is known to play an important role when voids significantly differ from ideal spheres (Mbiakop et al., 2015b; Song and Ponte-Castañeda, 2017b), *i.e.* approximately when one of the void axes ratios exceeds 2. For smaller deviations from sphericity, the effect on yield surfaces is deemed negligible and yield criteria developed for spherical cavities keep their validity (Hure, 2021). Experimental observations of intergranular void shapes during grain boundary ductile fracture are tricky and, to the authors' knowledge, have never been conducted. Dimples seen on fracture surfaces are usually quite round (see Table III.1), which may advocate for spheroidal cavities of symmetry axis perpendicular to the grain boundary. The fact that precipitates responsible for intergranular void nucleation are usually elongated along grain boundaries (Vasudévan and Doherty, 1987; Kuramoto et al., 1996) also suggests such void shapes. On the other hand, helium bubbles involved in the intergranular ductile fracture of irradiated metals are spherical (Miura et al., 2015).

It is therefore concluded that in order to enhance understanding and simulation of intergranular ductile fracture, there is a need for models predicting the yield surface of porous grain boundaries, with both spherical and ellipsoidal cavities; this is the goal set to the present study.

The paper is organized as follows: in a first part, a database of porous bi-crystal unit-cell limit-analysis simulations is gathered and described for an FCC material, including a larger set of crystallographic orientation couples and microstructure parameters than currently available in the literature. In a second part, a Gurson-type yield criterion for the growth of intergranular spherical voids is derived through limit analysis, along with heuristic corrections of the hydrostatic and the deviatoric terms. In the last part, a gauge surface accounting for intergranular ellipsoidal void shapes is obtained using a variational method. The results of the two yield functions are assessed against numerical homogenization results obtained in the first part. Finally, the implications of those models regarding the competition between intergranular and transgranular failure are briefly discussed.

1.2 Numerical homogenization

In the following, vectors are shown as $\underline{a}$ of norm a, second-order tensors as $\boldsymbol{a}$ and fourth-order tensors as $\mathbb{A}$, although $\mathbb{R}$ and $\mathbb{Z}$ still respectively refer to the set of real numbers and the set of integers — they shall be superscripted with a star if 0 is excluded from the set. Numerical limit-analysis simulations are performed in order to assess yield surfaces of porous grain boundaries (Madou and Leblond, 2012b); small strain assumption is thus used. Such kind of simulations differ from those existing in the porous bi-crystal literature (*e.g.* Dakshinamurthy et al. (2021)) as the idea is to evaluate yield stress for fixed parameters, either geometrical or material-based (perfect plasticity). Crystal plasticity constitutive laws modeling the grains are first described, and then the unit cells considered are detailed. $\boldsymbol{\sigma}$ stands as the (Cauchy) stress tensor.

1.2.1 Crystal plasticity constitutive laws

Additive decomposition of the total strain into elastic and plastic parts $\boldsymbol{\varepsilon} = \boldsymbol{\varepsilon}^{\mathrm{el}} + \boldsymbol{\varepsilon}^{\mathrm{p}}$ is considered, and elasticity obeys an isotropic Hooke law of Young modulus $Y = 10^3$ MPa and Poisson ratio $\nu = 0.49$. Plasticity is assumed to be related to the glide of dislocations, that can happen in a limited number of directions, called crystallographic slip systems, defined by a slip plane (whose normal is along unit vector $\underline{m}_s$) and a slip direction (of unit vector $\underline{n}_s$), and represented by the following symmetric Schmid tensor: $\boldsymbol{\mu}_s = \frac{1}{2}(\underline{m}_s \otimes \underline{n}_s + \underline{n}_s \otimes \underline{m}_s)$. Other plasticity mechanisms such as twinning are disregarded. A face-centered cubic (FCC) material is considered for numerical homogenization, with $K = 12$ independent slips systems — the $\{111\}\langle 110\rangle$ family. Using viscoplastic regularization, the plastic strain rate writes (Hutchinson, 1976):

$$\dot{\boldsymbol{\varepsilon}}^{\mathrm{p}} = \sum_{s=1}^{K} \left[\dot{\gamma}_0 \left(\frac{|\boldsymbol{\sigma} : \boldsymbol{\mu}_s|}{\tau_s^{\mathrm{c}}} \right)^n \mathrm{sgn}(\boldsymbol{\sigma} : \boldsymbol{\mu}_s) \right] \boldsymbol{\mu}_s = \sum_{s=1}^{K} \dot{\gamma}_s \boldsymbol{\mu}_s \tag{III.7}$$

where τ_s^{c} is the critical resolved shear stress of the s^{th} system, $\dot{\gamma}_0$ a reference slip-rate (set to $1\,\mathrm{s}^{-1}$) and $\dot{\gamma}_s$ the slip rate of system s. (τ_s^{c}) are fixed to the same value of $\tau^{\mathrm{c}} = 88$ MPa. n denotes the Norton exponent: the case $n \to +\infty$ corresponds to rate-independent plasticity while $n = 1$ represents linear Maxwell-type viscoelasticity. In the following, the value $n = 100$ will be chosen to stand for rate-independence.

1.2.2 Unit-cell computations

In order to study the mechanical behavior of porous grain boundaries, different periodic unit-cells can be chosen. Note that grain boundaries are not perfectly periodic structures, but this assumption is required by the FFT solver used. A microstructure composed of two single crystals of different crystallographic orientations (phases 1 and 2) regularly laminated along direction $\underline{e}_1$ and with periodic square arrays of cavities (phase 0) at $(\underline{e}_2, \underline{e}_3)$-grain boundaries is considered. Porosity — *i.e.* void volume fraction — is denoted f. Perfect bounding is assumed between the crystals. Such a periodic distribution corresponds to the configuration shown in Fig. III.2b, the width of crystal layers taken equal to the spatial period of cavities along $\underline{e}_2$ and $\underline{e}_3$. A simple way of alleviating computational burden consists of inserting cavities at every other boundary, leading to the cubical geometry of Fig. III.2a and dividing the unit-cell volume by two, provided that the two configurations approximately lead to the same predictions; such an assumption will be discussed in the following. Other configurations shown on Figs. III.2c,d,e will be studied later. Single crystal behavior is the one presented in Section III.1.2.1 while cavities are modeled as an elastic material of vanishing stiffness tensor. Note that other representative volume elements (RVE) could have been chosen (*e.g.* hollow sphere) for a numerical homogenization using FEM. Choosing a cuboid RVE allows to benefit from FFT solver efficiency.

Simulations are performed in the fast Fourier transform-based `AMITEX_FFTP` code (CEA, 2020) using periodic boundary conditions. Unit cells are discretized using cubical voxels. A unique material behavior (void, crystal 1,

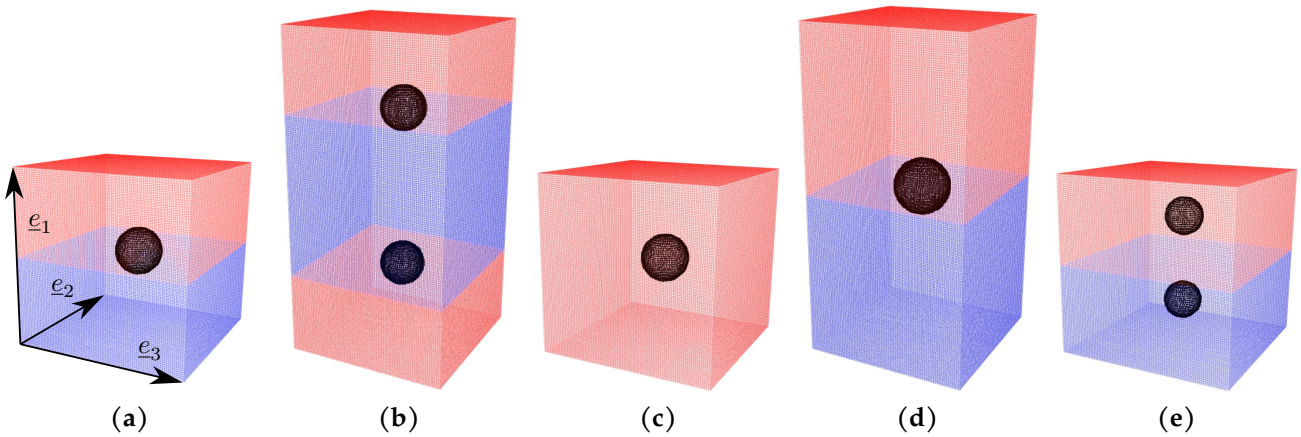

FIGURE III.2: Periodic unit-cell configurations considered in the numerical limit analysis: **(a)** porous boundary; **(b)** symmetric porous boundary, **(c)** porous single crystal, **(d)** elongated porous boundary and (e) porous laminate. Single crystals are shown in red/blue, and cavities are in black. All are pictured with 1% porosity and spherical voids.

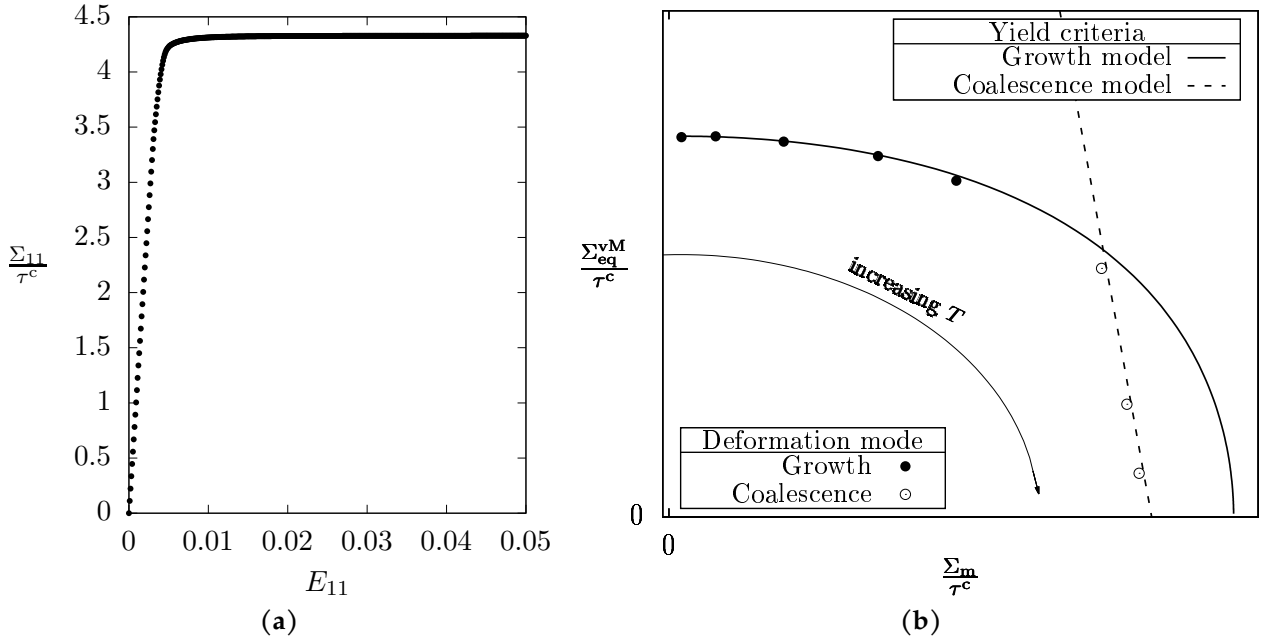

FIGURE III.3: **(a)** Stress saturation of Σ_{11} occurring during small strain yielding of a porous boundary with orientation couple #1 at $T = 1$, $\theta = 0$ and $f = 0.01$; **(b)** Sketch of a typical numerical yield surface (points) in a meridian half-plane (fixed θ), along with multi-surface plasticity modeling approach (lines).

and crystal 2) is assigned to each voxel. Application and validation of FFT numerical methods for (porous) crystals can be found in previous studies (Barrioz, 2019; Barrioz et al., 2019). Unit-cells are subjected to the macroscopic (volume-average) stress tensor $\boldsymbol{\Sigma}$ whose principal axes are aligned with unit-cell lattice directions and whose main stress component[1] is along $\underline{e}_1$:

$$\boldsymbol{\Sigma} = \Sigma_{11}\boldsymbol{\Sigma}^{(0)}(T,\theta) = \frac{\Sigma_{11}}{\cos\theta + \frac{3}{2}T}\begin{pmatrix} \cos\theta + \frac{3}{2}T & 0 & 0 \\ 0 & -\cos\left(\theta + \frac{\pi}{3}\right) + \frac{3}{2}T & 0 \\ 0 & 0 & -\cos\left(\theta - \frac{\pi}{3}\right) + \frac{3}{2}T \end{pmatrix} \tag{III.8}$$

where T is the stress triaxiality — *e.g.* the ratio between hydrostatic stress Σ_m and von Mises equivalent stress Σ_{eq}^{vM} — and θ is the Lode angle defined as (Danas and Ponte Castañeda, 2012):

$$\cos 3\theta = \frac{27}{2}\frac{\det\left(\boldsymbol{\Sigma} - \Sigma_m \boldsymbol{I}\right)}{\left(\Sigma_{eq}^{vM}\right)^3} \tag{III.9}$$

with $\theta \in \{0, \pi/3\}$ corresponding to axisymmetric loadings and $\theta = \pi/6$ to in-plane shear loadings. The loading is controlled by the linear increase of (volume-average) strain component E_{11} until small strain yielding of the unit-cell, which manifests by the saturation of $\boldsymbol{\Sigma}$ to values corresponding to the yield stress of the unit-cell (see Fig. III.3a). The macroscopic strain rate component D_{11} is set to $0.05\ s^{-1}$. In the limit $n = +\infty$, yield surfaces do not depend on this strain rate. Note that the elastic behavior of the crystals does not influence the plastic yielding — *i.e.* the saturated value of $\boldsymbol{\Sigma}$. In that sense, these unit-cell simulations are consistent with the theoretical framework of limit-analysis (Leblond et al., 2018).

Upon saturation, von Mises equivalent stress Σ_{eq}^{VM} and mean stress Σ_m are computed to draw the yield surface in the $\left(\Sigma_m, \Sigma_{eq}^{VM}\right)$ meridian plane. A porous material's typical numerical yield surface is shown in Fig. III.3b. Unit-cell simulations can be divided into two groups according to the deformation mode they display. Low stress triaxiality ratios correspond to diffuse plasticity (see Appendix III.1.B, Fig. III.16a) whereas localized plasticity occurs at high triaxiality ratios (see Appendix III.1.B, Fig. III.16c). The first deformation mode is referred to as void growth while the second is called void coalescence (Pineau et al., 2016): on Fig. III.3b, the relevant mode is indicated for each

[1] In the cases considered below, $\cos\theta + \frac{3}{2}T$ never vanish; such a situation would mean that the loading should be controlled using another principal axis.

numerical simulation — from now on, simulations involving coalescence will be identified as hollowed-out symbols. Details on the determination of the deformation mode of a given unit-cell simulation are given in Appendix III.1.B. In most studies in the literature, separate yield criteria are proposed to describe them; within a multi-surface plasticity framework, these yield criteria are considered simultaneously (Benzerga and Leblond, 2010; Keralavarma, 2017). Coalescence criteria are usually variations over Thomason's model (Thomason, 1985) which sets a limit value to the main principal macroscopic stress Σ_{I}. Thus, these models manifest as straight lines[2] in the meridian place (see Fig III.3b). Since the objective of this study is to provide a void growth model, the analytical yield surface will be checked to reproduce simulations displaying growth (full points) but special care will also be taken that the criterion is *exterior* to simulations displaying coalescence (hollowed-out points) in order for the multi-surface plasticity approach to be effective.

1.2.3 Simulation database

As in the case of porous single crystals (Sénac et al., 2022), yield surfaces are expected to depend on crystallographic orientations significantly. Therefore, forty random orientations gathered in twenty couples are studied here; see Table III.2 for their definition and colors with which they will be represented in all subsequent graphs. For fixed Lode angle θ, visualization of yield surfaces will be made in the plane $(\Sigma_{\mathrm{m}}, \Sigma_{\mathrm{eq}}^{\mathrm{vM}})$, *i.e.* by considering various stress triaxialities. This corresponds to yield surfaces' meridian half-planes. Since the matrix material behaves similarly under tension and compression, the macroscopic yield surface is centrally symmetric (*i.e.* the yield stress for (T, θ) is equal to that at $(-T, \pi/3 - \theta)$) so that it is enough to study the set of loadings for which $T > 0$ and $\theta \in [0, \pi/3]$. To cover the range from deviatoric stress-state to hydrostatic loading, T takes the following values: 0, $1/3$, 1, 2, 3, 6, 10, 40.

	#	Crystal 1			Crystal 2		
		ϕ_1 (°)	Φ (°)	ϕ_2 (°)	ϕ_1 (°)	Φ (°)	ϕ_2 (°)
●	1	93.48	53.17	315.41	40.96	84.69	136.94
●	2	65.60	112.22	83.99	166.48	40.56	139.94
●	3	109.49	111.84	171.00	124.35	34.17	267.58
●	4	117.83	107.35	66.79	141.70	100.97	29.13
●	5	16.78	55.01	63.50	142.68	53.37	29.46
	6	11.08	98.29	28.20	303.92	75.55	149.39
	7	134.39	133.33	7.13	266.58	63.38	310.06
	8	306.96	149.84	66.68	243.19	117.06	258.27
●	9	229.38	96.02	323.86	102.10	81.67	264.81
●	10	145.96	121.95	3.42	103.35	82.43	137.59
	11	73.67	120.61	85.47	302.65	57.31	202.39
	12	18.40	105.32	226.75	268.41	94.25	240.26
●	13	80.74	111.44	185.63	192.59	45.76	0.65
	14	352.79	112.15	125.60	228.63	93.54	261.97
	15	70.28	56.03	22.94	70.74	76.48	243.32
●	16	81.82	113.92	64.02	80.34	65.46	267.16
	17	120.04	67.52	178.16	328.21	119.29	201.63
	18	129.85	49.16	99.07	296.23	120.50	328.96
	19	230.74	161.52	140.50	81.97	64.24	149.44
	20	345.16	129.65	267.30	154.50	61.95	181.57

TABLE III.2: Euler angles (Bunge convention) of the 20 couples of random crystallographic orientations.

The equivalence of unit-cell configurations displayed in Fig. III.2a,b was checked on representative cases: no noticeable difference was seen on yield surfaces. This finding is no surprise: as long as cavities do not interact with each other between distinct $(\underline{e}_2, \underline{e}_3)$-planes (*e.g.* by necklace coalescence or out-of-plane shear-banding), the upper part of Fig. III.2b is independent of the lower part, thus both will have the same behavior as Fig. III.2a.

Before studying extensively porous bi-crystals, it is useful to assess differences between a porous grain boundary (Fig. III.2a) and porous single crystals (Fig. III.2c) of crystallographic orientations corresponding to the two constitutive grains of the bi-crystal. This was performed with spherical cavities considering all orientation couples with Norton exponents $n = 1$, 3, 10 and 100. Only data for $n = 100$ are shown in Fig. III.4 as other n displayed similar tendencies. An obvious remark is that a porous bi-crystal yield surface is reducible to neither of its crystal constituents' individual behavior, justifying the present study. Such a finding was already reported by Jeong et al. (2018) and Dakshinamurthy et al. (2021) who described porous bi-crystals showing intermediate yield stress compared to the two individual porous grains, corresponding to Fig. III.4a. However, due to the small number of orientation cou-

[2] Taking the equivalent von Mises stress of Eq. III.8 brings $\Sigma_{\mathrm{eq}}^{vM}\left(\cos\theta + \frac{3}{2}\frac{\Sigma_{\mathrm{m}}}{\Sigma_{\mathrm{eq}}^{vM}}\right) = \frac{3}{2}\Sigma_{11}$, which is a straight-line in a meridian plane, *i.e.* at fixed Lode angle θ.

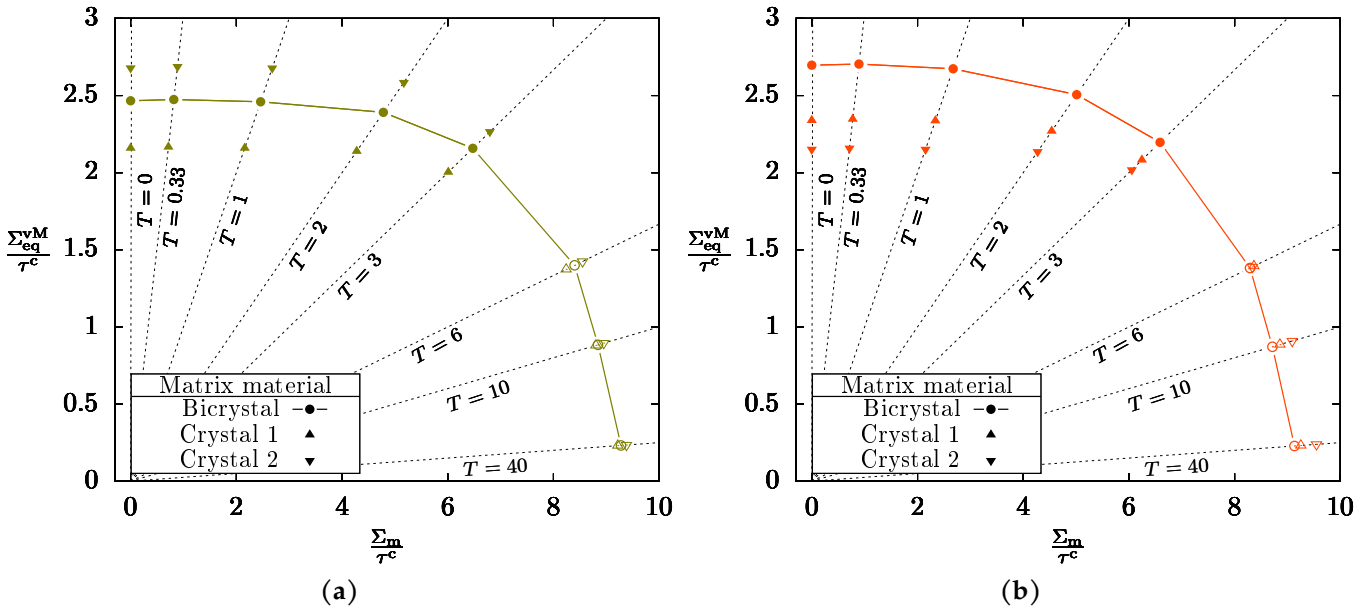

FIGURE III.4: Yield surfaces of porous bi-crystals (Fig. III.2a) and corresponding porous constitutive single crystals (Fig. III.2c) at $f = 0.005$, $n = 100$ and $\theta = 0$: **(a)** crystal orientation couple #3; **(b)** crystal orientation couple #2. Hollowed-out symbols mark simulations in which the deformation mode has been identified as void coalescence.

ples and triaxiality ratios studied in the existing literature, other possible bi-crystal behaviors were overlooked: in Fig. III.4b, the yield stress of the porous bi-crystal is greater than yield stresses of both porous single crystals from low to medium stress triaxialities and smaller at high triaxialities. However, in no instance was the porous bi-crystal yield stress smaller than both porous grain yield stresses for deviatoric loadings. This property shall be demonstrated in the limit of small porosities in Appendix III.1.C. Overall, for random orientations, spherical voids, axisymmetric loading conditions, and triaxialities ranging from $T = 0$ to $T = 3$, plastic yielding seems to occur for lower stress in at least one of the porous single crystal compared to the porous boundary. Such a general rule hints at the fact that a material with homogeneous porosity is more susceptible to transgranular ductile fracture than to intergranular ductile fracture; in order for such a failure mode to arise, boundaries have to be weakened compared to grain interiors: for instance greater porosity, different void shape, softer behavior, lower hardening capacity (see Pardoen et al. (2003) on that subject).

Since void growth yield criteria for single crystals are available, a legitimate question is whether such models could account for porous boundaries by delocalizing the cavity from either side of the interface. Instead of a unique void of volume f – the unit-cell has a volume of 1 – set at mid-height, voids of volume $f/2$ are located at mid-width of each crystal, effectively turning Fig. III.2a into Fig. III.2e. As shown in Fig. III.5a, the porous laminate unit-cell (Fig. III.2e) yield surface diverges significantly at high triaxialities from the porous boundary (Fig. III.2a) yield surface. The wider stress reversibility domain of the former makes it impossible to invoke earlier coalescence to explain such a discrepancy: unit-cells *do* have a different void growth behavior, with voids located at grain boundaries being more damaging than voids inside grains[3]. For lower Norton exponents n (Eq. III.7), discrepancies are smaller but still noticeable.

Finally, a necessary verification is to quantify the effect of unit-cell aspect ratio at fixed porosity: if this effect is negligible, simulations can be restricted to cubic cells. This is done by comparing Fig. III.2b,d unit-cell yield surfaces in Fig. III.5b. No noticeable discrepancy is seen from low to intermediate triaxialities between the two configurations. However, as the cavities are closer in the plane $(\underline{e}_2, \underline{e}_3)$ in the configuration Fig. III.2d, coalescence is more intense, leading to a strong contraction of the yield surface near the hydrostatic point. Since this deformation mode is not the subject of this study, it shall be considered in the following that unit-cell height — and more generally unit-cell geometry, see the discussion in Danas and Castañeda (2009) — has no effect on void growth plastic yielding.

Given the preliminary results gathered in this section, Fig. III.2a unit-cell configuration is chosen to assess void growth yield surfaces of porous grain boundaries. Using this unit-cell, three batches of simulations were conducted

[3]Note that it is not in contradiction to what have been said earlier about porous single crystals: voids in Fig. III.2e crystals are smaller so that both unit-cells Fig. III.2a,e have equal void volume fractions.

with the aforementioned set of crystal orientations and triaxiality ratios: a first set of computations was carried out with spherical voids at porosities $f \in \{0.001, 0.005, 0.01, 0.05, 0.1, 0.2, 0.3\}$ and $\theta = 0$; a second considered spherical voids at fixed porosity $f = 0.01$ but with a larger set of loadings: on the one hand $\theta \in \{\pi/6, \pi/3\}$ and on the other hand $\theta = 0$ with $\boldsymbol{\Sigma}$ subjected to rotations around $\underline{e}_2$ of $\alpha = \pi/4$ (main stress axis along $\underline{e}_1 + \underline{e}_3$) and $\pi/2$ (main stress axis along $\underline{e}_3$). Finally, simulations of ellipsoidal cavities were conducted at $\theta = 0$ and $f = 0.01$; more details on these geometries will be given in Section III.1.4. The ensuing database holds 800 simulations to validate the models. The results of the simulations will be presented in the next sections, when compared to theoretical results.

Since spherical cavities are discretized into cubic voxels, mesh convergence has to be checked. Cube edge discretization of $N = 300$ at $f = 0.01$ (which corresponds approximately to a cavity radius r of 30 voxel length) is taken as the converged value. Comparisons with $N = 45$ (6 voxels), 85 (10 voxels) and 150 (20 voxels) uncover respective maximum relative errors of 1.9%, 1.1%, and 0.5%. Given these findings, values $N = 85$ ($f \geq 0.01$), 95 ($f = 0.005$) and 162 ($f = 0.001$) are chosen for unit-cell containing spherical cavities[4]; similar considerations about minimum semi-axis drive the choice of mesh discretization for ellipsoidal cavities.

A first model is developed in the next section to predict yield surfaces of porous bi-crystals with spherical voids in the rate-independent limit.

1.3 Plastic yield criterion for spherical voids

In this section, an approximate yield criterion is proposed for rate-independent ($n \to +\infty$) porous bi-crystals with spherical voids using limit analysis. The yield function of a perfect crystal is regularized according to Arminjon (1991) and Gambin (1991):

$$\mathcal{F}_m^{\text{mono}}(\boldsymbol{\sigma}) = \left[\sum_{s=1}^{K} \left(\frac{|\boldsymbol{\sigma} : \boldsymbol{\mu}_s|}{\tau_s^c}\right)^m\right]^{2/m} - 1 \tag{III.10}$$

In the limit $m \to +\infty$, Schmid law is recovered. As stated in Paux et al. (2015), taking $m = 2$ in Eq. III.10 amounts to approximating the perfect crystal with a Hill-type material (Hill, 1948). This reduction is likely to be crude, but adopting it will allow to derive a yield criterion in Section III.1.3.1. Then, following a suitable heuristic, this yield surface will be adapted to the case $m \to +\infty$ in Section III.1.3.2.

In the analyses conducted in this section and the following one, the hypothesis that (τ_s^c) are close to their mean τ^c is made; this will allow substitution of τ_s^c by τ^c and *vice-versa* whenever it is necessary in the calculations. This as-

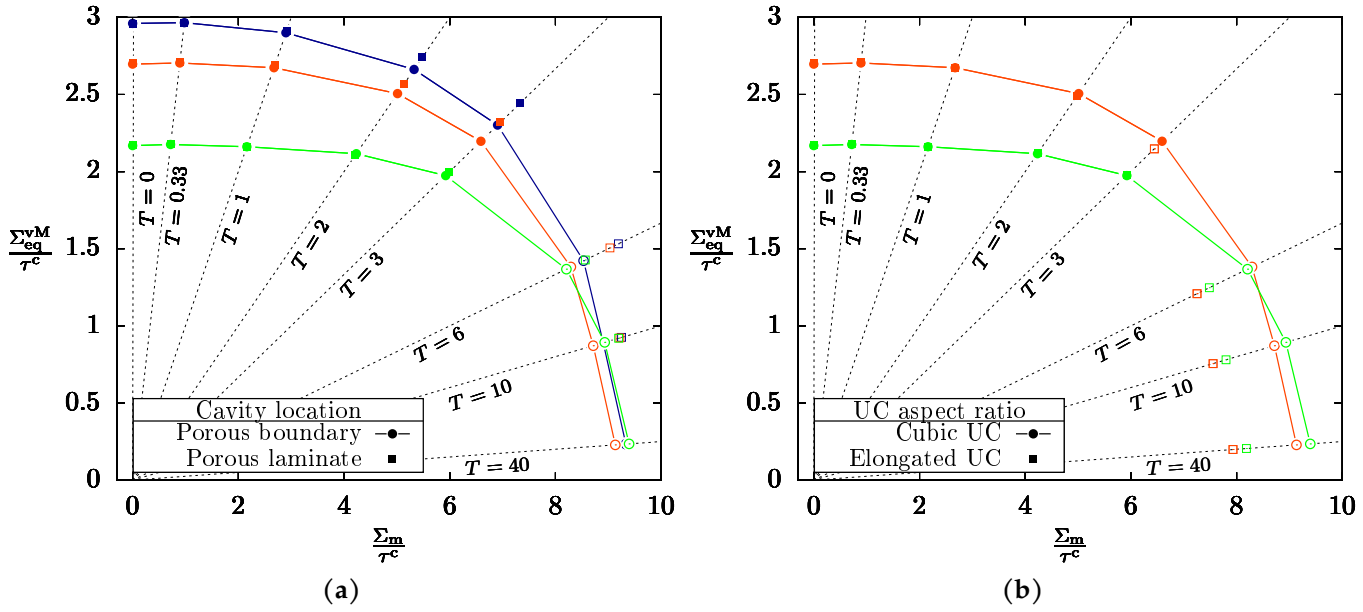

FIGURE III.5: Yield surfaces for different unit-cell configurations at $f = 0.005$, $n = 100$ and $\theta = 0$: **(a)** effect of void location (Fig. III.2a versus Fig. III.2e); **(b)** effect of unit-cell aspect ratio (Fig. III.2a versus Fig. III.2d). Hollowed-out symbols mark simulations in which the deformation mode has been identified as void coalescence.

[4] To be compared with 3, 16 and 32 voxels per cavity radius used respectively in Hure (2021), Vincent et al. (2014) and Wojtacki et al. (2020).

sumption seems acceptable in FCC materials but may be an issue in some HCP materials (Song and Ponte-Castañeda, 2017b).

1.3.1 Limit-analysis on porous Hill bi-materials

Following the limit-analysis framework used by Gurson (1977) for porous isotropic materials and specialized to porous Hill materials by Benzerga and Besson (2001), we consider a representative volume element of a material containing three phases i occupying volumes Ω_i, as pictured in Fig III.6. Phase 0 is a cavity of vanishing stiffness and volume fraction $f = (a/b)^3$ and phases 1 and 2 are perfectly plastic Hill materials of yield functions:

$$\mathcal{F}_2^{(i)}(\boldsymbol{\sigma}) = \left(\sigma_{\text{eq}}^{\text{H}}\right)^2 - 1 = \frac{3}{2}\boldsymbol{\sigma} : \mathbb{H}_i : \boldsymbol{\sigma} - 1 \tag{III.11}$$

where $\mathbb{H}_i$ are Hill stress anisotropy tensors — notice that contrary to the common formulation, they are *not* dimensionless. Matrix materials are incompressible, thus $\mathbb{J} : \mathbb{H}_i = \mathbb{H}_i : \mathbb{J} = 0$ with $\mathbb{J} = \frac{1}{3}\boldsymbol{I} \otimes \boldsymbol{I}$. For each material i, the associated equivalent strain rate is $d_{\text{eq}} = \sqrt{\frac{2}{3}\boldsymbol{d} : \mathbb{H}_i^* : \boldsymbol{d}}$ with $\mathbb{H}^*$ a tensor verifying $\mathbb{H}^* : \mathbb{H} = \mathbb{H} : \mathbb{H}^* = \mathbb{K}$, where $\mathbb{K} = \mathbb{I} - \mathbb{J}$. In a base of orthotropy, the components of $\mathbb{H}^*$ can be obtained from the components of $\mathbb{H}$ following the formulas given in Morin (2012) (Appendix A.2). More fundamentally, $\mathbb{H}^*$ is linked to $\mathbb{H}$ through linear algebra, as shown in Appendix III.1.A of the present work.

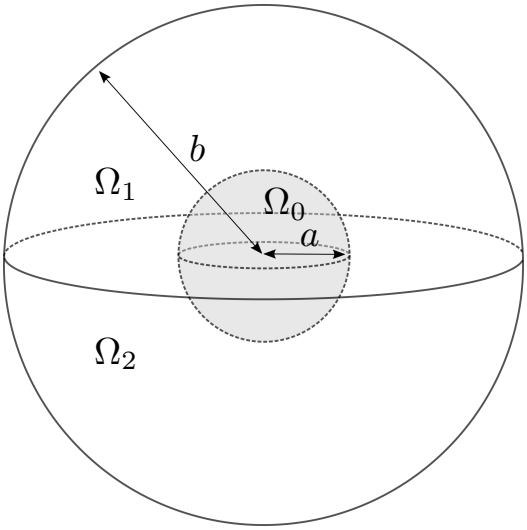

FIGURE III.6: Spherical unit-cell with a spherical cavity, used for the limit-analysis.

The unit-cell being subjected to prescribed uniform strain rate $\boldsymbol{D}$ on its boundary, the set $\mathcal{K}(\boldsymbol{D})$ of incompressible microscopic strain rate fields which are kinematically admissible with $\boldsymbol{D}$ is considered. The microscopic plastic dissipation associated with such a strain rate field $\dot{\boldsymbol{\varepsilon}}$ is :

$$\varpi\left(\dot{\boldsymbol{\varepsilon}}\left(\underline{x}\right)\right) \equiv \sup_{\widehat{\boldsymbol{\sigma}} \in \mathcal{C}(\underline{x})} \left(\widehat{\boldsymbol{\sigma}} : \dot{\boldsymbol{\varepsilon}}\left(\underline{x}\right)\right) = \sqrt{\frac{2}{3}\dot{\boldsymbol{\varepsilon}}\left(\underline{x}\right) : \mathbb{H}^*\left(\underline{x}\right) : \dot{\boldsymbol{\varepsilon}}\left(\underline{x}\right)} \tag{III.12}$$

where $\mathcal{C}(\underline{x})$ is the microscopic elasticity domain at point $\underline{x}$.

In the framework of limit analysis, any trial field $\dot{\boldsymbol{\varepsilon}} \in \mathcal{K}(\boldsymbol{D})$ gives an upper bound for the effective dissipation Π, defined as:

$$\Pi(\boldsymbol{D}) = \inf_{\dot{\boldsymbol{\varepsilon}} \in \mathcal{K}(\boldsymbol{D})} \left\langle \varpi\left(\dot{\boldsymbol{\varepsilon}}\left(\underline{x}\right)\right)\right\rangle_{\bigcup_i \Omega_i} = \frac{1-f}{2} \inf_{\dot{\boldsymbol{\varepsilon}} \in \mathcal{K}(\boldsymbol{D})} \left[\sum_{i=1}^{2} \left\langle \varpi\left(\dot{\boldsymbol{\varepsilon}}\left(\underline{x}\right)\right)\right\rangle_{\Omega_i}\right] \tag{III.13}$$

where $< \cdot >$ denotes volume averaging. From that upper bound Π^+, an approximate yield criterion is obtained since for a given strain rate $\boldsymbol{D}_0$, the macroscopic yield stress $\boldsymbol{\Sigma}$ is defined as the tangent vector to surface $\Pi^+(\boldsymbol{D})$ at point $\boldsymbol{D}_0$ (Suquet, 1982). Walking the footsteps of Benzerga and Besson (2001), the following strain rate field — which was already employed in Gurson (1977) — is chosen and expressed in spherical coordinates (r, θ, ϕ):

$$\dot{\boldsymbol{\varepsilon}} = \dot{\boldsymbol{\varepsilon}}_A + \dot{\boldsymbol{\varepsilon}}_B \quad \text{with} \quad \begin{cases} \dot{\boldsymbol{\varepsilon}}_A\left(\underline{x}\right) & = \dfrac{\text{Tr}(\boldsymbol{D})}{3}\left(\dfrac{b}{r}\right)^3 \left[-2\underline{e}_r \otimes \underline{e}_r + \underline{e}_\theta \otimes \underline{e}_\theta + \underline{e}_\phi \otimes \underline{e}_\phi\right] \\ \dot{\boldsymbol{\varepsilon}}_B & = \mathbb{K} : \boldsymbol{D} \end{cases} \tag{III.14}$$

Approximation of Eq. III.13 used in Benzerga and Besson (2001) relies on the computation of the mean square microscopic plastic dissipation over a sphere $\mathcal{S}(r)$ of radius r:

$$\left\langle \varpi\left(\dot{\boldsymbol{\varepsilon}}\right)^2 \right\rangle_{\mathcal{S}(r)} = \frac{1}{3}\sum_{i=1}^{2}\left[\dot{\boldsymbol{\varepsilon}}_B : \mathbb{H}_i^* : \dot{\boldsymbol{\varepsilon}}_B + 2\left\langle \dot{\boldsymbol{\varepsilon}}_A\right\rangle_{\mathcal{S}(r)\cap\Omega_i} : \mathbb{H}_i^* : \dot{\boldsymbol{\varepsilon}}_B + \left\langle \dot{\boldsymbol{\varepsilon}}_A : \mathbb{H}_i^* : \dot{\boldsymbol{\varepsilon}}_A\right\rangle_{\mathcal{S}(r)\cap\Omega_i}\right] \tag{III.15}$$

It is useful to remark that for a point $\underline{x}^1$ located on demi-sphere $\mathcal{S}(r)\cap\Omega_1$ and its symmetrical with respect to the origin $\underline{x}^2$ located on complementary demi-sphere $\mathcal{S}(r)\cap\Omega_2$, the local spherical frames are related: $(\underline{e}_r^2, \underline{e}_\theta^2, \underline{e}_\phi^2) = (-\underline{e}_r^1, \underline{e}_\theta^1, -\underline{e}_\phi^1)$.

Given the specific form of $\dot{\boldsymbol{\varepsilon}}_A$, the following relations are obtained:

$$\langle \dot{\boldsymbol{\varepsilon}}_A \rangle_{\mathcal{S}(r)\cap\Omega_1} = \langle \dot{\boldsymbol{\varepsilon}}_A \rangle_{\mathcal{S}(r)\cap\Omega_2} = \langle \dot{\boldsymbol{\varepsilon}}_A \rangle_{\mathcal{S}(r)} \tag{III.16}$$

Furthermore, it can be verified that:

$$\forall i \in \{1,2\},\ \langle \dot{\boldsymbol{\varepsilon}}_A : \mathbb{H}_i^* : \dot{\boldsymbol{\varepsilon}}_A \rangle_{\mathcal{S}(r)\cap\Omega_i} = \langle \dot{\boldsymbol{\varepsilon}}_A : \mathbb{H}_i^* : \dot{\boldsymbol{\varepsilon}}_A \rangle_{\mathcal{S}(r)} \tag{III.17}$$

Substitution of the present expressions into the development of Benzerga and Besson (2001) leads to the following yield criterion:

$$\left(\frac{3}{2}\boldsymbol{\Sigma} : \left[\frac{1}{2}\mathbb{H}_1^* + \frac{1}{2}\mathbb{H}_2^*\right]^* : \boldsymbol{\Sigma}\right) + 2qf\cosh\left(\frac{3\sqrt{2}}{\sqrt{\chi\left(\mathbb{H}_1^*\right)+\chi\left(\mathbb{H}_2^*\right)}}\Sigma_m\right) - 1 - (qf)^2 = 0 \tag{III.18}$$

$$\chi(\mathbb{H}^*) = \frac{8}{15}\left(h_{11}^* + h_{22}^* + h_{33}^* - h_{23}^* - h_{31}^* - h_{12}^*\right) + \frac{4}{5}\left(h_{44}^* + h_{55}^* + h_{66}^*\right) \tag{III.19}$$

where q is Tvergaard's adjustment parameter (Tvergaard, 1982) and h_{ij}^* are components of tensor $\mathbb{H}^*$ in the Voigt-Mandel notation, regardless of the chosen geometric frame. Eq. III.19 is obtained from the lengthy yet straightforward calculation of $\langle \dot{\boldsymbol{\varepsilon}}_A : \mathbb{H}_i^* : \dot{\boldsymbol{\varepsilon}}_A \rangle_{\mathcal{S}(r)}$ which involves the recasting of $\mathbb{H}_i^*$ from the bi-crystal frame of reference to the local spherical frame of reference. Note that Eq. III.19 is not directly found in Benzerga and Besson (2001) since this reference expressed χ as a function of eigenvalues of $\mathbb{H}$ whereas, in the present work, χ is a function of coefficients of $\mathbb{H}$ in an arbitrary basis. Equivalence of the two expressions can be obtained using Eq. III.52 presented in Appendix III.1.A. Therefore, in the limit where phase 1 and phase 2 are identical, $\left(\mathbb{H}_1^*\right)^* = \mathbb{H}_1$ and the criterion of Benzerga and Besson (2001) for porous Hill materials is recovered.

1.3.2 Porous bi-crystal correction

In the context of Eq. III.10 with the approximation $m = 2$, the results of Section III.1.3.1 can be specialized to perfectly-plastic crystals by setting the following stress anisotropy tensors:

$$\mathbb{H}_i = \frac{2}{3}\mathbb{S}_i \quad \text{with} \quad \mathbb{S}_i = \sum_{s=1}^{K} \frac{1}{\left(\tau_s^{(i),\mathrm{c}}\right)^2}\left[\boldsymbol{\mu}_k^{(i)} \otimes \boldsymbol{\mu}_k^{(i)}\right] \tag{III.20}$$

As stated in Paux et al. (2015), in the case of cubic crystal lattices with equivalent critical resolved shear stresses ($\tau_s^{\mathrm{c}} = \tau^{\mathrm{c}}$), $\mathbb{S}$ is a linear combination of deviatoric cubic projectors[5] $\mathbb{K}'$ and $\mathbb{K}''$ defined in Walpole (1981) with coefficients (α', α''):

$$\mathbb{K}' = \mathbb{G} - \mathbb{J}\,, \quad \mathbb{K}'' = \mathbb{I} - \mathbb{G} \quad \text{where} \quad \mathbb{G} = (\delta_{ij}\delta_{jk}\delta_{kl})_{ijkl} \tag{III.21}$$

written in the frame of orthotropy. Then, $\mathbb{S}^*$ can be obtained simply as its decomposition coefficients are $(1/\alpha', 1/\alpha'')$. However, crystal 1 and 2 orthotropy axes are not the same so the deviatoric term of Eq. III.18 cannot be expressed simply according to cubic projectors. Still, for a FCC crystal with $\tau_s^{\mathrm{c}} = \tau^{\mathrm{c}}$, $(\tau^{\mathrm{c}})^2\alpha' = 2$ and $(\tau^{\mathrm{c}})^2\alpha'' = 2/3$ so that Eq. III.19 writes $\chi = 33\left(\tau^{\mathrm{c}}\right)^2/5$.

As expected, Eq. III.18 is in poor agreement with porous bi-crystal unit-cell computations conducted in Section III.1.2.3 for quasi-rate independent behavior ($n = 100$). Following Paux et al. (2015), independent corrections of hydrostatic and deviatoric terms are conducted.

Hydrostatic point In the case of an FCC single crystal hollow sphere, Paux et al. (2018) determined that the value $\kappa' \equiv 3\tau^{\mathrm{c}}/\sqrt{\chi} \approx 0.49$ was needed to recover the plastic dissipation associated with microscopic strain rate $\dot{\epsilon} = \dot{\epsilon}_B$. A similar result ($\kappa' \approx 0.489$) was obtained in Hure (2019) using a simplified derivation. Eq. 16 of the latter reference, specialized to a voided bi-crystal, leads to:

$$\kappa' = \frac{3}{\langle M_1\left(\underline{x}, \dot{\boldsymbol{\varepsilon}}_B\right)\rangle_{\Omega_1} + \langle M_2\left(\underline{x}, \dot{\boldsymbol{\varepsilon}}_B\right)\rangle_{\Omega_2}} \quad \text{with} \quad M_i\left(\underline{x}, \dot{\boldsymbol{\varepsilon}}\right) = \frac{\sum_{s=1}^{K}\dot{\gamma}_k^{(i)}\left[\dot{\boldsymbol{\varepsilon}}\left(\underline{x}\right)\right]}{\sqrt{\frac{2}{3}\dot{\boldsymbol{\varepsilon}}\left(\underline{x}\right) : \dot{\boldsymbol{\varepsilon}}\left(\underline{x}\right)}} \tag{III.22}$$

[5] δ_{ij} stands for Kronecker delta.

Noticing that $M_i\left(-\underline{x},\dot{\boldsymbol{\varepsilon}_B}\right) = M_i\left(\underline{x},\dot{\boldsymbol{\varepsilon}_B}\right)$, we obtain that $\langle M_i\left(\underline{x},\dot{\boldsymbol{\varepsilon}}_B\right)\rangle_{\Omega_i} = \langle M_i\left(\underline{x},\dot{\boldsymbol{\varepsilon}}_B\right)\rangle_{\Omega_1\cup\Omega_2}$; therefore $\kappa \approx 0.489$ as in the case of the single crystal. It means that monocrystalline and bi-crystalline hollow spheres subjected to the hydrostatic microscopic field of Rice and Tracey (1969) have the same yield limit.

Deviatoric point Under deviatoric stress $\boldsymbol{\Sigma}$ and in the limit $f \to 0$, Eq. III.18 should recover the exact yield function of a pristine bi-crystal. As detailed in Appendix III.1.C, it writes:

$$\mathcal{F}_\infty^{\text{bi}}\left(\boldsymbol{\Sigma}\right) = \left[\min_{\boldsymbol{\Delta}_\infty}\max_{s\in[\![1,K]\!]}\left\{\frac{\left|\left(\boldsymbol{\Sigma}+\boldsymbol{\Delta}_\infty\right):\boldsymbol{\mu}_s^{(1)}\right|}{\tau_s^{(1),\text{c}}},\frac{\left|\left(\boldsymbol{\Sigma}-\boldsymbol{\Delta}_\infty\right):\boldsymbol{\mu}_s^{(2)}\right|}{\tau_s^{(2),\text{c}}}\right\}\right]^2 - 1 \tag{III.23}$$

where $\boldsymbol{\Delta}_\infty$ follows the stress continuity condition at the planar interface between the two crystals, parallel to $(\underline{e}_2,\underline{e}_3)$: $\boldsymbol{\Delta}_\infty = \mathbb{E}:\boldsymbol{\Delta}_\infty$ with $\mathbb{E} = \left(\boldsymbol{I}-\underline{e}_1\otimes\underline{e}_1\right)\overline{\otimes}\left(\boldsymbol{I}-\underline{e}_1\otimes\underline{e}_1\right)$ and $\left[\boldsymbol{A}\overline{\otimes}\boldsymbol{B}\right]_{ijkl} = \left(A_{ik}B_{jl}+A_{il}B_{jk}\right)/2$ (Dormieux and Kondo, 2010).

Having corrected the deviatoric and the hydrostatic points, the final yield surface is defined by the following Gurson-like criterion:

$$\mathcal{F}(\boldsymbol{\Sigma}) = \left[\min_{\boldsymbol{\Delta}_\infty}\max_{s\in[\![1,K]\!]}\left\{\frac{\left|\left(\boldsymbol{\Sigma}+\boldsymbol{\Delta}_\infty\right):\boldsymbol{\mu}_s^{(1)}\right|}{\tau_s^{(1),\text{c}}},\frac{\left|\left(\boldsymbol{\Sigma}-\boldsymbol{\Delta}_\infty\right):\boldsymbol{\mu}_s^{(2)}\right|}{\tau_s^{(2),\text{c}}}\right\}\right]^2 + 2qf\cosh\left(\kappa'\frac{\Sigma_m}{\tau^{\text{c}}}\right) - 1 - (qf)^2 = 0 \tag{III.24}$$

When crystal 1 and crystal 2 have the same orientation, Eq. III.24 reduces to the porous single crystal criterion of Paux et al. (2015) (Eq. III.49), as shown in Appendix III.1.C.

1.3.3 Assessment of yield surfaces

The assessment of the proposed yield criterion (Eq. III.24) is performed using the numerical homogenization results described in Section III.1.2. Whereas the limit analysis was carried out on a hollow sphere geometry (see Fig. III.6), FFT simulations could only be conducted on cuboids due to the periodicity assumption. As the criterion accounts for rate-independent crystals with spherical voids, only the unit-cell computations with $n = 100$ and spherical cavities are considered. As stated in the previous section, q requires calibration. Following Fritzen et al. (2012), it is supposed to depend on porosity f. Since the competitive deformation modes known as void growth and void coalescence are accounted for by multi-yield surface plasticity, it is of paramount importance that void coalescence points are within the elasticity domain predicted by the void growth criterion (see Section III.1.2.2 and Fig. III.3b). Therefore, $q(f)$ is set as the maximal q such as the simulations at porosity f, $\theta = 0$ and $\alpha = 0$ displaying void coalescence are within the elasticity domain and not outside. Only orientation couples that are not displayed in the graphs below were used in the calibration; therefore, the yield surfaces presented in Fig. III.7 serve as validation. Fitted values of $q(f)$ are presented in Table III.3; calibrated values follow the approximate relation $q(f) \approx (f+0.005)^{-0.15}$. By comparison, q have been set by previous studies on porous single crystals to 2.2 (Paux et al., 2015), 2 (Paux et al., 2018) and 1.66 (Sénac et al., 2022).

f	0.001	0.005	0.01	0.05	0.1	0.2	0.3
$q(f)$	2.14	1.97	1.85	1.57	1.45	1.24	1.17

TABLE III.3: Calibrated values of Tvergaard's parameter q at various porosities f.

Yield surfaces are shown in Fig. III.7. A good agreement is observed between the GTN-like model and simulations displaying void growth. In Fig. III.7a,b, it is shown that the influence of crystal orientation couples and porosity are captured well enough. In particular, the deviatoric point estimation based on the pristine bi-crystal yields excellent results for porosities $f \leq 0.01$; for higher porosities, increasing discrepancies are seen but good prediction quality is retained. In Fig. III.7c, the effect of the Lode angle θ on yield stresses is seen to be significant, especially for deviatoric loadings; this behavior is well-predicted by the model. However, some additional discussion is needed as, generally, Lode-angle effects on homogeneous yielding are believed to be two-fold:

- if the sound material has a Lode-dependent behavior, as in the case of crystals, then its influence on the yield locus of the corresponding porous material will be significant (Benallal, 2018);

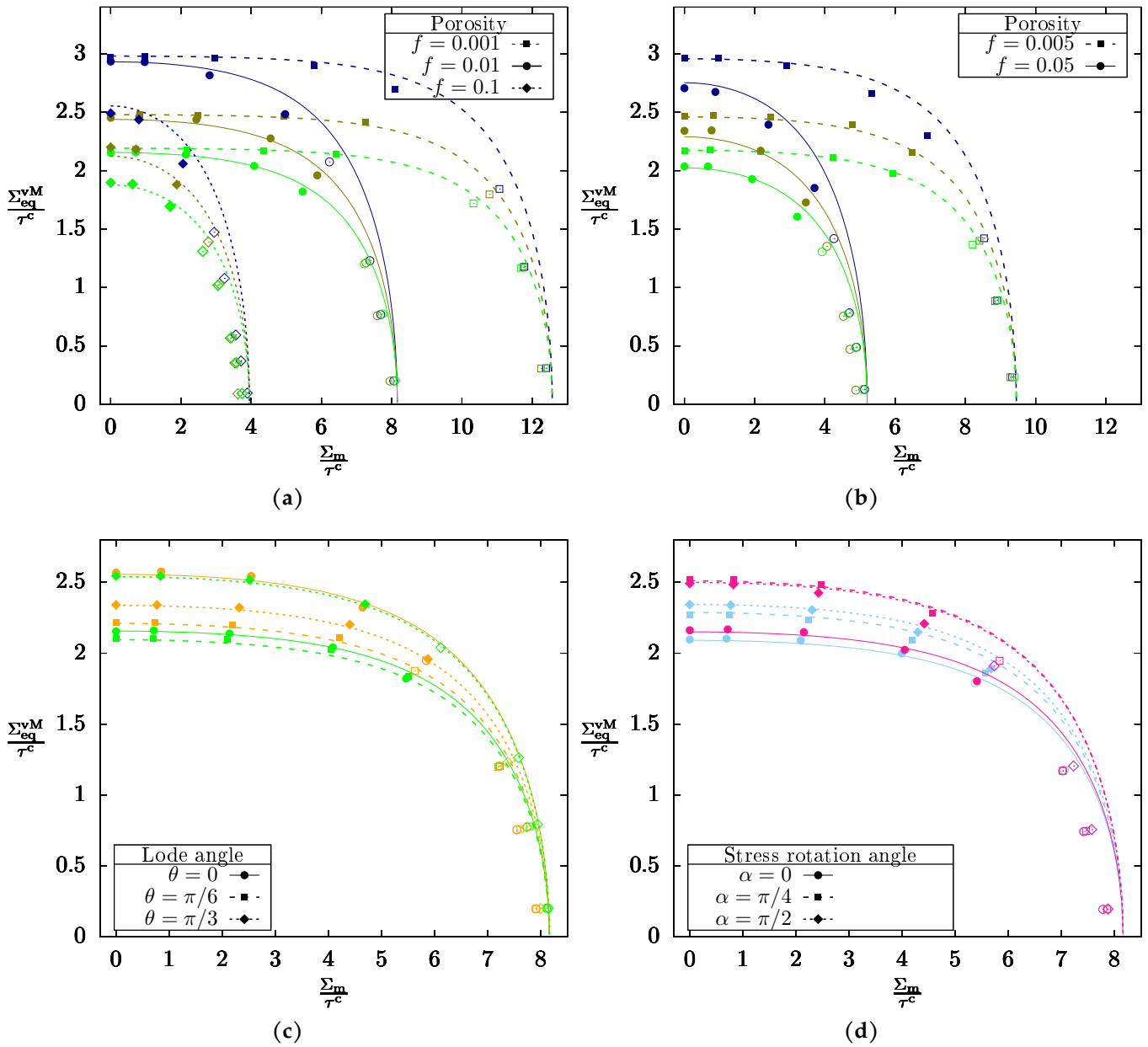

FIGURE III.7: Comparison of yield surfaces predicted by the GTN-like criterion (lines) and unit-cell computations conducted at $n = 100$ with spherical cavities (points): **(a)** porous boundary at $\theta = 0$ and porosities $f \in \{0.001, 0.01, 0.1\}$; **(b)** porous boundary at $\theta = 0$ and porosities $f \in \{0.005, 0.05\}$; **(c)** porous boundary at $f = 0.01$ and various Lode angles; **(d)** porous boundary at $f = 0.01$ and $\theta = 0$ with loading rotations of α around $\underline{e}_2$. Hollowed-out symbols mark simulations in which the deformation mode has been identified as void coalescence.

- as seen in the case of von Mises matrix, homogeneous yielding of porous Lode-independent materials also display Lode-dependence that can be incorporated into models (Danas et al., 2008; Cazacu et al., 2013; Benallal et al., 2014; Leblond and Morin, 2014; Cheng et al., 2015).

In the present case, only the first contribution, which is the dominant one, is accounted for by the model. However, the second contribution, despite being negligible regarding the stress values, may significantly influence yield surface normality and thus the porosity rate (Leblond and Morin, 2014) and then the failure locus (Vishwakarma and Keralavarma, 2019). There is no reason to believe that these findings, stated for von Mises materials, may differ for crystals; nevertheless, such considerations are neglected in this work — q is calibrated for $\theta = 0$ and expected to hold for other values of θ — and left for future research. Finally, in Fig. III.7d, it can be inferred that the model can account for main loading axes different from $\underline{e}_1$ ($\alpha = \pi/4$ and $\pi/2$), and applied stresses with shear components ($\alpha = \pi/4$). However, since GTN-like criteria have uncoupled deviatoric and hydrostatic terms, two configurations in which the deviatoric and hydrostatic points are similar are indistinguishable by the model, as seen with orientation couple #13

(plotted in pink) loaded with $\alpha = \pi/4$ and $\pi/2$; yet, unit-cell computations clearly show that these two configurations have distinct yield stresses at intermediate triaxialities.

Due to the calibration procedure, simulations displaying void coalescence are within yield surfaces of the void growth criterion. This way, a void coalescence criterion for porous boundaries can be used simultaneously with the GTN-like model without inconsistency (see Fig. III.3b).

In summary, the yield criterion presented in this section can predict satisfactorily void growth yield stresses for porous boundaries with spherical voids in the rate-independent limit. Improvement of the Gurson-like model to account for more general shapes could possibly be carried out following the lines of Monchiet et al. (2008), Keralavarma and Benzerga (2010) and Morin et al. (2015c) that extended the yield locus of Benzerga and Besson (2001) to Hill materials containing spheroidal or ellipsoidal cavities.

1.4 Viscoplastic potentials for porous bi-crystals with ellipsoidal voids

In order to obtain a criterion for porous grain boundaries with ellipsoidal voids, a variational approach is adopted in the following. Indeed, variational methods provide a homogenization alternative to limit analysis that has proven fruitful for the study of voided viscoplastic single crystals (Han et al., 2013; Mbiakop et al., 2015b; Song and Ponte-Castañeda, 2017a) and polycrystals (Lebensohn et al., 2011; Nervi and Idiart, 2015; Song and Ponte Castañeda, 2018). In particular, they are expected to yield viscoplastic potentials and to be more convenient to introduce void shape effects.

In that section, pristine single-crystal mechanical behavior is assumed to derive from the following viscoplastic stress potential:

$$u_n(\boldsymbol{\sigma}) = \sum_{s=1}^{K} \frac{\dot{\gamma}_0 \tau_s^{\mathrm{c}}}{n+1} \left(\frac{|\boldsymbol{\sigma} : \boldsymbol{\mu}_s|}{\tau_s^{\mathrm{c}}} \right)^{n+1}, \quad \dot{\boldsymbol{\varepsilon}} = \frac{\partial u_n}{\partial \boldsymbol{\sigma}} \tag{III.25}$$

The constitutive equation Eq. III.25$_b$ linking the stress potential and the plastic deformation rate is the same as Eq. III.7. Note that the Stokes-Rayleigh analogy (Hoff, 1954) enables an alternative interpretation of Eq. III.25 to viscoplasticity if the strain $\boldsymbol{\varepsilon}$ is substituted to the strain rate in Eq. III.25$_b$: when $n = 1$ the described material has a linear elastic behavior while $n > 1$ corresponds to non-linear elasticity. This is usually the paradigm that is adopted in variational approaches (Hashin and Shtrikman, 1963; Willis, 1977; Nemat-Nasser et al., 1993).

The concept of yield surface is extended for finite n by the gauge domain $\mathcal{G}$ introduced by Leblond et al. (1994):

$$\mathcal{G} = \left\{ \boldsymbol{\sigma},\, u_n(\boldsymbol{\sigma}) \leq \frac{\dot{\gamma}_0 \tau^{\mathrm{c}}}{n+1} \right\} \tag{III.26}$$

In this convenient framework, the normality rule is kept (Benzerga and Leblond, 2010) and viscoplastic yielding is studied through the description of the gauge surface $\partial\mathcal{G}$: gauge factor $\lambda(\boldsymbol{\sigma})$ is defined as the scalar such as $\lambda(\boldsymbol{\sigma}) \cdot \boldsymbol{\sigma} \in \partial\mathcal{G}$. In the limit $n \to +\infty$, $\partial\mathcal{G}$ recovers the classical concept of yield surface.

The potential U of the porous material represented by the unit-cell Ω writes:

$$U(\boldsymbol{\Sigma}) = \min_{\boldsymbol{\sigma} \in \mathcal{S}(\boldsymbol{\Sigma})} \langle u_n(\boldsymbol{\sigma}, \underline{x}) \rangle_{\Omega} \tag{III.27}$$

where $\mathcal{S}(\boldsymbol{\Sigma})$ is the set of statically admissible microscopic stress fields. Since potentials u for both void and single crystals are positively homogeneous of degree $n+1$, U inherits this property. Then, according to Euler's homogeneous function theorem combined with the macroscopic constitutive equation, $\boldsymbol{\Sigma} : \boldsymbol{D} = (n+1)U(\boldsymbol{\Sigma})$, enabling to compute U at yielding from macroscopic tensors. Therefore, when the unit cell is subjected to the loading described in Section III.1.2.2, it can be obtained that:

$$\lambda\left(\boldsymbol{\Sigma}_0\right) = \left(\frac{\boldsymbol{\Sigma}_0 : \boldsymbol{D}_0}{\dot{\gamma}_0 \tau^{\mathrm{c}}} \right)^{\frac{-1}{n+1}} \tag{III.28}$$

where $\boldsymbol{\Sigma}_0$ and $\boldsymbol{D}_0$ are the final converged values of the FFT computation. Eq. III.28 is used in the post-processing of viscoplastic numerical limit-analysis of Section III.1.2 and subsequent plotting of gauge surfaces: indeed, the numerical gauge stress is $\boldsymbol{\Sigma} = \lambda\left(\boldsymbol{\Sigma}_0\right) \cdot \boldsymbol{\Sigma}_0 \in \delta\mathcal{G}$. Note that when $n \to +\infty$, Eq. III.28 reduces to $\lambda\left(\boldsymbol{\Sigma}_0\right) = 1$ *i.e.* the numerical saturated stress is the sought yield stress.

1.4.1 Case $n = 1$: Hashin-Strikman estimates for periodical porous bi-crystals

The Hashin-Shtrikman bounds (Hashin and Shtrikman, 1963) on elastic moduli have been thoroughly used to study linear porous materials through the generalization of Willis (1977) who considered composites with random microstructure characterized by two-point correlation functions. Symmetries that allow analytic expressions are reviewed in Walpole (1981) and Torquato (1991). None of them are suited to the case of porous grain boundaries in which the three phases (cavity, grain 1, and grain 2) are such that cavities are always located at the interface between grains. Bi-crystals with porous boundaries have thus to be studied as periodical composites. A general framework to get bounds on elastic moduli of composites with periodic microstructure is provided by Nemat-Nasser et al. (1993) along with an explicit solution for two-phase composites. This section is devoted to obtaining such a solution for three-phase composites, and that estimate will be assessed in the case of linear porous bi-crystals ($n = 1$) in Section III.1.4.2.

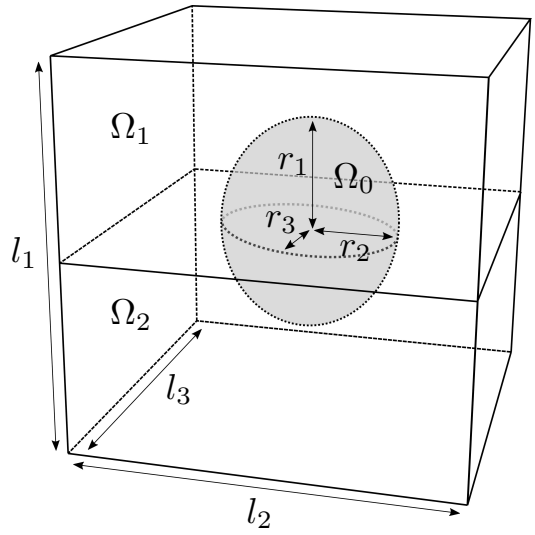

FIGURE III.8: Rectangular prismatic unit-cell with centered ellipsoidal cavity; void axes are aligned with unit-cell axes.

We consider a three-phase periodical composite characterized by the unit-cell of Fig. III.8 in which phase i occupies set Ω_i. Ω_0 is an ellipsoid of axes r_1, r_2 and r_3; void aspect ratios are defined as such: $w_2 = r_1/r_2$ and $w_3 = r_1/r_3$. The unit cell volume is taken as unity and the volume of phase i will be referred to as f_i. Each phase i is viscous linear material of pseudo-compliance[6] tensor $\mathbb{S}_i > 0$ so that $\dot{\boldsymbol{\varepsilon}} = \dot{\gamma}_0 \left(\mathbb{S}_i : \boldsymbol{\sigma}\right) / \tau^{\mathrm{c}}$. According to the Hashin-Strikman variational principle, every $\mathbb{S}$, rationalized as the pseudo-compliance tensor of a homogeneous comparison material, such as $\mathbb{S}_i - \mathbb{S} > 0$ (minimality condition) provide a lower bound for the macroscopic potential of the composite (Eq. 2.11 of Willis (1977) or Eq. 4.5a of Nemat-Nasser et al. (1993)):

$$U(\boldsymbol{\Sigma}) \geq \frac{\dot{\gamma}_0 \tau^{\mathrm{c}}}{2} \boldsymbol{\Sigma} : \overline{\mathbb{S}} : \boldsymbol{\Sigma} \quad \text{with} \quad \overline{\mathbb{S}} = \mathbb{S} + \sum_{i=0}^{2} f_i \mathbb{S}^{(i)} \tag{III.29}$$

According to Nemat-Nasser et al. (1993), tensors $\mathbb{S}^{(i)}$ are given by the following linear system within the space of symmetric fourth-order tensors:

$$\forall i \in [\![0,2]\!],\ \left(\mathbb{S}_i - \mathbb{S}\right)^{-1} : \mathbb{S}^{(i)} + \sum_{j=0}^{2} f_j \, \mathbb{A}_{ij} : \mathbb{S}^{(j)} - \mathbb{I} = 0 \tag{III.30}$$

where correlation tensors (or Eshelby sums) $\mathbb{A}_{ij}$ account for the interactions between phases and thus hold the microstructure information of the linear composite:

$$\mathbb{A}_{ij}(\mathbb{S}) = \sum_{\substack{\underline{\xi} = (2n_1\pi/l_1,\, 2n_2\pi/l_2,\, 2n_3\pi/l_3) \\ (n_1,n_2,n_3) \in \left(\mathbb{Z}^3\right)^*}} \mathrm{Re}\left[g_i\left(\underline{\xi}\right) g_j\left(-\underline{\xi}\right)\right] \underbrace{\left(\mathbb{S}^{-1} - \mathbb{S}^{-1} : \mathrm{sym}\left[\underline{\xi} \otimes \left(\underline{\xi} \cdot \mathbb{S}^{-1} \cdot \underline{\xi}\right)^{-1} \otimes \underline{\xi}\right] : \mathbb{S}^{-1}\right)}_{\mathbb{A}\left(\underline{\xi}, \mathbb{S}\right)} \tag{III.31}$$

$$\text{with} \quad g_j\left(\underline{\xi}\right) = \frac{1}{f_j} \int_{\underline{x} \in \Omega_j} e^{i \underline{\xi} \cdot \underline{x}} \tag{III.32}$$

where g_i is the Fourier transform of the characteristic function of Ω_i. Eq. III.31 differs from Nemat-Nasser et al. (1993) in that only the real part of $\mathbb{A}_{ij}$ is considered. Indeed, it is safely assumed that components of $\mathbb{S}^{(i)}$ are real-valued, allowing to focus attention on the real part of Eq. III.30. For conciseness, expressions of g-functions are provided in Appendix III.1.D for ellipsoidal cavities as well as elliptic-cylindrical cavities. However, explicit forms are not

[6] This terminology is motivated by the Stokes-Rayleigh analogy.

necessary to verify the following relations:

$$\begin{aligned} \mathbb{A}_{01} = \mathbb{A}_{02}\,, \quad \forall (i,j) \in [\![0,2]\!]^2,\, \mathbb{A}_{ij} = \mathbb{A}_{ji} \\ \mathbb{A}_{11} = \mathbb{A}_{22}\,, \quad f\mathbb{A}_{00} + (1-f)\mathbb{A}_{01} = 0 \\ f\mathbb{A}_{01} + \tfrac{1}{2}(1-f)\mathbb{A}_{11} + \tfrac{1}{2}(1-f)\mathbb{A}_{12} = 0 \end{aligned} \tag{III.33}$$

the last two deriving from the fact that $f_0 g_0 + f_1 g_1 + f_2 g_2 = 0$. Eq. III.33 implies that all correlation tensors can be expressed from $\mathbb{A}_{01}$ and $\mathbb{A}_{12}$. In order to solve the set of Eqs. III.30, it is convenient to introduce tensors $\mathbb{B}_i$:

$$\forall i \in [\![0,2]\!],\, \mathbb{B}_i = \frac{f}{2}\mathbb{A}_{01} + \frac{1-f}{2}\mathbb{A}_{12} - (\mathbb{S}_i - \mathbb{S})^{-1} \tag{III.34}$$

Non-commutative algebra finally yields the following expressions:

$$\begin{aligned} \mathbb{S}^{(0)} &= -\frac{1}{1-f}\left\{\mathbb{A}_{01}^{-1} + \frac{1}{2}\left[\left(\mathbb{B}_1 - \mathbb{B}_0\mathbb{B}_2^{-1}\mathbb{B}_0\right)^{-1}\left(\mathbb{I} + \mathbb{B}_0\mathbb{B}_2^{-1}\right) + \left(\mathbb{B}_2 - \mathbb{B}_0\mathbb{B}_1^{-1}\mathbb{B}_0\right)^{-1}\left(\mathbb{I} + \mathbb{B}_0\mathbb{B}_1^{-1}\right)\right]\right\} \\ \mathbb{S}^{(1)} &= -\frac{1}{1-f}\left(\mathbb{B}_1 - \mathbb{B}_0\mathbb{B}_2^{-1}\mathbb{B}_0\right)^{-1}\left(\mathbb{I} + \mathbb{B}_0\mathbb{B}_2^{-1}\right) \\ \mathbb{S}^{(2)} &= -\frac{1}{1-f}\left(\mathbb{B}_2 - \mathbb{B}_0\mathbb{B}_1^{-1}\mathbb{B}_0\right)^{-1}\left(\mathbb{I} + \mathbb{B}_0\mathbb{B}_1^{-1}\right) \end{aligned} \tag{III.35}$$

In the case of the porous linear bi-crystal, $\mathbb{S}_0 = \infty$ and $\mathbb{S}_1$ and $\mathbb{S}_2$ are given by Eq. III.20, corrected by a parameter $\kappa \to +\infty$ to regain inversibility:

$$\mathbb{S}_i = \sum_{s=1}^{K} \frac{1}{\left(\tau_s^{(i),c}\right)^2}\left[\boldsymbol{\mu}_s^{(i)} \otimes \boldsymbol{\mu}_s^{(i)}\right] + \frac{1}{\left(\tau^{(i),c}\right)^2}\frac{1}{3\kappa}\mathbb{J} \tag{III.36}$$

Since no obvious choice of $\mathbb{S}$ respecting the minimality condition exists, this condition is dropped and the homogeneous material is chosen to be the pristine bi-crystal: $\mathbb{S}$ is given by Eq. III.58. The left-hand expression of Eq. III.29 thus loses its bounding character and becomes an estimate of $U(\boldsymbol{\Sigma})$. Some degenerate cases are worth commenting on. On the one hand, when grain 1 and grain 2 have the same crystal orientation, $\mathbb{S} = \mathbb{S}_1 = \mathbb{S}_2$ and the modulus estimate reduces to:

$$\overline{\mathbb{S}} = \mathbb{S}_1 + \mathbb{A}_{00}\left(\mathbb{S}_1\right)^{-1} \tag{III.37}$$

which was already presented by Nemat-Nasser et al. (1993) (Eq. 6.5a). This approximated modulus is the periodical twin to the expression given by Willis (1977) (Eq. 3.16) in the context of random cavities and involving Eshelby inclusion integral:

$$\overline{\mathbb{S}} = \mathbb{S}_1 + \frac{f}{1-f}\left[\left\langle \mathbb{A}\left(\underline{\xi}, \mathbb{S}_1\right)\right\rangle_{\partial\Omega_0}\right]^{-1} \tag{III.38}$$

The absence of factor $f/(1-f)$ in Eq. III.37 may seem surprising, but it is simply hidden in $\mathbb{A}_{00}^{-1}$ as will be shown in Appendix III.1.E. On the other hand, when $f \to 0$, $\mathbb{A}_{12} \to -\mathbb{A}\left(\underline{e}_1, \mathbb{S}\right)$. Changing gear to $\mathbb{S} = \mathbb{S}_1$, the approximated pseudo-compliance becomes:

$$\overline{\mathbb{S}} = \mathbb{S}_1 + \left[2\left(\mathbb{S}_2 - \mathbb{S}_1\right)^{-1} + \mathbb{A}\left(\underline{e}_1, \mathbb{S}_1\right)\right]^{-1} \tag{III.39}$$

which is the result of Francfort and Murat (1986) (see Norris (1990) for a simplified presentation) for a pristine laminate. A similar agreement is found by choosing $\mathbb{S} = \mathbb{S}_2$. Therefore, setting $\mathbb{S}$ according to Eq. III.58 (or equivalently Eq. III.39) may yield $\overline{\mathbb{S}} = \mathbb{S}$; due to the intricate expressions it was not possible to derive equality but this conjecture was at least checked numerically on a few examples. In summary, the expressions are consistent in both extreme cases of pristine bi-crystals and porous single crystals.

1.4.2 Case $n = 1$: Assessment of gauge surfaces

In the previous section, a complete set of equations gives an estimate for the pseudo-compliance of the linear porous bicrystal and therefore an approximation for its potential. Analytical gauge surfaces are determined by the conjunction of Eq. III.29 and Eq. III.26:

$$\boldsymbol{\Sigma} \in \partial\mathcal{G} \quad \Leftrightarrow \quad \boldsymbol{\Sigma} : \overline{\mathbb{S}} : \boldsymbol{\Sigma} = 1 \tag{III.40}$$

$\kappa = 10^6$ is chosen in Eq. III.36, as higher values may cause instabilities when inverting tensors. $\mathbb{A}_{ij}$ series (Eq. III.33) are truncated from $(n_1, n_2, n_3) \in \left(\mathbb{Z}^3\right)^*$ to $\left([\![-100, 100]\!]^3\right)^*$ to ensure maximal accuracy; fewer terms would also lead to satisfying estimates, but such an investigation is outside the scope of this study. In order to assess this model, gauge surfaces are plotted in Fig III.9 and compared to numerical surfaces obtained using Eq. III.28 on unit-cell simulations.

As seen in Fig. III.9a, the estimates achieve very satisfying precision: variations of gauge stress according to

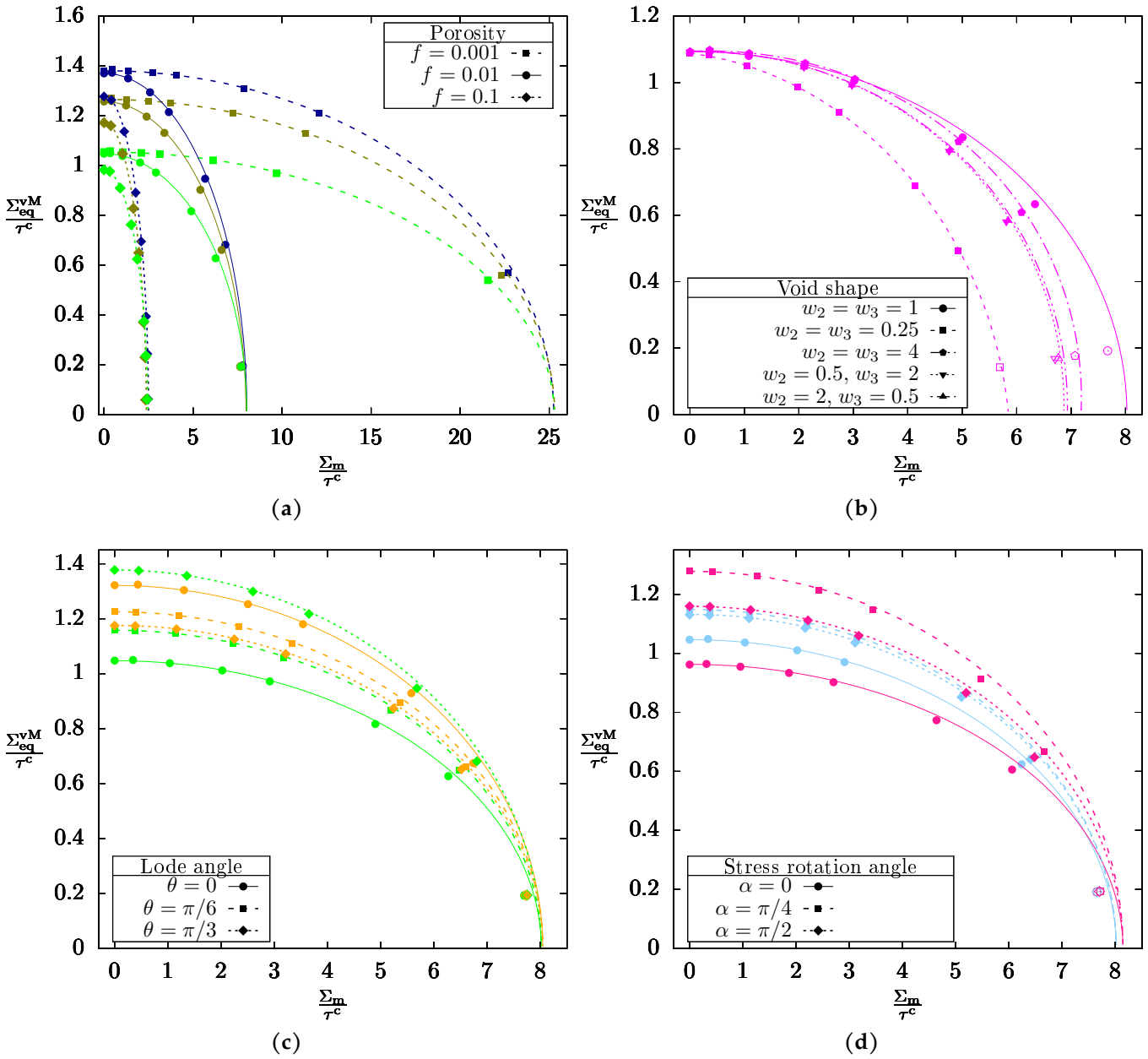

FIGURE III.9: Comparison of gauge surfaces predicted by variational estimates (lines) and unit-cell computations (points) at $n = 1$: (**a**) porous boundary at $\theta = 0$ and various spherical porosities; (**b**) porous boundary at $f = 0.01$ and $\theta = 0$ with ellipsoidal cavities of various shapes; (**c**) porous boundary with spherical cavity at $f = 0.01$ and various Lode angles; (**d**) porous boundary with spherical cavity at $f = 0.01$ and $\theta = 0$ with loading rotations of α around $\underline{e}_2$. Hollowed-out symbols mark simulations in which the deformation mode has been identified as void coalescence.

crystal orientations are perfectly accounted for, while the softening effect of porosity is correctly predicted in a wide range of f (in fact, for all the values considered in the unit-cell database: *i.e.* from $f = 0.001$ to $f = 0.3$). As in the case of single crystals, it can be noticed that porosity has a greater effect on the hydrostatic point than on the deviatoric point. Fig. III.9b assesses the impact of void shape; again, it is underlined that the proposed estimates are in agreement with unit-cell computations for all ellipsoidal geometries considered. For a given porosity, oblate cavities in the plane $(\underline{e}_2, \underline{e}_3)$ are found more damaging than prolate cavities, both of them displaying softer behavior than spherical cavities. Ellipsoidal cavities with $w_2 = 0.5$ and $w_3 = 2$ (and *vice-versa*) have intermediate gauge stresses between the two spheroidal void geometries. Lode angle influence is shown in Fig. III.9c: as in the case of single crystals (Paux et al., 2018), no general rule can be stated on the angle $\theta_{\max}$ at which the maximum yield stress is reached. Orientations displayed on the graph were chosen because of the important effect of θ, but this influence was noticed to be less important for other orientations. All these trends are quantitatively reflected in the model. All these findings do not depend on crystallographic orientations as they were seen on all couples present in the database. Finally, stress rotations were investigated in Fig. III.9d: $\alpha = \pi/2$ is a loading whose principal stress axis is along $\underline{e}_3$ while $\alpha = \pi/4$ have shear components since the main loading axis is along $\underline{e}_1 + \underline{e}_3$. Due to the complex interplay between loading directions and crystallographic orientations, the effect of α varies greatly according to the considered grain boundary. This is in contradiction with the findings of Wen and Yue (2007), Zhang et al. (2008) and Liu et al. (2009) who considered too few orientation couples to notice their influence. This conclusion will be seen to hold for other values of n (see Section III.1.4.4).

As explained in Appendix III.1.B, void coalescence was identified in a handful of simulations (see Fig III.9b,c,d). Although the model's predictions are not too far from these points, they are the computations where the discrepancy is the highest. Such a finding is unsurprising as the derivation conducted in the previous section is only supposed to account for voided boundaries where plasticity is diffuse.

1.4.3 Case $n > 1$: Heuristical variational extension

Variational methods of non-linear composite homogenization based on linear comparison materials have been widely used; see Castañeda and Suquet (1997) for a synthesis. In the aforementioned framework, the shear stresses on slip systems s are supposed to be homogeneous in each crystal i, *i.e.* $\tau_s^{(i)}(\underline{x}) = \overline{\tau}_s^{(i)}$. Injecting this hypothesis in Eq. III.27 means that the homogenized potential of a porous polycrystal of M grains (Song and Ponte-Castañeda, 2017a; Song and Ponte Castañeda, 2018) is sought in the form:

$$U^{\mathrm{LC}}(\boldsymbol{\Sigma}) = \sum_{i=1}^{M} f_i \left[\sum_{s=1}^{K} \frac{\dot{\gamma}_0 \tau_s^{(i),\mathrm{c}}}{n+1} \left(\frac{\overline{\tau}_s^{(i)}}{\tau_s^{(i),\mathrm{c}}} \right)^{n+1} \right] \tag{III.41}$$

In our study, only the cases $M = 1$ and $M = 2$ shall be considered. Note that there are $M+1$ phases due to the presence of a cavity of volume fraction $f_0 = f$, but the corresponding term does not appear in Eq. III.41 since the local stress potential of the void is 0. When $M = 1$, $f_1 = 1 - f$ and when $M = 2$, $f_1 = f_2 = (1-f)/2$. The homogenized resolved shear stresses $\overline{\tau}_s^{(i)}$ should be chosen in order to minimize the macroscopic potential and to fulfill the stress admissibility conditions. In linear comparison methods, $\left(\overline{\tau}_s^{(i)}\right)$ are solutions of a set of non-linear equations in which the pseudo-compliance $\overline{\mathbb{S}}$ of a well-chosen porous linear comparison material intervenes. Determining U requires solving a set of $m \times M \times K$ non-linear equations — integer m is contingent on the exact linear comparison method (*e.g.* variational method, second-order method). Therefore, Eq. III.41 is not analytic and may be too computationally expensive to implement in numerical simulations of ductile fracture, prompting the development of simpler expressions. In the case $M = 1$, Mbiakop et al. (2015b) has suggested the following analytic form for $\left(\overline{\tau}_s^{(i)}\right)$:

$$\overline{\tau}_s^{(i)} = \frac{1}{1-f} \sqrt{\left(\tau_s^{(i)}\right)^2 + \boldsymbol{\Sigma} : \left[\mathbb{A} + \left(q_{\mathbb{J}}(n,f)^2 - 1\right) \mathbb{J} : \mathbb{A} : \mathbb{J}\right] : \boldsymbol{\Sigma}} \quad \text{with} \quad \mathbb{A} = \frac{\left(\tau^{\mathrm{c}}\right)^2}{K} \left[(1-f)\overline{\mathbb{S}} - \mathbb{S}\right] \tag{III.42}$$

where $\tau_s^{(i)}$ is the resolved shear stress of the pristine crystal, $\mathbb{A}$ is linked to the pseudo-compliance $\overline{\mathbb{S}}$ of the linear porous crystal and $q_{\mathbb{J}}$ is a scalar depending on n and f. Since the work of Mbiakop et al. (2015b) focused on single crystal with random cavities, $\tau_s^{(i)} = \boldsymbol{\mu}_s : \boldsymbol{\Sigma}$, $\mathbb{S}$ is set by Eq. III.20$_b$ and $\overline{\mathbb{S}}$ is set by Eq. III.38. The substitution of Eq. III.42

into Eq. III.41 thus yields:

$$U^{\mathrm{LC}}_{\mathrm{mono}}(\boldsymbol{\Sigma}) = \frac{1}{(1-f)^n}\sum_{s=1}^{K}\frac{\dot{\gamma}_0\tau_s^{\mathrm{c}}}{n+1}\left[\frac{\sqrt{\boldsymbol{\Sigma}:\left(\boldsymbol{\mu}_s\otimes\boldsymbol{\mu}_s+\mathbb{A}+(q_J(n,f)^2-1)\,\mathbb{J}:\mathbb{A}:\mathbb{J}\right):\boldsymbol{\Sigma}}}{\tau_s^{\mathrm{c}}}\right]^{n+1} \tag{III.43}$$

which is exactly Eq. 40 of Mbiakop et al. (2015b). In the limit where f goes to 0, $\mathbb{A}=0$ so this expression reduces to the pristine single crystal potential (Eq. III.25). When $n=1$, if $q_J(1,f)$ is taken equal to 1 then Eq. III.43 reduces to the Hashin-Strikman estimate for linear porous single crystal (Eq. III.29$_a$ with $\overline{\mathbb{S}}$ given by Eq. III.38):

$$U^{\mathrm{LC}}_{\mathrm{mono}}(\boldsymbol{\Sigma}) = \frac{\dot{\gamma}_0\tau^{\mathrm{c}}}{2(1-f)}\left[\boldsymbol{\Sigma}:\left(\frac{K}{(\tau^{\mathrm{c}})^2}\mathbb{A}\right):\boldsymbol{\Sigma}+\sum_{s=1}^{K}\boldsymbol{\Sigma}:\left(\frac{1}{(\tau_s^{\mathrm{c}})^2}\boldsymbol{\mu}_s\otimes\boldsymbol{\mu}_s\right):\boldsymbol{\Sigma}\right] = \frac{\gamma_0\tau^{\mathrm{c}}}{2}\boldsymbol{\Sigma}:\overline{\mathbb{S}}:\boldsymbol{\Sigma} \tag{III.44}$$

Therefore, the expression of Mbiakop et al. (2015b) exhibits satisfying behavior in the limiting cases of a linear porous single crystal and a pristine non-linear single crystal. Next, Eq. III.42 is applied to the porous bicrystal case ($M=2$). From Appendix III.1.C, it is obtained that $\tau_s^{(i)} = \boldsymbol{\mu}_s^{(i)}:\left(\boldsymbol{\Sigma}\pm\widetilde{\boldsymbol{\Delta}_n}(\boldsymbol{\Sigma})\right)$ with $\widetilde{\boldsymbol{\Delta}_n}$ defined in Eq. III.55. As in Section III.1.4.1, $\mathbb{S}$ is set by Eq. III.39 (or equivalently Eq. III.58) and $\overline{\mathbb{S}}$ is set by Eq. III.29$_b$. Therefore, substitution of Eq. III.42 into Eq. III.41 yields:

$$U^{\mathrm{LC}}_{\mathrm{bi}}(\boldsymbol{\Sigma}) = \frac{1}{2(1-f)^n}\sum_{i=1}^{2}\sum_{s=1}^{K}\frac{\dot{\gamma}_0\tau_s^{(i),\mathrm{c}}}{n+1}\left[\frac{\sqrt{\left(\boldsymbol{\mu}_s^{(i)}:\left(\boldsymbol{\Sigma}\pm\widetilde{\boldsymbol{\Delta}_n}\right)\right)^2+\boldsymbol{\Sigma}:\left(\mathbb{A}+(q_J(n,f)^2-1)\,\mathbb{J}:\mathbb{A}:\mathbb{J}\right):\boldsymbol{\Sigma}}}{\tau_s^{(i),\mathrm{c}}}\right]^{n+1} \tag{III.45}$$

In the limit where f goes to 0, $\mathbb{A}=0$ so this expression reduces to the crystalline laminate potential (Eq. III.55). When $n=1$ and $q_J(1,f)$ is taken equal to 1, Eq. III.45 recovers the Hashin-Strikman estimate for the linear porous bi-crystal (Eq. III.29):

$$\begin{aligned} U^{\mathrm{LC}}_{\mathrm{bi}}(\boldsymbol{\Sigma}) &= \frac{\dot{\gamma}_0\tau^{\mathrm{c}}}{2(1-f)}\left[\boldsymbol{\Sigma}:\left(\frac{K}{(\tau^{\mathrm{c}})^2}\mathbb{A}\right):\boldsymbol{\Sigma}+\frac{1}{2}\sum_{s=1}^{K}\left(\frac{\boldsymbol{\mu}_s^{(1)}:\left(\boldsymbol{\Sigma}+\widetilde{\boldsymbol{\Delta}_1}\right)}{\tau_s^{(1),\mathrm{c}}}\right)^2+\left(\frac{\boldsymbol{\mu}_s^{(2)}:\left(\boldsymbol{\Sigma}-\widetilde{\boldsymbol{\Delta}_1}\right)}{\tau_s^{(2),\mathrm{c}}}\right)^2\right] \\ &= \frac{\dot{\gamma}_0\tau^{\mathrm{c}}}{2(1-f)}\left[\boldsymbol{\Sigma}:\left((1-f)\overline{\mathbb{S}}-\mathbb{S}\right):\boldsymbol{\Sigma}+\boldsymbol{\Sigma}:\mathbb{S}:\boldsymbol{\Sigma}\right] \quad \text{(see Eq. III.58)} \\ &= \frac{\dot{\gamma}_0\tau^{\mathrm{c}}}{2}\boldsymbol{\Sigma}:\overline{\mathbb{S}}:\boldsymbol{\Sigma} \end{aligned} \tag{III.46}$$

Therefore, the heuristic homogenized potential proposed here (Eq. III.45) is coherent with previous results in the limiting cases of a linear porous bi-crystal and a non-linear pristine bi-crystal. Until now, the value of q_J value was not discussed and was supposed to be 1. In that case, the use of Eq. III.43 and Eq. III.45 to predict gauge surfaces reveal that the estimated potential is too small at high trixialities, as is usually the case with variational estimates. q_J could be chosen to recover exact results for the hydrostatic behavior of porous crystals but unfortunately no such result is known. Instead, following Mbiakop et al. (2015b), the limiting case of crystals with an infinite number of equiangular equivalent slip systems ($K\to+\infty$ and $\tau_s^{(i),\mathrm{c}}=\tau^{\mathrm{c}}$) and spherical voids is considered and q_J is fixed so that this behavior is correctly predicted under pure hydrostatic loading. It is shown in Appendix III.1.E that this coherency condition writes:

$$q_J(n,f) = a\overline{g}_n\sqrt{\frac{20}{3f}}\left(\frac{1-f}{n(f^{-1/n}-1)}\right)^{\frac{n}{n+1}} \tag{III.47}$$

where $a=3/2$ for spherical voids and $\overline{g}_n$ is a constant that only depend on n. Note that:

$$q_J(1,f)=1 \;\Leftrightarrow\; \overline{g}_1 = \frac{1}{a}\sqrt{\frac{3}{20}} \tag{III.48}$$

Eq. III.47 can be qualitatively related to the hydrostatic behavior of Gurson-type yield criteria (see Paux et al., 2015 and Eq. III.24): under pure hydrostatic loading, the dependence on crystallographic orientations is thought to vanish, at least at the first order.

In summary, the heuristic variational model developed for viscoplastic bi-crystals with ellipsoidal voids is constituted by the conjunction of Eqs. III.45 and III.47.

1.4.4 Case $n > 1$: Assessment of gauge surfaces

Before carrying out an assessment of gauge surfaces, some additional discussion on $\overline{g}_n$ is needed. In Mbiakop et al. (2015b) as well as in Appendix III.1.E, an approximate argument based on a study of porous materials with Lode-dependent yield criteria (Benallal, 2018) lead to Eq. III.85, which gives an explicit value for $\overline{g}_n$. Values from Eq. III.85 and those given in Mbiakop et al. (2015b) are compared in Table III.4: they are very close for $n \in [\![1, 10]\!]$ but quite distinct[7] for $n = 100$. Unfortunately, when $n > 1$, using the value of $\overline{g}_n$ given by Eq. III.85 to predict gauge surfaces lead to gauge stresses at high triaxiality ratios that are significantly below the numerical gauge stresses provided by unit-cell simulations. For that reason, Eq. III.85 is discarded and $\overline{g}_n$ is set as a calibration parameter for $n > 1$. Note that the approximate nature of Eq. III.85 allows for such emancipation (see Appendix III.1.E). For a given n, $\overline{g}_n$ is chosen to minimize the mean square error in the prediction of gauge surfaces for porous boundaries with spherical voids and subjected to loadings with $\theta = 0$ and $\alpha = 0$. Only simulations that display void growth were considered; values obtained through this optimization procedure are reported in Table III.4 and shall be used in the graphs shown hereafter.

n		1	3	10	100
$\overline{g}_n$	Theoretical (Eq. III.73$_b$)	0.26	0.31	0.39	0.48
	Mbiakop et al. (2015b)	0.26	0.32	0.38	0.40
	Calibration	0.26	0.26	0.31	0.31

TABLE III.4: Values of $\overline{g}_n$ obtained by various methods.

In order to assess the heuristical extension presented in the previous section, gauge surfaces for $n = 3$, $n = 10$ and $n = 100$ are respectively shown in Fig. III.10, Fig. III.11 and Fig. III.12. Even if the predictions are satisfying in the range of n considered, it can be seen that agreement diminishes when n increases. This was expected since the rigorous estimate was only obtained for $n = 1$ and further extension to $n > 1$ is likely to become cruder as non-linearity grows. Thus, Fig. III.10 ($n = 3$) displays a better agreement than Fig. III.11 ($n = 10$) which itself shows better predictions

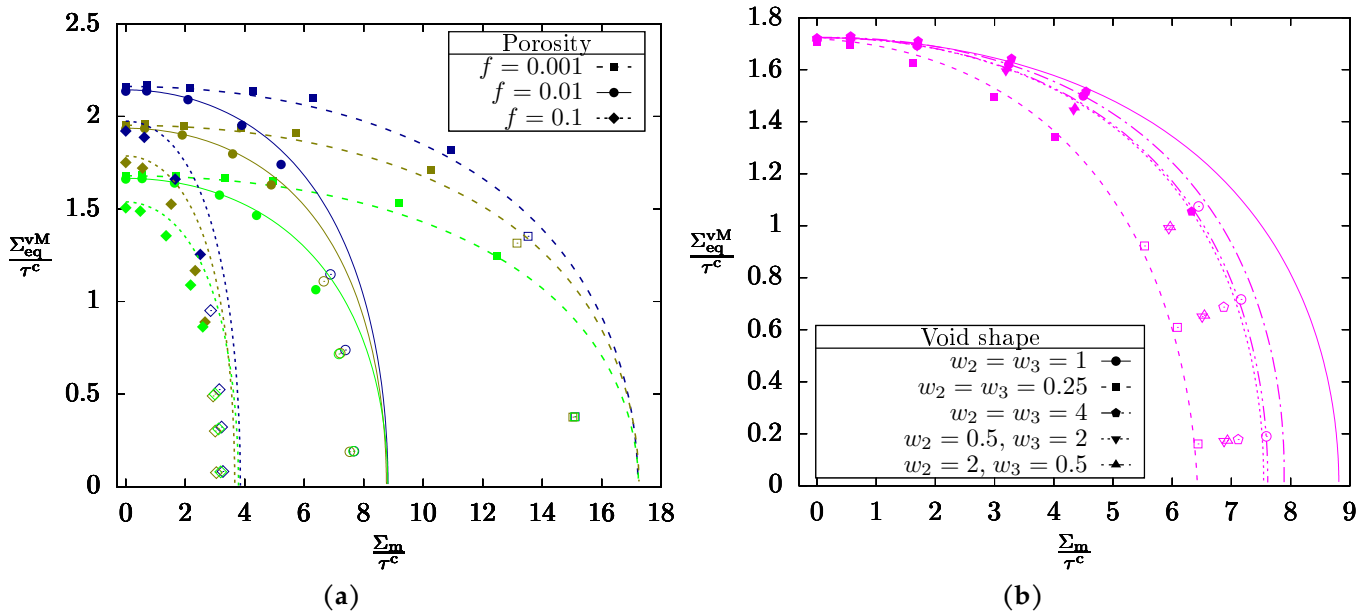

FIGURE III.10: Comparison of gauge surfaces predicted by variational estimates (lines) and unit-cell computations (points) at $n = 3$: **(a)** porous boundary at $\theta = 0$ and various spherical porosities; **(b)** porous boundary at $f = 0.01$ and $\theta = 0$ with ellipsoidal cavities of various shapes. Hollowed-out symbols mark simulations in which the deformation mode has been identified as void coalescence.

[7] This is no surprise since Mbiakop et al. (2015b) computed $\overline{g}_n$ for $n \in [\![1, 10]\!]$ from a formula akin to Eq. III.85 (although not explicitly given) and then extrapolated the numerical trend found in that interval to obtain $\overline{g}_{100}$.

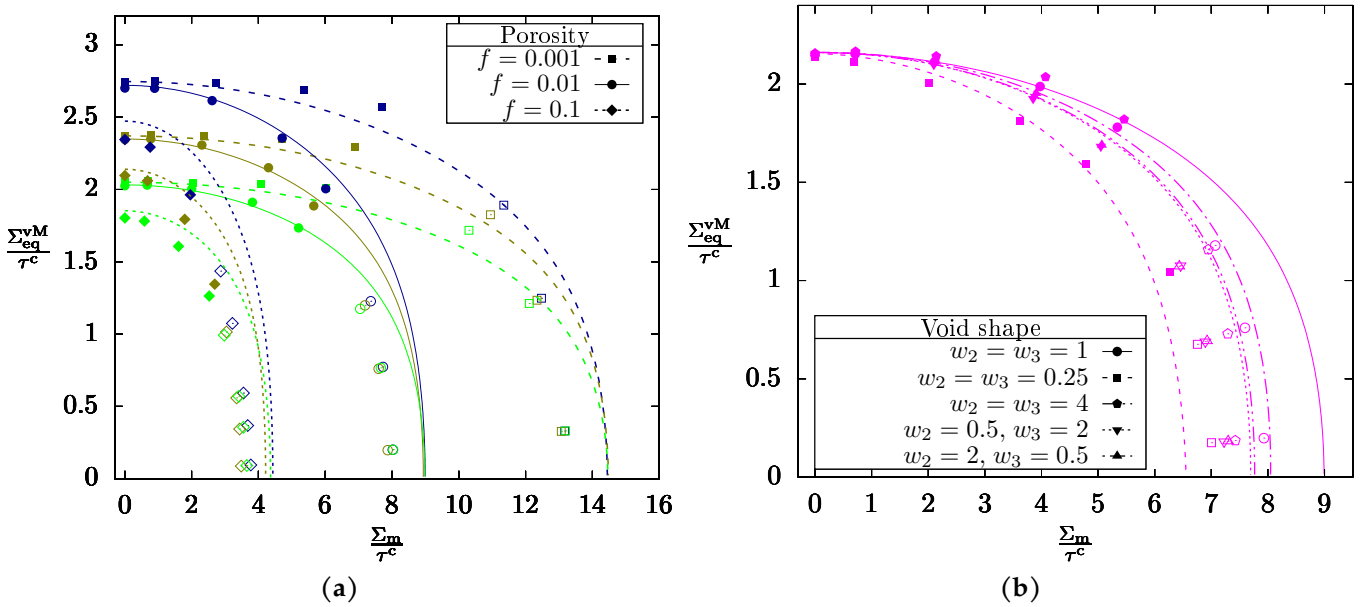

FIGURE III.11: Comparison of gauge surfaces predicted by variational estimates (lines) and unit-cell computations (points) at $n = 10$: **(a)** porous boundary at $\theta = 0$ and various spherical porosities; **(b)** porous boundary at $f = 0.01$ and $\theta = 0$ with ellipsoidal cavities of various shapes. Hollowed-out symbols mark simulations in which the deformation mode has been identified as void coalescence.

than Fig. III.12 ($n = 100$). Nevertheless, the variational model at $n = 100$ compares well with the Gurson-like locus (Fig III.7) in the void growth regime (full symbols). For all values of n, the combined effects of porosity and crystal orientation couples are well predicted (Figs. III.10-III.12a), as well as the influence of Lode angle and principal axes, which are only shown in the more challenging case ($n = 100$, see Fig. III.12c,d) for brevity. From these assessments, it can be inferred that gauge surfaces are correctly predicted for arbitrary loading configurations and that the model is fit for use in finite-element simulations. Furthermore, the results for ellipsoidal cavities presented in Figs. III.10-III.12b are quite satisfying regarding the void growth stage. The effect of oblate cavities along the grain boundary ($w_2 = w_3 = 0.25$) is particularly well predicted. The only disappointment comes from the asymmetry of the gauge surface for prolate cavities ($w_2 = w_3 = 4.0$) that is insufficiently marked in the model predictions, a discrepancy that increases with n and makes prolate cavities detrimental to material strength (similarly to the case $n = 1$, from which the heuristical extension is drawn) whereas they are beneficial to it. It can be seen in Mbiakop et al. (2015b) that the introduction of an additional parameter α_2 increased the influence of the microstructural tensor $\mathbb{A}$ on resolved shear stresses (Eq. III.42), enabling the reproduction of such effects at the cost of additional calibration.

It can be seen that increasing n fosters void coalescence (see also Fig. III.9), so that smaller sections of gauge surfaces belong to the void growth stage. A sharp transition can be seen (especially at $n = 100$) in the surfaces obtained by numerical homogenization: a first section with a high curvature at low triaxialities is supplemented by a straight-lined section at high triaxialities. This finding justifies the choice to model gauge surfaces with a multi-surface criterion (*e.g.* Keralavarma (2017)), only the void growth criterion being discussed here. This contrasts with other studies in which a unique yield criteria obtained in the dilute porosity regime is expected to account for all possible deformation modes: in Lebensohn et al. (2011), the estimations presented are naturally too stiff near the hydrostatic point due to the neglect of plastic localization, whereas the model presented in Mbiakop et al. (2015b) and Mbiakop et al. (2015a) displays degraded agreement at intermediate triaxialities in an effort to recover the hydrostatic point; remark that additional calibration parameters α_1 and α_2 that were needed at $n = 100$ (Mbiakop et al., 2015b) are not used here.

Finally, it is noted that the effect of choosing square periodicity of cavities in the plane $(\underline{e}_2, \underline{e}_3)$ has not been evaluated, but is believed to be minor given the fact that interactions between cavities are weak in the void growth stage. Nevertheless, Hashin-Strikman estimates for porous bi-crystals with planar randomness of cavities may be achieved by combining the derivations of Willis (1977) and Nemat-Nasser et al. (1993).

Even if it is not in the scope of this study, some considerations on computational efficiency may be stated. The GTN-like yield criterion is quite efficient provided that the value of $\mathbf{\Delta}_\infty$ is known. Since the normalized value of this

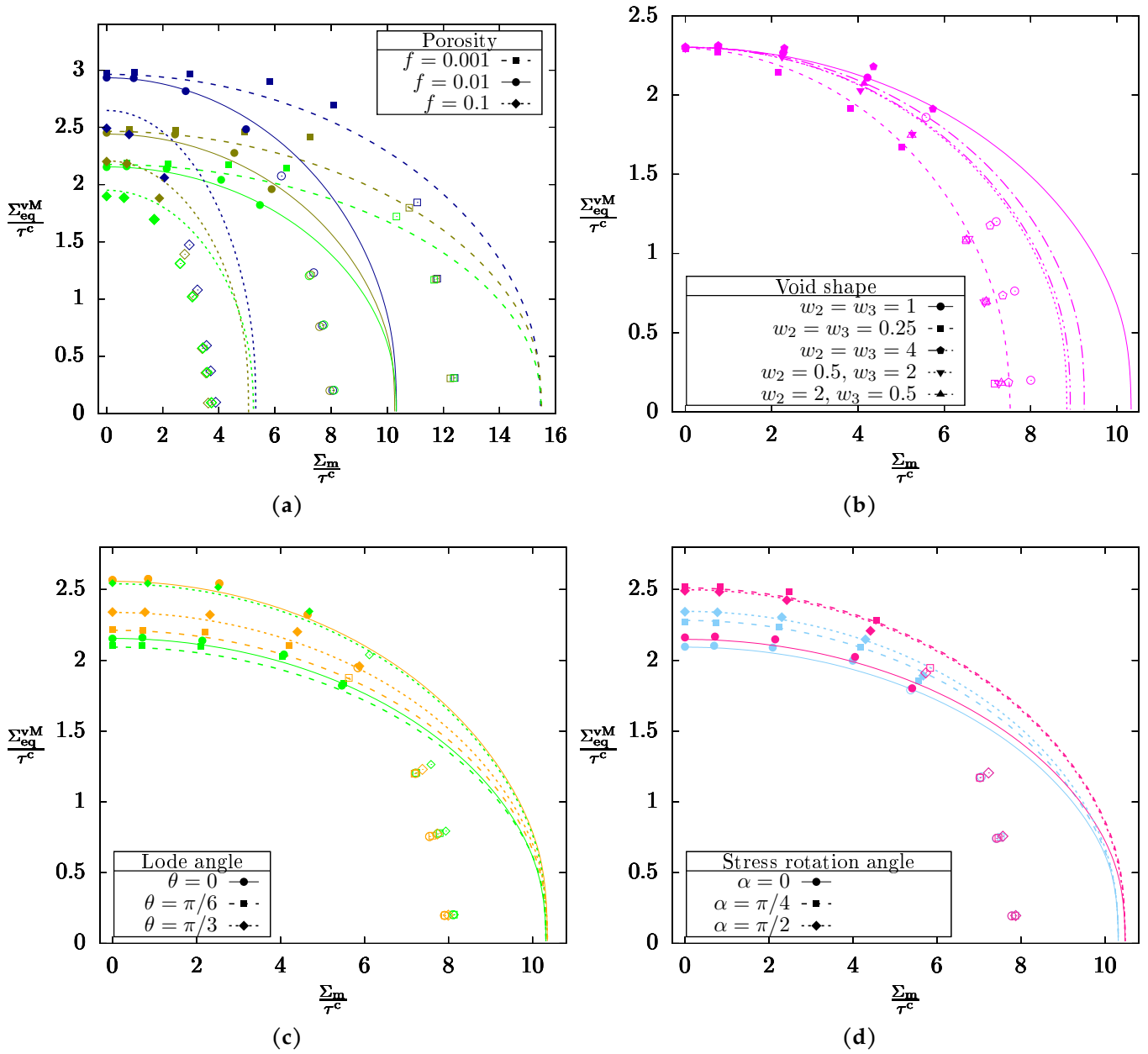

FIGURE III.12: Comparison of gauge surfaces predicted by variational estimates (lines) and unit-cell computations (points) at $n = 100$: **(a)** porous boundary at $\theta = 0$ and various spherical porosities; **(b)** porous boundary at $f = 0.01$ and $\theta = 0$ with ellipsoidal cavities of various shapes; **(c)** porous boundary with spherical cavity at $f = 0.01$ and various Lode angles; **(d)** porous boundary with spherical cavity at $f = 0.01$ and $\theta = 0$ with loading rotations of α around $\underline{e}_2$. Hollowed-out symbols mark simulations in which the deformation mode has been identified as void coalescence.

tensor only depends on the Lode angle and stress principal axes that may evolve slowly in ductile fracture simulations, optimization of Eq. III.55 will not be needed at every time step. Alternatively, using a surrogate model for $\boldsymbol{\Delta}_\infty$ would also accelerate simulations. Variational estimates (Eq. III.42) are more computation intensive with the determination of both $\overline{\mathbb{S}}$ and $\boldsymbol{\Delta}_n$, the latter being negligible compared to the former. Since $\overline{\mathbb{S}}$ only depends on porosity and void shape, its updates can be reduced to significant geometric evolutions, and accelerated by determining an optimal truncation for series $\mathbb{\Lambda}_{01}$ and $\mathbb{\Lambda}_{12}$ (Eq. III.31). It is also worth noting that computations can be alleviated by using a surrogate model for g_1 (Eq. III.62) or by considering elliptic-cylindrical voids for which function g_1 possesses a closed-form (see Appendix III.1.D).

1.5 Application to the competition between intergranular and transgranular void growth

The yield criteria proposed in the previous sections allow for discussing the competition between transgranular and intergranular ductile fracture. Since polycrystal ductile failure is an intricate phenomenon in which work hardening, texture evolution and strain localization play an essential role, definitive predictions of the dominant fracture mechanism are outside the scope of this study. However, given a microstructure with pre-existing cavities and a loading state, the two criteria derived in this study can predict the location — grain interiors or grain boundaries — where void growth will first occur.

As a first work example, let us consider a porous bi-crystal with a random distribution of spherical cavities, both at the grain boundary and within the grains, corresponding to the microstructure shown in Fig. III.13. Constant void volume fraction is assumed at the grain boundary and inside grains. Since Gurson-like criteria have been noticed to account for periodic arrays of voids as well as random distributions without additional calibration (Hure, 2021), Eq. III.24 is used to describe intergranular void growth and the following yield function (Paux et al., 2015) is chosen to account for transgranular void growth:

$$\lim_{m\to\infty}\left[\sum_{s=1}^{K}\left(\frac{|\boldsymbol{\Sigma}:\boldsymbol{\mu}_s|}{\tau_s^{\mathrm{c}}}\right)^m\right]^{2/m}+2qf\cosh\left(\kappa'\frac{\Sigma_m}{\tau^{\mathrm{c}}}\right)-1-(qf)^2=0 \quad \text{(III.49)}$$

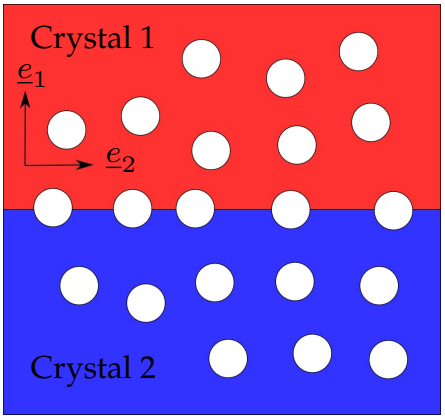

FIGURE III.13: Porous bi-crystal with a random distribution of spherical cavities.

with $\kappa' = 0.489$ and q given by Table III.3. Since yield functions only differ due to the deviatoric term, f and T have no influence on which of the grain boundary or grain interiors will experience plasticity first. In fact, it was proven in Appendix III.1.C that at constant porosity and loading state, the porous boundary (modeled by Eq. III.24) will always be harder than at least one of the two grain interiors (modeled by Eq. III.49). Hence, plasticity will first occur inside grains. This general prediction is in agreement with the experimental evidence that transgranular fracture is more common than intergranular ductile fracture, the latter being triggered by specific weakening of grain boundaries.

One of these weaknesses is the existence of a precipitate-free zone (PFZ) around grain boundaries of many precipitation-hardened alloys (see Fig. III.14a), which results in a significant decrease of the mean critical shear stress

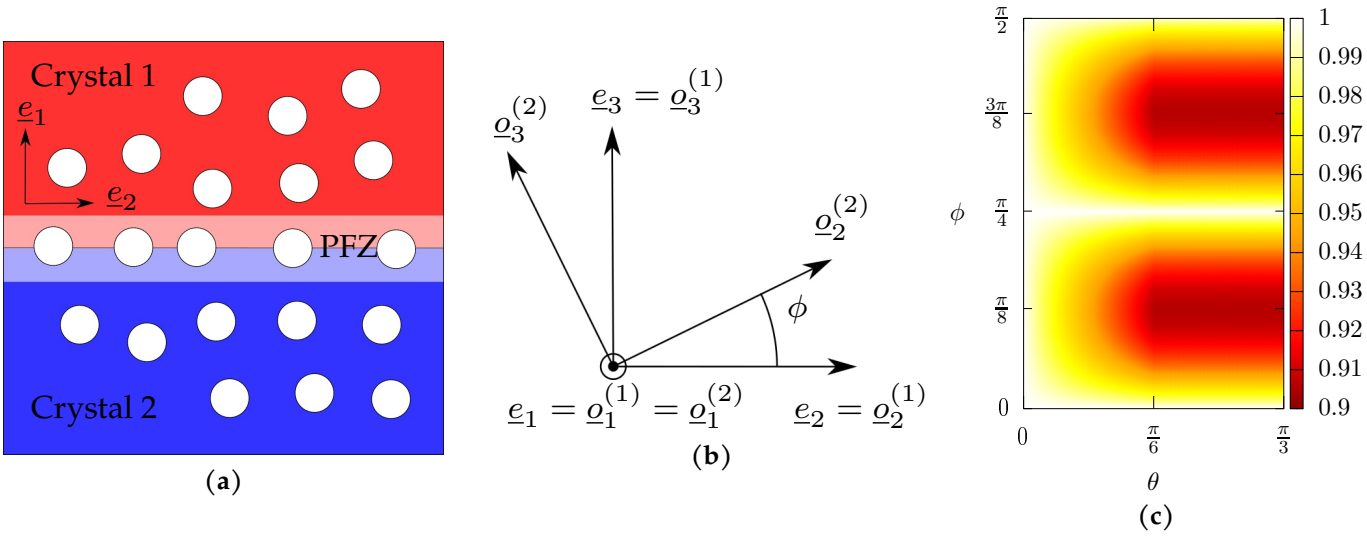

FIGURE III.14: Effect of crystal orientation and Lode angle θ on void growth inside a porous rate-independent bi-crystal with a soft precipitate-free zone (PFZ): **(a)** microstructure considered; **(b)** orientation mismatch ϕ between crystal 1 of orthotropy axes $(o_i^{(1)})$ and crystal 2 of orthotropy axes $(o_i^{(2)})$; **(c)** threshold $\tau^{\mathrm{c}}_{\mathrm{GB}}/\tau^{\mathrm{c}}_{\mathrm{GI}}$ below which plasticity occur first at grain boundaries as a function of ϕ and θ, at $T = 1/3$ and $f = 0.01$.

at grain boundaries. This critical shear stress is denoted τ^c_{GB} (Eq. III.24 is used with $\tau_s^{(1),c} = \tau_s^{(2),c} = \tau^c = \tau^c_{GB}$) while the grain interior critical shear stress is τ^c_{GI} (Eq. III.49 is used with $\tau_s^c = \tau^c = \tau^c_{GI}$). Restricting the analysis to a particular case of bi-crystals whose first crystal has orthotropy axes aligned with the frame of reference and whose second crystal has been rotated by an angle ϕ around $\underline{e}_1$ (see Fig. III.14b) — note that ϕ and $\phi + \pi/2$ result in the same crystal —, Fig. III.14c shows the critical shear stress mismatch required to trigger void growth at grain boundaries at $T = 1/3$ (simple tension) and $f = 0.01$. The axial symmetry in ϕ relatively to $\phi = \pi/4$ was expected because exchanging crystal 1 with crystal 2 does not influence the result. Remark that for $\phi \in \{0, \pi/2\}$ or $\theta = 0$, the two crystals are indistinguishable so yielding will occur both at the grain boundary and at grain interiors at $\tau^c_{GB} = \tau^c_{GI}$; decreasing τ^c_{GB} under this threshold will localize plasticity at grain boundaries. In all other situations, crystals have different behaviors under the prescribed loading so the threshold τ^c_{GB}/τ^c_{GI} displayed on Fig. III.14c will be below 1. Lode angle θ and crystal orientation mismatch ϕ have an influence on the threshold – although no influence of θ is reported when it exceeds a value of $\pi/6$. Identical trends exist for other stress triaxiality ratios T and void volume fractions f — even if these results need to be interpreted carefully due to the potential occurrence of void coalescence at high T and f. This is coherent with experimental results showing that some grain boundaries are more prone to intergranular fracture than others and provide a rationale for fracture surfaces exhibiting both transgranular and intergranular fracture (Deshpande et al., 1998). Note that inhomogeneities in the microstructure (Pommier et al., 2016) and grain boundary tilt angle relative to the loading (Gräf and Hornbogen, 1977) have also been put forward to justify such findings. Since PFZs usually have a higher work-hardening rate than grain interiors, the occurrence of plasticity at grain boundaries can be followed by grain interior plasticity once the PFZ has hardened (Thomas and Nutting, 1959). Therefore, the threshold given is an upper bound for the occurrence of ductile grain boundary failure, since τ^c_{GB} may be required to be much lower to account for subsequent fostered work-hardening; a full analysis of this effect was conducted by Pardoen et al. (2003) using isotropic GTN models.

Another weakness of grain boundaries that could enhance the occurrence of intergranular ductile fracture at constant void volume fraction is a different void aspect ratio. Indeed, elongated precipitates are common at grain boundaries (Kawabata and Izumi, 1976) and may lead to oblate intergranular voids. Thus, as a second example, microstructure shown in Fig. III.15a is considered, with spheroidal cavities of void aspect ratio $w = w_2 = w_3$ at the grain interface (see Section III.1.4.1 for the definition of these parameters), their volume being equal to the one of spherical voids located at grain interiors. The same crystal orientation couple as Fig. III.12b is chosen. Normalized yield stresses of grain interiors as well as the grain boundary are plotted in Fig. III.15b for $w = 1$ and $w = 0.25$ at two

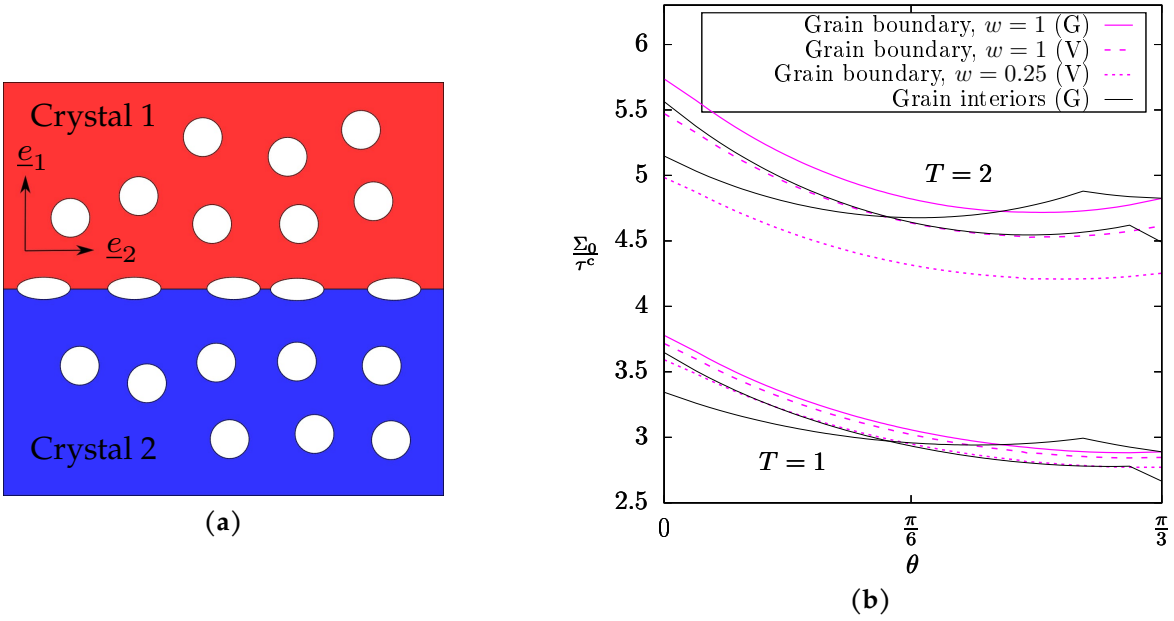

FIGURE III.15: Effect of intergranular void aspect ratio w, triaxiality T and Lode angle θ on void growth inside a porous rate-independent polycrystal of fixed orientation couple #10: **(a)** microstructure considered; **(b)** normalized yield stress Σ_0/τ^c at grain interiors and at the grain boundary as a function of θ for various w and T, computed either with Eq. III.24 (G) or Eq. III.42 (V).

different triaxialities. Porous single crystals are still modeled with Eq. III.49 but Gurson-like and variational criteria (Eqs. III.24 and III.42) are plotted for the porous boundary with $w = 1$; they are very close at $T = 1$ but the discrepancy increase with triaxiality — note that the two criteria coincide at the deviatoric point, at least when $f \to 0$. Despite this small inconsistency, the dependence in Lode angle θ is identical for the two criteria. Note that the brutal change in the slope of grain interior yield stress is not surprising; as pointed in Paux et al. (2018), it is related to a different set of slip systems being activated; no such vertexes are observed on grain boundary yield stress curves but no general rule can be stated on their absence as Eq. III.49 is a particular case of Eq. III.24. As seen in Fig. III.15b, transgranular yielding is favored at $T = 1$ for both $w = 1$ and $w = 0.25$, despite the expected softening effect of void aspect ratio reduction (see Fig. III.12b). The same conclusion holds at $T = 2$ and $w = 1$ when using Eq. III.24, as already pointed out in the previous case study. Due to the discrepancy between void growth criteria, this conclusion is challenged for $\theta > \pi/6$ when using the variational criterion, which underlines the importance of quantitative prediction of yield stresses as small errors can influence the failure mode. Finally, since void shape softening increases with T, it is no surprise that intergranular yielding is favored over transgranular yielding at $T = 2$ and $w = 0.25$.

1.6 Conclusion and perspectives

Large-scale simulation of intergranular ductile fracture requires the development of yield criteria for porous grain boundaries. This study focused on the void growth stage, *i.e.* the regime in which plastic deformation is not yet localized at the void scale. Using analytical homogenization techniques, two void growth yield criteria were derived for porous bi-crystal unit cells. The first yield locus (Eq. III.24), suited for rate-independent crystals with spherical voids, was obtained through limit-analysis of Hill plastic materials followed by heuristical corrections of the deviatoric and hydrostatic terms. This criterion is a Gurson-like expression, meaning that it can be easily implemented in mechanical solvers (FEM or FFT) that already hold similar models. Following a variational approach, an alternative criterion was derived for viscoplastic crystals of Norton exponent n: Hashin-Strikman estimates are obtained rigorously for $n = 1$ (Eqs. III.29, III.35), and a heuristical extension to $n > 1$ is proposed (Eq. III.42). Using a database of small strain unit-cell computations of porous grain boundaries, the agreement of models with respect to simulations was checked. Both criteria make satisfying predictions of yield surfaces for arbitrary macroscopic stress tensors (Fig. III.7c,d; Figs. III.9-III.12c,d) and crystal orientation couples (Fig. III.7a,b, Figs. III.9-III.12a). The span of porosities in which the models are validated is quite large ($f \in [0.001, 0.3]$), and the variational criterion predicts correctly gauge surfaces for ellipsoidal voids shapes whose axes are aligned with unit-cell axes (Figs. III.9-III.12b), which exclude the modeling of void rotation effects.

The derivation of intergranular void growth criteria, as performed in this paper, is an important milestone in simulating grain boundary ductile fracture. To describe the complete yield/gauge surfaces of voided grain boundaries, a void coalescence criterion should also be obtained, as performed in Hure (2019) for voided single crystals. Once the multi-surface criterion is complete, the addition of suitable evolution laws for microstructural parameters, such as porosity (*e.g.* Asim et al. (2019b)) and void shape, will constitute a full homogenized model, as was collected in Sénac et al. (2022) for porous single crystals. Thus, microstructure-informed simulations of the competition between transgranular and intergranular ductile fracture could be envisioned, as pioneered in Pardoen et al. (2003) for a given material, using isotropic models. Concomitantly, reference experiments are needed in order to assess theoretical models: namely, the hypothesis of perfect bonding between crystals made in crystal plasticity simulations and analytical homogenization has to be checked. Such confrontations at the bi-crystal scale are scarce (*e.g.* Zaefferer et al. (2003)) and were never performed in the presence of a voided boundary. Besides, if the material of interest displays intergranular voids of radius lower than the plasticity characteristic length, an extension of these criteria to account for size effects may be needed — see Khavasad and Keralavarma (2021) on that subject. Finally, at a different scale, it is paramount to compare porous polycrystal fracture predictions with actual experiments in the case of small aggregates so that the homogenization of crystallographic effects is validated.

1.A Definition and properties of Hill strain anisotropy tensor $\mathbb{H}^*$

For every orthonormal basis $(\underline{e}_1, \underline{e}_2, \underline{e}_3)$, the following set of vectors is a basis of the space of deviatoric symmetric second-order tensors $\mathscr{D}_2(\mathbb{R})$ (*i.e.* symmetric tensors $\boldsymbol{A}$ such that $\mathbb{J} : \boldsymbol{A} = 0$):

$$\left(\frac{\sqrt{3}+1}{2} \underline{e}_2 \otimes \underline{e}_2 + \frac{\sqrt{3}-1}{2} \underline{e}_3 \otimes \underline{e}_3, \frac{\sqrt{3}-1}{2} \underline{e}_2 \otimes \underline{e}_2 + \frac{\sqrt{3}+1}{2} \underline{e}_3 \otimes \underline{e}_3, \sqrt{2}\underline{e}_2 \otimes \underline{e}_3, \sqrt{2}\underline{e}_3 \otimes \underline{e}_1, \sqrt{2}\underline{e}_1 \otimes \underline{e}_2 \right) \tag{III.50}$$

Since $\mathscr{D}_2(\mathbb{R})$ is stabilized by $\mathbb{H}_i$, it is legitimate to consider its restriction $\overline{\mathbb{H}}_i$ to that subspace. The hypothesis that matrix materials can accommodate arbitrary isochoric deformation is made, *i.e.* $\overline{\mathbb{H}}_i$ admits an inverse tensor $\overline{\mathbb{H}}_i^*$. Tensors $\overline{\mathbb{H}}_i^*$ are then extended over the full space of symmetric second-order tensors $\mathscr{S}_2(\mathbb{R}) = \mathscr{D}_2(\mathbb{R}) \oplus \mathbb{R}\boldsymbol{I}$ by prescribing their value to 0 over the second set of the direct sum, yielding Hill strain anisotropy tensors $\mathbb{H}_i^*$ that verify $\mathbb{H}^* : \mathbb{H} = \mathbb{H} : \mathbb{H}^* = \mathbb{K}$.

The Voigt-Mandel condensation of $\mathbb{H}^*$ associated with an orthonormal basis of orthotropy $(\underline{e}_\mathrm{I}, \underline{e}_\mathrm{II}, \underline{e}_\mathrm{III})$ writes:

$$\mathbb{H}^* = \begin{pmatrix} h_{11}^* & h_{12}^* & h_{31}^* & 0 & 0 & 0 \\ h_{12}^* & h_{22}^* & h_{23}^* & 0 & 0 & 0 \\ h_{31}^* & h_{23}^* & h_{33}^* & 0 & 0 & 0 \\ 0 & 0 & 0 & h_{44}^* & 0 & 0 \\ 0 & 0 & 0 & 0 & h_{55}^* & 0 \\ 0 & 0 & 0 & 0 & 0 & h_{66}^* \end{pmatrix} \tag{III.51}$$

and it can be checked that this matrix admits an arrangement $(h_i^*)_{i\in[\![1,6]\!]}$ of its eigenvalues verifying the following relations:

$$\begin{aligned} h_{11}^* &= \tfrac{1}{9}\left(4h_1^* + h_2^* + h_3^*\right) & h_{23}^* &= \tfrac{1}{9}\left(h_1^* - 2h_2^* - 2h_3^*\right) & h_{44}^* &= h_4^* \\ h_{22}^* &= \tfrac{1}{9}\left(h_1^* + 4h_2^* + h_3^*\right) & h_{31}^* &= \tfrac{1}{9}\left(-2h_1^* + h_2^* - 2h_3^*\right) & h_{55}^* &= h_5^* \\ h_{33}^* &= \tfrac{1}{9}\left(h_1^* + h_2^* + 4h_3^*\right) & h_{12}^* &= \tfrac{1}{9}\left(-2h_1^* - 2h_2^* + h_3^*\right) & h_{66}^* &= h_6^* \end{aligned} \tag{III.52}$$

1.B Coalescence micromechanical indicator

The range of stress triaxialities and porosities covered in Section III.1.2 makes it likely that some unit cells undergo void coalescence instead of void growth. Therefore, an indicator is needed to filter out simulations that display deformation modes outside this study's scope. Two main macroscopic coalescence indicators have been proposed. First, coalescence by internal necking can be indicated by vanishing transverse strain rates D_{22}, D_{33} compared to D_{11}. However, this indicator cannot account for coalescence outside the $(\underline{e}_2, \underline{e}_3)$-plane such as shear-assisted coalescence (Hure, 2019) or coalescence in columns (Gologanu et al., 2001a). The extension proposed by Cadet et al. (2021) is based on the decrease rate of $\det(\dot{\boldsymbol{F}})$ — where $\boldsymbol{F}$ is the deformation gradient at the scale of the unit-cell — which experiences a drastic change when plasticity localizes. Unfortunately, in small strain simulations, unit cells are not expected to experience successive void growth and coalescence but rather a unique deformation mode, making this extension unsuitable. Second, the Rice criterion for plastic localization (Rice, 1976) is an alternative way of detecting the

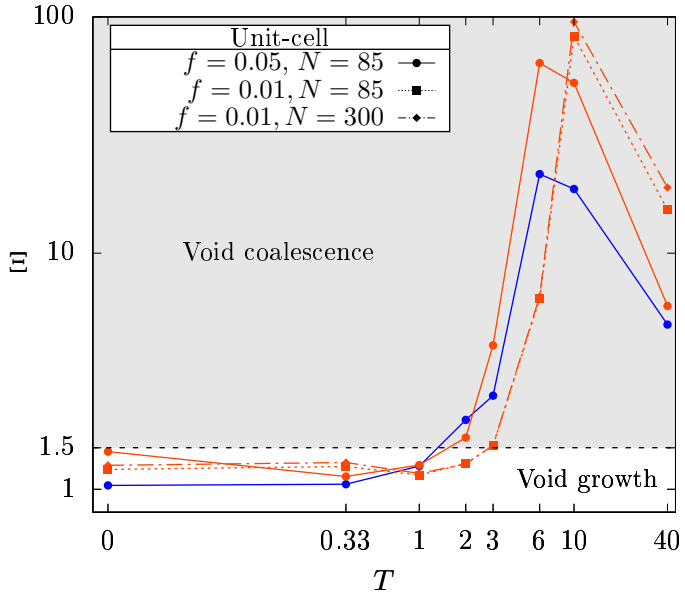

FIGURE III.17: Coalescence indicator Ξ as a function of triaxiality T at $\theta = 0$ and $n = 100$ for various porosities, mesh discretizations and crystal orientations.

onset of coalescence, as discussed in Vishwakarma and Keralavarma (2019) and Cadet et al. (2022). However, the start of inhomogeneous yielding under shear-dominated loadings is not detected by this criterion (Torki et al., 2021) and the fourth-order elastoplastic tangent stiffness tensor is not computed during FFT mechanical solving and thus cannot be obtained from unit-cell simulations.

In order to break this stalemate, advantage is taken from microscopic slip activity $\dot{\Gamma} = \sum_s |\dot{\gamma}_s|$ fields that are available upon plastic yielding for all simulations (Fig. III.16a,c). Statistical analysis of $\dot{\Gamma}$ values in voxels belonging to crystalline phases unveils different distributions according to the activated deformation mode, as shown in Fig. III.16b,d. In void growth situations (Fig. III.16a,b), plasticity is homogeneous around mean slip activity $\left\langle \dot{\Gamma} \right\rangle$ with very few voxels experiencing no yielding; this is in agreement with classical terminology of "diffuse plasticity". On the contrary, void coalescence is associated with large elastic zones in the unit cell (Fig. III.16c,d), leading to a distribution strongly weighted around 0 while mean slip activity $\left\langle \dot{\Gamma} \right\rangle$ is driven by voxels located in ligaments where plasticity localizes. Between these two well-identified extremes, few simulations remain ambiguous.

Based on the previous findings, the following coalescence indicator is proposed:

$$\Xi \geq \delta \quad \text{where} \quad \Xi = \frac{\left\langle \dot{\Gamma} \right\rangle}{\text{median}\left(\dot{\Gamma}\right)} \in [0, +\infty] \tag{III.53}$$

Ξ indicates the level of localization in the matrix and δ is an adjustable threshold. If $\Xi \geq \delta$, it means that the strain rate field deviates too much from a normal distribution, *i.e.* plasticity is no longer diffuse. For this study, a careful examination of the database ensured that the choice of $\delta = 1.5$ was satisfying for $n = 100$ and $\delta = 1.35$ for lower n. In

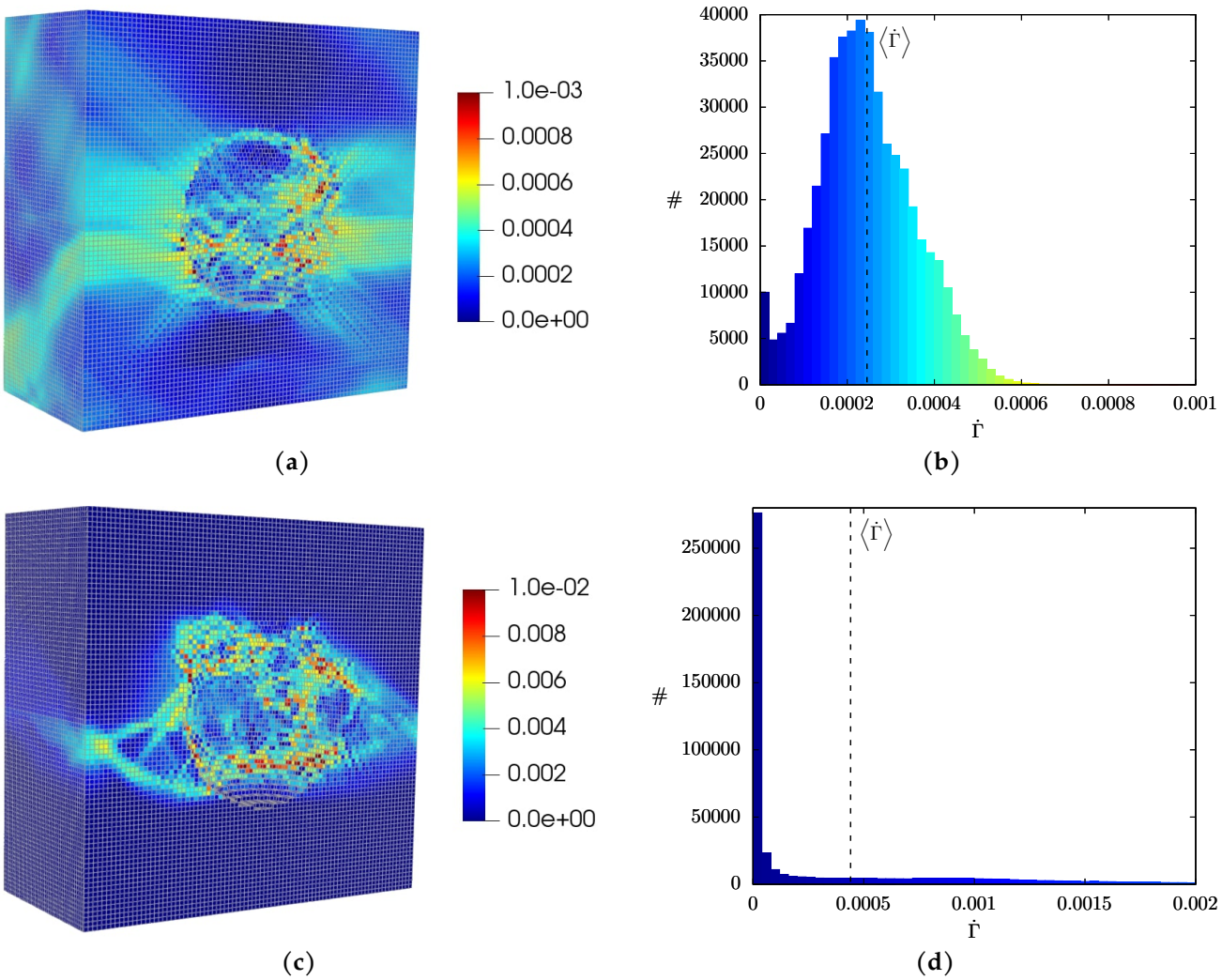

FIGURE III.16: Microscopic field **(a,c)** and corresponding histograms **(b,d)** of $\dot{\Gamma}$ at macroscopic plastic yielding for orientation couple #9, $\theta = 0$, $n = 100$ and $f = 0.05$: **(a,b)** $T = 0$; **(c,d)** $T = 10$.

Fig. III.17 are shown a few interesting properties of this indicator. First, Ξ is an increasing function of T from low to high triaxialities – as expected given the transition from growth to coalescence – but often exhibits a drop at very high triaxialities due to the transition from internal necking coalescence to multi-directional coalescence, a deformation mode in which localization takes place in a greater proportion of the unit-cell (this issue was briefly mentioned in Keralavarma (2017) and Keralavarma et al. (2020)). Second, when porosity increases, coalescence takes place at lower triaxialities. Finally, mesh discretization N has only a marginal effect on Ξ: indeed, in porous unit cells, strain localization is mainly controlled by the cavity size and not much by mesh refinement. Note that Chouksey et al. (2019) did propose another micromechanical indicator with less marked trends.

1.C Crystalline laminate mechanical analysis

Considering a unit-cell containing a crystalline laminate subjected to periodic boundary conditions, Hill-Mandel lemma $\boldsymbol{\Sigma} : \boldsymbol{D} = \langle \boldsymbol{\sigma} : \boldsymbol{d} \rangle_\Omega$ is verified with macroscopic stress $\boldsymbol{\Sigma}$ being the volume-average of the deviatoric microscopic field: $\boldsymbol{\Sigma} = \langle \boldsymbol{\sigma} \rangle_\Omega = \frac{1}{2}\left(\langle \boldsymbol{\sigma} \rangle_{\Omega_1} + \langle \boldsymbol{\sigma} \rangle_{\Omega_2}\right)$. Stress fields $\boldsymbol{\sigma}$ that are constant in each crystal are statistically admissible as long as $\boldsymbol{\sigma}^{(1)} = \boldsymbol{\Sigma} + \boldsymbol{\Delta}_n$ and $\boldsymbol{\sigma}^{(2)} = \boldsymbol{\Sigma} - \boldsymbol{\Delta}_n$ with $\boldsymbol{\Delta}_n$ an element of the space $\mathscr{C}_2(\mathbb{R})$ of symmetric second-order tensors satisfying the stress continuity condition at the planar interface. Then, every statically admissible field $\boldsymbol{\sigma}$ is such that:

$$\begin{aligned} \langle u(\boldsymbol{\sigma}) \rangle_\Omega &= \frac{1}{2}\left[\left\langle u_n^{(1)}(\boldsymbol{\sigma})\right\rangle_{\Omega_1} + \left\langle u_n^{(2)}(\boldsymbol{\sigma})\right\rangle_{\Omega_2}\right] \\ &\geq \frac{1}{2}\left[u_n^{(1)}\left(\langle \boldsymbol{\sigma} \rangle_{\Omega_1}\right) + u_n^{(2)}\left(\langle \boldsymbol{\sigma} \rangle_{\Omega_2}\right)\right] \\ &= \frac{1}{2}\left[u_n^{(1)}(\boldsymbol{\Sigma} + \boldsymbol{\Delta}_n) + u_n^{(2)}(\boldsymbol{\Sigma} - \boldsymbol{\Delta}_n)\right] \end{aligned} \tag{III.54}$$

due to the convexity of $u_n^{(1)}$ and $u_n^{(2)}$ in $\boldsymbol{\sigma}$ (potentials u are defined and discussed at the beginning of Section III.1.4). Therefore, minimizing the macroscopic stress potential over statically admissible stress fields (Eq. III.27) amounts to a minimization over crystal-wise constant fields, *i.e.* finding $\boldsymbol{\Delta}_n = \widetilde{\boldsymbol{\Delta}_n}$ so that U is minimal:

$$U(\boldsymbol{\Sigma}) = \min_{\boldsymbol{\Delta}_n \in \mathscr{C}_2(\mathbb{R})} \frac{1}{2}\left[u_n^{(1)}(\boldsymbol{\Sigma} + \boldsymbol{\Delta}_n) + u_n^{(2)}(\boldsymbol{\Sigma} - \boldsymbol{\Delta}_n)\right] \tag{III.55}$$

In the rate-independent limit, $n \to +\infty$ so Eq. III.23 is obtained. From Eq. III.55, it can be easily shown that the potential of the bi-crystal is lower than at least one of the corresponding single crystals:

$$U(\boldsymbol{\Sigma}) \leq U(\boldsymbol{\Sigma}, \boldsymbol{\Delta}_n = 0) \leq \max(U_1(\boldsymbol{\Sigma}), U_2(\boldsymbol{\Sigma})) \tag{III.56}$$

which proves that in the limit $f \to 0$, the porous bi-crystal will always be less prone to yielding at deviatoric loadings than one of the constitutive single crystals (see Section III.1.2.3). Note that when crystal 1 and crystal 2 are equal, $u_n^{(1)} = u_n^{(2)} = u_n$ and using the convexity of u_n on Eq. III.54 yield $U(\boldsymbol{\Sigma}) = u_n(\boldsymbol{\Sigma})$, *i.e.* the unnecessary stress continuity equation vanishes through the choice $\widetilde{\boldsymbol{\Delta}_n} = 0$.

For $n = 1$, an explicit resolution can be conducted. Indeed, Eq. III.55 can be rewritten using tensor $\mathbb{E}$ enforcing continuity at the planar interface (Hill, 1972), which enables to perform the minimization over the space of symmetric tensors:

$$U(\boldsymbol{\Sigma}) = \min_{\boldsymbol{\Delta} \in \mathscr{S}_2(\mathbb{R})} \frac{\dot{\gamma}_0 \tau^c}{4}\left[(\boldsymbol{\Sigma} + \mathbb{E} : \boldsymbol{\Delta}) : \mathbb{S}_1 : (\boldsymbol{\Sigma} + \mathbb{E} : \boldsymbol{\Delta}) + (\boldsymbol{\Sigma} - \mathbb{E} : \boldsymbol{\Delta}) : \mathbb{S}_2 : (\boldsymbol{\Sigma} - \mathbb{E} : \boldsymbol{\Delta})\right] \tag{III.57}$$

$\boldsymbol{\Delta}$-derivation and an inversion in the subspace of fourth-order tensors invariable by left or right double contraction with $\mathbb{E}$ (whose multiplicative identity is $\mathbb{E} : \mathbb{I} : \mathbb{E}$) yield:

$$\begin{aligned} \widetilde{\boldsymbol{\Delta}_1} &= \mathbb{D} : \boldsymbol{\Sigma} \quad \text{with} \quad \mathbb{D} = \mathbb{E} : \left[\mathbb{E} : (\mathbb{S}_1 + \mathbb{S}_2) : \mathbb{E}\right]^{-1} : \left[\mathbb{E} : (\mathbb{S}_2 - \mathbb{S}_1)\right] \\ U(\boldsymbol{\Sigma}) &= \frac{\dot{\gamma}_0 \tau^c}{2} \boldsymbol{\Sigma} : \overline{\mathbb{S}} : \boldsymbol{\Sigma} \quad \text{with} \quad \overline{\mathbb{S}} = \frac{1}{2}\mathbb{K} : \left[(\mathbb{I} + \mathbb{D}) : \mathbb{S}_1 : (\mathbb{I} + \mathbb{D}) + (\mathbb{I} - \mathbb{D}) : \mathbb{S}_2 : (\mathbb{I} - \mathbb{D})\right] : \mathbb{K} \end{aligned} \tag{III.58}$$

However, when $n > 1$, minimization amounts to finding the roots of high-degree polynomials of three variables, which seems to forbid explicit resolution. Thus, it must be resorted to numerical optimization to find $\widetilde{\boldsymbol{\Delta}_n}$. Nelder-Mead algorithm (Nelder and Mead, 1965) with multiple random starting points was found to be an efficient method to conduct this minimization.

Note that the constant character of microscopic stress fields in crystals is not retained when a cavity is present or when grain boundaries are not planar; indeed, stress continuity conditions at these interfaces applied to constant stress fields yield $\boldsymbol{\sigma} = 0$.

1.D Analytic expressions of g-functions

This section provides expressions of g_0 and g_1 for both ellipsoidal and elliptic-cylindrical voids with one axis along $\underline{e}_1$. g_2 is obtained immediately from g_1 by noticing that $g_2\left(\underline{\xi}\right) = g_1\left(-\underline{\xi}\right)$. The following notations, where $\odot$ is the Hadamard product, are introduced:

$$\phi = \left\|\underline{\xi} \odot r_1\underline{e}_1\right\|_2 \ , \ \zeta = \left\|\underline{\xi} \odot (r_2\underline{e}_2 + r_3\underline{e}_3)\right\|_2 \ , \ \eta = \left\|\underline{\xi} \odot (r_1\underline{e}_1 + r_2\underline{e}_2 + r_3\underline{e}_3)\right\|_2 \tag{III.59}$$

Voids without an axis along $\underline{e}_1$ do not follow the formulas given below and use must be made of the general expression Eq. III.32.

1.D.1 Ellipsoidal voids

The unit-cell configuration corresponding to ellipsoidal cavities is shown in Fig. III.19. After a variable substitution and the choice of the spherical coordinates of main axis along $\underline{\xi}$, g_0 can be expressed as:

$$g_0\left(\underline{\xi}\right) = \frac{3}{4\pi}\int_{r=0}^{1}\left(\int_{\theta=0}^{\pi}\left(\int_{\phi=0}^{2\pi} e^{i\eta r\cos\theta} r^2\sin\theta\,\mathrm{d}\phi\right)\mathrm{d}\theta\right)\mathrm{d}r = 3\,\frac{\sin\eta - \eta\cos\eta}{\eta^3} \tag{III.60}$$

g_1, on its part, requires the computation of the Fourier transform of the characteristic function of a cube and a demi-ball:

$$g_1\left(\underline{\xi}\right) = \frac{2}{1-f}\left[\frac{i}{n_1\pi}\sin\!\left(\frac{n_1\pi}{2}\right)^2\delta_{n_2,0}\delta_{n_3,0} - \int_{\underline{x}\in\Omega_0^+} e^{i\underline{\xi}\cdot\underline{x}}\right] \tag{III.61}$$

with $\Omega_0^+ = \{\underline{x}\in\Omega_0\,,\,\underline{x}\cdot\underline{e}_1 > 0\}$. Unfortunately, to the authors' knowledge, the latter do not possess a closed form, even if its real part is known. However, it can be expressed for $(n_2, n_3) \neq (0,0)$ as a one-dimensional integral (Eq. III.62$_b$) or as a series (Eq. III.62$_e$), the latter being numerically more efficient by two orders of magnitude:

$$\begin{aligned}
\int_{\underline{x}\in\Omega_0^+} e^{i\underline{\xi}\cdot\underline{x}} &= r_1r_2r_3\int_0^1\left(\int_0^{\sqrt{1-x_3^2}}\left(\int_0^{2\pi} e^{i\zeta r\cos\theta}e^{i\phi x_3} r\mathrm{d}\theta\right)\mathrm{d}r\right)\mathrm{d}x_3 \\
&= \frac{3f}{2\zeta}\int_0^1 e^{i\phi x_3}\sqrt{1-x_3^2}\,J_1\left(\zeta\sqrt{1-x_3^2}\right)\mathrm{d}x_3 \\
&= \frac{f}{2}\left[g_0\left(\underline{\xi}\right) + \frac{3}{\zeta}\,\mathrm{Im}\left(\int_0^1 e^{i\phi\sqrt{1-t^2}}\frac{t^2}{\sqrt{1-t^2}}J_1(\zeta t)\mathrm{d}t\right)\right] \\
&= \frac{f}{2}\left[g_0\left(\underline{\xi}\right) + i\frac{3}{\zeta}\sum_{n=0}^{+\infty}(-1)^n\frac{\phi^{2n+1}}{(2n+1)!}\int_0^1 t^2\left(1-t^2\right)^n J_1(\zeta t)\mathrm{d}t\right] \\
&= \frac{f}{2}\left[g_0\left(\underline{\xi}\right) + i\frac{3\phi}{\zeta^2}\sum_{n=0}^{+\infty}\left(-\frac{2\phi^2}{\zeta}\right)^n\frac{n!}{(2n+1)!}J_{n+2}(\zeta)\right]
\end{aligned} \tag{III.62}$$

where J_n is the n^{th} Bessel function. For $(n_2, n_3) = 0$, the following value is obtained:

$$\int_{\underline{x}\in\Omega_0^+} e^{i\underline{\xi}\cdot\underline{x}} = \frac{f}{2}\left[g_0\left(\underline{\xi}\right) + i\frac{3}{\phi^3}\left(1 - \cos\phi - \phi\sin\phi + \frac{1}{2}\phi^2\right)\right] \tag{III.63}$$

1.D.2 Elliptic-cylindrical voids

Given the additional computation time brought by evaluation of g_1 for ellipsoidal cavities, it may be more convenient to consider a laminate with elliptic cylindrical voids, shown in Fig. III.19. In that case, g-functions are Fourier transforms of characteristic functions of elliptic cylinders (or complementary of those for g_1 and g_2) and formulas are found

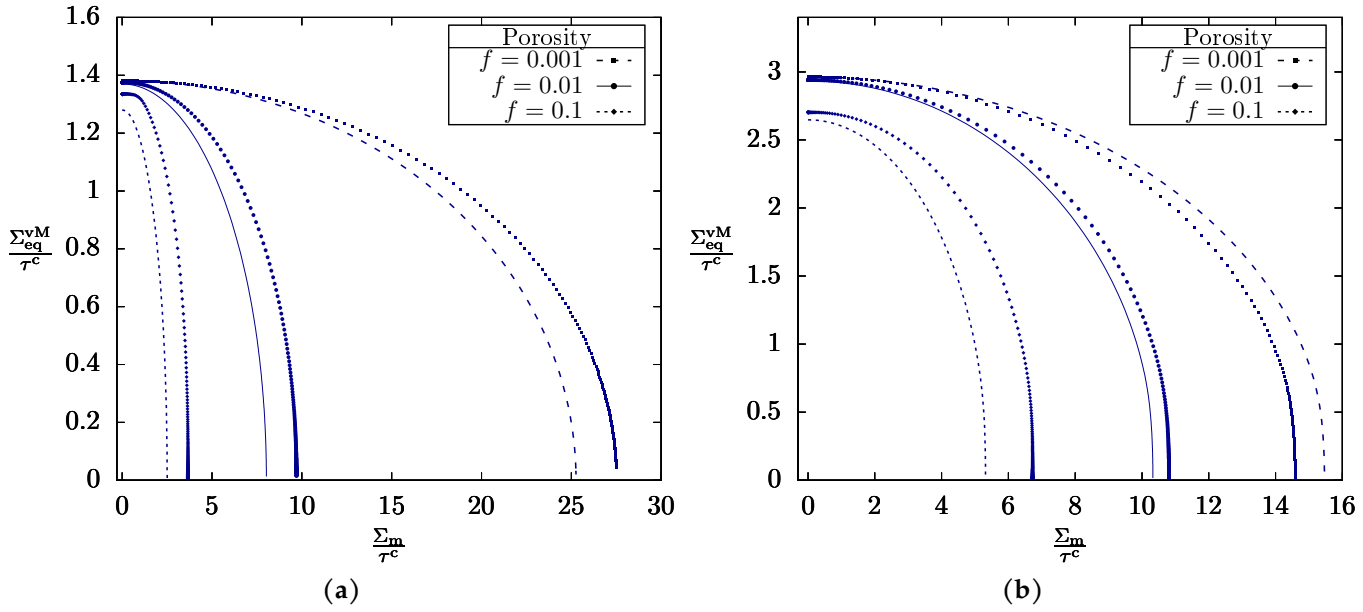

FIGURE III.18: Comparison of gauge surfaces predicted by variational estimates for spherical voids (lines) and equivalent cylindrical voids (points) at $\theta = 0$: **(a)** $n = 1$; **(b)** $n = 100$.

below:

$$g_0\left(\underline{\xi}\right) = 2\,\frac{\sin(\phi)}{\phi}\,\frac{J_1(\zeta)}{\zeta}$$
$$g_1\left(\underline{\xi}\right) = \frac{2}{1-f}\left[\frac{i}{n_1\pi}\sin\left(\frac{n_1\pi}{2}\right)^2\delta_{n_2,0}\delta_{n_3,0} - 2f\,\frac{\sin\left(\frac{\phi}{2}\right)}{\phi}\,\frac{J_1(\zeta)}{\zeta}e^{i\frac{\phi}{2}}\right] \tag{III.64}$$

keeping in mind that $\frac{J_1(\zeta)}{\zeta} \longrightarrow \frac{1}{2}$ when $\zeta \to 0$. All equations given in Sections III.1.4.1 and III.1.4.3 in the context of ellipsoidal voids are still valid for elliptic-cylindrical voids, except Eq. III.47 in which $a = \sqrt{3}$ for circular-cylindrical voids.

Given an ellipsoidal void of demi-axes (r_1, r_2, r_3), an equivalent elliptic-cylindrical void with dimensions $(r_1, r_2, \hat{r}_3)$ can be defined, with similar section in the plane $(\underline{e}_2, \underline{e}_3)$ and $\hat{r}_3$ chosen so that porosity f is kept constant between the two unit-cells. Comparisons of gauge surfaces of spherical cavities and equivalent cylindrical cavities are shown in Fig. III.18 for $n = 1$ and $n = 100$ at fixed Lode angle $\theta = 0$. At $n = 1$, the reversibility domain increases when the void shape is changed from spherical to cylindrical; this property is not retained at $n = 100$ due to different values of a in the heuristic extension. Regardless of n, a good agreement is reported when $f < 0.01$ for stress triaxialities ratios ranging from low to moderate — *i.e.* the part where void growth is active. However, this assessment should be pursued with other void shapes and more diverse loadings.

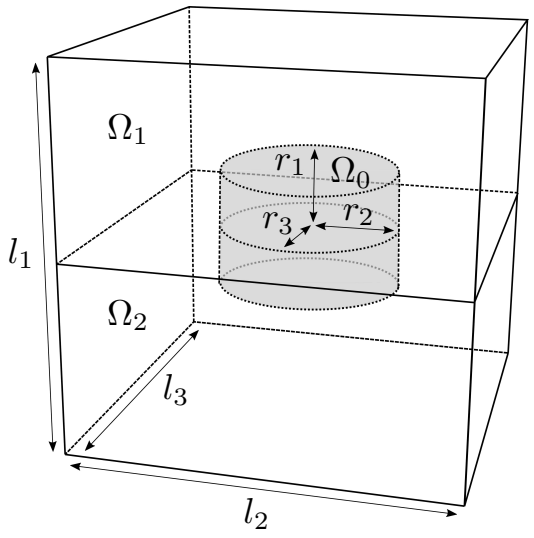

FIGURE III.19: Rectangular prismatic unit-cell with centered elliptic-cylindrical cavity; void axes are aligned with unit-cell axes.

1.E Porous crystal with infinite equivalent equiangular slip systems

1.E.1 Pristine crystal

In the principal frame $(\underline{e}_I, \underline{e}_{II}, \underline{e}_{III})$ of the Cauchy stress $\boldsymbol{\sigma}$, the following relation is verified:

$$\boldsymbol{\sigma} = \sigma_{\mathrm{m}}\boldsymbol{I} + \frac{2}{3}\sigma_{\mathrm{eq}}^{\mathrm{vM}}\boldsymbol{\sigma}^{(0)} \quad \text{with} \quad \boldsymbol{\sigma}^{(0)} = \begin{pmatrix} \cos\theta & 0 & 0 \\ 0 & -\cos\left(\theta + \frac{\pi}{3}\right) & 0 \\ 0 & 0 & -\cos\left(\theta - \frac{\pi}{3}\right) \end{pmatrix} \tag{III.65}$$

which means that when slip systems are equivalent, the plastic potential (Eq. III.25) writes as:

$$u_n(\boldsymbol{\sigma}) = \frac{\dot{\gamma}_0 \left(\tau^{\mathrm{c}}\right)^{-n}}{n+1} \left(\frac{2}{3}\sigma_{\mathrm{eq}}^{\mathrm{vM}}\right)^{n+1} \sum_{s=1}^{K} \left|\boldsymbol{\mu}_s : \boldsymbol{\sigma}^{(0)}\right|^{n+1} \tag{III.66}$$

In the limit of K equiangular slip systems with $K \to +\infty$, the Riemann summation theorem yields:

$$\frac{1}{K}\sum_{s=1}^{K} \left|\boldsymbol{\mu}_s : \boldsymbol{\sigma}^{(0)}\right|^{n+1} \longrightarrow \left\langle \left|\boldsymbol{\mu} : \boldsymbol{\sigma}^{(0)}(\theta)\right|^{n+1} \right\rangle_{\mathcal{S}} \tag{III.67}$$

where $\mathcal{S}$ is the set of all possible slip systems. Any slip system can be obtained by rotating an arbitrary slip system, *e.g.* $\underline{s}_0 = \underline{e}_I$, $\underline{m}_0 = \underline{e}_{II}$ and $\boldsymbol{\mu}_0 = \mathrm{sym}\left[\underline{e}_I \otimes \underline{e}_{II}\right]$. Therefore, the right-hand side of Eq. III.67 can be calculated by performing the following integration over the set $SO_3(\mathbb{R})$ of three-dimensional rotations with the (uniform and unit-normalized) Haar measure λ (Naimark, 1964):

$$\left\langle \left|\boldsymbol{\mu} : \boldsymbol{\sigma}^{(0)}(\theta)\right|^{n+1} \right\rangle_{\mathcal{S}} = \int_{SO_3(\mathbb{R})} \left|(\boldsymbol{R}^{\intercal} \cdot \boldsymbol{\mu}_0 \cdot \boldsymbol{R}) : \boldsymbol{\sigma}^{(0)}\right|^{n+1} \mathrm{d}\lambda(\boldsymbol{R}) \tag{III.68}$$

Recalling that $SO_3(\mathbb{R})$ can be parametrized with Euler angles $(\alpha_1, \alpha_2, \alpha_3) \in [0, 2\pi] \times [0, \pi] \times [0, 2\pi]$ with

$$\boldsymbol{R}(\alpha_1, \alpha_2, \alpha_3) = \begin{pmatrix} \cos\alpha_1 & -\sin\alpha_1 & 0 \\ \sin\alpha_1 & \cos\alpha_1 & 0 \\ 0 & 0 & 1 \end{pmatrix} \cdot \begin{pmatrix} 1 & 0 & 0 \\ 0 & \cos\alpha_3 & -\sin\alpha_3 \\ 0 & \sin\alpha_3 & \cos\alpha_3 \end{pmatrix} \cdot \begin{pmatrix} \cos\alpha_3 & -\sin\alpha_3 & 0 \\ \sin\alpha_3 & \cos\alpha_3 & 0 \\ 0 & 0 & 1 \end{pmatrix} \tag{III.69}$$

in the frame $(\underline{e}_I, \underline{e}_{II}, \underline{e}_{III})$, the integral can be recast as:

$$\left\langle \left|\boldsymbol{\mu} : \boldsymbol{\sigma}^{(0)}(\theta)\right|^{n+1} \right\rangle_{\mathcal{S}} = \frac{1}{8\pi^2} \int_0^{2\pi}\int_0^{\pi}\int_0^{2\pi} \left|\left[\boldsymbol{R}(\alpha_1, \alpha_2, \alpha_3)^{\intercal} \cdot \boldsymbol{\mu}_0 \cdot \boldsymbol{R}(\alpha_1, \alpha_2, \alpha_3)\right] : \boldsymbol{\sigma}^{(0)}\right|^{n+1} \sin\alpha_2 \, \mathrm{d}\alpha_3 \mathrm{d}\alpha_2 \mathrm{d}\alpha_1 \tag{III.70}$$

Restricting the analysis to odd n, a general form for this integral can be obtained using a formal computation tool:

$$\left\langle \left|\boldsymbol{\mu} : \boldsymbol{\sigma}^{(0)}(\theta)\right|^{n+1} \right\rangle_{\mathcal{S}} = a_n - \sum_{k=1}^{\lfloor \frac{n+1}{6} \rfloor} b_{k,n} \cos(6k\theta) \quad \text{with} \quad a_n,\, b_{k,n} > 0 \tag{III.71}$$

For instance:

$$a_1 = \frac{3}{20} \; ; \quad a_3 = \frac{27}{560} \; ; \quad a_5 = \frac{1269}{64064} \; , \quad b_{1,5} = \frac{27}{32032} \; ; \quad a_7 = \frac{5751}{622336} \; , \quad b_{1,7} = \frac{81}{77792} \tag{III.72}$$

In the limit $K \to +\infty$, the sum over k in Eq. III.66 will contain an infinity of terms. For the potential u_n to remain finite, τ^{c} must decrease with K at a rate suggested by Eq. III.67. Therefore, the pristine single crystal is considered with renormalized CRSS $\tau^{\mathrm{c}} = K^{1/n}\sigma^c$, so that:

$$u_n(\boldsymbol{\sigma}) \underset{K\to+\infty}{\longrightarrow} u_\infty(\boldsymbol{\sigma}) = \frac{\dot{\gamma}_0 \left(\sigma^{\mathrm{c}}\right)^{-n}}{n+1} \left(g_n(\theta)\, \sigma_{\mathrm{eq}}^{\mathrm{vM}}\right)^{n+1} \quad \text{where} \quad g_n(\theta) = \frac{2}{3}\left\langle \left|\boldsymbol{\mu} : \boldsymbol{\sigma}^{(0)}(\theta)\right|^{n+1} \right\rangle_{\mathcal{S}}^{\frac{1}{n+1}} \tag{III.73}$$

Thus, in the limit $K \to +\infty$, the pristine single crystal becomes an isotropic material of Lode angle-dependent potential. Using the analytical form of Eq. III.71, it can be shown that $g_n\left(\frac{\pi}{3}\right) = g_n(0)$, $g_n'(0) = g_n'\left(\frac{\pi}{3}\right) = 0$ and

$g_n(\theta) + g_n''(\theta) \geq 0$, which will be useful in what follows. Note that in the limit in which $n \to +\infty$, the single crystal becomes a perfectly plastic Tresca material, as already pointed out by other studies (Cailletaud, 2009; Mbiakop et al., 2016), which means that:

$$g_\infty(\theta) \propto \frac{1}{\cos\left(\theta - \frac{\pi}{6} - \left\lfloor \frac{3\theta}{\pi} \right\rfloor \frac{\pi}{3}\right)} \tag{III.74}$$

Functions g_1 and g_∞ are plotted in Fig. III.20; all other g_n for odd n lie in between in a continuum from g_1 to g_∞ as n increases.

1.E.2 Hollow sphere under hydrostatic loading

It is recalled that Benallal (2018) demonstrated that a hollow sphere with an isotropic perfect-plastic matrix following a yield function expressed as:

$$\mathcal{F}(\boldsymbol{\sigma}) = \left[\frac{\sigma_{\text{eq}}^{\text{vM}}}{\sigma^{\text{c}}} g(\theta)\right]^2 - 1 \tag{III.75}$$

with g a smooth function verifying $g(\theta) + g''(\theta) \geq 0$ and subjected to pure hydrostatic tension has the same yield strength as a hollow sphere made of a perfectly plastic von Mises material of uniaxial tension yield limit σ^0:

$$\sigma^0 = \frac{1}{\sqrt{g\left(\frac{\pi}{3}\right)^2 + g'\left(\frac{\pi}{3}\right)^2}} \sigma^{\text{c}} \tag{III.76}$$

while under pure hydrostatic compression, this result becomes:

$$\sigma^0 = \frac{1}{\sqrt{g(0)^2 + g'(0)^2}} \sigma^{\text{c}} \tag{III.77}$$

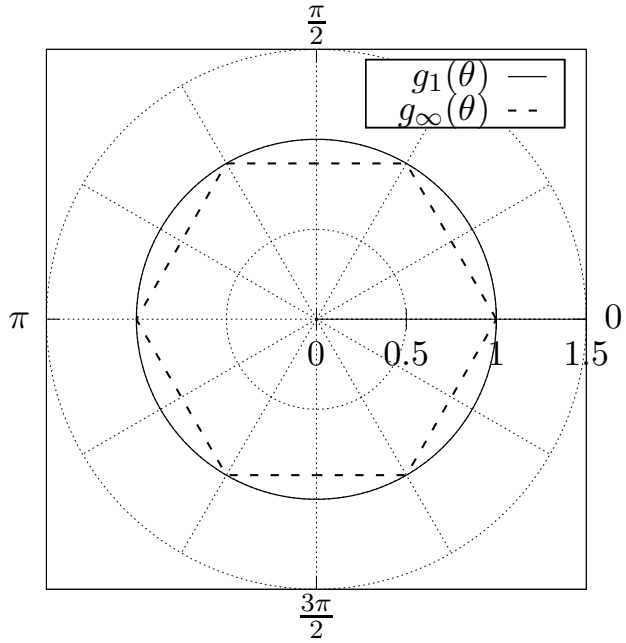

FIGURE III.20: Polar plot of normalized functions $g_n(\theta)/g_n(0)$ where θ is the angular coordinate. This representation corresponds to the π-plane of gauge surfaces.

Mbiakop et al. (2015b) made the (unstated) hypothesis that a similar equivalence was true for viscoplastic materials. If such a result is at least approximately verified, Eqs. III.76 and III.77 can be used with g_n instead of g. Since g_n is $\frac{\pi}{3}$-periodic, Eqs. III.76 and III.77 are identical. This means that a hollow sphere of viscoplastic single crystal with $K \to +\infty$ would then have the same plastic potential under pure hydrostatic loading as a hollow sphere of viscoplastic von Mises material of parameters $(\dot{\varepsilon}_0, \sigma_0) = (\dot{\gamma}_0, \sigma^{\text{c}}/g_n(0))$ in the case where n is finite (in the case $n = +\infty$, Tresca yield function is not smooth).

On the one hand, the plastic potential of a hollow sphere in a viscoplastic von Mises matrix of reference stress σ^{c} subjected to hydrostatic loading, as found in Leblond et al. (1994), writes:

$$U(\Sigma_{\text{m}}) = \frac{\dot{\gamma}_0}{n+1} \frac{(a g_n(0) \Sigma_{\text{m}})^{n+1}}{\left[\sigma^{\text{c}}\, n \left(f^{-\frac{1}{n}} - 1\right)\right]^n} \text{ with } a = \frac{3}{2} \text{ (spherical void)} \tag{III.78}$$

On the other hand, when $\tau_s^{\text{c}} = K^{1/n}\sigma^c$ and $K \to +\infty$, Eq. III.41 becomes:

$$U(\Sigma_{\text{m}}) = \frac{\dot{\gamma}_0}{n+1} \frac{(q_{\text{J}} \Sigma_{\text{m}})^{n+1}}{\left[\sigma^{\text{c}}(1-f)\right]^n} \left(\sqrt{\lim_{K \to +\infty} \left[(1-f)\frac{(\tau^{\text{c}})^2}{K} \boldsymbol{I} : \overline{\mathbb{S}} : \boldsymbol{I}\right]}\right)^{n+1} \tag{III.79}$$

Thus, Eq. III.78 and Eq. III.79 can be equated using the hollow sphere equivalence discussed previously. However, before proceeding, the quantity $\boldsymbol{I} : \left(\overline{\mathbb{S}}/K\right) : \boldsymbol{I}$ of Eq. III.79 should be evaluated in the limit $K \to +\infty$. First, according to

Böhlke and Bertram (2001), the pseudo-compliance tensor of a pristine crystal with infinite equiangular slip systems[8] becomes isotropic:

$$\frac{\left(\tau^{\mathrm{c}}\right)^2}{K}\mathbb{S}_i \underset{K\to+\infty}{\longrightarrow} \mathbb{S}_{\mathrm{iso}} \text{ with } \mathbb{S}_{\mathrm{iso}} = \frac{1}{3\kappa}\mathbb{J} + \frac{1}{2\mu_0}\mathbb{K} \text{ where } \mu_0 = 5 \tag{III.80}$$

Then, following Nemat-Nasser et al. (1993), $\mathbb{A}$ associated with an isotropic matrix is such that:

$$\begin{aligned}\frac{1}{\mu}\left[\mathbb{A}\left(\underline{\xi}, \frac{1}{3\kappa}\mathbb{J} + \frac{1}{2\mu}\mathbb{K}\right)\right]_{ijkl} &= \delta_{ik}\delta_{jl} + \delta_{il}\delta_{jk} - \frac{1}{\xi^2}(\delta_{ik}\xi_j\xi_l + \delta_{il}\xi_j\xi_k + \delta_{jk}\xi_i\xi_l + \delta_{jl}\xi_i\xi_k) \\ &+ \frac{6\kappa - 4\mu}{3\kappa + 4\mu}\left[\delta_{ij}\delta_{kl} - \frac{1}{\xi^2}(\delta_{ij}\xi_k\xi_l + \delta_{kl}\xi_i\xi_j)\right] + \frac{4}{\xi^4}\frac{3\kappa + \mu}{3\kappa + 4\mu}\xi_i\xi_j\xi_k\xi_l\end{aligned} \tag{III.81}$$

which yields, in the case of a random distribution of spherical voids:

$$\left\langle \mathbb{A}\left(\frac{1}{3\kappa}\mathbb{J} + \frac{1}{2\mu}\mathbb{K}\right)\right\rangle_{\Omega_0} = \frac{12\kappa\mu}{3\kappa + 4\mu}\mathbb{J} + h(\kappa, \mu)\mathbb{K} \tag{III.82}$$

where h is a coefficient depending on κ and μ that do not need to be detailed here. Alternatively, if the voids are distributed periodically with a cubic unit-cell, Eq. III.81 provides the following result:

$$\mathbb{A}_{00}\left(\frac{1}{3\kappa}\mathbb{J} + \frac{1}{2\mu}\mathbb{K}\right) = \frac{12\kappa\mu}{3\kappa + 4\mu}\left(\sum_{\underline{\xi}} \left|g_0\left(\underline{\xi}\right)\right|^2\right)\mathbb{J} + h'(\kappa, \mu)\mathbb{K}' + h''(\kappa, \mu)\mathbb{K}'' \quad \text{with} \quad \sum_{\underline{\xi}} \left|g_0\left(\underline{\xi}\right)\right|^2 = \frac{1 - f}{f} \tag{III.83}$$

with h' and h'' are coefficients depending on κ and μ and where the last equality is obtained using three-dimensional Parseval identity. Note that the factor $f/(1-f)$, whose absence may have surprised in Eq. III.37, is recovered as a normalization factor. Finally, considering Eq. III.82 (respectively Eq. III.83) in the limit $(\kappa, \mu) \to (+\infty, 5)$ and injecting it in Eq. III.38 (respectively Eq. III.37) that defines $\overline{\mathbb{S}}$ brings:

$$\frac{\left(\tau^{\mathrm{c}}\right)^2}{K}\boldsymbol{I} : \overline{\mathbb{S}} : \boldsymbol{I} \underset{K\to+\infty}{\longrightarrow} \frac{3}{20}\frac{f}{1 - f} \tag{III.84}$$

Equating Eq. III.78 and Eq. III.79 thus leads to:

$$q_{\mathrm{J}} = a\, g_n(0)\sqrt{\frac{20}{3f}}\left(\frac{1 - f}{n(f^{-1/n} - 1)}\right)^{\frac{n}{n+1}} \tag{III.85}$$

which is the condition on q_{J} that is necessary to recover the exact potential in the limit $K \to +\infty$. Note that this result does not depend on the number of crystals in the matrix (since they all become the same isotropic material in the limit $K \to +\infty$) nor on the distribution of cavities — *i.e.* random or with cubic periodicity.

[8] Remember that in the limit $K \to +\infty$, $\left(\tau^{\mathrm{c}}\right)^2 \mathbb{S}_i$ goes to infinity and needs renormalization by K to yield a finite value.

2 Intergranular void coalescence criterion

In the previous section, two yield criteria for intergranular void growth were obtained and did show satisfying accuracy compared to numerical results. As depicted in Fig. III.3b, these criteria must be supplemented by a study of intergranular void coalescence so that the full yield criterion of porous grain boundaries can be predicted using a multi-surface framework. On the one hand, the void coalescence criterion should encompass both internal necking and shear-assisted coalescence, since experimental occurrences of these coalescence modes were seen on intergranular ductile fracture surfaces (*e.g.* Fig. III.22). On the other hand, no observation of intergranular necklace coalescence exists in the literature; thus, this process is not believed to be of significant interest in the modeling of intergranular ductile fracture and shall be neglected in the following.

It should be kept in mind that homogenizing a porous material always results in a simplification of the microstructure: for instance, the void shape is approximated to an ellipsoid whose axes are aligned with those of the unit cell, excluding non-spherical shapes, asymmetries, and void rotation. No strain hardening is considered in this chapter but when the matrix material can experience it, its strong spatial heterogeneity can make it very difficult to homogenize with a single internal variable, as was shown in Section II.1. Crystal lattice rotation poses a similar challenge because it can vary significantly throughout the representative volume element of a porous (poly)crystal. Ling et al. (2016) has quantified this effect for porous single crystals at triaxialities $T \geq 1$, Chen et al. (2019) has performed a statistical analysis of this effect on porous bi-crystals at various T and Dakshinamurthy et al. (2021) presented a lattice rotation cartography for a unique porous grain boundary at $T = 0$ and various Lode parameters (see Fig. III.21). In this last study, the lattice rotation in crystal #2 is so inhomogeneous that it may not be considered as a single crystal anymore when ε_{eq} reaches 0.45. Naturally, crystal lattice rotation heterogeneity increases with strain so that it will have a greater impact on void coalescence than on void growth. Coalescence is most probably controlled by the crystallographic orientation in the intervoid ligament rather than the average crystallographic orientation of each half-crystal. Nevertheless, this heterogeneity is neglected here and its modeling is left for future research so that only porous bi-crystals with homogeneous crystallographic orientation from either side of the grain boundary are considered. Therefore, in the remaining of this sub-chapter, a coalescence yield criterion will be sought for a porous crystalline microstructure akin to that of Fig. III.1. This content is reprinted from a scientific paper (Sénac et al., 2024).

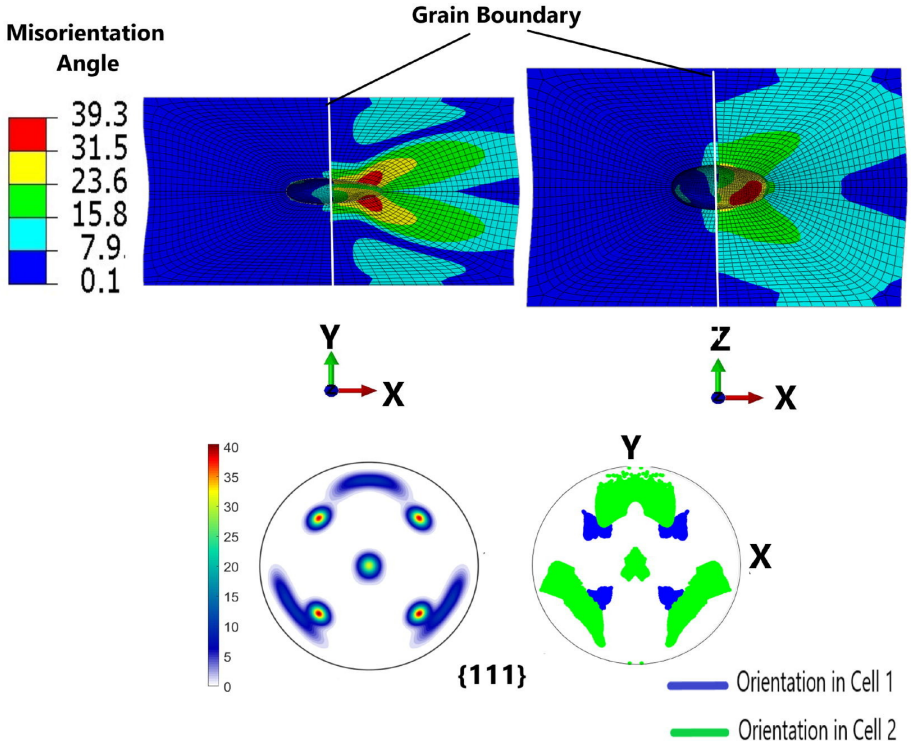

FIGURE III.21: Crystal lattice misorientation angle relatively to the initial crystallographic orientations, taken at $\varepsilon_{\text{eq}} = 0.45$. The main loading axis is along X, with $T = 0$ and $L = -1$. The pole figures present the density plot and the discrete plot of crystallographic orientations of material elements in the deformed state (Dakshinamurthy et al., 2021).

Yield criterion for intergranular void coalescence under combined tension and shear

Cédric Sénac, Jérémy Hure, Benoît Tanguy

Submitted for publication

Abstract

Intergranular ductile fracture is a failure mode that may arise in many metallic alloys used in industrial applications. It manifests as the successive nucleation, growth, and coalescence of cavities at grain boundaries. Thus, simulation of intergranular ductile fracture in polycrystals requires modeling those three different stages at the scale of grain boundaries, *i.e.* at the interface between two different crystals. In this study, a yield criterion for the coalescence of cavities at the interface between two isotropic materials obeying Mises plasticity is first developed by limit analysis in order to provide some insights into that phenomenon. This criterion is checked against numerical limit analysis under combined tension and shear and is found to agree with unit-cell simulations quantitatively. The model is then extended to crystals so as to account for the complex coupling between loading state, crystallographic orientations, and void microstructure in intergranular coalescence. This second criterion is also assessed through comparisons to numerical limit analysis for an FCC crystal lattice. The agreement is very good in the case of coalescence by internal necking and the trends displayed by coalescence under combined tension and shear are captured correctly. Some implications of the model on the competition between transgranular and intergranular ductile fracture are discussed. Finally, by combining this model with an existing criterion for void growth at grain boundaries, a multi-surface yield function relevant to intergranular ductile fracture is obtained and compared to unit-cell simulations.

2.1 Introduction

The phenomenon of void nucleation, growth and coalescence is among metallic alloys' dominant ductile failure modes. On the one hand, void growth manifests as a relatively independent enlargement of cavities, with diffuse plasticity at the scale of voids. On the other hand, void coalescence is characterized by strong interactions between cavities with strain localizing in specific zones linking voids (Pineau et al., 2016). These ductile fracture processes can be transgranular as well as intergranular; in the former, the damage develops through the grains whereas in the latter, the phenomenon of void growth and coalescence happen at grain boundaries due to intense intergranular plastic flow (Vasudévan and Doherty, 1987). In that case, fracture surfaces display intergranular facets covered in fine dimples originating from the coalescence of grain boundary cavities. As in transgranular fracture, intergranular coalescence can occur by necking of the intervoid ligament — in which case dimples are round or equiaxed, as shown in Fig. III.22a — or by shear-assisted coalescence — in which case elongated dimples are seen, as in Fig. III.22b. A more detailed description of these two important coalescence modes can be found in Benzerga and Leblond (2010).

A broad class of metallic alloys can experience transgranular or intergranular ductile fracture depending on microstructure and loading conditions; some fractographies even reveal mixed damaging processes. For instance, the failure mode of precipitation-hardened alloys is especially sensitive to the aging treatment that can foster transgranular or intergranular ductile fracture: this is the case in aluminum alloys (Suresh et al., 1987; Kuramoto et al., 1996; Decreus et al., 2013; Poole et al., 2019), nickel superalloys (Mills, 1980; Chang et al., 2014), metastable β-titanium alloys (Foltz et al., 2011; Li et al., 2017) and magnesium alloys (Zheng et al., 2008; Xiao et al., 2022). Steel overheating during austenitization treatment has a similar effect (Tsun, 1953; Schulz and McMahon, 1973). Finally, neutron-irradiated metals in which transmutation produces helium bubbles are also a type of material where competition between ductile damage phenomena happens, *e.g.* austenitic stainless steels (Hojná, 2017) and nickel-based alloys (Judge et al., 2015; Howard et al., 2019). For a more detailed overview of alloys prone to intergranular ductile fracture, see Sénac et al. (2023a). Cases in which intergranular ductile fracture prevails are usually associated with reduced elongation compared to transgranular ductile fracture occurrences, so that predicting the dominant damage process is of paramount importance (Pardoen et al., 2003).

Since seminal contributions five decades ago (*e.g.* Rice and Tracey (1969), Gurson (1977), and Thomason (1985)), considerable efforts have been made to model ductile failure through homogenization of the mechanical behavior

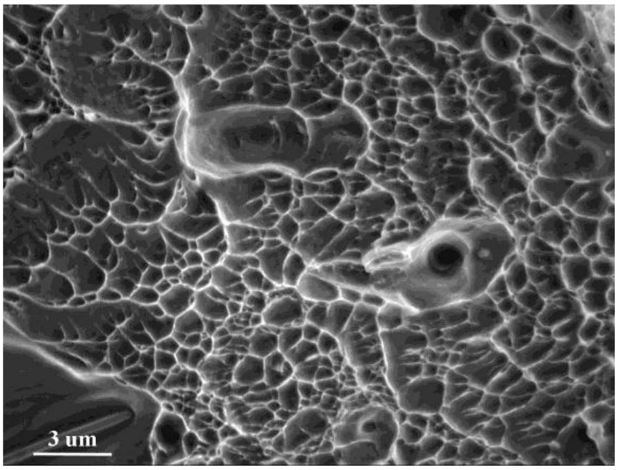

(**a**) Coalescence by internal necking

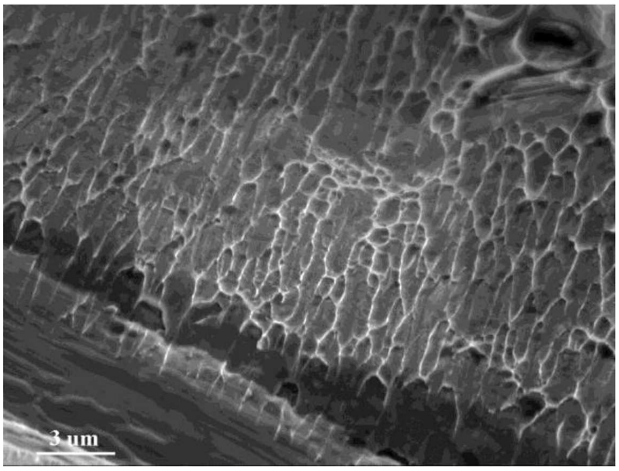

(**b**) Shear-assisted coalescence

FIGURE III.22: Secondary electron micrographs of the dimples seen on intergranular facets of the fracture surface of an Al-Mg-Si alloy with low manganese content subjected to an oil quench after being heat-treated at 560°C (Poole et al., 2019).

of porous materials. These achievements are extensively reviewed in Benzerga and Leblond (2010). Most of these models are relevant for polycrystalline materials where voids are significantly larger than the grain size, so that the matrix material at the scale of the voids is composed of many grains and can be described by conventional plasticity models. However, any physically-based modeling of the differences between intergranular and transgranular ductile fracture needs to tackle the issue at a scale below, that of voids smaller than the grain size. As it happens, interest in the effective behavior of porous single crystals has risen in the last twenty-five years. On the one hand, significant numerical results have been gathered on void growth and coalescence inside single crystals, considering different geometries: spherical voids in tetragonal cells (Liu et al., 2007; Yang and Dong, 2009; Liu et al., 2010; Ha and Kim, 2010; Yerra et al., 2010; Selvarajou et al., 2019; Guo et al., 2020; Sénac et al., 2022; Indurkar et al., 2022) and cylindrical voids in a cylindrical cell (Hure, 2019; Sénac et al., 2023b). On the other hand, intergranular void growth has been studied in several works (Wen and Yue, 2007; Liu et al., 2009; Yang and Dong, 2009; Li et al., 2015; Jeong et al., 2018; Chen et al., 2019; Asim et al., 2019a; Dakshinamurthy et al., 2021; Zhu et al., 2022; Sénac et al., 2023a). However, to the authors' knowledge, only one study did focus on the issue of intergranular void coalescence (Liu et al., 2010); it was also incidentally evoked in Sénac et al. (2023a). In the work of Liu et al. (2010), it was shown that when the orientation mismatch between the two grains increases, significant strain incompatibilities arise at the grain boundary, triggering void coalescence along the interface. On the contrary, void coalescence through the interface is impaired by high-angle boundaries.

Fostered by these numerical homogenization studies, analytical homogenization of porous materials has been extended to single crystals with internal cavities in several models designed to account either for void growth (Han et al., 2013; Paux et al., 2015; Mbiakop et al., 2015b; Ling et al., 2016; Song and Ponte-Castañeda, 2017a; Srivastava et al., 2017; Khavasad and Keralavarma, 2021) or coalescence (Yerra et al., 2010; Hure, 2019). As a result, simulations of crystal plasticity-based transgranular ductile fracture of samples have been enabled (Scherer et al., 2021; Frodal et al., 2021; Khadyko et al., 2021). On the contrary, the physically-based modeling of intergranular ductile fracture is mostly missing. Recently, two yield criteria of intergranular void growth were developed (Sénac et al., 2023a) but the modeling of intergranular void coalescence is still lacking; the present study aims to fill this gap.

The paper is organized as follows: in a first part, the microstructure studied — an array of cavities at the interface between two materials with different mechanical properties — is detailed and the fundamentals of limit analysis are briefly recalled. In a second part, a yield criterion for void coalescence in a Mises bi-material is obtained through limit analysis and assessed against numerical homogenization results. In a third part, the isotropic yield criterion is extended to account for crystal plasticity, thus obtaining a limit-load criterion for intergranular coalescence. Its validation is also carried out by comparing analytical results to unit-cell computations. The last part discusses the implications of the crystalline criterion regarding the competition between intergranular and transgranular failure and proposes a multi-surface yield criterion for intergranular ductile fracture.

2.2 Problem statement

In the following, vectors are shown as $\underline{a}$ of norm a, second-order tensors as $\boldsymbol{a}$ and fourth-order tensors as $\mathbb{A}$. Finally, the symmetric tensor product is denoted $\odot$.

2.2.1 Porous material description

As a first approximation, a porous grain boundary (Fig. III.23a) is modeled as a void array with hexagonal lattice at the interface between two different materials (Fig. III.23b). Perfect bounding is assumed between the two sound phases. An approximation of this material is provided by a cylindrical unit-cell Ω of main axis along $\underline{e}_3$ (Fig. III.23c) and whose origin is taken at the center of the void. Up to a rotation of the material orientation, $\underline{e}_1$ can be chosen along the imposed shear in the plane normal to $\underline{e}_3$, if any. The unit cell half-height is called H and its radius R; it contains a coaxial cylindrical void ω and is characterized by three dimensionless ratios:

$$\chi = \frac{r}{R} \ , \quad c = \frac{h}{H} \ , \quad w = \frac{h}{r} \tag{III.86}$$

χ is the (transverse) ligament size ratio, c is the axial ligament size ratio and w is the void aspect ratio. If $w > 1$, the void is elongated (which would correspond to a prolate cavity), and $w < 1$ means that the void is flat (which would correspond to an oblate cavity).

As unit cell simulations have shown that coalescence corresponds to the appearance of elastic unloading on both vertical sides of the void (*e.g.* Morin et al. (2015b)), the following boundary conditions for the velocity field $\underline{v}$ are considered:

$$\underline{v}\left(|z| > h\right) = \mathrm{sgn}(z) H \left[2D_{31}\underline{e}_1 + D_{33}\underline{e}_3\right] \tag{III.87}$$

which corresponds to the presence of rigid regions above and below the void (Fig. III.23c). As discussed in Torki et al. (2015), these boundary conditions allow to consider yielding under combined tension and shear. The associated volume-averaged macroscopic strain rate tensor $\boldsymbol{D}$ is equal to:

$$\boldsymbol{D} \equiv \frac{1}{|\Omega|}\int_\Omega \boldsymbol{d}\,\mathrm{d}V = \frac{1}{|\Omega|}\int_{\partial\Omega} \underline{v}\odot\underline{n}\,\mathrm{d}S = \begin{pmatrix} 0 & 0 & D_{31} \\ 0 & 0 & 0 \\ D_{31} & 0 & D_{33} \end{pmatrix} \tag{III.88}$$

with $\boldsymbol{d}$ the microscopic strain rate tensor and $\underline{n}$ the local unit vector normal to the surface boundary $\partial\Omega$ of Ω. The microscopic Cauchy stress tensor is referred to as $\boldsymbol{\sigma}$ and the macroscopic one as $\boldsymbol{\Sigma}$, these tensors being related by $\boldsymbol{\Sigma} = \int_\Omega \boldsymbol{\sigma}/\left|\Omega\right|$.

2.2.2 Kinematic limit analysis

In this work, the macroscopic behavior of the unit cell is studied using kinematic limit analysis (Suquet, 1982). Limit analysis relies on finding a (trial) velocity field that is both kinematically admissible (*i.e.* compatible with the boundary conditions) and plastically admissible (*i.e.* consistent with the macroscopic behavior). This study considers only rigid perfectly-plastic materials. This trial velocity field is then used to estimate the yield surface (Benzerga and Leblond, 2010). The set of trial velocity fields considered is denoted $\mathcal{K}\left(\boldsymbol{D}\right)$. The microscopic plastic dissipation of such a velocity field is:

$$\varpi\left(\underline{v}\left(\underline{x}\right)\right) \equiv \sup_{\boldsymbol{\sigma}^*\in\mathscr{C}} \left(\boldsymbol{\sigma}^* : \boldsymbol{d}\left(\underline{x}\right)\right) \tag{III.89}$$

where $\boldsymbol{d}$ is the strain rate field deriving from $\underline{v}$ and $\mathscr{C}$ is the microscopic elasticity domain of the matrix. Each element $\underline{v} \in \mathcal{K}\left(\boldsymbol{D}\right)$ provides an upper bound Π_+ for the macroscopic dissipation Π, defined as:

$$\Pi(\boldsymbol{D}) = \inf_{\underline{v}\in\mathcal{K}(\boldsymbol{D})} \frac{1}{|\Omega|}\int_\Omega \varpi\left(\underline{v}\left(\underline{x}\right)\right)\,\mathrm{d}V \tag{III.90}$$

If the velocity field exhibits a discontinuity $\Delta\underline{v} = |\Delta\underline{v}|\,\underline{t}$ on a given surface $\mathcal{S}_d$ of normal $\underline{n}$ ($\underline{t}$ and $\underline{n}$ are unit vectors such that $\underline{n}\cdot\underline{t} = 0$), an additional dissipation term has to be added to the total macroscopic dissipation Π_+ (Salençon,

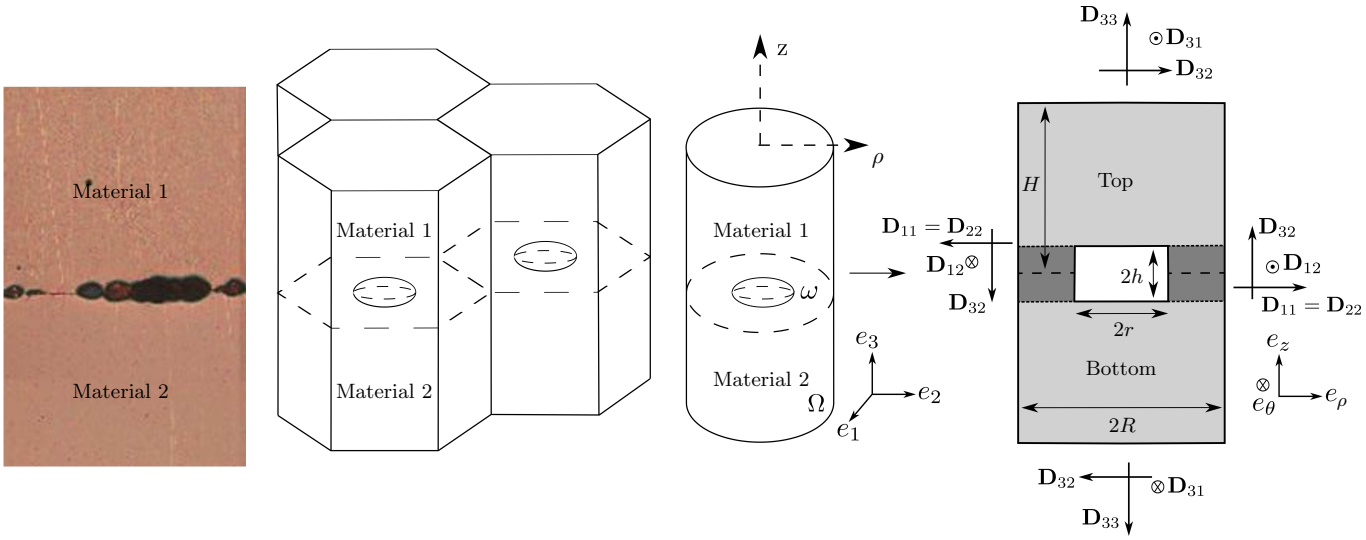

FIGURE III.23: Microstructure considered: (a) real grain boundary with cavities (micrograph from Perez-Bergquist et al. (2011)); (b) idealized microstructure with a periodic array of intergranular voids of hexagonal lattice; (c) approximation of the hexagonal unit-cell with a cylindrical unit-cell.

1983):

$$\Pi_+^{\text{surf}}(\boldsymbol{D}) = \frac{|\Delta \underline{v}|}{|\Omega|} \int_{\mathcal{S}_d} \sup_{\boldsymbol{\sigma}^* \in \mathscr{C}} \left(\boldsymbol{\sigma}^* : \boldsymbol{d}^{(\mathrm{I})} \right) \quad \text{with} \quad \boldsymbol{d}^{(\mathrm{I})} = \underline{t} \odot \underline{n} \tag{III.91}$$

which is obtained from evaluating the volume dissipation over a fictive layer of finite width e around $\mathcal{S}_d$, in the limit where $e \to 0$. In the hypothetical case in which the discontinuity surface is located at an interface between two materials of different elasticity domains $\mathscr{C}_1$ and $\mathscr{C}_2$, the surface term would become:

$$\Pi_+^{\text{surf}}(\boldsymbol{D}) = \frac{|\Delta \underline{v}|}{2\,|\Omega|} \left[\int_{\mathcal{S}_d} \sup_{\boldsymbol{\sigma}^* \in \mathscr{C}_1} \left(\boldsymbol{\sigma}^* : \boldsymbol{d}^{(\mathrm{I})} \right) \mathrm{d}S + \int_{\mathcal{S}_d} \sup_{\boldsymbol{\sigma}^* \in \mathscr{C}_2} \left(\boldsymbol{\sigma}^* : \boldsymbol{d}^{(\mathrm{I})} \right) \mathrm{d}S \right] \tag{III.92}$$

because half of the fictive layer would be in material 1 and the other would be in material 2. Comparison of Eqs III.91 and III.92 shows that surface discontinuities will never occur at a material interface but will instead be slightly relocated in the material where the microscopic dissipation associated with $\boldsymbol{d}^{(\mathrm{I})}$ is lower.

For the boundary conditions considered, Hill-Mandel lemma (*e.g.* Nemat-Nasser and Hori (1993)) allows to write that:

$$\forall \boldsymbol{D} \ , \quad \boldsymbol{\Sigma} : \boldsymbol{D} \leq \Pi\left(\boldsymbol{D}\right) \tag{III.93}$$

which is used to assess the yield surface. Indeed, a stress $\boldsymbol{\Sigma}$ on the yield surface of the material verifies Eq. III.93 with at least one strain rate $\boldsymbol{D}$ for which equality is reached. It means that the hyperplane $\boldsymbol{\Sigma} : \boldsymbol{D}$ must be tangent to surface $\Pi(\boldsymbol{D})$. On the one hand, if Π is differentiable at the point $\boldsymbol{D}_0$ where multi-dimensional tangency occur, then tangency implies that:

$$\boldsymbol{\Sigma} : \boldsymbol{D}_0 = \Pi(\boldsymbol{D}_0) \ , \quad \boldsymbol{\Sigma} = \frac{\partial \Pi}{\partial \boldsymbol{D}}(\boldsymbol{D}_0) \tag{III.94}$$

On the other hand, if Π is not differentiable, then multi-dimensional tangency becomes:

$$\boldsymbol{\Sigma} : \boldsymbol{D}_0 = \Pi(\boldsymbol{D}_0) \ , \quad \boldsymbol{\Sigma} \in \partial\Pi(\boldsymbol{D}_0) \tag{III.95}$$

with $\partial\Pi(\boldsymbol{D}_0)$ denoting the subdifferential of Π at point $\boldsymbol{D}_0$, *i.e.* the set of subgradients $\boldsymbol{S}$ such that

$$\Pi(\boldsymbol{D}) - \Pi(\boldsymbol{D}_0) \geq \boldsymbol{S} : (\boldsymbol{D} - \boldsymbol{D}_0) \tag{III.96}$$

For each trial velocity field, Eq. III.90 provides an upper-bound Π_+ of the macroscopic dissipation Π and thus an upper-bound of the yield surface (through Eq. III.94$_b$ or Eq. III.95$_b$). In the following, for each trial field, the corresponding

Π_+ and its subsequent upper bounds will still be denoted Π for convenience.

2.3 Void coalescence in a von Mises bi-material

In order to provide first insights on intergranular void coalescence, a simplified model will be presented in this part. This is achieved with a yield criterion derived in the case of a von Mises bi-material with a porous interface.

2.3.1 Material description and trial velocity fields

In a perfectly-plastic von Mises material of yield limit σ_0, the microscopic plastic dissipation associated with a strain rate $\boldsymbol{d}$ writes:

$$\varpi\left(\boldsymbol{d}\right) = \sigma_0 d_{\text{eq}} \quad \text{with} \quad d_{\text{eq}} = \sqrt{\frac{2}{3}\boldsymbol{d}:\boldsymbol{d}} \tag{III.97}$$

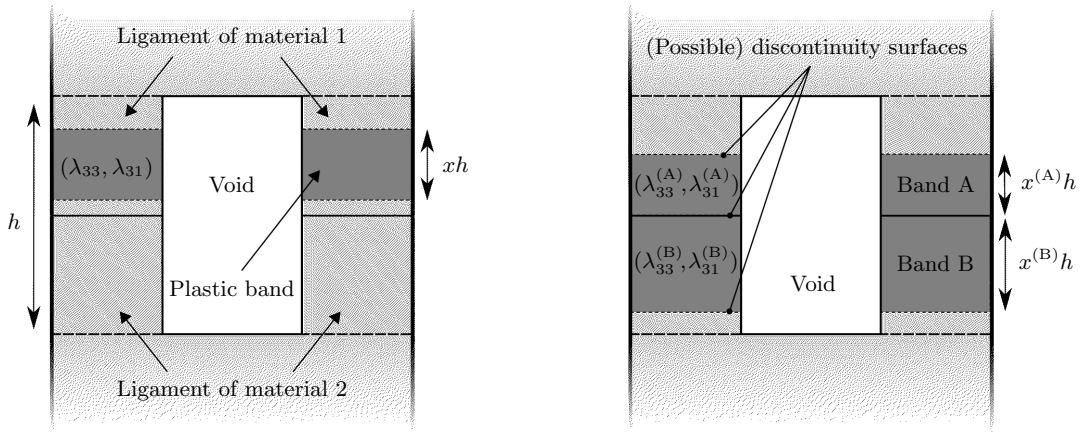

FIGURE III.24: Sketches of the intervoid ligament: (a) localization band (Eq. III.98) of height xh in the ligament; (b) velocity discontinuity surfaces that can appear between a rigid zone and a localization band or between two adjacent localization bands such as band A and band B.

In the following, the problem of void coalescence at the interface of a bi-material is specialized to the idealized case of a bi-material whose two phases follow von Mises plasticity with different yield limits $\sigma_0^{(1)} > \sigma_0^{(2)}$. According to Torki et al. (2015), on the unit-cell shown in Fig. III.23c, the boundary conditions associated with a macroscopic strain rate $\boldsymbol{D}_0 = \lambda_{33} D_{33}\left(\underline{e}_3 \otimes \underline{e}_3\right) + \lambda_{31} D_{31}\left(\underline{e}_1 \odot \underline{e}_3\right)$ (where $\lambda_{33}, \lambda_{31} \geq 0$) can be accommodated by inserting a horizontal layer in one of the materials of the ligament, the velocity field being:

$$v_\rho = \frac{\lambda_{33} D_{33}}{2xc}\left(\frac{R^2}{\rho} - \rho\right) + \frac{2(z-z_0)}{xc}\lambda_{31} D_{31}\cos\theta\ , \quad v_\theta = -\frac{2(z-z_0)}{xc}\lambda_{31} D_{31}\sin\theta\ , \quad v_z = \frac{\lambda_{33} D_{33}}{xc}(z-z_0) \tag{III.98}$$

where xh is the height of the localization layer ($x \in \left[0, \frac{1}{2}\right]$) and z_0 the z-coordinate of its center, while the rest of the structure is rigid (Fig. III.24a). On the one hand, a sound approximation[9] of the macroscopic volume dissipation associated with this layer has been computed in the same reference:

$$\Pi^{\text{vol}}\left(\sigma_0, \lambda_{33}, \lambda_{31}\right) = \sigma_0 \sqrt{\left(g^{\text{vol}} \lambda_{33} D_{33}\right)^2 + \left(g^{\text{sh}} \lambda_{31} D_{31}\right)^2} \tag{III.99}$$

where σ_0 is the yield stress of the material in which the band is located. On the other hand, the surface dissipation of each velocity discontinuity surface is obtained from Eq. III.91 combined with Eq. III.97. It depends on the yield stress σ_0 of the material in which the surface is located and on the characteristics of the two adjacent zones $i \in \{A, B\}$ (Fig. III.24b), namely width ratio $x^{(i)}$, strain rate ratio $\lambda_{33}^{(i)}$ (this ratio is null in the case of a rigid zone) and yield stress $\sigma_0^{(i)}$:

$$\Pi^{\text{surf}}\left(\sigma_0^{(\text{A})}, \sigma_0^{(\text{B})}, x^{(\text{A})}, x^{(\text{B})}, \lambda_{33}^{(\text{A})}, \lambda_{33}^{(\text{B})}\right) = \min\left(\sigma_0^{(\text{A})}, \sigma_0^{(\text{B})}\right) g^{\text{surf}} \left| \left(\frac{\lambda_{33}^{(\text{A})}}{x^{(\text{A})}} - \frac{\lambda_{33}^{(\text{B})}}{x^{(\text{B})}}\right) D_{33} \right| \tag{III.100}$$

[9] In Torki et al. (2017), it is shown that computing the exact dissipation has a negligible effect on yield surfaces whereas it significantly complicates the theoretical derivation.

The aforementioned g-functions are (Benzerga and Leblond, 2014; Torki et al., 2015):

$$g^{\text{vol}} = \frac{1}{\sqrt{3}}\left[2 - \sqrt{1+3\chi^4} + \log\frac{1+\sqrt{1+3\chi^4}}{3\chi^2}\right] \ , \quad g^{\text{surf}} = \frac{\chi^3 - 3\chi + 2}{6\sqrt{3}\chi w} \ , \quad g^{\text{sh}} = \frac{2}{\sqrt{3}}\left(1-\chi^2\right) \tag{III.101}$$

Due to the linearity of the macroscopic strain rate $\boldsymbol{D}$ with respect to the microscopic velocity field $\underline{v}$ (Eq. III.88), a ligament with several plastic layers i which could individually accommodate loadings $\boldsymbol{D}^{(i)} = (\lambda_{33}^{(i)} D_{33}, \lambda_{31}^{(i)} D_{31})$ with $\sum_i \lambda_{33}^{(i)} = \sum_i \lambda_{31}^{(i)} = 1$ will thus accommodate the loading $\boldsymbol{D} = (D_{33}, D_{31})$. Therefore, the trial velocity field is searched in the form of multiple bands of the type described by Eq. III.98, either in material 1 or in material 2 (Fig. III.25a). By convention, the volume of bands never extends in both materials — even if one of the surface discontinuities can be fictively located at an infinitesimal distance on the other side of the interface, as shown in the previous section.

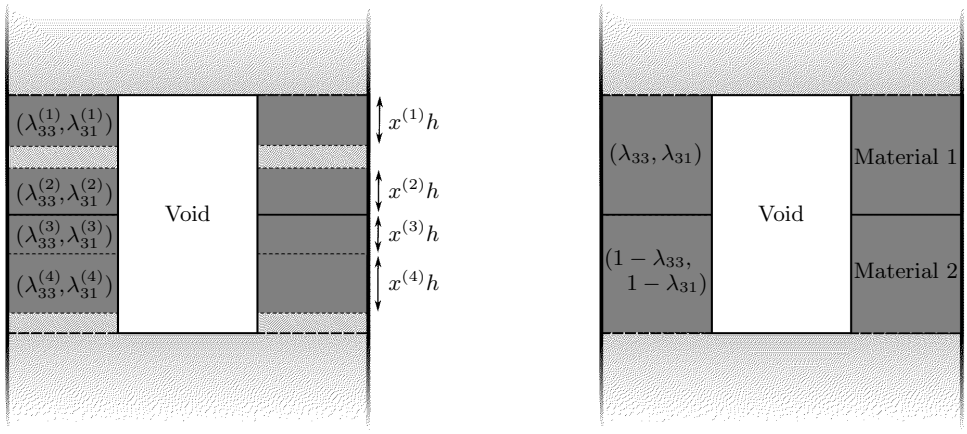

FIGURE III.25: Search of the optimal trial field: (a) example of trial velocity field considered; (b) two-band geometry of the optimal trial field.

2.3.2 Macroscopic dissipation

The next step is to find the number and position of localization bands allowing to minimize the macroscopic dissipation (Eq. III.90). The associated trial field, referred to as the optimal trial field, will be determined through a handful of *lemmata*, whose proof can be found in Appendix III.2.A.

Lemma 1. *In the optimal trial field, all bands are conterminous.*

Lemma 2. *The optimal trial field has a maximum of one band in each material.*

Lemma 3. *Each band can be chosen of maximal width.*

Combining them, it is obtained that there are only two bands (see Fig. III.25b): one that occupies entirely material 1 and that accommodates the loading $(\lambda_{33}D_{33}, \lambda_{31}D_{31})$, and one that occupies entirely material 2 and that accommodates the loading $((1-\lambda_{33})D_{33}, (1-\lambda_{31})D_{31})$, where $(\lambda_{33}, \lambda_{31}) \in [0,1]^2$. Each of those bands is possibly rigid (*i.e.* $\lambda_{33} = \lambda_{31} \in \{0,1\}$). Since material 2 is softer than material 1, the discontinuity surface between the two bands is located in material 2 (see Section III.2.2.2 and Eq. III.100). Therefore, finding the optimal trial field amounts to finding the minimum of the following macroscopic dissipation over $(\lambda_{33}, \lambda_{31}) \in [0,1]^2$:

$$\Pi(\lambda_{33},\lambda_{31}) = \sigma_0^{(1)}\sqrt{\left(\lambda_{33}g^{\text{vol}}D_{33}\right)^2 + \left(\lambda_{31}g^{\text{sh}}D_{31}\right)^2} + \sigma_0^{(2)}\sqrt{\left[(1-\lambda_{33})g^{\text{vol}}D_{33}\right]^2 + \left[(1-\lambda_{31})g^{\text{sh}}D_{31}\right]^2} + 2g^{\text{surf}}\left|D_{33}\right|\left[\lambda_{33}\sigma_0^{(1)} + \left(\left|2\lambda_{33}-1\right| + (1-\lambda_{33})\right)\sigma_0^{(2)}\right] \tag{III.102}$$

The detailed minimization can be found in Appendix III.2.B. In the following, a simplified approach is conducted by only considering limiting values of the yield stress contrast $\epsilon = (\sigma_0^{(1)} - \sigma_0^{(2)})/\sigma_0^{(1)}$. On the one hand, when $\epsilon \to 0$, materials 1 and 2 are almost identical. Thus, application of Lemma 2 and Lemma 3 brings that there is only one band

extending in the full height of the ligament, *i.e.* $\lambda_{33} = \lambda_{31} = \frac{1}{2}$. That means that plasticity occurs equally in both materials. On the other hand, when $\epsilon \to 1$, Eq. III.102 simplifies as:

$$\frac{\Pi(\lambda_{33}, \lambda_{31})}{\sigma_0^{(1)}} \longrightarrow \sqrt{\left(\lambda_{33} g^{\text{vol}} D_{33}\right)^2 + \left(\lambda_{31} g^{\text{sh}} D_{31}\right)^2} + 2 g^{\text{surf}} \left|D_{33}\right| \lambda_{33} \tag{III.103}$$

which reaches its minimum at $\lambda_{33} = \lambda_{31} = 0$. That means that material 2 is so soft that plasticity localizes entirely in it.

Supposing that these extreme cases are sufficient to describe the general situation, the following approximation is done to obtain the macroscopic dissipation:

$$\min_{\lambda_{33}, \lambda_{31}} \Pi\left(\lambda_{33}, \lambda_{31}\right) \approx \min\left\{\Pi(0,0), \Pi\left(\frac{1}{2}, \frac{1}{2}\right)\right\} \tag{III.104}$$

In cases where $D_{33} = 0$ or $D_{31} = 0$, the macroscopic dissipation corresponding to the set of trial velocity fields chosen in Section III.2.3.1 is exactly given by the right-hand side of Eq. III.104, as shown in Appendix III.2.B.

2.3.3 Yield surface

According to Eq. III.104, the yield surface for intergranular coalescence can be found from the two individual surfaces related to macroscopic dissipations $\Pi(0,0)$ and $\Pi\left(\frac{1}{2}, \frac{1}{2}\right)$. In Torki et al. (2015), it was proven using Eqs. III.94-III.95 that the yield surface associated with a macroscopic dissipation of the form $\Pi = \sqrt{a^2 D_{33}^2 + b^2 D_{31}^2} + c\left|D_{33}\right|$ writes:

$$\left(\frac{\left\{\left|\Sigma_{33}\right| - c\right\}_+}{a}\right)^2 + \left(2\frac{\Sigma_{31}}{b}\right)^2 - 1 = 0 \tag{III.105}$$

where $\{\cdot\}_+ = \max(0, \cdot)$. This result is specialized to $\Pi(0,0)$ and $\Pi\left(\frac{1}{2}, \frac{1}{2}\right)$ to obtain the corresponding surfaces:

$$\Pi(0,0) \quad : \quad \left(\frac{\left\{\left|\Sigma_{33}\right| - 4\sigma_0^{(2)} g^{\text{surf}}\right\}_+}{\sigma_0^{(2)} g^{\text{vol}}}\right)^2 + \left(2\frac{\Sigma_{31}}{\sigma_0^{(2)} g^{\text{sh}}}\right)^2 - 1 = 0 \tag{III.106}$$

$$\Pi\left(\frac{1}{2}, \frac{1}{2}\right) \quad : \quad \left(2\frac{\left\{\left|\Sigma_{33}\right| - \left[\sigma_0^{(1)} + \sigma_0^{(2)}\right] g^{\text{surf}}\right\}_+}{\left[\sigma_0^{(1)} + \sigma_0^{(2)}\right] g^{\text{vol}}}\right)^2 + \left(4\frac{\Sigma_{31}}{\left[\sigma_0^{(1)} + \sigma_0^{(2)}\right] g^{\text{sh}}}\right)^2 - 1 = 0 \tag{III.107}$$

Then, the void coalescence elasticity domain of the bi-material is obtained by intersecting elasticity domains corresponding to coalescence confined in the softest constitutive material (Eq. III.106) and to plasticity in ligaments of both materials (Eq. III.107). Note that when $\sigma_0^{(1)} = \sigma_0^{(2)}$, Eqs. III.106 and III.107 do not coincide because localization in both materials is favored over localization in material 1 (see Lemma 2).

For a porous homogeneous von Mises material of yield stress σ_0, the internal necking criterion writes (Benzerga and Leblond, 2014):

$$\Sigma_{33} = \text{sgn}(D_{33})\sigma_0\left(g^{\text{vol}} + 2g^{\text{surf}}\right) \tag{III.108}$$

whereas coalescence in pure shear occurs when (Torki et al., 2015):

$$\Sigma_{31} = \text{sgn}(D_{31})\sigma_0 \frac{g^{\text{sh}}}{2} \tag{III.109}$$

Both of these expressions have been shown by Torki et al. (2015) and Torki et al. (2017) to require a correction in order to improve the agreement to numerical results and recover an acceptable yield criterion in the limit $w \to 0$. The calibration led in the aforementioned studies resulted in the correction of g^{vol}, g^{sh} and g^{surf}:

$$\hat{g}^{\text{vol}} = b g^{\text{vol}} \ , \quad \hat{g}^{\text{sh}} = \left[1 + \left(l_0 + l_1\chi\right)\hat{w}\right] g^{\text{sh}} \ , \quad \hat{g}^{\text{surf}} = \frac{\left(t_0 + t_1\chi\right)\hat{w}}{1 + \left(t_0 + t_1\chi\right)\hat{w}^{\frac{4}{3}}} g^{\text{surf}}$$

$$\text{with} \quad \begin{cases} b & = 0.9 \\ (l_0, l_1) & = (0.035, -0.15) \\ (t_0, t_1) & = (-0.84, 12.9) \end{cases} \tag{III.110}$$

where $\hat{w}$ is the effective void aspect ratio seen by the material. In the case investigated here of a bi-material, each ligament is of half-width: $\hat{w} = w/2$. This correction is adopted in the following[10]. In the next section, this model is assessed using unit-cell simulations.

2.3.4 Numerical assessment

The analytical coalescence criterion is validated by resorting to numerical limit analysis. For future reference, all unit-cell simulation types performed for this work are summarized in Table III.5 which describes in a condensed notation their main differences and the location where they are used in this article. All details pertaining to these simulations will be provided in the main text.

Method	Unit-cell	Mesh	Matrix	Boundary conditions	Use
FEM	Cylindrical	Fig III.26a	Mises bi-material	$\boldsymbol{D} = (D_{33}, 0)$, pseudo-periodic	Figs. III.27 and III.28
FFT	Hexagonal	Fig III.26b	Mises bi-material	$\boldsymbol{D} = (D_{33}, D_{31})$, fully periodic	Figs. III.29, III.30 and III.38
FFT	Cylindrical	Fig III.26c	Single crystal	$\boldsymbol{D} = (D_{33}, 0)$, pseudo-periodic	Eq. III.124 and Fig. III.35
FFT	Cylindrical	Fig III.26c	Bi-crystal	$\boldsymbol{D} = (D_{33}, 0)$, pseudo-periodic	Figs. III.31, III.32 and III.35
FFT	Hexagonal	Fig III.26b	Single crystal	$\boldsymbol{D} = (0, D_{31})$, fully periodic	Eq. III.125
FFT	Hexagonal	Fig III.26b	Bi-crystal	$\boldsymbol{D} = (D_{33}, D_{31})$, fully periodic	Figs. III.33, III.34, III.36 and III.39
FFT	Hexagonal	Fig III.26b	Single crystal	$\boldsymbol{D} = (D_{33}, D_{31})$, fully periodic	Fig. III.36

TABLE III.5: Summary of the unit-cell simulations performed for calibration and numerical assessment. Cylindrical voids coaxial to the unit-cell are used in each simulation.

First, the case of internal necking ($D_{31} = 0$) is considered. Small strain finite element simulations are conducted on the unit-cell shown in Fig. III.23c using the FEM solver `Cast3M` (CEA, 2018). Axisymmetric simulations are performed with the mesh shown in Fig III.26a; it holds 38400 quadratic quadrangular elements, mesh convergence being duly checked. The upper half is a von Mises material with yield stress $\sigma_0^{(1)}$ while the lower half has a yield stress $\sigma_0^{(2)} < \sigma_0^{(1)}$. The height of the unit-cell is determined by fixing $c = 0.3$; this choice has no effect on the results presented hereafter, as long as c is small enough.

Vertical displacements of the nodes lying on the boundaries $\mathcal{S}_{\text{top}}$ and its symmetric $\mathcal{S}_{\text{bottom}}$ are constrained to have the same absolute value, while horizontal displacements on $\mathcal{S}_{\text{lat}}$ are set to zero. These boundary conditions are consistent with an imposed macroscopic strain rate $\boldsymbol{D} = D_{33}\underline{e}_3 \otimes \underline{e}_3$ (Torki et al., 2017). The macroscopic stress Σ_{33} is computed by averaging the microscopic stress field $\boldsymbol{\sigma}$ over Ω. The displacement is then increased linearly until small strain yielding of the unit-cell occurs. This manifests by the saturation of Σ_{33} to values corresponding to the internal necking stress of the unit cell, which can be seen as a yield stress.

Numerical and analytical internal necking stresses of the bi-material are displayed according to the yield stress contrast ϵ in Fig III.27. In Fig. III.27a, it is seen that coalescence is fostered when χ increases, which is in line with results observed in mono-materials by Benzerga and Leblond (2014). The model captures quantitatively this trend, as well as the fact that the internal necking stress is lower when w increases, as shown in Fig. III.27b. Note that the data related to strain rate fields was reported in the graph after careful examination of the equivalent plastic strain field of each numerical limit analysis simulation. Interestingly, as the yield stress contrast ϵ increases, the predicted velocity field changes from one occupying both materials to one that is confined in the soft material. For instance, Fig. III.28 shows this transition for $\chi = w = 0.5$. The existence of two distinct localization patterns was expected: on the one hand, $\sigma_0^{(2)} \ll \sigma_0^{(1)}$ is intuitively associated with a full localization in material 2; on the other hand, $\sigma_0^{(2)} = \sigma_0^{(1)}$ is the mono-material case, in which the thicker the ligament is, the lower the internal stress is. Plotting $\Sigma_{33}/\sigma_0^{(2)}$ in Fig. III.27 enables to show distinctly the localization change by the transition from a parabolic curve to a horizontal line. The critical stress ratio at which the localization pattern changes is correctly predicted by the model and its evolution regarding χ and w is captured well. For instance, a high w means the optimal trial field can more easily fit in the soft material. Thus, void coalescence in bi-materials is satisfactorily predicted despite the crude nature of the

[10] With the correction of Eq. III.110, the yield surface loses its rigourous upper bounding character for pure internal necking. In the presence of shear, the original expression nor its correction by Eq. III.110 are upper bounds.

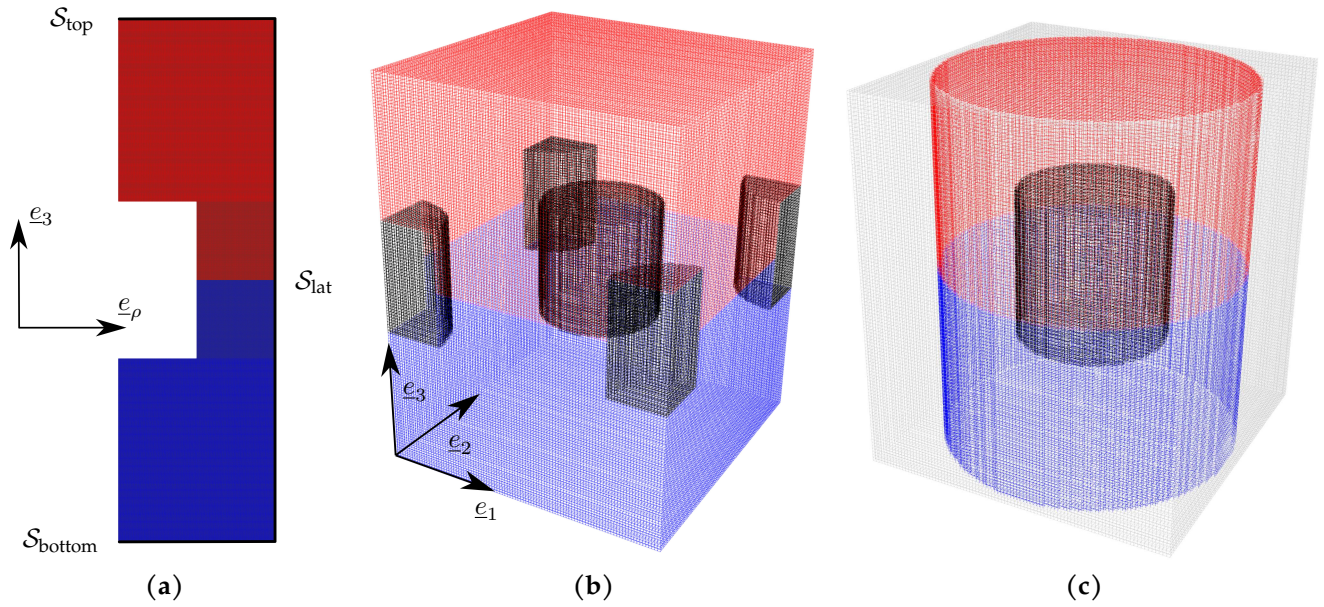

FIGURE III.26: Meshes used for numerical limit analysis at $\chi = 0.5$ and $w = 1$: (a) FEM axisymmetric mesh used for the internal necking simulations; (b) FFT 3D mesh with hexagonal periodicity for coalescence under combined tension and shear; (c) FFT 3D mesh with axial symmetry used for internal necking simulations of anisotropic materials.

set of trial fields used in Section III.2.3.3.

Second, the case of coalescence under combined tension and shear is considered. The macroscopic shear strain is responsible for the breaking of the axial symmetry. Therefore, a three-dimensional mesh of the unit cell is needed. These computations being computer-intensive, fast Fourier transform modeling using `AMITEX_FFTP` code is preferred over finite element modeling in order to increase efficiency. This numerical method, introduced in Moulinec and Suquet (1998), allows to solve the mechanical equilibrium equations of periodic unit cells with an iterative algorithm based on the Lippman-Schwinger equation and discrete Green operator. `AMITEX_FFTP` solver (CEA, 2020) uses the fixed point scheme proposed in Moulinec and Suquet (1998), but with filtered discrete Green operator (Gélébart

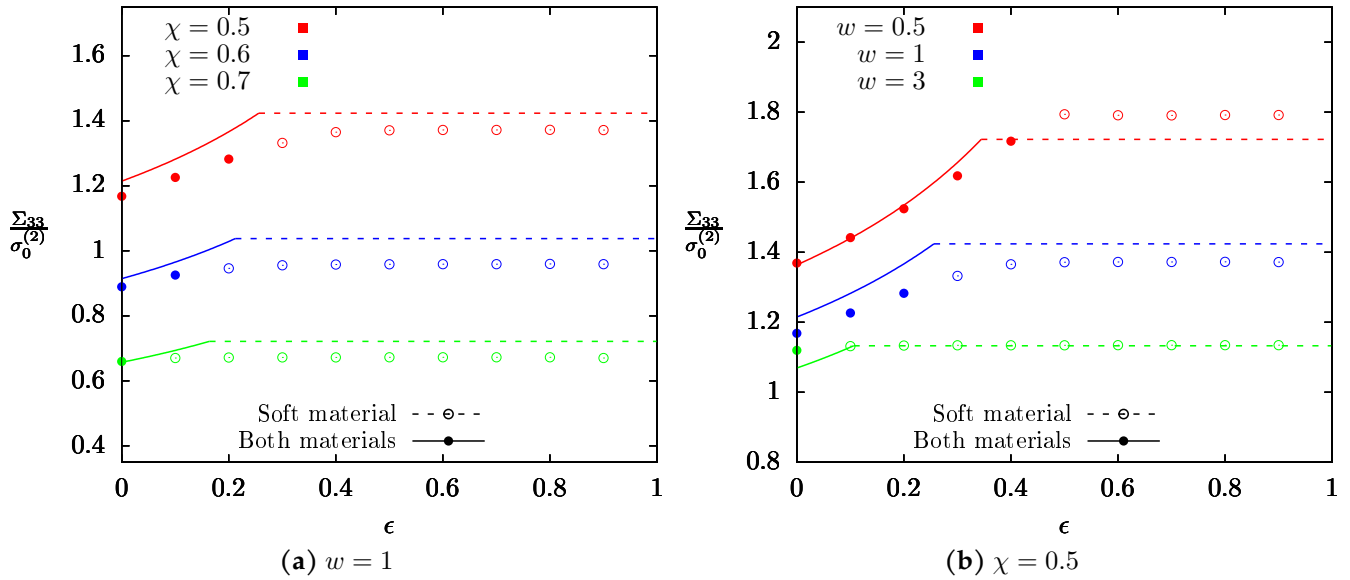

FIGURE III.27: Dependence of internal necking coalescence stress Σ_{33} on the yield stress contrast ϵ as predicted by the model (lines) and computed numerically through FEM unit-cell simulations (points): (a) for various χ with $w = 1$; (b) for various w at $\chi = 0.5$. Plasticity can either extend in both materials (full lines and symbols) or be confined to the softest material (dotted lines and hollowed-out symbols).

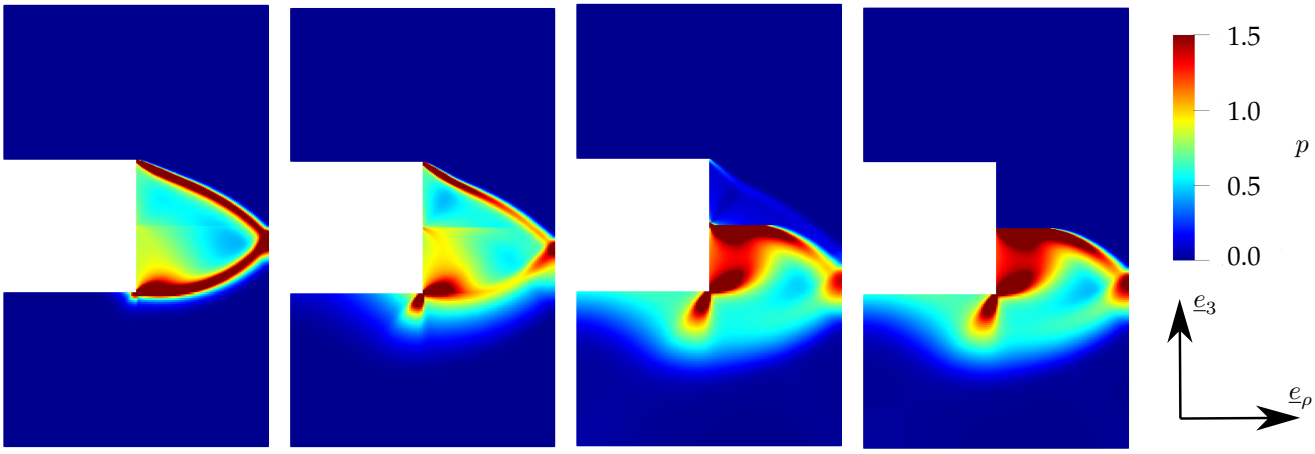

(a) $\epsilon = 0.3$ **(b)** $\epsilon = 0.4$ **(c)** $\epsilon = 0.5$ **(d)** $\epsilon = 0.6$

FIGURE III.28: Microscopic fields of equivalent plastic strain $p = \int d_{\text{eq}} \mathrm{d}t$ (arbitrary units) for internal necking simulations carried out at $\chi = w = 0.5$ with increasing yield stress contrast ϵ.

and Ouaki, 2015) and convergence acceleration (Ramière and Helfer, 2015) that both contribute to improving the convergence and reducing the sensibility to material contrast (differences in local stiffness) encountered in the original implementation.

Since FFT simulations require periodic boundary conditions and a cuboid mesh made of cubic voxels, it is returned to the hexagonal array of voids of Fig. III.23b whose approximation is the cylindrical unit-cell of Fig. III.23c. In the unit-cell obtained from the hexagonal array of voids, χ is defined as $\sqrt{f_{\text{b}}}$, f_{b} being the porosity in the median horizontal plane, *i.e.* the ratio of the void surface on the section of the unit-cell. It means that the radius of cavities is given by $\hat{r} = \chi/\sqrt{2\pi}$. The resulting mesh is shown in Fig. III.26b (Fig. III.26c will be commented later). Its section in the plane $(\underline{e}_1, \underline{e}_2)$ holds $N \times N$ cuboids with $N = 100$. The number of cuboids M along $\underline{e}_3$ is chosen so that $c = 0.3$, *i.e.* $M = (w\chi N) \,/\, \left(\sqrt{2\pi}c\right)$. Simulations are conducted with periodic boundary conditions at an imposed macroscopic strain rate $\boldsymbol{D} = D_{33}\underline{e}_3 \otimes \underline{e}_3 + 2D_{31}\underline{e}_1 \odot \underline{e}_3$ with various ratios D_{31}/D_{33} until stress saturation occurs. The macroscopic stresses $(\Sigma_{33}, \Sigma_{31})$ are computed by averaging the microscopic stress field $\boldsymbol{\sigma}$ over the unit-cell. It is checked that no discrepancy arises between the cylindrical unit cell and the hexagonal unit cell when used to compute the internal necking stress, which ensures that the definition of χ is valid. Again, mesh discretization is assessed and found satisfying.

Note that material interfaces — and later grain boundaries — are not supposed to be periodic structures along $\underline{e}_3$, but this assumption is required by the FFT solver that is used to assess the model. As long as the height of the periodic microstructure along $\underline{e}_3$ is sufficient, it is believed that the coalescence process will not be hindered by the interaction between neighboring planes of cavities (Tekoğlu et al., 2012).

The results for various yield stress contrasts ϵ are shown in Fig. III.29 in the plane $(\Sigma_{31}, \Sigma_{33})$. The internal necking case $(D_{31} = 0)$ generates no macroscopic shear stress and thus corresponds to the axis $\Sigma_{31} = 0$. Similarly, the pure shear case $(D_{33} = 0)$ result sits on the axis $\Sigma_{33} = 0$. The model and the simulations being symmetric relatively to the axes $\Sigma_{31} = 0$ and $\Sigma_{33} = 0$, only a fourth of the plane is shown. It is seen that the yield stress contrast has an important influence on the yield surface. The dependence of the whole yield surface on w is visible by comparing the case $\epsilon = 0.1$ in Fig. III.29a and Fig. III.29c. The model correctly accounts for both these effects. It is seen that the analytic yield surface is quantitatively accurate for pure shear and internal necking but that a discrepancy appears in mixed coalescence modes. This observation was also made by Torki et al. (2017) in mono-materials: it originates mainly from the fact that the trial field for combined shear and tension is not accurate enough and has almost nothing to do with the approximations performed subsequently to the choice of the trial field. As a reminder, these two approximations are: simplification of the volume dissipation of a localization band (Eq. III.99), and heuristic minimization of Eq. III.102 (Eq. III.104).

Regarding the localization of plasticity, three types of yield surfaces can be distinguished. In the first kind, corresponding to low s, internal necking occurs in the soft material. Since an increase of the shear strain D_{31} can only increase the tendency to localization in the soft material, the full yield surface is obtained for strain rate fields con-

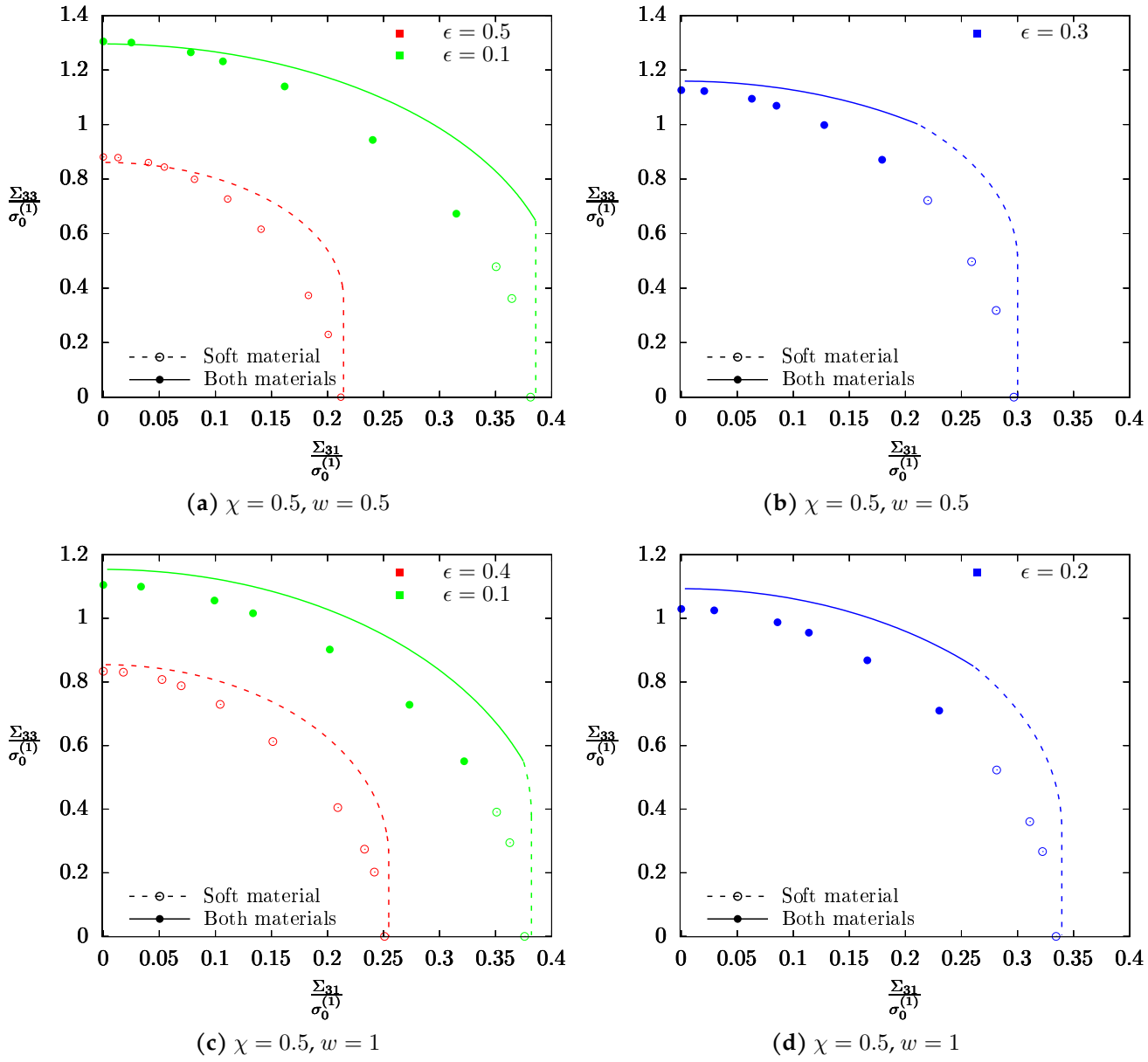

(a) $\chi = 0.5, w = 0.5$ **(b)** $\chi = 0.5, w = 0.5$

(c) $\chi = 0.5, w = 1$ **(d)** $\chi = 0.5, w = 1$

FIGURE III.29: Coalescence yield surface under combined tension and shear in the plane $(\Sigma_{31}, \Sigma_{33})$ as predicted by the model (lines) and computed numerically through FFT unit-cell simulations (points) for $\chi = 0.5$ and two different values of w. Various yield stress contrasts ϵ are considered. The strain rate field can either extend in both materials (full lines and symbols) or be confined to the softest material (dotted lines and hollowed-out symbols).

fined in the soft material. For $\chi = w = 0.5$, this is the case at $s = 0.5$ (and lower values of s), as seen in Fig. III.29a; for $\chi = 0.5$ and $w = 1$, this behavior is seen at $s = 0.6$ (and lower values of s), as shown in Fig. III.29c. At intermediate yield stress ratios s, internal necking occurs in both materials and localization shifts to the softer material at a finite ratio D_{31}/D_{33}, which corresponds to Figs. III.29b,d. Finally, at high s, the full yield surface is obtained for strain rates that extend in both materials, except the part that corresponds to pure coalescence in shear ($D_{33} = 0$) which occurs exclusively in the softer material since the width of the shear band can be as thin as necessary without increasing the macroscopic dissipation. This is seen at $s = 0.9$ in Figs. III.29a,c. The model displays the three types of yield surfaces in agreement with numerical simulations and the transition in localization from both materials to the soft material is satisfyingly predicted. Naturally, when w increases, localization in the soft material increases so the boundaries of the three aforementioned regimes shift toward higher s.

Microscopic fields of cumulated plastic strain are shown in Fig. III.30. Coherently with what the model predicts in Fig. III.29d, the strain rate field extends in both materials under internal necking (Fig. III.30a) and is confined to the soft material in pure shear (Fig. III.30b).

As a last note, it is emphasized that the yield criterion of Section III.2.3.3 predicts systematically that void coales-

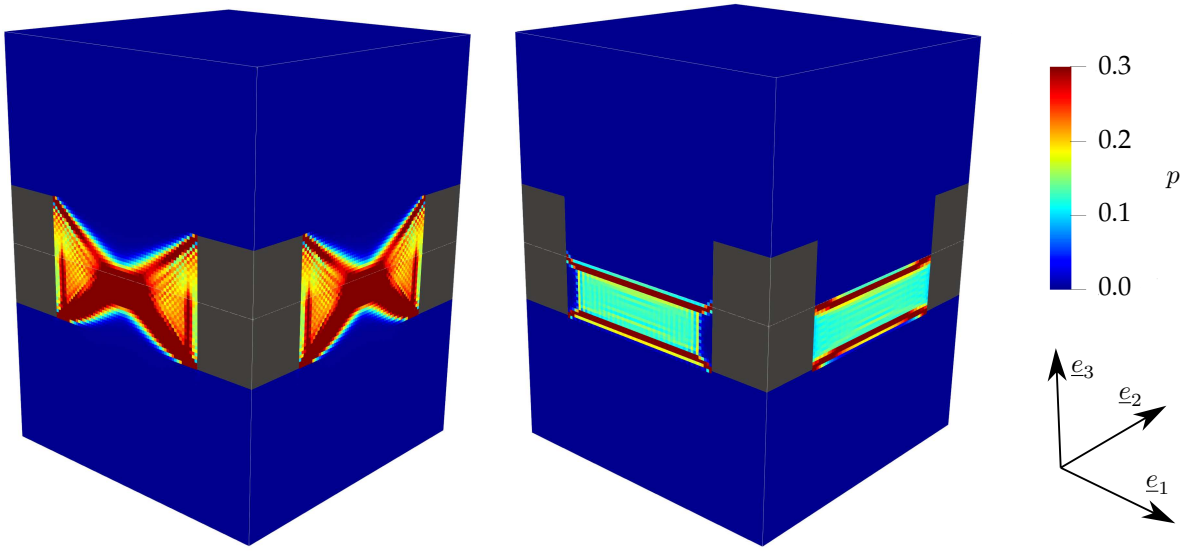

(a) $D_{31} = 0$ **(b)** $D_{33} = 0$

FIGURE III.30: Microscopic fields of equivalent plastic strain $p = \int d_{\text{eq}} \mathrm{d}t$ (arbitrary units) for simulations carried out at $\chi = 0.5$, $w = 1$ and $\epsilon = 0.3$. Voids are shown in dark gray.

cence in a von Mises bi-material happens at lower stress compared to the case of a mono-material of yield stress $\sigma_0^{(2)}$ and at a higher stress than a mono-material of yield stress $\sigma_0^{(1)}$. Unit-cell computations confirm this finding — see for instance Fig. III.27 in which the point at $\epsilon = 0$ (*i.e.* the numerical result of the mono-material of yield stress $\sigma_0^{(2)}$) is below all other points. Yet, it does not mean coalescence is hindered in the bi-material compared to the soft material *in all generality* but simply *at equal microstructure parameters*. Indeed, ductile fracture is a complex process in which geometry evolution is paramount. For instance, the finite-strain study of Li and Guo (2002), which simulated the mechanical loading of voids at the interface of two different Mises materials, did show that a yield stress or a strain hardening capacity mismatch between the two phases fostered void coalescence compared to a similar process in a homogeneous matrix. This can be explained by the fact that localization in the ligament of the soft half-material — which is twice thinner than the corresponding ligament of the mono-material — triggers a faster damaging process.

In conclusion, the model developed in Section III.2.3.3 based on the set of trial fields described by Eq. III.98 is accurate enough to predict coalescence under combined tension and shear at the interface of two Mises materials. In particular, the model discriminates correctly the situations in which plasticity localizes in the soft material from the cases in which plasticity occurs in both materials. In the next part, an approach inspired by the method used above will be applied to grain boundaries in order to study intergranular void coalescence.

2.4 Void coalescence at a crystal interface

The criterion presented in the previous part cannot be directly applied to study intergranular coalescence due to the inherent difference between isotropic plasticity and crystal plasticity. In this part, the unit-cell of Fig. III.23c is still considered, but each matrix material will follow the constitutive laws of a single crystal with a given orientation. Perfect bonding is assumed at the crystal interface; in the following, this interface will be called *grain boundary* even if no mechanical model of grain boundary is considered in the current work. An extended model is then developed using an approximate method relying on average Taylor factors and originating from the study of coalescence in porous single crystals by Hure (2019).

2.4.1 Single crystal matrix behavior

In a single crystal, plasticity is assumed to be related to the glide of dislocations, that can happen in a limited number of directions, called crystallographic slip systems, defined by a slip plane (whose normal is along unit vector $\underline{m}_s$) and a slip direction (of unit vector $\underline{n}_s$), and represented by the following symmetric Schmid tensor: $\boldsymbol{\mu}_s = \frac{1}{2}(\underline{m}_s \otimes \underline{n}_s + \underline{n}_s \otimes \underline{m}_s)$. Other plasticity mechanisms such as twinning are disregarded. A face-centered cubic (FCC) material is considered, with $K = 12$ independent slips systems — the $\{111\}\langle 110\rangle$ family. Using viscoplastic

regularization, the plastic strain rate writes (Hutchinson, 1976):

$$\boldsymbol{d} = \sum_{s=1}^{K} \left[\dot{\gamma}_0 \left(\frac{|\boldsymbol{\sigma} : \boldsymbol{\mu}_s|}{\tau_0} \right)^n \operatorname{sgn}(\boldsymbol{\sigma} : \boldsymbol{\mu}_s) \right] \boldsymbol{\mu}_s = \sum_{s=1}^{K} \dot{\gamma}_s \boldsymbol{\mu}_s \tag{III.111}$$

where τ_0 is the critical resolved shear stress (identical for all slip systems), $\dot{\gamma}_0$ a reference slip-rate and $\dot{\gamma}_s$ the slip rate of system s. n denotes the Norton exponent: the case $n \to +\infty$ corresponds to rate-independent plasticity, which is of interest here.

The local Taylor factor associated with a single crystal subjected to a strain rate $\boldsymbol{d}$ is defined as:

$$M(\boldsymbol{d}) = \frac{\sum_{s=1}^{K} \dot{\gamma}_s(\boldsymbol{d})}{d_{\text{eq}}^{\text{iso}}} \quad \text{with} \quad d_{\text{eq}}^{\text{iso}} = \sqrt{\frac{2}{3} \boldsymbol{d} : \boldsymbol{d}} \tag{III.112}$$

where $d_{\text{eq}}^{\text{iso}}$ is the von Mises equivalent deformation rate. In rate-independent plasticity, $(\dot{\gamma}_s)$ are determined from $\boldsymbol{d}$ as the set that verifies $\sum \dot{\gamma}_s \boldsymbol{\mu}_s = \boldsymbol{d}$ while minimizing $\sum |\dot{\gamma}_s|$. Since this problem is a minimization under linear hard constraints involving inequalities, it can be solved through classical linear programming algorithms (see Van Houtte (1988) for this specific case). M strongly depends on the crystallographic orientation through the set of Schmid tensors $(\boldsymbol{\mu}_s)$. This quantity is of great interest to our study since, in a single crystal, the microscopic plastic dissipation writes:

$$\sup_{\boldsymbol{\sigma}^* \in \mathscr{C}} \boldsymbol{\sigma}^* : \boldsymbol{d} = \sum_{s=1}^{K} \tau_0 \dot{\gamma}_s = M(\boldsymbol{d}) \tau_0 d_{\text{eq}}^{\text{iso}} \tag{III.113}$$

Eq. III.113 can then be used to re-apply the limit analysis framework of Section III.2.3 considering $\sigma_0 = M(\boldsymbol{d})\tau_0$.

2.4.2 Approximate macroscopic dissipation

At the macroscopic scale, the following approximation[11] can be performed on a zone A occupying volume $\Omega_{\text{A}} \subset \Omega$:

$$\Pi^{(\text{A})} = \frac{1}{|\Omega|} \int_{\Omega_{\text{A}}} M(\boldsymbol{d}) \tau_0 d_{\text{eq}}^{\text{iso}} \, \mathrm{d}V \approx \left(\frac{1}{|\Omega_{\text{A}}|} \int_{\Omega_{\text{A}}} M(\boldsymbol{d}) \, \mathrm{d}V \right) \left(\frac{1}{|\Omega|} \int_{\Omega_{\text{A}}} \tau_0 d_{\text{eq}}^{\text{iso}} \, \mathrm{d}V \right) = \left(\frac{1}{|\Omega_{\text{A}}|} \int_{\Omega_{\text{A}}} M(\boldsymbol{d}) \, \mathrm{d}V \right) \Pi_{\text{iso}}^{(\text{A})} \tag{III.114}$$

with $\Pi_{\text{iso}}^{(\text{A})}$ the corresponding dissipation in an equivalent isotropic material of uniaxial yield stress τ_0. The dependence of the mean Taylor factor on loading and geometry can be established by keeping in mind that $M(\boldsymbol{d})$ is homogeneous of degree 0, *i.e.* colinear strain rates tensors share the same Taylor factor. Additional details can be found in Hure (2019).

Since the set of trial fields constituted of a finite number of localization bands described by Eq. III.98 has been shown in Section III.2.3 to lead to a void coalescence yield surface for porous von Mises bi-materials in good agreement with numerical simulations, it will be adopted for the void coalescence of porous grain boundaries as well.

Before anything else, the macroscopic dissipation associated with a single localization band located in one of the single crystals has to be evaluated. On the one hand, the volume term of the macroscopic dissipation of a localization band in the absence of shear can be estimated using Eq. III.114:

$$\begin{aligned} \Pi^{\text{vol}} &\approx \tau_0 \underbrace{\left(\frac{1}{\pi(1-\chi^2)} \int_{\chi}^{1} \int_{0}^{2\pi} M\left(\boldsymbol{d}^{\text{vol}}\right) \rho \, \mathrm{d}\theta \, \mathrm{d}\rho \right)}_{M_2(\chi)} g^{\text{vol}} \lambda_{33} \left| D_{33} \right| \\ \text{with} \quad \boldsymbol{d}^{\text{vol}} &= -\frac{1}{2} \left(1 + \frac{R^2}{\rho^2} \right) \underline{e}_r \otimes \underline{e}_r + \frac{1}{2} \left(-1 + \frac{R^2}{\rho^2} \right) \underline{e}_\theta \otimes \underline{e}_\theta + \underline{e}_z \otimes \underline{e}_z \end{aligned} \tag{III.115}$$

where $\boldsymbol{d}^{\text{vol}}$ is the strain rate associated with the trial velocity field of Eq. III.98 when $D_{31} = 0$. On the other hand, the volume term of the macroscopic dissipation under pure shear can be written as:

$$\Pi^{\text{vol}} \approx \tau_0 M_3 g^{\text{sh}} \lambda_{31} \left| D_{31} \right| \quad \text{where} \quad M_3 \equiv M\left(\boldsymbol{d}^{\text{sh}}\right) \quad \text{with} \quad \boldsymbol{d}^{\text{sh}} \propto \underline{e}_1 \odot \underline{e}_3 \tag{III.116}$$

[11] The average of a product writes as: $\langle AB \rangle = \langle A \rangle \langle B \rangle \left(1 + \left\langle \frac{A - \langle A \rangle}{\langle A \rangle} \frac{B - \langle B \rangle}{\langle B \rangle} \right\rangle \right)$. The second term is the normalized covariance of A and B. In the case in which A is independent from B or that of small relative variations of quantities A and B — which is solely postulated but could be verified numerically — the first term is the leading one.

where $\boldsymbol{d}^{\text{sh}}$ is the strain rate associated with the trial velocity field of Eq. III.98 when $D_{33} = 0$. Following Hure (2019), an approximation of the volume term in the general case ($D_{33} \neq 0$ and $D_{31} \neq 0$) can be inspired by Eq. III.99:

$$\Pi^{\text{vol}} \approx \tau_0 \sqrt{\left(M_2 g^{\text{vol}} \lambda_{33} D_{33}\right)^2 + \left(M_3 g^{\text{sh}} \lambda_{31} D_{31}\right)^2} \tag{III.117}$$

Finally, the surface dissipation associated with a tangential velocity discontinuity surface can be approximated by:

$$\begin{aligned} \Pi^{\text{surf}} &\approx \tau_0 \min\left(M_1^{(\text{A})}, M_1^{(\text{B})}\right) g^{\text{surf}} \left| \left(\frac{\lambda_{33}^{(\text{A})}}{x^{(\text{A})}} - \frac{\lambda_{33}^{(\text{B})}}{x^{(\text{B})}} \right) D_{33} \right| \\ \text{with} \quad M_1 &= \left(\frac{1}{2\pi} \int_0^{2\pi} M\left(\boldsymbol{d}^{\text{surf}}\right) \mathrm{d}\theta \right) \quad \text{and} \quad \boldsymbol{d}^{\text{surf}} \propto \underline{e}_r \odot \underline{e}_z \end{aligned} \tag{III.118}$$

where $\boldsymbol{d}^{\text{surf}}$ is the strain rate associated with the tangential velocity leap at the discontinuity surface.

Given the form of volume and surface dissipations (Eq. III.117 and III.118), Lemmata 1, 2 and 3, initially established for a Mises bi-material, still hold for grain boundaries. This means that there is a single localization band – possibly rigid – in each crystal and each of those bands is of maximal width. Besides, the surface discontinuity between the two bands is located in the crystal whose yield stress relative to the velocity leap $\Delta \underline{v}$ is the lowest, *i.e.* the crystal with the lowest M_1. Thus, an upper bound of the macroscopic dissipation of the unit cell is obtained by minimization over $(\lambda_{33}, \lambda_{31}) \in [0,1]^2$ of the function:

$$\begin{aligned} \Pi(\lambda_{33}, \lambda_{31}) = \tau_0 \Bigg\{ & 2 g^{\text{surf}} |D_{33}| \left[\left(M_1^{(1)} \lambda_{33} + \min\left(M_1^{(1)}, M_1^{(2)}\right) |2\lambda_{33} - 1| \right) \sigma_0^{(1)} + M_1^{(2)} (1 - \lambda_{33}) \right] + \\ & \sqrt{\left(M_2^{(1)} \lambda_{33} g^{\text{vol}} D_{33}\right)^2 + \left(M_3^{(1)} \lambda_{31} g^{\text{sh}} D_{31}\right)^2} + \sqrt{\left[M_2^{(2)} (1 - \lambda_{33}) g^{\text{vol}} D_{33}\right]^2 + \left[M_3^{(2)} (1 - \lambda_{31}) g^{\text{sh}} D_{31}\right]^2} \Bigg\} \end{aligned} \tag{III.119}$$

A detailed attempt to minimize Eq. III.119 is provided in Appendix III.2.C. In the following, a simplification inspired by the Mises bi-material will be conducted. Three limiting cases are considered:

- if crystal 1 is significantly softer than crystal 2 whatever the loading considered, then plasticity will localize only in crystal 2, *i.e.* $\lambda_{33} = \lambda_{31} = 1$;
- if crystal 2 is significantly softer than crystal 1 whatever the loading considered, then plasticity will localize only in crystal 2, *i.e.* $\lambda_{33} = \lambda_{31} = 0$;
- if crystal 1 and crystal 2 display a similar hardness whatever the loading considered, then plasticity will be of similar intensity in both crystals, *i.e.* $\lambda_{33} = \lambda_{31} = \frac{1}{2}$.

The assumption that the underlying physics of the limiting cases are enough to describe more general situations is made; therefore, the minimization of Eq. III.119 yields:

$$\min_{\lambda_{33}, \lambda_{31}} \Pi\left(\lambda_{33}, \lambda_{31}\right) \approx \min\left\{ \Pi(0,0), \Pi\left(\frac{1}{2}, \frac{1}{2}\right), \Pi(1,1) \right\} \tag{III.120}$$

It is shown in Appendix III.2.C that Eq. III.120 is exact when $D_{33} = 0$ or $D_{31} = 0$.

2.4.3 Yield surface

According to Eq. III.120, the yield surface for intergranular coalescence is obtained from the three individual surfaces related to macroscopic dissipations $\Pi(0,0)$, $\Pi\left(\frac{1}{2}, \frac{1}{2}\right)$ and $\Pi(1,1)$. Using the result obtained by Torki et al. (2015) (Eq. III.105), the following surfaces are obtained:

$$\Pi(0,0) \quad : \quad \left(\frac{\left\{ |\Sigma_{33}| - 2\tau_0 \left[M_1^{(2)} + \min\left(M_1^{(1)}, M_1^{(2)}\right) \right] g^{\text{surf}} \right\}_+}{\tau_0 M_2^{(2)} g^{\text{vol}}} \right)^2 + \left(2 \frac{\Sigma_{31}}{\tau_0 M_3^{(2)} g^{\text{sh}}} \right)^2 - 1 = 0 \tag{III.121}$$

$$\Pi\left(\frac{1}{2},\frac{1}{2}\right) \quad : \quad \left(2\frac{\left\{|\Sigma_{33}|-2\tau_0\left[M_1^{(1)}+M_1^{(2)}\right]g^{\text{surf}}\right\}_+}{\tau_0\left[M_2^{(1)}+M_2^{(2)}\right]g^{\text{vol}}}\right)^2+\left(4\frac{\Sigma_{31}}{\tau_0\left[M_3^{(1)}+M_3^{(2)}\right]g^{\text{sh}}}\right)^2-1=0 \tag{III.122}$$

$$\Pi\left(1,1\right) \quad : \quad \left(\frac{\left\{|\Sigma_{33}|-2\tau_0\left[M_1^{(1)}+\min\left(M_1^{(1)},M_1^{(2)}\right)\right]g^{\text{surf}}\right\}_+}{\tau_0 M_2^{(1)}g^{\text{vol}}}\right)^2+\left(2\frac{\Sigma_{31}}{\tau_0 M_3^{(1)}g^{\text{sh}}}\right)^2-1=0 \tag{III.123}$$

The effective coalescence elasticity domain is defined as the intersection of elasticity domains corresponding to these three types of strain localization. As a side note, notice that, contrary to the model of void coalescence in single crystals of Hure (2019), no minimization has to be conducted to determine the plane of coalescence — each plane corresponding to a set of average Taylor factors. Indeed, intergranular coalescence is characterized by a coalescence plane located at the grain boundary, which removes any ambiguity in the definition of the effective yield criterion.

2.4.4 Numerical assessment

In order to assess the model presented in Section III.2.4.3, numerical limit analysis is performed on porous grain boundaries. A set of 20 couples of random crystallographic orientations is investigated numerically. Their definition can be found in Table III.2, relative to the axes given in Fig. III.23c of the present study. In general, the orthotropy axes of crystals are not aligned with the axes of the simulation, so three-dimensional computations have to be conducted. The fast Fourier transform-based `AMITEX_FFTP` code is used with periodic boundary conditions. Small strain assumption is used, with crystal plasticity constitutive equations (Eq. III.111) for matrix materials. These constitutive equations have been implemented in the `MFront` code generator (Helfer et al., 2015), using an implicit discretization solved with a Newton-Raphson algorithm. Details of the numerical implementation can be found in Hure et al. (2016). Crystal elasticity is chosen to obey an isotropic Hooke law of Young modulus $Y = 10^3$ MPa and Poisson ratio $\nu = 0.49$. As a classical result of limit analysis, the results presented in the following do not depend on these values. τ_0, $\dot{\gamma}_0$ and n have been set to 88 MPa, 1 s^{-1} and 100, respectively. These parameter values ensure a negligible strain rate dependency for all simulations performed.

2.4.5 Coalescence by internal necking

First, the case of internal necking is considered. In order to mimic the cylindrical unit-cell of Fig. III.23c within the periodic cubic grid of FTT simulations, the mesh of Fig. III.26c is used. In this mesh, the cylindrical unit cell is laterally

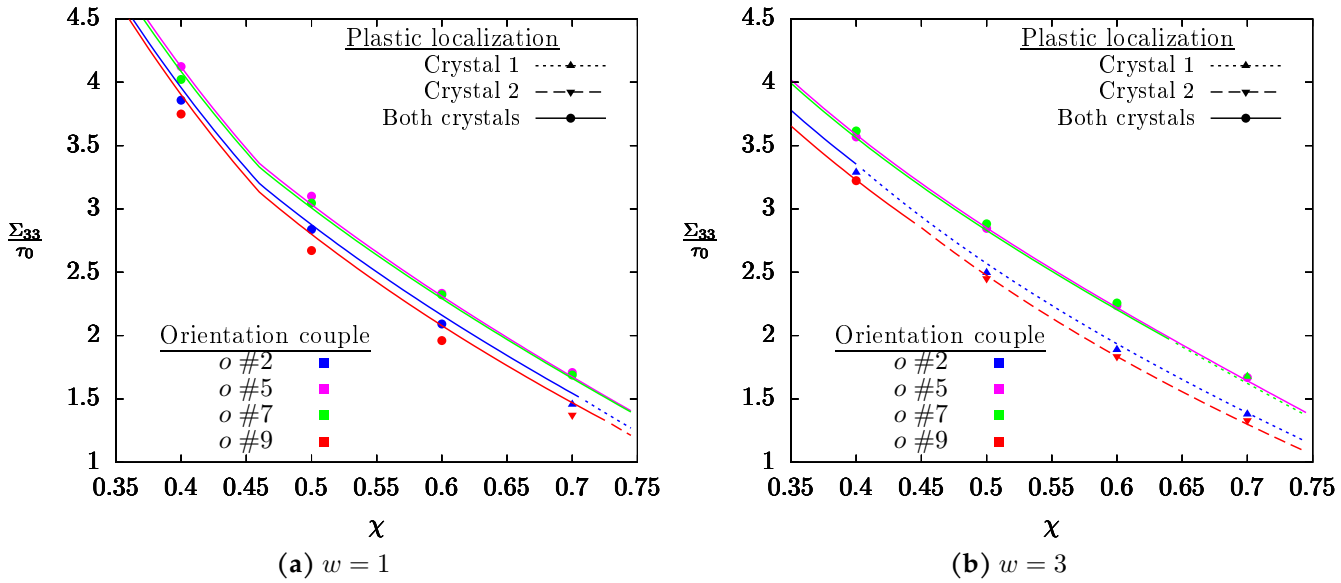

(a) $w = 1$ **(b)** $w = 3$

FIGURE III.31: Comparison of the internal necking stress computed by numerical limit analysis (points) and predicted by the model (lines) for various orientation couples (different colors) and microstructure parameters. Plasticity can either extend in both crystals (full lines and circular symbols) or be confined into a unique crystal (dashed lines and triangular symbols).

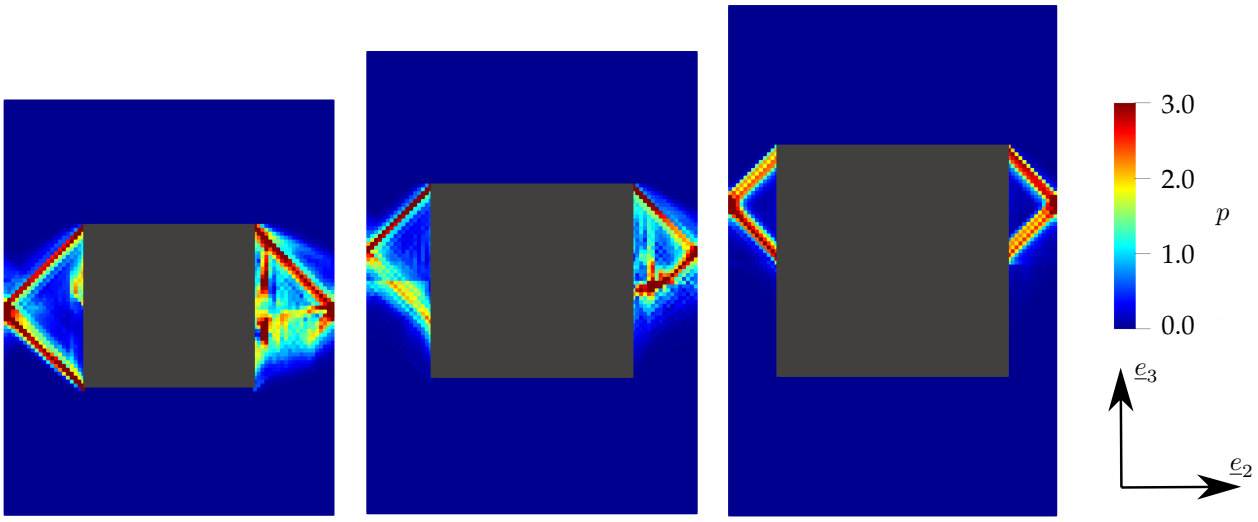

(a) $\chi = 0.5$ **(b)** $\chi = 0.6$ **(c)** $\chi = 0.7$

FIGURE III.32: Microscopic fields of equivalent plastic strain p (arbitrary units) for internal necking simulations carried out for orientation couple #2 at $w = 1$ and increasing χ. The fields are shown in the median plane $(\underline{e}_2, \underline{e}_3)$ and the void is depicted in gray.

embedded in a cuboid of fictive material. This fictive material is an elastic medium with Young's modulus Y_{33} and shear moduli G_{31}, G_{32} equal to zero, and (almost)-infinite Young's moduli Y_{11}, Y_{22} and shear modulus G_{12}; details can be found in Barrioz et al. (2018a). Crystal plasticity is assigned to the voxels inside the cylindrical unit cell, with a different crystallographic orientation on each side of the median horizontal plane, and an elastic material with zero stiffness is set to the voxels of the cylindrical void. The radius of the cylinder is of $N = 100$ voxels and the height of the unit cell is chosen so that $c = 0.4$, which is low enough so that c does not influence the results. As always, mesh convergence is checked so that results can be relied upon. The macroscopic strain rate prescribed to the cuboid unit-cell is $\boldsymbol{D} = D_{33}\underline{e}_3 \otimes \underline{e}_3$ with $D_{33} = 10^{-4}\ \mathrm{s}^{-1}$. The definition of the fictive material ensures that the cylindrical unit-cell is subjected to uniaxial extension devoid of macroscopic shear stress Σ_{31} since the lateral surfaces of the cylinder can shear freely in horizontal planes. Upon loading, the macroscopic stress Σ_{33} saturates at the internal necking stress.

As in the isotropic case, a numerical correction is performed on the model before carrying out its assessment. In the isotropic case, it was justified because the real velocity field differed sufficiently from the considered set of trial fields to cause discrepancies, especially when $w \to 0$. In the grain boundary case, the real velocity field is even farther from the putative velocity fields of Section III.2.4.3. Thus, the numerical correction should diverge from the isotropic case. The mesh of Fig. III.26c is used to perform numerical limit analysis of internal necking in single crystals, for $\chi \in \{0.4, 0.5, 0.6, 0.7\}$, $w \in \{0.5, 1, 3\}$ and the two crystal orientations of the first 10 orientation couples. Then, by comparing these results to the model of Hure (2019) — which is the crystalline counterpart of that of Torki et al. (2017) — a calibration suggests substituting g^{vol} and g^{surf} of Section III.2.4.3 by:

$$\tilde{g}^{\mathrm{vol}} = \alpha(\chi, w)\hat{g}^{\mathrm{vol}} \quad , \quad \tilde{g}^{\mathrm{surf}} = \alpha(\chi, w)\hat{g}^{\mathrm{surf}} \quad \text{with} \quad \alpha(\chi, w) = \max\left[1.15 - 0.76(\chi + 0.2w - 0.2), 0.775 + 0.025w\right] \tag{III.124}$$

This correction is adopted in the following.

Reverting to the case of porous grain boundaries, the internal necking stress computed by numerical limit analysis is compared to the one predicted by the model in Fig. III.31 for a handful of crystallographic orientation couples. It is seen that the predictions of the model are quite satisfying and that it reproduces correctly the evolution of Σ_{33} with χ for $w = 1$ (Fig. III.31a) and $w = 3$ (Fig. III.31b). Note that the agreement over a large span of parameters w and χ is obtained partly due to the calibration of $\alpha(w, \chi)$. Despite the differences between crystal orientations being weak, they are well accounted for by the analytical criterion. For instance, notice that the fact that orientation couples #5 and #7 are closer to each other at high χ for $w = 1$ is correctly foreseen, as well as the fact that these two orientations are almost indistinguishable at $w = 3$. As shown in Hure (2019), weak variations between orientation couples are intrinsic to FCC crystals: for instance, HCP crystals display a stronger anisotropy so that the model would uncover greater differences in coalescence stress. Finally, note that the differences in coalescence stress between crystal orientations increase in

relative value with w and χ.

In Fig. III.31, it is seen that the model is capable of predicting the shift in strain localization that occurs with increasing χ. Indeed, as was pointed out in Section III.2.3.4, a higher ligament size ratio favors localization in a unique (softer) material over localization in both materials. This behavior is seen for orientation couples #2 and #9 at $w = 1$ and for all orientation couples except #5 at $w = 3$. The former is detailed in Fig. III.32: at $\chi = 0.5$, the numerical strain rate field occupies both crystals; at $\chi = 0.6$, it shifts to the upper half of the unit-cell but lingers partially in the lower half; at $\chi = 0.7$, the transition is over and the strain rate field lies entirely in crystal 1. Interestingly, the model predicts all those changes with a reasonable accuracy[12] and can distinguish whether crystal 1 is softer than crystal 2 (relatively to the coalescence strain rate field) or the other way around. The dependence of this transition on the crystallographic orientations is significant: for instance, at $w = 3$, orientation couple #2 makes its transition from both crystals to crystal 1 between $\chi = 0.3$ and $\chi = 0.4$ whereas the transition from both crystals to crystal 2 for orientation couple #1 occurs after $\chi = 0.7$ (see Fig. III.31b). Thus, the fact that the model can correctly estimate the threshold at which the localization pattern changes is quite valuable.

2.4.6 Coalescence under combined tension and shear

Having verified that the model performs well for coalescence by internal necking, the case of coalescence under combined tension and shear is next considered. The mesh relying on the fictive material (Fig. III.26c) can no longer be used because the fictive material cannot transmit shear strain along $\underline{e}_1 \odot \underline{e}_3$. Therefore, the unit-cell with hexagonal periodicity of Fig. III.23b is used, as in the isotropic case. The mesh of Fig. III.26b is defined similarly as in Section III.2.3.4 and loaded so that the macroscopic strain rate is $\boldsymbol{D} = D_{33}\underline{e}_3 \otimes \underline{e}_3 + 2D_{31}\underline{e}_1 \odot \underline{e}_3$ with a fixed ratio D_{31}/D_{33} and $\max(D_{33}, D_{31}) = 10^{-4}$ s^{-1}. The macroscopic stresses Σ_{33} and Σ_{31} are computed by averaging the saturated microscopic stress field $\boldsymbol{\sigma}$ over the unit cell. Contrary to the isotropic case, the numerical yield surface generally exhibits no axial symmetry. In particular, the boundary conditions associated with $D_{31} = 0$ (respectively $D_{33} = 0$) do not necessary yield $\Sigma_{31} = 0$ (respectively $\Sigma_{33} = 0$). However, the constitutive equation of crystal plasticity (Eq. III.111) is an odd function of $\boldsymbol{\sigma}$, which means that the macroscopic yield surface has a central symmetry. Thus, only the half-plane $(\Sigma_{33}, \Sigma_{31})$ with $\Sigma_{33} > 0$ will be shown.

A calibration similar to that concerning internal necking is conducted for pure shear ($D_{33} = 0$). Numerical limit analysis of coalescence in porous single crystals with the mesh of Fig. III.26b and the same range of microstructure parameters and crystal orientations as before suggests replacing g^{sh} of the isotropic model by

$$\tilde{g}^{\text{sh}} = \beta \hat{g}^{\text{sh}} \tag{III.125}$$

with $\beta = 0.9$. This correction is adopted for the rest of the study.

Returning to porous grain boundaries, a comprehensive comparison of numerical limit analysis results to model predictions is given in Fig. III.33. In Fig. III.33a, it is seen that an increase of χ significantly reduces the elasticity domain and that the model quantitatively captures the effect of χ. It confirms on the whole surface what was noticed in Fig. III.31 for the single point corresponding to internal necking ($\Sigma_{31} = 0$). As shown in Fig. III.33b, the gradual contraction of the yield surface with increasing w is also satisfyingly accounted for by the model. Besides, at $w = 3$, a section of the numerical yield surface is associated with localization in crystal 1, which is correctly predicted by the model even if the precise boundaries of this domain are not quantitatively foreseen. The change in the localization pattern with increasing shear strain rate is shown in Fig. III.34: at dominant axial strain (Fig. III.34a), plasticity localizes in crystal 1, which is the softer of the two crystals relatively to this loading; then, when the shear strain increases (Fig. III.34b), plasticity extends in both crystals; finally, under pure shear strain (Fig. III.34c), plasticity occurs dominantly in crystal 2, which is the softest of the two crystals relatively to this loading.

Numerical results for a handful of crystallographic orientations and their analytical counterparts are shown in Fig. III.33c. It confirms the fact that coalescence yield surfaces of grain boundaries can differ significantly, not only in internal necking (which was shown in Fig. III.31) but also under combined tension and shear. The model captures the influence of crystal orientations under pure shear and internal necking well, but discrepancies arise under combined

[12] Notice that the shear bands at 45° displayed in Fig. III.32 bear a troubling resemblance to that of the coalescence model of Brown and Embury (1973). In a cylindrical cell, this model predicts that coalescence happens for $\chi \geq 1/(1+\hat{w})$ with $\hat{w}$ the effective void aspect ratio. Coalescence occurring solely in the upper (or lower) half of the cell is associated with $\hat{w} = w/2$, leading to $\chi > 0.66$ ($w = 1$) — a threshold that is coherent with Fig. III.32 — and $\chi > 0.4$ ($w = 3$). However, for other orientation couples, shear bands are less marked or not at 45° so that predictions of the qualitative model degrade significantly (see Fig. III.31).

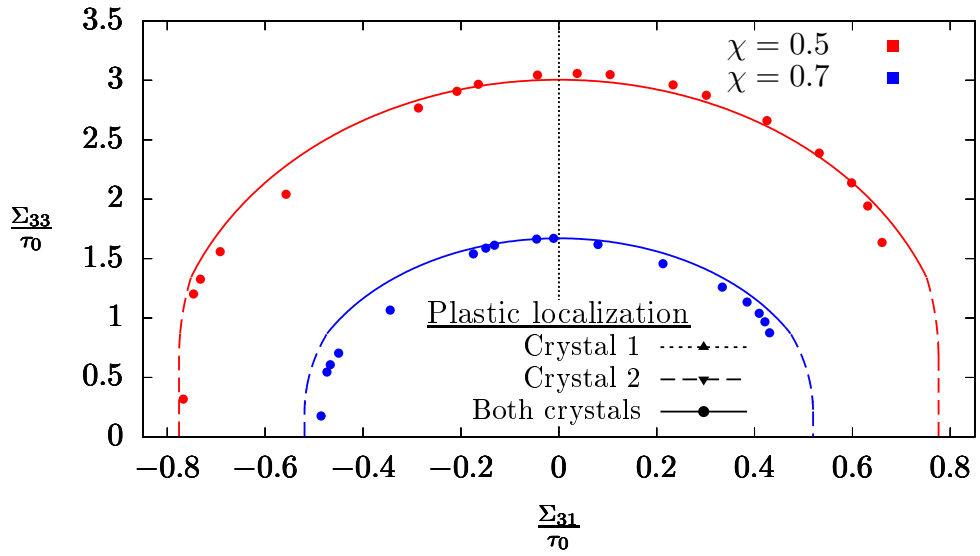

(**a**) Orientation couple #1, $w = 1$

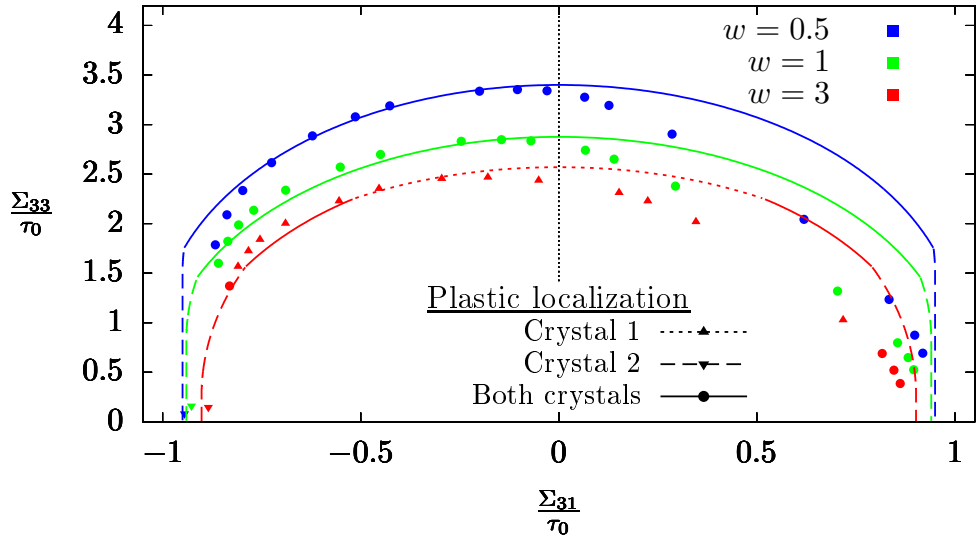

(**b**) Orientation couple #2, $\chi = 0.5$

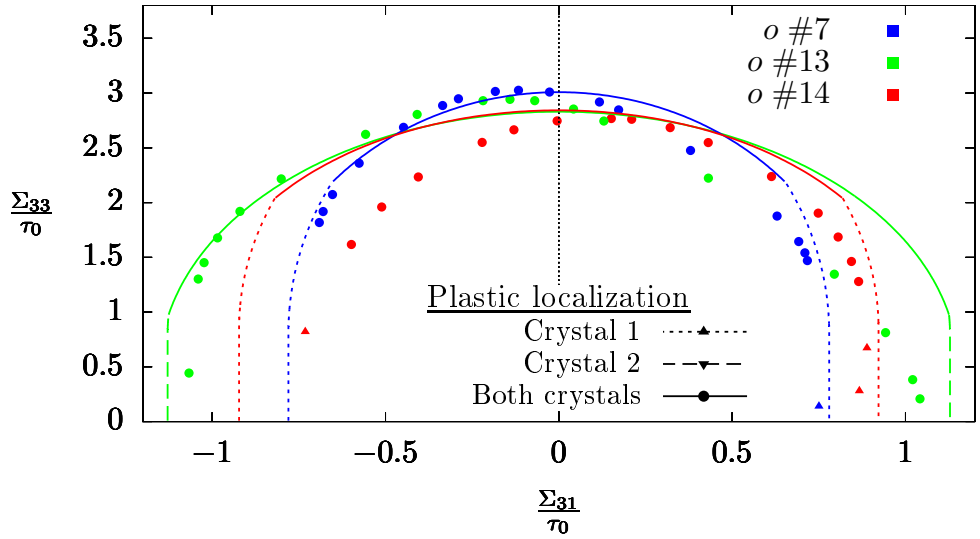

(**c**) $\chi = 0.5$, $w = 1$

FIGURE III.33: Coalescence yield surface in the plane $(\Sigma_{31}, \Sigma_{33})$ as predicted by the model (lines) and computed numerically through FFT unit-cell simulations (points). The effect of various parameters (in different colors) is assessed: (a) ligament size ratio χ; (b) void aspect ratio w; (c) crystallographic orientations. Plasticity can either extend in both crystals (full lines and circular symbols) or be confined into a unique crystal (dashed lines and triangular symbols).

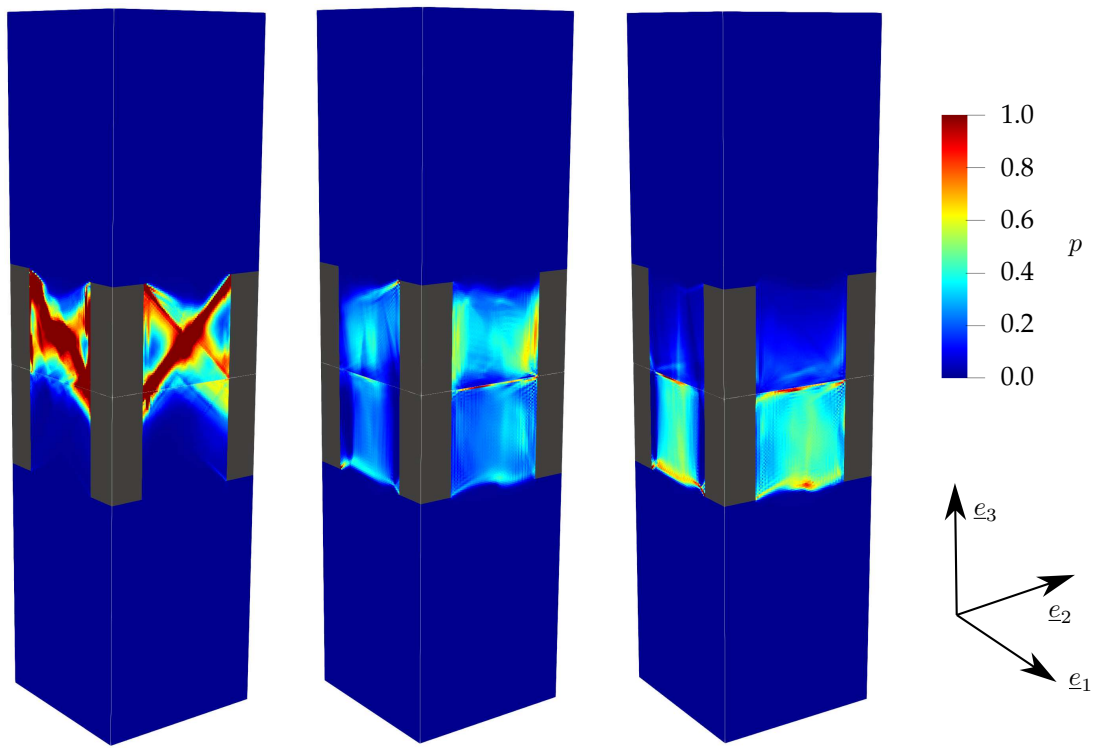

(a) $D_{31} = 0$ **(b)** $D_{31} = 7D_{33}$ **(c)** $D_{33} = 0$

FIGURE III.34: Microscopic fields of equivalent plastic strain $p = \int d_{\text{eq}} \mathrm{d}t$ (arbitrary units) for simulations carried out at $\chi = 0.5$, $w = 3$ and orientation number #2.

tension and shear. Part of this error already existed in the isotropic case (see Fig. III.29) but a new source of inconsistency is specific to crystals. Indeed, as stated before, whereas the model — which was adapted from the isotropic case — predicts an axial symmetry relatively to $\Sigma_{33} = 0$ and $\Sigma_{31} = 0$, no such symmetry exists in numerical yield surfaces. This was already visible in the study of coalescence in single crystals by Hure (2019) (see FCC orientation $[\bar{1}25]$). The asymmetry is related to the absence of equivalence of $(\underline{e}_1, \underline{e}_3)$ and $(-\underline{e}_1, \underline{e}_3)$ for the crystal orientation couple considered. When this asymmetry is weak, as in the case of orientation couple #1 (Fig. III.33a) and orientation couple #7 (Fig. III.33c), the agreement between the model and numerical results is very satisfying. On the contrary, if this asymmetry is significant, as in the case of orientation couple #2 (Fig. III.33b) and orientation couples #13 and #14 (Fig. III.33c), the model disagrees with numerical results on a large section of the yield surface. For instance, the numerical yield surface of orientation couple #14 is well reproduced by the model for $\Sigma_{31} > 0$ but a large deviation appears for $\Sigma_{31} < 0$.

It is seen in Fig. III.33 that plasticity localization predicted by the model falls in two alternative cases: either internal necking favors a strain rate field that occupies both crystals (see orientation couple #7 in Fig. III.33c) and increasing shear strain will gradually localize plasticity in the softest (relatively to shear strain) of the two crystals, or internal necking is characterized by strain localization in a unique crystal (see orientation couple #2, $w = 3$ in Fig. III.33b) and increasing shear strain will first extend plasticity to both crystals and then confine it to a unique crystal, different from the first one. Indeed, it seems that a crystal cannot be simultaneously softer relative to pure shear and to uniaxial tension than another given crystal. This contrasts with the isotropic case in which material 2 was softer for all possible loadings and in which the yield surface could be entirely determined by the sub-criterion associated with localization in the soft material (see for instance the porous bi-material with $s = 0.5$ in Fig. III.29a). This prediction of the coalescence model seems confirmed by part of the numerical results (see orientation couples #2, #7, and #14 in Fig. III.33). Yet, a third case arises among numerical surfaces: when the two crystals have pure shear yield stresses that are close, unit-cell computations point out that, under dominant shear, plasticity can extend in both crystals with equivalent intensity. This is seen for orientation couple #1 in Fig. III.33a ($M_3^{(1)} = 2.03$ and $M_3^{(2)} = 2.20$) and for orientation couple #13 in Fig. III.33c ($M_3^{(1)} = 3.08$ and $M_3^{(2)} = 2.96$). The model cannot predict this situation since the theoretical dissipation of a shear band does not depend on its width — g^{surf} only depends on χ —, which

seems to be an oversimplification. A more realistic velocity field for pure shear would have to be chosen to alleviate this shortcoming. More generally, it should be remembered that the model predicts a flat part related to $D_{33} = 0$ that is too large compared to numerical surfaces where that loading condition is usually reduced to a single point. This explains that the model sometimes predicts plastic localization in a unique crystal while numerical simulations reveal a strain rate field occupying both crystals (*e.g.* Fig. III.33b). Correcting such a deviation would require using a velocity field without tangential discontinuity, such as the one given in Keralavarma and Chockalingam (2016).

In this section, the model has been compared to numerical limit analysis results. On the one hand, it has been validated on coalescence by internal necking for which it predicts accurately the dependence on crystallographic orientations and microstructure parameters and foresees correctly the different localization patterns in the ligament. On the other hand, it has shown promising capabilities to estimate yield surfaces for coalescence under combined tension and shear, reproducing correctly trends associated with microstructure parameters and crystal orientations. Yet, the latter use is subjected to a few shortcomings: first, for orientation couples with strong asymmetry regarding the given shear strain, some sections of the yield surface will display a significant discrepancy; then, strain localization patterns foreshown by the model are in qualitative agreement with numerical results but sometimes lack quantitative agreement.

2.5 Discussion

2.5.1 Effect of the localization pattern on ductility

Even if this study focuses on deriving an intergranular coalescence criterion on a fixed geometry, some rationalization of the full process of intergranular ductile fracture may be attempted. The early work of Li and Guo (2002) on porous interfaces has shown that, when a yield stress mismatch existed between two Mises materials, the fracture strain was lower in the porous bi-material than in corresponding porous Mises mono-materials. Coalescence by internal necking was seen to occur exclusively in the soft half of the porous interface. In the absence of shear, this numerical finding can be interpreted in the light of the two porous interface coalescence modes evidenced in the present work: coalescence in the full ligament and coalescence in the soft half-ligament. The enhanced damage observed by Li and Guo (2002) can be explained qualitatively through the evolution equation for χ associated with internal necking in Mises materials (Benzerga, 2000; Benzerga, 2002):

$$\dot{\chi} = \frac{1}{2c}\left(\frac{1}{\chi} - \chi\right) D_{33} \tag{III.126}$$

Specialized to the two possible internal necking regimes of a porous interface, it yields for the same initial ligament size ratio χ_0:

$$\dot{\chi}_{\text{soft half-ligament}}\left(\chi_0\right) = 2\dot{\chi}_{\text{full ligament}}\left(\chi_0\right) \tag{III.127}$$

since the height ratio c of the effective ligament is twice smaller when plasticity localizes in the soft ligament. This means that when internal necking occurs exclusively in the soft material, interface coalescence is approximately twice as fast as bulk coalescence or as interface coalescence with localization in the entire ligament. Therefore, predicting the dominant coalescence mode is paramount to assessing the ductility of a porous grain boundary.

2.5.2 Competition between transgranular and intergranular void coalescence

The model derived in the previous part allows for a discussion of the competition between transgranular and intergranular ductile fractures. Ductile fracture usually occurs by successive nucleation, growth, and coalescence of cavities; thus, the nucleation and growth stages will significantly determine the fracture mode. Nonetheless, since coalescence is associated with a brutal loss of stress-bearing capacity, it may play an important part in the competition between transgranular and intergranular fractures. In the following, void coalescence in porous grain boundaries and their corresponding porous single crystals is studied using the simplified microstructure shown in Fig. III.23, meaning that cavities preexist the ductile fracture process. In the case of porous single crystals, material 1 and material 2 are the same crystalline matrix material. The model used to describe coalescence in porous single crystals is the one given in Hure (2019), which predicts the following yield surface under combined tension and shear:

$$\left(\frac{\left(|\Sigma_{33}| - 2\tau_0 M_1 g^{\text{surf}}\right)_+}{\tau_0 M_2 g^{\text{vol}}}\right)^2 + \left(2\frac{\Sigma_{31}}{\tau_0 M_3 g^{\text{sh}}}\right)^2 - 1 = 0 \tag{III.128}$$

with M_1, M_2 and M_3 the average Taylor factors associated with the crystal orientation. The model used for intergranular void coalescence is the one from Section III.2.4.3. In both cases, models are compared to unit-cell computations conducted along the same lines as in Section III.2.4.4, using only the first 8 orientation couples of Table III.2.

First, the case of internal necking is assessed in Fig. III.35. The quantitative agreement between models and unit-cell results is excellent for orientation couple #2 (Fig. III.35a). This case, in which the internal necking stress of the grain boundary lies between the stresses of corresponding single crystals, covers approximately half of the orientation couples investigated here, and is especially favored by high w and χ. The orientation couples pertaining to that regime for $\chi \geq 0.5$ are: for $w = 0.5$, couples #1 to #3; for $w = 1$, couples #1, #2, #3 and #5; for $w = 3$, couples #1 to #5. This means that in the case of a homogeneous distribution of cavities between grain interiors and grain boundaries, internal necking will be transgranular since one of the two single crystals will be more prone to this deformation mode than the grain boundary. However, the remainder of crystal orientation couples follows the trend shown in Fig. III.35b, *i.e.* the coalescence stress of both single crystals is close and internal necking is favored at the grain boundary compared to constitutive single crystals. Unfortunately, the model cannot predict such a phenomenon, even if it correctly estimates the value of the coalescence stress of the grain boundary. Indeed, according to the model presented in this article and the one taken from Hure (2019), the coalescence susceptibility of the grain boundary will always be intermediate between its two constitutive single crystals. This numerical finding has significant consequences since it means that intergranular void coalescence can have precedence over transgranular coalescence without specific grain boundary weakening. This contrasts with what was shown about void growth in the authors' previous work (Sénac et al., 2023a): at equivalent damage, transgranular void growth is always favored over intergranular void growth. If significant growth is needed to trigger coalescence, then the competition will be dominated by the difference in void growth rates. However, in many cases (*e.g.* Schulz and McMahon (1973), Hojná (2017), and Demkowicz (2020)), grain boundary voids exhibit minimal growth before coalescence so that intergranular ductile fracture may be controlled by coalescence.

A similar analysis is performed on coalescence under combined tension and shear; some of its results are displayed in Fig. III.36. As for internal necking, some grain boundaries display a median coalescence susceptibility compared to their constitutive single crystals over the whole yield surface, *e.g.* orientation couple #3 in Fig. III.36a. These cases are mimicked correctly by the conjunction of coalescence models. However, for some orientation couples such as #9 (see Fig. III.36b, $-0.9 < \Sigma_{31} < -0.5$), there are portions of the yield surface for which the grain boundary is more susceptible to coalescence than its corresponding single crystals. Again, models are unable to predict such behaviors, which calls for additional development in the future.

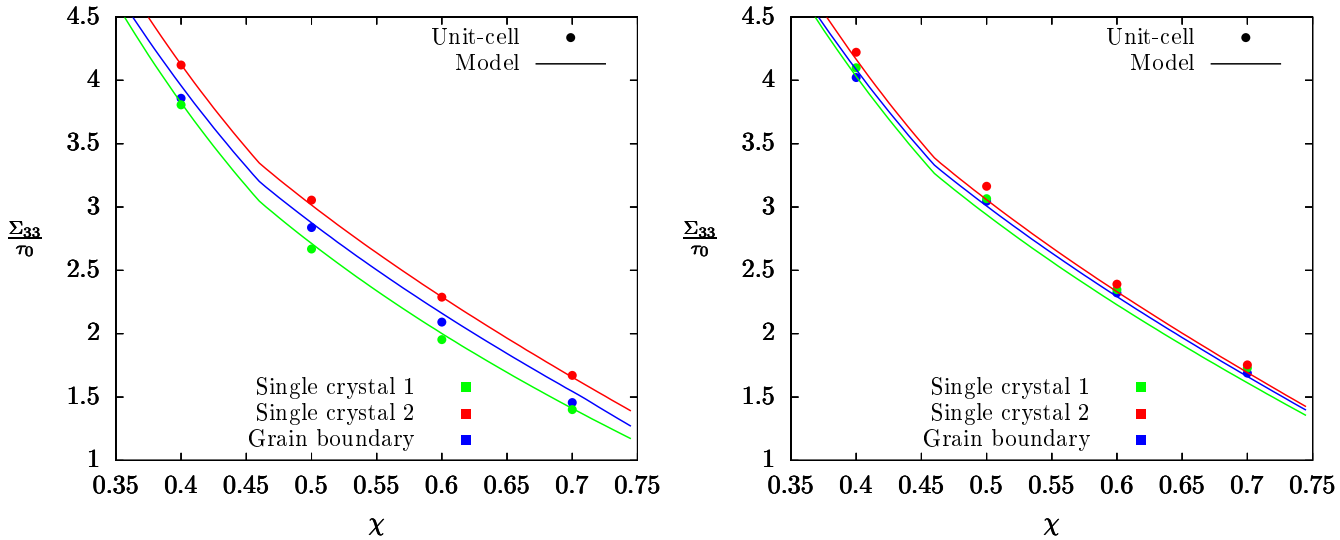

(**a**) Orientation couple #2, $w = 1$ (**b**) Orientation couple #7, $w = 1$

FIGURE III.35: Internal necking stress as a function of χ for a porous grain boundary and corresponding porous single crystals, as computed by numerical limit analysis (points) and predicted by the models (lines).

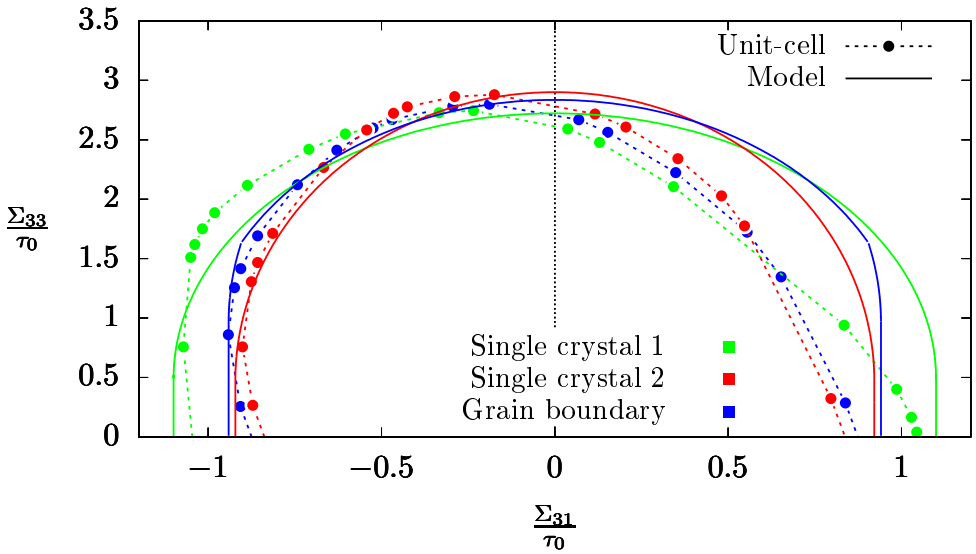

(**a**) Orientation couple #3, $\chi = 0.5$, $w = 1$

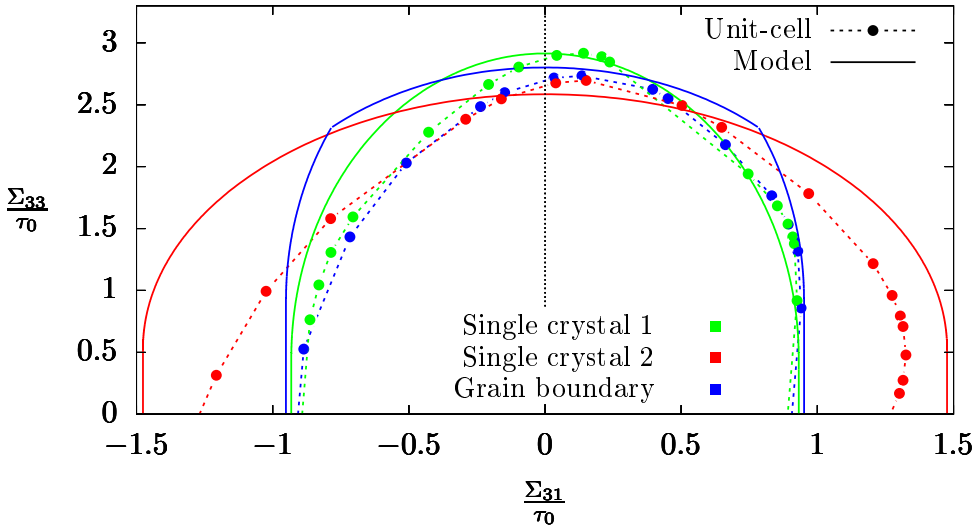

(**b**) Orientation couple #9, $\chi = 0.5$, $w = 1$

FIGURE III.36: Coalescence yield surface in the plane $(\Sigma_{31}, \Sigma_{33})$ as predicted by the models (lines) and computed numerically through FFT unit-cell simulations (points) for a porous grain boundary and corresponding porous single crystals.

2.5.3 Intergranular void growth and coalescence by internal necking

As underlined in the introduction, grain boundary ductile fracture occurs by successive intergranular void growth and coalescence. In order to predict the entire yield surface of a porous grain boundary, the effective criterion has to incorporate both growth and coalescence. A convenient way of reaching this goal is combining available intergranular void growth and coalescence criteria in a multi-surface framework, as described in Benzerga and Leblond (2010). This method amounts to intersecting elasticity domains obtained by individual criteria in order to obtain the final yield surface. Note that this approach has already been successfully applied to transgranular ductile fracture of porous single crystals (Scherer et al., 2021; Sénac et al., 2022). In the case of intergranular ductile fracture, the chosen void growth criterion is the variational criterion ($n = 100$) of Sénac et al. (2023a) because it allows considering non-spherical cavities.

In order to be consistent with the aforementioned study, the unit cell of the periodic microstructure considered is a cubic bicrystal containing a spheroidal cavity at the grain boundary. Even if the orientation couple definitions are identical in both studies, note that the grain boundary plane is now $(\underline{e}_2, \underline{e}_3)$, meaning that $\underline{e}_1$ is normal to the putative coalescence plane. The void aspect ratio w is now defined as the ratio of the semi-axis along $\underline{e}_1$ to the equatorial radius of the spheroid. Combined with the porosity f — understood as the void volume fraction of the unit cell —, they define the cavity entirely. In the cylindrical unit-cell, the transverse ligament ratio χ is both the square root of

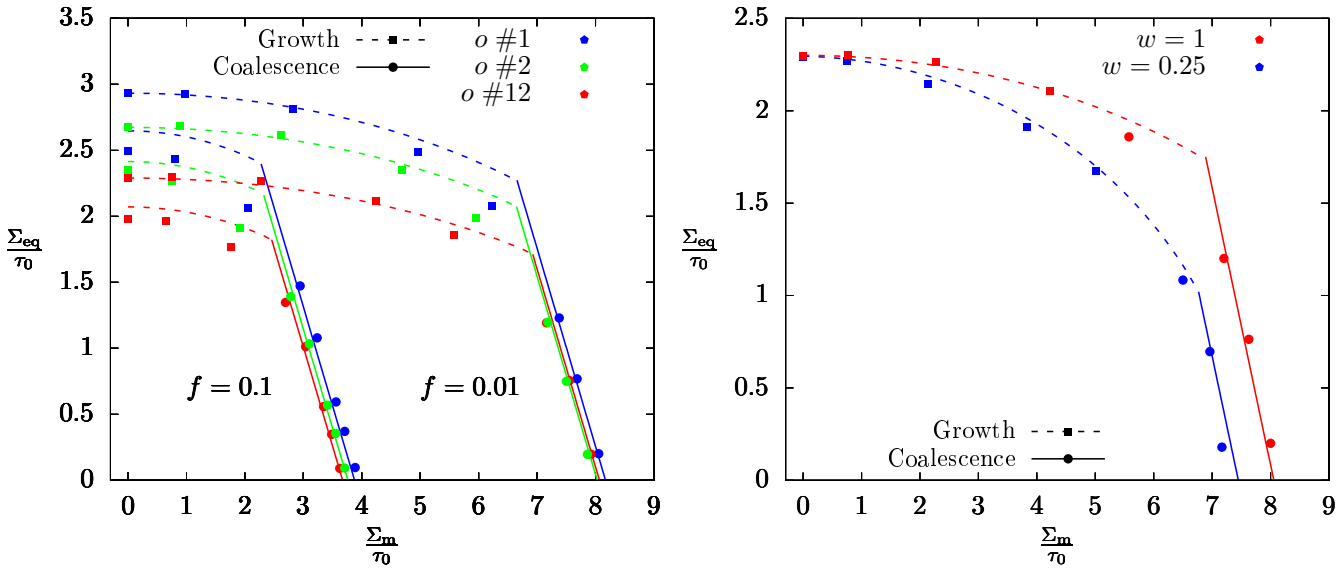

(a) $w = 1$ (b) Orientation couple #10, $f = 0.01$

FIGURE III.37: Yield surface of porous grain boundaries plotted in the meridian plane (Σ_m, Σ_{eq}) as predicted by the multi-surface criterion (lines) and by unit-cell simulations (points). Various effects are studied: (a) different orientation couples and porosities f; (b) different void aspect ratios w. Sections belonging to void coalescence and void growth are distinguished graphically, while the deformation mode experienced by each unit-cell simulation was determined using a numerical indicator (Sénac et al., 2023a).

the void volume fraction in the horizontal band containing the cavity (definition #1) and the ratio between the cavity radius and the void spacing (definition #2). In the cubic unit-cell, such choices lead to:

$$\chi = \left(\alpha \frac{f}{w}\right)^{\frac{1}{3}} \tag{III.129}$$

with $\alpha = \alpha_1 \equiv \sqrt{\frac{\pi}{6}}$ (definition #1) and $\alpha = \alpha_2 \equiv \frac{6}{\pi}$ (definition #2). In this work, the intermediate choice of $\alpha = \alpha_1\alpha_2 = \sqrt{\frac{6}{\pi}}$ is made. The unit-cell is subjected to axisymmetric loading with a main axis along $\underline{e}_1$ and a fixed stress triaxiality T, which is defined as the ratio of hydrostatic stress $\Sigma_m = \frac{1}{3}\mathrm{Tr}(\boldsymbol{\Sigma})$ to the equivalent von Mises stress Σ_{eq}. Numerical results are extracted from Sénac et al. (2023a). More details about unit-cell geometry, mechanical loading and numerical simulations can be found in the aforementioned study. Note that given the axisymmetric loading, coalescence can only happen by uniaxial extension, *i.e.* internal necking.

An excerpt of the comparison between the multi-surface yield criterion and unit-cell results is displayed in Fig. III.37. Note that the coalescence criterion has been applied to a different unit-cell geometry — spheroidal void in a cubic cell — than that on which it was developed and validated — cylindrical void in a cylindrical cell — without additional calibration. Despite this source of discrepancy, its agreement with unit-cell simulations is very satisfying. As expected, coalescence occurs at high T while void growth dominates at low T. In Fig. III.37a, it is shown that the combined yield criterion predicts the effect of crystal orientation couples and porosity well. Using Eq. III.129, $f = 0.01$ corresponds to $\chi = 0.24$ and $f = 0.1$ to $\chi = 0.52$. Understandably, increasing f fosters coalescence over growth, leading to a larger coalescence section in the yield surface. The orientation effect is seen to be more important on void growth than on void coalescence; still, it should not be neglected, especially at a high porosity (as underlined in Section III.2.4.5, differences between crystallographic orientation couples are more marked when χ is high) as is shown with $f = 0.1$ in Fig. III.37a. In Fig. III.37b, it is seen that the effect of the void aspect ratio w is also well accounted for by the combined model. It can thus be concluded that the multi-surface criterion can be used to estimate the yielding of porous grain boundaries under proportional axisymmetric loading for a large span of microstructure parameters, which was the goal of the present study.

2.6 Conclusion and perspectives

Any physically-based modeling of intergranular ductile fracture requires the development of criteria for the growth and coalescence of cavities at crystal interfaces. This study has dwelt upon the phenomenon of coalescence of intergranular cavities. In a first approach, porous grain boundaries were approximated by a von Mises bi-material with cavities at the internal interface. Using limit analysis on a set of simple trial velocity fields inspired by Benzerga and Leblond (2014) and Torki et al. (2015), a yield criterion for coalescence under combined tension and shear was obtained. The model suggests that plasticity will always occur in the ligament of the soft material and shall only extend in the ligament of the hard material if the yield stress mismatch is weak, the void aspect ratio is low or the distance between voids is significant. Predicting the localization pattern correctly is considered paramount for predicting the fracture strain since localization in the soft half-ligament significantly reduces ductility compared to localization in the entire ligament. To validate the yield criterion, unit-cell computations with an identical geometry were conducted using finite-element modeling and fast Fourier transform solving. On the one hand, an examination of the numerical strain rate fields confirmed the qualitative outcomes of the model. On the other hand, quantitative agreement was noticed in predicting the yield surface over an extensive range of parameters, for both internal necking and tension with superimposed shear.

Although convincing, this first model could not account for intergranular coalescence since a crystal with a given orientation cannot be said to be unequivocally softer than another with a different orientation. In the second part of the study, an extended model has been developed based on the isotropic yield criterion using an approximate method relying on average Taylor factors first proposed in Hure (2019). Numerical limit analysis was then performed on grain boundaries with FCC crystal lattice with and without the presence of additional shear with respect to the coalescence plane. The analytical criterion led to coalescence stress predictions in good agreement with numerical results, capturing the effects of crystallographic orientations, void shape and size. Yet, the absence of asymmetry of analytic yield surfaces under combined tension and shear was shown to be a weakness of the current modeling. The implications of the proposed criterion on the competition between transgranular and intergranular coalescence have also been studied. In some cases, the intergranular coalescence yield surface was seen to be slightly interior to the corresponding transgranular coalescence yield surfaces, which the model cannot predict. Finally, the very first criterion of combined growth and coalescence of intergranular cavities was obtained by gathering the present model and a criterion of grain boundary void growth of Sénac et al. (2023a). When compared to numerical results of spheroidal voids in cubic unit cells, this multi-surface criterion bore promising results on the prediction of the transition between void growth and coalescence by internal necking.

This work offers many perspectives. First, it paves the way for studying other crystal lattices, as the model can apply to arbitrary sets of slip systems. Less symmetric crystals such as hexagonal-close-packed lattices should especially be investigated since the influence of crystallography on the yield surface will be larger than what has been shown in this study. Second, it establishes a basis for building enhanced criteria that alleviate the shortcomings of the proposed yield surface. Since it relies on the assumption of a periodic array of voids, its relevance for porous materials with a random distribution of voids remains to be assessed. Besides, it has been shown by Tekoğlu and Koçhan (2022) that out-of-plane shear components can influence the plastic yielding of porous materials, which remains to be included in ductile fracture modeling. Third, it constitutes the first step in developing a homogenized model for intergranular coalescence. Indeed, simulating ductile fracture requires a precise accounting of strain hardening and microstructure evolution in a finite-strain framework. For instance, it was shown in Yerra et al. (2010) that void coalescence in single crystals is quite dependent on the local critical resolved stresses. Once such evolution laws are available, a complete model for successive intergranular growth and coalescence could be designed, similarly to what was done for transgranular ductile fracture in Sénac et al. (2022). At that point, simulation of the competition between transgranular ductile fracture and intergranular ductile fracture will be in reach, as initially performed with isotropic models in the seminal contribution of Pardoen et al. (2003). Finally, the analytical coalescence criterion and numerical-analysis results must be validated by model experiments of intergranular coalescence to assess the quality of predictions and the basic hypotheses of the mechanical analysis — among which the perfect bonding between crystals.

2.A Location and number of localization bands

Lemma 1. *In the optimal trial field, all bands are conterminous.*

Supposing that there is a rigid band between two plastic bands A and B, the following relationship is verified:

$$\Pi^{\text{surf}}\left(\sigma_0^{(\text{A})}, x^{(\text{A})}, \lambda_{33}^{(\text{A})}\right) + \Pi^{\text{surf}}\left(\sigma_0^{(\text{B})}, x^{(\text{A})}, \lambda_{33}^{(\text{A})}\right) > \Pi^{\text{surf}}\left(\min\left[\sigma_0^{(\text{A})}, \sigma_0^{(\text{B})}\right], x^{(\text{A})}, x^{(\text{B})}, \lambda_{33}^{(\text{A})}, \lambda_{33}^{(\text{B})}\right) \tag{III.130}$$

while volume terms remain constant. This means that moving bands to close the rigid gap decreases the macroscopic dissipation. □

Lemma 2. *The optimal trial field has a maximum of one band in each material.*

It is enough to show that if the trial field contains two adjacent bands $i \in \{\text{A}, \text{B}\}$ of widths $\left(x^{(i)}\right)$ and strain rate ratios $\left(\lambda_{33}^{(i)}, \lambda_{31}^{(i)}\right)$ located in the same material of yield stress σ_0, reduction of the macroscopic dissipation can be achieved by their replacement by a unique band C of width $x^{(\text{A})} + x^{(\text{B})}$ and strain ratios $\left(\lambda_{33}^{(\text{A})} + \lambda_{33}^{(\text{B})}, \lambda_{31}^{(\text{A})} + \lambda_{31}^{(\text{B})}\right)$. This fact is evidently true for the volume terms due to the inequality $\sqrt{a} + \sqrt{b} > \sqrt{a+b}$ for $a, b > 0$:

$$\Pi^{\text{vol}}\left(\sigma_0, \lambda_{33}^{(\text{A})}, \lambda_{31}^{(\text{A})}\right) + \Pi^{\text{vol}}\left(\sigma_0, \lambda_{33}^{(\text{B})}, \lambda_{31}^{(\text{B})}\right) > \Pi^{\text{vol}}\left(\sigma_0, \lambda_{33}^{(\text{A})} + \lambda_{33}^{(\text{B})}, \lambda_{31}^{(\text{A})} + \lambda_{31}^{(\text{B})}\right) \tag{III.131}$$

Surface terms require a more delicate handling. First, it is underlined that[13]

$$\frac{\lambda_{33}^{(\text{A})} + \lambda_{33}^{(\text{B})}}{x^{(\text{A})} + x^{(\text{B})}} \in \left]\frac{\lambda_{33}^{(\text{A})}}{x^{(\text{A})}}, \frac{\lambda_{33}^{(\text{B})}}{x^{(\text{B})}}\right[\quad \text{since} \quad \frac{\lambda_{33}^{(\text{A})}}{x^{(\text{A})}} \neq \frac{\lambda_{33}^{(\text{B})}}{x^{(\text{B})}} \tag{III.132}$$

The other horizontal surface of A is in contact with band A_0 (which can be rigid, *i.e.* with no strain rate) and the other horizontal surface of B is in contact with band B_0 (*idem*). Note that the boundary between B and B_0 can be located in an adjacent material of yield stress $\hat{\sigma}_0 \leq \sigma_0$. Then, the following inequalities are verified:

$$\begin{aligned}
&\sigma_0\left|\frac{\lambda_{33}^{(\text{A}_0)}}{x^{(\text{A}_0)}} - \frac{\lambda_{33}^{(\text{A})}}{x^{(\text{A})}}\right| + \sigma_0\left|\frac{\lambda_{33}^{(\text{A})}}{x^{(\text{A})}} - \frac{\lambda_{33}^{(\text{B})}}{x^{(\text{B})}}\right| > \sigma_0\left|\frac{\lambda_{33}^{(\text{A}_0)}}{x^{(\text{A}_0)}} - \frac{\lambda_{33}^{(\text{A})}}{x^{(\text{A})}}\right| + \sigma_0\left|\frac{\lambda_{33}^{(\text{A})}}{x^{(\text{A})}} - \frac{\lambda_{33}^{(\text{A})} + \lambda_{33}^{(\text{B})}}{x^{(\text{A})} + x^{(\text{B})}}\right| \geq \sigma_0\left|\frac{\lambda_{33}^{(\text{A}_0)}}{x^{(\text{A}_0)}} - \frac{\lambda_{33}^{(\text{A})} + \lambda_{33}^{(\text{B})}}{x^{(\text{A})} + x^{(\text{B})}}\right| \\
&\hat{\sigma}_0\left|\frac{\lambda_{33}^{(\text{B}_0)}}{x^{(\text{B}_0)}} - \frac{\lambda_{33}^{(\text{B})}}{x^{(\text{B})}}\right| + \sigma_0\left|\frac{\lambda_{33}^{(\text{B})}}{x^{(\text{B})}} - \frac{\lambda_{33}^{(\text{A})}}{x^{(\text{A})}}\right| > \hat{\sigma}_0\left|\frac{\lambda_{33}^{(\text{B}_0)}}{x^{(\text{B}_0)}} - \frac{\lambda_{33}^{(\text{A})}}{x^{(\text{A})}}\right| + \hat{\sigma}_0\left|\frac{\lambda_{33}^{(\text{A})}}{x^{(\text{A})}} - \frac{\lambda_{33}^{(\text{A})} + \lambda_{33}^{(\text{B})}}{x^{(\text{A})} + x^{(\text{B})}}\right| \geq \hat{\sigma}_0\left|\frac{\lambda_{33}^{(\text{B}_0)}}{x^{(\text{B}_0)}} - \frac{\lambda_{33}^{(\text{A})} + \lambda_{33}^{(\text{B})}}{x^{(\text{A})} + x^{(\text{B})}}\right|
\end{aligned} \tag{III.133}$$

By summing the two previous inequalities, it is obtained that the surface dissipation associated with band C is inferior to the original surface dissipation:

$$\Pi^{\text{surf}}_{\text{A}_0,\text{A}} + 2\Pi^{\text{surf}}_{\text{A,B}} + \Pi^{\text{surf}}_{\text{B,B}_0} > \Pi^{\text{surf}}_{\text{A}_0,\text{C}} + \Pi^{\text{surf}}_{\text{C,B}_0} \tag{III.134}$$

Thus, there is a maximum of one band in each material. □

Lemma 3. *Each band can be chosen of maximal width.*

The band in material 1 is denoted A, and the band in material 2 is denoted B, one of them possibly rigid. Band A accommodates the loading $(\lambda_{33}D_{33}, \lambda_{31}D_{31})$ while band B accommodates the loading $((1-\lambda_{33})D_{33}, (1-\lambda_{31})D_{31})$. Surface terms read:

$$\Pi^{\text{surf}} = \left[\sigma_0^{(1)}\frac{\lambda_{33}}{x^{(\text{A})}} + \sigma_0^{(2)}\left|\frac{\lambda_{33}}{x^{(\text{A})}} - \frac{1-\lambda_{33}}{x^{(\text{B})}}\right| + \sigma_0^{(2)}\frac{1-\lambda_{33}}{x^{(\text{B})}}\right] g^{\text{surf}}\,|D_{33}| \tag{III.135}$$

whose $x^{(\text{A})}$ and $x^{(\text{B})}$-derivatives are negative, which means that the choice $x^{(\text{A})} = x^{(\text{B})} = \frac{1}{2}$ can be done for the optimal trial field. □

[13] It is recalled that $]y_1, y_2[= \{ty_1 + (1-t)y_2\,,\ t \in]0,1[\}$.

2.B Explicit resolution for the Mises bi-material

2.B.1 Macroscopic dissipation

Π is convex[14] with respect to $(\lambda_{33}, \lambda_{31})$, so every local minimum is a global minimum on $[0,1]^2$. The partial derivatives of Π write:

$$\frac{\partial \Pi}{\partial \lambda_{33}} = \frac{\sigma_0^{(1)} \lambda_{33} (g^{\text{vol}} D_{33})^2}{\sqrt{\left(\lambda_{33} g^{\text{vol}} D_{33}\right)^2 + \left(\lambda_{31} g^{\text{sh}} D_{31}\right)^2}} - \frac{\sigma_0^{(2)} (1-\lambda_{33}) (g^{\text{vol}} D_{33})^2}{\sqrt{\left[(1-\lambda_{33}) g^{\text{vol}} D_{33}\right]^2 + \left[(1-\lambda_{31}) g^{\text{sh}} D_{31}\right]^2}} + 2 g^{\text{surf}} |D_{33}| \left\{ \sigma_0^{(1)} + \sigma_0^{(2)} \left[2 \text{sgn}\left(2\lambda_{33} - 1\right) - 1 \right] \right\} \tag{III.136}$$

$$\frac{\partial \Pi}{\partial \lambda_{31}} = \frac{\sigma_0^{(1)} \lambda_{31} (g^{\text{sh}} D_{31})^2}{\sqrt{\left(\lambda_{33} g^{\text{vol}} D_{33}\right)^2 + \left(\lambda_{31} g^{\text{sh}} D_{31}\right)^2}} - \frac{\sigma_0^{(2)} (1-\lambda_{31}) (g^{\text{sh}} D_{31})^2}{\sqrt{\left[(1-\lambda_{33}) g^{\text{vol}} D_{33}\right]^2 + \left[(1-\lambda_{31}) g^{\text{sh}} D_{31}\right]^2}} \tag{III.137}$$

It can be verified that:

$$\frac{\partial \Pi}{\partial \lambda_{31}} \left(\frac{1}{2}, 0 \right) < 0 \ , \quad \frac{\partial \Pi}{\partial \lambda_{31}} \left(\frac{1}{2}, \frac{1}{2} \right) > 0 \tag{III.138}$$

Thus, through the intermediate value theorem, there exists $\hat{\lambda}_{31} \in]0, \frac{1}{2}[$ such that $\frac{\partial \Pi}{\partial \lambda_{31}} \left(\frac{1}{2}, \hat{\lambda}_{31} \right) = 0$. It can be noticed that $\hat{\lambda}_{31}$ is the root of the following fourth-order polynomial

$$P(X) = 4 \left(g^{\text{sh}} D_{31} \right)^2 \left[\left(\sigma_0^{(1)} \right)^2 - \left(\sigma_0^{(2)} \right)^2 \right] X^2 (X-1)^2 + \left(g^{\text{vol}} D_{33} \right)^2 \left[\left(\sigma_0^{(1)} \right)^2 X^2 - \left(\sigma_0^{(2)} \right)^2 (X-1)^2 \right] \tag{III.139}$$

and thus admits no analytical formula in general. In order to determine the minimum of Π, several additional *lemmata* are needed.

Lemma 4. *The minimum of* Π *is reached for* $\lambda_{31} < \frac{1}{2}$ *and* $\lambda_{33} \leq \frac{1}{2}$.

First, supposing that the minimum $(\lambda_{33}, \lambda_{31})$ is reached on $]\frac{1}{2}, 1] \times [\frac{1}{2}, 1]$, an absurdity is reached:

$$\Pi(\lambda_{33}, \lambda_{31}) > \Pi(1-\lambda_{33}, 1-\lambda_{31}) \tag{III.140}$$

stemming from the fact that $\sigma_0^{(1)} > \sigma_0^{(2)}$. Then, it is supposed that the minimum $(\lambda_{33}, \lambda_{31})$ is reached on $[0, \frac{1}{2}] \times [\frac{1}{2}, 1]$. It is obtained:

$$\frac{\partial \Pi}{\partial \lambda_{31}} (\lambda_{33}, \lambda_{31}) > \frac{\partial \Pi}{\partial \lambda_{31}} \left(\frac{1}{2}, \frac{1}{2} \right) > 0 \tag{III.141}$$

due to the fact that $\frac{\partial \Pi}{\partial \lambda_{31}}$ is a strictly decreasing function of λ_{33} and a strictly increasing function of λ_{31}. Thus, it is not a minimum.

The previous developments have shown that $\lambda_{31} < \frac{1}{2}$. Supposing that a minimum exists at $(\lambda_{33}, \lambda_{31}) \in]\frac{1}{2}, 1[\times]0, \frac{1}{2}[$, the nullity of partial derivatives brings:

$$\frac{\sigma_0^{(1)} (g^{\text{vol}} D_{33})^2}{\sqrt{\left(\lambda_{33} g^{\text{vol}} D_{33}\right)^2 + \left(\lambda_{31} g^{\text{sh}} D_{31}\right)^2}} \left[\lambda_{33} - (1-\lambda_{33}) \frac{\lambda_{31}}{1-\lambda_{31}} \right] = -2 g^{\text{surf}} |D_{33}| \left(\sigma_0^{(1)} + \sigma_0^{(2)} \right) \leq 0 \tag{III.142}$$

which implies that $\lambda_{31} \geq \lambda_{33}$, *i.e.* $\lambda_{31} > \frac{1}{2}$, which is absurd.

It remains to exclude the possibility of a minimum reached on points of the form $(1, \lambda_{31})$ with $\lambda_{31} < \frac{1}{2}$ and points of the form $(\lambda_{33}, 0)$ with $\lambda_{33} > \frac{1}{2}$. This is achieved by noticing the following properties:

$$\begin{aligned} &\forall \lambda_{33} > 0, \frac{\partial \Pi}{\partial \lambda_{31}} (\lambda_{33}, 0) < 0 \quad \text{so the minimum is not reached on } \lambda_{31} = 0 \text{ when } \lambda_{33} > 0 \\ &\forall \lambda_{31} > 0, \frac{\partial \Pi}{\partial \lambda_{33}} (1, \lambda_{31}) > 0 \quad \text{so the minimum is not reached on } \lambda_{33} = 1 \text{ when } \lambda_{31} < 1 \end{aligned} \tag{III.143}$$

□

[14] For instance, this result can be established through an elementary calculation of its second-order partial derivatives.

Lemma 5. *The minimum of* Π *is reached for* $(\lambda_{33}, \lambda_{31}) = \left(\frac{1}{2}, \hat{\lambda}_{31}\right)$ *if and only if* $\dfrac{\partial \Pi}{\partial \lambda_{33}}\left(\dfrac{1}{2}^{-}, \hat{\lambda}_{31}\right) \leq 0$.

At point $\left(\frac{1}{2}, \hat{\lambda}_{31}\right)$, the partial derivatives of Π are such that:

$$\frac{\partial \Pi}{\partial \lambda_{33}}\left(\frac{1}{2}^{-}, \hat{\lambda}_{31}\right) \leq 0\,, \quad \frac{\partial \Pi}{\partial \lambda_{33}}\left(\frac{1}{2}^{+}, \hat{\lambda}_{31}\right) > \frac{\partial \Pi}{\partial \lambda_{33}}\left(\frac{1}{2}^{+}, \frac{1}{2}\right) > 0\,, \quad \frac{\partial \Pi}{\partial \lambda_{31}}\left(\frac{1}{2}, \hat{\lambda}_{31}\right) = 0 \tag{III.144}$$

where the second inequality emerges from the fact that $\frac{\partial \Pi}{\partial \lambda_{33}}$ is a strictly decreasing function of λ_{31}. Eq. III.144 means that a local minimum is located there. This minimum is global due to the convexity of Π. □

Lemma 6. *If* $\dfrac{\partial \Pi}{\partial \lambda_{33}}\left(\dfrac{1}{2}^{-}, \dfrac{1}{2}\right) \geq 0$, *then the minimum of* Π *is reached for* $\lambda_{33} = \lambda_{31} = 0$.

The minimum is denoted as $(\lambda_{33}, \lambda_{31}) \in [0, \frac{1}{2}] \times [0, \frac{1}{2}[$. On the one hand, if $\lambda_{33} > \lambda_{31}$, it is obtained that:

$$\frac{\partial \Pi}{\partial \lambda_{33}}(\lambda_{33}, \lambda_{31}) > \frac{\partial \Pi}{\partial \lambda_{33}}(\lambda_{33}, \lambda_{33}) = \frac{\partial \Pi}{\partial \lambda_{33}}\left(\frac{1}{2}^{-}, \frac{1}{2}\right) \geq 0 \tag{III.145}$$

since $\frac{\partial \Pi}{\partial \lambda_{33}}$ is strictly decreasing with respect to λ_{31} and homogeneous of degree 0 on $]\frac{1}{2}, 1] \times [0, 1]$, which is absurd. On the other hand, if $\lambda_{31} > \lambda_{33}$, it is obtained that

$$\frac{\partial \Pi}{\partial \lambda_{31}}(\lambda_{33}, \lambda_{31}) > \frac{\partial \Pi}{\partial \lambda_{31}}(\lambda_{31}, \lambda_{31}) = \frac{\partial \Pi}{\partial \lambda_{31}}\left(\frac{1}{2}, \frac{1}{2}\right) > 0 \tag{III.146}$$

since $\frac{\partial \Pi}{\partial \lambda_{31}}$ is a strictly decreasing with respect to λ_{33} and homogeneous of degree 0, which is absurd. Therefore, $\lambda_{33} = \lambda_{31}$. However, for $\lambda_{33} > 0$, it is obtained that:

$$\frac{\partial \Pi}{\partial \lambda_{31}}(\lambda_{33}, \lambda_{33}) = \frac{\partial \Pi}{\partial \lambda_{31}}\left(\frac{1}{2}, \frac{1}{2}\right) > 0 \tag{III.147}$$

which means that $\lambda_{31} = \lambda_{33} = 0$. □

These theoretical results hint at the fact that two major situations can arise: in the first case, there is one plastic band in material 2 accommodating the full strain rate ($\lambda_{33} = \lambda_{31} = 0$); in the second case, there is one plastic band in each material with no surface discontinuity and a dominant shear in material 2 ($\lambda_{33} = \frac{1}{2}$, $\lambda_{31} = \hat{\lambda}_{31} < \frac{1}{2}$). However, it has been checked numerically that the reciprocal of Lemma 6 is invalid. Furthermore, in some exotic situations, a third intermediate case has been noticed, with a minimum reached at $\lambda_{33} \in]0, \frac{1}{2}[$, $\lambda_{31} < \lambda_{33}$. Since the macroscopic dissipation associated with this intermediate case is usually very close to the macroscopic dissipation of one of the two extreme values of λ_{33} ($\lambda_{33} = 0$ and $\lambda_{33} = \frac{1}{2}$), the total macroscopic dissipation can be approximated with great confidence by:

$$\min_{\lambda_{33}, \lambda_{31}} \Pi\left(\lambda_{33}, \lambda_{31}\right) \approx \min\left\{\Pi(0,0), \Pi\left(\frac{1}{2}, \hat{\lambda}_{31}\right)\right\} \tag{III.148}$$

The previous result only applies when $D_{33}, D_{31} > 0$. Adapting the same reasoning with $D_{33} = 0$ brings an optimal trial field with a unique band of indeterminate finite width in the material 2, meaning that

$$\Pi = \sigma_0^{(2)} g^{\mathrm{sh}} \left|D_{31}\right| \tag{III.149}$$

When $D_{31} = 0$, $\frac{\partial \Pi}{\partial \lambda_{33}}$ no longer depends on λ_{31}. As a result, Lemma 5 and 6 cover the whole range of situations, which brings Eq. III.148 as an exact result — still with no dependence[15] on λ_{31}:

$$\min_{\lambda_{33}} \Pi\left(\lambda_{33}\right) = \min\left\{\Pi(0), \Pi\left(\frac{1}{2}\right)\right\} \tag{III.150}$$

This means that there can be either one band in material 2 or two bands with no velocity discontinuity.

[15] Note that when $D_{31} \to 0$, $\hat{\lambda}_{31} \to \frac{\sigma_0^{(2)}}{\sigma_0^{(1)} + \sigma_0^{(2)}}$.

2.B.2 Yield surface

According to Eq. III.148, the yield surface for intergranular coalescence is the intersection of two individual elasticity domains related to macroscopic dissipations $\Pi(0,0)$ and $\Pi\left(\frac{1}{2},\hat{\lambda}_{31}\right)$. The corresponding yield surfaces are derived separately using Eq. III.94, except at the non-differentiable point $D_{33}=0$ at which Eq. III.95 is employed instead.

Surface corresponding to $\Pi=\Pi(0,0)$ (plasticity in the soft material only)

- $D_{33}\neq 0$:

$$\Sigma_{33}=\frac{\partial\Pi}{\partial D_{33}}=\operatorname{sgn}(D_{33})\,\sigma_0^{(2)}\left[g^{\text{vol}}\frac{g^{\text{vol}}}{\sqrt{\left(g^{\text{vol}}\right)^2+\left(g^{\text{sh}}\frac{D_{31}}{D_{33}}\right)^2}}+4g^{\text{surf}}\right]$$
$$\Sigma_{31}=\frac{1}{2}\frac{\partial\Pi}{\partial D_{31}}=\operatorname{sgn}(D_{31})\,\sigma_0^{(2)}\frac{g^{\text{sh}}}{2}\frac{g^{\text{sh}}}{\sqrt{\left(g^{\text{vol}}\frac{D_{33}}{D_{31}}\right)^2+\left(g^{\text{sh}}\right)^2}} \tag{III.151}$$

- $D_{33}=0$:

$$|\Sigma_{33}|\leq 4\sigma_0^{(2)}g^{\text{surf}}\ ,\quad \Sigma_{31}=\operatorname{sgn}(D_{31})\,\frac{\sigma_0^{(2)}g^{\text{sh}}}{2} \tag{III.152}$$

Surface corresponding to $\Pi=\Pi\left(\frac{1}{2},\hat{\lambda}_{31}\right)$ (plasticity in both materials)

- $D_{33}\neq 0$: Eq. III.94 is applied to $\hat{\Pi}(D_{33},D_{31})=\Pi(D_{33},D_{31},\hat{\lambda}_{31}(D_{33},D_{31}))$:

$$\Sigma_{33}=\frac{\partial\hat{\Pi}}{\partial D_{33}}=\frac{\partial\Pi}{\partial D_{33}}+\frac{\partial\hat{\lambda}_{31}}{\partial D_{33}}\frac{\partial\Pi}{\partial\hat{\lambda}_{31}}\ ,\quad \Sigma_{31}=\frac{1}{2}\frac{\partial\hat{\Pi}}{\partial D_{31}}=\frac{1}{2}\left(\frac{\partial\Pi}{\partial D_{31}}+\frac{\partial\hat{\lambda}_{31}}{\partial D_{31}}\frac{\partial\Pi}{\partial\hat{\lambda}_{31}}\right) \tag{III.153}$$

For typical values of χ, w and $\sigma_0^{(2)}/\sigma_0^{(1)}$, it can be checked numerically that the second term — originating from the variation of $\hat{\lambda}_{31}$ — is negligible compared to the first term when the ratio D_{31}/D_{33} does not reach values that are too large. Therefore, the yield surface is given by the following equations:

$$\Sigma_{33}=\operatorname{sgn}(D_{33})\left\{\left(\sigma_0^{(1)}+\sigma_0^{(2)}\right)g^{\text{surf}}+\frac{g^{\text{vol}}}{2}\left[\sigma_0^{(1)}\frac{\frac{1}{2}g^{\text{vol}}}{\sqrt{\left(\frac{1}{2}g^{\text{vol}}\right)^2+\left(\hat{\lambda}_{31}g^{\text{sh}}\frac{D_{31}}{D_{33}}\right)^2}}\right.\right.$$
$$\left.\left.+\sigma_0^{(2)}\frac{\frac{1}{2}g^{\text{vol}}}{\sqrt{\left(\frac{1}{2}g^{\text{vol}}\right)^2+\left(\left[1-\hat{\lambda}_{31}\right]g^{\text{sh}}\frac{D_{31}}{D_{33}}\right)^2}}\right]\right\} \tag{III.154}$$

$$\Sigma_{31}=\operatorname{sgn}(D_{31})\,\frac{g^{\text{sh}}}{2}\left[\sigma_0^{(1)}\hat{\lambda}_{31}\frac{\hat{\lambda}_{31}g^{\text{sh}}}{\sqrt{\left(\frac{1}{2}g^{\text{vol}}\frac{D_{33}}{D_{31}}\right)^2+\left(\hat{\lambda}_{31}g^{\text{sh}}\right)^2}}\right.$$
$$\left.+\sigma_0^{(2)}\left(1-\hat{\lambda}_{31}\right)\frac{\left(1-\hat{\lambda}_{31}\right)g^{\text{sh}}}{\sqrt{\left(\frac{1}{2}g^{\text{vol}}\frac{D_{33}}{D_{31}}\right)^2+\left(\left[1-\hat{\lambda}_{31}\right]g^{\text{sh}}\right)^2}}\right] \tag{III.155}$$

for $|\Sigma_{33}|\geq\left(\sigma_0^{(1)}+\sigma_0^{(2)}\right)g^{\text{surf}}$. When plotted simultaneously in the plane $(\Sigma_{31},\Sigma_{33})$, the approximate (Eqs. III.154-III.155) and the exact (Eq. III.153) yield surfaces cannot be distinguished, justifying the aforementioned simplification.

- $D_{33}=0$:

$$|\Sigma_{33}|\leq\left(\sigma_0^{(1)}+\sigma_0^{(2)}\right)g^{\text{surf}}\ ,\quad \Sigma_{31}=\operatorname{sgn}(D_{31})\,\frac{\sigma_0^{(2)}g^{\text{sh}}}{2} \tag{III.156}$$

A comparison between the simplified model (Section III.2.3.3) and the detailed model (Appendix III.2.B.2) is presented in Fig. III.38. Note that the detailed model is quasi-exact in the sense that no visible difference exists between the yield surfaces it predicts and those obtained through a numerical minimization of Eq III.102 (not shown here). It can be seen in Fig. III.38 that yield stresses predicted by the models are quite close. However, the normal to the yield surface and the predicted localization of plasticity can display higher variations. Finally, note that the detailed model produces continuous yield surfaces whereas the ones of the simplified model exhibit a non-differentiable vertex.

2.C Explicit resolution for the grain boundary

2.C.1 Macroscopic dissipation

The λ_{31}-derivative of Π writes

$$\frac{\partial \Pi}{\partial \lambda_{33}} = \frac{\tau_0 \lambda_{33} \left(M_2^{(1)} g^{\mathrm{vol}} D_{33}\right)^2}{\sqrt{\left(M_2^{(1)} \lambda_{33} g^{\mathrm{vol}} D_{33}\right)^2 + \left(M_3^{(1)} \lambda_{31} g^{\mathrm{sh}} D_{31}\right)^2}} - \frac{\tau_0 (1-\lambda_{33}) \left(M_2^{(2)} g^{\mathrm{vol}} D_{33}\right)^2}{\sqrt{\left[M_2^{(2)} (1-\lambda_{33}) g^{\mathrm{vol}} D_{33}\right]^2 + \left[M_3^{(2)} (1-\lambda_{31}) g^{\mathrm{sh}} D_{31}\right]^2}} + 2\tau_0 g^{\mathrm{surf}} |D_{33}| \left[M_1^{(1)} + 2 \min\left(M_1^{(1)}, M_1^{(2)}\right) \mathrm{sgn}\left(2\lambda_{33} - 1\right) - M_1^{(2)}\right] \quad \text{(III.157)}$$

$$\frac{\partial \Pi}{\partial \lambda_{31}} = \frac{\tau_0 \lambda_{31} \left(M_3^{(1)} g^{\mathrm{sh}} D_{31}\right)^2}{\sqrt{\left(M_2^{(1)} \lambda_{33} g^{\mathrm{vol}} D_{33}\right)^2 + \left(M_3^{(1)} \lambda_{31} g^{\mathrm{sh}} D_{31}\right)^2}} - \frac{\tau_0 (1-\lambda_{31}) \left(M_3^{(2)} g^{\mathrm{sh}} D_{31}\right)^2}{\sqrt{\left[M_2^{(2)} (1-\lambda_{33}) g^{\mathrm{vol}} D_{33}\right]^2 + \left[M_3^{(2)} (1-\lambda_{31}) g^{\mathrm{sh}} D_{31}\right]^2}} \quad \text{(III.158)}$$

Finding the point at which Π reaches its minimum is more complex than in the isotropic case. In particular, it can be verified that Lemmata 4 and 5 do not hold for crystals; in fact, for arbitrary values of average Taylor factors, the minimum of Π can be located at every possible point of $[0,1]^2$. However, similarly to the isotropic function (Eq. III.102), the minimum of Π is epitomized by a finite set of values for λ_{33}: $\lambda_{33} \in \{0, \frac{1}{2}, 1\}$. It means that, for a given set of parameters, there is a high likelihood that the minimum of Π is effectively reached over that subset or that the minimum of Π over this subset provides a very good estimate of the global minimum. Therefore, the minimum of Π will only be sought over this reduced domain. It is thus supposed that crystal 1 ($\lambda_{33} = 1$) or crystal 2 ($\lambda_{33} = 0$) accommodates the full axial strain rate, or that there is one axial plastic band in each crystal with no surface discontinuity at the grain

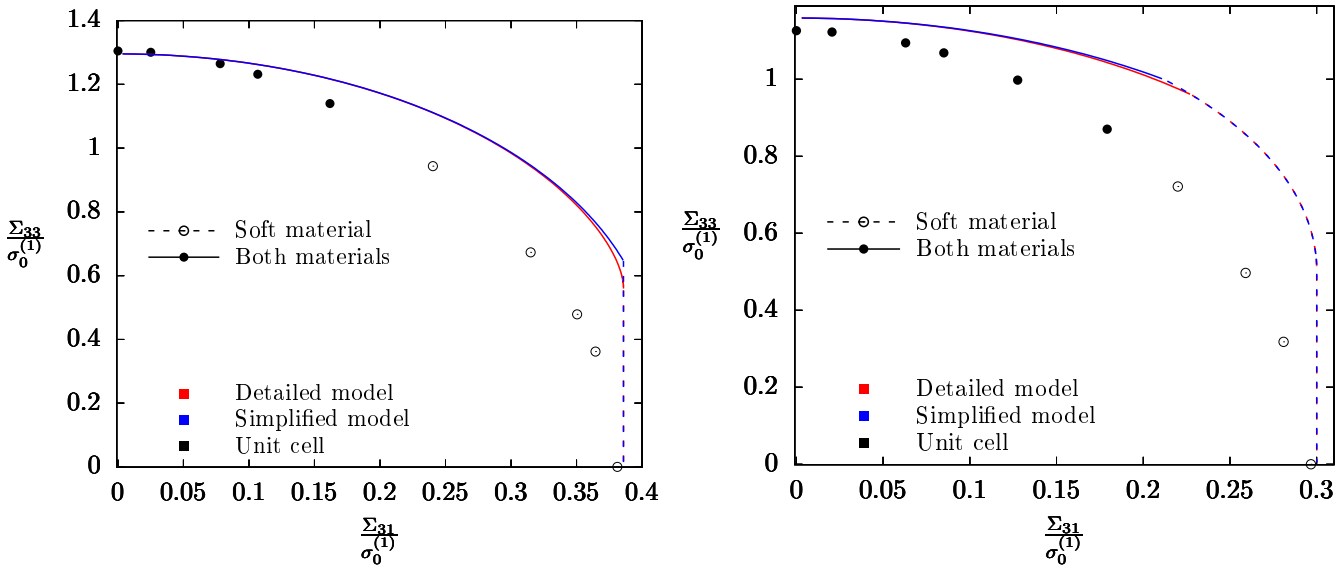

(a) $\chi = 0.5$, $w = 0.5$, $\epsilon = 0.1$ **(b)** $\chi = 0.5$, $w = 0.5$, $\epsilon = 0.3$

FIGURE III.38: Coalescence yield surface in the plane $(\Sigma_{31}, \Sigma_{33})$ as predicted by the models (lines) and computed numerically through FFT unit-cell simulations (points) for two different values of ϵ. The strain rate field can either extend in both materials (full lines and symbols) or be confined to the softest material (dotted lines and hollowed-out symbols).

boundary ($\lambda_{33} = \frac{1}{2}$).

In the case where the full axial strain is accommodated by crystal 1 ($\lambda_{33} = 1$), two situations can be distinguished. On the one hand, if $M_3^{(1)} \leq M_3^{(2)}$, then $\frac{\partial \Pi}{\partial \lambda_{31}}(1, \lambda_{31}) < 0$ for all $\lambda_{31} < 1$. Thus, the minimum of Π is obtained for $\lambda_{31}^+ = 1$. On the other hand, if $M_3^{(1)} \geq M_3^{(2)}$, then the minimum of Π is obtained for the unique value $\lambda_{31}^+ \in]0, 1]$ that verifies:

$$\lambda_{31}^+ = \min \left[1, \frac{g^{\text{vol}}}{g^{\text{sh}}} \frac{|D_{33}|}{|D_{31}|} \frac{M_2^{(1)}}{M_3^{(1)}} \frac{M_3^{(2)}}{\sqrt{\left(M_3^{(1)}\right)^2 - \left(M_3^{(2)}\right)^2}} \right] \tag{III.159}$$

which emerges from the condition $\frac{\partial \Pi}{\partial \lambda_{31}}(1, \lambda_{31}) = 0$. In both situations, the macroscopic potential becomes:

$$\Pi\left(1, \lambda_{31}^+\right) = \tau_0 \left\{ \sqrt{\left(M_2^{(1)} g^{\text{vol}} D_{33}\right)^2 + \left(M_3^{(1)} \lambda_{31}^+ g^{\text{sh}} D_{31}\right)^2} + M_3^{(2)} \left(1 - \lambda_{31}^+\right) g^{\text{sh}} |D_{31}| \right.$$
$$\left. + 2 g^{\text{surf}} \left[M_1^{(1)} + \min\left(M_1^{(1)}, M_1^{(2)}\right) \right] |D_{33}| \right\} \tag{III.160}$$

Supposing that the minimum of Π is obtained for $\lambda_{33} = 0$ — *i.e.* the axial strain localizes in crystal 2 —, the optimal λ_{31} is given by

$$\lambda_{31}^- = \begin{cases} 0 & \text{if } M_3^{(2)} \leq M_3^{(1)} \\ \max \left[0, 1 - \dfrac{g^{\text{vol}}}{g^{\text{sh}}} \dfrac{|D_{33}|}{|D_{31}|} \dfrac{M_2^{(2)}}{M_3^{(2)}} \dfrac{M_3^{(1)}}{\sqrt{\left(M_3^{(2)}\right)^2 - \left(M_3^{(1)}\right)^2}} \right] & \text{if } M_3^{(2)} > M_3^{(1)} \end{cases} \tag{III.161}$$

and the macroscopic potential becomes

$$\Pi\left(0, \lambda_{31}^-\right) = \tau_0 \left\{ M_3^{(1)} \lambda_{31}^- g^{\text{sh}} |D_{31}| + \sqrt{\left(M_2^{(2)} g^{\text{vol}} D_{33}\right)^2 + \left[M_3^{(2)} \left(1 - \lambda_{31}^-\right) g^{\text{sh}} D_{31}\right]^2} \right.$$
$$\left. + 2 g^{\text{surf}} \left[\min\left(M_1^{(1)}, M_1^{(2)}\right) + M_1^{(2)} \right] |D_{33}| \right\} \tag{III.162}$$

In the last case, the axial strain is accommodated by both crystals with no surface discontinuity at the grain boundary, meaning that $\lambda_{33} = \frac{1}{2}$. As for the isotropic model, the optimal λ_{31} is the value $\hat{\lambda}_{31} \in]0, 1[$ that cancels $\frac{\partial \Pi}{\partial \lambda_{31}}$. This value exists and is unique because $\frac{\partial \Pi}{\partial \lambda_{31}}\left(\frac{1}{2}, \lambda_{31}\right)$ is a strictly increasing function that takes a strictly negative value at $\lambda_{31} = 0$ and a strictly positive value at $\lambda_{31} = 1$. The macroscopic potential then writes:

$$\Pi\left(\frac{1}{2}, \hat{\lambda}_{31}\right) = \tau_0 \left\{ \sqrt{\left(\frac{1}{2} M_2^{(1)} g^{\text{vol}} D_{33}\right)^2 + \left(M_3^{(1)} \hat{\lambda}_{31} g^{\text{sh}} D_{31}\right)^2} + \sqrt{\left(\frac{1}{2} M_2^{(2)} g^{\text{vol}} D_{33}\right)^2 + \left(M_3^{(2)} \left[1 - \hat{\lambda}_{31}\right] g^{\text{sh}} D_{31}\right)^2} \right.$$
$$\left. + 2 g^{\text{surf}} \left(M_1^{(1)} + M_1^{(2)}\right) |D_{33}| \right\} \tag{III.163}$$

Finally, the estimate of the total macroscopic dissipation is obtained from the three cases treated above:

$$\min_{\lambda_{33}, \lambda_{31}} \Pi\left(\lambda_{33}, \lambda_{31}\right) \approx \min \left\{ \Pi(0, \lambda_{31}^-), \Pi\left(\frac{1}{2}, \hat{\lambda}_{31}\right), \Pi(1, \lambda_{31}^+) \right\} \tag{III.164}$$

The previous results were derived for $D_{33}, D_{31} > 0$. Adapting the same reasoning with $D_{33} = 0$ brings an optimal trial field with a unique band of indeterminate finite width in the crystal whose M_3 is lower:

$$\Pi = \tau_0 \min\left(M_3^{(1)}, M_3^{(2)}\right) g^{\text{sh}} |D_{31}| \tag{III.165}$$

When $D_{31} = 0$, $\frac{\partial \Pi}{\partial \lambda_{33}}$ is a shifted Heaviside step function — in particular, the step occurs at $\lambda_{33} = \frac{1}{2}$ —, which

brings the same alternative as Eq. III.164 as an *exact result*:

$$\min_{\lambda_{33}} \Pi\left(\lambda_{33}\right) = \min\left\{\Pi(0), \Pi\left(\frac{1}{2}\right), \Pi(1)\right\} \tag{III.166}$$

This means that there can be either a unique plastic band in one of the crystals or two bands with no velocity discontinuity.

2.C.2 Yield surface

According to Eq. III.164, the approximate yield surface of the grain boundary subjected to void coalescence is obtained by the intersection of three individual elasticity domains corresponding to macroscopic dissipations $\Pi(0, \lambda_{31}^{-})$, $\Pi\left(\frac{1}{2}, \hat{\lambda}_{31}\right)$ and $\Pi(1, \lambda_{31}^{+})$, each of the corresponding yield surfaces being itself deduced from the fundamental equations of limit analysis (Eqs. III.94-III.95). As in the isotropic case (see III.2.B.2), the perturbation terms of the form $\frac{\partial \lambda_{31}}{\partial D_{ij}} \frac{\partial \Pi}{\partial \lambda_{31}}$ are neglected.

Surface corresponding to $\Pi = \Pi\left(1, \lambda_{31}^{+}\right)$ (axial strain accommodated by crystal 1 only)

- $D_{33} \neq 0$:

$$\Sigma_{33} = \operatorname{sgn}\left(D_{33}\right) \tau_0 \left\{ M_2^{(1)} g^{\text{vol}} \frac{M_2^{(1)} g^{\text{vol}}}{\sqrt{\left(M_2^{(1)} g^{\text{vol}}\right)^2 + \left(M_3^{(1)} \lambda_{31}^{-} g^{\text{sh}} \frac{D_{31}}{D_{33}}\right)^2}} + 2 g^{\text{surf}} \left[M_1^{(1)} + \min\left(M_1^{(1)}, M_1^{(2)}\right)\right] \right\}$$
$$\Sigma_{31} = \operatorname{sgn}\left(D_{31}\right) \tau_0 g^{\text{sh}} \left[M_3^{(1)} \lambda_{31}^{-} \frac{M_3^{(1)} \lambda_{31}^{-} g^{\text{sh}}}{\sqrt{\left(M_2^{(1)} g^{\text{vol}} \frac{D_{33}}{D_{31}}\right)^2 + \left(M_3^{(1)} \lambda_{31}^{-} g^{\text{sh}}\right)^2}} + M_3^{(2)} \left(1 - \lambda_{31}^{-}\right) \right] \tag{III.167}$$

- $D_{33} = 0$:

$$\left|\Sigma_{33}\right| \leq 2\tau_0 \left[M_1^{(1)} + \min\left(M_1^{(1)}, M_1^{(2)}\right)\right] g^{\text{surf}}, \quad \Sigma_{31} = \operatorname{sgn}\left(D_{31}\right) \tau_0 \min\left(M_3^{(1)}, M_3^{(2)}\right) \frac{g^{\text{sh}}}{2} \tag{III.168}$$

Surface corresponding to $\Pi = \Pi\left(0, \lambda_{31}^{-}\right)$ (axial strain accommodated by crystal 2 only)

- $D_{33} \neq 0$:

$$\Sigma_{33} = \operatorname{sgn}\left(D_{33}\right) \tau_0 \left\{ M_2^{(2)} g^{\text{vol}} \frac{M_2^{(2)} g^{\text{vol}}}{\sqrt{\left(M_2^{(2)} g^{\text{vol}}\right)^2 + \left(M_3^{(2)} \left[1 - \lambda_{31}^{+}\right] g^{\text{sh}} \frac{D_{31}}{D_{33}}\right)^2}} + 2 g^{\text{surf}} \left[\min\left(M_1^{(1)}, M_1^{(2)}\right) + M_1^{(2)}\right] \right\}$$
$$\Sigma_{31} = \operatorname{sgn}\left(D_{31}\right) \tau_0 g^{\text{sh}} \left[M_3^{(1)} \lambda_{31}^{+} + M_3^{(2)} \left(1 - \lambda_{31}^{+}\right) \frac{M_3^{(2)} \left(1 - \lambda_{31}^{+}\right) g^{\text{sh}}}{\sqrt{\left(M_2^{(2)} g^{\text{vol}} \frac{D_{33}}{D_{31}}\right)^2 + \left(M_3^{(2)} \left[1 - \lambda_{31}^{+}\right] g^{\text{sh}}\right)^2}} \right] \tag{III.169}$$

- $D_{33} = 0$:

$$\left|\Sigma_{33}\right| \leq 2\tau_0 \left[M_1^{(2)} + \min\left(M_1^{(1)}, M_1^{(2)}\right)\right] g^{\text{surf}}, \quad \Sigma_{31} = \operatorname{sgn}\left(D_{31}\right) \tau_0 \min\left(M_3^{(1)}, M_3^{(2)}\right) \frac{g^{\text{sh}}}{2} \tag{III.170}$$

Surface corresponding to $\Pi\left(\frac{1}{2}, \hat{\lambda}_{31}\right)$ (axial strain accommodated by both crystals)

- $D_{33} \neq 0$:

$$\Sigma_{33} = \operatorname{sgn}(D_{33})\,\tau_0 \left\{ 2g^{\text{surf}} \left(M_1^{(1)} + M_1^{(2)} \right) + \frac{g^{\text{vol}}}{2} \left[M_2^{(1)} \frac{\frac{1}{2} M_2^{(1)} g^{\text{vol}}}{\sqrt{\left(\frac{1}{2} M_2^{(1)} g^{\text{vol}} \right)^2 + \left(M_3^{(1)} \hat{\lambda}_{31} g^{\text{sh}} \frac{D_{31}}{D_{33}} \right)^2}} + M_2^{(2)} \frac{\frac{1}{2} M_2^{(2)} g^{\text{vol}}}{\sqrt{\left(\frac{1}{2} M_2^{(2)} g^{\text{vol}} \right)^2 + \left(M_3^{(2)} \left[1 - \hat{\lambda}_{31} \right] g^{\text{sh}} \frac{D_{31}}{D_{33}} \right)^2}} \right] \right\}$$

$$\Sigma_{31} = \operatorname{sgn}(D_{31})\,\tau_0 \frac{g^{\text{sh}}}{2} \left[M_3^{(1)} \hat{\lambda}_{31} \frac{M_3^{(1)} \hat{\lambda}_{31} g^{\text{sh}}}{\sqrt{\left(\frac{1}{2} M_2^{(1)} g^{\text{vol}} \frac{D_{33}}{D_{31}} \right)^2 + \left(M_3^{(1)} \hat{\lambda}_{31} g^{\text{sh}} \right)^2}} + M_3^{(2)} \left(1 - \hat{\lambda}_{31} \right) \frac{M_3^{(2)} \left(1 - \hat{\lambda}_{31} \right) g^{\text{sh}}}{\sqrt{\left(\frac{1}{2} M_2^{(2)} g^{\text{vol}} \frac{D_{33}}{D_{31}} \right)^2 + \left(M_3^{(2)} \left[1 - \hat{\lambda}_{31} \right] g^{\text{sh}} \right)^2}} \right] \tag{III.171}$$

- $D_{33} = 0$:

$$|\Sigma_{33}| \leq \tau_0 \left(M_1^{(1)} + M_1^{(2)} \right) g^{\text{surf}}\,, \quad \Sigma_{31} = \operatorname{sgn}(D_{31})\,\tau_0 \min\left(M_3^{(1)}, M_3^{(2)} \right) \frac{g^{\text{sh}}}{2} \tag{III.172}$$

A comparison between the simplified model (Section III.2.4.3) and the detailed model (Appendix III.2.C.2) is presented in Fig. III.39. As in the case of the Mises bi-material, the detailed model is indistinguishable from the surface obtained by numerical minimization of Eq. III.119 (not shown here). The differences seen between models are more important than in the isotropic case; in particular, the prediction of the localization pattern can vary significantly. The observed discrepancies depend on the crystal orientation couple considered; orientation couple #2 chosen in Fig. III.39 is close to the average behavior.

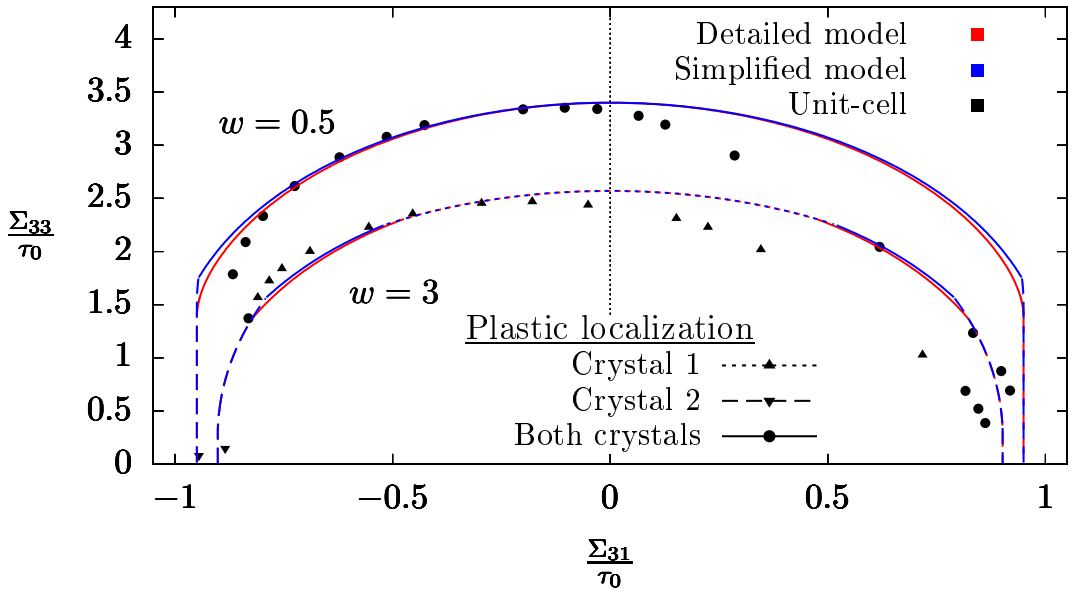

FIGURE III.39: Coalescence yield surface in the plane $(\Sigma_{31}, \Sigma_{33})$ as predicted by the models (lines) and computed numerically through FFT unit-cell simulations (points) for orientation couple #2 at $\chi = 0.5$. Plasticity can either extend in both crystals (full lines and circular symbols) or be confined into a unique crystal (dashed lines and triangular symbols).

3 Homogenized model for intergranular void growth

3.1 Description of the homogenized model

In this section, a homogenized model for intergranular void growth at finite strain is proposed based on the yield criterion developed in Section III.1. Its objective is to predict — at least qualitatively — the mechanical behavior of a porous grain boundary (Fig. III.2a). With such a model, physical-based[16] simulation of intergranular ductile fracture becomes closer.

In order to conduct a preliminary assessment of the current ability to predict intergranular void growth, this first model is kept as simple as possible. In particular, it is confined to axisymmetric loadings (see Fig. III.40) and does not incorporate any strain hardening. This last restriction is motivated by the findings of Section II.1 in which it is seen that an efficient way to homogenize hardening in single crystals is still lacking. Furthermore, the finite strain framework with multiplicative decomposition of the deformation gradient is adopted. Finally, note that the model presented below can be used in the limiting case of two identical grains, in which case it becomes a model of transgranular void growth similar to that of Section II.1, except for the finite strain framework used.

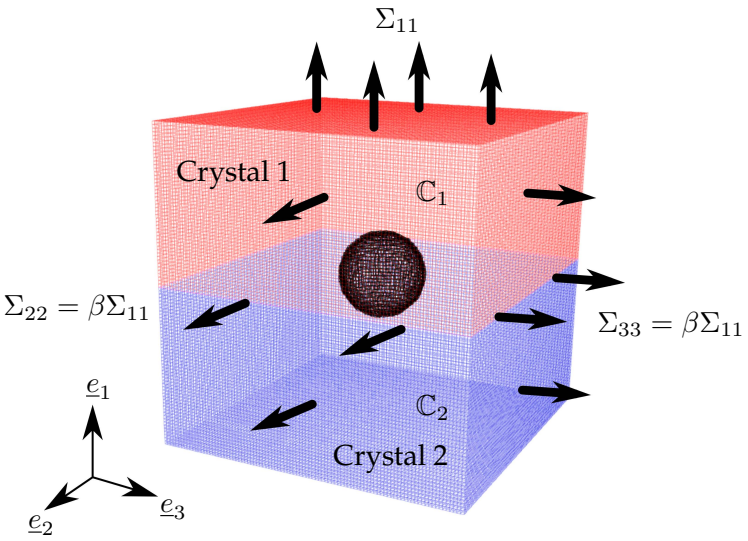

FIGURE III.40: Porous bi-crystalline unit-cell subjected to asymmetric loading of main axis $\underline{e}_1$. β is linked to the stress triaxiality by Eq. III.188.

3.1.1 Finite strain framework

In the following, the multiplicative decomposition of deformation gradient $\boldsymbol{F}$ into elastic and plastic parts (Kröner, 1959; Lee, 1969; Mandel, 1973) is assumed:

$$\boldsymbol{F} = \boldsymbol{F}_\mathrm{e}\boldsymbol{F}_\mathrm{p} \tag{III.173}$$

The material orientation is the same in the original configuration and in the unique isoclinic intermediate local configuration obtained after application of $\boldsymbol{F}_\mathrm{p}$ (see Fig. III.41).

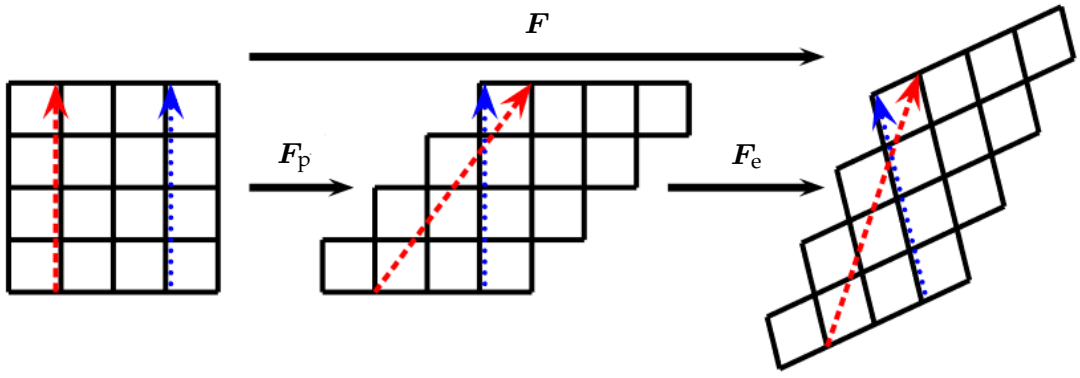

FIGURE III.41: Sketch of the effect of the gradient deformation $\boldsymbol{F}$ on the material considered: the evolution of material lines (red arrow) and material orientation (blue arrow) highlighted by Mandel (1973) is shown (Forest, 2023).

[16] As a side note, remark that data-based modeling of intergranular ductile fracture can also be envisioned. For instance, when there are few possible grain boundaries due to thermodynamical stability, simple calibration can be conducted (see Asim et al. (2019a)). However, when the entire space of grain boundaries has to be covered, machine learning techniques seem to be required (*e.g.* Guo et al. (2022a) and Ling et al. (2023) for transgranular ductile fracture). This subject shall not be pursued here.

On the one hand, elastic strains can be described by the elastic Green-Lagrange tensor:

$$\boldsymbol{e}_{\mathrm{GL}} = \frac{1}{2}\left(\boldsymbol{F}_{\mathrm{e}}^{\mathrm{T}} \cdot \boldsymbol{F}_{\mathrm{e}} - \boldsymbol{I}\right) = \frac{1}{2}\left(\boldsymbol{C}_{\mathrm{e}} - \boldsymbol{I}\right) \tag{III.174}$$

where $\boldsymbol{C}_{\mathrm{e}}$ is the right Cauchy–Green deformation tensor. On the other hand, the plastic spatial velocity gradient $\boldsymbol{L}_{\mathrm{p}}$ is defined as:

$$\boldsymbol{L}_{\mathrm{p}} = \dot{\boldsymbol{F}}_{\mathrm{p}} \cdot \boldsymbol{F}_{\mathrm{p}}^{-1} \tag{III.175}$$

The second Piola-Kirchhoff stress tensor $\boldsymbol{\Pi}$ and the Mandel stress tensor $\boldsymbol{M}$ are defined as:

$$\boldsymbol{\Pi} = \det(\boldsymbol{F}_{\mathrm{e}})\, \boldsymbol{F}_{\mathrm{e}}^{-1} \cdot \boldsymbol{\Sigma} \cdot \boldsymbol{F}_{\mathrm{e}}^{-\mathrm{T}} \quad , \qquad \boldsymbol{M} = \boldsymbol{C}_{\mathrm{e}} \cdot \boldsymbol{\Pi} \tag{III.176}$$

where $\boldsymbol{\Sigma}$ is the Cauchy stress tensor. Neglecting the volume change associated with elasticity, previous definitions allow writing the internal power as Han, 2012:

$$\boldsymbol{\Sigma} : \boldsymbol{D} = \boldsymbol{\Pi} : \dot{\boldsymbol{e}}_{\mathrm{GL}} + \boldsymbol{M} : \boldsymbol{L}_{\mathrm{p}} \tag{III.177}$$

where $\boldsymbol{D}$ is the eulerian strain tensor. Eq. III.177 indicates that, within this framework, the second Piola-Kirchhoff stress tensor should be used to describe elasticity, while the Mandel stress tensor is relevant for plasticity (Miehe et al., 2002).

3.1.2 Constitutive equations

In this section, the constitutive equations of a simple homogenized model for intergranular void growth are presented within the finite strain framework described in Section III.3.1.1. The stiffness tensor of the porous grain boundary is fixed to the stiffness tensor of the pristine grain boundary, with no influence of damage. It is recalled that this fourth-order tensor expresses as (see Eq. III.39 and Francfort and Murat (1986)):

$$\mathbb{C} = \left\{\mathbb{C}_1^{-1} + \left[2\left(\mathbb{C}_2^{-1} - \mathbb{C}_1^{-1}\right)^{-1} + \mathbb{\Lambda}\right]^{-1}\right\}^{-1} \quad \text{where} \quad \mathbb{\Lambda} = \mathbb{C}_1 - \mathbb{C}_1 : \mathrm{sym}\left[\underline{e}_1 \otimes \left(\underline{e}_1 \cdot \mathbb{C}_1 \cdot \underline{e}_1\right)^{-1} \otimes \underline{e}_1\right] : \mathbb{C}_1 \tag{III.178}$$

with $\mathbb{C}_1$ and $\mathbb{C}_2$ the stiffness tensors of the corresponding single crystals (see Fig. III.40). The elasticity law then writes:

$$\boldsymbol{\Pi} = \mathbb{C} : \boldsymbol{e}_{\mathrm{GL}} \tag{III.179}$$

No strain hardening is considered, so the growth yield criterion writes:

$$\phi_{\mathrm{g}} = \sigma_{\mathrm{g}}^{*} - \tau_0 \tag{III.180}$$

where τ_0 is the critical resolved shear stress of the pristine single crystal. The equivalent stress σ_{g}^{*} is defined by $S_{\mathrm{g}}(\sigma_{\mathrm{g}}^{*}) = 0$. Based on Eq. III.177 and following the path laid by Ling et al. (2016), S_{g} (Eq. III.24) is extended at finite strains using the Mandel stress $\boldsymbol{M}$:

$$S_{\mathrm{g}}(\sigma_{\mathrm{g}}^{*}, \boldsymbol{M}, f) \equiv \left(\frac{\left(\sum_{s=1}^{N}\left|\boldsymbol{\mu}_s^{(1)} : (\boldsymbol{M} + M'_{11}\boldsymbol{\Delta})\right|^n + \sum_{s=1}^{N}\left|\boldsymbol{\mu}_s^{(2)} : (\boldsymbol{M} - M'_{11}\boldsymbol{\Delta})\right|^n\right)^{\frac{1}{n}}}{\sigma_{\mathrm{g}}^{*}}\right)^2 + 2qf\cosh\left(\kappa\frac{M_{\mathrm{m}}}{\sigma_{\mathrm{g}}^{*}}\right) - 1 - (qf)^2 \tag{III.181}$$

where $M_{\mathrm{m}} = \mathrm{Tr}(\boldsymbol{M})/3$ and $\boldsymbol{M'} = \boldsymbol{M} - M_{\mathrm{m}}\boldsymbol{I}$. $\boldsymbol{\mu}_s^{(i)}$ is the non-symmetric Schmid tensor associated with the slip system s of crystal i (Eq. II.3). $n \to +\infty$ is a regularization parameter to remove vertexes from the yield surface to avoid convergence issues. q is a calibration parameter whose value will be discussed later, and κ is a numerical parameter set to 0.489 (see Section III.1.3.2 and Hure (2019)). Finally, symmetric tensor $\boldsymbol{\Delta}$ is the grain boundary normalized stress mismatch tensor from infinitesimal strain theory, which is defined as (see Appendix III.1.C):

$$\boldsymbol{\Delta} = \underset{\boldsymbol{\delta}\in\mathcal{S}_3(\mathbb{R})}{\mathrm{argmin}} \max_{s\in[\![1,N]\!]} \max\left[\left|\boldsymbol{\mu}_s^{(1)} : (\boldsymbol{\Sigma} + \Sigma_{11}\boldsymbol{\delta})\right|, \left|\boldsymbol{\mu}_s^{(2)} : (\boldsymbol{\Sigma} - \Sigma_{11}\boldsymbol{\delta})\right|\right] \tag{III.182}$$

Note that since $\boldsymbol{\mu}_s^{(1)} : \boldsymbol{I} = 0$, $\boldsymbol{\Delta}$ does not depend on the stress triaxiality ratio T of the Cauchy stress $\boldsymbol{\Sigma}$. However, it is dependent on the Lode angle θ and the three scalars (*e.g.* Euler angles) that define the rotation of the Cauchy stress $\boldsymbol{\Sigma}$ to its principal frame of reference. Thus, $\boldsymbol{\Delta}$ must be determined numerically for each set of those parameters. In the present work, only axisymmetric Cauchy stress tensors will be considered so that $\boldsymbol{\Delta}$ will be fixed for each crystallographic orientation couple.

In the associated plasticity framework that is adopted here, the flow rule is given by the yield surface through the normality rule:

$$\boldsymbol{L}_{\mathrm{p}} = \dot{p}\frac{\partial \phi_{\mathrm{g}}}{\partial \boldsymbol{M}} = \dot{p}\boldsymbol{n}_{\mathrm{g}} \quad \text{where} \quad \boldsymbol{n}_{\mathrm{g}} = \frac{\partial \sigma_{\mathrm{g}}^*}{\partial \boldsymbol{M}} \tag{III.183}$$

where $\dot{p}$ is the plastic multiplier and the expression of $\boldsymbol{n}_{\mathrm{g}}$ is given in Appendix III.3.A.2.

The void growth yield criterion described above only accounts for spherical voids. Thus, the evolution equation $\dot{w} = 0$ is adopted for the aspect ratio w. The porosity f, taken as the void volume fraction in the intermediate configuration, can then be determined by considering the incompressibility of the matrix material (Gurson, 1977):

$$\dot{f} = (1-f)\mathrm{Tr}\left(\boldsymbol{L}_{\mathrm{p}}\right) = (1-f)\dot{p}\mathrm{Tr}\left(\boldsymbol{n}_{\mathrm{g}}\right) \tag{III.184}$$

which can be integrated into:

$$f = 1 - \frac{1-f_0}{\det\left(\boldsymbol{F}_{\mathrm{p}}\right)} \tag{III.185}$$

with f_0 the initial porosity. Finally, the crystallographic orientations of the grain boundary are supposed to rotate at the same rate as the material orientation — linked to $\boldsymbol{F}_{\mathrm{e}}$ — so that no derogatory evolution laws (*e.g.* Mbiakop (2015)) are implemented.

Note that when crystal #1 and crystal #2 have the same crystallographic orientation, the model recovers the transgranular fracture model of Section II.1.3 in the limit of small transformations (and before coalescence sets in). Furthermore, when $f = 0$ and the crystals are identical, the model amounts to classical crystal perfect-plasticity at arbitrary strain (see Section II.1.2.1), although numerical stability is reached here by regularization (parameter n) instead of viscoplasticity (parameters m and K).

3.1.3 Numerical implementation

The constitutive equations detailed in Section III.3.1.2 form a set of nonlinear differential equations which is integrated numerically for each increment of deformation gradient $\Delta\boldsymbol{F}$. The state variables are the Green-Lagrange strain tensor $\boldsymbol{e}_{\mathrm{GL}}$, the porosity f, and the cumulated plastic strain p. A fourth state variable, named `broken`, identifies the state of the material element: if the porosity reaches a certain critical threshold $f_{\mathrm{c}} = 0.99/q$, `broken` is set to `true` and the stress drops to 0; this variable is only used to ease the numerical convergence. Other parameters involved in the constitutive equations can be deduced from these state variables, such as stress tensors $\boldsymbol{\Pi}$ and $\boldsymbol{M}$ which are obtained directly from $\boldsymbol{e}_{\mathrm{GL}}$ and the elastic part $\boldsymbol{F}_{\mathrm{e}}$ of the deformation gradient that is linked to the successive increments $\Delta\boldsymbol{F}$ and Δp. The equivalent matrix stresses σ_{g}^* is obtained by solving Eq. III.181, given a porosity f and a Mandel stress $\boldsymbol{M}$. The discretized versions of the set of equations to be solved are:

$$\begin{aligned}
\mathcal{R}_{\Delta \boldsymbol{e}_{\mathrm{GL}}} &= \boldsymbol{e}_{\mathrm{GL}} + \Delta\boldsymbol{e}_{\mathrm{GL}} - \frac{1}{2}\left(\boldsymbol{F}_{\mathrm{e}}^{\mathrm{T}}\boldsymbol{F}_{\mathrm{e}} - \boldsymbol{I}\right) &&= 0 \\
\mathcal{R}_{\Delta p} &= \frac{\sigma_{\mathrm{g}}^*\left(f, \boldsymbol{e}_{\mathrm{GL}}\right)}{\tau_0} - 1 &&= 0 \\
\mathcal{R}_{\Delta f} &= \Delta f - (1-f)\Delta p \mathrm{Tr}\left[\boldsymbol{n}_g\left(f, \boldsymbol{e}_{\mathrm{GL}}\right)\right] &&= 0
\end{aligned} \tag{III.186}$$

where the flow direction $\boldsymbol{n}_{\mathrm{g}}$ (and its $\boldsymbol{M}$-derivative) is detailed in Appendix III.3.A.2.

A fully implicit integration scheme for the set of Eqs. III.186 would solve the equations considering that the value of each variable corresponds to the one at the end of the time step. To alleviate the numerical difficulties due to the highly non-linear nature of Eqs. III.186, a mixed Newton-Raphson / fixed-point algorithm is used. Eqs. III.186$_{a,b}$ are solved by a Newton Raphson algorithm with respect to the increments of elastic stain tensor $\Delta\boldsymbol{e}_{\mathrm{GL}}$ and of plastic multiplier Δp, the state variable f being constant. The Newton-Raphson algorithm requires the computation of the

Algorithm 2 Numerical integration of constitutive equations between time m (variables X_m) and time $m+1$ (variables X_{m+1}).

Require: State variables $\{\boldsymbol{e}_{\mathrm{GL},m}, f_m, \texttt{broken}\}$ and state $\boldsymbol{F}_{\mathrm{e},m}$ at the beginning of the time step
Require: Increment of deformation gradient $\Delta\boldsymbol{F} = \boldsymbol{F}_{m+1}\boldsymbol{F}_m^{-1}$
if `broken` **then**
  $\{\boldsymbol{e}_{\mathrm{GL},m+1}, \boldsymbol{F}_{\mathrm{e},m+1}, f_{m+1}\} \leftarrow \{\boldsymbol{e}_{\mathrm{GL},m}, \boldsymbol{F}_{\mathrm{e},m}, f_m\}$
else
  Elastic predictor $\boldsymbol{F}_{\mathrm{e}}^{\mathrm{trial}} = \Delta\boldsymbol{F}\cdot\boldsymbol{F}_{\mathrm{e},m}$ ▷ Elastic prediction
  Green-Lagrange strain tensor predictor $\boldsymbol{e}_{\mathrm{GL}}^{\mathrm{trial}} = \frac{1}{2}\left(\boldsymbol{F}_{\mathrm{e}}^{\mathrm{trial,T}}\boldsymbol{F}_{\mathrm{e}}^{\mathrm{trial}} - \boldsymbol{I}\right)$
  Second Piola-Kirchoff stress tensor predictor $\boldsymbol{\Pi}^{\mathrm{trial}} = \mathbb{C} : \boldsymbol{e}_{\mathrm{GL}}^{\mathrm{trial}}$
  Mandel stress tensor predictor $\boldsymbol{M}^{\mathrm{trial}} = \left(\boldsymbol{I} + 2\boldsymbol{e}_{\mathrm{GL}}^{\mathrm{trial}}\right)\cdot\boldsymbol{\Pi}^{\mathrm{trial}}$
  if $\sigma_{\mathrm{g}}^{*}\left(\boldsymbol{M}^{\mathrm{trial}}, f_m\right) \leq \tau_0$ **then** ▷ Elastic evolution
    $\left\{\boldsymbol{e}_{\mathrm{GL},m+1}, \boldsymbol{F}_{\mathrm{e},m+1}, f_{m+1}\right\} \leftarrow \left\{\boldsymbol{e}_{\mathrm{GL}}^{\mathrm{trial}}, \boldsymbol{F}_{\mathrm{e}}^{\mathrm{trial}}, f_m\right\}$
  else ▷ Elasto-plastic evolution
    $\Delta f \leftarrow 0$
    repeat ▷ Fixed-point algorithm for Δf
      $\{\Delta\boldsymbol{e}_{\mathrm{GL}}, \Delta p\} \leftarrow \{0, 0\}$
      Compute $\mathcal{R}_{\Delta\boldsymbol{e}_{\mathrm{GL}}}$, $\mathcal{R}_{\Delta p}$ from $\boldsymbol{e}_{\mathrm{GL},m}$ and $\boldsymbol{F}_{\mathrm{e},m}$
      repeat ▷ Newton-Raphson algorithm on $\Delta\boldsymbol{e}_{\mathrm{GL}}$ and Δp
        $\begin{pmatrix}\Delta\boldsymbol{e}_{\mathrm{GL}}\\ \Delta p\end{pmatrix} \leftarrow \begin{pmatrix}\Delta\boldsymbol{e}_{\mathrm{GL}}\\ \Delta p\end{pmatrix} - \underset{\sim}{\boldsymbol{J}}^{-1}\begin{pmatrix}\mathcal{R}_{\Delta\boldsymbol{e}_{\mathrm{GL}}}\\ \mathcal{R}_{\Delta p}\end{pmatrix}$
        $\boldsymbol{\Pi} = \mathbb{C} : \left(\boldsymbol{e}_{\mathrm{GL},m} + \Delta\boldsymbol{e}_{\mathrm{GL}}\right)$
        $\boldsymbol{M} = \left[\boldsymbol{I} + 2\left(\boldsymbol{e}_{\mathrm{GL},m} + \Delta\boldsymbol{e}_{\mathrm{GL}}\right)\right] : \boldsymbol{\Pi}$
        $\Delta\boldsymbol{F}_{\mathrm{p}}^{-1} = \dfrac{\boldsymbol{I} - \Delta p\boldsymbol{n}_{\mathrm{g}}}{\sqrt[3]{\det\left(\boldsymbol{I} - \Delta p\boldsymbol{n}_{\mathrm{g}}\right)}}$
        $\boldsymbol{F}_{\mathrm{e}} = \boldsymbol{F}_{\mathrm{e}}^{\mathrm{trial}}\cdot\Delta\boldsymbol{F}_{\mathrm{p}}^{-1}$
        Compute $\mathcal{R}_{\Delta\boldsymbol{e}_{\mathrm{GL}}}$, $\mathcal{R}_{\Delta p}$ from $\boldsymbol{M}$ and $\boldsymbol{F}_{\mathrm{e}}$
      until $\max\left[\left|\mathcal{R}_{\Delta\boldsymbol{e}_{\mathrm{GL}}}\right|, \left|\mathcal{R}_{\Delta p}\right|\right] \leq \epsilon$
      $\Delta f \leftarrow (1-f)\Delta p\mathrm{Tr}\left(\boldsymbol{n}_g\right)$
    until $\left|\Delta f^{k+1} - \Delta f^{k}\right| \leq \epsilon$
    $\left\{\boldsymbol{e}_{\mathrm{GL},m+1}, \boldsymbol{F}_{\mathrm{e},m+1}, f_{m+1}\right\} \leftarrow \left\{\boldsymbol{e}_{\mathrm{GL},m} + \Delta\boldsymbol{e}_{\mathrm{GL}}, \boldsymbol{F}_{\mathrm{e}}, f_m + \Delta f\right\}$
    if $f > f_c$ **then**
      `broken` $\leftarrow$ `true` ▷ Material failure
    end if
  end if
end if
$\boldsymbol{\Sigma} = \dfrac{1}{\det\left(\boldsymbol{F}_{\mathrm{e}}\right)}\boldsymbol{F}_{\mathrm{e}}\cdot\boldsymbol{\Pi}\cdot\boldsymbol{F}_{\mathrm{e}}^{\mathrm{T}}$

partial derivatives of Eqs. III.186$_{a,b}$ which define the Jacobian $\underset{\sim}{\boldsymbol{J}}$ of the system:

$$\begin{aligned}
\frac{\partial\mathcal{R}_{\Delta\boldsymbol{e}_{\mathrm{GL}}}}{\partial\Delta\boldsymbol{e}_{\mathrm{GL}}} &= \mathbb{I} + \Delta p\left[\frac{\partial\boldsymbol{e}_{\mathrm{GL}}}{\partial\left(\Delta\boldsymbol{F}_{\mathrm{p}}^{-1}\right)} : \frac{\partial\boldsymbol{n}_{\mathrm{g}}}{\partial\boldsymbol{M}} : \frac{\partial\boldsymbol{M}}{\partial\Delta\boldsymbol{e}_{\mathrm{GL}}}\right] & \frac{\partial\mathcal{R}_{\Delta\boldsymbol{e}_{\mathrm{GL}}}}{\partial\Delta p} &= \frac{\partial\boldsymbol{e}_{\mathrm{GL}}}{\partial\left(\Delta\boldsymbol{F}_{\mathrm{p}}^{-1}\right)} : \boldsymbol{n}_{\mathrm{g}}\\
\frac{\partial\mathcal{R}_{\Delta p}}{\partial\Delta\boldsymbol{e}_{\mathrm{GL}}} &= \left[\boldsymbol{n}_{\mathrm{g}} : \frac{\partial\boldsymbol{M}}{\partial\Delta\boldsymbol{e}_{\mathrm{GL}}}\right] & \frac{\partial\mathcal{R}_{\Delta p}}{\partial\Delta p} &= 0
\end{aligned} \tag{III.187}$$

where partial derivatives are detailed in Appendix III.3.A.1. Upon convergence of the Newton-Raphson algorithm, Eq. III.186$_c$ is used to compute the increment of f. These two steps are repeated until stationarity of Δf. This algorithm ensures a fully implicit integration scheme of the system defined by Eqs. III.186. The consistent tangent operator, required for some finite element solvers, can be computed based on Eq. III.187 (Helfer, 2020). The numerical integration has been implemented in the `MFront` code generator (Helfer et al., 2015), and the different steps are summarized in Algorithm 2.

3.2 Numerical assessment

3.2.1 Porous unit cell simulations

In order to construct a database upon which the homogenized model can be validated, eight different random FCC crystallographic orientation couples are chosen (first eight couples of Table III.2). Cubic unit cells containing a centered single spherical void at the boundary of two single crystals (see Fig. III.42a) are considered, with an initial porosity of $f_0 = 0.01$. The unit-cell is meshed with 40^3 voxels, consistently with the FFT mesh of Section II.1.2.2 which held 41^3 voxels. Voxels are allowed a unique material law among three possibilities. The voxels representing the cavity have a vanishing stiffness tensor whereas voxels corresponding to single crystals follow finite strain crystal plasticity laws (described in Section II.1.2.1). Viscoplastic parameters $K = 0.1$ MPa and $m = 20$ are chosen to reproduce rate independence at the considered strain rate (see below). Finally, the cubic symmetry elasticity modulus values are taken from Table II.2.

Periodic boundary conditions are used along with axisymmetric loading conditions (as in Ling et al. (2016)), principal axes being aligned with the initial axes of the cell (see Fig. III.40):

$$\boldsymbol{\Sigma} = \Sigma_{11} \begin{pmatrix} 1 & 0 & 0 \\ 0 & \beta & 0 \\ 0 & 0 & \beta \end{pmatrix} \quad , \qquad T = \frac{\Sigma_{\mathrm{m}}}{\Sigma_{\mathrm{eq}}^{\mathrm{vM}}} = \frac{1+2\beta}{3(1-\beta)} \tag{III.188}$$

where $\Sigma_{\mathrm{m}} = \frac{1}{3}\,\mathrm{Tr}(\boldsymbol{\Sigma})$ is the hydrostatic stress and $\Sigma_{\mathrm{eq}}^{\mathrm{vM}}$ is the equivalent von Mises stress associated to the macroscopic Cauchy stress tensor $\boldsymbol{\Sigma}$. Four different values of stress triaxiality are used: $T \in \{0, \frac{1}{3}, 1, 2, 3\}$. Simulations have been performed under finite strain in the FFT-based solver `AMITEX_FFTP` (CEA, 2020). Mechanical loading is applied by imposing one component of the macroscopic deformation gradient rate $\dot{F}_{11} = 10^{-4}\ \mathrm{s}^{-1}$, reminding that the constitutive equations used are almost rate-independent. Selected simulations have been performed to check consistency of the results and discretization convergence. The method used to enforce a constant stress triaxiality in `AMITEX_FFTP` is in the spirit of the work of Kabel et al. (2016) and extended to impose proportionality on the Cauchy stress tensor. Combining the different crystallographic orientations and stress triaxialities, 40 finite strain porous grain boundary unit-cell simulations results have been gathered.

The void shape can be obtained by post-processing the unit cell simulations; it is approximated to an ellipsoid of axes r_1, r_2 and r_3 along $\underline{e}_1$, $\underline{e}_2$ and $\underline{e}_3$. The void aspect ratios are defined as $w_2 = r_1/r_2$ and $w_3 = r_1/r_3$. Since `AMITEX_FFTP` provides the mean deformation gradient $\boldsymbol{F}$ in each material, the void axes r_i are the diagonal terms of the void mean deformation gradient $\boldsymbol{F}_{\mathrm{void}}$. This approach amounts to neglecting the rotation of the void, which is acceptable for $T \geq \frac{1}{3}$ at relatively small strains. A more complete approach would rely on the polar decomposition:

$$\boldsymbol{F}_{\mathrm{void}} = \boldsymbol{R}\boldsymbol{U} \quad \text{where} \quad \boldsymbol{U} = \left(\boldsymbol{F}_{\mathrm{void}}^{\mathrm{T}}\boldsymbol{F}_{\mathrm{void}}\right)^{\frac{1}{2}} \quad \text{and} \quad \boldsymbol{R} = \boldsymbol{F}_{\mathrm{void}}\boldsymbol{U}^{-1} \tag{III.189}$$

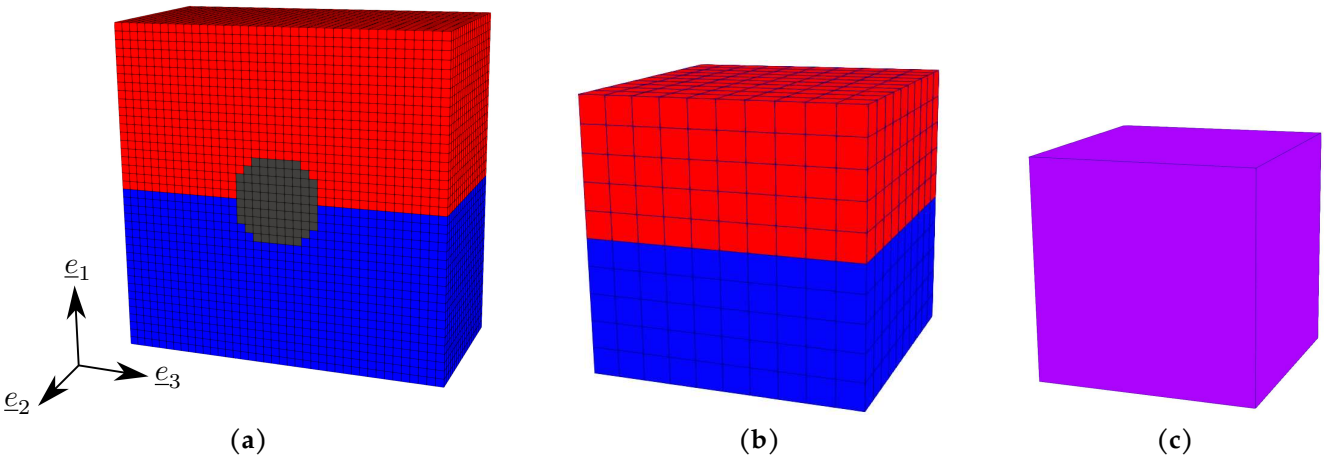

FIGURE III.42: Meshes used to perform the FFT computations: (a) unit cell simulation with $f = 0.01$ (half of the mesh is shown); (b) unit cell simulation with $f = 0$; (c) homogenized model with a single voxel. For unit-cell simulations, the void is shown in dark grey whereas the voxels which follow single crystal plasticity are colored in blue and red.

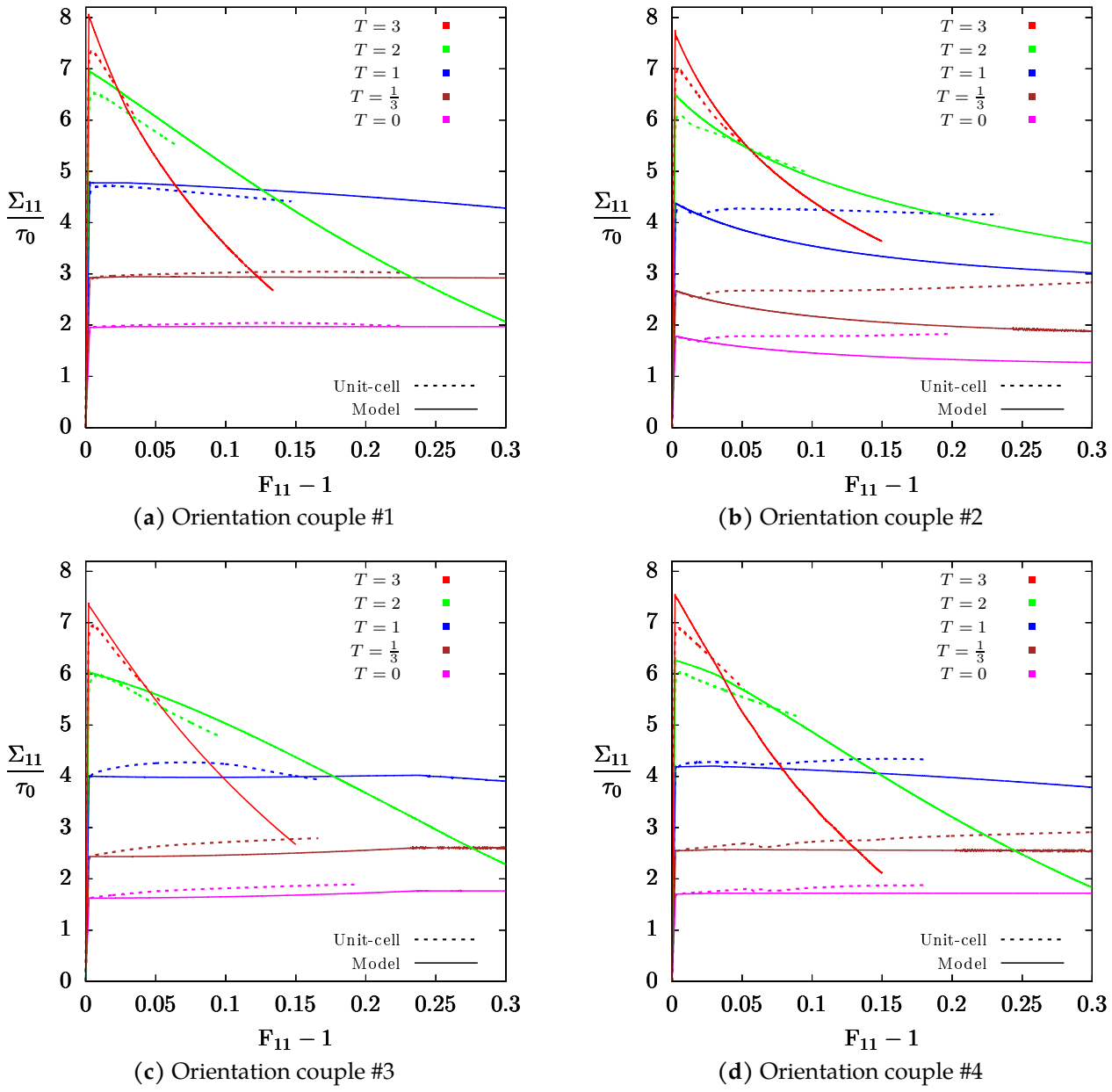

(a) Orientation couple #1 (b) Orientation couple #2

(c) Orientation couple #3 (d) Orientation couple #4

FIGURE III.43: Stress-strain curves corresponding to the homogenized model and the unit cell computations with $f_0 = 0.01$. Various fixed stress triaxiality ratios T and four different crystallographic orientation couples are considered.

with the void axes obtained from the eigenvalues of $\boldsymbol{U}$ and three Euler angles characterizing the rotation $\boldsymbol{R}$ would be required.

For completeness, it is mentioned that unit-cell computations were also carried out on the eight orientation couples with $f = 0$ using the mesh with 10^3 voxels shown in Fig. III.42. Given elastic moduli values, elastic strain can be neglected compared to plastic strain. Thus, the unit cell is considered incompressible, meaning that loading with $T = 0$ is enough to characterize all stress triaxiality ratios.

3.2.2 Comparison to the homogenized model

The predictions of the homogenized model presented in Section III.3.1 are compared to the unit-cell simulations by considering a single material cubic voxel (Fig. III.42c) whose behavior law is that of the model and which is subjected to the same loadings as in Section III.3.2.1 using `AMITEX_FFTP`. The material law, implemented in `MFront` (see Section III.3.1.3), is used with an initial porosity of $f_0 = 0.01$. The parameters of the yield criterion (Eq. III.181) are set to $n = 5000$ and $q = 1.85$; the value of q is chosen according to the calibration performed on small strain simulations for $f = 0.01$ (see Table III.3).

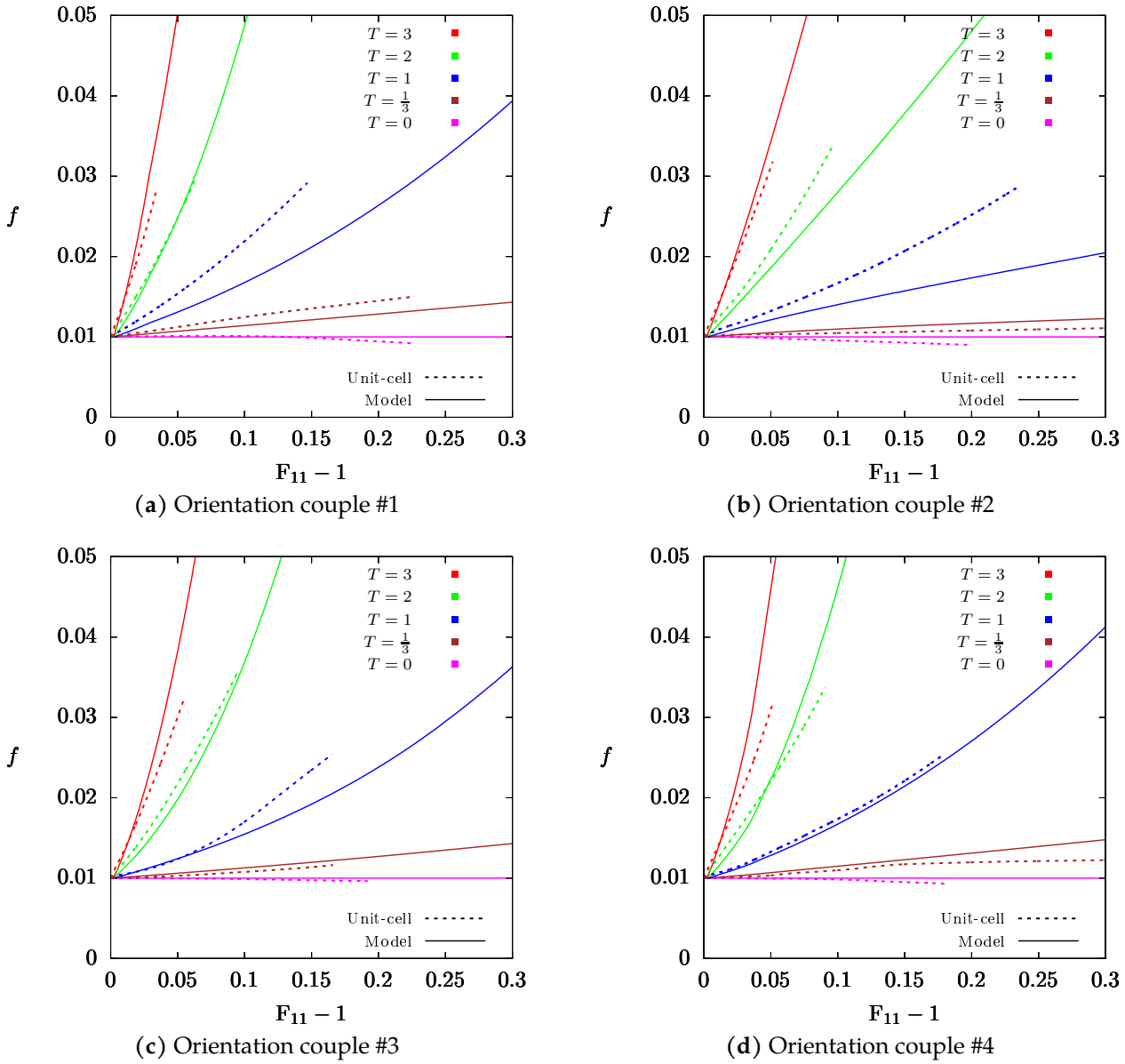

(**a**) Orientation couple #1 (**b**) Orientation couple #2

(**c**) Orientation couple #3 (**d**) Orientation couple #4

FIGURE III.44: Porosity f evolution predicted by the homogenized model and the unit cell computations at various fixed stress triaxiality ratios T and for four different crystallographic orientation couples. The initial porosity has been set to $f_0 = 0.01$.

The results are displayed in Figs. III.43-III.45. The effect of stress triaxiality on the macroscopic stress-strain curves is assessed in Fig. III.43 for four different orientation couples. As in the original model of Gurson (1977), the increase of Σ_{11} with T is well captured. This agreement is achieved mainly due to the quality of the yield stress prediction. Similarly to the small strain study (see Fig. III.7), it can be seen that the yield stress at high triaxialities ($T \geq 2$) can be overvalued by a maximum of 10%. A better agreement could be obtained by increasing the value of q — which was not performed in the small strain study due to considerations linked to void coalescence. The evolution of the stress with increasing strain is generally well predicted, especially at $T = 0$ and $T = \frac{1}{3}$ which are generally associated with smaller variations of Σ_{11}. Orientation couple #2 (Fig. III.43b) stands in contrast with the other three orientation couples because the homogenized model fails to predict the second increase of stress seen for $T \leq 1$, which underlines the approximate nature of evolution equations.

A similar agreement is obtained when considering the effect of T on the porosity evolution, as shown in Fig. III.44. As foresaw by the law of Rice and Tracey (1969) and evidenced by earlier porous grain boundary unit cell computations (Chen et al., 2019; Dakshinamurthy et al., 2021), porosity increases exponentially with the stress triaxiality ratio. It can be seen that a good prediction of the slope of the stress-strain curve (*e.g.* Fig. III.43a at $T = 2$, Fig. III.43d at $T = 1$ and 2) is usually associated with a sound prediction of porosity increase (*e.g.* Fig. III.44a at $T = 2$, Fig. III.44d

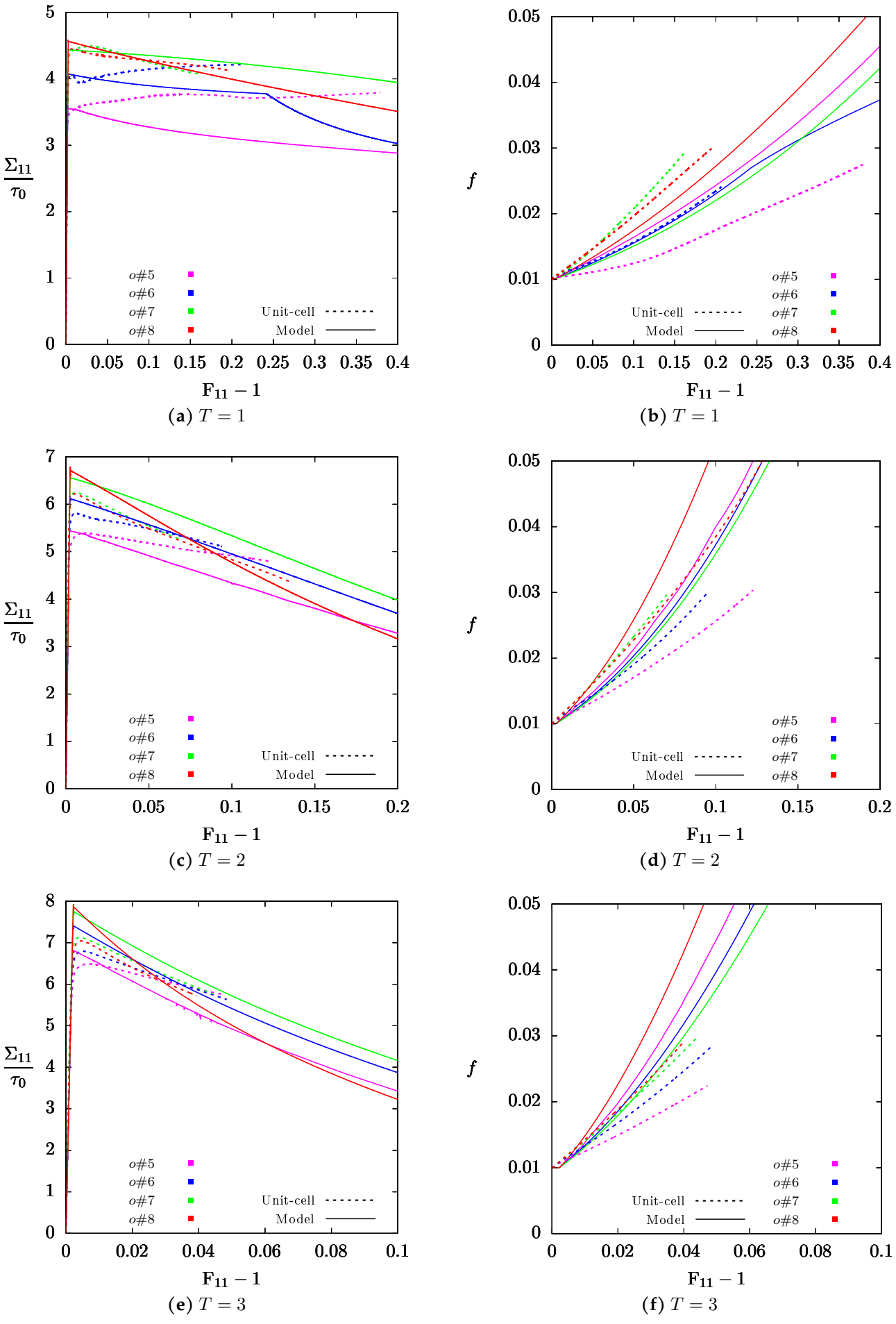

(**a**) $T = 1$ (**b**) $T = 1$

(**c**) $T = 2$ (**d**) $T = 2$

(**e**) $T = 3$ (**f**) $T = 3$

FIGURE III.45: Effect of the crystallographic orientation couples on the stress-strain curves (**a,c,e**) and porosity evolution (**b,d,f**) for various fixed stress triaxiality ratios. The homogenized model predictions are compared to corresponding unit cell results.

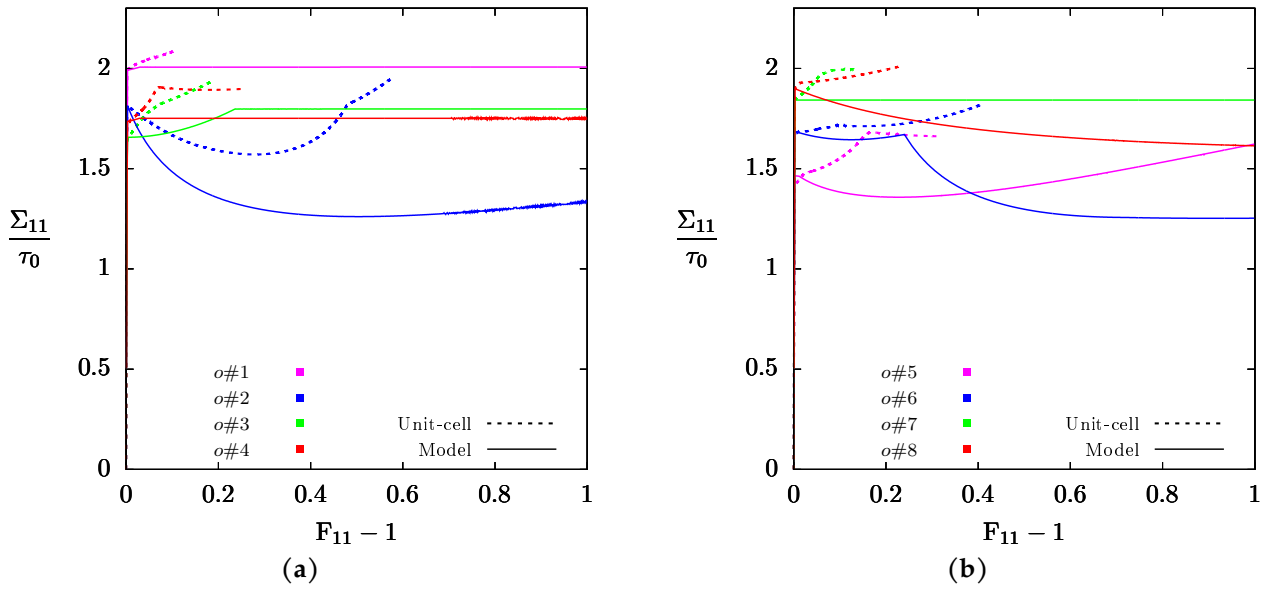

FIGURE III.46: Stress-strain curves corresponding to the homogenized model and the unit cell computations at $T = 0$ for pristine grain boundaries ($f = 0$).

at $T = 1$ and 2), which is not a surprise since void growth is the leading cause for softening. At $T = 0$, no evolution of porosity is predicted since Eq. III.181 does not depend anymore on the hydrostatic (Mandel) stress so that the homogenized material can be considered incompressible. This outcome is not far from the unit-cell simulations that indicate only mild void contraction — at least for the relatively small strain considered here.

The effect of T being satisfactorily captured for a fixed orientation couple, the effect of the orientation couple is now studied at fixed stress triaxiality ratios in Fig. III.45. Results are less favorable, especially at $T = 1$ (Fig. III.45a) where softening due to void growth and structural hardening due to crystal lattice rotation compete. It can be seen that hardening prevails for couples #5 and #6, resulting in significant discrepancies between the homogenized model and the unit cell results. This adverse effect is greatly reduced for $T \geq 2$ (Fig. III.45c,e) since softening becomes dominant and differences between orientation couples are less critical. It can be seen that quantitative agreement can only be reached around plastic yielding, since discrepancies appear both in stress-strain (Fig. III.45a,c,e) and porosity-strain curves (Fig. III.45b,d,f) with increasing strain. However, some qualitative features are correctly predicted, such as the fact that the stress-strain curve of couple #8 crosses that of couples #5 and #6 for $T \geq 2$ (Fig. III.45c,e) due to a faster porosity increase (Fig. III.45d,f).

3.2.3 Discussion

Despite the achievements of the homogenized model proposed here, it is useful to ponder over its shortcomings. Since the finite strain framework adopted here is adapted to crystal plasticity (Helfer and Ling, 2014; Abatour et al., 2021), discrepancies can only arise from two sources: incomplete modeling of the mechanical behavior of the pristine bicrystal[17] or overly simplified modeling of void growth. The available evidence supports both types of errors.

- First, comparing the homogenized model predictions for $f = 0$ and the corresponding unit cell results (Fig. III.46) shows that the finite strain model of the pristine bicrystal displays important limitations, even if some trends are qualitatively predicted. These shortcomings may come from the loss of validity of $\boldsymbol{\Delta}$ with increasing deformation — for instance, stress homogeneity in half-crystals rely on the flatness of the grain boundary — or from the fact that the two crystallographic orientations can rotate at a different rate.

- Second, the void growth may be too simplified by the model. For instance, it was shown in Dakshinamurthy et al. (2021) that porosity evolution could significantly differ between the two half-crystals, especially when the yield stress mismatch — regarding the considered mechanical loading — is high. The neglect of non-spherical void shapes is also an issue that can be solved using the more complicated intergranular void growth yield

[17] Note that this whole discrepancy source does not exist for porous single crystal homogenized models since the case $f = 0$ reduces to classical crystal plasticity; modeling porous bicrystals is thus more difficult.

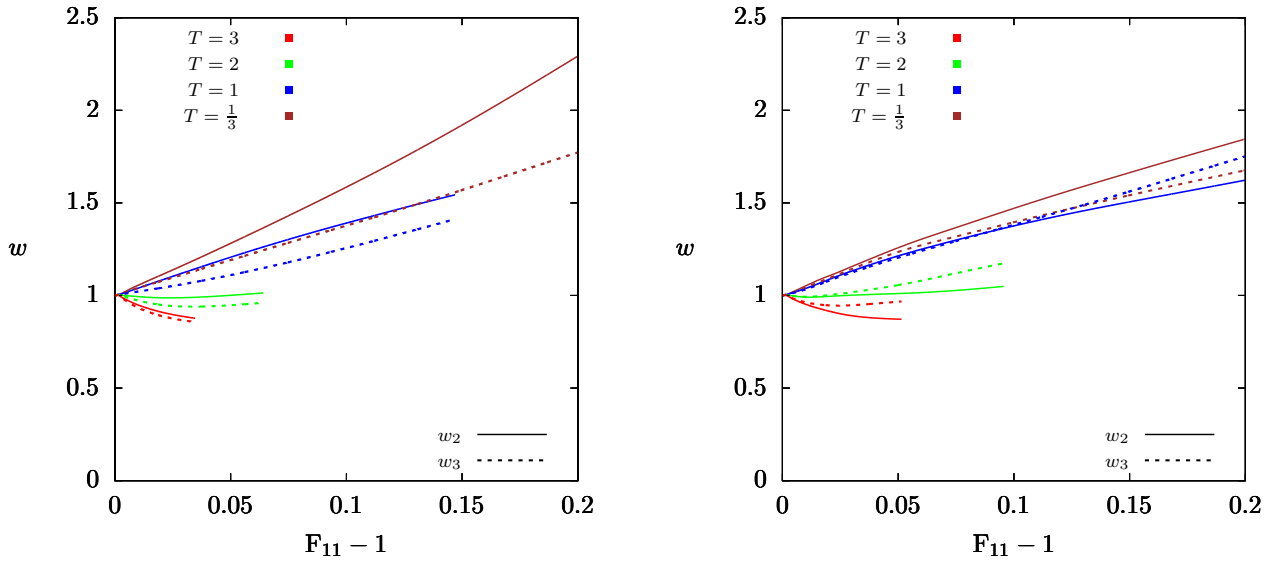

(**a**) Orientation couple #1 (**b**) Orientation couple #2

FIGURE III.47: Evolution of void aspect ratios w_2 and w_3 in unit cell simulations at various stress triaxiality ratios.

criterion of Section III.1.4. However, this discrepancy is mild for $T \geq 2$ since deviations from sphericity are relatively low (see Fig. III.47). Finally, the void likely impacts the lattice rotation of half-crystals with macroscopic consequences, as is the case for porous single crystals.

3.3 Conclusion

In the preceding, a first homogenized model for intergranular void growth was proposed in a finite strain framework fit for crystal plasticity. It relies upon the Gurson-like yield criterion for spherical cavities obtained using small strain limit analysis, along with a plastic flow given by the normality rule. This model enables the simulation of intergranular ductile fracture under axisymmetric loading with limited complexity. When assessed against corresponding porous grain boundary unit cell simulations, it shows a satisfying agreement by predicting correctly the effect of stress triaxiality ratio and qualitatively the effect of crystallographic orientation couples, at least for relatively small strains. This study of a simple model is useful to assess the current state of intergranular ductile fracture prediction.

Future enhancements to the model may be required to reach quantitative agreement, such as a more refined homogenization of pristine grain boundaries. The model should then be compared to porous unit-cell simulations at larger strain by performing dedicated computations or using numerical results already available in the literature for hardenable crystals (Jeong et al., 2018; Dakshinamurthy et al., 2021). The central perspective of this work would then be the use of this model — possibly with an additional intergranular void coalescence criterion — together with a homogenized model of transgranular ductile fracture to simulate the competition between ductile fracture modes, which would be a significant achievement.

3.A Expression of useful derivatives

3.A.1 Finite strain quantities

First, the operator $\underline{\otimes}$ is defined as such: it produces a fourth-order tensor $\mathbb{A}$ from two second-order tensors $\boldsymbol{B}$ and $\boldsymbol{C}$ so that $A_{ijkl} = B_{ik}C_{jl}$. This operator is useful when deriving a tensorial product (Helfer and Ling, 2014):

$$\frac{\partial(\boldsymbol{BC})}{\partial \boldsymbol{B}} = \boldsymbol{I} \underline{\otimes} \boldsymbol{C}^{\mathrm{T}} \quad \text{and} \quad \frac{\partial(\boldsymbol{BC})}{\partial \boldsymbol{C}} = \boldsymbol{B} \underline{\otimes} \boldsymbol{I} \tag{III.190}$$

Then, the following formulas are obtained:

$$\begin{aligned}\frac{\partial \boldsymbol{e}_{\mathrm{GL}}}{\partial\left(\Delta \boldsymbol{F}_{\mathrm{p}}^{-1}\right)} &= \frac{1}{2}\frac{\partial\left(\boldsymbol{F}_{\mathrm{e}}^{\mathrm{T}}\boldsymbol{F}_{\mathrm{e}}\right)}{\partial \boldsymbol{F}_{\mathrm{e}}} : \left(\boldsymbol{F}_{\mathrm{e}}^{\mathrm{trial}} \underline{\otimes} \boldsymbol{I}\right) \\ \frac{\partial \boldsymbol{M}}{\partial \Delta \boldsymbol{e}_{\mathrm{GL}}} &= 2\boldsymbol{I} \underline{\otimes} \boldsymbol{\Pi}^{\mathrm{T}} + \left[\left(\boldsymbol{I} + 2\boldsymbol{e}_{\mathrm{GL}}\right) : \mathbb{C}\right] \underline{\otimes} \boldsymbol{I}\end{aligned} \tag{III.191}$$

3.A.2 Growth yield criterion

Numerical implementation of the constitutive equations in the `MFront` code generator requires analytical expressions of the yield criterion flow direction and its partial derivative with respect to $\boldsymbol{M}$. They are provided below.

Useful notations

$$\hat{\boldsymbol{\mu}}_k^{(1)} \equiv \boldsymbol{\mu}_k^{(1)} + \left|\boldsymbol{\Delta} : \boldsymbol{\mu}_k^{(1)}\right| \left(\underline{e}_1 \otimes \underline{e}_1\right) : \mathbb{K} \quad , \qquad \hat{\boldsymbol{\mu}}_k^{(2)} \equiv \boldsymbol{\mu}_k^{(2)} - \left|\boldsymbol{\Delta} : \boldsymbol{\mu}_k^{(2)}\right| \left(\underline{e}_1 \otimes \underline{e}_1\right) : \mathbb{K} \tag{III.192}$$

$$S_{\mathrm{g}}^{(0)} \equiv \sum_{k=1}^{N} \left|\boldsymbol{\mu}_k^{(1)} : \left(\boldsymbol{M} + M'_{11}\boldsymbol{\Delta}\right)\right|^n + \sum_{k=1}^{N} \left|\boldsymbol{\mu}_k^{(2)} : \left(\boldsymbol{M} - M'_{11}\boldsymbol{\Delta}\right)\right|^n \tag{III.193}$$

$$\begin{aligned}\boldsymbol{S}_{\mathrm{g}}^{(\mathbf{1})} \equiv &\sum_{k=1}^{N} \operatorname{sgn}\left[\boldsymbol{\mu}_k^{(1)} : \left(\boldsymbol{M} + M'_{11}\boldsymbol{\Delta}\right)\right] \left|\boldsymbol{\mu}_k^{(1)} : \left(\boldsymbol{M} + M'_{11}\boldsymbol{\Delta}\right)\right|^{n-1} \hat{\boldsymbol{\mu}}_k^{(1)} \\ &+ \sum_{k=1}^{N} \operatorname{sgn}\left[\boldsymbol{\mu}_k^{(2)} : \left(\boldsymbol{M} - M'_{11}\boldsymbol{\Delta}\right)\right] \left|\boldsymbol{\mu}_k^{(2)} : \left(\boldsymbol{M} - M'_{11}\boldsymbol{\Delta}\right)\right|^{n-1} \hat{\boldsymbol{\mu}}_k^{(2)}\end{aligned} \tag{III.194}$$

$$\mathbb{S}_{\mathrm{g}}^{(2)} \equiv \sum_{k=1}^{N} \left|\boldsymbol{\mu}_k^{(1)} : \left(\boldsymbol{M} + M'_{11}\boldsymbol{\Delta}\right)\right|^{n-2} \hat{\boldsymbol{\mu}}_k^{(1)} \otimes \hat{\boldsymbol{\mu}}_k^{(1)} + \sum_{k=1}^{N} \left|\boldsymbol{\mu}_k^{(2)} : \left(\boldsymbol{M} - M'_{11}\boldsymbol{\Delta}\right)\right|^{n-2} \hat{\boldsymbol{\mu}}_k^{(2)} \otimes \hat{\boldsymbol{\mu}}_k^{(2)} \tag{III.195}$$

Flow direction

$$\frac{\partial S_{\mathrm{g}}}{\partial \boldsymbol{M}} = \frac{2}{\sigma_{\mathrm{g}}^*}\left[\frac{1}{\sigma_{\mathrm{g}}^*}\left(S_{\mathrm{g}}^{(0)}\right)^{\frac{2}{n}-1} \boldsymbol{S}_{\mathrm{g}}^{(\mathbf{1})} + \frac{1}{3} q f \kappa \sinh\left(\kappa \frac{M_{\mathrm{m}}}{\sigma_{\mathrm{g}}^*}\right) \boldsymbol{I}\right] \tag{III.196}$$

$$\frac{\partial S_{\mathrm{g}}}{\partial \sigma_{\mathrm{g}}^*} = -\frac{2}{(\sigma_{\mathrm{g}}^*)^2}\left[\frac{1}{\sigma_{\mathrm{g}}^*}\left(S_{\mathrm{g}}^{(0)}\right)^{\frac{2}{n}} + q f \kappa \sinh\left(\kappa \frac{M_{\mathrm{m}}}{\sigma_{\mathrm{g}}^*}\right) M_{\mathrm{m}}\right] \tag{III.197}$$

$$\boldsymbol{n}_{\mathrm{g}} = \frac{\partial \sigma_{\mathrm{g}}^*}{\partial \boldsymbol{M}} = -\left(\frac{1}{\frac{\partial S_{\mathrm{g}}}{\partial \sigma_{\mathrm{g}}^*}}\right) \frac{\partial S_{\mathrm{g}}}{\partial \boldsymbol{M}} \tag{III.198}$$

Flow direction first-order derivative

$$\frac{\partial^2 S_{\mathrm{g}}}{\partial \boldsymbol{M}^2} = \frac{2}{\left(\sigma_{\mathrm{g}}^*\right)^2}\left[\left(S_{\mathrm{g}}^{(0)}\right)^{\frac{2}{n}-2}\left((n-1) S_{\mathrm{g}}^{(0)} \mathbb{S}_{\mathrm{g}}^{(2)} - (n-2)\boldsymbol{S}_{\mathrm{g}}^{(\mathbf{1})} \otimes \boldsymbol{S}_{\mathrm{g}}^{(\mathbf{1})}\right) + \frac{1}{9} q f \kappa^2 \cosh\left(\kappa \frac{M_{\mathrm{m}}}{\sigma_{\mathrm{g}}^*}\right) \boldsymbol{I} \otimes \boldsymbol{I}\right] \tag{III.199}$$

$$\frac{\partial^2 S_{\mathrm{g}}}{\partial \boldsymbol{M} \partial \sigma_{\mathrm{g}}^*} = -\frac{2}{(\sigma_{\mathrm{g}}^*)^2}\left[\frac{2}{\sigma_{\mathrm{g}}^*}\left(S_{\mathrm{g}}^{(0)}\right)^{\frac{2}{n}-1} \boldsymbol{S}_{\mathrm{g}}^{(\mathbf{1})} + \frac{1}{3} q f \kappa \sinh\left(\kappa \frac{M_{\mathrm{m}}}{\sigma_{\mathrm{g}}^*}\right) \boldsymbol{I} + \frac{1}{3}\frac{q f \kappa^2}{\sigma_{\mathrm{g}}^*} \cosh\left(\kappa \frac{M_{\mathrm{m}}}{\sigma_{\mathrm{g}}^*}\right) M_{\mathrm{m}} \boldsymbol{I}\right] \tag{III.200}$$

$$\frac{\partial^2 S_{\mathrm{g}}}{(\partial \sigma_{\mathrm{g}}^*)^2} = \frac{2}{(\sigma_{\mathrm{g}}^*)^3}\left[\frac{3}{\sigma_{\mathrm{g}}^*}\left(S_{\mathrm{g}}^{(0)}\right)^{\frac{2}{n}} + 2 q f \kappa \sinh\left(\kappa \frac{M_{\mathrm{m}}}{\sigma_{\mathrm{g}}^*}\right) M_{\mathrm{m}} + \frac{q f \kappa^2}{\sigma_{\mathrm{g}}^*} \cosh\left(\kappa \frac{M_{\mathrm{m}}}{\sigma_{\mathrm{g}}^*}\right) M_{\mathrm{m}}^2\right] \tag{III.201}$$

$$\frac{\partial \boldsymbol{n}_{\mathrm{g}}}{\partial \boldsymbol{M}} = \frac{\partial^2 \sigma_{\mathrm{g}}^*}{\partial \boldsymbol{M}^2} = -\left(\frac{1}{\frac{\partial S_{\mathrm{g}}}{\partial \sigma_{\mathrm{g}}^*}}\right)\left[\frac{\partial^2 S_{\mathrm{g}}}{\partial \boldsymbol{M}^2} + \frac{\partial^2 S_{\mathrm{g}}}{\partial \boldsymbol{M} \partial \sigma_{\mathrm{g}}^*} \otimes \frac{\partial \sigma_{\mathrm{g}}^*}{\partial \boldsymbol{M}}\right] + \left(\frac{1}{\frac{\partial S_{\mathrm{g}}}{\partial \sigma_{\mathrm{g}}^*}}\right)^2 \left[\frac{\partial S_{\mathrm{g}}}{\partial \boldsymbol{M}} \otimes \left(\frac{\partial^2 S_{\mathrm{g}}}{\partial \boldsymbol{M} \partial \sigma_{\mathrm{g}}^*} + \frac{\partial^2 S_{\mathrm{g}}}{(\partial \sigma_{\mathrm{g}}^*)^2}\frac{\partial \sigma_{\mathrm{g}}^*}{\partial \boldsymbol{M}}\right)\right] \tag{III.202}$$

4 Ductile fracture of a helium-implanted austenitic steel

In this chapter, intergranular ductile fracture was modeled at the scale of porous grain boundaries using dedicated yield criteria for void growth and void coalescence. Validation was sought by comparison against porous crystal plasticity simulations. The interesting predictions the analytical models have enabled are satisfying on their own, but the sight of the final applications should not be lost in this process. Indeed, the goal of such studies is to foresee the mechanical behavior and ultimately, the fracture, of real materials. Thus, experimental confirmations of the results obtained so far are needed.

Almost all occurrences of intergranular ductile fracture involve materials with a significant number of grains and no access to local mechanical data (*e.g.* Vasudévan and Doherty (1987)), which means that the homogenized model predictions can only be assessed macroscopically. Calibration of model parameters using these experiments can probably lead to phenomenological agreement, but that does not mean underlying physics are captured correctly. On the contrary, assessing analytical criteria at the microscopic scale through model experiments increases confidence in the physically-based approach. This sub-chapter is devoted to such a model experiment. In order to study the ductile fracture of grain boundaries, a model material with coarse grains is developed so that samples with a unique grain boundary in the gauge section can be obtained. Helium implantation of the material of interest is then performed in order to create voids at the grain boundary (see Section I.1.2.2). This way, the void nucleation stage is excluded from the study, which permits, at least in principle, a comparison between the experimental results and models of intergranular void growth and coalescence.

The main stages of the experimental procedure are summarized in Fig. III.48. The first part details sample preparation, irradiation conditions and implanted sample characterization. Then, the mechanical testing results and fracture surface analysis are carried out in the second part.

4.1 Sample description

4.1.1 Model material

Since a great wealth of data exists on the mechanical behavior and microstructure of austenitic stainless steels and given the fact that they are extensively used in the nuclear field, the research of a model material is restricted to this class of alloys. Three cuboid ingots of size $50\ \text{mm} \times 30\ \text{mm} \times 8\ \text{mm}$ are machined in three different steel grades: 304L, 316L, and a Fe-15Cr-15Ni-Ti alloy called AIM1 whose composition are given in Table III.6. The initial grain size of the 304L steel is $25 \pm 19\ \mu\text{m}$, that of the 316L is unknown and that of AIM1 is $18 \pm 4\ \mu\text{m}$. In a first stage, heat treatments are carried out to obtain very large crystals (ideally over the millimeter) to be able to conduct mechanical testing on a single grain boundary. An AIM1 control ingot is also drilled so that a thermocouple can measure the temperature at its center during the subsequent heat treatment. The four samples are individually subjected to annealing for four hours in an air furnace at $1250\ ^\circ\text{C}$ and immediately water-quenched to stabilize the phases (for 304 steel) and avoid

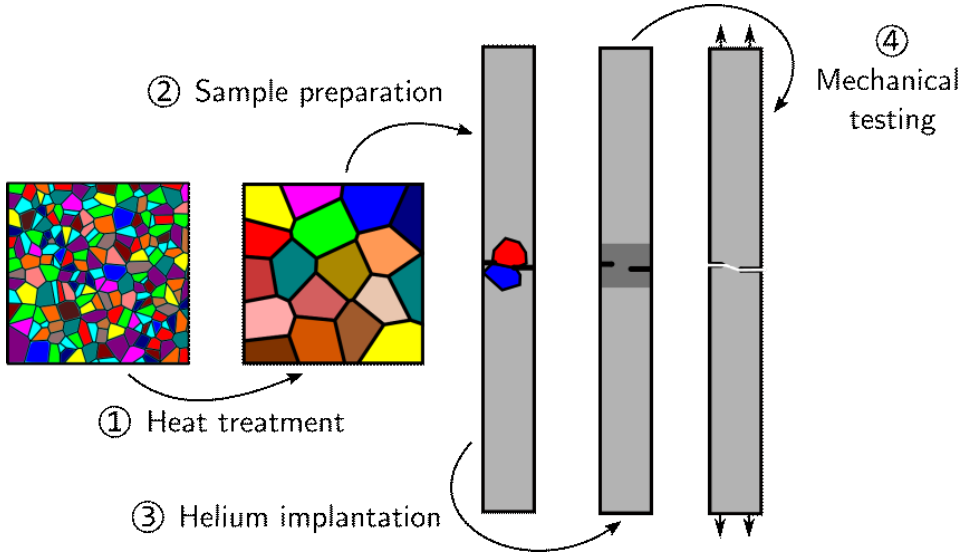

FIGURE III.48: Sketch of the experimental procedure used in this sub-chapter.

Element	Ni	Cr	Mo	Mn	Si	Ti	C	P	N	S
304L weight percentage	8.55	18.75	0.020	1.650	0.450	< 0.05	0.010	0.012	0.10	0.002
316L weight percentage	10.001	16.541	2.027	1.815	0.619	-	0.016	0.026	0.0222	0.0009
AIM1 weight percentage	15.02	14.28	1.51	1.42	0.84	0.399	0.091	0.046	0.006	0.009

TABLE III.6: Elemental weight composition of 304L (Barrioz et al., 2019), 316L and AIM1 steels used in this study. AIM1 steel is from a 2015 cast by Aubert & Duval (reference HR 228401) and its density is $\rho = 7.96$ g $\cdot$ cm^{-3}. Fe is the remaining weight percentage.

unwanted precipitation. This heat treatment is conducted at the Laboratory of Technologies for Extreme Materials (LTMEx) at CEA Saclay. The temperature at the center of the control specimen stabilizes at 1180 °C after 15 minutes, as seen in Fig. III.49. This discrepancy relative to the target temperature (1250 °C) is due to the inhomogeneity of the steady-state temperature inside the furnace; indeed, the heating system is enslaved to a single thermocouple located at a remote location inside the furnace.

A material slice is taken in each of the three specimina. These slices are mechanically polished using standard polishing techniques up to 0.25 µm diamond paste and then electro-chemically etched in order to reveal grain boundaries, including twin boundaries. The electrochemical attack is carried out with an electrolytic solution of nitric acid HNO_3 concentrated to 60% and a stainless steel cathode, the anode — *i.e.* the sample — being placed in front of the cathode at a distance of around 5 centimeters. A constant intensity of 0.1 A is then enforced for approximately 2 minutes to obtain satisfying results. Three optical micrographs showing the grain morphology are shown in Fig. III.51. The average grain size that is obtained varies from 75 ± 50 µm for the 304L grade to around 110 ± 100 µm for the 316L grade and approximately 320 ± 220 µm for the AIM1 grade. The grain size for AIM1 is checked using EBSD, confirming that the electrochemical etching did reveal all the grain boundaries. In Fig. III.51a,b, the second phase is composed of ferrite grains, as is verified by EBSD analysis. On Fig. III.51c, the orange particles with square section and diameter of 6 ± 4 µm are Ti(C,N) inclusions while dark particles with round shapes and diameter of 5 ± 3 µm are probably (Ti,Mo)C inclusions, both being well-known second-phase particles in AIM1 (Courtin, 2015).

Since the AIM1 alloy exhibits the most important grain growth, this material is chosen and subjected to an additional heat treatment of six hours at 1250 °C in the same furnace and immediately water-quenched. A grain morphology examination is carried out again in Fig. III.52: it is seen that the average grain size reaches around 410 ± 200 µm (see Fig. III.52a) and that the length of some grains can exceed 1 mm (Fig. III.52b). This grain size is believed to be saturating (see for instance grain growth kinetics in Stanley and Perrotta (1969)) so no further heat treatment is conducted. Ti(C,N) inclusions are not noticed anymore while individual (Ti,Mo)C inclusions have grown to 18 ± 8 µm diameter and seem to have coalesced in many locations. A significant part of them are intergranular inclusions, which have probably blocked further migration of the grain boundaries. Following that examination, the AIM1 sample is tempered at 450 °C during 5 hours in an air furnace in order to relieve internal stresses induced by the quench, which may have resulted in the bending of thin samples machined from the ingot.

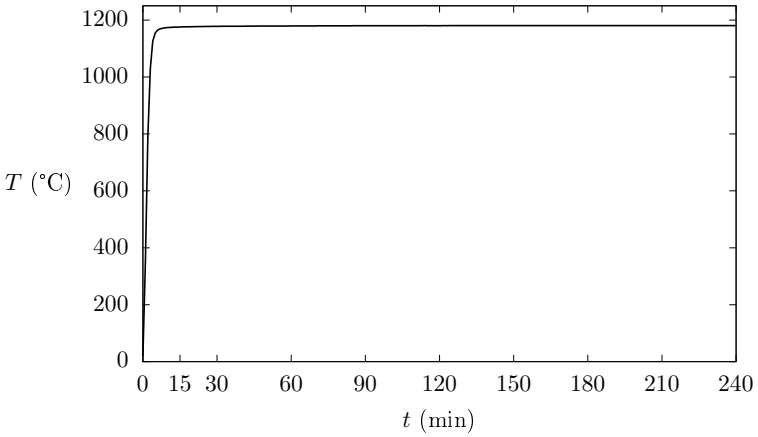

FIGURE III.49: Temperature measured at the center of the AIM1 control specimen during the 4-hour heat treatment at 1250 °C.

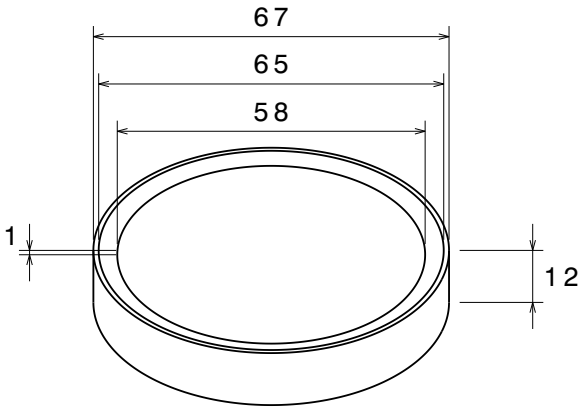

FIGURE III.50: Aluminum support for manual mechanical polishing; dimensions are given in mm.

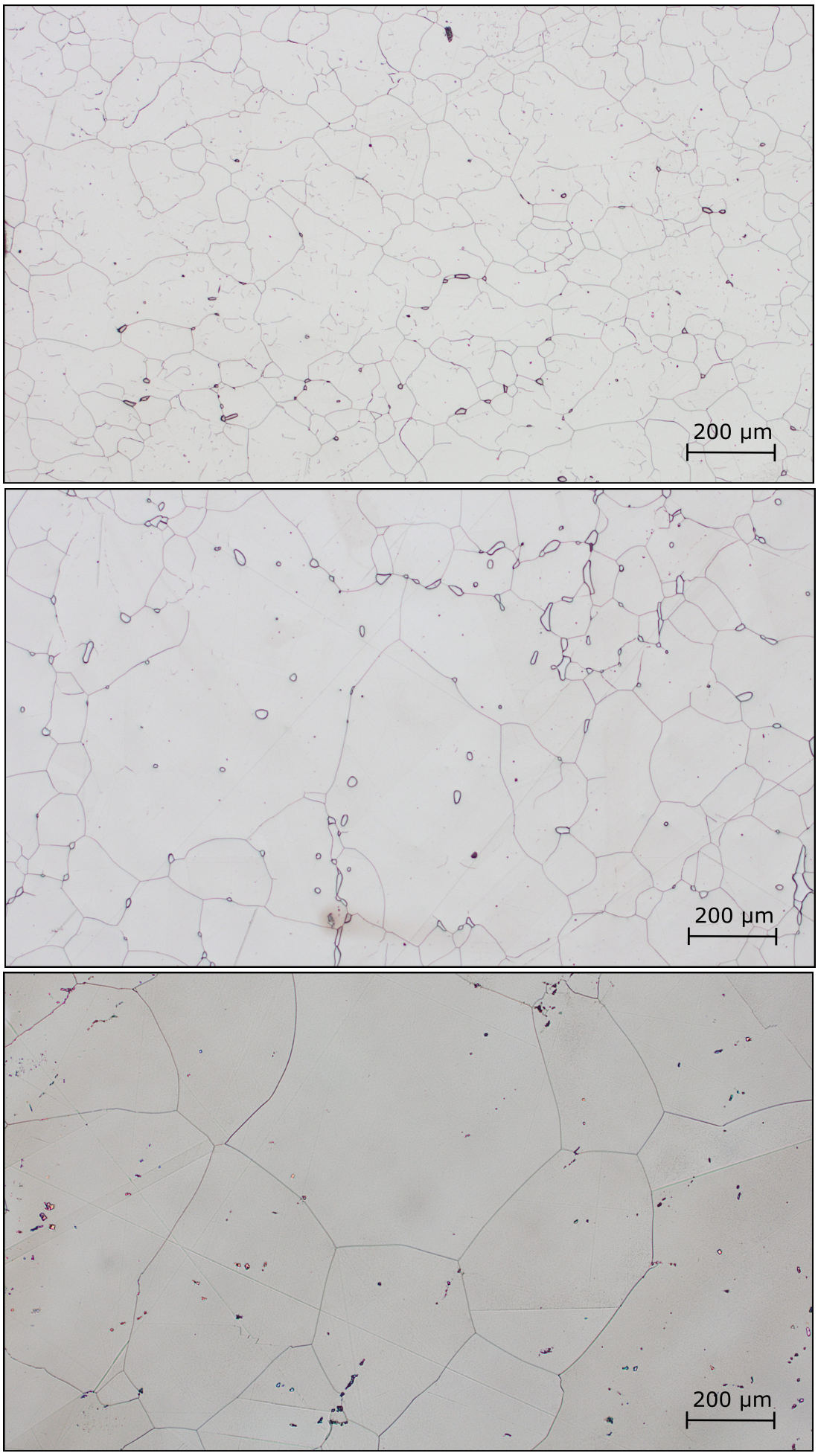

FIGURE III.51: Optical micrographs of electro-chemically etched samples showing the grain morphology after the first heat treatment (4 hours at 1200 °C): (**a**) 304L; (**b**) 316L; (**c**) AIM1.

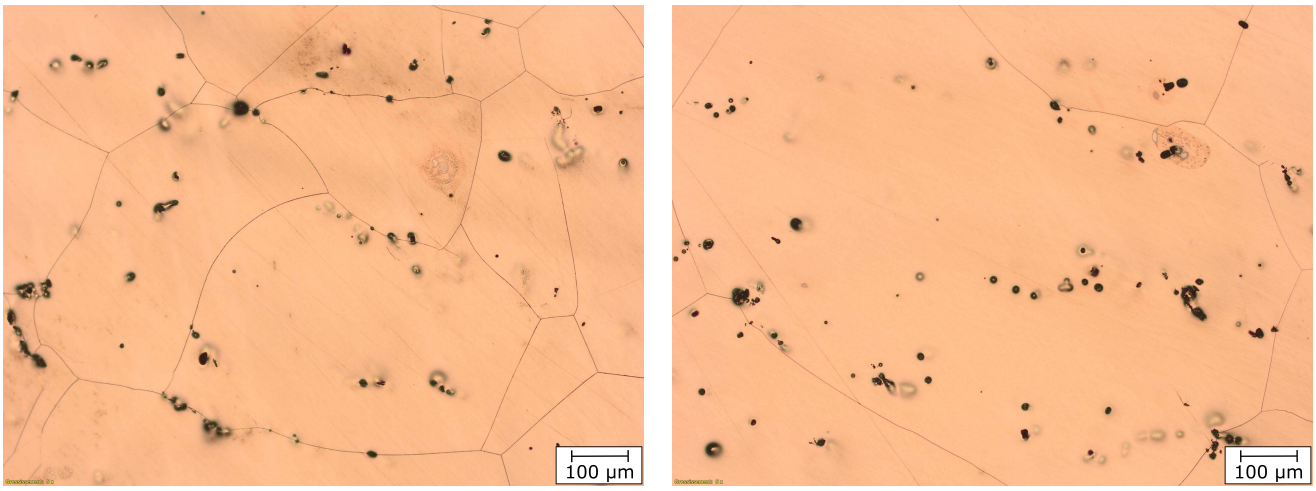

(a) (b)

FIGURE III.52: Optical micrographs of the AIM1 sample after the second heat treatment (6 hours at 1200°C).

4.1.2 Sample preparation

The main stages of the sample preparation are summarized graphically in Fig. III.53 and described in greater length in the following.

To obtain thin samples, rectangular sheets of 800 µm thickness are prepared from the heat-treated AIM1 ingot by electrical discharge machining. First, these sheets are glued on an aluminum support (see Fig. III.50) with CrystalBond wax so that the wax film between the sheets and the support is of minimal thickness and as plane as possible. Then, the samples are thinned down to 45 µm by mechanical polishing following a technique developed in Barrioz (2019): SiC grinding paper with grit of 320 is used up to 200 µm thickness, grit of 600 up to 100 µm and grit of 1200 until the final thickness. This thickness is chosen to enable helium implantation in the samples' bulk (see Section III.4.1.3). The 1 mm thick flange on the aluminum support — which broadens during the thinning process — helps to balance the mechanical polishing. Furthermore, four cardinal points are marked on the flange. The thickness of the flange is regularly measured on these points with a dial indicator — every 100 µm removal at the beginning of thinning up to 5 µm removal at the end of thinning — to ensure the parallelism of the samples faces. Any deviation is corrected by offsetting the point on which pressure is applied on the support. However, below 80 µm thickness, increased thinning of the support flanges as well as the edges of the steel sheet is noticed. To alleviate this phenomenon, a significant thickness of wax should encompass the sample on all sides. Moreover, only the center part of the sheet, where the faces are almost parallel, should be used. After this process, the sheets are mirror polished using standard polishing techniques: successive use of 3 µm, 1 µm, and 0.25 µm diamond paste, and then vibratory polishing performed during 4 hours with a colloidal silica solution (particle size of 0.05 µm, pH = 7) to remove any surface hardening from previous polishing steps. It is checked that the thickness loss due to the stages performed after thinning can be neglected. The sheets are cleaned carefully on a fine polishing cloth soaked with soap and water, and then with ethanol. Finally, the thin sheets are unstuck by heating the wax. The wax is removed by immersing the sheets in a beaker full of acetone in an ultrasonic cleaner. The same stage is subsequently performed with a beaker full of ethanol. The full thinning and polishing process takes about four hours.

Following that stage, it is expected that there is only one grain in the thickness of AIM1 sheets, since the average grain size is around five times the thickness of the sheets. Thinned sheets are stuck on a metal support using strong machining scotch and six rectangular samples (denoted B2 to B7) of length $l_1^0 = 20$ mm, width $l_2 = 1$ mm and thickness $l_3 = 45 \pm 2$ µm are machined arbitrarily in the center zone of sheets using micro-milling, with 0.1 mm precision on l_1^0 and l_2. The corresponding frame of reference $(\underline{e}_1, \underline{e}_2, \underline{e}_3)$ is defined for each sample. A control sample (denoted B1) of width $l_2 = 2$ mm is also prepared. Samples are then unstuck by immersing the machining scotch in acetone for 24 hours.

In order to reveal grain boundaries, surface abrasion is carried out using the focused ion beam (FIB) of a FEI Helios 650 NanoLab SEM-FIB with a Ga ions beam. Indeed, the differential abrasion speed experienced by crystals induces a contrast that can reveal the grain microstructure. Several mappings are performed by imaging each zone

of interest with the maximal ion intensity available (65 nA). With such intensity, an area of 0.6 mm^2 is imaged in approximately two hours. Grain boundaries that are both long and whose projection on the observed surface displays an angle inferior to 45° relatively to $\underline{e}_1$ are chosen in each sample. Two through-thickness notches are then drilled in the sample using FIB to ensure that only the grain boundaries of interest will be loaded mechanically. This process takes four to seven hours, depending on the notch radius. The grain morphology and notches are shown in Fig. III.54 for the six tensile samples (B2 to B7). The length of each sample is then reduced to $l_1 = 18$ mm using precision scissors and ensuring that the notches are located at mid-length of each sample.

EBSD mapping is performed using a JEOL IT300 SEM with tungsten filament equipped with an OXFORD EBSD detector to access the crystallographic orientations of grains from either side of each chosen grain boundary. Orientations are given in Table III.7 according to the frame of reference $(\underline{e}_1, \underline{e}_2, \underline{e}_3)$ of the sample. The grain boundaries of B2 and B4 are (twin) **Σ3**-boundaries while the grain boundaries of B5 and B7 display respective misorientations of 43.5° and 50.8°. In sample B6, the misorientation between crystal 1 and crystal 2 is 53.7° whereas it is 56.8° between crystal 1 and crystal 3.

Sample	Crystal	ϕ_1 (°)	Φ (°)	ϕ_2 (°)
B2	1	213.0	143.1	234.8
	2	319.3	157.4	282.9
B3	1	29.2	157.2	31.1
B4	1	191.4	155.3	208.1
	2	30.6	137.9	57.7
B5	1	267.5	130.0	225.6
	2	234.5	137.4	239.6
B6	1	1.3	133.3	13.0
	2	205.5	127.8	239.0
	3	298.0	134.3	290.6
B7	1	250.6	140.6	266.4
	2	0.1	139.2	252.1

TABLE III.7: Euler angles (Bunge convention) of the crystals in the notch zone of samples, according to the numbering given in Fig. III.54.

4.1.3 Helium implantation

Irradiation sample holder Before helium implantation, the seven samples (B1 to B7) are put in the rectangular area of 18.2 mm per 10 mm (shown in green) of the specimen support of Fig. III.55 using plastic tweezers. The length of the samples is horizontal, their width is vertical, and the polished surface is facing forward. The cumulated width of the samples being 8 mm, the remaining 2 mm is used to space evenly the samples, which is more convenient to manipulate them. The specimen support is then closed using the irradiation mask (also presented in Fig. III.55), which is held tight by four M2 screws (shown in blue). The samples are thus maintained between the irradiation mask's extra thickness and the flanges of the specimen holder (shown in brown) but are still able to lengthen or widen due to thermal expanse. The irradiation mask has a transmission slot of 10 mm per 1 mm (shown in orange) so that an area of 1 mm length centered on the FIB notches is implanted in each sample. This enables to reduce the activation of the samples by ensuring that only the area of interest (1 mm × 10 mm) is irradiated. The specimen support has a window on the rear side to allow temperature measurements from the back of the specimen. Two vertical M3 screws at the bottom of the specimen holder (shown in red) are used to fix the sample holder on the implantation set-up. Finally, the last couple of M2 screws (shown in magenta) are used to attach a piece of graph paper in front of the transmission slot of the irradiation mask. This paper darkens when irradiated so that it is used to adjust the position of the ion beam before the implantation. Once the beam is correctly aligned with the

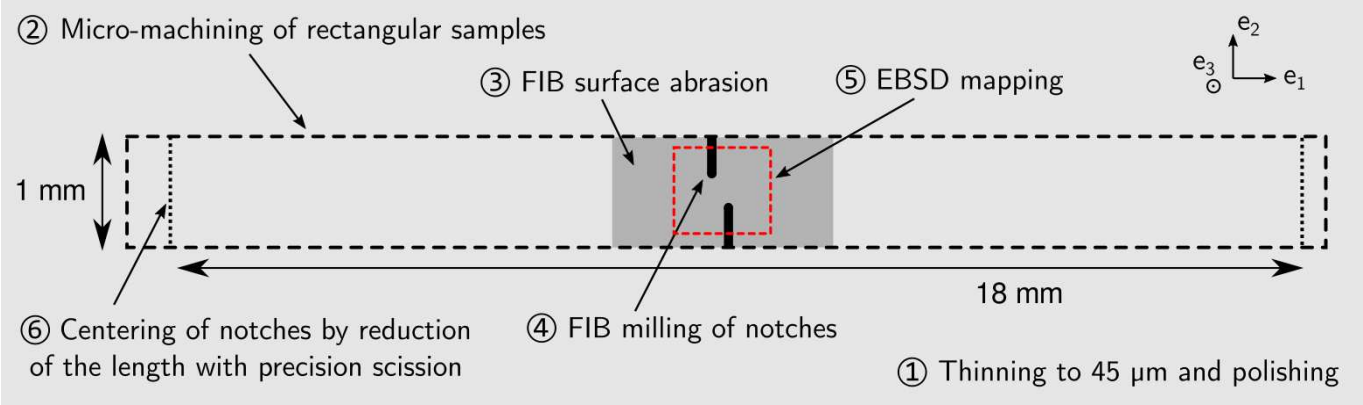

FIGURE III.53: Sketch of the successive stages of sample preparation.

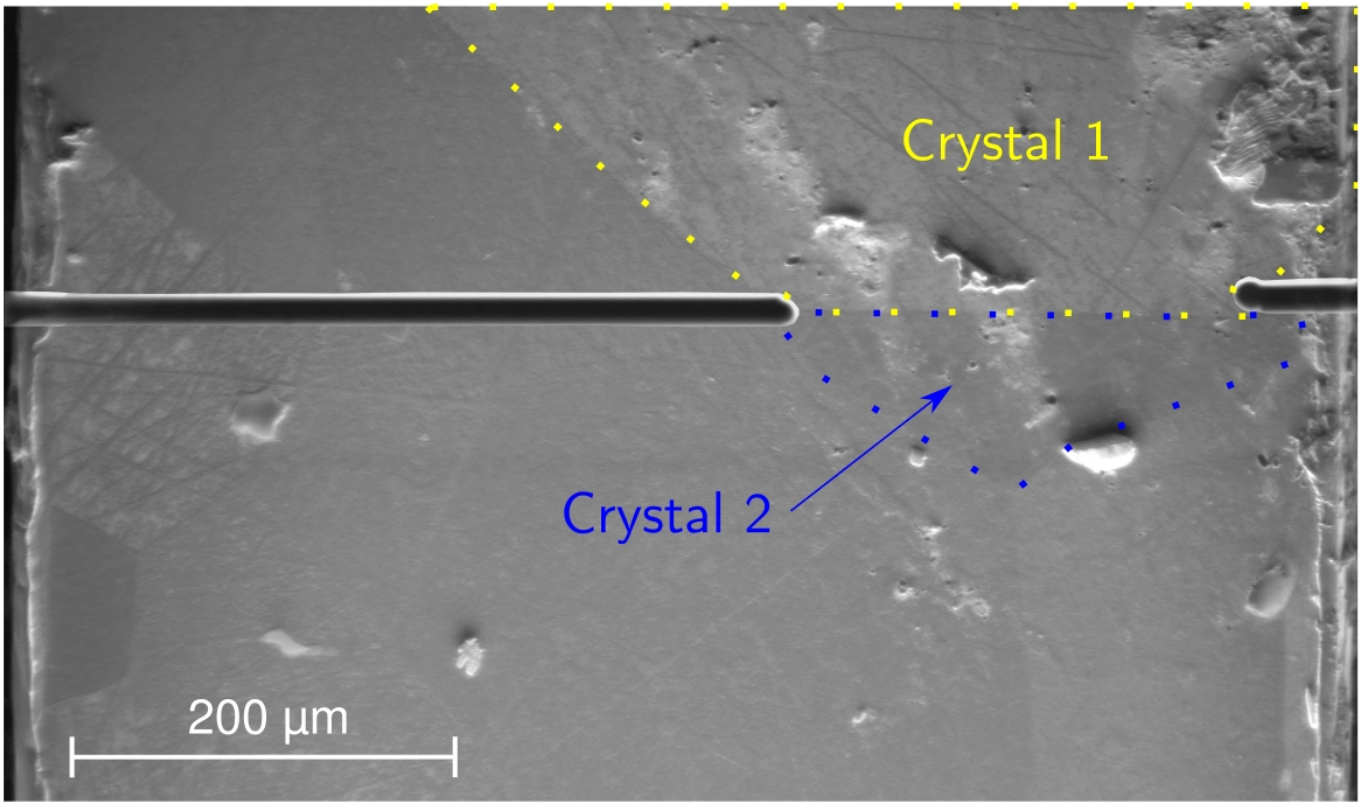

(**a**) Sample B2 (notch radius of 7 µm)

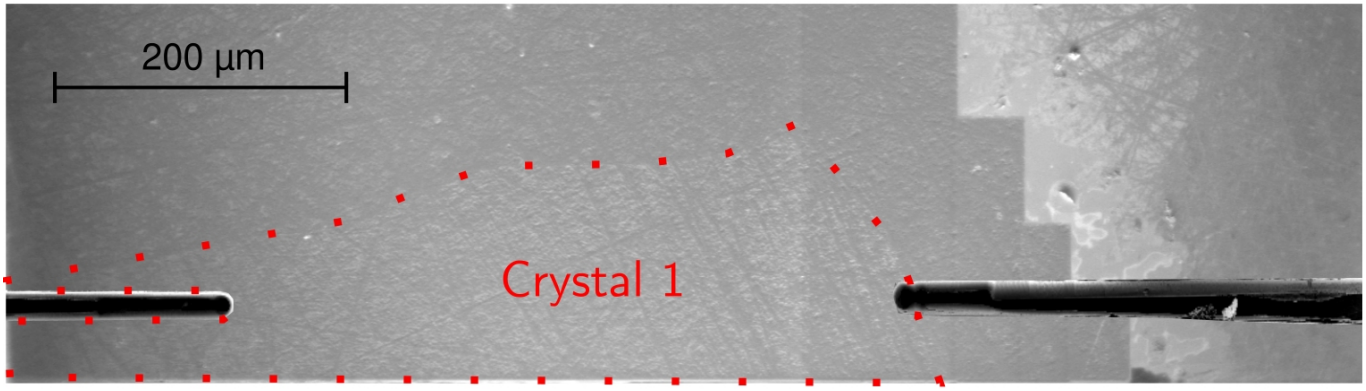

(**b**) Sample B3 (notch radius of 7 µm)

FIGURE III.54: Morphology of the gauge area of samples after the drilling of FIB notches. Imaging is performed with the ionic beam (30 kV, 65 pA). Micrographs after and before milling are merged to allow the visualization of crystals. By convention, $\underline{e}_1$ points upward.

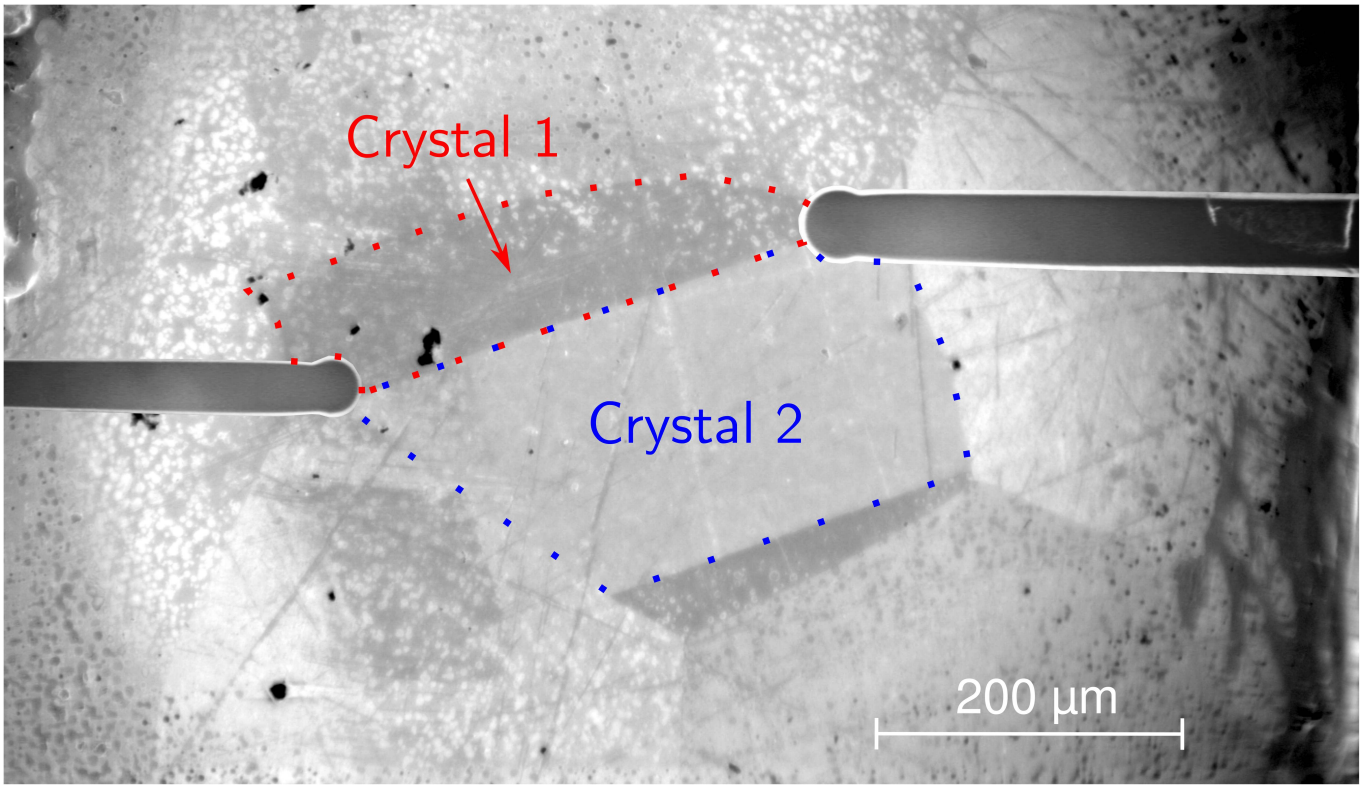

(**c**) Sample B4 (notch radius of 20 µm)

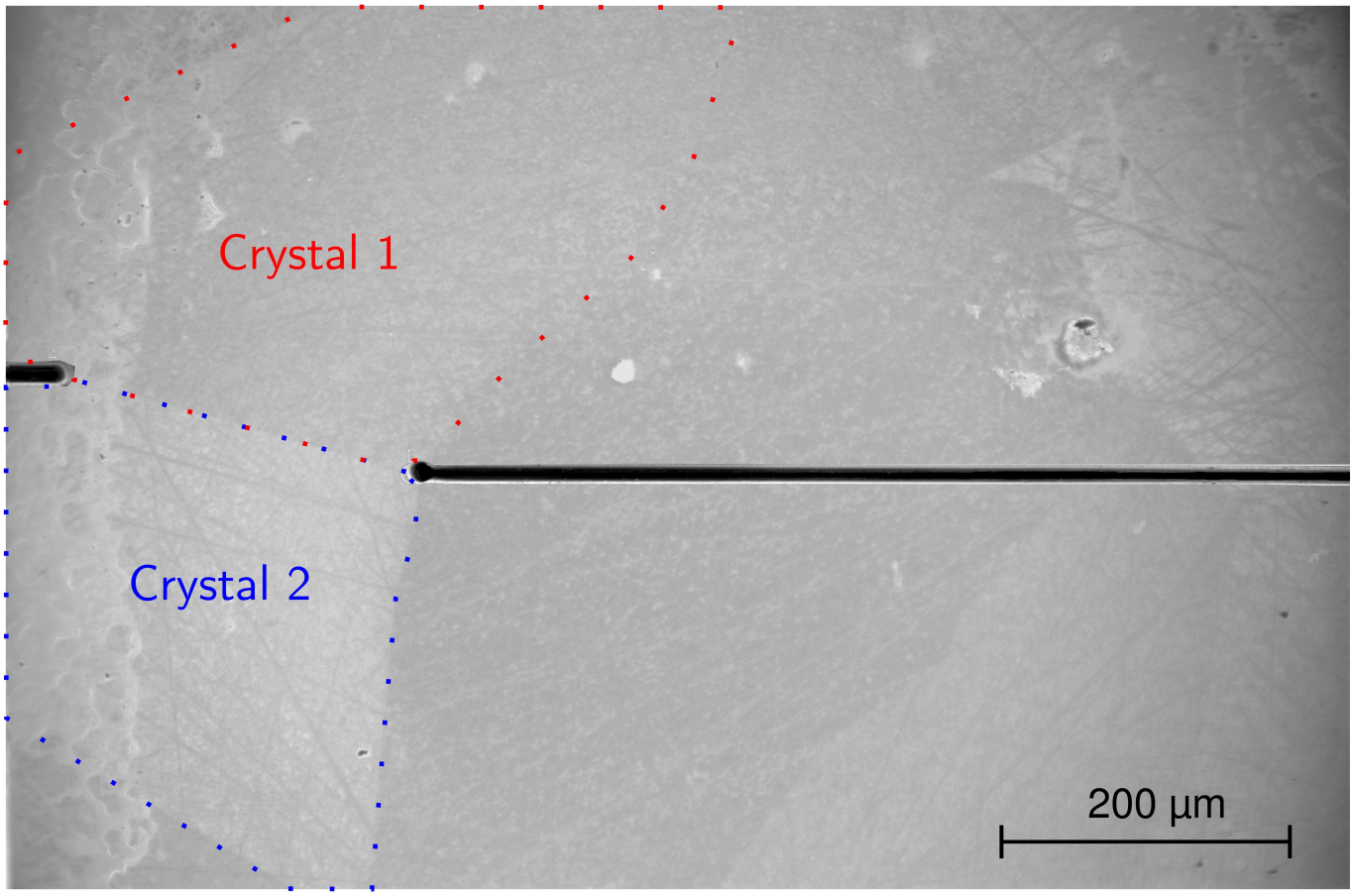

(**d**) Sample B5 (notch radius of 7 µm)

FIGURE III.54: Morphology of the gauge area of samples after the drilling of FIB notches. Imaging is performed with the ionic beam (30 kV, 65 pA). Micrographs after and before milling are merged to allow the visualization of crystals. By convention, $\underline{e}_1$ points upward.

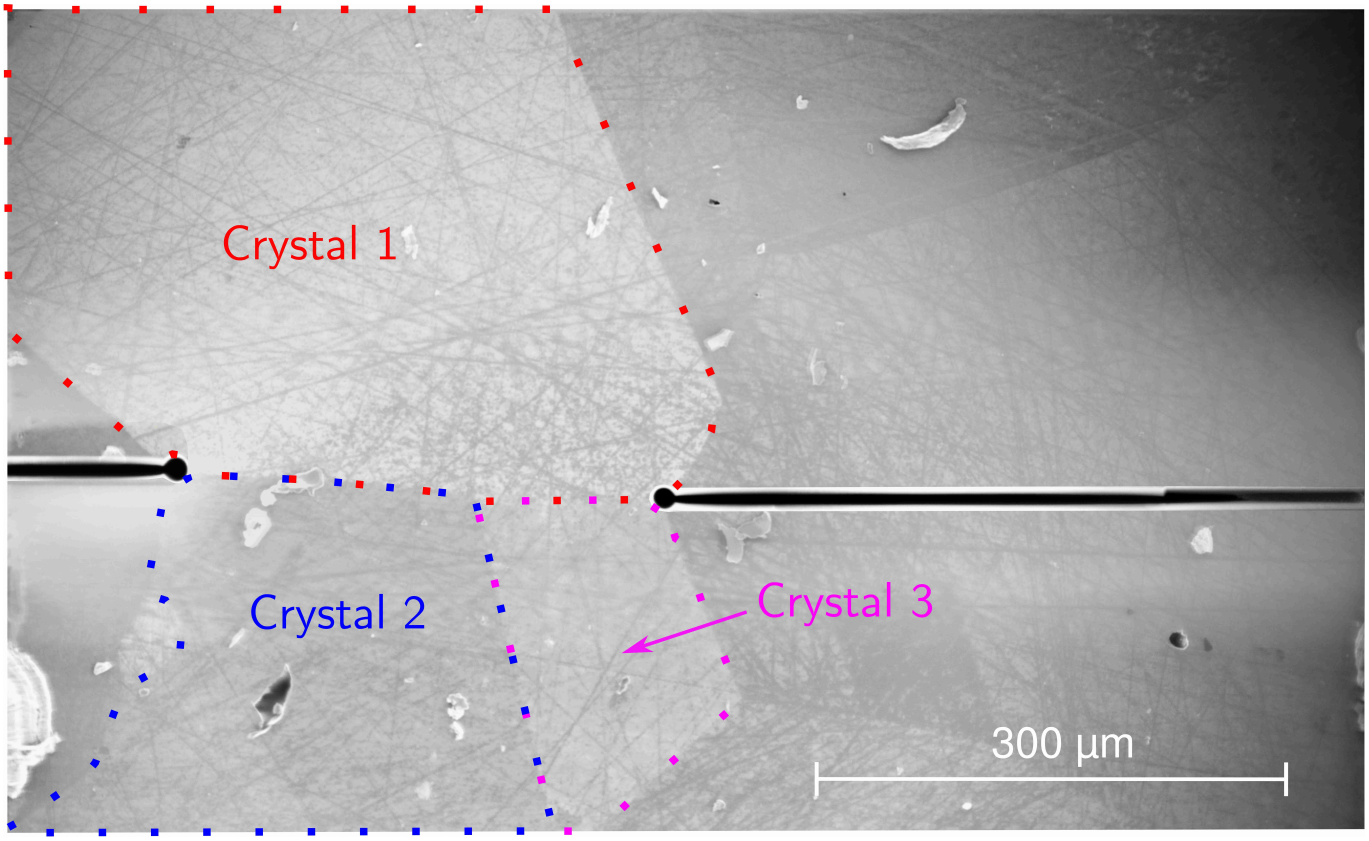

(**e**) Sample B6 (notch radius of 7 µm)

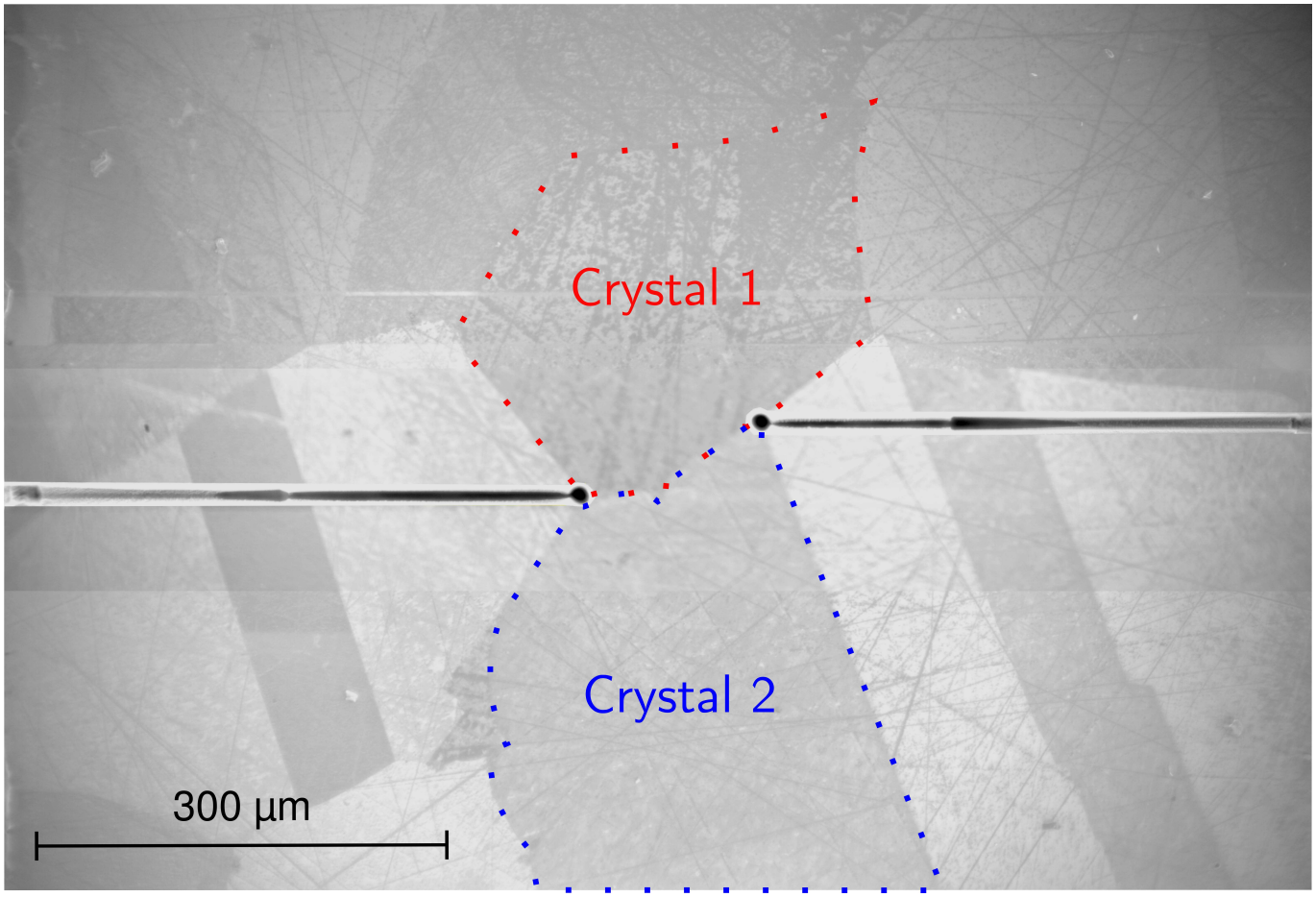

(**f**) Sample B7 (notch radius of 7 µm)

FIGURE III.54: Morphology of the gauge area of samples after the drilling of FIB notches. Imaging is performed with the ionic beam (30 kV, 65 nA). Micrographs after and before milling are merged to allow the visualization of crystals. By convention, $\underline{e}_1$ points upward.

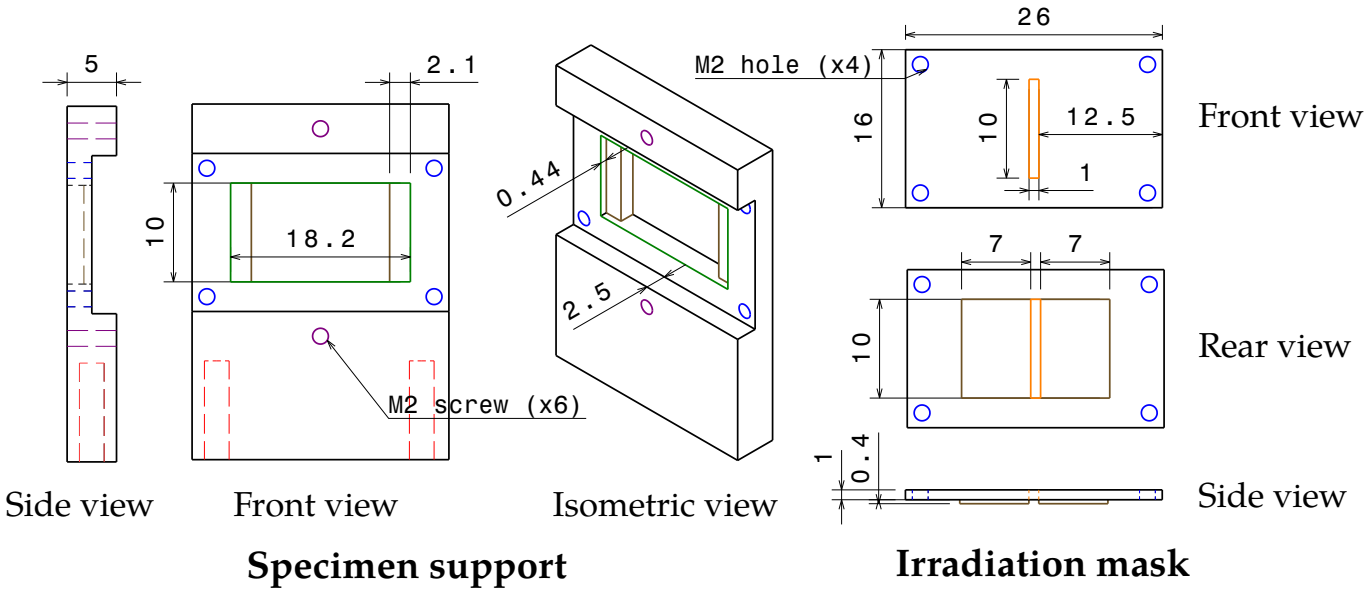

FIGURE III.55: Sample holder designed for helium implantation; dimensions related to the samples are given in millimeters, other are omitted for the sake of readability.

collimation window, the paper is removed and the implantation can begin.

Implantation conditions The objective of the irradiation is to obtain a concentration of helium in the bulk of the samples that would be sufficient to trigger intergranular fracture. Based on the study of Miura et al. (2015), a target concentration of 1.8 atomic percent is set. Furthermore, contrary to neutrons, ions have difficulty penetrating dense matter due to electronic interactions. Thus, a high-energy beam is required to implant the samples at an important thickness. Therefore, the helium implantation is conducted at the cyclotron of CEMHTI at CRNS Orléans (Fig. III.56). The scaling and realization of the irradiation stems from a collaboration with Dr. Thierry Sauvage of CEMHTI and Dr. Jia-Chao Chen of Paul Scherer Institute (Switzerland). The implantation set-up inside the irradiation cell is shown in Fig. III.58. The cyclotron beam is composed of 28 MeV α particles whose remaining energy is 25 MeV after crossing the vacuum window (25 µm-thick Hastelloy foil) which guarantees a high vacuum in the beam line. Behind the vacuum window, the irradiation chamber is under a purified helium atmosphere to avoid oxidation of the samples. Since a mono-energetic beam of 25 MeV α-particles would be implanted at a depth of 116 µm with little dispersion (see Fig. III.57), it is necessary to reduce that energy (the maximal energy needed to penetrate 45 µm is 14 MeV) and modulate it to obtain an almost-homogeneous helium concentration through the sample thickness. Thus, multi-energy implantation is fulfilled with an aluminum degrader wheel with 24 different thicknesses ranging from 165 to 271 µm. Implantation is only carried out from one side of the specimina. The obtained helium profile will be detailed later (Fig. III.59).

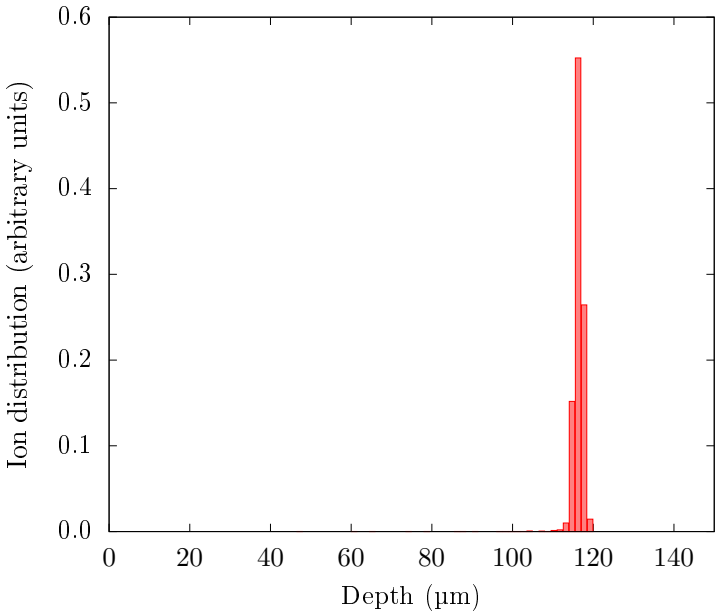

FIGURE III.57: Implanted helium depth distribution profile for a 25 MeV mono-energy incident beam on AIM1 steel, as computed by SRIM-2013 (Ziegler et al., 2010). The discrete distribution has steps of 1.5 µm width and its integral is normalized to 1.

The beam size is adjusted using four quadrants cooled with demineralized water. The aperture between horizontal quadrants corresponds to 3 mm while the distance for vertical quadrants is 12 mm. The implantation area is

(**a**)

(**b**)

FIGURE III.56: Cyclotron of CEMHTI: (**a**) exterior view of the irradiation cell whose entry is closed by a reinforced door, with the helium gas cooling and purification system on the right-hand side; (**b**) control room of the cyclotron, which continuously require two operators.

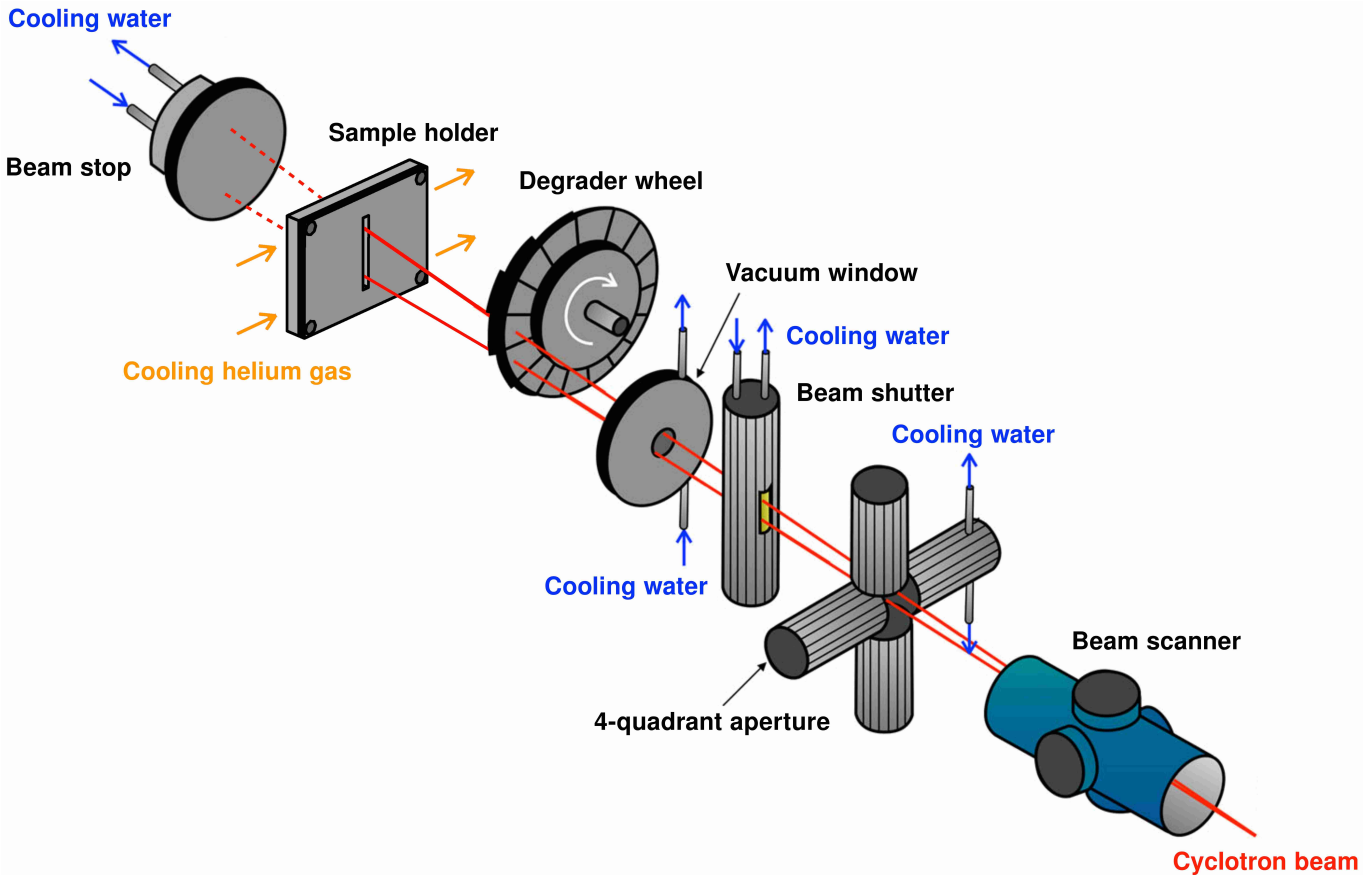

FIGURE III.58: Sketch of the helium implantation set-up CH3ILDS (Chamber for Hydrogen or Helium Homogeneous Implantation at Large Depth in Sample) receiving the cyclotron beam, adapted from Villacampa et al. (2017).

larger than the area of interest to maximize homogeneity. Before the 4-quadrant aperture, the beam size is 6-7 mm. During implantation, currents on each quadrant are monitored to ensure the stability along $\underline{e}_1$ and $\underline{e}_2$ of the upstream beam. The beam is scanned with a Lissajous pattern in the plane $(\underline{e}_1,\underline{e}_2)$ with a frequency of 7 Hz and a resolution of 15, *i.e.* a dwell time of 2 seconds.

The temperature is monitored from the backside of the specimens by a pyrometer. The irradiation temperature is limited to 200°C to avoid microstructure changes in the material. Since the very energetic beam induces heating of

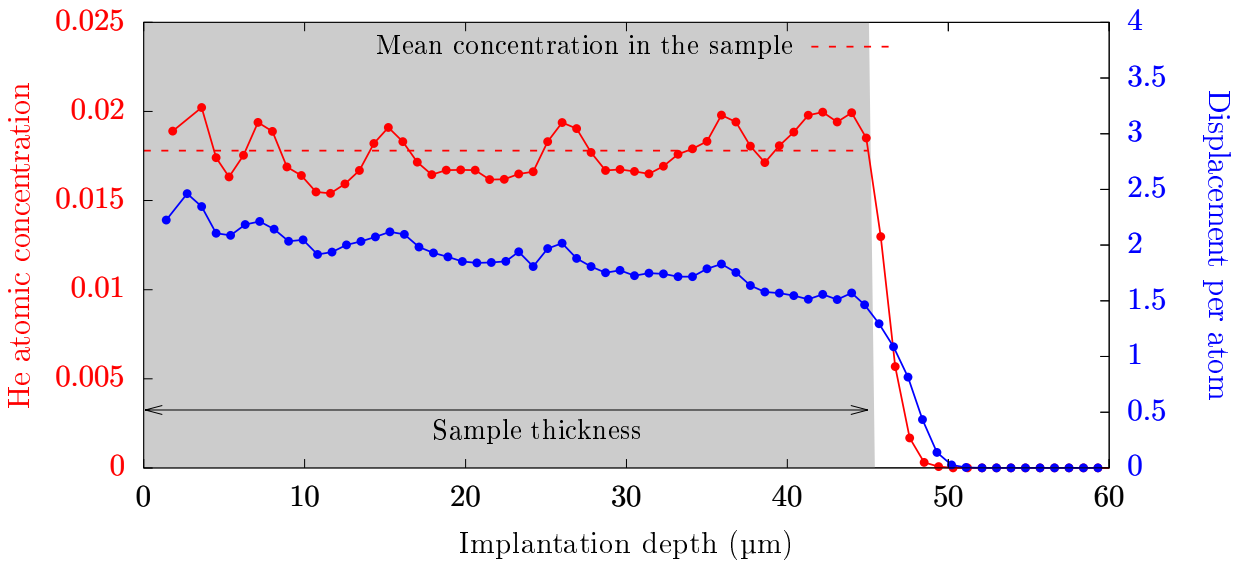

FIGURE III.59: Simulated helium atomic concentration and displacement per atom profiles in AIM1 steel after implantation. The average helium atomic concentration throughout the thickness of the samples used here is shown with a dashed line.

the samples, temperature control is conducted with an adjustable jet of purified helium gas at 18°C (see Fig. III.56a) geared towards the samples in the irradiation chamber. Thus, when the beam is on, the temperature is 200 ± 10 °C. Temperature homogeneity across the irradiated area's main axis is regularly checked with the pyrometer.

The beam intensity directed at the target is measured each hour by a beam stop located in the high vacuum zone — between the vacuum windows and the beam shaping section — with an error inferior to 7%. The beam stop is cooled by demineralized water. The raw average intensity during the $\Delta t = 45.3$ hours (across four consecutive days) of irradiation is $I = 5.46$ µA. Intensity measurements should be scaled down by a factor $f_c = 1.1$ because secondary electrons generated by the beam stop due to the incident α beam are also measured. The implantation fluence is then:

$$F = \frac{I\,\Delta t}{S\,q_\alpha\,f_c} \tag{III.203}$$

where $q_\alpha = 3.2 \cdot 10^{-19}$ C is the elementary charge of α particles and $S = 10$ mm^2 is the implanted area. Thus, $F = 7.02 \cdot 10^{18}$ He $\cdot$ cm^{-2}, which corresponds to an average flux of $4.30 \cdot 10^{13}$ He $\cdot$ cm^{-2} $\cdot$ s^{-1}. Since the atomic density of the target is $N = 8.55 \cdot 10^{22}$ at. $\cdot$ cm^{-3} and the irradiated depth is $e = 46$ µm (note that $e > l_3$), the final mean helium atomic concentration is $c_{\mathrm{He}} = F/(eN) = 1.78\%$. This corresponds to an average He implantation rate of 393 appm $\cdot$ h^{-1}.

The helium profile in the implanted AIM1 is calculated by `SRIM-2013` (Ziegler et al., 2010) by carrying one computation per distinct thickness of aluminum degrader; three layers are modeled: a layer of aluminum of a given thickness, a layer of helium gas that is supposed not to interact with the incident beam, and a layer of AIM1 with infinite thickness. The helium concentration profile in AIM1 is then obtained by summing the individual ion distributions corresponding to the chosen degrader thicknesses; it is shown in Fig. III.59. As can be seen, the implanted concentration does not vary much around its average. The vacancy production rate (in vacancy per He atom and per unit length) is also computed by `SRIM` with Kinchin–Pease (K–P) approach as described by Stoller et al. (2013) with a displacement energy for Fe, Cr and Ni of 40 eV (ASTM E521, 2006). The number of displacements per atom d is linked to the vacancy production rate v and the fluence F through $d = Fv\rho/M$, where ρ and M are respectively the density and the molar mass of the target material. Contrary to the helium concentration, the damage profile decreases with increasing depth, as shown in Fig. III.59. Nevertheless, the extreme values (1.46 dpa on the back side of the specimen and 2.46 dpa on the front side) do not wander too far from the average (1.88 dpa), so this variation is disregarded when interpreting mechanical tests.

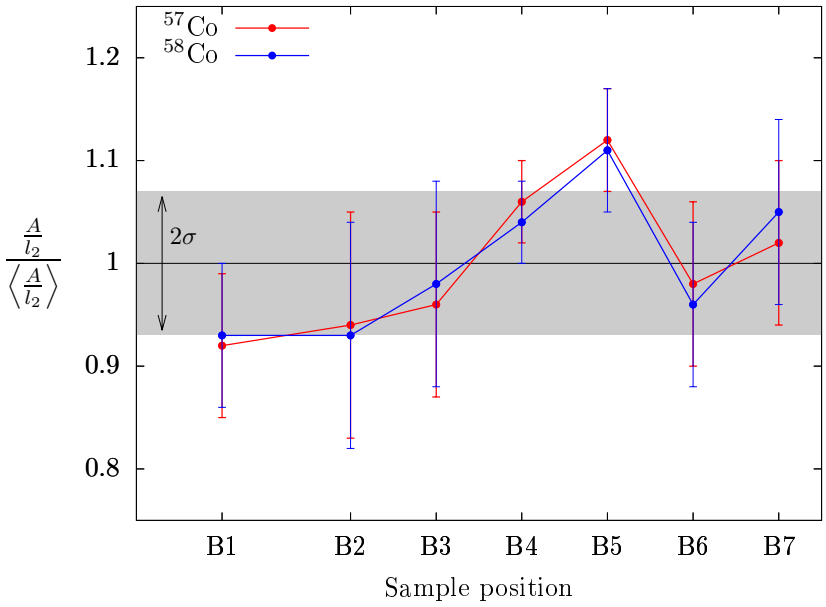

FIGURE III.60: Normalized activity A to sample width l_2 ratio for ^{57}Co and ^{58}Co radioisotopes. The error bars combine width and activity measurement uncertainties. The standard deviation $\sigma = 7\%$ is reported on the graph.

4.1.4 Quantification of the implantation homogeneity

Due to the high energy of α particles used, the samples did activate under irradiation, with two significant radioisotopes produced: ^{57}Co (half-life of 270 days) and ^{58}Co (half-life of 70 days). For instance, the reaction $^{56}\mathrm{Fe} + \alpha \rightarrow {}^{58}\mathrm{Co}$ is activated for energies superior to 7.5 MeV. The homogeneity of the implantation was checked by counting the activity of ^{57}Co (122 keV peak) and ^{58}Co (811 keV peak) with a High-Purity Germanium (HPGe) radiation detector. The thickness and the collimation being identical for all samples, the helium concentration is proportional to A/l_2, with A the activity (measured during 1000 seconds). The results are gathered in Fig. III.60. As expected, there is a concentration peak for the samples in the middle (B4, B5) compared to samples on the edges (B1, B2, B6). However, the standard deviation of the normalized activity (and thus helium concentration) is only 7%. Combined with the uncertainty on the beam intensity, it means that the total relative error on the helium content is 10%: $c_{\mathrm{He}} = 1.78 \pm 0.18\%$

Since the activity quantification was carried out 61 days after the end of the irradiation, the total activity at the end of irradiation can be computed using depletion laws: $1.35 \cdot 10^4$ Bq of ^{57}Co and $2.53 \cdot 10^4$ Bq of ^{58}Co. On the same day, a measure of the γ-radioactivity outside of the membrane box of sample B2 brought $0.5\ \mu\mathrm{Sv} \cdot \mathrm{h}^{-1}$, for a background noise of $0.2\ \mu\mathrm{Sv} \cdot \mathrm{h}^{-1}$. The total activation (α, β, γ) measures over the front side of a 1 mm-width sample never exceed 50 counts per second (value reported for B5), for a background noise of 1.25 ± 0.25 counts per second.

4.1.5 Quantification of oxidation after implantation

Upon disassembly of the sample holder, it was noticed at the optical microscope that an oxide had developed on the back side of some samples (see Fig. III.61a), despite the helium atmosphere and the 200°C temperature threshold. Thus, it appeared necessary to quantify this oxidation to ensure that it would not influence the mechanical and fracture behavior of the samples.

Nuclear reaction analysis (NRA) is performed to estimate the chemical contamination according to depth in irradiated samples without causing any mechanical alteration. NRAs are carried out with 900 keV deuterons and a detection angle of 178° on the back side of sample B1; this choice is more convenient because the NRA beam area is 1 mm^2 can fit in the 2 mm width. The analyzed depth is material-dependent; it is approximately 1 µm for austenitic stainless steels. α particles from reaction $^{16}\mathrm{O}(\mathrm{d},\alpha)^{14}\mathrm{N}$ and protons from $^{12}\mathrm{C}(\mathrm{d},\mathrm{p})^{13}\mathrm{C}$ are detected at 178° and are used to quantify the oxygen and carbon that sorbed into the sample during irradiation. Peak areas corresponding to

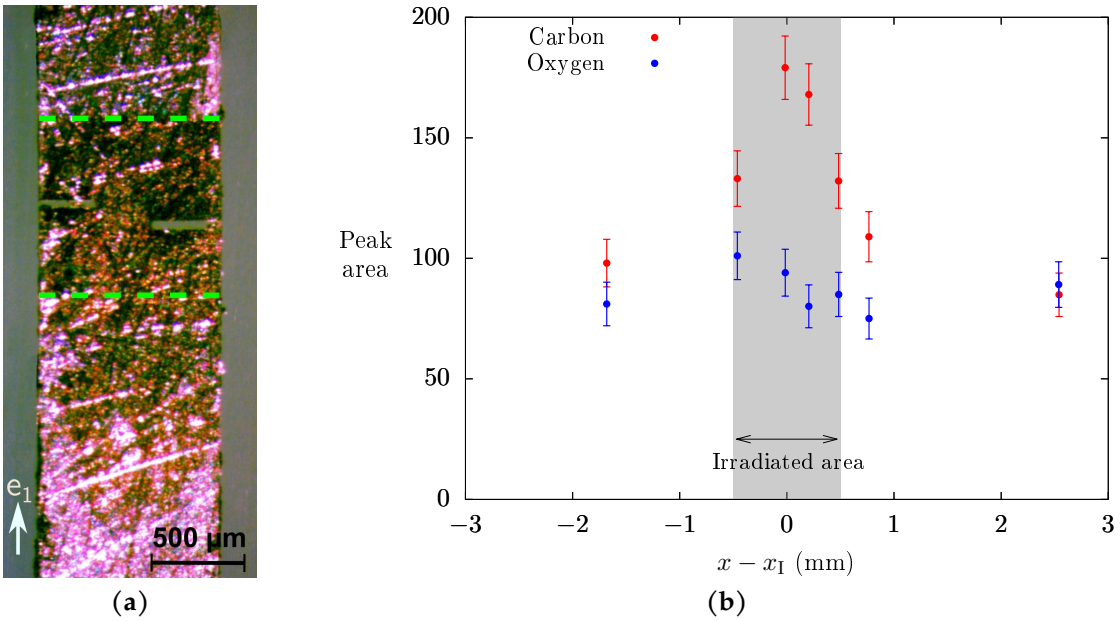

FIGURE III.61: Contamination of the samples' back side: (a) optical micrograph of the back surface of B4 sample after irradiation, with the implanted area shown between green dashed lines; (b) NRA data for carbon and oxygen on the back surface of B1 sample, around the irradiated zone. The measured area of the peaks (arbitrary units) corresponding to the nuclear reaction of oxygen (centered on channel 541) and carbon (centered on channel 615) are obtained from the NRA counting spectra (counts versus channel).

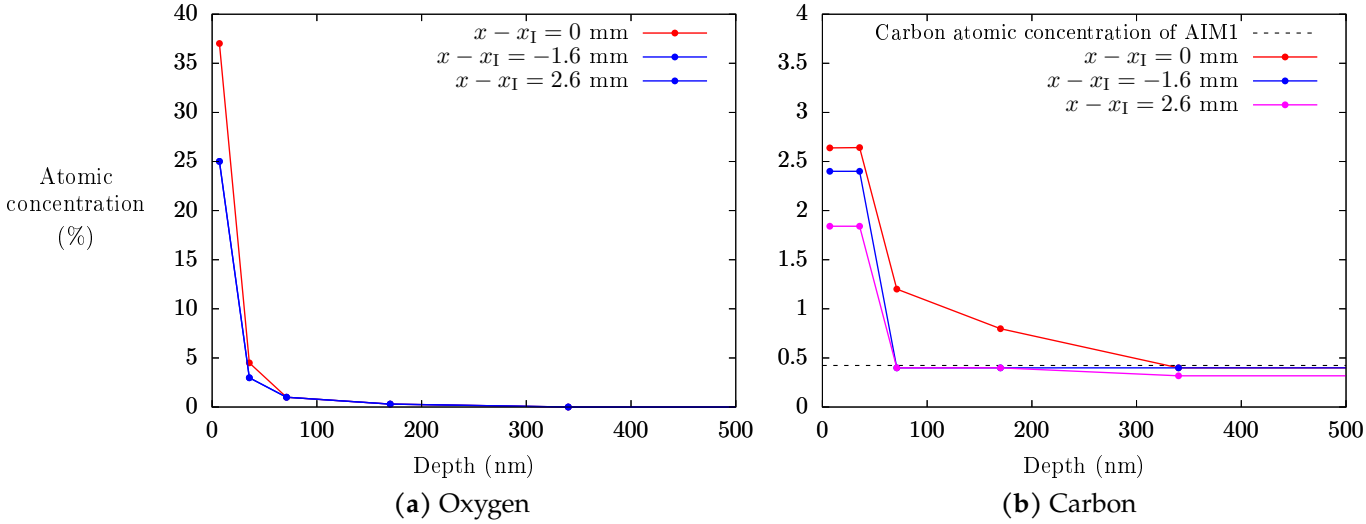

(**a**) Oxygen (**b**) Carbon

FIGURE III.62: Atomic concentration profiles obtained by NRA on three locations of the back surface of sample B1. Note that two indistinguishable profiles were represented with the same color in (**a**).

the two reactions are measured on several points of B1 with a reduced 5 μC charge to identify the irradiated zone precisely. Carbon contamination is almost always observed after intense ionic implantation (*e.g.* Wang et al. (2017), Was et al. (2017), and Gigax et al. (2017)). Based on this finding, the contrast in the data for carbon is used to determine precisely the irradiated zone. Since the beam area size (1 mm) is equal to the width of the irradiated area, the center of the area of maximal measured carbon content corresponds precisely to the center of the irradiated area: every deviation from it along $\underline{e}_1$ reduces the measured excess carbon content. The x-coordinate of the center of the irradiated area is denoted x_I. On Fig. III.61b, it can be seen on the one hand that oxygen content seems relatively constant over a zone that extends outside the irradiated zone — this is consistent with the observation of Fig. III.61a —, which means that it is due exclusively to the environment. The absence of oxide on the front side of specimina is probably linked to the fact that they are mirror-polished while their backside is in a raw machined state and thus exhibits a significant roughness. On the other hand, the implantation chamber environment is responsible for only part of the excess carbon content since a large surface peak is noticed in the irradiated zone (see Fig. III.61b).

Spectra were also acquired at 43 μC on three locations of sample B1 to obtain reliable counting statistics. The atom $\cdot$ cm^{-2} quantification is done by comparison of NRA spectra to simulations performed with the software `SIMNRA`. The calibration is performed with a 200 nm layer of SiO_2 deposed on silicon (oxygen measurement), and a vitreous carbon bulk (carbon measurement). Depth profiles of oxygen and carbon are obtained with an approximate depth resolution of 15 nm for oxygen and 30 nm for carbon; they are shown in Fig. III.62. Depth measures in atom $\cdot$ cm^{-2} were converted to nm using the density of AIM1. The oxygen contamination is measured up to 200 nm while the carbon contamination can be measured up to 100 nm (unirradiated material) or 400 nm (irradiated material). With increasing depth, the carbon concentration is seen to saturate around the concentration expected for AIM1 steel, *i.e.* 0.42 atomic percent (see Fig. III.62b). The uncertainty of that high-depth measurement is due to insufficient statistical evidence in the corresponding part of the carbon peak. More generally, the confidence in NRA results is limited by the roughness displayed by the back surfaces of samples.

It is concluded from this analysis that oxygen contamination is negligible in the case of the B1 sample. However, central samples such as B4 (Fig. III.61a) have experienced higher temperatures during irradiation so that the oxide layer on their back side may be thicker than that of B1. As will be seen on later SEM micrographs (see Fig. III.72), their thickness can reach up to 1 or 2 μm. However, the temperature inhomogenity was measured to be less than 30 °C. Thus, the dispersion of oxidation intensity probably stems from different roughness of the rear surfaces. In any case, as oxides usually have low fracture toughness, they are not believed to influence the mechanical behavior of samples.

Based on literature observations (Was et al., 2017), carbon contamination is believed to occur on the samples' front and back surfaces. NRA analyses have concluded that carbon contamination from the back surface does not reach the bulk of the material and thus cannot influence the fracture behavior of the sample. However, no front surface measurements were carried out, so an effect of carbon contamination originating from this side cannot be entirely ruled out. Indeed, the contamination on the front side could be either greater (due to the larger beam intensity) or

lower (due to the better surface state).

4.1.6 Post-implantation annealing

In order to obtain larger helium bubbles with an increased spacing, an annealing of one hour at 800 °C is performed on samples B5 and B6. The temperature profile is displayed on Fig. III.63. No quench is done after the annealing so the cooling rate is rather slow. Indeed, the annealing is conducted under high vacuum with a pressure inferior to $8 \cdot 10^{-4}$ Pa during the whole heating duration. Optical examination reveals no further oxidation due to annealing.

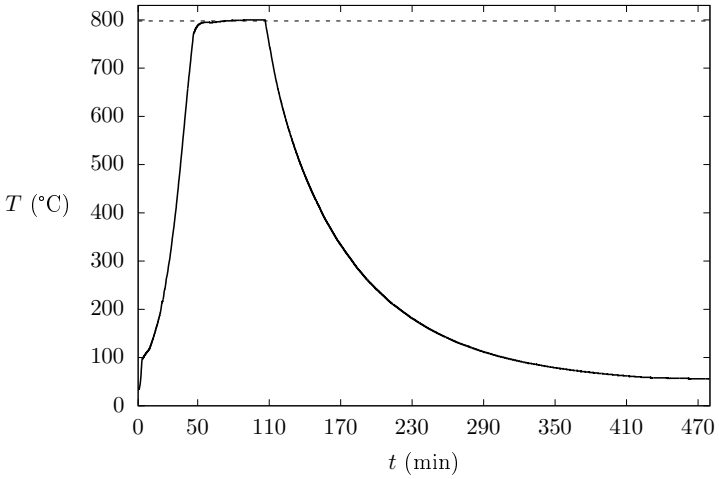

FIGURE III.63: Temperature profile of the annealing conducted on samples B5 and B6. The average temperature measured next to the samples during the one-hour peak is 798 °C (dashed line).

4.1.7 Characterization of irradiation defects

In order to gather data on helium bubbles and Frank loops produced by irradiation, TEM lamellae are prepared from sample B1 using the ZEISS NVision40 SEM-FIB of Paul Scherer Institute with the help of Dr. Peng Bi. The irradiated area of sample B1 is subjected to surface abrasion as described in Section III.4.1.2 in order to reveal grain boundaries. Two grain boundaries whose crystals are different from each other are chosen. EBSD measurements reveal that the first grain boundary is a general high-angle boundary with a misorientation of 53° while the second grain boundary is a thermal twinning boundary (*i.e.* **Σ3** boundary) with a misorientation of 60°. Carbon deposition of a rectangle of 30 µm length, centered on the grain boundary, and 2.5 µm width is performed. Then, one lamina is milled in each grain boundary using FIB drilling so that the lamina length is perpendicular to the grain boundary (see Fig. III.64). The dimensions of these raw laminae are approximately: length of 30 µm, width of 10 µm and thickness of 4 µm. Once laminae are lifted out and fixed on the TEM grid, they are thinned into TEM lamellae of 100 nm thickness using the following process on both sides (tilt angle of $54 \pm 1°$ and tension of 30 kV): 3 nA mill up to 1 µm thickness; 1.5 nA to 700 nm; 700 pA to 400 nm; 300 pA to 300 nm; 150 or 80 pA to 150 nm; 40 pA to 100 nm. The final cleaning for removal of defects induced by the FIB machining is carried out at 3 kV and 200 pA with a tilt angle of 5° for a duration of 30 seconds. The lamina is only thinned on a length of 10 µm approximately centered on the grain boundary (Fig. III.65).

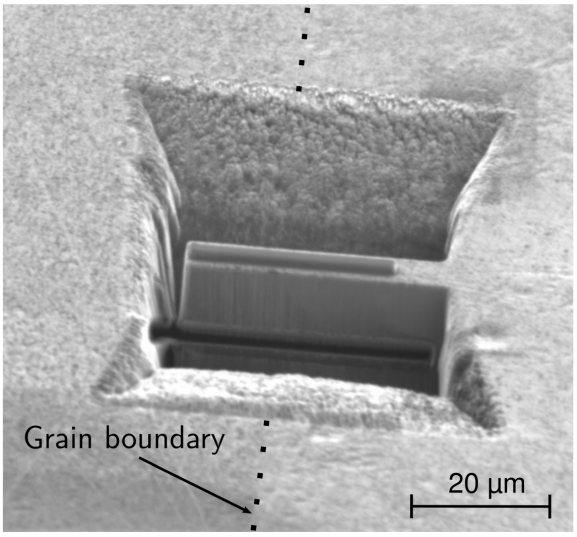

(**a**) Lamina #1

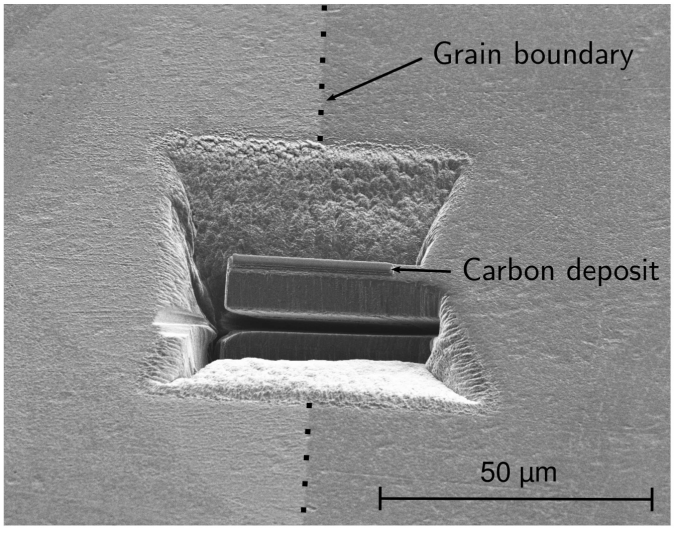

(**b**) Lamina #2

FIGURE III.64: Position of laminae (after carbon deposition, FIB sputtering and bottom cut) relative to the grain boundary.

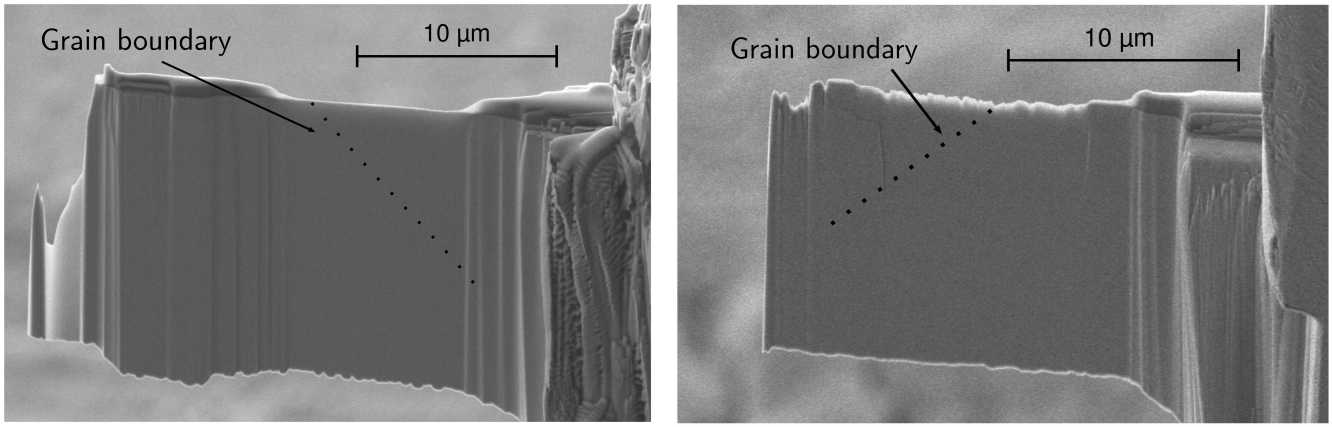

(**a**) Lamella #1 (**b**) Lamella #2

FIGURE III.65: Final lamellae obtained after FIB thinning.

The lamellae are then thinned additionally using the argon ion polishing system GATAN PIPS II at 500 V, enabling the removal of all remaining milling defects. They are observed by Dr. Solène Rouland of GPM (Physics of Materials Group) in the JEOL JEM ARM-200F TEM of Rouen University using a tension of 200 kV. Thickness maps of the samples are obtained through Gatan Imaging Filter (GIF) (Gubbens et al., 2010) which uses the electron energy loss spectroscopy (EELS) log-ratio technique (Malis et al., 1988) which compares EFTEM unfiltered and zero-loss images. The thickness is then obtained as a multiplier of the effective mean free path λ of electrons in the material. Consistently with literature values on austenitic stainless steels (Iakoubovskii et al., 2008; Desormeaux et al., 2016; Villacampa et al., 2018), the 200 kV electron mean free path in AIM1 steel was taken to be $\lambda \approx 110$ nm.

To visualize Frank loops, the reciprocal lattice rod (rel-rod) technique (Edwards et al., 2003) is used with an objective aperture of 5 µm. The TEM lamina #1 is tilted a few degrees away from <110> zone axis while maintaining the two-beam condition of $\mathbf{g} = <311>$. Two {111} stacking fault variants (out of four) are shown in Fig. III.66. The mean thickness of the area of Fig. III.66a is 121 nm while that of Fig. III.66b is 91 nm. The diameter of the white

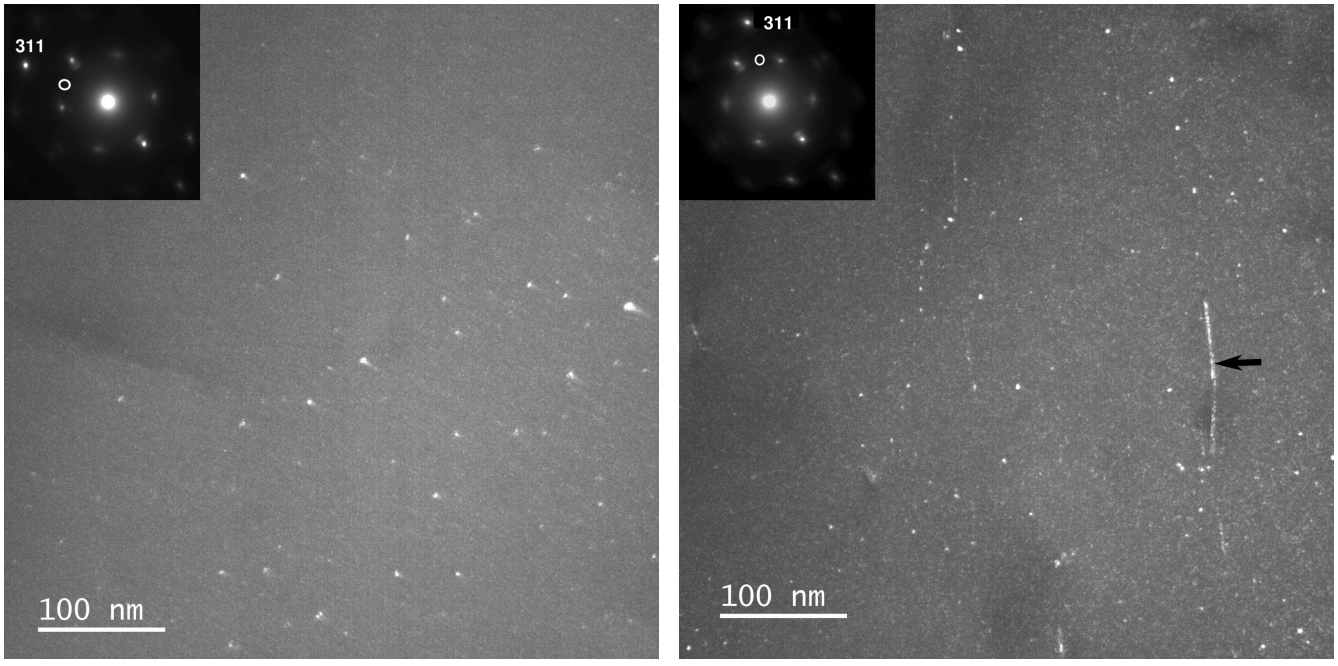

(**a**) (**b**)

FIGURE III.66: Dark-field relrod micrographs of lamella #2 in two imaging conditions described in the insets. The white circle in the diffraction pattern is the aperture position for relrod images. The white lines, including the one marked by a black arrow, were identified as dislocations using bright-field imaging.

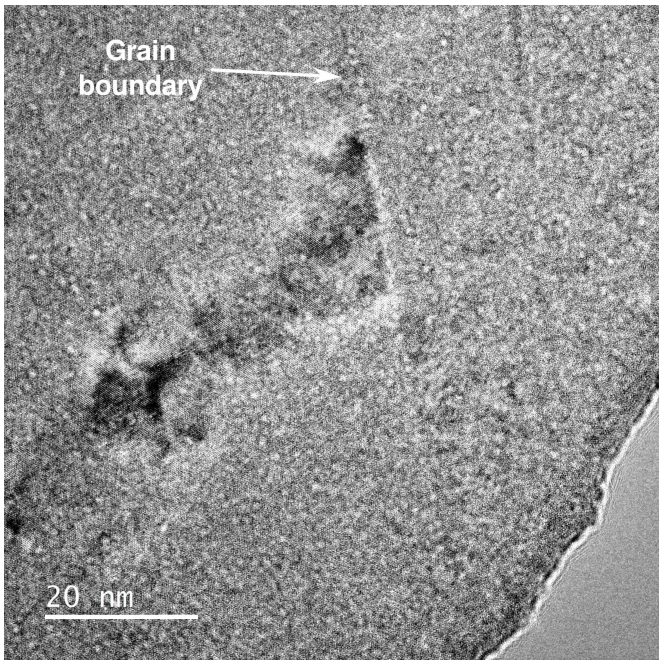

(**a**) 300k magnification, under-focus of 300 nm

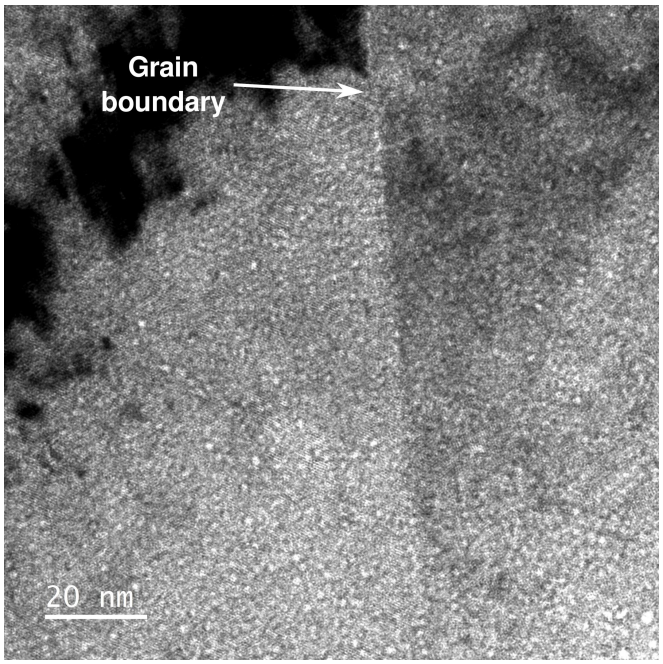

(**b**) 200k magnification, under-focus of 600 nm, objective aperture of 15 µm

FIGURE III.67: Bright-field micrographs of lamella #2 revealing helium bubbles.

dots seen in Fig. III.66 is 2.8 ± 1.0 nm: due to this small size, they cannot be unequivocally identified as Frank loops as other objects may lead to similar observations (*i.e.* nano-precipitates, black dots). However, these dots were not visible under standard bright-field and dark-field images, which may exclude nano-precipitates, and black dots are often interpreted as small Frank loops (*e.g.* Pokor et al. (2004) and Chen et al. (2015)). From rel-rod observations, it is estimated that the total density of white dots is $2.3 \pm 1.0 \cdot 10^{21} \mathrm{m}^{-3}$. Manual counting of the white dots in Fig. III.66a and Fig. III.66b was carried out; dividing these numbers by the surface times the thickness gave access to the density of dots for the two stacking fault variants of Fig. III.66: the total density of alleged Frank loops was then obtained by multiplying this value by a factor of 2.

To uncover the helium bubbles, the bright-field through-focal series technique is used with grain boundary edge-on condition, which means that the sample is tilted so that the incident electron beam is parallel to the grain boundary plane. Since the lamellae thickness is larger than 20 times the diameter of helium bubbles (around 1 nm), no bubbles are seen in focus images and it is resorted to defocusing. Villacampa et al. (2018) has shown that, at constant defocus, under-focus measurements provide a better estimate of bubble size than over-focus measurements. Therefore, only under-focus micrographs will be shown; in those conditions, helium bubbles appear as clear zones surrounded by a bright fringe followed by a dark fringe. At a magnification of 100k, Villacampa et al. (2018) determined that an under-focus of 600 nm was optimal and that this defocus should decrease at higher magnification. In the observations carried out on our lamellae at 200k and 300k magnification, under-focus between 300 nm and 600 nm provides the best conditions to image helium bubbles. This differs significantly from the study of Miura et al. (2015) in

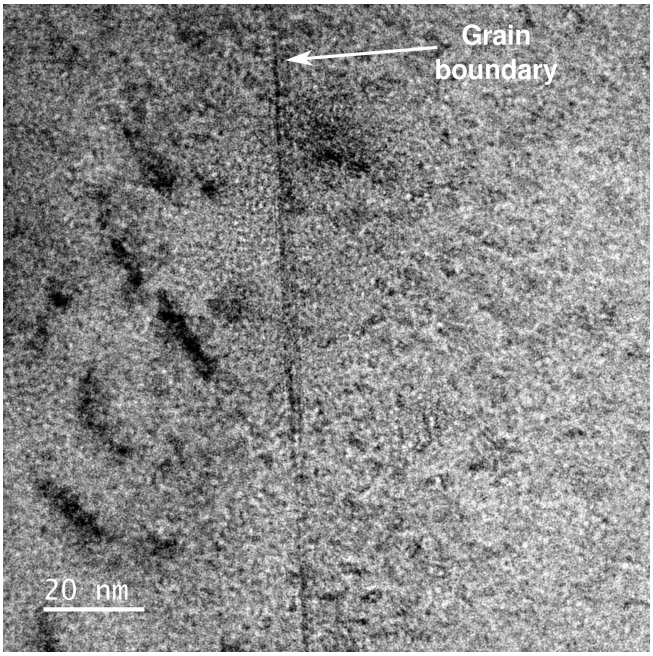

FIGURE III.68: Bright-field micrographs of lamella #1 revealing helium bubbles: 200k magnification, under-focus of 300 nm, objective aperture of 15 µm

which a defocus of 1 µm was used; this discrepancy may be rooted in the higher tension (300 kV) used by these researchers. More generally, Yao et al. (2012) have shown that under-focus values over 1 µm should be avoided when imagining tiny helium bubbles — whose diameter is inferior to 2 nm — in steel because it leads to an overestimation of the bubble diameter.

On the one hand, the random high-angle grain boundary is shown in Fig. III.68. A dense distribution of helium bubbles can be seen in grain interiors, with no denuded zone around the grain boundary. The grain boundary itself is covered in bubbles with a density that might be superior to that of grain interiors. The transgranular helium bubble diameter is 1.8 ± 0.3 nm, while the intergranular helium bubble size is smaller: 1.5 ± 0.2 nm. Both these values are obtained manually (statistics on a dozen intergranular bubbles and a few tens of transgranular bubbles) in a zone where the thickness of the sample is only 10 nm (the edge of the sample, part of which is shown in Fig. III.68a) in order to minimize the bubble overlap; an under-focus of 600 nm was used to obtain a good contrast. Since intergranular bubbles overlap, the spacing of intergranular helium bubbles is impossible to measure confidently. Thus, the areal density could not be accessed directly. However, at the thin edge of the specimen, two measurements bring an average intergranular bubble spacing of approximately 5 nm. Note that all the values pertaining to grain boundary helium bubbles are similar to those measured by Miura et al. (2015) (diameter of 1.5 nm, spacing of 7 nm) for close implantation conditions (1.15 helium atomic %, irradiation temperature of 200°C, no annealing). Using the method proposed by Villacampa et al. (2018) to link the area coverage to the bubble size and spacing, the grain boundary void coverage is estimated to be around 4%. On the other hand, the twin boundary is shown in Fig. III.67 where it can be noted that the boundary is almost free of helium bubbles, which hints at very different helium bubble nucleation propensity between coincidence site lattice (CSL) boundaries and general boundaries. The density of helium bubbles in grain interiors of lamella #1 is measured to be $2.0 \pm 0.5 \cdot 10^{24}$, which yields an initial porosity of $f_0 \approx 0.050$. A similar value is obtained in lamella #2.

In conclusion, the objective of implanting intergranular helium bubbles at grain boundaries has been reached. The characterization of irradiation defects in specimen annealed after implantation is to be conducted in the future. However, based on the study of Villacampa et al. (2018), it expected that all implantation damage is healed by annealing and that the diameter of helium bubbles is expected to be around 4 nm.

4.2 Fracture behavior

4.2.1 Mechanical testing

Tensile experiments are performed using a Proxima tension micromachine from MicroMecha. The samples are pinched at their ends to impose the displacement. The machine is operated by enforcing a constant $0.5\ \mu m \cdot s^{-1}$ displacement rate to the mobile crosshead. A Sensy loading cell (model 2962) with a maximum capacity of 200 N is used to measure the applied tensile force. Mechanical testing is recorded using a Keyence numerical optical microscope (model VHX-970FN with VH-Z20R/Z100R lenses). Testing is conducted at room temperature.

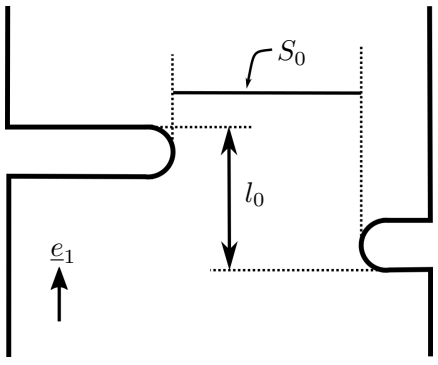

FIGURE III.69: Sketch defining S_0 and l_0 for a given sample.

Fractured samples are shown in Fig. III.70. Two fracture modes were observed. On the one hand, specimens B2, B5, and B6 experienced significant plasticity with an irregular crack path that does not seem to follow the grain boundaries evidenced in Fig. III.54. Cracking of sample B2 initiated on the left-hand side notch and progressed towards the right-hand side notch, while that of samples B5 and B6 initiated at the notches and progressed inward. Thus, this fracture mode is identified as transgranular. On the other hand, the cracking of sample B7 was brutal and followed the grain boundary shown in Fig. III.54f, which points to intergranular fracture.

The stress-strain curves of the mechanical tests are displayed in Fig. III.71. The length variation Δl is the value enforced by the micro-machine. The gauge length l_0 is defined as the distance between the notches (including the width of each notch) in direction $\underline{e}_1$ and the initial section S_0 is the area perpendicular to $\underline{e}_1$ located between the two notches (see Fig. III.69). Both these values are given in Table III.8 for each sample. The local stress at fracture initiation corresponds conventionally to a true plastic strain of $\varepsilon^{\mathrm{p}} = 0.01$. This value, as well as the local maximal stress and the local plastic strain at fracture, is reported in Table III.8. Stress at fracture initiation is rather close (around 330 MPa)

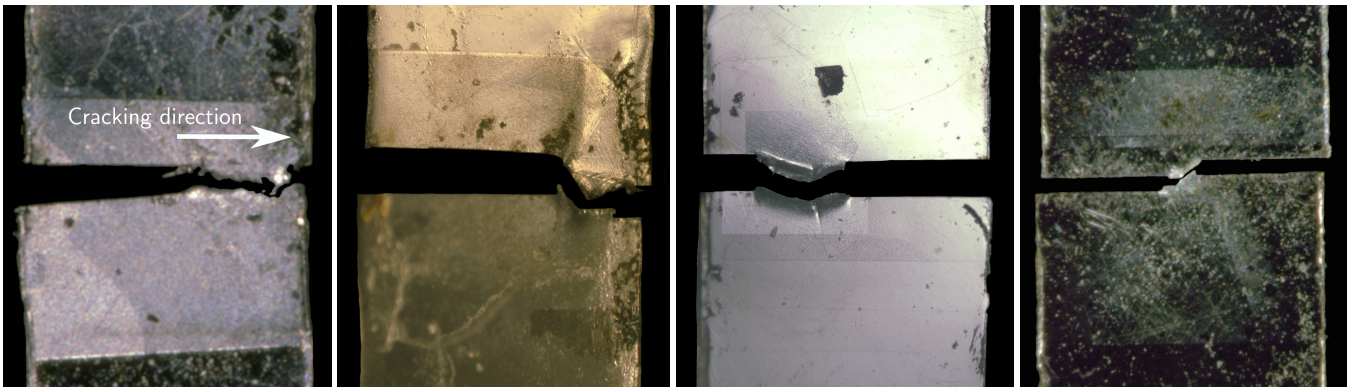

(**a**) Sample B2 (**b**) Sample B5 (**c**) Sample B6 (**d**) Sample B7

FIGURE III.70: Optical micrographs of the fractured samples. Clear areas are zones where FIB surface abrasion was performed (see Section III.4.1.2).

Sample	**Initial section** S_0 (mm^2)	**Gauge length** l_0 (µm)	**Fracture initiation stress** (MPa)	**Maximal stress** (MPa)	**Fracture plastic strain**
B2	$1.10 \cdot 10^{-2}$	25	362	429	0.283
B5	$1.29 \cdot 10^{-2}$	82	361	746	0.334
B6	$2.00 \cdot 10^{-3}$	34	300	370	0.174
B7	$5.08 \cdot 10^{-3}$	70	975	1002	0.012

TABLE III.8: Results of micromechanical testing. Stresses and strains are local quantities at the notch zone (see Fig. III.69).

for all transgranular fracture occurrences (B2, B5, and B6) — despite the difference in crystallographic orientations — and differs from that of B7 which is larger. The same specimina exhibits a plastic strain at fracture that is significantly higher than the one of B7. These two findings corroborate the fact that sample B7 fails intergranularly. However, it should be noted that one intergranular crack initiates at the left notch of sample B5 (seen on the rear surface, not shown here) at the same time as transgranular cracking but the transgranular crack eventually prevails. This explains the three different slopes seen in the stress-strain curve of B5: first, elasticity, second, simultaneous intergranular and transgranular cracking and finally, transgranular cracking only. The fact that intergranular cracking was not as catastrophic in B5 as in B2 seems to indicate that this failure mode is more ductile and may be the intergranular ductile

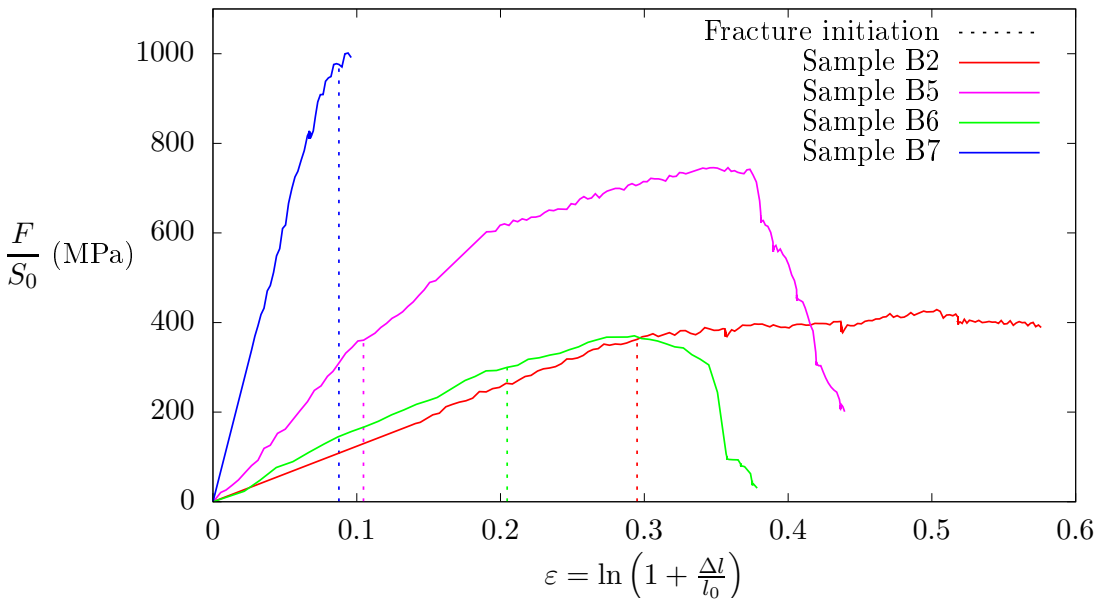

FIGURE III.71: Nominal stress versus true strain curves of the micromechanical tests; strain at fracture initiation is indicated by a dashed line.

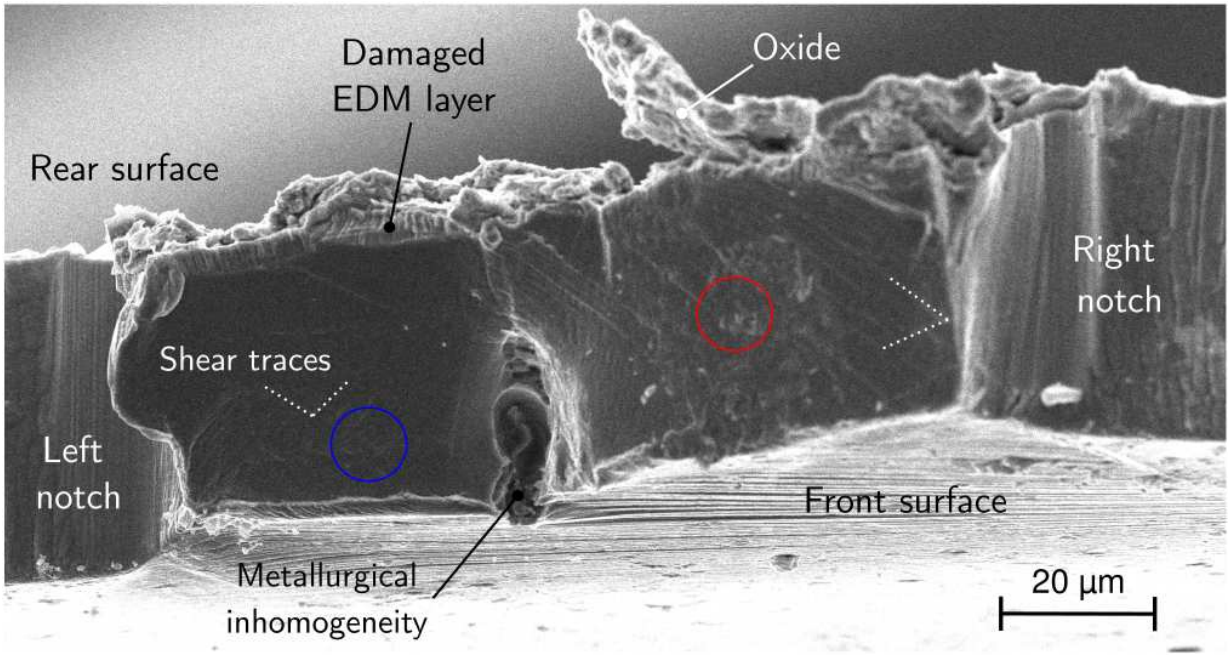

FIGURE III.72: SEM examination (20 kV, secondary electrons) of the lower fracture surface of sample B7. The red circle marks the location whose corresponding area on the upper fracture surface is shown at higher magnification in Fig. III.73. The blue circle marks the location which is shown at higher magnification in Fig. III.74.

fracture observed by Miura et al. (2015). Finally, it is noticed that the fracture of annealed specimina (B5 and B6) is less brutal than as-irradiated specimina (B2 and B7), which is probably linked to the fact that helium bubbles that are larger and less dense may undergo significant plastic growth before coalescence.

4.2.2 Fracture surface investigation

The fractographic observations are performed on a JEOL IT800 SHL SEM of the platform MACLE at CNRS-Orléans. The fracture surface of sample B7 is shown in Fig. III.72. It can be seen that the oxide layer on the rear surface is much thicker (around 2 µm) than the estimation made from sample B1; at some locations, it has delaminated from the sample. This oxide's growth has probably been favored by the damaged layer (whose thickness is measured on the fracture surface to be between 1 µm and 4 µm) produced by electrical discharge machining. Yet, these two layers did not influence the fracture process of the remaining pristine material, which failed along a grain boundary. The

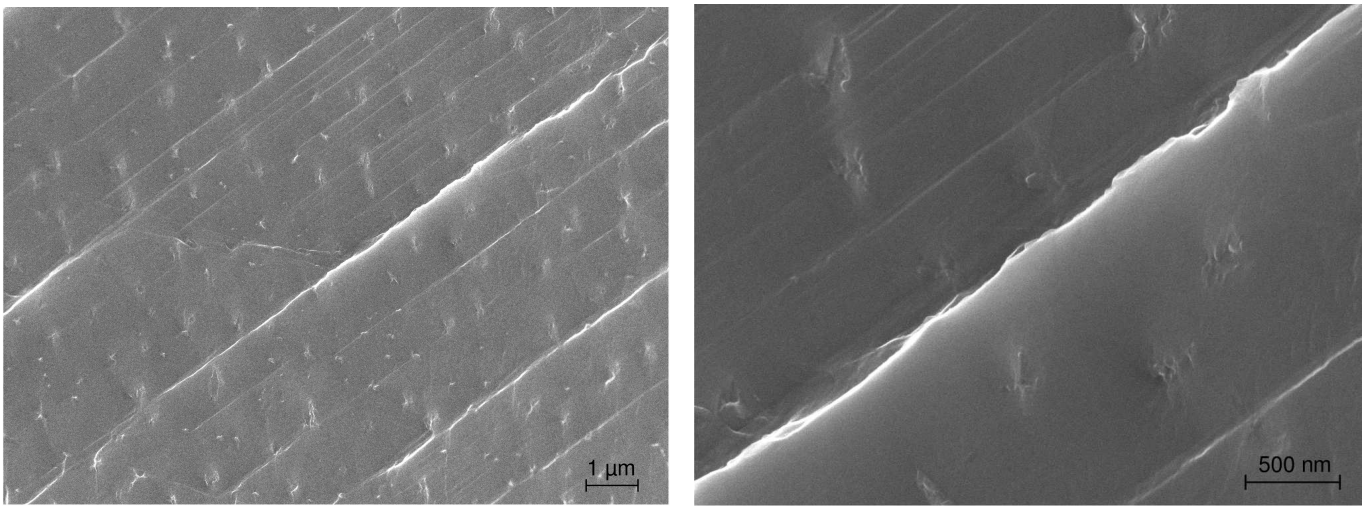

(**a**) (**b**)

FIGURE III.73: SEM micrographs (20 kV, upper hybrid detector) of the upper fracture surface of sample B7. Image (**b**) is an enlargement of (**a**).

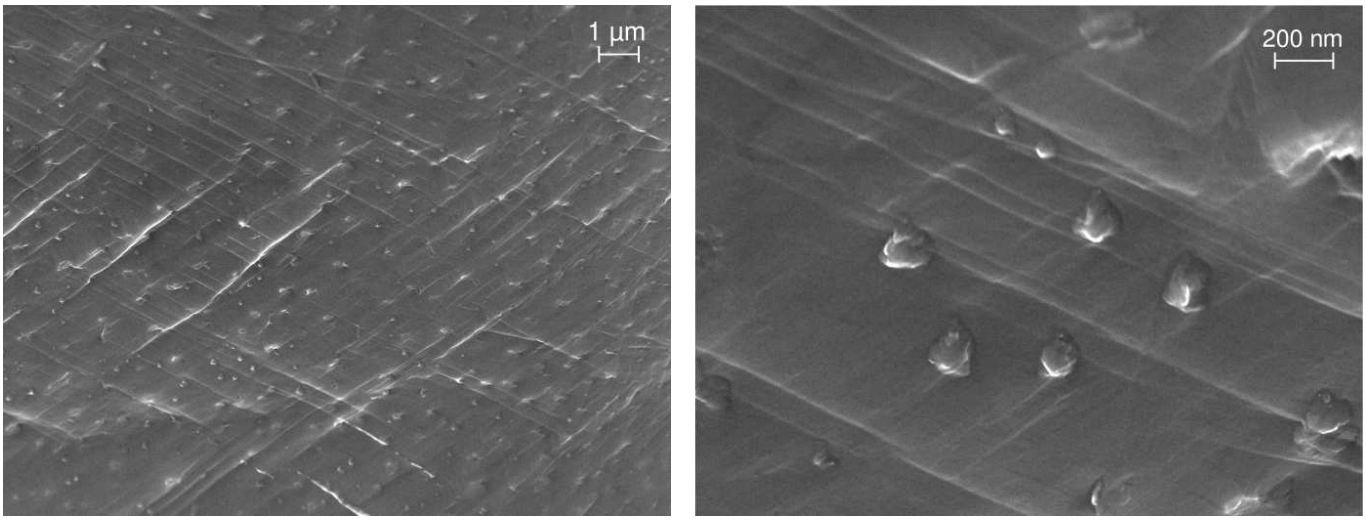

FIGURE III.74: SEM micrographs (20 kV, upper hybrid detector) of the lower fracture surface of sample B7. Image (**b**) is an enlargement of (**a**).

fracture surface is flat on each of its two planes (see also Fig. III.70b) and bears the traces of shear steps. A metallurgical inhomogeneity with the shape of a (Ti,Mo)C inclusion can also be noticed; yet, an EDS analysis (Oxford Instruments ULTIM MAX 100, detector size of 100 mm^2) states that despite an enrichment in titanium, molybdenum and carbon, this volume is chemically close from the matrix material. Furthermore, the FIB surface abrasion (Fig. III.54e) displayed no contrast between crystal 1 and this inhomogeneity area, meaning they have close crystallographic orientations. Thus, it is concluded that it is a former (Ti,Mo)C inclusion that dissolved into crystal 1 during one of the prior heat treatments. Contrary to the rest of the material, this volume fractured transgranularly because it was energetically favorable for the crack to circumvent it. Higher magnification micrographs of the intergranular fracture surface are provided in Figs. III.73 and III.74. Two different families of shear planes can seen on Fig. III.74a, but only one is noticed in Fig. III.74a. These intergranular facets covered with shear traces can be related to the observations of intergranular fracture in aluminum alloys (Figs. I.14c and I.15a) (Kuramoto et al., 1996) and neutron-irradiated austenitic steel (Figs. I.35 and I.36c) (Fukuya et al., 2008). Such well-defined bands can arise from the shearing of sessile irradiation defects induced by irradiation (a deformation mode usually known as dislocation channelling (Byun and Hashimoto, 2006)) or by localized deformation twinning (Griffiths, 2023). However, a phenomenon implying void growth and coalescence of nanometric bubbles cannot be ruled out since the magnification is insufficient to check the presence of dimples at the nano-scale. Besides, dimples of 100 nm length can be distinguished on the top of the main shear steps (*e.g.* Fig. III.73b), which may indicate a role of cavity growth in this fracture process. Intergranular precipitates of a mean diameter of 100 nm can also be seen in Fig. III.74. This is the first time that grain boundary precipitates are observed in AIM1 steel. The absence of dimples around precipitates indicates that no void nucleation happened at their location, ruling out classical intergranular ductile fracture.

The fracture surface of sample B2 is shown in Fig. III.75. It presents various features that indicate a mixed fracture mode:

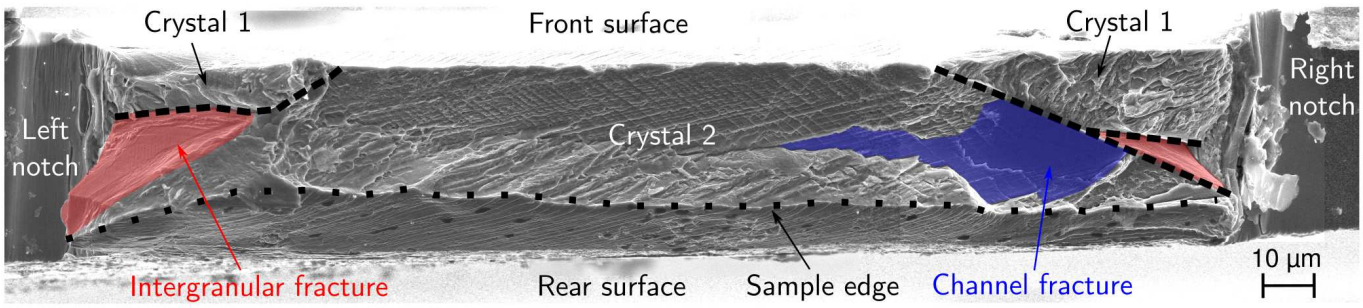

FIGURE III.75: SEM examination (20 kV, secondary electrons) of the upper fracture surface of sample B2.

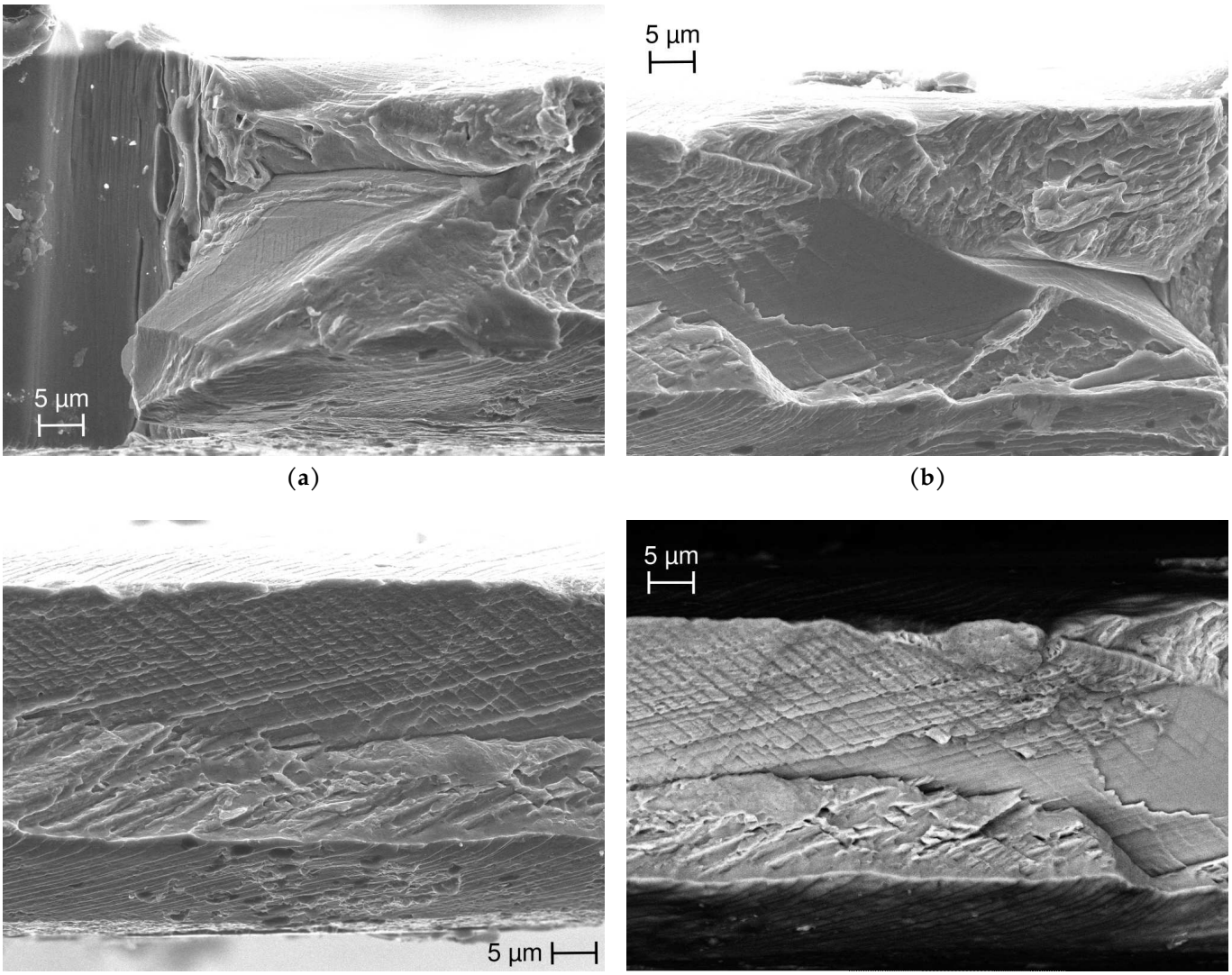

(**a**) (**b**)

(**c**) (**d**)

FIGURE III.76: SEM micrographs (20 kV) of the upper fracture surface of sample B2. Images (**a-c**) are from secondary electrons while (**d**) is obtained from back-scattered electrons.

- First, the red zones are associated with intergranular fracture: they display polyhedral shapes with flat facets and the grain boundaries (shown with thick dashed lines in Fig. III.75) are well defined, as can be seen in Fig. III.76a,b. It can be noticed that even if the intersection of the grain boundary (between crystal 1 and crystal 2) and the front surface is perpendicular to $\underline{e}_1$ (as was shown in Fig. III.54a), the grain boundary itself is not perpendicular to $\underline{e}_1$ but slanted. Thus, intergranular fracture was less favored than in sample B7. It is also underlined that this grain boundary may be devoid of helium bubbles since B2 corresponds to a twin boundary. Indeed, the twin boundary of Section III.4.1.7 displayed no intergranular bubbles; this absence could greatly favor transgranular fracture over intergranular fracture.

- Then, it can be seen that the remaining part of the fracture surface is transgranular. On the one hand, the two zones corresponding to crystal 1 experienced a classical transgranular ductile fracture process. On the other hand, the transgranular fracture of crystal 2 is seen to have occurred in two steps. In the initial stage, a necking phenomenon occurred, especially on the back of the sample, as seen in Fig. III.75 where the fracture surface edge is not parallel to the rest of the rear surface. Then, void nucleation and growth fostered by localized shear bands occurred. Indeed, it can be seen in Fig. III.76c that a net of shear steps is well-marked on the fracture surface, and that dimples are located at each intersection of these shear planes (Fig. III.76d). Notice that the fracture surface is seen to form a valley parallel to the edges of the sample and that the slope descending from the front surface is that on which shear bands are best defined.

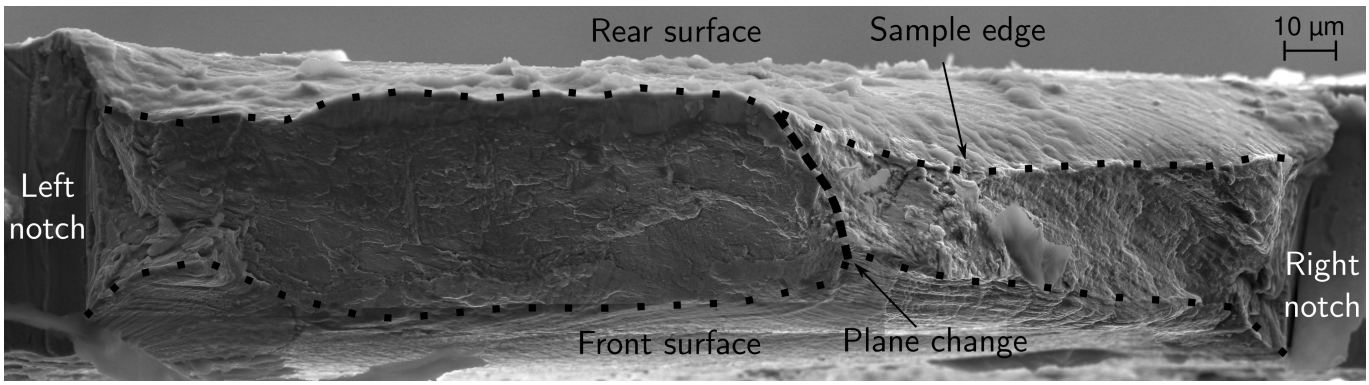

FIGURE III.77: SEM examination (20 kV, secondary electrons) of the lower fracture surface of sample B5.

- Finally, channel fracture is suspected to have occurred in a part of the transgranular fracture surface of crystal 2 that is drawn in Fig. III.75. Channel fracture is a failure mode triggered by intense plastic localization and can be identified by its terraced plate-like surfaces (Garner, 2012). In our case, the aforementioned area is characterized by two parallel flat planes separated by a small step (Fig. III.76b) and by an absence of dimples (Fig. III.76d). Its appearance is very close to that of the intergranular fracture surfaces, but can be distinguished from it by two points: first, the aforementioned step whose serrated profile would not be found on an intergranular facet; second, the fact that it makes a significant angle with the nearby grain boundary. Channel fracture is often observed in neutron-irradiated austenitic steels at intermediate irradiation doses (around 50 dpa) or higher (*e.g.* Hunter et al. (1972), Mills (1988), Huang (1992), Mills (1997), and Margolin et al. (2016)). The occurrence of channel fracture at such a low level of damage (1.8 dpa) highlights the potential influence of helium bubbles. Determining the precise mechanism responsible for this fracture mode requires further investigation as the discussion is still open in the literature. Indeed, channel fracture is usually attributed to dislocation channeling (Garner, 2012), but some authors attribute channel fracture to localized twinning and/or martensite formation in the presence of numerous unshearable gas bubbles (Griffiths, 2023; Changizian et al., 2023) as is the case here.

The very different fracture modes displayed by samples B2 and B7 explain, together with the influence of crystallographic orientations, the variation of mechanical properties seen in Fig. III.71. The chosen experimental conditions seem adapted to study the influence of crystallography on the competition between fracture modes.

Intriguingly, the observed fracture modes differ significantly from the transgranular cleavage seen for 316L steel implanted at room temperature with 1% helium atomic content and loaded at room temperature and 300°C (Ullmaier and Chen, 2003). Instead, they seem more in line with the results of Miura et al. (2015) on 316 steel micro-samples

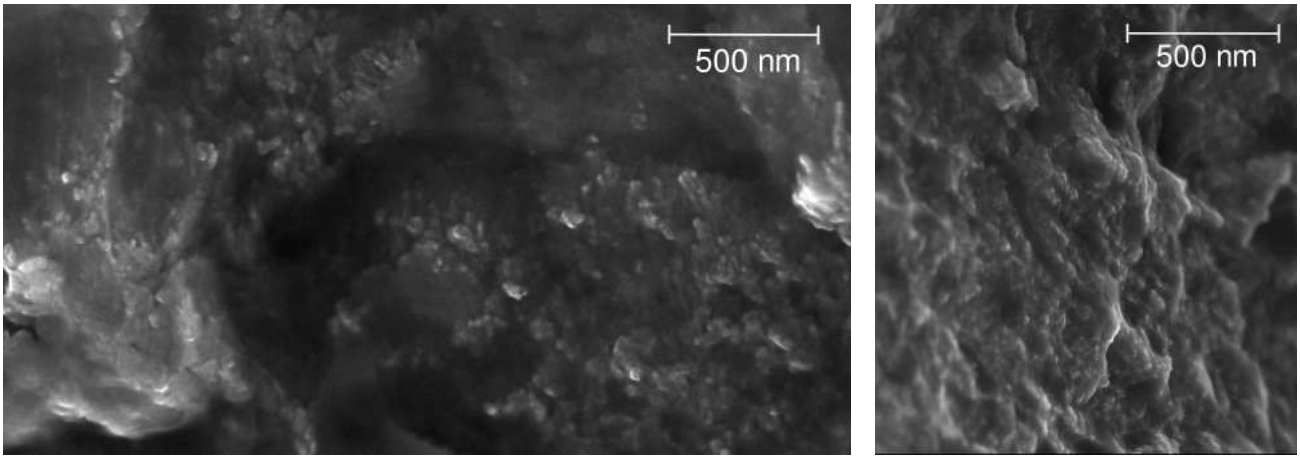

(**a**) (**b**)

FIGURE III.78: SEM micrographs (20 kV, upper hybrid detector) of the lower fracture surface of sample B5: (**a**) comes from the leftmost plane while (**b**) is from the rightmost plane.

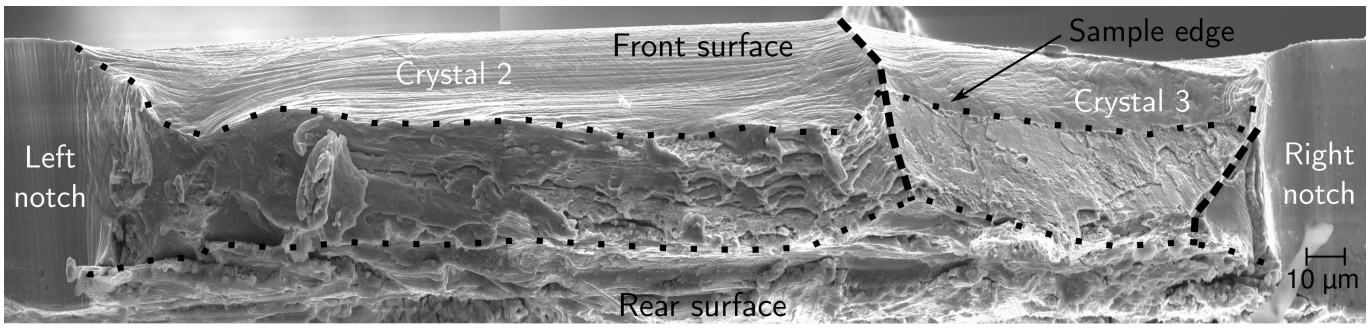

FIGURE III.79: SEM examination (20 kV, secondary electrons) of the upper fracture surface of sample B6.

tested at room temperature; in this study, transgranular ductile fracture was noticed below 2% helium atomic content and intergranular fracture above that threshold. Thus, the observed competition between transgranular and intergranular fracture at 1.8% helium atomic content in AIM1 steel is consistent with the literature. Closer comparison reveals that the transgranular ductile fracture of sample C of Miura et al. (2015) (1% He, no annealing) displays a fracture surface with both dimples and necking as sample B2 (Fig. III.75). Furthermore, the net of shear traces that are barely visible on the intergranular fracture of sample D (2% He, no annealing) is reminiscent of what is observed on sample B7 (Fig. III.72). This suggests that results obtained on very thin samples (300 nm) can hint at what happens on thicker samples (45 µm). The observation of deformation twins associated with the intergranular fracture of 316 steel sample C (Miura et al., 2015) advocate for twinning being the deformation mode responsible for the shear steps seen on fracture surfaces of B2 and B7. This is corroborated by the fact that intense deformation twinning occurs

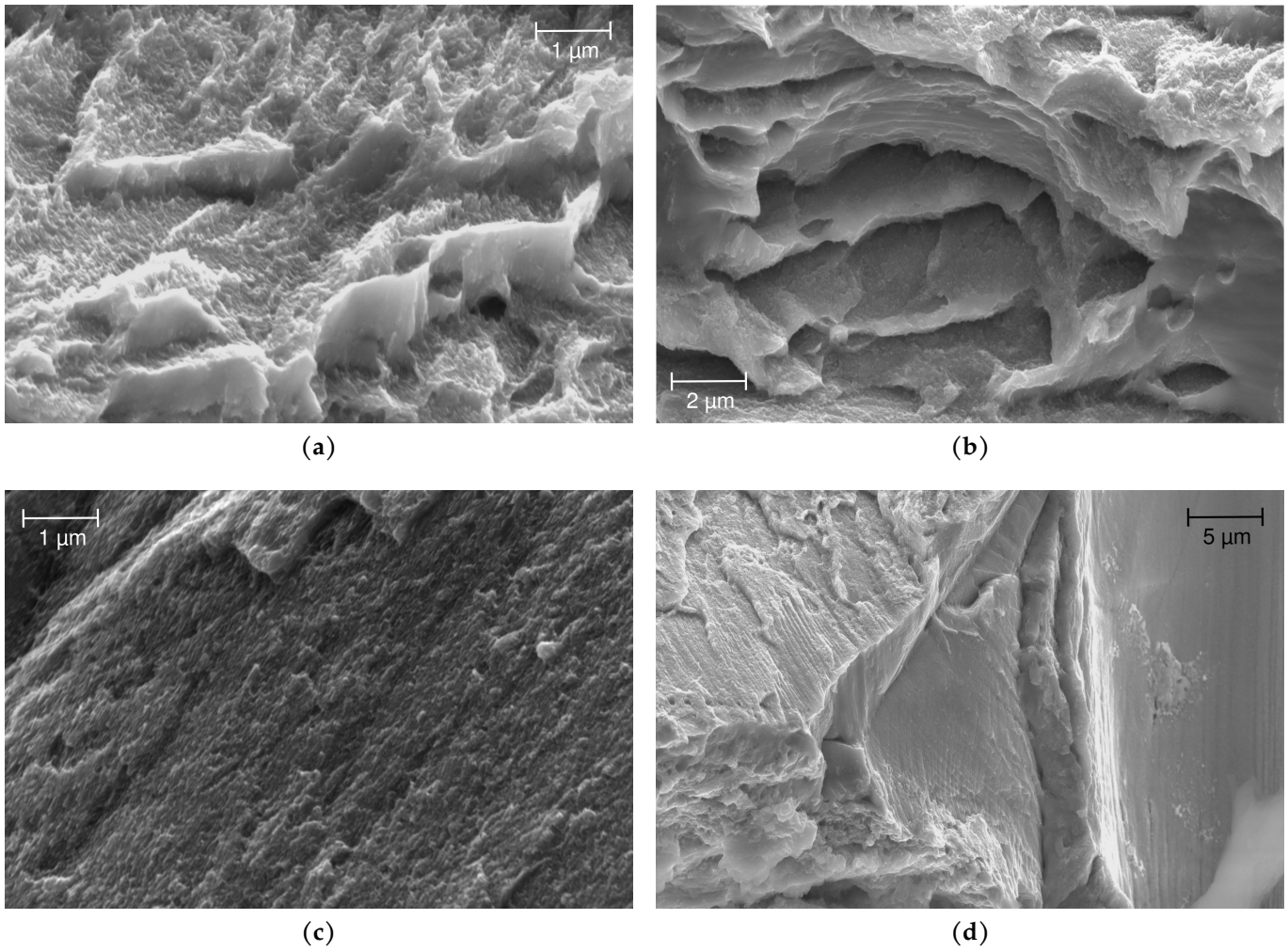

FIGURE III.80: SEM micrographs (20 kV, secondary electrons) of the upper (**a,b,d**) and lower (**c**) fracture surfaces of sample B6.

in unirradiated AIM1 loaded at room temperature (Curtet et al., 2020). However, these preliminary results must be investigated further and completed to draw definitive conclusions.

Samples that were annealed after implantation both displayed transgranular ductile fracture. The fracture surface of sample B5 is shown in Fig. III.77 and presents two fracture planes. It can be noticed that significant necking occurred, especially on the rightmost plane. Shear traces are also seen on the fracture surface but are less marked than on sample B2. If these traces were linked to dislocation channeling, removing sessile defects by annealing has likely diminished the localization of deformation. A higher magnification micrograph of each of the fracture planes (Fig. III.78) shows the existence of nanometric dimple-like features that may be linked to helium bubbles that may have initiated the process of transgranular ductile fracture.

The fracture surface of sample B6, shown in Fig. III.79, also displays significant necking as well as two fracture planes. Each plane corresponds to a different grain. A cracked oxide layer similar to that of B7 can be noticed on the rear surface. Dimples are seen on the fracture surface at higher magnification, with a clear separation of scale between fine dimples of around 50 nm diameter (see Fig. III.80a,c) and macroscopic cavities with a size of a few microns (Fig. III.80b). No decohesion or cracking of precipitates is witnessed. Thus, fine dimples are believed to originate from the plastic growth of helium bubbles (initial diameter of approximately 4 nm). The coalescence of many of these bubbles then forms macroscopic cavities, as evidenced by the nanometric features on the edges of the macroscopic voids shown in Fig. III.80b. Finally, it should be pointed out that a plate-like surface can be found next to the right notch (Fig. III.80d). It presents the same aspect that the channel fracture zone of sample B2 and could be linked to the existence of a fourth crystal in the volume loaded, meaning that the surface separating this terraced area from the more ductile zone is a grain boundary.

4.3 Temporary conclusion

The experimental procedure described here has reached the objective of creating conditions favorable to observe intergranular (ductile?) fracture. Due to time limitations, the remaining two samples (B3 and B4) were not mechanically tested. Further investigation could be carried out on these specimina by choosing an appropriate heat treatment to modify the size of helium bubbles or by increasing the test temperature to 300 °C to suppress deformation twinning in AIM1 (see Curtet et al. (2020)).

In any case, as was put forward in the introduction of Section III.4, the valuable experimental data gathered here should be compared to numerical and analytical results to increase the confidence of physical-based modeling of ductile fracture (both transgranular and intergranular). In particular, the fact that the material studied here experiences a competition between transgranular and intergranular fracture should be used to assess the compared predictions of transgranular and intergranular fracture homogenized models. Such a task will be attempted in future work.

5 Conclusion and perspectives

In the first part of this chapter, contributions to intergranular ductile fracture prediction were made using the micromechanical framework of porous material homogenization, which was originally developed for transgranular ductile fracture. The following developments were conducted:

- First, two yield criteria for intergranular void growth were derived in Section III.1 using alternative methods: on the one hand, a Gurson-like criterion for spherical cavities emerging from kinematic limit-analysis, and on the other hand, a viscoplastic potential for ellipsoidal cavities obtained through an approximate variational method relying on linear composite comparison. Both criteria were validated against an extensive database of small strain bicrystal unit cell simulations, exhibiting very satisfying agreement with a single calibration parameter for each model. Finally, these yield functions were compared to the transgranular ductile fracture criterion of Paux et al. (2015) to get a first assessment of the competition between intergranular and transgranular ductile fracture. In particular, it was evidenced that intergranular void growth can only occur if grain boundaries are weakened compared to grain interiors.

- Then, an estimate of the limit load for intergranular void coalescence under combined tension and shear was developed in Section III.2 through limit analysis, first on a simple Mises bi-material and then on a bicrystal. It evidenced two competing coalescence modes: one in which plasticity localizes in the softer material, and another in which plasticity occurs in the full intervoid ligament. The determination of the dominant coalescence mode is of paramount importance since localization in a single material is believed to be much more damaging. The limit load for intergranular void coalescence was checked against relevant unit cell simulations, highlighting a qualitative agreement. The coalescence model was then applied to competition between intergranular and transgranular coalescence. Finally, it was used in a multi-surface yield criterion in conjunction with the Gurson-like intergranular void growth criterion of Section III.1 and compared to numerical results from small strain unit cell simulations under axisymmetric loading, showing excellent agreement.

- Eventually, a homogenized model for intergranular void growth built on the Gurson-like criterion of Section III.1 was proposed in Section III.3 within a finite strain framework relying on the multiplicative decomposition of the deformation gradient. No strain hardening was considered. The homogenized model was numerically implemented and compared to a database of finite strain unit cell simulations of porous bicrystals subjected to axisymmetric loading with various stress triaxiality ratios. The agreement between the model and simulations is satisfying at relatively small strains. Still, discrepancies appear at larger strains, especially for $T = 1$, which can be linked to the neglect of the local variations of lattice rotation in the two crystals.

The second part of this chapter was devoted to an experimental investigation of ductile fracture in an austenitic stainless steel with large grains (around $500\ \mu\text{m}$) implanted with helium. Indeed, due to its low solubility, helium forms bubbles at grain boundaries and in the interior of grains; these bubbles can then act as nucleated cavities and lead to intergranular ductile fracture. The objective of these model experiments was first to validate a protocol to study to study the competition between ductile failure modes and second to compare experimental data to predictions of the models developed previously. Specimina were thin lamellae ($45\ \mu\text{m}$) in which fine notches were drilled by focused ion beam in order to have a unique grain boundary in the effective section of each specimen. Irradiation was designed in collaboration with CEMHTI and PSI teams to reach 1.8 atomic percent of helium, which was expected from the literature to be sufficient to trigger intergranular fracture. Samples were then loaded in a micro-tensile machine until fracture, revealing both intergranular and transgranular fractures. Bubble characterization was carried out in TEM, fracture surfaces were observed at SEM and EBSD analyses were performed to gather the microstructural data relevant to the study of fracture. The results of this study are currently under analysis so that the comparison of experimental data to model predictions shall be presented in the future.

Natural extensions of the intergranular ductile fracture modeling carried out in this chapter include the following:

- application to crystal lattices that are more anisotropic than FCC crystals, *e.g.* HCP crystals. In the HCP case, twinning systems may also be accounted for using a similar framework as slip systems;

- improvement of the void coalescence criterion to account for the asymmetry in the plane $(\Sigma_{33}, \Sigma_{31})$;

- development of a homogenized model including both void growth (as currently done in Section III.3) and coalescence in layers (based on the criterion of Section III.2);

On the other hand, longer-term perspectives foreseen to pursue the prediction of intergranular fracture are:

- to conduct model experiments of fracture using bicrystals to assess the assumption that grain boundaries can be modeled with perfect bonding interfaces in the context of ductile fracture;
- to improve the modeling of microstructure evolution at finite strain, which is still a major issue due to its highly coupled nature, even in pristine bicrystals. In particular, homogenizing hardening and crystal lattice rotation is a significant challenge.

Detailed prospects about the simulation of the competition between transgranular and intergranular ductile fracture will be found in the general conclusion.

Conclusion and perspectives

A broad class of metallic alloys used in industrial fields — *e.g.* nuclear, aerospace, oil and gas — exhibits a ductile fracture mode by void nucleation, growth, and coalescence at operating temperatures. These three successive (or simultaneous) processes involve plasticity, which is the irreversible deformation of the material. Void nucleation usually occurs due to inclusions that fracture or decohere from the alloy matrix. Still, initial porosity can also exist in the material due to its aging under service, *e.g.* irradiation or creep cavities. Void growth under mechanical loading manifests as the slow increase of the volume of cavities when voids are small enough to be independent of each other. Larger voids finally interact, leading to a fast increase of porosity known as void coalescence. At this stage, strain localizes in specific zones linking voids — the ligaments — and fracture soon occurs by void linkage, resulting in a macro-crack. Ductile fracture can be either transgranular or intergranular: in the former, the previous mechanism occurs inside grains, whereas in the latter, the phenomenon of void growth and coalescence happens at grain boundaries. For a given material, both types of fracture can occur depending on its microstructure and the thermo-mechanical loading applied, and a drastic reduction of ductility usually accompanies intergranular ductile fracture. Thus, a careful understanding of the competition between intergranular and transgranular ductile fracture is necessary to ensure that metallic alloys manifest sufficient toughness.

The objective of this work was to make modeling and simulation contributions toward the prediction of the competition between ductile failure modes. To reach this goal, this work has adopted a micromechanical approach to transgranular ductile fracture and intergranular ductile fracture at the crystal scale through the homogenization of porous materials. This choice has enabled to capitalize on decades of research that have already proved their worth in accounting for ductile fracture. Besides, the development of an experimental methodology to validate the modeling work was pursued.

Main results

The results gathered in this manuscript pertain to the modeling and simulation of ductile fracture and cover both transgranular and intergranular failure modes. They are detailed below, following brief reminders of the state of the art anterior to this work:

1. **Transgranular ductile fracture:** Modeling of porous single crystals carried out in the last years have led to the development of void growth (Han et al., 2013; Paux et al., 2015; Paux et al., 2018; Mbiakop et al., 2015b) and coalescence in layers (Hure, 2019) yield criteria. Void growth criteria have been included successfully in homogenized models (Ling et al., 2016; Scherer et al., 2021) used to perform ductile tearing simulations (Scherer et al., 2021; Khadyko et al., 2021). The efforts that were carried out here sought to extend these results along two axes:

    - First, a homogenized model accounting for both void growth and coalescence in porous single crystals was proposed in Section II.1.3 from existing yield criteria for growth (Paux et al., 2015) and coalescence by internal necking (Hure, 2019). To assess the quality of this model and that of Scherer et al. (2021), a database of porous single crystal unit-cell computations loaded under finite strain was gathered and described in Section II.1.2. A comparison between predictions of the models and numerical results was provided in Section II.1.2, revealing that qualitative agreement could be achieved on the material behavior in the absence of strain hardening or with saturating strain hardening of single crystals. However, reproducing numerical results of porous crystals whose hardening is unbounded is still a challenge. It was also noticed that deformation gradient multiplicative decomposition was necessary to account for structural hardening effects

due to crystal lattice rotation. Finally, two-dimensional plane strain and three-dimensional ductile tearing simulations of test samples were conducted using the homogenized model with no strain regularization. It proved the ability to conduct large-scale simulations with such a refined local model. Crack propagation was considered in both mono- and polycrystalline samples, highlighting the effect of microstructure on macroscopic load-displacement curve, local fields of stress and damage, crack path, and fracture toughness.

- Simultaneously, the study of strain localization patterns in anisotropic materials was enhanced by the development of a full yield surface accounting for the four main modes of yielding under axisymmetric loading: void growth, coalescence by internal necking, coalescence in columns, and columnar shielding. This full criterion was derived for both porous Hill (1948) materials (Section II.3.3) and porous single crystals (Section II.3.4), the latter being the result of main interest regarding the objective set to this thesis. Both were assessed against corresponding numerical limit analysis simulations with very satisfying results. Finally, evolution laws for microstructure parameters were obtained by sequential limit analysis for Hill materials in an attempt to propose a full homogenized model. As only qualitative evaluation of these laws was provided, quantitative assessment is still necessary.

2. **Intergranular ductile fracture:** At the beginning of this work, modeling of porous grain boundaries was still limited, and simulation was confined to unit-cell computations (*e.g.* Jeong et al. (2018), Chen et al. (2019), and Dakshinamurthy et al. (2021)). Thus, there was a lot to be done to reach the same level of development as transgranular ductile fracture.

   - First, a detailed review of occurrences of intergranular ductile fracture in engineering metallic materials was gathered in Chapter I.2, a work that extends the study of Vasudévan and Doherty (1987) which focused on precipitation-hardened aluminum alloys.
   - Second, two yield criteria for intergranular void growth were derived using different methodologies. On the one hand, a Gurson-like criterion for spherical cavities was obtained using limit analysis (Section III.1.3). On the other hand, an approximated variational method led to a more complex criterion accounting for ellipsoidal cavities (Section III.1.4). Both were assessed using numerical limit analysis computations (Section III.1.2) and were seen to provide a satisfying prediction of the yield surface as well as quantitative estimates for the influence of the Lode angle, stress rotations, void volume fraction, and void aspect ratios (if applicable).

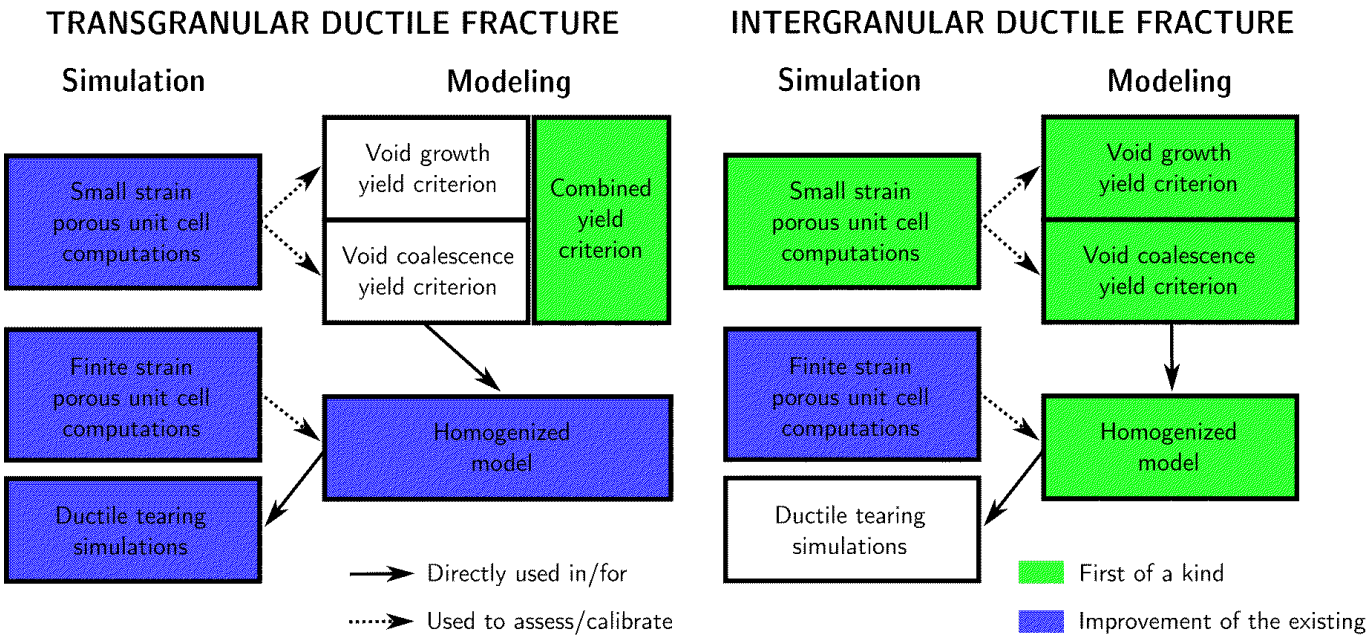

FIGURE III.81: Graphical summary of this work's main simulation and modeling results, belonging either to transgranular or intergranular ductile fracture at the crystal scale.

- Then, an intergranular void coalescence criterion under combined tension and shear was drawn from limit analysis. A first step involving a Mises bimaterial with cavities at the internal interface was necessary to grasp the basic principles of such a coalescence process (see Section III.2.3) before extending the results to bicrystals with cavities at the grain boundary (see Section III.2.4). As in the void growth case, void coalescence small strain simulations were carried out to validate the criteria, which showed good agreement.
- Next, a homogenized model of intergranular void growth was proposed from the Gurson-like criterion with deformation gradient multiplicative decomposition framework in Section III.3. Its numerical implementation was described and its results were compared to a database of finite strain porous unit-cell computations. The effect of stress triaxiality was reproduced quantitatively but challenges remain to account correctly for crystallographic effects at finite strains, especially for $T = 1$.
- Finally, a model experiment for the competition between intergranular and transgranular ductile fracture was described in Section III.4. An austenitic stainless steel with large grains was implanted with 1.8 atomic percent of helium to obtain gas bubbles — which can act as nucleated cavities — at grain boundaries and inside grains. Notches were previously machined in each sample using Focused Ion Bean (FIB) drilling to localize strain on a unique grain boundary. Samples have then been loaded *in-situ* at room temperature with a tensile micro-machine, exhibiting both intergranular and transgranular fracture. Load-displacement curves were collected along with TEM characterization of helium bubbles and SEM fractographies.

A summary of the modeling and simulation achievements is shown in Fig. III.81.

Short-term prospects

A handful of developments were envisioned during this thesis but were not carried out due to a lack of time. They can be considered as short-term prospects to this work:

1. **Transgranular ductile fracture:** To model more accurately this fracture mode, the homogenized model of Section II.1 should be supplemented with missing localization modes:

   - shear-assisted coalescence, which is a major concern for low-triaxiality loadings and for which a yield criterion was proposed in Hure (2019);
   - coalescence in columns, which has an influence on the fracture strain of some material microstructures and for which a model was put forward in Section II.3;

   Following the findings of Section II.1, the finite strain framework of the homogenized model should also be updated to multiplicative decomposition of the deformation gradient, along the lines of what was done in Section III.3, and the numerical assessment performed anew. Finally, unit-cell simulations for random arrays of cavities in single crystals would be needed to assess the effect of void distribution. In particular, the results of Cadet et al. (2022) — according to which shear-assisted coalescence generally occurs before coalescence by internal necking for random distributions of cavities in isotropic media — should be checked on single crystals.

2. **Intergranular ductile fracture:** The most obvious efforts needed to enhance the modeling of intergranular ductile fracture presented in this work are the following:

   - The homogenized model of intergranular ductile fracture presented in Section III.3 should be supplemented with the intergranular coalescence criterion of Section III.2. The simplified evolution laws used for transgranular void coalescence can be easily adapted for the two modes of coalescence in layers — localization in the softest crystal and localization in both crystals —, as seen with Eq. III.127. This way, a comprehensive numerical assessment of the homogenized model with finite-strain unit-cell simulations of intergranular void growth and coalescence (as in Section II.1 for transgranular ductile fracture) could be carried out.
   - The assumption that grain boundaries can be modeled mechanically as perfect bonding interfaces for ductile fracture needs to be qualified with dedicated model experiments. They could adapt the set-up developed in Barrioz et al. (2018b) and Barrioz et al. (2019) to intergranular ductile fracture: *i.e.* using thin bicrystalline samples with an intergranular hole drilled by FIB, which would then be loaded mechanically.

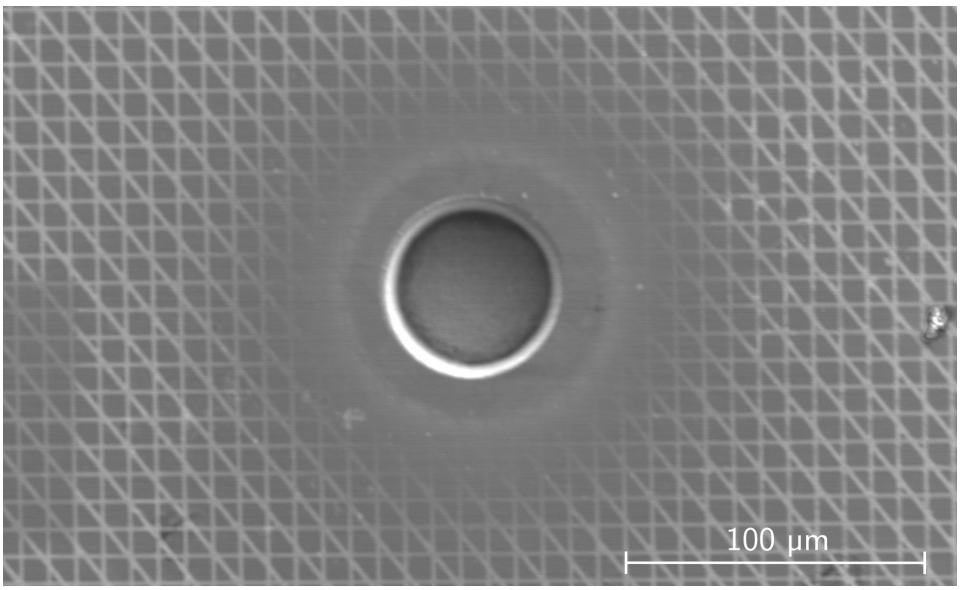

FIGURE III.82: FIB hole drilled in an austenitic stainless steel sample on which a gold microgrid for digital image correlation with steps of 10 µm was previously marked. The microgrid was deposited at Centre des Matériaux (Mines ParisTech) using a method described in Annex 12 of Chaumun (2016). The damage suffered by the grid around the hole suggests that drilling from behind would lead to better results than drilling from the front as done here.

Using a microgrid (see Fig. III.82) would enable to recover deformations around the cavity through digital image correlation and compare them to corresponding crystal plasticity FEM simulations using perfect bonding at the grain boundary. Refined modeling for grain boundaries will be needed in case of discrepancies between the simulated and measured displacement fields.

3. **Competition between ductile fracture modes:** As highlighted in the previous section, the present work has made contributions to enable the prediction of the competition between transgranular and intergranular ductile fracture:

   - Future work should harvest this progress by performing ductile fracture simulations on simplified materials with both failure modes to assess the effect of microstructure parameters (see Pardoen et al. (2003) and Fourmeau et al. (2015)). This means that analyses carried out in Sections III.1.5 and III.2.5.2 should be extended to finite-strain simulations with homogenized models for transgranular and intergranular fracture. However, it will require to mesh grain boundary zones with classical FEM elements, leading to the choice of an intergranular zone thickness. This will create a mesh dependence that must be handled carefully. Note that triple points (points where three grains meet) should not be meshed by dedicated elements (*e.g.* Fourmeau et al. (2015)) in a first time, but given their propensity to nucleate voids (see Section I.1.2), their effect has to be investigated in further work.
   - Experimental results of Section III.4 have yet to be analyzed in light of the analytical yield criterion used in the previous sections.

Long-term prospects

Two main long-term prospects are envisioned for this work. The first one concerns validation of the results detailed in the previous section, and the second one deals with their possible application:

1. **Experimental validation:** As regularly evoked throughout this document, there is a real need for reliable experiments involving the ductile fracture of oligo-crystals to validate or challenge micromechanical modeling. Indeed, crystal plasticity effects are best noticed when samples present few grains (or even a single grain) in the area loaded mechanically. Many challenges are associated with this type of testing. The first one is the relatively small size of grains in most industrial alloys (*e.g.* about 10 µm in austenitic stainless steels) because the

size of grains has an adverse effect on most mechanical properties except creep resistance. This hurdle requires either to use micro-samples of industrial alloys or model alloys with bigger grains (ideally 1 mm of diameter), each time with size effect issues. The second one is the difficulty of acquiring reliable *in-situ* three-dimensional experimental data (*i.e.* with fast and non-destructive techniques), a reason that makes samples with very low thickness quite attractive. A third one is the fact that the microstructure should be simple enough to make meaningful comparisons between, on the one hand, experiments and, on the other hand, explicit simulations or homogenized models. Indeed, this is a mandatory first step towards simulating complex microstructure. Without a dedicated model for void nucleation, this implies that cavities should pre-exist in the material (machined voids, helium bubbles, lack-of-fusion defects, etc.) or at least be nucleated at low strains. Carrying these model experiments, albeit challenging, should prove very valuable to assess the micromechanical prediction of transgranular/intergranular ductile fracture, *i.e.* qualify the situations in which the model/simulation compares satisfyingly with the measured data and identify the mechanisms that need additional examination.

2. **Prediction of the competition between ductile fracture modes:** As highlighted in the previous section, predicting the competition between transgranular ductile fracture and intergranular ductile fracture is an important prospect of this work. In the long run, it is envisioned that homogenized models will enable the study of this competition in engineering materials — for instance precipitation-hardened aluminum alloys — with more realistic texture, grain morphology, and population of void nuclei (*e.g.* Pardoen et al. (2010)). The results of the latter shall be compared to available macroscopic experimental data to validate the qualitative trends shown by simulations. Finally, these simulations could be used to predict the fracture toughness of alloy microstructures on which no experimental data is available, leading to predictions that could:

   - improve or accelerate the development of materials in which intergranular ductile fracture would be banned, effectively enhancing their ductility;
   - ease the constitution of safety cases of existing materials by assessing the current security margins or justify lifetime extension due to increased confidence.

Résumé du manuscrit

Le corps du manuscrit étant rédigé en langue anglaise, le texte suivant est un résumé détaillé de la thèse en langue française.

Contexte scientifique

La rupture ductile intergranulaire est un mode de ruine qui présente les trois phénomènes successifs — ou éventuellement simultanés — suivants :

1. la germination de cavités, qui se manifeste par la création de vides dans le matériau par décohésion atomique ou condensation de lacunes, ces deux processus étant favorisés par l'existence de concentration de contraintes — glissement aux joints de grains, empilement de dislocations, présence de cavités adjacentes — qui se produisent habituellement aux particules intergranulaires de seconde phase des matériaux industriels. Quelques fois, les cavités ne sont pas créées par un chargement mécanique quasi-statique mais préexistent dans le matériau, *e.g.* cavités d'irradiation, cavités issues d'impacts (dites « de spallation ») et bulles d'hélium.
2. la croissance de cavités, qui est caractérisée par une augmentation du volume des cavités intergranulaires sans interaction entre elles du fait de l'écoulement plastique aux joints de grains. La plasticité peut prendre la forme de plusieurs modes de déformations — glissement de dislocations, fluage-dislocation, maclage — et peut parfois être précédée ou évincée par la diffusion de lacunes aux joints de grains — une spécificité de la rupture intergranulaire. Un paramètre adimensionnel ξ est introduit dans l'étude bibliographique afin de distinguer les cas relevant de la diffusion de ceux associés à la plasticité.
3. la coalescence de cavités, qui est définie par l'augmentation de volume des vides dès lors qu'ils interagissent. De ce fait, les cavités coalescent en une unique fissure intergranulaire, ou en de multiples fissures qui coalescent elles-mêmes dans un second temps. Pour certains auteurs, la rupture ductile intergranulaire est contrôlée presque entièrement par la coalescence de cavités, contrairement à la rupture ductile transgranulaire pour laquelle la croissance de cavités joue un rôle majeur.

Les surfaces de ruptures associées avec ce mode de rupture présentent des facettes intergranulaires couvertes de fines cupules, ce qui permet de les distinguer de deux autres modes de rupture avec lesquels la rupture ductile intergranulaire présente des points communs :

- la rupture fragile intergranulaire, qui ne présente pas de cupules du fait de l'absence de plasticité ;
- la rupture ductile transgranulaire, dont les surfaces sont exemptes de facettes intergranulaires car la coalescence des cavités n'a pas lieu aux joints de grains.

La confusion entre ces modes de rupture et la rupture ductile intergranulaire peut parfois être causée par une résolution insuffisante des observations fractographiques. La déformation à rupture associée à la rupture ductile intergranulaire est généralement supérieure à celle de la rupture fragile intergranulaire — car la déformation plastique en est absente — et inférieure à celle de le rupture ductile transgranulaire. Cette dernière constatation s'explique par le fait que la rupture ductile intergranulaire est souvent associée avec une moindre croissance de cavités, comme en témoignent les cupules de taille inférieure sur les surfaces de rupture.

Contexte industriel

La rupture ductile intergranulaire peut être observée dans de nombreux matériaux industriels — qu'ils soient irradiés ou non — sous diverses conditions de sollicitation. Les alliages à durcissement structural sont particulièrement ex-

posés à ce mode de rupture à basse température homologue (le rapport entre la température et la température de fusion du matériau concerné), quelle que soit la structure du réseau cristallin (*e.g.* cubique à faces centrées, cubique centré, hexagonal compact). En premier lieu, les alliages d'aluminium forment la classe de matériaux dans laquelle la rupture ductile intergranulaire a été mise en évidence pour la première fois. Parmi les alliages les plus cités, on trouve Al-Zn-Mg, Al-Cu et Al-Mg-Si. Les alliages d'aluminium contenant du lithium, divisés en trois générations successives, sont une catégorie à part entière de matériaux vulnérable à la rupture intergranulaire par croissance et coalescence de cavités. Tous les alliages d'aluminium à durcissement structural présentent des zones exemptes de précipités autour des joints de grains ; plus molles que l'intérieur des grains, elles jouent un rôle important dans la localisation de la plasticité. Après les alliages d'aluminium, la deuxième classe de matériaux dans laquelle la rupture ductile intergranulaire est le plus couramment observée est constituée des superalliages de nickel : par exemple, l'Inconel X-750, le MAR-M200 et l'Inconel 718. L'absence de zones exemptes de précipités dans certains de ces alliages révèle un phénomène élémentaire alternatif dans lequel la précipitation intergranulaire est si préjudiciable que des zones molles autour des joints de grains ne sont pas nécessaires pour favoriser la croissance de cavités intergranulaires. Des comportements similaires sont observés dans d'autres matériaux métalliques : le magnésium allié avec des terres rares (*e.g.* Mg-11Gd-2Nd-0.4Zr) présente ce mode de ruine à un durcissement structural spécifique ; par ailleurs, les alliages de titane à phase β métastable sont sujets à de la rupture intergranulaire à cupules du fait de précipités de phase α aux joints de grains, ce qui est un obstacle à leur usage plus large dans l'industrie aérospatiale.

D'autre matériaux que les alliages à durcissement structural sont susceptibles de présenter de la rupture ductile intergranulaire. Ainsi, la surchauffe d'acier contenant du souffre au cours d'un traitement d'austénitisation favorise ce mode de ruine en augmentant la précipitation de sulfure de manganèse aux joints de grains. Par ailleurs, la rupture ductile intergranulaire peut être causée par l'irradiation neutronique, particulièrement quand des bulles d'hélium sont formées aux joints de grains comme cela a pu être observé dans les aciers austénitiques et les alliages à base nickel. Finalement, il faut mentionner que la rupture intergranulaire à haute température peut aussi être considérée comme ductile quand la contribution de la plasticité à la croissance des cavités surpasse l'intensité des phénomènes de diffusion de lacunes aux joints de grains mis en jeu par le fluage. Des exemples de telles situations sont la sollicitation à forte vitesse de déformation et la fissuration en relaxation des aciers austénitiques, ainsi que la rupture de l'Inconel X-750.

Approche micromécanique de la rupture ductile

À la suite de contributions fondatrices datant d'un demi-siècle (Rice and Tracey, 1969; Gurson, 1977; Thomason, 1985), la prédiction de la rupture ductile à fondement physique a été tentée par le biais d'approches micromécaniques fondées sur l'homogénéisation des matériaux poreux. Dans ce cadre d'étude, les trois étapes de la rupture ductile sont supposées être prises en compte par des modèles dédiés. Toutefois, la compréhension de la germination des cavités étant toujours limitée, ce travail adopte l'hypothèse selon laquelle les cavités préexistent dans le matériau ou apparaissent très tôt sous chargement mécanique. De fait, seulement la croissance et la coalescence de cavités sont modélisées, et ce différemment en fonction de l'échelle à laquelle les vides se situent :

- si les cavités sont *plus grandes que les grains*, le matériau autour des vides peut être représenté de manière satisfaisante par des lois de plasticité phénoménologiques comme celles de Mises (1913) et Hill (1948) ;
- si les cavités se trouvent *à l'échelle cristalline*, l'approche fondée sur la plasticité phénoménologique peut toujours être adoptée pour représenter le comportement moyen des cavités ; toutefois, cette approche ne tient qu'imparfaitement compte de la microstructure car l'effet de la plasticité cristalline n'est plus négligeable, ce qui crée un besoin pour des modèles pour cristaux poreux et pour joints de grains poreux.

Dans le premier cas, une abondante littérature scientifique a développé des critères de plasticité adaptés à des applications diverses (cavités sphériques, cavités ellipsoïdales, matériaux anisotropes, effets de taille etc.). De plus, des modèles homogénéisés rassemblant des critères pour la croissance et la coalescence de cavités ainsi que des lois d'évolution pour la microstructure ont été utilisés pour simuler la rupture ductile transgranulaire. Dans le second cas, seulement une poignée d'études sur les monocristaux poreux sont disponibles. En particulier, il n'existe aucun modèle homogénéisé complet fondé sur des critères de plasticité pour monocristaux poreux, pas plus que de critère pour la coalescence de cavités en colonnes. De plus, la modélisation des joints de grains poreux est un domaine en

grande partie inexploré. De fait, la simulation de la rupture ductile intergranulaire à fondement physique repose la plupart du temps sur le maillage explicite des fissures (comme dans les calculs XFEM) et des cavités (comme dans les calculs de cellules-unité poreuses) aux joints de grains.

Contributions à l'étude micromécanique de la rupture transgranulaire

Dans une première partie, des contributions à l'étude de la rupture ductile transgranulaire sont faites en utilisant le formalisme micromécanique de l'homogénéisation des matériaux poreux. En effet, la simulation de la rupture ductile établie sur des bases physiques ne peut se permettre de prendre explicitement en considération toutes les cavités d'un matériau et requiert de fait la dérivation de modèles homogénéisés capables de reproduire correctement la croissance et la coalescence graduelles des vides par un comportement mécanique moyenné. Tandis que la majeure partie de la littérature s'est concentrée sur une approche qui considère des cavités plus grandes que la taille de grains, ce travail est principalement dédié à la prise en compte des cavités à l'intérieur des monocristaux, puisqu'il s'agit d'une situation observée dans beaucoup d'alliages industriels.

Les modèles homogénéisés reposent avant tout sur des critères de plasticité pour matériau poreux qui doivent décrire aussi précisément que possible le seuil auquel la déformation irréversible se produit et donc tenir compte des différents modes de déformations. Dans ces travaux de thèse, deux approches concurrentes sont adoptées :

- Etant donné que la rupture ductile a lieu par croissance et coalescence de cavités, le critère de plasticité peut être obtenu à partir des critères correspondant à chacun de ces deux modes de déformation. Deux des études de cette partie mettent en pratique cette démarche :
  - Tout d'abord, un modèle homogénéisé pour monocristaux poreux est proposé à partir de critères de plasticité déjà disponibles dans la littérature scientifique pour la croissance et la striction interne transgranulaires de cavités, ainsi que de lois d'évolution ad hoc pour les variables internes. Ce modèle est validé à partir d'une base de données extensive de simulations explicites de cellules-unité contenant une cavité initialement sphérique au sein d'un monocristal d'orientation cristallographique donnée. La comparaison montre un accord satisfaisant lorsque l'écrouissage cristallin sature, mais souligne une difficulté à homogénéiser un écrouissage trop intense. Le modèle est également comparé au modèle homogénéisé de Scherer et al. (2021), mettant en évidence qu'une prise en compte des rotations du réseau cristallin au sein du formalisme de grandes transformations apparaît nécessaire.
  - Ensuite, ce modèle homogénéisé est utilisé pour réaliser des simulations de déchirure ductile d'éprouvettes mono- et poly-cristallines en deux dimensions sous l'hypothèse des déformations planes. Ces calculs montrent un effet de l'orientation des grains sur le comportement à la rupture des éprouvettes, à la fois sur la courbe de charge, sur les champs locaux de contrainte et d'endommagement, et sur le trajet de fissuration. Une première simulation de déchirure ductile d'un polycristal en trois dimensions est aussi effectuée. Ces réalisations montrent que la simulation de composants et l'optimisation de propriétés matériau fondées sur la prise en compte de la microstructure sont possibles avec ces approches.
- Dans une approche alternative, le critère de plasticité peut être obtenu en combinant des critères pour la localisation graduelle de la déformation en couches d'une part, et en colonnes d'autre part. En se plaçant dans ce cadre, une surface de plasticité incorporant à la fois la croissance de cavités, la coalescence par striction interne et la coalescence en colonnes est développée par analyse limite cinématique pour les matériaux anisotropes, qu'ils suivent la loi phénoménologique de Hill ou les équations de la plasticité cristalline. En effet, il est nécessaire de tenir compte de la coalescence en colonnes pour prédire correctement la rupture ductile dans des situations variées, comme des observations expérimentales et des simulations numériques le mettent en évidence. Enfin, les lois d'évolution des paramètres microstructuraux associées à cette surface de plasticité sont obtenues par analyse limite séquentielle afin de développer un modèle homogénéisé complet.

Contributions à l'étude micromécanique de la rupture intergranulaire

Une seconde partie rassemble les contributions à la prédiction de la rupture ductile intergranulaire. Dans un premier temps, le formalisme micromécanique de l'homogénéisation des matériaux poreux est transposé de la rupture ductile transgranulaire vers la rupture ductile intergranulaire. Cette approche conduit aux avancées suivantes :

- Premièrement, deux critères de plasticité pour la croissance de cavités intergranulaires sont obtenus par le biais de méthodes différentes : d'une part, un critère de type Gurson pour les cavités sphériques est développé par l'analyse limite cinématique, et d'autre part, un potentiel viscoplastique macroscopique est dérivé pour une interface cristalline avec des cavités ellipsoïdales en utilisant une méthode variationnelle reposant sur la comparaison avec un composite linéaire. Ces deux critères sont validés grâce à une large base de données de calculs de cellules-unité réalisés sous l'hypothèse des petites perturbations ; l'utilisation d'un unique paramètre de calibration pour chaque modèle conduit à un accord très satisfaisant. Finalement, ces deux critères de plasticité sont comparés à la surface de plasticité de Paux et al. (2015) correspondant à la rupture ductile transgranulaire afin d'obtenir une première estimation de la compétition entre ruptures ductiles intergranulaire et transgranulaire. En particulier, il est mis en évidence que la croissance de cavités intergranulaires ne peut se produire que si les joints de grains sont suffisamment affaiblis par rapport à l'intérieur des grains.

- Ensuite, une estimation de la charge limite correspondant à la coalescence intergranulaire de cavités sous traction et cisaillement combinés est développé par le biais de l'analyse limite cinématique, dans un premier temps sur un simple bi-matériau de Mises et ensuite sur un bi-cristal. Deux modes de coalescence concurrents sont mis en lumière : dans l'un, la plasticité est localisée quasi-exclusivement dans le matériau le plus mou , tandis que dans l'autre, la plasticité est observée dans l'entièreté du ligament reliant les cavités. La détermination du mode de coalescence qui prévaut est d'une importance capitale car la localisation de la plasticité dans le matériau le plus mou a probablement des effets délétères sur la ductilité du joint de grains. La charge limite pour la coalescence intergranulaire de cavités est vérifiée grâce aux calculs de cellules-unité correspondants, et présente un accord qualitatif avec ces derniers. Ce modèle théorique est aussi appliqué à la compétition entre la coalescence transgranulaire et la coalescence intergranulaire. Finalement, il est employé en conjonction avec le critère de type Gurson pour la croissance de cavités intergranulaires au sein d'un formalisme multi-surfaces et comparé à des résultats de simulation de cellules-unité sollicitées de manière axisymétrique dans l'hypothèse des petites perturbations, révélant un excellent accord.

- Enfin, un modèle homogénéisé pour la croissance de cavités intergranulaires fondé sur le critère de plasticité de type Gurson est proposé dans un formalisme de grandes transformations reposant sur la décomposition multiplicative du gradient de la transformation. Dans cette première tentative, l'écrouissage n'est pas pris en compte. Le modèle homogénéisé est implémenté numériquement et comparé à une base de données de simulations de cellules-unité de joints de grains poreux en grandes transformations avec des chargements axisymétriques correspondant à divers taux de triaxialité des contraintes. La correspondance entre le modèle et les simulations est satisfaisant pour des petites déformations. Néanmoins, des différences apparaissent aux déformations plus importantes, et ce particulièrement pour $T = 1$. Cette limitation du modèle peut être lié à une prise en compte insuffisante des rotations locales du réseau cristallin, qui peuvent-être très hétérogènes dans les deux grains.

Dans le reste de cette partie, une investigation expérimentale de la rupture ductile d'un acier austénitique inoxydable avec des gros grains (autour de 500 µm) implanté aux ions hélium est menée. En effet, du fait de sa solubilité limitée, l'hélium forme des bulles dans le matériau, à la fois aux joints de grains et à l'intérieur des grains. Ces bulles peuvent ensuite se comporter comme des germes de cavités et conduire à de la rupture ductile intergranulaire. L'objectif de ces expériences-modèles est premièrement de valider un protocole pour étudier la compétition entre rupture intergranulaire et rupture transgranulaire et deuxièmement de comparer les données expérimentales aux prédictions des modèles développés dans le reste de la thèse. Les échantillons sont de fines lames (45 µm d'épaisseur) rectangulaires dans lesquelles de petites entailles sont usinées par faisceau ionique focalisé dans le but d'avoir un unique joint de grains dans la section utile de chaque éprouvette. Les orientations de ces grains sont relevées par EBSD. L'irradiation en cyclotron est dimensionnée en collaboration avec les équipes du CEMHTI (CNRS Orléans) et l'Institut Paul Scherer (Suisse) afin d'atteindre une concentration atomique d'hélium de 1.8 %. D'après la littérature, ce taux est suffisant pour déclencher de la rupture intergranulaire. Les échantillons sont ensuite chargés mécaniquement dans une machine de micro-traction jusqu'à la rupture, révélant pour certains de la rupture intergranulaire, pour d'autres de la rupture transgranulaire et pour les derniers un faciès mixte. La caractérisation des défauts d'irradiation (boucles de Frank et bulles d'hélium) sont réalisés au MET et les faciès de rupture sont analysés au MEB haute résolution afin de collecter des données relatives au processus de rupture. Les résultats expérimentaux quantitatifs sont toujours en cours d'analyse afin d'être comparés dans le futur aux prédictions de modèles de rupture ductile.

Perspectives à court terme

Un certain nombre de développement ont été envisagés dans cette thèse mais n'ont pas pu être réalisés faute de temps. Ils peuvent servir de perspectives à brève échéance pour ce travail :

1. **Rupture ductile transgranulaire :** Afin de modéliser de manière plus précise ce mode de ruine, le modèle homogénéisé proposé doit être complété avec les modes de localisation plastique manquants :

   - la coalescence assistée par cisaillement, qui est d'une importance majeure pour les chargement à faible taux de triaxialité des contraintes et pour laquelle un critère de plasticité a été proposé dans Hure (2019) ;
   - la coalescence en colonnes, qui a une influence significative sur la déformation à rupture de certaines microstructures de matériaux et pour laquelle un modèle a été proposé dans cette thèse ;

   En se fondant sur les conclusions de l'analyse du modèle homogénéisé transgranulaire, la prise en compte des grandes transformations pourrait aussi être améliorée en adoptant le formalisme de décomposition multiplicative du gradient de la transformation, comme cela a été fait pour le modèle homogénéisé intergranulaire. L'évaluation numérique du modèle devrait alors être recommencé depuis le début. Des simulations de cellules-unité avec des répartitions aléatoires de cavités sont également nécessaires afin d'étudier les effets de la distribution des vides. En particulier, les résultats de Cadet et al. (2022) — selon lesquels la coalescence assistée par cisaillement se produit généralement avant la coalescence par striction interne quand les cavités sont réparties de manière aléatoire — seraient intéressants à vérifier sur les monocristaux poreux. Enfin, la régularisation du modèle homogénéisé par l'introduction d'une longueur interne afin d'éviter une dépendance pathologique à la taille de maille dans les calculs mécaniques apparait nécessaire.

2. **Rupture ductile intergranulaire :** Les efforts les plus évidents pour améliorer la modélisation de la rupture ductile intergranulaire présentée dans cette thèse sont les suivants:

   - Le modèle homogénéisé de rupture ductile intergranulaire devrait être complété par le critère de coalescence intergranulaire de cavités proposé dans ce travail. Les lois d'évolution simplifiées utilisées pour la coalescence transgranulaire de cavités peuvent être facilement adaptées pour les deux modes de coalescence en couches — localisation dans le cristal le plus mou et localisation dans les deux cristaux en même temps — mis en évidence. De cette manière, une évaluation complète du modèle homogénéisé avec des simulations de cellules-unité de la croissance et coalescence de cavités intergranulaires en grandes transformations (comme cela a été le cas pour la rupture ductile transgranulaire) pourrait être conduite.
   - L'hypothèse selon laquelle les joints de grains peuvent être modélisés mécaniquement par des interfaces de contact parfait dans le contexte de la rupture ductile doit être vérifié par des expériences-modèles dédiées. Dans cette optique, le protocole utilisé par Barrioz et al. (2018b) and Barrioz et al. (2019) pourrait être adapté à la rupture ductile intergranulaire, ce qui consisterait en l'utilisation d'éprouvettes bi-cristallines avec un trou intergranulaire percé par faisceau ionique focalisé et qui seraient ensuite chargées mécaniquement. L'emploi d'une micro-grille permettrait de remonter aux déformations expérimentales par corrélation d'images et de les comparer à celles prédites par les simulations de plasticité cristalline avec contact parfait à l'interface. Dans le cas de différences trop importantes entre les champs de déplacement, une modélisation plus poussée du joint de grains sera nécessaire.

3. **Compétition entre les modes de rupture ductile :**

   - Les avancées permises par ces travaux de thèse peuvent être poursuivies en réalisant des simulations de rupture ductile sur des matériaux simplifiés dans lesquels les deux modes de ruines sont possibles afin d'étudier les effets des paramètres microstructuraux (voir citetPardoen2003,Fourmeau2015). Cela suggère d'étendre les analyses de cette étude à des simulations en grandes transformations avec des modèles homogénéisés pour les ruptures ductiles transgranulaire et intergranulaire. Cependant, cela requerra de mailler les zones intergranulaires dans les calculs par éléments finis, menant à un choix de l'épaisseur de la zone intergranulaire et à une dépendance en la taille de mailles qui ne doit pas être négligée. Dans un premier temps, les points triples (c'est-à-dire les endroits où trois grains se rencontrent) ne devraient pas

être maillés par des éléments dédiés, mais étant donné leur propension à faire germer des cavités, leur modélisation devra être considérée avec plus d'attention dans un second temps.

- Les résultats expérimentaux sur l'acier implanté à l'hélium doivent toujours être analysées à la lumière des modèles de rupture ductile développés dans la thèse.

Perspectives à long terme

Deux développements à long terme sont envisagés pour ce travail. Le premier concerne la validation des résultats théoriques et numériques, et le second a pour sujet leurs possibles applications:

1. **Validation expérimentale :** Afin de valider ou de questionner les modélisations micromécaniques, il y a un besoin vital d'expériences fiables sur la rupture ductile d'oligo-cristaux. En effet, les effets de la plasticité cristalline sont mieux mis en évidence dans des éprouvettes présentant un faible nombre de grains — voire un monocristal — dans la zone utile chargée mécaniquement. La réalisation de ce type de tests suppose de relever un certain nombre de défis. Le premier est la taille de grains relativement petite de beaucoup d'alliages industriels (*e.g.* approximativement 10 µm dans les aciers austénitiques inoxydables) car la taille des grains a un effet délétère sur la plupart des propriétés mécaniques à l'exception de la résistance au fluage. Cet obstacle nécessite d'utiliser soit des micro-éprouvettes d'alliages industriels, soit des alliages-modèles avec des grains de plus grande taille (idéalement 1 mm de diamètre), à chaque fois avec des effets de taille problématiques. Le deuxième défi est la difficulté d'acquérir in-situ des données expérimentales fiables en trois dimensions (*i.e.* avec des techniques rapides et non-destructives), ce qui rend intéressantes les éprouvettes de très faible épaisseur. Un troisième est le fait que la microstructure devrait être assez simple pour faire des comparaisons satisfaisantes entre, d'une part, les expériences, et d'autres part, les simulations explicites ou les modèles homogénéisés. En effet, les cas simples sont un premier pas requis avant de simuler des microstructures plus complexes. Sans un modèle dédié pour la germination de cavités, cela signifie que les cavités doivent préexister dans le matériau (trous usinés, bulles d'hélium, défauts de manque de fusion, etc.) ou au moins apparaître à de faibles déformations. La conduite de ces expériences-modèles, bien que contraignante, apporterait des données d'une grande valeur pour évaluer la prédiction micromécanique de la rupture ductile, c'est-à-dire identifier les situations dans lesquelles le modèle ou les simulations sont cohérents avec les données expérimentales et mettre en évidence les mécanismes qui doivent être étudiés plus profondément.

2. **Prédiction de la compétition entre les modes de rupture ductile :** Il est envisagé que les modèles homogénéisés permettent l'étude de cette compétition dans les matériaux industriels — par exemple les alliages d'aluminium à durcissement structural — avec une texture, une morphologie de grains et des populations de germes de cavités réalistes (*e.g.* Pardoen et al. (2010)). Les résultats de ces simulations devront alors être comparés aux données expérimentales disponibles afin de valider les tendances qualitatives présentes numériquement. Enfin, ces simulations pourront être utilisées pour prédire la ténacité de microstructures d'alliages pour lesquelles des données expérimentales ne sont pas disponibles, menant à des estimations qui pourront :

   - améliorer ou accélérer le développement de matériaux dans lesquels la rupture ductile intergranulaire serait empêchée, augmentant efficacement leur ductilité ;
   - faciliter la constitution de dossiers de sûreté pour des matériaux existants en étudiant les marges de sécurité actuelles ou en justifiant des extensions de durée de vie du fait d'une confiance augmentée.

Bibliography

Abatour, M., Ammar, K., Forest, S., Ovalle Rodas, C., Osipov, N., and Quilici, S. (2021). *A generic formulation of anisotropic thermo-elastoviscoplasticity at finite deformations for Finite Element codes*. Tech. rep. Centre des Matériaux Mines ParisTech and Transvalor.

Abbas, M. (2016). *Model of great deformations GDEF_LOG*. Tech. rep. EDF / Code_Aster.

Alarcon, O., Nazar, A., and Monteiro, W. (1991). "The effect of microstructure on the mechanical behavior and fracture mechanism in a 7050-T76 aluminum alloy". *Materials Science and Engineering: A* 138 (2), pp. 275–285.

Anderson, P. M. and Shewmon, P. G. (2000). "Stress redistribution and cavity nucleation near a diffusively growing grain boundary cavity". *Mechanics of Materials* 32 (3), pp. 175–191.

Anoukou, K., Pastor, F., Dufrenoy, P., and Kondo, D. (2016). "Limit analysis and homogenization of porous materials with Mohr-Coulomb matrix: Part I - Theoretical formulation". *Journal of the Mechanics and Physics of Solids* 91, pp. 145–171.

Arkell, D. and Pfeil, P. (1964). "Transmission electron microscopical examination of irradiated austenitic steel tensile specimens". *Journal of Nuclear Materials* 12 (2), pp. 145–152.

Arminjon, M. (1991). "A regular form of the Schmid law: Application to the ambiguity problem". *Textures and Microstructures* 14-18, pp. 1121–1128.

Ashmawi, W. M. and Zikry, M. A. (2001). "Prediction of grain-boundary interfacial mechanisms in polycrystalline materials". *Journal of Engineering Materials and Technology* 124 (1), pp. 88–96.

Asim, U. B., Siddiq, M. A., and Kartal, M. E. (2019a). "A CPFEM based study to understand the void growth in high strength dual-phase titanium alloy (Ti-10V-2Fe-3Al)". *International Journal of Plasticity* 122, pp. 188–211.

Asim, U. B., Siddiq, M. A., and Kartal, M. E. (2019b). "Representative volume element (RVE) based crystal plasticity study of void growth on phase boundary in titanium alloys". *Computational Materials Science*.

ASTM E1820 (2017). "Standard test method for measurement of fracture toughness". *Annual Book of ASTM Standards*.

ASTM E521 (2006). "Standard practice for neutron radiation damage simulation by charged-particle irradiation". *Annual Book of ASTM Standards*.

Auzoux, Q. (2004). "Fissuration en relaxation des aciers inoxydables austénitiques - Influence de l'écrouissage sur l'endommagement intergranulaire". PhD thesis. École nationale supérieure des Mines de Paris.

Auzoux, Q., Allais, L., Caës, C., Monnet, I., Gourgues, A. F., and Pineau, A. (2010). "Effect of pre-strain on creep of three AISI 316 austenitic stainless steels in relation to reheat cracking of weld-affected zones". *Journal of Nuclear Materials* 400 (2), pp. 127–137.

Barnes, R. S. (1965). "Embrittlement of stainless steels and nickel-based alloys at high temperature induced by neutron radiation". *Nature* 206, pp. 1307–1310.

Barrioz, P., Hure, J., and Tanguy, B. (2018a). "On void shape and distribution effects on void coalescence". *Journal of Applied Mechanics* 86.

— (2018b). "Void growth and coalescence in irradiated copper under deformation". *Journal of Nuclear Materials* 502, pp. 123–131.

— (2019). "Effect of dislocation channeling on void growth to coalescence in FCC crystals". *Materials Science and Engineering: A* 749, pp. 255–270.

Barrioz, P.-O. (2019). "Rupture ductile des matériaux CFC irradiés". PhD thesis. Université Paris-Saclay.

Bayerschen, E., McBride, A., Reddy, B., and Böhlke, T. (2016). "Review on slip transmission criteria in experiments and crystal plasticity models". *Journal of Materials Science* 51 (1), pp. 2243–2258.

Becker, R., Needleman, A., Suresh, S., Tvergaard, V., and Vasudevan, A. (1989). "An analysis of ductile failure by grain boundary void growth". *Acta Metallurgica* 37 (1), pp. 99–120.

Benallal, A., Desmorat, R., and Fournage, M. (2014). "An assessment of the role of the third stress invariant in the Gurson approach for ductile fracture". *European Journal of Mechanics - A/Solids* 47, pp. 400–414.

Benallal, A. (2018). "On some features of the effective behaviour of porous solids with J2- and J3-dependent yielding matrix behaviour". *Comptes Rendus Mécanique* 346 (2), pp. 77–88.

Bennetch, J. and Jesser, W. (1981). "Microstructural aspects of He embrittlement in type 316 stainless steel". *Journal of Nuclear Materials* 104, pp. 809–813.

Benzerga, A. A., Besson, J., Batisse, R., and Pineau, A. (2001). "Synergistic effects of plastic anisotropy and void coalescence on fracture mode in plane strain". *Modelling and Simulation in Materials Science and Engineering* 10 (1), pp. 73–102.

Benzerga, A. A. (2002). "Micromechanics of coalescence in ductile fracture". *Journal of the Mechanics and Physics of Solids* 50, pp. 1331–1362.

Benzerga, A. A. and Besson, J. (2001). "Plastic potentials for anisotropic porous solids". *European Journal of Mechanics - A/Solids* 20, pp. 397–434.

Benzerga, A. A., Besson, J., and Pineau, A. (2004a). "Anisotropic ductile fracture: Part I – Experiments". *Acta Materialia* 52, pp. 4623–4638.

— (2004b). "Anisotropic ductile fracture: Part II – Theory". *Acta Materialia* 52, pp. 4639–4650.

Benzerga, A. A. and Leblond, J.-B. (2010). "Ductile fracture by void growth to coalescence". *Advances in Applied Mechanics* 44, pp. 169–305.

— (2014). "Effective yield criterion accounting for microvoid coalescence". *Journal of Applied Mechanics* 81.

Benzerga, A. A., Leblond, J.-B., Needleman, A., and Tvergaard, V. (2016). "Ductile failure modeling". *International Journal of Fracture* 201, pp. 29–80.

Benzerga, A. A. (2000). "Rupture ductile des tôles anisotropes". PhD thesis. École nationale supérieure des Mines de Paris.

Besson, J. (2010). "Continuum models of ductile fracture: A review". *International Journal of Damage Mechanics* 19, pp. 3–52.

Besson, J. and Foerch, R. (1998). "Object-oriented programming applied to the finite element method: Part I - General concepts". *Revue Européenne des Éléments Finis* 7, pp. 535–566.

Biswas, P., Narasimhan, R., and Kumar, A. (2013). "Interaction between a notch and cylindrical voids in aluminum single crystals: Experimental observations and numerical simulations". *Journal of the Mechanics and Physics of Solids* 61 (4), pp. 1027–1046.

Böhlke, T. and Bertram, A. (2001). "Isotropic orientation distributions of cubic crystals". *Journal of the Mechanics and Physics of Solids* 49, pp. 2459–2470.

Borodin, O. V., Bryk, V. V., Kalchenko, A. S., A., Parkhomenko, I. N. A., and Voyevodin, V. N. (2004). "Swelling and post-irradiated deformation structures in 18Cr-10Ni-Ti irradiated with heavy ions". *Journal of Nuclear Materials* 229-233, pp. 630–633.

Boyce, B. L., Clark, B. G., Lu, P., Carroll, J. D., and Weinberger, C. R. (2013). "The morphology of tensile failure in tantalum". *Metallurgical and Materials Transactions A* 44 (10), pp. 4567–4580.

Bramfitt, B. L. and Marder, A. R. (1977). "A study of the delamination behavior of a very low-carbon steel". *Metallurgical Transactions A* 8, pp. 1263–1273.

Briant, C. (1988). "Intergranular fracture in metals". *Journal de Physique* 49 (C5), pp. 3–23.

Bringa, E., Traiviratana, S., and Meyers, M. (2010). "Void initiation in FCC metals: Effect of loading orientation and nanocrystalline effects". *Acta Materialia* 58, pp. 4458–4477.

Bron, F. and Besson, J. (2006). "Simulation of the ductile tearing for two grades of 2024 aluminum alloy thin sheets". *Engineering Fracture Mechanics* 73 (11), pp. 1531–1552.

Brown, L. M. and Embury, J. D. (1973). "The initiation and growth of voids at second phase particles". *3rd International Conference on the strength of metals and alloys*, pp. 164–168.

Bui, H. D. (1969). "Évolution des frontières d'élasticité des métaux cubiques avec l'écrouissage et relation de comportement élasto-plastique des métaux cubiques". PhD thesis. Université Pierre et Marie Curie.

Busso, E. P. and Cailletaud, G. (2005). "On the selection of active slip systems in crystal plasticity". *International Journal of Plasticity* 21 (11), pp. 2212–2231.

Byun, T. and Hashimoto, N. (2006). "Strain localization in irradiated materials". *Nuclear Engineering and Technology* 38, pp. 619–638.

Cadet, C., Besson, J., Flouriot, S., Forest, S., Kerfriden, P., Lacourt, L., and Rancourt, V. de (2022). "Strain localization analysis in materials containing randomly distributed voids: Competition between extension and shear failure modes". *Journal of the Mechanics and Physics of Solids* 166.

Cadet, C., Besson, J., Flouriot, S., Forest, S., Kerfriden, P., and Rancourt, V. de (2021). "Ductile fracture of materials with randomly distributed voids". *International Journal of Fracture* 230, pp. 193–223.

Cailletaud, G. (2009). "An overview of the anatomy of crystal plasticity models". *Advanced Engineering Materials* 11 (9), pp. 710–716.

Carpenter, R. (1967). "Deformation and fracture of gold-platinum polycrystals strengthened by spinodal decomposition". *Acta Metallurgica* 15 (8), pp. 1297–1308.

Castañeda, P. P. and Suquet, P. (1997). "Nonlinear composites". *Advances in Applied Mechanics* 34, pp. 171–302.

Cawthorne, C. and Fulton, E. (1967). "Voids in irradiated stainless steel". *Nature* 216, pp. 575–576.

Cazacu, O., Revil-Baudard, B., Chandola, N., and Kondo, D. (2014). "New analytical criterion for porous solids with Tresca matrix under axisymmetric loadings". *International Journal of Solids and Structures* 51, pp. 861–874.

Cazacu, O., Revil-Baudard, B., Lebensohn, R. A., and Gărăjeu, M. (2013). "On the combined effect of pressure and third invariant on yielding of porous solids with von Mises matrix". *Journal of Applied Mechanics* 80 (6).

CEA (2018). "Cast3M". *www-cast3M.cea.fr*.

— (2020). "AMITEX_FFTP". *www.maisondelasimulation.fr/projects/amitex/html/*.

Chabaud-Reytier, M., Allais, L., Caes, C., Dubuisson, P., and Pineau, A. (2003). "Mechanisms of stress relief cracking in titanium stabilised austenitic stainless steel". *Journal of Nuclear Materials* 323 (1), pp. 123–137.

Chang, L., Sun, W., Cui, Y., Zhang, F., and Yang, R. (2014). "Effect of heat treatment on microstructure and mechanical properties of the hot-isostatic-pressed Inconel 718 powder compact". *Journal of Alloys and Compounds* 590, pp. 227–232.

Changizian, P., Yao, Z., Long, F., Topping, M., Xu, S., Daymond, M., and Griffiths, M. (2023). "Mechanical behavior of cold-worked, precipitation-hardened Inconel X-750 before and after helium-implantation". *Materials Characterization* 199.

Chaumun, E. (2016). "Corrosion sous contrainte de l'alliage 82 en vapeur d'eau hydrogénée à 400°C : Influence de la microstructure et du comportement mécanique sur l'amorçage". PhD thesis. École nationale supérieure des Mines de Paris.

Chen, C., Li, S., and Wang, Z. (1998). "Characteristics of strain and resolved shear stress in a bicrystal with the grain boundary perpendicular to the tensile axis". *Materials Science and Engineering: A* 247 (1), pp. 15–22.

Chen, C., Li, S., Wen, J., and Jia, W. (2000). "Finite element analysis about effects of stiffness distribution on stresses and elastic strain energy near the triple junction in a tricrystal". *Materials Science and Engineering: A* 282 (1), pp. 170–176.

Chen, C. W. and Machlin, E. S. (1956). "On the mechanism of intercrystalline cracking". *Acta Metallurgica* 4, pp. 655–656.

Chen, D., Murakami, K., Dohi, K., Nishida, K., Soneda, N., Li, Z., Liu, L., and Sekimura, N. (2015). "Radiation defects formed in ion-irradiated 316L stainless steel model alloys with different Si additions". *Materials Transactions* 56, pp. 1549–1552.

Chen, I.-W. and Argon, A. (1981). "Diffusive growth of grain-boundary cavities". *Acta Metallurgica* 29 (10), pp. 1759–1768.

Chen, T., Sakidja, R., Ching, W., and Zhou, C. (2019). "Crystal plasticity modeling of void growth on grain boundaries in Ni-based superalloys". *JOM* 71.

Chen, X., Asay, J. R., Dwivedi, S. K., and Field, D. P. (2006). "Spall behavior of aluminum with varying microstructures". *Journal of Applied Physics* 99 (2), p. 023528.

Chen, Y., Pedersen, K., Clausen, A., and Hopperstad, O. (2009). "An experimental study on the dynamic fracture of extruded AA6xxx and AA7xxx aluminium alloys". *Materials Science and Engineering: A* 523 (1), pp. 253–262.

Cheng, L., Monchiet, V., Morin, L., de Saxcé, G., and Kondo, D. (2015). "An analytical Lode angle dependent damage model for ductile porous materials". *Engineering Fracture Mechanics* 149, pp. 119–133.

Cheng, M., Li, C., Tang, M., Lu, L., Li, Z., and Luo, S. (2018). "Intragranular void formation in shock-spalled tantalum: Mechanisms and governing factors". *Acta Materialia* 148, pp. 38–48.

Chouksey, M. and Basu, S. (2021). "Exploration of subsequent yield surfaces through unit cell simulations". *International Journal of Solids and Structures* 219-220, pp. 11–22.

Chouksey, M., Keralavarma, S. M., and Basu, S. (2019). "Computational investigation into the role of localisation on yield of a porous ductile solid". *Journal of the Mechanics and Physics of Solids* 130, pp. 141–164.

— (2020). "Exploring subtle features of yield surfaces of porous, ductile solids through unit cell simulations". *Mechanics of Materials* 151.

Clayton, J. D. (2011). "Mechanical twinning in crystal plasticity". *Nonlinear mechanics of crystals*. Springer Netherlands, pp. 379–421.

Coble, R. L. (1963). "A model for boundary diffusion controlled creep in polycrystalline materials". *Journal of Applied Physics* 34 (6), pp. 1679–1682.

Cordero, N., Forest, S., Busso, E., Berbenni, S., and Cherkaoui, M. (2012). "Grain size effects on plastic strain and dislocation density tensor fields in metal polycrystals". *Computational Materials Science* 52 (1), pp. 7–13.

Courtin, L. (2015). "Optimisation de la transformation à froid des tubes de gaîne en acier austénitique 15-15TI AIM1". PhD thesis. Université de Poitiers.

Crépin, J., Bretheau, T., and Caldemaison, D. (1996). "Cavity growth and rupture of β-treated zirconium: A crystallographic model". *Acta Materiala* 12, pp. 4927–4935.

Curran, D., Seaman, L., and Shockey, D. (1987). "Dynamic failure of solids". *Physics Reports* 147 (5), pp. 253–388.

Curtet, E., Kedjar, B., Mompiou, F., Bahsoun, H., Pailloux, F., Courcelle, A., Bono, M., Olier, P., and Thilly, L. (2020). "Loss of ductility in optimized austenitic steel at moderate temperature: A multi-scale study of deformation mechanisms". *Materialia* 9, p. 100562.

Dakshinamurthy, M., Kowalczyk-Gajewska, K., and Vadillo, G. (2021). "Influence of cristallographic orientation on the void growth at the grain boundary in bi-crystals". *International Journal of Solids and Structures* 212, pp. 61–79.

Danas, K. and Castañeda, P. P. (2009). "A finite-strain model for anisotropic viscoplastic porous media: Part I - Theory". *European Journal of Mechanics- A/Solids* 28, pp. 387–401.

Danas, K., Idiart, M., and Castañeda, P. P. (2008). "A homogenization-based constitutive model for isotropic viscoplastic porous media". *International Journal of Solids and Structures* 45 (11), pp. 3392–3409.

Danas, K. and Ponte Castañeda, P. (2012). "Influence of the Lode parameter and the stress triaxiality on the failure of elasto-plastic porous materials". *International Journal of Solids and Structures* 49 (11), pp. 1325–1342.

Dayalan, I., Frank Crasta, P., Pradhan, S., and Gupta, R. (2020). "A review on stress relaxation cracking in austenitic stainless steel". *Proceedings of International Conference on Intelligent Manufacturing and Automation*. Ed. by H. Vasudevan, V. K. N. Kottur, and A. A. Raina. Springer Singapore, pp. 427–434.

DebRoy, T., Wei, H., Zuback, J., Mukherjee, T., Elmer, J., Milewski, J., Beese, A., Wilson-Heid, A., De, A., and Zhang, W. (2018). "Additive manufacturing of metallic components – Process, structure and properties". *Progress in Materials Science* 92, pp. 112–224.

Decreus, B., Deschamps, A., Donnadieu, P., and Ehrström, J. (2013). "On the role of microstructure in governing fracture behavior of an aluminum–copper–lithium alloy". *Materials Science and Engineering: A* 586, pp. 418–427.

Demkowicz, M. J. (2020). "A threshold density of helium bubbles induces a ductile-to-brittle transition at a grain boundary in nickel". *Journal of Nuclear Materials* 533.

Deshpande, N. U., Gokhale, A., Denzer, D. K., and Liu, J. (1998). "Relationship between fracture toughness, fracture path, and microstructure of 7050 aluminum alloy: Part I - Quantitative characterization". *Metallurgical and Materials Transactions A* 29, pp. 1191–1201.

Desormeaux, M., Rouxel, B., Motta, A., Kirk, M., Bisor, C., de Carlan, Y., and Legris, A. (2016). "Development of radiation damage during in-situ Kr^{++} irradiation of FeNiCr model austenitic steels". *Journal of Nuclear Materials* 475, pp. 156–167.

Dhooge, A., Dolby, R., Sebille, J., Steinmetz, R., and Vinckier, A. (1978). "A review of work related to reheat cracking in nuclear reactor pressure vessel steels". *International Journal of Pressure Vessels and Piping* 6 (5), pp. 329–409.

Dhooge, A. and Vinckier, A. (1987). "Reheat cracking - A review of recent studies". *International Journal of Pressure Vessels and Piping* 27 (4), pp. 239–269.

Ding, M.-S., Du, J.-P., Wan, L., Ogata, S., Tian, L., Ma, E., Han, W.-Z., Li, J., and Shan, Z.-W. (2016). "Radiation-induced Helium nanobubbles enhance ductility in submicron-sized single-crystalline copper". *Nano Letters* 16 (7), pp. 4118–4124.

Dormieux, L. and Kondo, D. (2010). "An extension of Gurson model incorporating interface stresses effects". *International Journal of Engineering Science* 48, pp. 575–581.

Edwards, D. J., Garner, F. A., Bruemmer, S. M., and Efsing, P. (2009). "Nano-cavities observed in a 316SS PWR flux thimble tube irradiated to 33 and 70 dpa". *Journal of Nuclear Materials* 384 (3), pp. 249–255.

Edwards, D., Simonen, E., Garner, F., Greenwood, L., Oliver, B., and Bruemmer, S. (2003). "Influence of irradiation temperature and dose gradients on the microstructural evolution in neutron-irradiated 316SS". *Journal of Nuclear Materials* 317, pp. 32–45.

Enakoutsa, K. and Leblond, J.-B. (2009). "Numerical implementation and assessment of the GLPD micromorphic model of ductile rupture". *European Journal of Mechanics - A/Solids* 28 (3), pp. 445–460.

English, C. A., Murphy, S. M., and Perks, J. M. (1990). "Radiation-induced segregation in metals". *Journal of the Chemical Society* 86 (8), pp. 1263–1271.

Evans, H. E. (1984). *Mechanisms of creep fracture*. Elsevier Applied Science.

Fabregue, D. and Pardoen, T. (2008). "A constitutive model for elastoplastic solids containing primary and secondary voids". *Journal of the Mechanics and Physics of Solids* 56, pp. 719–741.

Fleck, R., Taplin, D., and Beevers, C. (1975). "An investigation of the nucleation of creep cavities by 1 MV electron microscopy". *Acta Metallurgica* 23 (4), pp. 415–424.

Foltz, J. W., Welk, B., Collins, P. C., Fraser, H. L., and Williams, J. C. (2011). "Formation of grain boundary α in β Ti alloys: Its role in deformation and fracture behavior of these alloys". *Metallurgical and Materials Transactions A* 42, pp. 645–650.

Ford, I. J. (1992). "Intergranular fracture of fast reactor irradiated stainless steel". *Acta Metallurgica* 40 (1), pp. 113–122.

Forest, S. (2023). "Lois de comportement élasto-visco-plastique des matériaux en transformations finies". 2023 Mecatmat symposium, Aussois (France).

Forest, S. and Rubin, M. (2016). "A rate-independent crystal plasticity model with a smooth elastic–plastic transition and no slip indeterminacy". *European Journal of Mechanics - A/Solids* 55, pp. 278–288.

Fourmeau, M., Marioara, C., Børvik, T., Benallal, A., and Hopperstad, O. (2015). "A study of the influence of precipitate-free zones on the strain localization and failure of the aluminium alloy AA7075-T651". *Philosophical Magazine* 95 (28-30), pp. 3278–3304.

Francfort, G. and Murat, F. (1986). "Homogenization and optimal bounds in linear elasticity". *Archive for Rational Mechanics and Analysis* 94, pp. 307–334.

Franciosi, P., Berveiller, M., and Zaoui, A. (1980). "Latent hardening in copper and aluminium single crystals". *Acta Metallurgica* 28 (3), pp. 273–283.

Franciosi, P. and Zaoui, A. (1982). "Multislip in fcc crystals a theoretical approach compared with experimental data". *Acta Metallurgica* 30 (8), pp. 1627–1637.

Fritzen, F., Forest, S., Bohlke, T., Kondo, D., and Kanit, T. (2012). "Computational homogenization of elasto-plastic porous metals". *International Journal of Plasticity* 29, pp. 102–119.

Frodal, B. H., Thomesen, S., Børvik, T., and Hopperstad, O. S. (2021). "On the coupling of damage and single crystal plasticity for ductile polycrystalline materials". *International Journal of Plasticity* 142.

Frost, H. J. and Ashby, M. F. (1982). *Deformation-mechanism maps: The plasticity and creep of metals and ceramics*. Pergamon Press.

Fu, J. and Zhang, Y. (2020). "Mechanism of crack initiation and propagation of 316LN stainless steel during the high temperature tensile deformation". *Materials Research Express* 7 (8).

Fujii, K., Fukuya, K., Furutani, G., Torimaru, T., Kohyama, A., and Katoh, Y. (2001). *Proceedings of the Tenth International Symposium on Environmental Degradation of Materials in Nuclear Power Systems - Water Reactors*, CD format.

Fukuya, K., Fujii, K., Nakano, M., and Nakajima, N. (2001). *Proceedings of the Tenth International Symposium on Environmental Degradation of Materials in Nuclear Power Systems - Water Reactors*, CD format.

Fukuya, K., Nishioka, H., Fujii, K., Kamaya, M., Miura, T., and Torimaru, T. (2008). "Fracture behavior of austenitic stainless steels irradiated in PWR". *Journal of Nuclear Materials* 378 (2), pp. 211–219.

Fukuya, K. (2013). "Current understanding of radiation-induced degradation in light water reactor structural materials". *Journal of Nuclear Science and Technology* 50 (3), pp. 213–254.

Fukuya, K. and Fujii, K. (2001). "Swelling in cold-worked 316 stainless steels irradiated in a PWR". *INSS Journal* 8, pp. 156–165.

Fukuya, K., Fujii, K., Nishioka, H., and Kitsunai, Y. (2006). "Evolution of microstructure and microchemistry in cold-worked 316 stainless steels under PWR irradiation". *Journal of Nuclear Science and Technology* 43 (2), pp. 159–173.

Gallican, V. and Hure, J. (2017). "Anisotropic coalescence criterion for nanoporous materials". *Journal of the Mechanics and Physics of Solids* 108, pp. 30–48.

Gambin, V. (1991). "Crystal plasticity based on yield surfaces with rounded-off corners". *Zeitschrift für Angewandte Mathematik und Mechanik* 71, pp. 265–268.

Gan, Y. X., Kysar, J. W., and Morse, T. L. (2006). "Cylindrical void in a rigid-ideally plastic single crystal: Part II - Experiments and simulations". *International Journal of Plasticity* 22, pp. 39–72.

Garner, F. A. (2012). "Radiation damage in austenitic steels". *Comprehensive Nuclear Materials* 4, pp. 33–95.

Garner, F. A. (2020). "Radiation-induced damage in austenitic structural steels used in nuclear reactors". *Comprehensive nuclear materials*. Ed. by R. J. Konings and R. E. Stoller. Second edition. Elsevier, pp. 57–168.

Gélébart, L. and Ouaki, F. (2015). "Filtering material properties to improve FFT-based methods for numerical homogenization". *Journal of Computational Physics* 294, pp. 90–95.

Gigax, J. G., Kim, H., Aydogan, E., Garner, F. A., Maloy, S., and Shao, L. (2017). "Beam-contamination-induced compositional alteration and its neutron-atypical consequences in ion simulation of neutron-induced void swelling". *Materials Research Letters* 5 (7), pp. 478–485.

Gologanu, M., Leblond, J.-B., and Devaux, J. (1994). "Approximate models for ductile metals containing nonspherical voids —- Case of axisymmetric oblate ellipsoidal cavities". *Journal of Engineering Materials and Technology* 116 (3), pp. 290–297.

— (2001a). "Theoretical models for void coalescence in porous ductile solids - II. Coalescence "in columns"". *International Journal of Solids and Structures* 38 (32), pp. 5595–5604.

Gologanu, M., Leblond, J.-B., Perrin, G., and Devaux, J. (1997). "Recent extention of Gurson's model for porous ductile metals". *Continuum micromechanics*. Springer, pp. 61–130.

— (2001b). "Theoretical models for void coalescence in porous ductile solids - I. Coalescence "in layers"". *International Journal of Solids and Structures* 38 (32), pp. 5581–5594.

Goods, S. and Nieh, T. (1983). "Mechanisms of intergranular cavity nucleation and growth during creep". *Scripta Metallurgica* 17 (1), pp. 23–30.

Gräf, M. and Hornbogen, E. (1977). "Observation of ductile intercrystalline fracture of an Al-Zn-Mg alloy". *Acta Metallurgica* 25, pp. 883–889.

Greenwood, J. (1952). "Intercrystalline cracking of metals". *The Journal of the Iron and Steel Institute* 174 (8), p. 380.

Greenwood, J., Miller, D., and Suiter, J. (1954). "Intergranular cavitation in stressed metals". *Acta Metallurgica* 2 (2), pp. 250–258.

Griffiths, M. (2021). "Effect of neutron irradiation on the mechanical properties, swelling and creep of austenitic stainless steels". *Materials* 14 (10).

— (2023). "Strain localisation and fracture of nuclear reactor core materials". *Journal of Nuclear Engineering* 4 (2), pp. 338–374.

Griffiths, M., Bickel, G., and Douglas, S. (2012). "Irradiation-induced embrittlement of Inconel 600 flux detectors in CANDU reactors". *Journal of Energy and Power Engineering* 6, pp. 188–194.

Griffiths, M. and Boothby, R. (2020). "Radiation effects in nickel-based alloys". *Comprehensive nuclear materials*. Ed. by R. J. Konings and R. E. Stoller. Second edition. Elsevier, pp. 334–371.

Gubbens, A., Barfels, M., Trevor, C., Twesten, R., Mooney, P., Thomas, P., Menon, N., Kraus, B., Mao, C., and McGinn, B. (2010). "The GIF Quantum, a next generation post-column imaging energy filter". *Ultramicroscopy* 110 (8), pp. 962–970.

Güler, B., Şimşek, Ü., Yalçinkaya, T., and Efe, M. (2018). "Grain-scale investigations of deformation heterogeneities in aluminum alloys". *AIP Conference Proceedings* 1960 (1).

Guo, H.-J., Ling, C., Busso, E. P., Zhong, Z., and Li, D.-F. (2020). "Crystal plasticity based investigation of micro-void evolution under multi-axial loading conditions". *International Journal of Plasticity* 129.

Guo, H.-J., Ling, C., Li, D.-F., Li, C.-F., Sun, Y., and Busso, E. P. (2022a). "A data-driven approach to predicting the anisotropic mechanical behaviour of voided single crystals". *Journal of the Mechanics and Physics of Solids* 159.

Guo, Y., Li, F., Suo, T., Tang, Z., and Li, Y. (2013). "A close observation on the deformation behavior of bicrystal copper under tensile loading". *Mechanics of Materials* 62, pp. 80–89.

Guo, Y., Burnett, T. L., McDonald, S. A., Daly, M., Sherry, A. H., and Withers, P. J. (2022b). "4D imaging of void nucleation, growth, and coalescence from large and small inclusions in steel under tensile deformation". *Journal of Materials Science & Technology* 123, pp. 168–176.

Gurson, A. (1977). "Continuum theory of ductile rupture by void nucleation and growth: Part I - Yield criteria and flow rules for porous ductile media". *Journal of Engineering Materials and Technology* 99, pp. 2–15.

Gurtin, M. E. (2008). "A theory of grain boundaries that accounts automatically for grain misorientation and grain-boundary orientation". *Journal of the Mechanics and Physics of Solids* 56 (2), pp. 640–662.

Ha, S. and Kim, K. (2010). "Void growth and coalescence in fcc single crystals". *International Journal of Mechanical Sciences* 52, pp. 863–873.

Halphen, B. and Nguyen, Q. (1975). "Sur les matériaux standard généralisés". *Journal de Mécanique* 14, pp. 39–63.

Han, X., Besson, J., Forest, S., Tanguy, B., and Bugat, S. (2013). "A yield function for single crystals containing voids". *International Journal of Solids and Structures* 50, pp. 2115–2131.

Han, X. (2012). "Modélisation de la fragilisation due au gonflement dans les aciers inoxydables austénitiques irradiés". PhD thesis. CEA, École nationale supérieure des Mines de Paris.

Han, Y. and Chaturvedi, M. (1987). "Steady state creep deformation of superalloy Inconel 718". *Materials Science and Engineering* 89, pp. 25–33.

Hancock, J. W. (1976). "Creep cavitation without a vacancy flux". *Metal Science* 10 (9), pp. 319–325.

Hashimoto, N., Kasada, R., Raj, B., and Vijayalakshmi, M. (2020). "Radiation effects in ferritic steels and advanced ferritic-martensitic steels". *Comprehensive nuclear materials*. Ed. by R. J. Konings and R. E. Stoller. Second edition. Elsevier, pp. 226–254.

Hashin, Z. and Shtrikman, S. (1963). "A variational approach to the theory of the elastic behaviour of multiphase materials". *Journal of the Mechanics and Physics of Solids* 11 (2), pp. 127–140.

Helfer, T. and Ling, C. (2014). *Écriture de lois de comportement mécaniques en grandes transformations avec le générateur de codes `MFront`*. Tech. rep. CEA.

Helfer, T., Michel, B., Proix, J., Salvo, M., Sercombe, J., and Casella, M. (2015). "Introducing the open-source `MFront` code generator: Application to mechanical behaviours and material knowledge management within the PLEIADES fuel element modelling platform". *Computers & Mathematics with Applications* 70, pp. 994–1023.

Helfer, T. (2020). *Assisted computation of the consistent tangent operator of behaviours integrated using an implicit scheme: Theory and implementation in `Mfront`*. Tech. rep. CEA.

Herzig, C. and Mishin, Y. (2005). "Grain boundary diffusion in metals". *Diffusion in condensed matter: Methods, materials, models*. Springer Berlin Heidelberg, pp. 337–366.

Hill, R. (1948). "A theory of the yielding and plastic flow of anisotropic metals". *Proceedings of the Royal Society of London A* 193, pp. 281–297.

— (1967). "The essential structure of constitutive laws for metal composites and polycrystals". *Journal of the Mechanics and Physics of Solids* 15 (2), pp. 79–95.

— (1972). "An invariant treatment of interfacial discontinuities in elastic composites". *Continuum Mechanics and Related Problems of Analysis*, pp. 597–604.

Hoff, N. J. (1954). "Approximate analysis of structures in the presence of moderately large creep deformations". *Quarterly of Applied Mathematics* 12 (1), pp. 49–55.

Hojná, A. (2017). "Overview of intergranular fracture of neutron irradiated austenitic stainless steels". *Metals* 7, p. 392.

Hornbogen, E. and Kreye, H. (1982). "The mechanism of pseudo-intercrystalline brittleness of precipitation-hardened alloys and tempered steels". *Journal of Materials Science* 17, pp. 979–988.

Hosseini, N., Nieto-Fuentes, J., Dakshinamurthy, M., Rodríguez-Martínez, J., and Vadillo, G. (2022). "The effect of material orientation on void growth". *International Journal of Plasticity* 148.

Howard, C., Judge, C., and Hosemann, P. (2019). "Applying a new push-to-pull micro-tensile testing technique to evaluate the mechanical properties of high dose Inconel X-750". *Materials Science and Engineering: A* 748, pp. 396–406.

Huang, F. H. (1984). "The fracture characterization of highly irradiated type 316 stainless steel". *International Journal of Fracture* 25, pp. 181–193.

— (1992). "Comparison of fracture behavior for low-swelling ferritic and austenitic alloys irradiated in the Fast Flux Test Facility (FFTF) to 180 dpa". *Engineering Fracture Mechanics* 43 (5), pp. 733–748.

Hughes, A. and Caley, J. (1963). "The effects of neutron irradiation at elevated temperatures on the tensile properties of some austenitic stainless steels". *Journal of Nuclear Materials* 10 (1), pp. 60–62.

Hull, D. and Rimmer, D. E. (1959). "The growth of grain-boundary voids under stress". *Philosophical Magazine* 4 (42), pp. 673–687.

Hunter, C., Fish, R., and Holmes, J. (1972). "Channel fracture in irradiated EBR-II type 304 stainless steel". *Transactions of the American Nuclear Society* 15, pp. 254–255.

Hure, J., El Shawish, S., Cizelj, L., and Tanguy, B. (2016). "Intergranular stress distributions in polycrystalline aggregates of irradiated stainless steel". *Journal of Nuclear Materials* 476, pp. 231–242.

Hure, J. (2019). "A coalescence criterion for porous single crystals". *Journal of the Mechanics and Physics of Solids* 124, pp. 505–525.

— (2021). "Yield criterion and finite strain behavior of random porous isotropic materials". *European Journal of Mechanics - A/Solids* 85.

Hure, J. and Barrioz, P.-O. (2016). "Theoretical estimates for flat voids coalescence by internal necking". *European Journal of Mechanics - A/Solids* 60, pp. 217–226.

Hure, J., Courcelle, A., and Turque, I. (2022). "A micromechanical analysis of swelling-induced embrittlement of neutron-irradiated austenitic stainless steels". *Journal of Nuclear Materials* 565.

Hutchinson, J. W. (1976). "Bounds and self-consistent estimates for creep of polycrystalline materials". *Proceedings of the Royal Society of London A* 348 (1652), pp. 101–127.

Iakoubovskii, K., Mitsuishi, K., Nakayama, Y., and Furuya, K. (2008). "Mean free path of inelastic electron scattering in elemental solids and oxides using transmission electron microscopy: Atomic number dependent oscillatory behavior". *Physical Review B* 77.

Idaho National Laboratory (2011). *Analytical neutronics studies correlating fast neutron fluence to material damage in carbon, silicon, and silicon carbide*. Tech. rep. INL/EXT-11-22880. US Department of Energy.

Idiart, M. (2006). "Macroscopic behavior and field statistics in viscoplastic composites". PhD thesis. École polytechnique.

Indurkar, P. P., Joshi, S. P., and Benzerga, A. A. (2022). "On the micromechanics of void mediated failure in HCP crystals". *Journal of the Mechanics and Physics of Solids* 165.

Jeong, W., Lee, C., Moon, J., Jang, D., and Lee, M. G. (2018). "Grain scale reprensentative volume element simulation to investigate the effect of crystal orientation on void growth in single and multi-crystals". *Metals* 8 (6), p. 436.

Joëssel, L., Vincent, P.-G., Gărăjeu, M., and Idiart, M. I. (2018). "Viscoplasticity of voided cubic crystals under hydrostatic loading". *International Journal of Solids and Structures* 147, pp. 156–165.

Judge, C. D., Gauquelin, N., Walters, L., Wright, M., Cole, J. I., Madden, J., Botton, G. A., and Griffiths, M. (2015). "Intergranular fracture in irradiated Inconel X-750 containing very high concentrations of helium and hydrogen". *Journal of Nuclear Materials* 457, pp. 165–172.

Judge, C. D., Griffiths, M., Waters, L., Wright, M., Bickel, G., Woo, O., Stewart, M., and Douglas, S. (2012). "Embrittlement of nickel alloys in a CANDU reactor environment". *Effects of Radiation on Nuclear Materials* 25, pp. 161–175.

Kabel, M., Fliegener, S., and Schneider, M. (2016). "Mixed boundary conditions for FFT-based homogenization at finite strains". *Computational Mechanics* 57, pp. 193–210.

Kant, R. and Dupont, J. (2019). "Stress relief cracking susceptibility in high temperature alloys". *Welding Journal* 98, pp. 29s–49s.

Kasana, S. S. and Pandey, O. (2021). "Effect of heat treatment on microstructure and mechanical properties of boron containing Ti-stabilized AISI-321 steel for nuclear power plant application". *Materials Today Communications* 26, p. 101959.

Kassner, M. and Pérez-Prado, M.-T. (2000). "Five-power-law creep in single phase metals and alloys". *Progress in Materials Science* 45 (1), pp. 1–102.

Kassner, M. and Hayes, T. (2003). "Creep cavitation in metals". *International Journal of Plasticity* 19 (10), pp. 1715–1748.

Kassner, M., Kennedy, T., and Schrems, K. (1998). "The mechanism of ductile fracture in constrained thin silver films". *Acta Materialia* 46 (18), pp. 6445–6457.

Kawabata, T. and Izumi, O. (1976). "Ductile fracture in the interior of precipitate free zone in an Al-6.0%Zn-2.6%Mg alloy". *Acta Metallurgica* 24, pp. 817–825.

Keralavarma, S. M. and Benzerga, A. A. (2010). "A constitutive model for plastically anisotropic solids with non-spherical voids". *Journal of the Mechanics and Physics of Solids* 58, pp. 874–901.

Keralavarma, S. M. and Chockalingam, S. (2016). "A criterion for void coalescence in anisotropic ductile materials". *International Journal of Plasticity* 82, pp. 159–176.

Keralavarma, S. M., Hoelscher, S., and Benzerga, A. A. (2011). "Void growth and coalescence in anisotropic solids". *International Journal of Solids and Structures* 48, pp. 1696–1710.

Keralavarma, S. M., Reddi, D., and Benzerga, A. A. (2020). "Ductile failure as a constitutive instability in porous plastic solids". *Journal of the Mechanics and Physics of Solids* 139.

Keralavarma, S. M. (2017). "A multi-surface plasticity model for ductile fracture simulations". *Journal of the Mechanics and Physics of Solids* 103, pp. 100–120.

Khadyko, M., Frodal, B. H., and Hopperstad, O. S. (2021). "Finite element simulation of ductile fracture in polycrystalline materials using a regularized porous crystal plasticity model". *International Journal of Fracture* 228, pp. 15–31.

Khaleel, M., Zbib, H., and Nyberg, E. (2001). "Constitutive modeling of deformation and damage in superplastic materials". *International Journal of Plasticity* 17 (3), pp. 277–296.

Khavasad, P. H. and Keralavarma, S. M. (2021). "Effective yield criterion for a porous single crystal accounting for void size effects". *Mechanics of Materials* 160.

— (2023). "Size-dependent yield criterion for single crystals containing spherical voids". *International Journal of Solids and Structures* 283.

Kikuchi, M., Shiozawa, K., and Weertman, J. (1981). "Void nucleation in astroloy: theory and experiments". *Acta Metallurgica* 29 (10), pp. 1747–1758.

Kikuchi, M. and Weertman, J. (1980). "Mechanism for nucleation of grain boundary voids in a nickel base superalloy". *Scripta Metallurgica* 14 (7), pp. 797–799.

Klueh, R. L. (1990). "Helium effects on the mechanical properties of neutron-irradiated Cr-Mo ferritic steels". *Conference on the effect of irradiation on materials of fusion reactors*.

Koiter, W. T. (1953). "Stress-strain relations, uniqueness and variational theorems for elastic-plastic materials with a singular yield surface". *Quarterly of Applied Mathematics* 11, pp. 350–354.

Koplik, J. and Needleman, A. (1988). "Void growth and coalescence in porous plastic solids". *International Journal of Solids and Structures* 24, pp. 835–853.

Kröner, E. (1959). "Allgemeine kontinuumstheorie der versetzungen und eigenspannungen". *Archive for Rational Mechanics and Analysis* 4, pp. 273–334.

Kubin, L., Devincre, B., and Hoc, T. (2008). "Modeling dislocation storage rates and mean free paths in face-centered cubic crystals". *Acta Materialia* 56 (20), pp. 6040–6049.

Kuhlmann-Wilsdorf, D. and Wilsdorf, H. G. F. (1964). "Dislocation movements in metals". *Science* 144 (3614), pp. 17–25.

Kuramoto, S., Itoh, G., and Kanno, M. (1996). "Intergranular fracture in some precipitation-hardened aluminum alloys at low temperatures". *Metallurgical and Materials Transactions A* 27A, pp. 3081–3088.

Kuroda, T. (2000). "Helium bubble formation in YAG laser weldment of helium-implanted stainless steel". *Vacuum* 59, pp. 301–312.

Kysar, J. W. (2001). "Continuum simulations of directional dependence of crack growth along a copper/sapphire bicrystal interface. Part I: experiments and crystal plasticity background". *Journal of the Mechanics and Physics of Solids* 49 (5), pp. 1099–1128.

Lebensohn, R., Idiart, M., Castañeda, P. P., and Vincent, P.-G. (2011). "Dilatational viscoplasticity of polycrystalline solids with intergranular cavities". *Philosophical Magazine* 91 (22), pp. 3038–3067.

Leblond, J.-B., Perrin, G., and Devaux, J. (1995). "An improved Gurson type model for hardenable ductile metals". *European Journal of Mechanics - A/Solids* 14, pp. 499–527.

Leblond, J., Perrin, G., and Suquet, P. (1994). "Exact results and approximate models for porous viscoplastic solids". *International Journal of Plasticity* 10 (3), pp. 213–235.

Leblond, J.-B., Kondo, D., Morin, L., and Remmal, A. (2018). "Classical and sequential limit analysis revisited". *Comptes Rendus Mécanique* 346 (4), pp. 336–349.

Leblond, J.-B. and Morin, L. (2014). "Gurson's criterion and its derivation revisited". *Journal of Applied Mechanics* 81 (5).

Lee, E. H. (1969). "Elastic-plastic deformation at finite strains". *Journal of Applied Mechanics* 36 (1), pp. 1–6.

Lemaitre, J. (1985). "A continuous damage mechanics model for ductile fracture". *Journal of Engineering Materials and Technology* 107 (1), pp. 83–89.

Leonard, K. J. and Taylor, C. N. (2020). "Radiation effects in refractory metals and alloys". *Comprehensive nuclear materials*. Ed. by R. J. Konings and R. E. Stoller. Second edition. Elsevier, pp. 372–397.

Lewandowski, J. and Holroyd, N. (1990). "Intergranular fracture of AlLi alloys: Effects of aging and impurities". *Materials Science and Engineering A* 123, pp. 219–227.

Lewis, E. E. (2008). *Fundamentals of nuclear reactor physics*. Elsevier.

Li, C., Li, B., Huang, J., Ma, H., Zhu, M., Zhu, J., and Luo, S. (2016). "Spall damage of a mild carbon steel: Effects of peak stress, strain rate and pulse duration". *Materials Science and Engineering: A* 660, pp. 139–147.

Li, H., Li, J., Tang, B., Fan, J., and Yuan, H. (2017). "Simulation of intergranular ductile cracking in β titanium alloys based on a micro-mechanical damage model". *Materials* 10 (11).

Li, S., Grossbeck, M., Zhang, Z. W., Shen, W., and Chin, B. (2011). "The effect of Helium on welding irradiated materials". *Welding Journal* 90, pp. 19s–26s.

Li, S.-W., Wen, Z.-X., Yue, Z.-F., and Gao, J. (2015). "Creep behavior and life assessment of anisotropic bicrystals with a void and without void in different kinds of grain boundaries". *Materialwissenschaft und Werkstofftechnik* 46 (12), pp. 1169–1176.

Li, Z. and Guo, W. (2002). "The influence of plasticity mismatch on the growth and coalescence of spheroidal voids on the bimaterial interface". *International Journal of Plasticity* 18 (2), pp. 249–279.

Lin, H. T. and Chin, B. A. (1991). "Helium-induced weld cracking in austenitic and martensitic steels". *Journal of Materials Science* 26, pp. 2063–2070.

Lin, H. T., Grossbeck, M. L., and Chin, B. A. (1990). "Cavity microstructure and kinetics during gas tungsten arc welding of helium-containing stainless steel". *Metallurgical Transactions A* 21, pp. 2585–2596.

Lin, H.-T. and Braski, D. (1994). "Degradation in the weldability of a helium-containing vanadium alloy". *Journal of Nuclear Materials* 217 (1-2), pp. 209–212.

Lin, Y., Li, L., He, D.-G., Chen, M.-S., and Liu, G.-Q. (2017). "Effects of pre-treatments on mechanical properties and fracture mechanism of a nickel-based superalloy". *Materials Science and Engineering: A* 679, pp. 401–409.

Ling, C. (2017). "Simulation de la rupture ductile intragranulaire des aciers irradiés. Effets de l'anisotropie cristalline et du gradient de déformations". PhD thesis. École nationale supérieure des Mines de Paris.

Ling, C., Besson, J., Forest, S., Tanguy, B., Latourte, F., and Bosso, E. (2016). "An elastoviscoplastic model for porous single crystals at finite strains and its assessment based on unit cell simulations". *International Journal of Plasticity* 84, pp. 58–87.

Ling, C., Tanguy, B., Besson, J., Forest, S., Latourte, F., and Bosso, E. (2015). "Multi-scale simulation of uniaxial tension of single crystal and polycrystalline irradiated FCC steels specimens". ICMM4 conference, Berkeley (USA), May 27-29.

Ling, C., Li, D.-F., and Busso, E. P. (2023). "Porous single crystals under triaxial creep loadings: A data-driven modelling approach". *International Journal of Plasticity* 169.

Liu, M., Nambu, S., Zhou, K., Wang, P. F., Lu, G., Lu, C., Tieu, K. A., and Koseki, T. (2019). "On the influence of grain boundary misorientation on the severe plastic deformation of aluminum bicrystals: A three-dimensional crystal plasticity finite element method study." *Metallurgical and Materials Transactions A* 50, pp. 2399–2412.

Liu, W., He, Z., Yao, W., Li, M., and Tang, J. (2014). "XFEM simulation of the effects of microstructure on the intergranular fracture in high strength aluminum alloy". *Computational Materials Science* 84, pp. 310–317.

Liu, W., Huang, H., and Tang, J. (2010). "FEM simulation of void coalescence in FCC crystals". *Computational Materials Science* 50 (2), pp. 411–418.

Liu, W., Qiu, Q., Chen, Y., and Tang, C. (2016a). "Simulation of PFZ on intergranular fracture based on XFEM and CPFEM". *Journal of Central South University* 23, pp. 2500–2505.

Liu, W., Zhang, X., and Tang, J. (2009). "Study on the growth behavior of voids located at the grain boundary". *Mechanics of Materials* 41 (7), pp. 799–809.

Liu, W., Zhang, X., Tang, J., and Du, Y. (2007). "Simulation of void growth and coalescence behavior with 3D crystal plasticity theory". *Computational Materials Science* 40, pp. 130–139.

Liu, W., Ji, Y., Tan, P., Zang, H., He, C., Yun, d., Zhang, C., and Yang, Z. (2016b). "Irradiation induced microstructure evolution in nanostructured materials: A review". *Materials* 9, p. 105.

Lobb, R. C. and Evans, H. E. (1987). "The high-temperature oxidation of AGR fuel cladding". *Materials for nuclear reactor core applications*. Vol. 1, pp. 335–340.

Loyer-Prost, M., Puichaud, A.-H., Flament, C., Rouesne, E., and Béchade, J.-L. (2023). "Impact of intragranular misorientation on void swelling and inter-granular cavities after ion irradiation in standard and additive manufacturing 316L austenitic steels". *Journal of Nuclear Materials* 573, p. 154102.

Lu, F., Guang, Z., and Ke-shi, Z. (2003). "Grain boundary effects on the inelastic deformation behavior of bicrystals". *Materials Science and Engineering: A* 361 (1), pp. 83–92.

Lucki, G., Chambron, W., Watanabe, S., and Verdone, J. (1975). "Vacancies supersaturation induced by fast neutron irradiation in FeNi alloys". *IV^{th} inter-American conference on materials technology*. Vol. 2.

Ludtka, G. and Laughlin, D. (1982). "The influence of microstructure and strength on the fracture mode and toughness of 7XXX series aluminum alloys". *Metallurgical Transactions A* 13, pp. 411–425.

Luo, S.-N., Germann, T. C., Desai, T. G., Tonks, D. L., and An, Q. (2010). "Anisotropic shock response of columnar nanocrystalline Cu". *Journal of Applied Physics* 107 (12).

Lynch, S. P. (1991a). "Fracture of 8090 Al-Li plate - Part I: Short transverse fracture toughness". *Materials Science and Engineering: A* 136, pp. 25–43.

— (1991b). "Mechanisms of intergranular fracture". *Grain Boundary Chemistry and Intergranular Fracture*. Vol. 46. Materials Science Forum. Trans Tech Publications Ltd, pp. 1–24.

Lynch, S. P., Muddle, B., and Pasang, T. (2001). "Ductile-to-brittle fracture transitions in 8090 Al–Li alloys". *Acta Materialia* 49, pp. 2863–2874.

Lynch, S. P., Muddle, B. C., and Pasang, T. (2002). "Mechanisms of brittle intergranular fracture in Al-Li alloys and comparison with other alloys". *Philosophical Magazine A* 82 (17-18), pp. 3361–3373.

Lynch, S. P., Wilson, A. R., and Byrnes, R. T. (1993). "Effects of ageing treatments on resistance to intergranular fracture of 8090 Al–Li alloy plate". *Materials Science and Engineering: A* 172 (1), pp. 79–93.

Madou, K. and Leblond, J.-B. (2012a). "A Gurson-type criterion for porous ductile solids containing arbitrary ellipsoidal voids I : Limit-analysis of some representative cell". *Journal of the Mechanics and Physics of Solids* 60, pp. 1020–1036.

— (2012b). "A Gurson-type criterion for porous ductile solids containing arbitrary ellipsoidal voids—II: Determination of yield criterion parameters". *Journal of the Mechanics and Physics of Solids* 60 (5), pp. 1037–1058.

Maire, E. and Withers, P. (2014). "Quantitative X-ray tomography". *International Materials Reviews* 59, pp. 1–43.

Malis, T. F., Cheng, S. C., Egerton, R. F., and Egerton, R. F. (1988). "EELS log-ratio technique for specimen-thickness measurement in the TEM". *Journal of Electron Microscopy Technique* 82, pp. 193–200.

Mandel, J. (1973). "Équations constitutives et directeurs dans les milieux plastiques et viscoplastiques". *International Journal of Solids and Structures* 9 (6), pp. 725–740.

Mannan, S. and Sivaprasad, P. (2016). "Austenitic stainless steels for in-core applications of fast breeder reactors". *Reference module in materials science and materials engineering*. Elsevier.

Mansur, L. and Grossbeck, M. (1988). "Mechanical property changes induced in structural alloys by neutron irradiations with different helium to displacement ratios". *Journal of Nuclear Materials* 155-157, pp. 130–147.

Margolin, B., Sorokin, A., Shvetsova, V., Minkin, A., Potapova, V., and Smirnov, V. (2016). "The radiation swelling effect on fracture properties and fracture mechanisms of irradiated austenitic steels: Part I - Ductility and fracture toughness". *Journal of Nuclear Materials* 480, pp. 52–68.

Margolin, B., Kursevich, I., Sorokin, A., and Neustroev, V. (2009). "The relationship of radiation embrittlement and swelling for austenitic steels for WWER internals". *American Society of Mechanical Engineers, Pressure Vessels and Piping Division*. Vol. 6.

Matsuda, K., Tsukiyama, J., Uetani, Y., and Ikeno, S. (2008). "Effect of crystal grain orientation on grain boundary fracture in peak-aged polycrystalline Al-Mg-Si alloys". *Journal of Japan Institute of Light Metals* 58 (8), pp. 388–394.

Matthews, J. and Preusser, T. (1987). "On the failure of fast reactor fuel pins". *Nuclear Engineering and Design* 101 (3), pp. 281–303.

Mbiakop, A., Constantinescu, A., and Danas, K. (2015a). "A model for porous single crystals with cylindrical voids of elliptical cross-section". *International Journal of Solids and Structures* 64-65, pp. 100–119.

— (2015b). "An analytical model for porous single cristals with ellipsoidal voids". *Journal of the Mechanics and Physics of Solids* 84, pp. 436–467.

Mbiakop, A. (2015). "Nonlinear homogenization in porous creeping single crystals: Modeling, numerical implementation and applications to fracture and fatigue". PhD thesis. École polytechnique.

Mbiakop, A., Danas, K., and Constantinescu, A. (2016). "A homogenization based yield criterion for a porous Tresca material with ellipsoidal voids". *International Journal of Fracture* 200, pp. 209–225.

McClintock, F. A. (1968). "A criterion for ductile fracture by the growth of holes". *Journal of Applied Mechanics* 35 (2), p. 363.

McClintock, F. A. and Argon, A. (1966). *Mechanical behaviour of materials*. Addison-Wesley.

McLean, D. (1966). "The physics of high temperature creep in metals". *Reports on Progress in Physics* 29 (1), pp. 1–33.

Mear, M. and Huntchinson, J. (1985). "Influence of yield surface curvature on flow localization in dilatant plasticity". *Mechanics of Materials* 4, pp. 395–407.

Miehe, C., Apel, N., and Lambrecht, M. (2002). "Anisotropic additive plasticity in the logarithmic strainspace: Modular kinematic formulation and implementation based on incremental minimization principles for standard materials". *Computer Methods in Applied Mechanics and Engineering* 191, pp. 5383–5425.

Mills, W. (1980). "The deformation and fracture characteristics of Inconel X-750 at room temperature and elevated temperatures". *Metallurgical Transactions A* 11, pp. 1039–1047.

Mills, W. J. (1997). "Fracture toughness of type 304 and 316 stainless steels and their welds". *International Materials Reviews* 42 (2), pp. 45–82.

— (1988). "Fracture toughness of irradiated stainless steel alloys". *Nuclear technology* 82, pp. 290–303.

Mises, R. von (1913). "Mechanik der festen körper im plastisch-deformablen zustand". *Nachrichten von der Gesellschaft der Wissenschaften zu Göttingen*. Mathematisch-Physikalische Klasse 1, pp. 582–592.

Miura, T., Fujii, K., and Fukuya, K. (2015). "Micro-mechanical investigation for effects of helium on grain boundary fracture of austenitic steel". *Journal of Nuclear Materials* 457, pp. 279–290.

Moës, N., Dolbow, J., and Belytschko, T. (1999). "A finite element method for crack growth without remeshing". *International Journal for Numerical Methods in Engineering* 46 (1), pp. 131–150.

Molkeri, A., Srivastava, A., Osovski, S., and Needleman, A. (2020). "Influence of grain size distribution on ductile intergranular crack growth resistance". *Journal of Applied Mechanics* 87 (3).

Monchiet, V., Cazacu, O., Charkaluk, E., and Kondo, D. (2008). "Macroscopic yield criteria for plastic anisotropic materials containing spheroidal voids". *International Journal of Plasticity* 24 (7), pp. 1158–1189.

Morere, B., Ehrström, J.-C., Gregson, P. J., and Sinclair, I. (1998). "Microstructural effects on fracture toughness in AA7010 plate". *Metallurgical and Materials Transactions A* 31A, pp. 2503–2515.

Morin, L., Kondo, D., and Leblond, J. (2015a). "Numerical assessment, implementation and application of an extended Gurson model accounting for void size effects". *European Journal of Mechanics - A/Solids* 51, pp. 183–192.

Morin, L. (2012). "Influence de l'effet de forme et de taille des cavités, et de l'anisotropie plastique sur la rupture ductile". PhD thesis. Université Pierre et Marie Curie.

Morin, L., Leblond, J.-B., and Benzerga, A. A. (2015b). "Coalescence of voids by internal necking : Theoretical estimates and numerical results". *Journal of the Mechanics and Physics of Solids* 75, pp. 140–158.

Morin, L., Leblond, J.-B., Benzerga, A. A., and Kondo, D. (2016a). "A unified criterion for the growth and coalescence of microvoids". *Journal of the Mechanics and Physics of Solids* 97, pp. 19–36.

Morin, L., Leblond, J.-B., and Kondo, D. (2015c). "A Gurson-type criterion for plastically anisotropic solids containing arbitrary ellipsoidal voids". *International Journal of Solids and Structures* 77, pp. 86–101.

Morin, L., Leblond, J.-B., and Tvergaard, V. (2016b). "Application of a model of plastic porous materials including void shape effects to the prediction of ductile failure under shear-dominated loadings". *Journal of the Mechanics and Physics of Solids* 94, pp. 148–166.

Morin, L., Michel, J.-C., and Leblond, J.-B. (2017). "A Gurson-type layer model for ductile porous solids with isotropic and kinematic hardening". *International Journal of Solids and Structures* 118, pp. 167–178.

Moulinec, H. and Suquet, P. (1998). "A numerical method for computing the overall response of nonlinear composites with complex microstructure". *Computer Methods in Applied Mechanics and Engineering* 157, pp. 69–94.

Nahshon, K. and Hutchinson, J. (2008). "Modification of the Gurson model for shear failure". *European Journal of Mechanics - A/Solids* 27 (1), pp. 1–17.

Naimark, M. (1964). *Linear Representations of the Lorentz Group*. Pergamon.

Needleman, A. and Rice, J. (1980). "Plastic creep flow effects in the diffusive cavitation of grain boundaries". *Acta Metallurgica* 28 (10), pp. 1315–1332.

Nelder, J. A. and Mead, R. (1965). "A simplex method for function minimization". *The Computer Journal* 7, pp. 308–313.

Nemat-Nasser, S. and Hori, M. (1993). *Micromechanics: Overall properties of heterogeneous materials*. Elsevier, pp. 27–64.

Nemat-Nasser, S., Yu, N., and Hori, M. (1993). "Bounds and estimates of overall moduli of composites with periodic microstructure". *Mechanics of Materials* 15 (3), pp. 163–181.

Nervi, J. and Idiart, M. (2015). "Bounding the plastic strength of polycrystalline voided solids by linear-comparison homogenization techniques". *Proceedings of the Royal Society of London A* 471.

Neustroev, V. and Garner, F. (2009). "Severe embrittlement of neutron irradiated austenitic steels arising from high void swelling". *Journal of Nuclear Materials* 286-288, pp. 157–160.

Nix, W. (1988). "Mechanisms and controlling factors in creep fracture". *Materials Science and Engineering: A* 103 (1), pp. 103–110.

Noell, P., Caroll, J., Hattar, K., Clark, B., and Boyce, B. (2017). "Do voids nucleate at grain boundaries during ductile rupture ?" *Acta Materiala* 137, pp. 103–114.

Noell, P., Caroll, J., and Boyce, B. (2018). "The mechanisms of ductile fracture". *Acta Materiala* 161, pp. 83–98.

Norris, A. N. (1990). "The effective moduli of layered media — A new look at an old problem". *Micromechanics and Inhomogeneity*. Springer New York, pp. 321–339.

Onimus, F., Doriot, S., and Béchade, J.-L. (2020). "Radiation effects in zirconium alloys". *Comprehensive nuclear materials*. Ed. by R. J. Konings and R. E. Stoller. Second edition. Elsevier, pp. 1–56.

Osovski, S., Srivastava, A., Williams, J., and Needleman, A. (2015). "Grain boundary crack growth in metastable titanium β alloys". *Acta Materialia* 82, pp. 167–178.

Østby, E., Thaulow, C., and Zhang, Z. (2007). "Numerical simulations of specimen size and mismatch effects in ductile crack growth – Part I: Tearing resistance and crack growth paths". *Engineering Fracture Mechanics* 74 (11), pp. 1770–1792.

Paccou, E. (2019). "Étude de l'évolution des propriétés mécaniques et de la sensibilité à la fissuration intergranulaire en fonction de la microstructure d'irradiation d'un acier 304 irradié aux ions lourds". PhD thesis. Université de Toulouse.

Paccou, E., Tanguy, B., and Legros, M. (2019). "Micropillar compression study of Fe-irradiated 304L steel". *Scripta Materialia* 172, pp. 56–60.

Pala, R. and Dzioba, I. (2018). "Influence of delamination on the parameters of triaxial state of stress before the front of the main crack". *AIP Conference Proceedings* 2029 (1).

Pardoen, T., Dumont, D., Deschamps, A., and Brechet, Y. (2003). "Grain boundary versus transgranular ductile failure in aluminium alloys". *Journal of the Mechanics and Physics of Solids* 51 (4), pp. 637–665.

Pardoen, T. and Hutchinson, J. (2003). "Micromechanics-based model for trends in toughness of ductile metals". *Acta Materiala* 51, pp. 133–148.

Pardoen, T. (1998). "Ductile fracture of cold-drawn copper bars: Experimental investigation and micromechanical modeling". PhD thesis. Université Catholique de Louvain.

Pardoen, T. and Hutchinson, J. (2000). "An extended model for void growth and coalescence". *Journal of the Mechanics and Physics of Solids* 48, pp. 2467–2512.

Pardoen, T., Scheyvaerts, F., Simar, A., Tekoğlu, C., and Onck, P. R. (2010). "Multiscale modeling of ductile failure in metallic alloys". *Comptes Rendus Physique* 11 (3), pp. 326–345.

Pasang, T., Symonds, N., Moutsos, S., Wanhill, R., and Lynch, S. (2012). "Low-energy intergranular fracture in Al–Li alloys". *Engineering Failure Analysis* 22, pp. 166–178.

Paux, J., Brenner, R., and Kondo, D. (2018). "Plastic yield criterion and hardening of porous single crystals". *International Journal of Solids and Structures* 132-133, pp. 80–95.

Paux, J., Morin, L., Brenner, R., and Kondo, D. (2015). "An approximate yield criterion for porous single crystals". *European Journal of Mechanics - A/Solids* 51, pp. 1–10.

Pavinich, W. and Raj, R. (1977). "Fracture at elevated temperature". *Metallurgical Transactions A* 8, pp. 1917–1933.

Peirce, D., Asaro, R. J., and Needleman, A. (1983). "Material rate dependence and localized deformation in crystalline solids". *Acta Metallurgica* 31 (12), pp. 1951–1976.

Peralta, P., Schober, A., and Laird, C. (1993). "Elastic stresses in anisotropic bicrystals". *Materials Science and Engineering: A* 169 (1), pp. 43–51.

Perez-Bergquist, A., Escobedo, J., Trujillo, C., Cerreta, E., Gray, G., Brandl, C., and Germann, T. (2012). "The role of the structure of grain boundary interfaces during shock loading". Vol. 1426, pp. 1359–1362.

Perez-Bergquist, A., Cerreta, E. K., Trujillo, C. P., F., C., and Gray, G. T. (2011). "Orientation dependence of void formation and substructure deformation in a spalled copper bicrystal". *Scripta Materialia* 65 (12), pp. 1069–1072.

Pineau, A., Benzerga, A. A., and Pardoen, T. (2016). "Failure of metals: Part I - Brittle and ductile fracture". *Acta Materiala* 107, pp. 424–483.

Plancher, E., Tajdary, P., Auger, T., Castelnau, O., Favier, V., Loisnard, D., Marijon, J.-B., Maurice, C., Michel, V., Robach, O., and Stodolna, J. (2019). "Validity of crystal plasticity models near grain boundaries: A contribution of elastic strain measurements at the micron scale". *Journal of Materials Science* 71 (10), pp. 3543–3551.

Plateau, J., Henry, G., and Crussard, C. (1957). "Quelques nouvelles applications de la microfractographie". *Revue de métallurgie* 54 (3), pp. 200–216.

Pokor, C., Brechet, Y., Dubuisson, P., Massoud, J.-P., and Barbu, A. (2004). "Irradiation damage in 304 and 316 stainless steels experimental investigation and modeling. Part I: Evolution of the microstructure". *Journal of Nuclear Materials* 326, pp. 19–29.

Pommier, H., Busso, E. P., Morgeneyer, T. F., and Pineau, A. (2016). "Intergranular damage during stress relaxation in AISI 316L-type austenitic stainless steels: Effect of carbon, nitrogen and phosphorus contents". *Acta Materialia* 103 (4), pp. 893–908.

— (2017). "Local approach to stress relaxation cracking in a AISI 316L-type austenitic stainless steel: Tomography damage quantification and FE simulations". *Engineering Fracture Mechanics* 183 (4), pp. 170–179.

Ponte Castañeda, P. (1991). "The effective mechanical properties of nonlinear isotropic composites". *Journal of the Mechanics and Physics of Solids* 39, pp. 45–71.

Poole, W., Wang, X., Embury, J., and Lloyd, D. (2019). "The effect of manganese on the microstructure and tensile response of an Al-Mg-Si alloy". *Materials Science and Engineering: A* 755, pp. 307–317.

Potirniche, G., Hearndon, J., Horstemeyer, M., and Ling, X. (2006). "Lattice orientation effects on void growth and coalescence in FCC single crystals". *International Journal of Plasticity* 22, pp. 921–942.

Qin, W., Chauhan, A., and Szpunar, J. (2018). "Helium bubble nucleation at grain boundaries and its influence on intergranular fracture". *Philosophical Magazine* 99, pp. 1–20.

Raj, R. and Ashby, M. (1975). "Intergranular fracture at elevated temperature". *Acta Metallurgica* 23 (6), pp. 653–666.

Ramière, I. and Helfer, T. (2015). "Iterative residual-based vector methods to accelerate fixed point iterations". *Computers and Mathematics with Applications* 70 (9), pp. 2210–2226.

Ratcliffe, R. T. and Greenwood, G. W. (1965). "The mechanism of cavitation in magnesium during creep". *Philosophical Magazine* 12 (115), pp. 59–69.

Rawl, D. E., Caskey, G. R., and Donovan, J. A. (1980). "Low temperature helium embrittlement of tritium-charged stainless steel". *109th Annual AIME Meeting*.

Reddi, D., Areej, V., and Keralavarma, S. M. (2019). "Ductile failure simulations using a multi-surface coupled damage-plasticity model". *International Journal of Plasticity* 118, pp. 190–214.

Requena, G., Maire, E., Leguen, C., and Thuillier, S. (2014). "Separation of nucleation and growth of voids during tensile deformation of a dual phase steel using synchrotron microtomography". *Materials Science and Engineering: A* 589, pp. 242–251.

Rice, J. R. and Tracey, D. M. (1969). "On the ductile enlargement of voids in triaxial stress fields". *Journal of the Mechanics and Physics of Solids* 17, pp. 201–217.

Rice, J. R. (1976). "The localization of plastic deformation". *14th International Congress on Theoretical and Applied Mechanics*, pp. 207–220.

Riedel, H. (1987). *Fracture at high temperatures*. Springer Verlag.

Rieth, M., Falkenstein, A., Graf, P., Heger, S., Jäntsch, U., Klimiankou, M., Materna-Morris, E., and Zimmermann, H. (2004). *Creep of the austenitic steel AISI 316 L(N): Experiments and models*. Tech. rep. FZKA 7065. Institut für Materialforschung Programm Kernfusion.

Ringdalen, I. G., Jensen, I. J. T., Marioara, C. D., and Friis, J. (2021). "The role of grain boundary precipitates during intergranular fracture in 6xxx series aluminium alloys". *Metals* 11 (6).

Rivalin, F., Besson, J., Pineau, A., and Di Fant, M. (2001). "Ductile tearing of pipeline-steel wide plates: II. Modeling of in-plane crack propagation". *Engineering Fracture Mechanics* 68 (3), pp. 347–364.

Rodriguez, A., Mansoor, B., Ayoub, G., Colin, X., and Benzerga, A. A. (2020). "Effect of UV-aging on the mechanical and fracture behavior of low density polyethylene". *Polymer Degradation and Stability* 180.

Roters, F., Eisenlohr, P., Hantcherli, L., Tjahjanto, D., Bieler, T., and Raabe, D. (2010). "Overview of constitutive laws, kinematics, homogenization and multiscale methods in crystal plasticity finite-element modeling: Theory, experiments, applications". *Acta Materiala* 58 (4), pp. 1152–1211.

Rousselier, G. (1981). "Finite deformation constitutive relations including ductile fracture damage". *Three-dimensional Constitutive Equations of Damage and Fracture*, pp. 331–355.

Rowcliffe, A. (1966). "The observation of helium bubbles in irradiated 20%Cr-25%Ni-Ti stainless steel". *Journal of Nuclear Materials* 18 (1), pp. 60–65.

Rowcliffe, A., Mansur, L., Hoelzer, D., and Nanstad, R. (2009). "Perspectives on radiation effects in nickel-base alloys for applications in advanced reactors". *Journal of Nuclear Materials* 392 (2), pp. 341–352.

Saeidi, N., Ashrafizadeh, F., Niroumand, B., Forouzan, M. R., and Barlat, F. (2015). "Influence of bainite morphology on ductile fracture behavior in a 0.C-CrMoNi steel". *Steel Research International* 86 (5), pp. 528–535.

Salençon, J. (1983). *Calcul à la rupture et analyse limite*. Presses de l'école nationale des Ponts et chaussées, pp. 43–60.

Scherer, J.-M., Besson, J., Forest, S., Hure, J., and Tanguy, B. (2021). "A strain gradient plasticity model of porous single crystal ductile fracture". *Journal of the Mechanics and Physics of Solids* 156.

Scherer, J.-M. and Hure, J. (2019). "A size-dependent ductile fracture model: Constitutive equations, numerical implementation and validation". *European Journal of Mechanics - A/Solids* 76, pp. 135–145.

Scheyvaerts, F., Onck, P., Tekoğlu, C., and Pardoen, T. (2011). "The growth and coalescence of ellipsoidal voids in plane strain under combined shear and tension". *Journal of the Mechanics and Physics of Solids* 59, pp. 373–397.

Schulz, B. and McMahon, C. (1973). "Fracture of alloy steels by intergranular microvoid coalescence as influenced by composition and heat treatment". *Metallurgical Transactions* 4, pp. 2485–2489.

Sekio, Y., Yamashita, S., Sakaguchi, N., and Takahashi, H. (2015). "Void denuded zone formation for Fe–15Cr–15Ni steel and PNC316 stainless steel under neutron and electron irradiations". *Journal of Nuclear Materials* 458, pp. 355–360.

Selvarajou, B., Joshi, S., and Benzerga, A. A. (2019). "Void growth and coalescence in hexagonal close packed crystals". *Journal of the Mechanics and Physics of Solids* 125, pp. 198–224.

Sénac, C., Hure, J., and Tanguy, B. (2023a). "Void growth yield criteria for intergranular ductile fracture". *Journal of the Mechanics and Physics of Solids* 172.

— (2023b). "Yield surface for void growth and coalescence of porous anisotropic materials under axisymmetric loading". *Journal of the Mechanics and Physics of Solids* 179.

— (2024). "Yield criterion for intergranular void coalescence under combined tension and shear". *International Journal of Plasticity* 173.

Sénac, C., Scherer, J.-M., Hure, J., Helfer, T., and Tanguy, B. (2022). "Homogenized constitutive equations for porous single crystals plasticity". *European Journal of Mechanics - A/Solids* 95.

Sénac, C., Hure, J., and Helfer, T. (2021a). *Homogenized material law for porous single crystal ductile fracture through void growth and coalescence*. Version v1.0.

Sénac, C., Scherer, J.-M., and Hure, J. (2021b). *Porous single crystal unit-cell simulation database for ductile fracture by void growth and coalescence*. Version v1.0.

Seo, D., Toda, H., Kobayashi, M., Uesugi, K., Takeuchi, A., and Suzuki, Y. (2015). "In situ observation of void nucleation and growth in a steel using X-ray tomography". *ISIJ International* 55, pp. 1474–1482.

Shiraishi, H. (1996). "Evaluation of helium embrittlement by two dimensional elastic—plastic finite element method". *Journal of Nuclear Materials* 233-237, pp. 985–990.

Shoemaker, L. E., Smith, G. D., Baker, B. A., and Poole, J. M. (2007). "Fabricating nickel alloys to avoid stress relaxation cracking". *Proceedings of the Corrosion conference*.

Siddiq, A. (2019). "A porous crystal plasticity constitutive model for ductile deformation and failure in porous single crystals". *International Journal of Damage Mechanics* 28 (2), pp. 233–248.

Skallerud, B. and Zhang, Z. (1997). "A 3D numerical study of ductile tearing and fatigue crack growth under nominal cyclic plasticity". *International journal of solids and structures* 34 (24), pp. 3141–3161.

Song, D. and Ponte-Castañeda, P. (2017a). "A finite-strain homogenization model for viscoplastic porous single crystals: Part I - Theory". *Journal of the Mechanics and Physics of Solids* 107, pp. 560–579.

— (2017b). "A finite-strain homogenization model for viscoplastic porous single crystals: Part II - Applications". *Journal of the Mechanics and Physics of Solids* 107, pp. 580–602.

Song, D. and Ponte Castañeda, P. (2018). "A multi-scale homogenization model for fine-grained porous viscoplastic polycrystals: I – Finite-strain theory". *Journal of the Mechanics and Physics of Solids* 115, pp. 102–122.

Srivastava, A., Revil-Baudard, B., Cazacu, O., and Needleman, A. (2017). "A model for creep of porous crystals with cubic symmetry". *International Journal of Solids and Structures* 110-111, pp. 67–79.

Stanley, J. and Perrotta, A. (1969). "Grain growth in austenitic stainless steels". *Metallography* 2 (4), pp. 349–362.

Steglich, D., Brocks, W., Heerens, J., and Pardoen, T. (2008). "Anisotropic ductile fracture of Al 2024 alloys". *Engineering Fracture Mechanics* 75 (12), pp. 3692–3706.

Stoller, R., Toloczko, M., Was, G., Certain, A., Dwaraknath, S., and Garner, F. (2013). "On the use of SRIM for computing radiation damage exposure". *Nuclear Instruments and Methods in Physics Research Section B: Beam Interactions with Materials and Atoms* 310, pp. 75–80.

Stopher, M. A. (2017). "The effects of neutron radiation on nickel-based alloys". *Materials Science and Technology* 33 (5), pp. 518–536.

Stout, M. G. and Gerberich, W. W. (1978). "Structure/property/continuum synthesis of ductile fracture in Inconel alloy 718". *Metallurgical Transactions A* 9.

Suquet, P. (1982). "Plasticité et homogénéisation". PhD thesis. Université Pierre et Marie Curie.

Suresh, S., Vasudevan, A., Tosten, M., and Howell, P. (1987). "Microscopic and macroscopic aspects of fracture in lithium-containing aluminum alloys". *Acta Metallurgica* 35 (1), pp. 25–46.

Tan, J. and Tan, M. (2003). "Superplasticity and grain boundary sliding characteristics in two stage deformation of Mg–3Al–1Zn alloy sheet". *Materials Science and Engineering: A* 339 (1), pp. 81–89.

Tang, H., Acharya, A., and Saigal, S. (2005). "Directional dependence of crack growth along the interface of a bicrystal with symmetric tilt boundary in the presence of gradient effects". *Mechanics of Materials* 37 (5), pp. 593–606.

Taylor, G. (1938). "Plastic strains in metals". *Journal of the Institute of Metals* 62, pp. 307–324.

Taylor, M., Zbib, H., and Khaleel, M. (2002). "Damage and size effect during superplastic deformation". *International Journal of Plasticity* 18 (3), pp. 415–442.

Tedmon, C. S., Vermilyea, D. A., and Rosolowski, J. H. (1971). "Intergranular corrosion of austenitic stainless steel". *Journal of The Electrochemical Society* 118 (2), p. 192.

Tekoğlu, C. and Koçhan, B. (2022). "Unit cell calculations under fully characterized stress states". *International Journal of Plasticity* 156.

Tekoğlu, C., Leblond, J.-B., and Pardoen, T. (2012). "A criterion for the onset of void coalescence under combined tension and shear". *Journal of the Mechanics and Physics of Solids* 60, pp. 1363–1381.

Thomas, G. and Nutting, J. (1957). "The plastic deformation of aged aluminum alloys". *Journal of the Institute of Metals* 86, pp. 7–14.

— (1959). "The ageing characteristics of aluminum alloys". *Journal of the Institute of Metals* 88, pp. 81–90.

Thomason, P. F. (1985). "Three-dimensional models for the plastic limit-loads at incipient failure of the intervoid matrix in ductile porous solids". *Acta Metallurgica* 33, pp. 1079–1085.

Thomesen, S., Hopperstad, O. S., Myhr, O. R., and Børvik, T. (2020). "Influence of stress state on plastic flow and ductile fracture of three 6000-series aluminium alloys". *Materials Science and Engineering: A* 783.

Thorsen, P., Bilde-Sørensen, J., and Singh, B. (2004). "Bubble formation at grain boundaries in helium implanted copper". *Scripta Materialia* 51 (6), pp. 557–560.

Torki, M. E., Benzerga, A. A., and Leblond, J.-B. (2015). "On void coalescence under combined tension and shear". *Journal of Applied Mechanics* 82.

Torki, M. E., Keralavarma, S. M., and Benzerga, A. A. (2021). "An analysis of Lode effects in ductile failure". *Journal of the Mechanics and Physics of Solids* 153.

Torki, M. E., Medrano, F. A., Benzerga, A. A., and Leblond, J.-B. (2023). "A model of void coalescence in columns". *Journal of the Mechanics and Physics of Solids* 171.

Torki, M. E., Tekoğlu, C., Leblond, J.-B., and Benzerga, A. A. (2017). "Theoretical and numerical analysis of void coalescence in porous ductile solids under arbitrary loadings". *International Journal of Plasticity* 91, pp. 160–181.

Torki, M. E. and Benzerga, A. A. (2022). "Ductile fracture in plane stress". *Journal of Applied Mechanics* 89 (1).

Torki, M. E. (2019). "A unified criterion for void growth and coalescence under combined tension and shear". *International Journal of Plasticity* 119, pp. 57–84.

Torki, M. E. and Benzerga, A. A. (2018a). "Micromechanics-based constitutive relations for post-localization analysis". *MethodsX* 5, pp. 1431–1439.

Torki, M. E. and Benzerga, A. A. (2018b). "A mechanism of failure in shear bands". *Extreme Mechanics Letters* 23, pp. 67–71.

Torquato, S. (1991). "Random heterogeneous media: Microstructure and improved bounds on effective properties". *Applied Mechanics Reviews* 44 (2), pp. 37–76.

Trinkaus, H. and Singh, B. (2003). "Helium accumulation in metals during irradiation – where do we stand?" *Journal of Nuclear Materials* 323 (2), pp. 229–242.

Tsun, K. (1953). "The overheating and burning of steel". *Symposium on industrial failure of engineering metals and alloys*, pp. 95–104.

Tvergaard, V. (1982). "On localization in ductile materials containing spherical voids". *International Journal of Fracture* 18, pp. 237–252.

Tvergaard, V. and Needleman, A. (1984). "Analysis of the cup-cone fracture in a round tensile bar". *Acta Metallurgica* 52, pp. 157–169.

Ullmaier, H. and Chen, J. (2003). "Low temperature tensile properties of steels containing high concentrations of helium". *Journal of Nuclear Materials* 318, pp. 228–233.

Unwin, P. T. and Smith, G. C. (1969). "The microstructure and mechanical properties of Al-6% Zn-3% Mg". *Journal of the Institute of Metals* 97, pp. 299–310.

Van Houtte, P. (1988). "A comprehensive mathematical formulation of an extended Taylor–Bishop–Hill model featuring relaxed constraints, the Renouard–Wintenberger theory and a strain rate sensitivity model". *Texture, Stress, and Microstructure* 8, pp. 313–350.

Varley, P., Day, M., and Sendorek, A. (1957). "The structure and mechanical properties of high-purity aluminium-zinc-magnesium alloys". *Journal of the Institute of Metals* 86, pp. 337–351.

Vasudévan, A. K. and Doherty, R. D. (1987). "Grain boundary ductile fracture in precipitation hardened aluminium alloys". *Acta Metallica* 35 (6), pp. 1193–1219.

Venkiteswaran, P. K. and Taplin, D. M. R. (1974). "The creep fracture of Inconel X-750 at 700°C". *Metal Science* 8 (1), pp. 97–106.

Villacampa, I., Chen, J. C., Spätig, P., Seifert, H. P., and Duval, F. (2017). "Helium effects on IASCC susceptibility in as-implanted solution annealed, cold-worked and post-implantation annealed 316L steel". *Corrosion Engineering, Science and Technology* 52 (8), pp. 567–577.

— (2018). "Helium bubble evolution and hardening in 316L by post-implantation annealing". *Journal of Nuclear Materials* 500, pp. 389–402.

Vincent, L., Renault-Laborne, A., and Rouesne, E. (2022). *Fluage long terme du 316L(N): Analyse de données historiques et études des effets du vieillissement sur le développement et la résistance mécanique des précipités*. Tech. rep. LC2M/NT/2022-4028/A. CEA, pp. 46–72.

Vincent, P., Moulinec, H., Joëssel, L., Idiart, M., and Gărăjeu, M. (2020). "Porous polycrystal plasticity modeling of neutron-irradiated austenitic stainless steels". *Journal of Nuclear Materials* 542.

Vincent, P.-G., Suquet, P., Monerie, Y., and Moulinec, H. (2014). "Effective flow surface of porous materials with two populations of voids under internal pressure: II - Full-field simulations". *International Journal of Plasticity* 56, pp. 74–98.

Vishnu, A., Vadillo, G., and Rodríguez-Martinez, J. (2023). "Void growth in ductile materials with realistic porous microstructures". *International Journal of Plasticity* 167.

Vishwakarma, V. and Keralavarma, S. M. (2019). "Micromechanical modeling and simulation of the loading path dependence of ductile failure by void growth and coalescence". *International Journal of Solids and Structures* 166, pp. 135–153.

Walpole, L. (1981). "Elastic behavior of composite materials: Theoretical foundations". *Advances in Applied Mechanics* 21, pp. 169–242.

Wan, J. and Yue, Z. (2004). "Stress distribution near grain boundary in anisotropic bicrystals and tricrystals". *Applied Mathematics and Mechanics* 25, pp. 19–46.

Wang, C., Grossbeck, M., Aglan, H., and Chin, B. (1996). "The effect of an applied stress on the welding of irradiated steels". *Journal of Nuclear Materials* 239, pp. 85–89.

Wang, H., Tian, Y., Ye, Q., Wang, Q., Wang, Z., and Wang, G. (2022). "Effect of delamination on ductile fracture during the impact test in ultra-heavy steel". *Journal of Materials Engineering and Performance* 31 (10), pp. 7843–7855.

Wang, J., Toloczko, M., Kruska, K., Schreiber, D. K., Edwards, D. J., Zhu, Z., and Zhang, J. (2017). "Carbon contamination during ion irradiation - Accurate detection and characterization of its effect on microstructure of ferritic/martensitic steels". *Scientific Reports* 7.

Wanhill, R., Symonds, N., Merati, A., Pasang, T., and Lynch, S. (2013). "Five helicopter accidents with evidence of material and/or design deficiencies". *Engineering Failure Analysis* 35, pp. 133–146.

Was, G. (2007). *Fundamentals of radiation materials science: Metals and alloys*. Springer.

Was, G., Taller, S., Jiao, Z., Monterrosa, A., Woodley, D., Jennings, D., Kubley, T., Naab, F., Toader, O., and Uberseder, E. (2017). "Resolution of the carbon contamination problem in ion irradiation experiments". *Nuclear Instruments and Methods in Physics Research Section B: Beam Interactions with Materials and Atoms* 412, pp. 58–65.

Watanabe, T. and Davies, P. W. (1978). "Grain boundary sliding and intergranular fracture behaviour of copper bicrystals". *Philosophical Magazine A* 37 (5), pp. 649–681.

Wen, J., Huang, Y., Hwang, K., Kiu, C., and Li, M. (2005). "The modified Gurson model accounting for the void size effect". *International Journal of Plasticity* 21, pp. 381–395.

Wen, Z. X. and Yue, Z. F. (2007). "On the crystallographic study of growth characterization of isolated void in the grain boundary". *Computational Materials Science* 40 (1), pp. 140–146.

Westinghouse (2020). *Westinghouse technology systems manual: Section 3.1 - Reactor vessel and internals*. Tech. rep. Rev 0909. USNRC HRTD.

Wilkinson, D. (1987). "The effect of time dependent void density on grain boundary creep fracture — I. Continuous void coalescence". *Acta Metallurgica* 35 (6), pp. 1251–1259.

Willis, J. (1977). "Bounds and self-consistent estimates for the overall properties of anisotropic composites". *Journal of the Mechanics and Physics of Solids* 25 (3), pp. 185–202.

Wojtacki, K., Vincent, P.-G., Suquet, P., Moulinec, H., and Boittin, G. (2020). "A micromechanical model for the secondary creep of elasto-viscoplastic porous materials with two rate-sensitivity exponents: Application to a mixed oxide fuel". *International Journal of Solids and Structures* 184, pp. 99–113.

Woo, O., Judge, C. D., Nordin, H., Finlayson, D., and Andrei, C. (2011). "The microstructure of unirradiated and neutron irradiated Inconel X750". *Microscopy and Microanalysis* 17 (S2), pp. 1852–1853.

Wu, Q. and Zikry, M. (2016). "Microstructural modeling of transgranular and intergranular fracture in crystalline materials with coincident site lattice grain-boundaries: Σ3 and Σ17b bicrystals". *Materials Science and Engineering: A* 661, pp. 32–39.

Wu, R. and Sandström, R. (1995). "Creep cavity nucleation and growth in 12Cr–Mo–V steel". *Materials Science and Technology* 11 (6), pp. 579–588.

Wu, W.-P., Li, N.-L., and Li, Y.-L. (2016). "Molecular dynamics-based cohesive zone representation of microstructure and stress evolutions of nickel intergranular fracture process: Effects of temperature". *Computational Materials Science* 113, pp. 203–210.

Xiao, L., Chen, X., Ning, H., Jiang, P., Liu, Y., Chen, B., Yin, D., Zhou, H., and Zhu, Y. (2022). "Unexpected high-temperature brittleness of a Mg-Gd-Y-Ag alloy". *Journal of Magnesium and Alloys* 10 (9), pp. 2510–2515.

Xu, S., Griffiths, M., Scarth, D. A., and Graham, D. (2022). "Microstructure-based polycrystalline finite element modeling of Inconel X-750 irradiated in a CANDU reactor". *Engineering Fracture Mechanics* 276.

Yalçinkaya, T., Özdemir, İ., and Fırat, A. O. (2018). "Three dimensional grain boundary modeling in polycrystalline plasticity". *AIP Conference Proceedings* 1960 (1).

Yang, M. and Dong, X. (2009). "Simulation of lattice orientation effects on void growth and coalescence by crystal plasticity". *Acta Metallurgica Sinica (English Letters)* 22 (1), pp. 40–50.

Yao, B., Edwards, D. J., Kurtz, R. J., Odette, G. R., and Yamamoto, T. (2012). "Multislice simulation of transmission electron microscopy imaging of helium bubbles in Fe". *Journal of Electron Microscopy* 61 (6), pp. 393–400.

Yerra, S. K., Tekoğlu, C., Scheyvaerts, F., Delannay, L., Houtte, P. V., and Pardoen, T. (2010). "Void growth and coalescence in single crystals". *International Journal of Solids and Structures* 47, pp. 1016–1029.

Zaefferer, S., Kuo, J.-C., Zhao, Z., Winning, M., and Raabe, D. (2003). "On the influence of the grain boundary misorientation on the plastic deformation of aluminum bicrystals". *Acta Materialia* 51 (16), pp. 4719–4735.

Zhang, K., Hopperstad, O. S., Holmedal, B., and Dumoulin, S. (2014). "A robust and efficient substepping scheme for the explicit numerical integration of a rate-dependent crystal plasticity model". *International Journal for Numerical Methods in Engineering* 99 (4), pp. 239–262.

Zhang, X. M., Liu, W. H., Tang, J., and Ye, L. Y. (2008). "Influence of crystallographic orientation on growth behavior of spherical voids". *Journal of Central South University of Technology* 15, pp. 159–164.

Zheng, K. Y., Dong, J., Zeng, X. Q., and Ding, W. J. (2008). "Effect of precipitation aging on the fracture behavior of Mg–11Gd–2Nd–0.4Zr cast alloy". *Materials Characterization* 59 (7), pp. 857–862.

Zhou, H., Wang, P., and Lu, S. (2021). "Investigation on the effects of grain boundary on deformation behavior of bicrystalline pillar by crystal plasticity finite element method". *Crystals* 11 (8).

Zhu, J., Liu, J., Huang, M., Li, Z., and Zhao, L. (2022). "Investigation on intragranular and intergranular void growth and their competition in polycrystalline materials". *International Journal of Plasticity* 159.

Zhu, Q., Shao, J.-L., and Wang, P. (2023a). "The dynamic response of He bubble in bicrystal copper under uniaxial compression and tension". *Journal of Nuclear Materials* 574.

— (2023b). "The growth and coalescence of helium bubbles in bicrystal copper under tension". *Journal of Nuclear Materials* 582.

Zhu, X. W., Foster, M. E., and Sills, R. B. (2023c). "Molecular dynamics studies of helium bubble effects on grain boundary fracture vulnerabilities in an FeNiCrH austenitic stainless steel". *Journal of Nuclear Materials* 574.

Ziegler, J. F., Ziegler, M. D., and Biersack, J. P. (2010). "SRIM – The stopping and range of ions in matter". *Nuclear Instruments and Methods in Physics Research Section B: Beam Interactions with Materials and Atoms* 268, pp. 1818–1823.

Zinkle, S. and Lucas, G. E. (2003). *Deformation and fracture mechanisms in irradiated FCC and BCC metals*. Tech. rep. DOE-ER-0313/34. US Department of Energy.